Cancer Cell

Volume 22
Number 3

September 11, 2012

www.cellpress.com

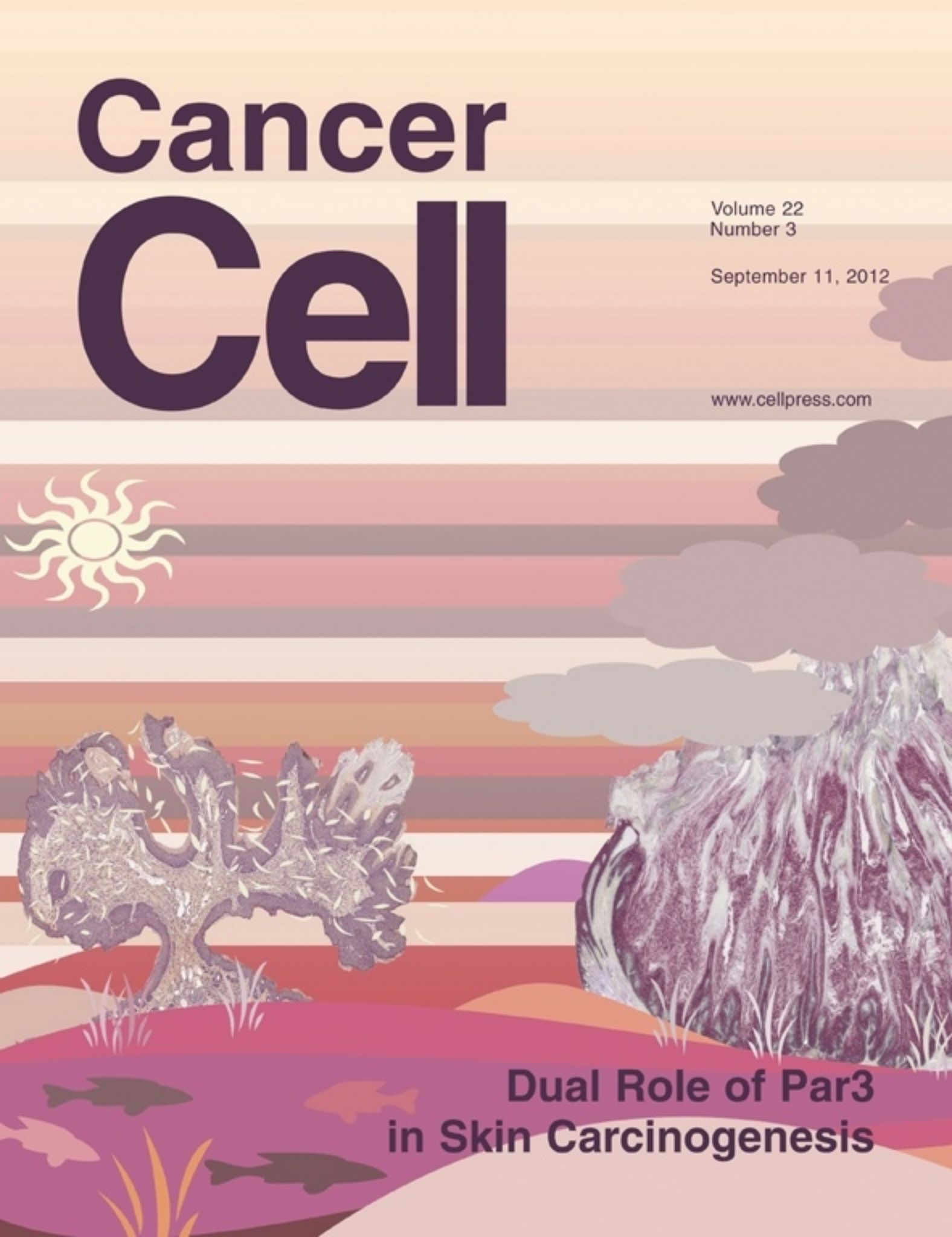

Dual Role of Par3 in Skin Carcinogenesis

Cancer Cell
Article

Integrative Analysis Reveals an Outcome-Associated and Targetable Pattern of p53 and Cell Cycle Deregulation in Diffuse Large B Cell Lymphoma

Stefano Monti,[1,8,9] Bjoern Chapuy,[2,8] Kunihiko Takeyama,[2,10] Scott J. Rodig,[5] Yansheng Hao,[2] Kelly T. Yeda,[2] Haig Inguilizian,[4] Craig Mermel,[1] Treeve Currie,[5,11] Ahmet Dogan,[6] Jeffery L. Kutok,[5,12] Rameen Beroukhim,[1] Donna Neuberg,[3] Thomas M. Habermann,[7] Gad Getz,[1] Andrew L. Kung,[4] Todd R. Golub,[1,4] and Margaret A. Shipp[2,*]
[1]Cancer Program, Broad Institute, Cambridge, MA 02142, USA
[2]Department of Medical Oncology
[3]Department of Biostatistics
[4]Department of Pediatric Oncology
Dana-Farber Cancer Institute, Boston, MA 02215, USA
[5]Department of Pathology, Brigham and Women's Hospital, Boston, MA 02115, USA
[6]Department of Laboratory Medicine and Pathology, College of Medicine
[7]Division of Hematology
Mayo Clinic, Rochester, MN 55905, USA
[8]These authors contributed equally to this work
[9]Present address: Section of Computational Biomedicine, Boston University School of Medicine, Boston, MA 02118, USA
[10]Present address: Sanofi-Aventis K. K., 163-1488 Tokyo, Japan
[11]Present address: Novartis, Cambridge, MA 02139, USA
[12]Present address: Infinity Pharmaceuticals, Cambridge, MA 02139, USA
*Correspondence: margaret_shipp@dfci.harvard.edu
http://dx.doi.org/10.1016/j.ccr.2012.07.014

SUMMARY

Diffuse large B cell lymphoma (DLBCL) is a clinically and biologically heterogeneous disease with a high proliferation rate. By integrating copy number data with transcriptional profiles and performing pathway analysis in primary DLBCLs, we identified a comprehensive set of copy number alterations (CNAs) that decreased p53 activity and perturbed cell cycle regulation. Primary tumors either had multiple complementary alterations of p53 and cell cycle components or largely lacked these lesions. DLBCLs with p53 and cell cycle pathway CNAs had decreased abundance of p53 target transcripts and increased expression of E2F target genes and the Ki67 proliferation marker. CNAs of the CDKN2A-TP53-RB-E2F axis provide a structural basis for increased proliferation in DLBCL, predict outcome with current therapy, and suggest targeted treatment approaches.

INTRODUCTION

Diffuse large B cell lymphoma (DLBCL) is the most common non-Hodgkin lymphoma in adults and a clinically and genetically heterogeneous disorder. With current immunochemotherapy, over 60% of patients with DLBCL can be cured; however, the remaining patients succumb to their disease (Friedberg and Fisher, 2008). Despite recent advances in the molecular understanding of DLBCL pathogenesis, clinical risk factor models are still used to identify patients who are unlikely to be cured with current therapy. The most widely used model is the International Prognostic Index (IPI), an outcome predictor based on easily measurable clinical parameters including age, performance status, serum lactate dehydrogenase (LDH), Ann Arbor stage, and number of extranodal disease sites (Shipp et al., 1993). Although the IPI is robust and reproducible, the link between the included

Significance

In spite of advances in the molecular understanding of DLBCL pathogenesis, clinical models are still used to identify high-risk patients who then receive empiric therapy. In DLBCLs, which have infrequent inactivating somatic mutations of *TP53* and *RB1*, the current studies define an alternative copy number-dependent mechanism of deregulating p53 and cell cycle. This genetic signature predicts outcome and suggests targeted approaches to treatment such as pan cyclin-dependent kinase inhibition.

clinical parameters and underlying biology or targeted treatment remains to be defined.

In previous studies, increased cellular proliferation has also been associated with unfavorable outcome in DLBCL. Indirect indices of cellular proliferation included elevated serum LDH as a component of the IPI and increased expression of the Ki67 nuclear antigen (Grogan et al., 1988; Salles et al., 2011).

DLBCLs largely originate from germinal center (GC) B cells, which have high growth rates and increased genomic instability (Klein and Dalla-Favera, 2008). GC B cells undergo somatic hypermutation (SHM) of their immunoglobulin variable region genes and class-switch recombination (CSR) to alter their immunoglobulin subtype. The rapid proliferation rate and errors in CSR and SHM predispose normal GC B cells to malignant transformation. As a consequence, DLBCLs exhibit multiple low frequency genetic alterations including chromosomal translocations, somatic mutations, and copy number alterations (CNAs).

Given the numbers and types of genetic alterations in DLBCL, investigators have sought additional comprehensive classification systems to identify groups of tumors with similar molecular traits. Transcriptional profiling has been used to define DLBCL subsets that share certain features with normal B cell subtypes (''cell-of-origin'' [COO] classification) (Lenz and Staudt, 2010). COO-defined DLBCLs include ''germinal center B cell'' (GCB) and ''activated B cell'' (ABC) types and an additional group of unclassified tumors. The COO-defined tumor groups are characterized by certain biological features, most notably increased NFκB activity and less favorable outcome in ABC-type DLBCLs (Lenz and Staudt, 2010). However, the outcome differences in GCB and ABC-type DLBCLs may be less striking in patients treated with current rituxan-containing combination chemotherapy regimens (Fu et al., 2008; Lenz et al., 2008a). An alternative transcriptional profiling classification, termed comprehensive consensus clustering, identifies DLBCL subtypes solely on the basis of distinctions within primary tumors and includes the three groups: ''B cell receptor,'' ''oxidative phosphorylation,'' and ''host-response'' (Chen et al., 2008; Monti et al., 2005).

To date, genetic alterations in DLBCL have largely been analyzed as single features or in association with the defined transcriptional subtypes (Bea et al., 2005; Lenz et al., 2008b). The platforms that were previously used to define CNAs in DLBCL had lower resolution, and concordant assessments of transcript abundance and copy number (CN) were more limited. For these reasons, the precise boundaries of CNAs, the associated candidate ''driver genes,'' and implicated pathways require further definition.

The earlier observations regarding cellular proliferation in DLBCL prompted additional analyses of certain individual cell cycle components and regulators. Cell cycle progression is controlled by series of cyclin-dependent kinases (CDKs), which are complexed with specific cyclins (Malumbres and Barbacid, 2009). The cyclin D-dependent kinases 4 and 6 (CDK4/CDK6) and the cyclin E-associated kinase 2 (CDK2) sequentially phosphorylate the retinoblastoma (RB) proteins, releasing the E2F transcription factors and promoting cell cycle progression. The A-type cyclins also activate CDK2 and CDK1 promoting S phase transition and the onset of mitosis. CDK activity is regulated by inhibitors, such as the INK4 family member $p16^{INK4A}$ (at the *CDKN2A* locus), and certain p53 targets, such as p21, among others (Malumbres and Barbacid, 2009). Individual cell cycle components and regulators reported to be perturbed in small numbers of DLBCLs include *CDKN2A* (ARF and $p16^{INK4A}$), p53 and its target p21, cyclin D3, and RB1 (Jardin et al., 2010; Pasqualucci et al., 2011; Sánchez-Beato et al., 2003; Winter et al., 2010; Young et al., 2008). Recent deep sequencing analyses confirm earlier reports of *TP53* somatic mutations in approximately 20% of DLBCLs (Morin et al., 2011; Pasqualucci et al., 2011; Lohr et al., 2012), a much lower percentage than in certain nonhematologic malignancies (Cancer Genome Atlas Research Network, 2008, 2011). The relatively low frequency of *TP53* somatic alterations in primary human DLBCLs suggests that additional bases of p53 deficiency remain to be defined.

Herein, we integrate CN data with transcriptional profiles and perform pathway analyses to identify core deregulated and targetable pathways in primary DLBCLs.

RESULTS

Mapping Recurrent CNAs in Primary DLBCL

Recurrent CNAs in the 180 primary DLBCLs were detected using the Genomic Identification of Significant Targets in Cancer (GISTIC) algorithm. Within the identified regions of significant CN gain or loss, narrower peaks of maximally significant CN change were identified (Supplemental Experimental Procedures available online). We found 47 recurrent CNAs, including 21 copy gains and 26 copy losses, with frequencies of 4% to 27% (Figure 1; Table S1). The GISTIC-defined CNAs range from narrow focal alterations, such as amplification peak 2p16.1 to chromosome arm and whole-chromosome alterations, including gain of 1q, loss of 6q, and gain of chromosome 7 (Figure 1).

Comparison of CNAs in DLBCLs and Nonhematologic Cancers

To distinguish between CNAs that are unique to DLBCL and those that are found in other tumors, we compared the DLBCL GISTIC analysis to that of 2,433 nonhematologic cancers (Beroukhim et al., 2010). The CNAs in DLBCLs and the nonhematologic cancers were visualized with a mirror plot (Figure 2), and the CNA overlap in the two series was computed (Figure S1A; Supplemental Experimental Procedures). Seven of 21 (33%) regions of copy gain and 16/26 (62%) regions of copy loss were common to both series; additional regions of copy gain exhibited partial overlap (Figures 2 and S1A). Examples of shared alterations include gains of chromosome 7 and chromosome 1q and loss of chromosome 6q, suggesting a broader role for these alterations in multiple tumor types. In contrast, 9/21 (43%) regions of copy gain and 10/26 (38%) regions of copy loss were only identified in DLBCL, including gains of 2p16.1 and 19q13.42 (Figures 2 and S1A). These DLBCL-selective CNAs were largely absent in a lymphoid malignancy of non-GC origin (Figure S1B).

Integrative Analysis of CNAs and Transcript Abundance

We anticipated that DLBCL CNAs would alter the corresponding gene transcript levels and prioritized genes with the most significant association between transcript abundance and CNA. All genes within the 47 defined CNA peaks and regions (Table S2) were analyzed for the association between transcript abundance and the presence/absence of the gene alteration (peak or region) across the DLBCL series. The ''cis-signature'' of a given CNA

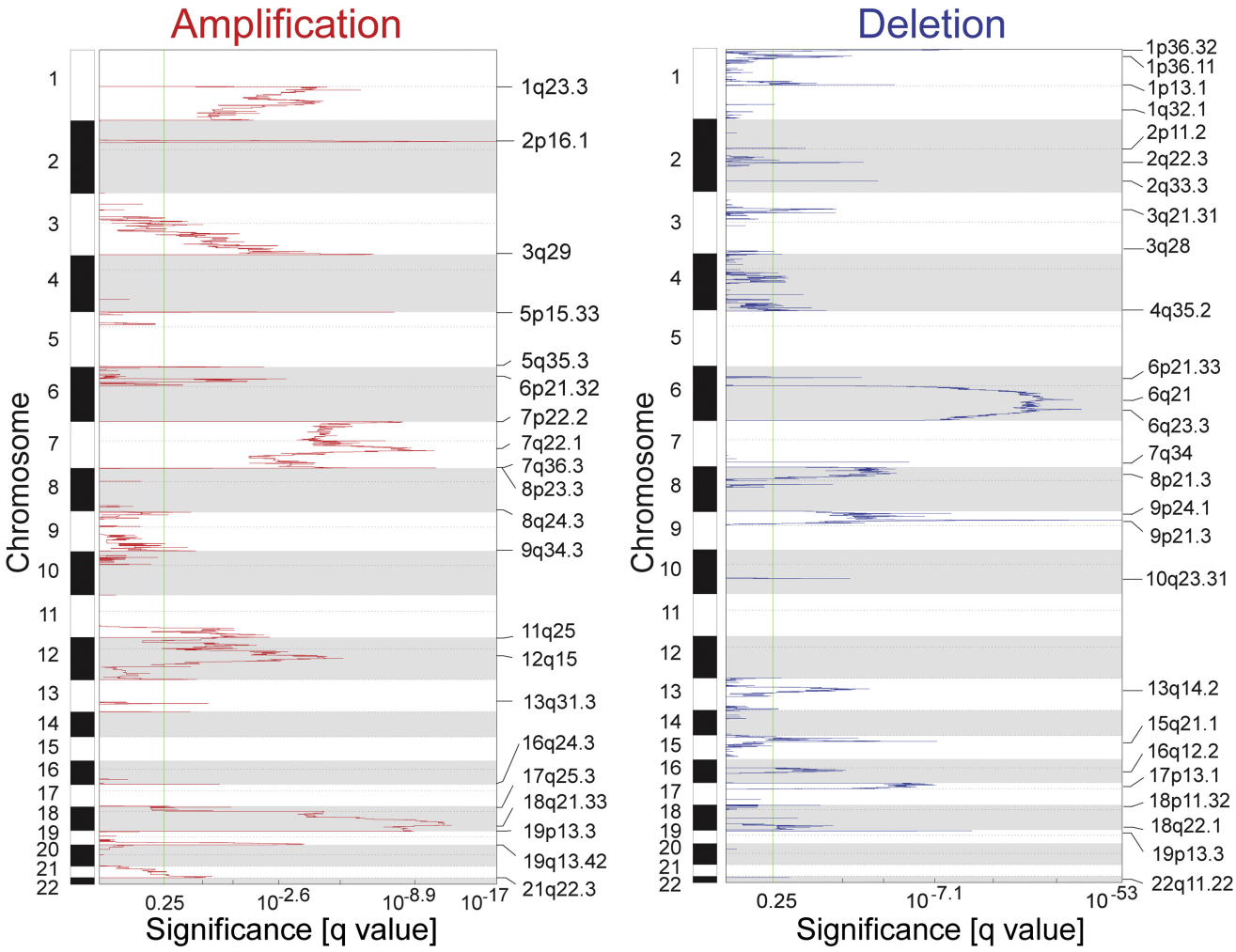

ID	Band	Peak boundaries	Top 5 genes in peak	n (%)
A1	1q23.3	chr1:159,738,009 -159,946,881	*FCRLA, FCGR2B, FCGR2C*	27 (15)
A2	2p16.1	chr2: 60,847,200 - 61,000,748	*PAPOLG, REL*	28 (16)
A3	3q29	chr3:196,744,162 - 197,538,400	*PPP1R2, PCYT1A, TFRC, APOD*	28 (16)
A4	5p15.33	chr5:1,322,366 -1,339,296		27(15)
A5	5q35.3	chr5:178,985,164 -179,067,227	*CANX*	23 (13)
A6	6p21.32	chr6: 32,798,809 - 32,867,250		21 (12)
A7	7p22.2	chr7:1-3,921,089	*HEATR2, NUDT1, UNC84A, C7ORF20, FTSJ2*	37 (21)
A8	7q22.1	chr7:100,846,670 -101,680,144		35(19)
A9	7q36.3	chr7:157,625,912 -157,638,632		37(21)
A10	8p23.3	chr8: 957,635 - 979,854	*ERICH1*	14 (8)
A11	8q24.3	chr8:144,510,826 -146,274,826	*SLC39A4, CYC1, GPR172A, RPL8, GPAA1*	19 (11)
A12	9q34.3	chr9:137,683,556 -140,273,252	*PHPT1, TUBB2C, EDF1, C9ORF86, PMPCA*	19 (11)
A13	11q25	chr11:133,857,250 -134,137,032		21(12)
A14	12q15	chr12: 67,637,703 -69,005,611	*RAB3IP, CNOT2, YEATS4, CCT2, CPSF6*	24(13
A15	13q31.3	chr13: 90,639,856 - 91,276,232		14 (8)
A16	16q24.3	chr16: 88,172,338 - 88,190,375		11 (6)
A17	17q25.3	chr17: 78,224,811-78,241,606		14 (8)
A18	18q21.33	chr18: 59,013,889 - 59,028,583	*BCL2*	33 (18)
A19	19p13.3	chr19: 211,999 - 2,134,174	*NDUFS7, RPS15, GPX4, CDC34, DAZAP1*	16 (9)
A20	19q13.42	chr19: 60,201,501- 60,985,512	*U2AF2, ISOC2, NAT14, HSPBP1, PPP1R12C*	18 (10)
A21	21q22.3	chr21: 41,771,455 - 45,917,251	*PFKL, U2AF1, ICOSLG, CSTB, PDXK*	17 (9)

ID	Band	Peak boundaries	Top 5 genes in peak	n (%)
D1	1p36.32	chr1: 2,916,416 - 3,752,748	*LRRC47, WDR8, KIAA0495*	25 (14)
D2	1p36.11	chr1: 27,103,658 - 27,413,812		16 (9)
D3	1p13.1	chr1:116,871,939 -116,913,482	*CD58*	14 (8)
D4	1q32.1	chr1: 204,650,261- 205,216,469	*RASSF5, IKBKE, IL10, PIGR*	8 (4)
D5	2p11.2	chr2: 84,971,942 - 85,173,585	*TMSB10, KCMF1*	11 (6)
D6	2q22.3	chr2:144,682,679 -145,762,089		13 (7)
D7	2q33.3	chr2: 206,441,809 - 20,6444,766		12 (7)
D8	3p21.31	chr3: 47,813,898 - 49,878,068	*DALRD3, ARIH2, UQCRC1, USP4, IHPK2*	14 (8)
D9	3q28	chr3:190,827,809 -191,035,064		9 (5)
D10	4q35.2	chr4:188,898,040 -189,271,117		13 (7)
D11	6p21.33	chr6: 31,275,478 - 31,434,938	*HLA-B, HLA-C*	12 (7)
D12	6q21	chr6:106,531,795 -106,686,165	*PRDM1*	49 (27)
D13	6q23.3	chr6:138,075,988 -138,381,526	*TNFAIP3*	44 (24)
D14	7q34	chr7:142,055,362 -142,213,197		20 (11)
D15	8p21.3	chr8:19,407,049 - 20,687,278	*INTS10, ATP6V1B2*	19 (11)
D16	9p24.1	chr9: 5,096,681- 5,099,576	*JAK2*	23 (13)
D17	9p21.3	chr9: 21,953,431- 21,978,391	*CDKN2A*	43 (24)
D18	10q23.31	chr10: 90,587,609 - 90,765,608	*FAS, STAMBPL1, ANKRD22*	12 (7)
D19	13q14.2	chr13: 47,078,937 - 47,858,483	*MED4, RB1, NUDT15, SUCLA2, ITM2B*	16 (9)
D20	15q21.1	chr15: 42,726,553 - 42,813,414	*B2M*	19 (11)
D21	16q12.2	chr16: 52,040,758 - 52,209,001	*RBL2*	13 (7)
D22	17p13.1	chr17: 7,483,385 - 7,964,774	*TRAPPC1, CHD3, LSMD1, TP53, JMJD3*	22 (12)
D23	18p11.32	chr18:1,895,359 -1,976,213	*METTL4*	11 (6)
D24	18q22.1	chr18: 63,756,690 - 64,116,269	*TXNDC10*	14 (8)
D25	19p13.3	chr19: 6,486,980 - 6,571,909		15 (8)
D26	22q11.22	chr22: 20,835,282 - 21,596,117	*PRAME*	14 (8)

Figure 1. Recurrent CNAs in Newly Diagnosed DLBCLs

GISTIC summary plots of the significant CN gains (left panel, red) and CN losses (right panel, blue) in 180 primary DLBCLs are displayed by chromosomal position (y axis). FDR q values <.25 (right of the green line, x axis) are considered statistically significant. The chromosomal bands, GISTIC peak boundaries, frequencies of alterations (n [%]), and top five genes by integrative analyses of CN and transcript abundance are listed below.

See also Tables S1, S2, and S3.

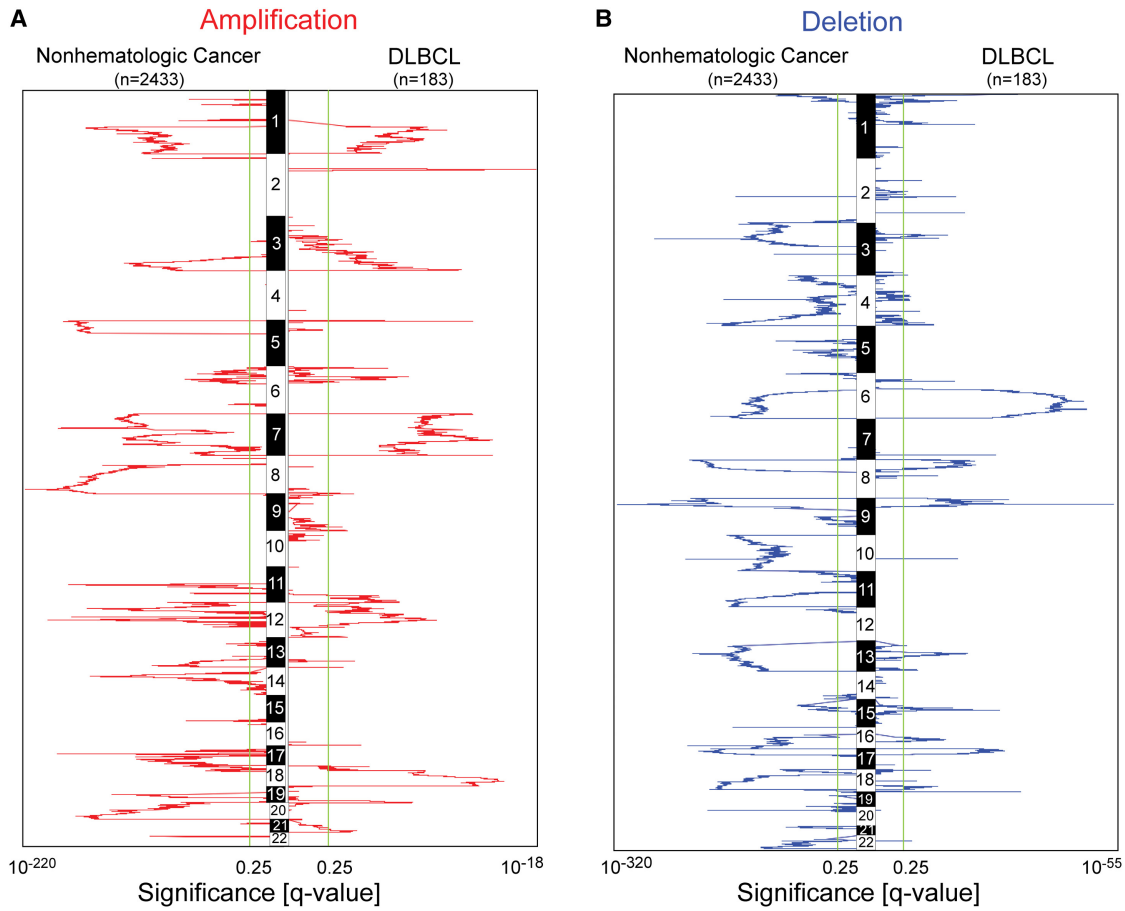

Figure 2. Comparison of CNAs in Primary DLBCLs and Nonhematologic Cancers

The GISTIC-defined recurrent CNAs in the 180 primary DLBCLs (B) are compared to those in 2,433 nonhematologic cancers from a publicly available database (A; Beroukhim et al., 2010) in a mirror plot with chromosome position on the y axis, significance (q value) on the x axis, CN gain in red and CN loss in blue. Green line denotes FDR values <.25.

See also Figure S1.

was defined as the set of within-peak (or within-region) genes with the most significant association between CN and transcript abundance (false discovery rate [FDR] q values $\leq$ .25; top five peak transcripts; Figure 1; Table S1; complete list, Table S3).

CNAs of Genes with Known Roles in Lymphomagenesis

The two genes most closely associated with the 6q21 and 6q23.3 copy loss were *PRDM1* (*BLIMP1*) and *TNFAIP3* (*A20*), respectively (Figure 1; Table S1). Both genes are confirmed tumor suppressors that can be inactivated by several mechanisms, including copy loss (Calado et al., 2010; Kato et al., 2009; Pasqualucci et al., 2006). Deletion of the ubiquitin-editing enzyme, TNFAIP3, contributes to lymphoid transformation, in part, by deregulating NFκB signaling (Shembade et al., 2010). Inactivation of the PRDM1 transcriptional repressor promotes lymphomagenesis by blocking normal plasma cell differentiation (Mandelbaum et al., 2010).

The additional tumor suppressor genes, *CDKN2A*, *RB1*, *FAS,* and *TP53* were closely associated with 9p21.3, 13q14.2, 10q23.31, and 17p13.1 copy loss, respectively (Figure 1), consistent with earlier analyses (Jardin et al., 2010; Sánchez-Beato et al., 2003). Furthermore, two well-known oncogenes were tightly linked with amplification peaks, *REL* at 2p16.1 and *BCL2* at 18q21.33 (Figure 1). Copy gains of 2p16.1/*REL* and 12q15 were more frequent in GCB DLBCLs whereas gains of 18q21.32/*BCL2* and 19q13.42 were more common in ABC tumors, as described (Table S1) (Bea et al., 2005; Lenz et al., 2008b). Given the identification of known CNAs in DLBCL, the integrative analysis will likely define additional CNAs and genes with previously unappreciated roles in the disease.

CNAs of Newly Identified Genes in DLBCL

The genes most closely associated with amplification of 1q23.3 (seen in 15% of DLBCLs) encode the low-affinity receptors for the IgG Fc receptors, *FCGR2B* (*CD32B*) and *FCGR2C*, and the related protein, *FCRLA* (*FCRL1*) (Figure 1). Increased FCGR2B expression was previously associated with adverse outcome in DLBCL (Camilleri-Broët et al., 2004), and *FCGR2C* CN variation and overexpression were linked with certain autoimmune diseases (Breunis et al., 2008). In addition, FCRLA was preferentially expressed in B cells and postulated to be an activating coreceptor (Leu et al., 2005).

Genes associated with amplification of the 19q13.42 region include protein arginine methyl tranferase 1 (*PRMT1*) and

BCL2L12 (Table S1). PRMT1 specifically dimethylates histone H4 at arginine 3, which generally serves as an activation signal (Nicholson et al., 2009). In addition, PRMT1 modifies transcription factors including FOXO1 (Yamagata et al., 2008) and signaling intermediaries such as the Igα subunit of the B cell receptor (Infantino et al., 2010). BCL2L12 is an atypical BCL2 family member with cytoplasmic and nuclear roles. Cytoplasmic BCL2L12 inhibits caspases 3 and 7, whereas nuclear BCL2L12 interacts with p53 and inhibits its binding to target gene promoters (Stegh and DePinho, 2011).

CNAs of Genes Required for Tumor Immune Recognition

In addition to identifying individual genes targeted by specific CNAs, we noted several alterations that perturbed genes required for tumor immune recognition. Copy loss of 6q21.33 decreased the abundance of the major histocompatibility complex (MHC) class I molecules, HLA-B and HLA-C, at the peak, and the MHC class I polypeptide-related sequences A and B, MICA and MICB, in the region (Figure 1; Table S1). In addition, copy loss of 15q21.1 and 1p13.1 reduced the abundance of the peak β2 microglobulin (β2M) and CD58 transcripts, respectively (Figure 1), and 19p13.3 copy loss decreased the levels of the region TNFSF9 (CD137L) transcripts (Table S1).

The β2M polypeptide associates with histocompatibility complex antigen (HLA) class I heavy chains on the cell surface to present antigen. In the absence of β2M, stable antigen-HLA class I complexes cannot be formed. Both HLA class I and *B2M* copy loss were previously described in large B cell lymphomas of immunoprivileged sites (Booman et al., 2008; Jordanova et al., 2003), and inactivating mutations and deletions of *B2M* were recently reported in DLBCLs (Challa-Malladi et al., 2011; Pasqualucci et al., 2011).

The 6q21.33 region genes, *MICA* and *MICB* (Table S1), encode ligands of the activating NKG2D receptor, which is expressed by natural killer (NK) cells and a subset of T cells (Raulet, 2003). Decreased expression of these NKG2D ligands likely limits an innate NK-cell mediated antitumor immune response.

The 1p13.1 peak gene, *CD58* (*LFA3*) (Figure 1), encodes a member of the immunoglobulin superfamily that is a ligand for the costimulatory CD2 receptor on T and NK cells. CD58 was recently reported to be the target of inactivating somatic mutations in a small subset of DLBCLs (Challa-Malladi et al., 2011; Pasqualucci et al., 2011), providing additional evidence that *CD58* loss promotes tumor immune escape.

The 19p13.3 region gene, *TNFSF9* (Table S1), encodes the ligand for the CD137 costimulatory receptor, which is expressed by follicular dendritic cells (FDC) and primed $CD8^+$ memory T cells (Middendorp et al., 2009). Interactions between TNFSF9 on GC B cells and CD137 on FDC and T cells regulate the GC B cell response, and *TNFSF9* loss promotes the development of GCB lymphomas (Middendorp et al., 2009).

Pathway Enrichment Analyses Reveal Coordinate Deregulation of p53 Signaling and Cell Cycle

After identifying CNAs of several genes required for tumor immune recognition, we sought a more comprehensive method to characterize additional pathways perturbed by CNAs in DLBCL. We first defined global *cis*-acting peak or region signatures as the union of all individual *cis*-acting peak or region signatures (Figure 3Aa). Thereafter, we performed pathway enrichment of the global signatures using a curated series of gene sets and ranked the results by FDR (Figures 3Aa and 3B, top pathways; Table S4, full analysis). In the global peak signature, 13 of 15 of the most significantly enriched gene sets reflect related aspects of p53 signaling, apoptosis, and cell cycle regulation (Figure 3B, top panel; FDR < .10). Although the gene sets have different names, they include common genes that are targeted by CNAs—*TP53*, *CDKN2A*, *RB1,* and *RBL2* (all copy loss) and *BCL2* (copy gain) (Figure 3B, top panel).

In the global region signature, the most significantly enriched gene set is the "p53 signaling pathway" (Figure 3B, bottom panel, FDR .0003). Additional p53 pathway components altered by CNAs include the p53 modifiers, *MDM2*, *MDM4*, and *RFWD2* (*COP1*) (all copy gain); p53 targets, *PERP*, *SCOTIN*, *TNFRSF10* (*DR5*/TRAIL receptor), and *FAS* (all copy loss); and critical cell cycle regulators, *CCND3* (cyclin D3), *CDK4*, *CDK6*, and *CDK2* (all copy gain) (Figure 3B, bottom panel).

Components of the p53, Apoptotic, and Cell Cycle Pathways Perturbed by CNAs

CNAs of p53, apoptotic, and cell cycle pathway members are illustrated in Figure 4.

p53 Pathway

CNAs of p53 pathway components all had the same predicted downstream effect—decreased abundance of functional p53 and reduced levels of associated p53 targets. Copy loss of *CDKN2A*, at 9p21.3, occurs in 24% of DLBCLs (Figure 4). The two alternative transcripts derived from the *CDKN2A* locus, $p16^{INK4A}$, and ARF have complementary roles in p53 signaling and cell cycle regulation. ARF interferes with binding of the MDM2 E3 ligase to p53, decreasing its ubiquitylation and proteasomal degradation (Brooks and Gu, 2006). As a consequence, *CDKNA2* deletion (ARF loss) and *MDM2* (12q15) amplification both increase the ubiquitylation and subsequent degradation of p53 (Figure 4). Two additional E3 ligases with complementary but largely nonoverlapping functions in destabilizing cellular p53 levels, MDM4 and RFWD2 (COP1), are increased by 1q23.3 copy gain (Figure 4) (Dornan et al., 2004).

Moreover, *TP53* itself and two positive p53 modifiers, *RPL26* and *KDM6B* (*JMJD3*), are targeted by 17p13.1 copy loss (Figure 4). The H3K27 demethylase, KDM6B, participates in the active removal of the repressive methyl mark from $p16^{INK4A}$-ARF, contributing to its transcriptional activation (Agger et al., 2009). Therefore, *KDM6B* copy loss represents an additional mechanism of indirectly reducing functional p53 activity (Figure 4). KDM6B also directly modulates p53 methylation, cellular distribution, and function (Sola et al., 2011). The other positive modifier of p53 activity, RPL26, binds to the 5′ untranslated region (UTR) of TP53, promotes its translation, and significantly increases stress-induced p53 levels (Chen and Kastan, 2010; Takagi et al., 2005) (Figure 4). RPL26 is also a target of MDM2, which polyubiquitylates the ribosomal protein and enhances its proteasomal degradation (Ofir-Rosenfeld et al., 2008) (Figure 4). In addition, the recently identified negative modulator of p53 transcriptional activity, *BCL2L12* (at 19q13.42), is amplified in a subset of DLBCLs (Figure 4).

Apoptotic Pathways

Independent of its role in regulating p53, *BCL2L12* amplification limits apoptosis by blocking the effector caspases 3 and 7

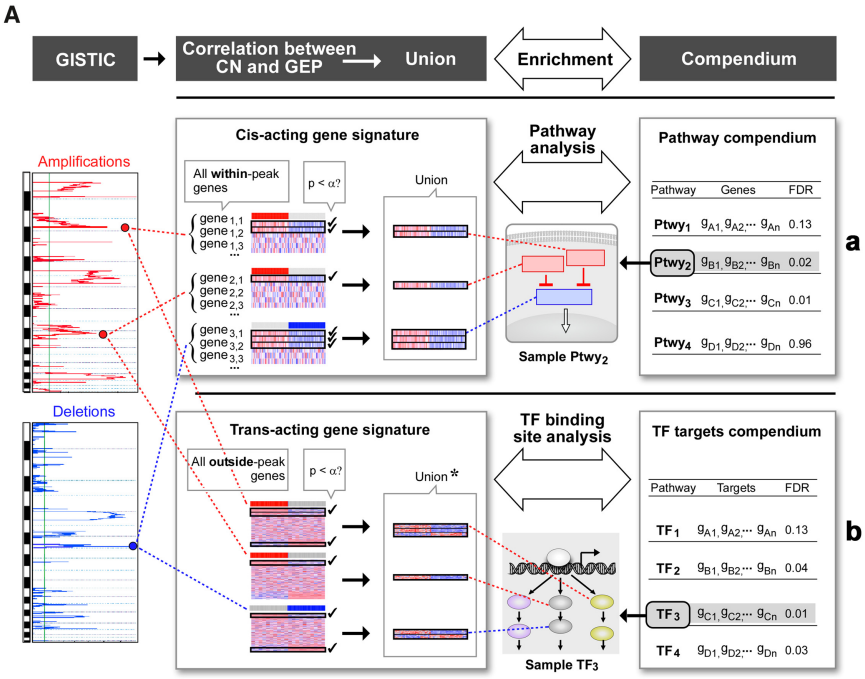

B

	Pathway / Category	FDR	Set annotated (out of 173)	Category annotated (out of 18590)	Hits (Amplifications / Deletions)
PEAK	HSA00051_FRUCTOSE_AND_MANNOSE_METABOLISM	< 0.01	6	42	TSTA3, PHPT1, RDH13, PFKL, PFKFB4, GMPPB
	G1PATHWAY	0.03	4	28	RB1 TP53 CDKN2A CDC25A
	HSA00190_OXIDATIVE_PHOSPHORYLATION	0.03	7	128	CYC1, ATP5D, UQCR, NDUFS7, NDUFV3, UQCRC1, ATP6V1B2
	RBPATHWAY	0.03	3	13	RB1 TP53 CDC25A
	ARFPATHWAY	0.04	3	16	RB1 TP53 CDKN2A
	P53PATHWAY	0.04	3	16	BCL2 RB1 TP53
	TELPATHWAY	0.05	3	18	BCL2 RB1 TP53
	HSA05030_AMYOTROPHIC_LATERAL_SCLEROSIS	0.05	3	19	BCL2 TP53 GPX1
	TIDPATHWAY	0.05	3	19	RB1 TP53 JAK2
	HSA04110_CELL_CYCLE	0.05	6	115	RB1 TP53 CDKN2A RBL2 CDC25A MAD1L1
	CELLCYCLEPATHWAY	0.07	3	23	RB1 CDKN2A CDC25A
	G2PATHWAY	0.07	3	24	TP53 CDC25A CDC34
	CELL_CYCLE_KEGG	0.07	5	90	RB1 TP53 CDKN2A CDC25A MAD1L1
	HSA05223_NON_SMALL_CELL_LUNG_CANCER	0.07	4	54	RB1 TP53 CDKN2A RASSF5
	ST_PAC1_RECEPTOR_PATHWAY ...	0.10	2	8	CAMP, DAG1
REGION	HSA04115_P53_SIGNALING_PATHWAY ...	0.0003	22**	68	TP53 CDKN2A SCOTIN PERP TNFRSF10B FAS RFWD2 MDM4 CCND3 CDK6 CDK4 CDK2 MDM2 PMAIP1 SESN1 CYCS EI24 CHEK1 SIAH1 ATR ZMAT3 SERPINE1

C

Pathway / Category	FDR	Set annotated (out of 4353)	Category annotated (out of 18590)
SGCGSSAAA_V$E2F1DP2_01	0.1	61	171
V$E2F_Q4	0.1	78	238
V$E2F1DP2_01	0.1	77	239
V$E2F1DP1_01	0.1	77	239
V$E2F4DP2_01	0.1	77	239
V$E2F_02	0.1	77	239
V$E2F4DP1_01	0.1	78	243
...			

Figure 3. Pathway and TF Binding Site Enrichment

(A) Schema for pathway and TF binding site enrichment. (a) Pathway analysis. For each GISTIC peak and region, a "cis-acting gene signature" was defined, which included the genes within a GISTIC alteration with a significant (FDR <.25) correlation between CN and gene expression (left panel). The global *cis*-acting signature, the union of all individual *cis*-acting signatures, was analyzed for pathway enrichment using a pathway compendium (C2, MSigDB). (b) TF binding site analysis schema. The "trans-acting signature" of each CNA (those genes outside the CNA with the most significant association between transcript abundance and the CNA) was defined (left panel), and the union of the cis- and *trans*-acting signatures was then tested for enrichment of genes with common TF binding sites using a TF binding site compendium (C3, MSigDB).

(B) Pathway analysis. The results of global *cis*-acting signature pathway enrichment, separated for peaks (upper panel) and regions (lower panel), were ranked by FDR (FDR $\leq$ .10, peaks; top set, region; amplified genes in red, deleted genes in blue). In the region pathway analysis, the set annotation is "out of 1,893" instead of "out of 173"(**).

(C) TF binding site analysis. The results were ranked by FDR (FDR $\leq$ .1 shown here).

See also Table S4.

(Figure 4). An additional means of perturbing the intrinsic apoptotic pathway is *BCL2* copy gain (18q21.33) (Figure 4). Copy loss also decreases the abundance of several p53 targets that promote apoptosis, including the extrinsic apoptotic pathway components, *FAS*, *TNFRF10B*, *SCOTIN*, and *PERP* (Figure 4) (Beaudry et al., 2010; Bourdon et al., 2002; Wilson et al., 2009).

Cell Cycle Degregulation

The loss of $p16^{INK4A}$ and decreased abundance of p53 targets, such as p21 and GADD45, relieve repression of the cell cycle components, CCND3 (cyclin D3), CDK2, and CDK1, respectively (Figure 4). In addition, *CDK2*, *CCND3*, and the cyclin D-associated CDKs, *CDK4*, and *CDK6*, are increased by copy gain (Figure 4). In addition, *RB1* and the related RB locus, *RBL2* (p130), are targeted by copy loss in a subset of DLBCLs (Figure 4). RB1 is also a recognized target of the MDM2 E3 ligase (Polager and Ginsberg, 2009).

Signature of E2F Activation

We next sought an unbiased approach to assess the relationship between CNA-dependent changes and the abundance of E2F target genes. Because transcription factors (TF), such as E2F, will target genes outside the identified CNAs, we first defined the "trans-acting signature" of each CNA (those genes outside the CNA with the most significant association between transcript abundance and the CNA; Figure 3Ab). The union of the cis- and *trans*-acting signatures, termed the "global cis/trans-acting transcriptional signature," was then tested for

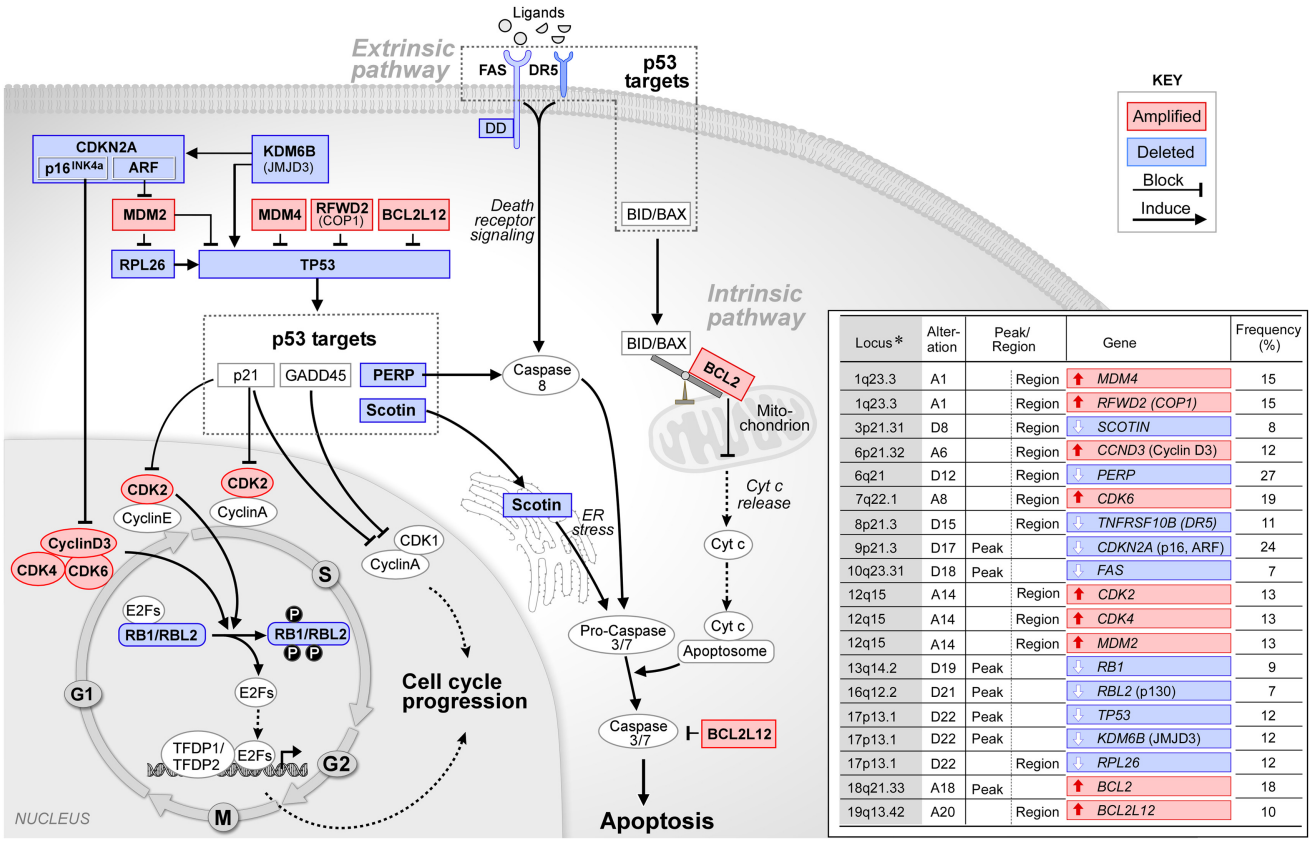

Locus*	Alter-ation	Peak/ Region	Gene	Frequency (%)
1q23.3	A1	Region	↑ *MDM4*	15
1q23.3	A1	Region	↑ *RFWD2 (COP1)*	15
3p21.31	D8	Region	↓ *SCOTIN*	8
6p21.32	A6	Region	↑ *CCND3* (Cyclin D3)	12
6q21	D12	Region	↓ *PERP*	27
7q22.1	A8	Region	↑ *CDK6*	19
8p21.3	D15	Region	↓ *TNFRSF10B (DR5)*	11
9p21.3	D17	Peak	↓ *CDKN2A* (p16, ARF)	24
10q23.31	D18	Peak	↓ *FAS*	7
12q15	A14	Region	↑ *CDK2*	13
12q15	A14	Region	↑ *CDK4*	13
12q15	A14	Region	↑ *MDM2*	13
13q14.2	D19	Peak	↓ *RB1*	9
16q12.2	D21	Peak	↓ *RBL2* (p130)	7
17p13.1	D22	Peak	↓ *TP53*	12
17p13.1	D22	Peak	↓ *KDM6B* (JMJD3)	12
17p13.1	D22	Region	↓ *RPL26*	12
18q21.33	A18	Peak	↑ *BCL2*	18
19q13.42	A20	Region	↑ *BCL2L12*	10

Figure 4. Components of the p53, Apoptotic, and Cell Cycle Pathways Perturbed by CNAs

Components include genes identified by the cis-signature pathway enrichment (Figure 3B) and three recently described p53 modifiers and cis-signature genes, *RPL26*, *KDM6B/JMJD3*, and *BCL2L12*, that are not captured by the current annotated gene sets. Amplified genes, red; deleted genes, blue. For each CNA, the locus, peak, or region gene and frequency of alteration are noted (right).

enrichment of genes with common TF binding sites (Figure 3Ab). The "global cis/trans-acting transcriptional signature" was significantly enriched for genes containing E2F binding sites; specifically, 7/7 of top-ranked binding sites were either E2F, E2F/DP1, or E2F/DP2 (Figure 3C; full list in Table S4). Therefore, DLBCL CNAs are tightly associated with cell cycle deregulation and increased abundance of E2F target genes.

Patterns of CNAs of Pathway Components

The analysis of CNAs that perturb p53 signaling, apoptosis, and cell cycle regulation also illustrates four important principles. First, a single CNA may alter several genes, which synergistically modulate the same pathway, as in 17p13.1 copy loss decreasing expression of p53 itself and the p53 modifiers, RPL26 and KDM6B (JMJD3) (Figure 4). Second, several CNAs may modify the same pathway. For example, 1q23.3 copy gain (*MDM4* and *RFWD2*), 9p21.3 copy loss (*CDKN2A*), 12q15 copy gain (*MDM2*), 17p13.1 copy loss (*TP53*, *RPL26*, and *KDM6B*), and 19q13.42 copy gain (*BCL2L12*) all function to decrease p53 activity (Figure 4). Third, certain single CNAs may alter complementary pathways, such as 12q15 amplification (*CDK2*, *CDK4*, and *MDM2*), enhancing cell cycle progression and reducing p53 activity (Figure 4). Fourth, multiple CNAs may modify complementary pathways such as p53 signaling, apoptosis, and cell cycle regulation (Figure 4).

CNAs of p53 Pathway and Cell Cycle Components in Individual Primary DLBCLs

After comprehensively defining CNAs that perturb p53 signaling and cell cycle pathways in DLBCLs, we assessed the patterns and combinations of alterations that occur in individual tumors. When the primary DLBCLs were clustered in the space of the CNAs that alter p53 pathway and cell cycle components, 66% (118/180) of tumors had multiple alterations (termed "complex") whereas the remaining 34% of tumors lacked these lesions (designated "clean"; Figure 5A). Primary DLBCLs with single copy loss of 17p13.1 (*TP53/RPL26/KDM6B*) often had CNAs perturbing an additional p53 modifier – 9p21.3 (*CDKN2A/ARF*), 19q13.42 (*BCL2L12*), 12q15 (*MDM2*), or 1q23.3 (*MDM4/RFWD2*) (Figure 5A). Of interest, CNAs of the respective p53 modifiers, *CDKN2A* (ARF, 9p21.3), *MDM2* (12q15), and *MDM4/RFWD2* (1q23.3) occurred in largely separate groups of tumors (Figure 5A). DLBCLs with CNAs of p53 pathway members frequently exhibited concurrent alterations of additional cell cycle components such as *CCND3* (6p21.32), *CDK6* (7q22.1), *CDK2/CDK4* (12q15), and/or *RB1* (13q14.2) or *RBL2* (16q12.2) (Figure 5A). Tumors with "complex" patterns of p53 pathway and cell cycle components also had more total CNAs than DLBCLs with "clean" p53/cell cycle signatures (Figure 5A, bottom panel, Σ all CNAs, "complex" versus "clean" $p < .0001$

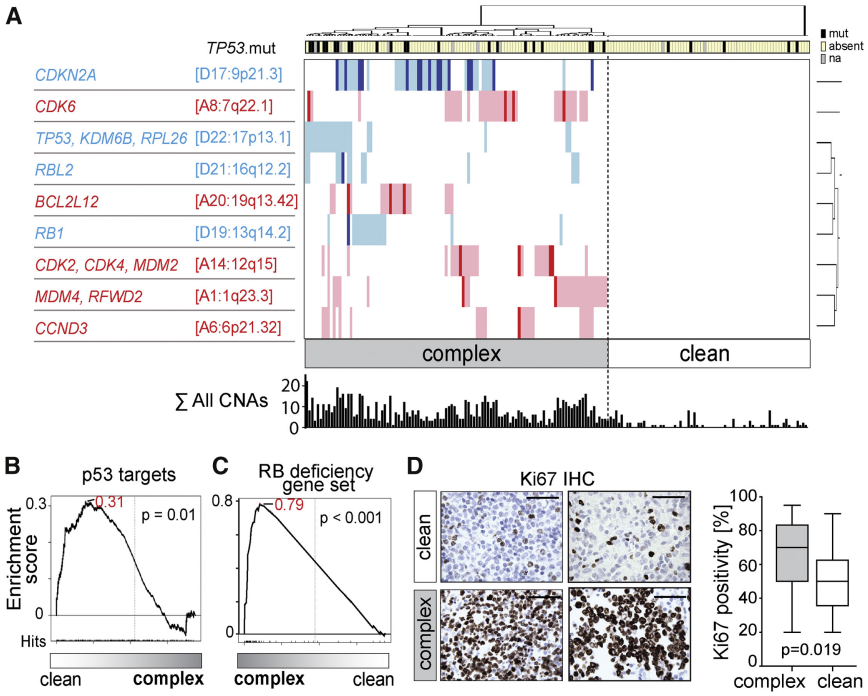

Figure 5. CNAs of p53 Pathway and Cell Cycle Components in Individual Primary DLBCLs

(A) Primary DLBCLs clustered in the space of CNAs that alter p53 pathway and cell cycle components. CNAs and perturbed genes on the left (rows) and individual tumors on top (columns). CN gains, red; CN losses, blue; color intensity corresponds to the magnitude of the CNA. Tumors with CNAs of multiple p53 pathway and cell cycle components, "complex"; DLBCLs without these lesions, "clean". Total CNAs (Σ all CNAs) in "complex" versus "clean" DLBCLs under heat map, $p < .0001$, Mann-Whitney U test. *TP53* mutations in "complex" versus "clean" DLBCLs at top, 22% versus 7%, $p < 0.005$, Fisher's one-sided exact test.

(B) GSEA of p53 targets in "clean" versus "complex" DLBCLs. The 19K genes in the genome were sorted from highest (left, white) to lowest (right, gray) relative expression in "clean" versus the "complex" DLBCLs (horizontal axis). The p53 targets (V.P53_02, described in Figure S2C) were located within the sorted genome and their positions (hits) were found to be significantly skewed toward the left end of the sorted list (positive enrichment score, 0.31), reflecting their statistically significant overexpression in "clean" as compared to "complex" DLBCLs ($p = 0.01$).

(C) GSEA of a RB deficiency gene set in "complex" versus "clean" DLBCLs. GSEA was performed as in (B) except that genes were sorted from highest to lowest expression in "complex" versus "clean" DLBCLs (horizontal axis). The positions of RB-deficiency gene set members (hits) were significantly skewed toward the left end of the sorted list reflecting their overexpression in "complex" DLBCLs (positive enrichment score 0.79, $p < 0.001$).

(D) Ki67 immunohistochemistry of "complex" and "clean" DLBCLs. Representative "clean" (upper micrographs) and "complex" DLBCLs (lower micrographs) (left). Scale bar represents 50 μm. Percentage Ki67-positive tumor cells in "complex" and "clean" DLBCLs ($p = 0.019$, Mann-Whitney U test) visualized as Box-Plot (median, line; 25% and 75% quartile, box; whiskers, minimum to maximum) (right).

See also Figure S2 and Table S5.

and Figure S2A) and more frequent *TP53* mutations (Figure 5A top panel, "complex" 22% versus "clean" 7%, $p < 0.005$; Figure S2; Table S5). The patterns of "complex" versus "clean" CNAs of p53 pathway and cell cycle components and the association between "complex" signature and total CNAs were confirmed in an independent series of 79 primary DLBCLs (Figure S2B).

To further characterize "complex" versus "clean" tumors, we performed gene set enrichment analysis (GSEA) with publicly available series of p53 target genes and a RB-deficiency gene set, which included multiple E2F targets (Knudsen and Knudsen, 2008). The GSEA computational method identifies statistically significant, concordant differences in the transcript abundance of a previously defined set of genes (such as p53 targets) in two biological states (ie, "clean" versus "complex" primary DLBCLs) (Subramanian et al., 2005). The p53 target transcripts were significantly less abundant in "complex" DLBCLs, directly linking their genetic signature of p53 deficiency with decreased p53 activity (Figures 5B and S2C). Furthermore, the RB-deficiency gene set was significantly enriched in "complex" DLBCLs suggesting that these tumors had increased E2F-mediated cell cycle progression (Figure 5C). Consistent with these observations, DLBCLs with "complex" CNA patterns also had significantly higher proliferation indices as determined by Ki67 immunostaining (Figure 5D).

Structural Complexity as a Significant Predictor of Outcome

We next assessed the prognostic significance of the "complex" CNA pattern in the subset of patients who were treated with rituxan, cyclophosphamide, adriamycin, oncovin, and prednisone (R-CHOP) and had long-term follow up (Tables S6 and S7). Patients with "complex" CNA patterns had a 5 year overall survival of only 62%, whereas those with "clean" CNA signatures were all cured (Figure 6A; $p = .001$). The association between CN complexity and outcome was independent of transcriptional COO categories (Figure S3).

We next assessed the relationship of CN complexity and the clinical IPI risk model. Although the IPI was highly predictive of outcome (low/low-intermediate versus high-intermediate/high; Figure 6B, left panel), the CNA pattern significantly increased prognostic accuracy (Figure 6B, middle and right panels). In both the low/low-intermediate and high-intermediate/high-risk groups, patients whose tumors had "complex" CNAs had significantly shorter overall survivals, whereas all patients with "clean" CNA patterns were cured (Figure 6B, middle and right panels). The contribution of the CNA pattern to IPI outcome stratification was also confirmed by a Cox-proportional hazard model ($p < .001$; Supplemental Experimental Procedures). Taken together, these data provide a structural basis for deregulated cell cycle,

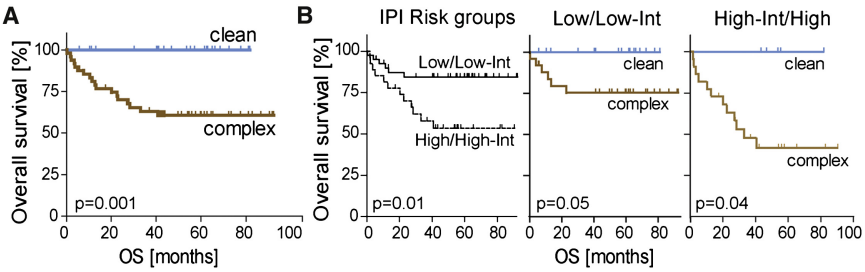

Figure 6. Prognostic Significance of "Complex" versus "Clean" CNA Pattern in DLBCLs

(A) Overall survival of R-CHOP treated DLBCL patients with "complex" versus "clean" CNA patterns (p = .001, log rank test).

(B) CNA patterns in IPI risk groups. Overall survival of R-CHOP treated DLBCL patients in low/low-intermediate and high-intermediate/high IPI risk groups (left). Overall survival of low/low-intermediate and high-intermediate/high risk patients with "complex" versus "clean" CNA patterns (middle and right).

See also Figure S3 and Tables S6 and S7.

increased cellular proliferation, and unfavorable outcome in DLBCL.

Targeting Deregulated Cell Cycle with Broad-Acting CDK Inhibitors

The predictive value of the "complex" CNA pattern and its association with deregulated cell cycle and increased activation of CDK4/6, CDK2, and likely CDK1 (Figure 4) prompted us to assess the activity of a broad-acting CDK inhibitor, such as flavopiridol (Lapenna and Giordano, 2009), in DLBCL. We used a panel of DLBCL cell lines derived from patients with relapsed/refractory disease; all lines have decreased or absent p53 activity and CNAs of cell cycle components including *CDKN2A*, *CCND3*, *CDK4*, *CDK6*, *CDK2*, and/or copy loss of *RB1* (Figure S4A). Flavopiridol, which inhibits CDK4/6, CDK2, and CDK1 (and CDK9), decreased the cellular proliferation of the DLBCL cell lines at nanomolar doses (Figure 7A). Similar results were obtained with a second pan-CDK inhibitor, AT-7519 (Figure S4B). Of interest, a DLBCL cell line with single copy *RB1* loss (DHL7), was less sensitive to lower doses of flavopiridol (Figure 7A) consistent with *RB1* being downstream of the targeted CDKs.

In these DLBCL cell lines, treatment with the pan-CDK inhibitor decreased S phase and induced cell cycle arrest (Figure 7B). In addition, the broad-acting CDK inhibitor increased apoptosis, as assessed by subG1 peaks and Annexin V/7-AAD staining (Figures 7B and 7C), and decreased the phosphorylation of RB1 at CDK4/6 and CDK2-specific sites (pS780 and pT821, respectively) (Figures 7D and S4B). In multiple DLBCL xenograft models, flavopiridol treatment significantly reduced tumor growth and lymphoma infiltration of bone marrow and spleen (Figures 8A–8C and S5). Taken together, these data suggest that genetically driven cell cycle deregulation in DLBCL may be amenable to targeted therapy.

DISCUSSION

Using a combination of high-density (HD)-SNP arrays, gene expression profiling, and pathway analyses, we have comprehensively defined CNAs, associated candidate driver genes, and perturbed signaling pathways in a large series of newly diagnosed DLBCLs. The precision of the HD-SNP platform allowed us to precisely determine the boundaries of recurrent CNAs and distinguish alterations that were unique to DLBCL from ones that were shared with nonhematologic malignancies. The multiple low frequency CNAs prompted us to systematically evaluate the alterations and associated genes with pathway analyses. The approach revealed a large complementary set of CNAs that decreased p53 activity and perturbed cell cycle regulation. The CNA-associated signature of p53 deficiency and cell cycle deregulation was highly predictive for outcome and potentially amenable to targeted therapy.

p53 Deficiency

The CNA-associated pattern of deregulated p53 signaling was detected in 66% of newly diagnosed DLBCLs, of note because somatic inactivating mutations of *TP53* are much less common in DLBCLs than in multiple epithelial malignancies. For example, only 16% of tumors in the current series of primary DLBCLs exhibited hemizygous *TP53* mutations, and the majority of these were in "complex" tumors with additional CNAs of p53 pathway members. All of the CNAs of p53 modulators and signaling pathway components had the same functional effect—decreased abundance of functional p53 and reduced levels of p53 targets. In addition to identifying previously described CNAs of p53 modifiers, such as *CDKN2A* (ARF) and *MDM2* and *TP53* itself, we found CNAs of the p53 regulators *MDM4*, *RFWD2*, and *BCL2L12* in DLBCL. We also defined a "deletion block" on chromosome 17p13 that includes two additional p53 modifiers, *KDM6B* and *RPL26*, as well as *TP53*. The concurrent loss of *TP53*, *RPL26*, and *KDM6B* may perturb p53 signaling to a greater degree than anticipated in tumors with hemizygous 17p13 deletions. The gain of both *MDM4* and *RFWD2* at 1q23.3 delineates an additional "amplicon block" that serves to decrease p53 activity. These insights regarding genetic mechanisms that reduce normal p53 activity in DLBCL may inform targeted treatment strategies. For example, two recently developed p53 inhibitors are predicated on disrupting the interaction between functional p53 and the p53 modifiers, MDM2 and MDM4 (Bernal et al., 2010; Shangary and Wang, 2008).

Perturbed Cell Cycle Regulation

Besides copy loss of the cyclin D-dependent kinase inhibitor, $p16^{INK4A}$, we identified copy gain of *CDK4*, *CDK6*, and *CCND3*, the most abundant and essential D-type cyclin in germinal center B cells (Cato et al., 2011). In addition to the likely relief of p53/p21-dependent CDK2 inhibition, we also found copy gain of *CDK2* in association with *CDK4* (and *MDM2*) in a chromosome 12q15 "amplicon block" and copy loss of both *RB1* and *RBL2*. There was a highly significant CNA-associated signature of

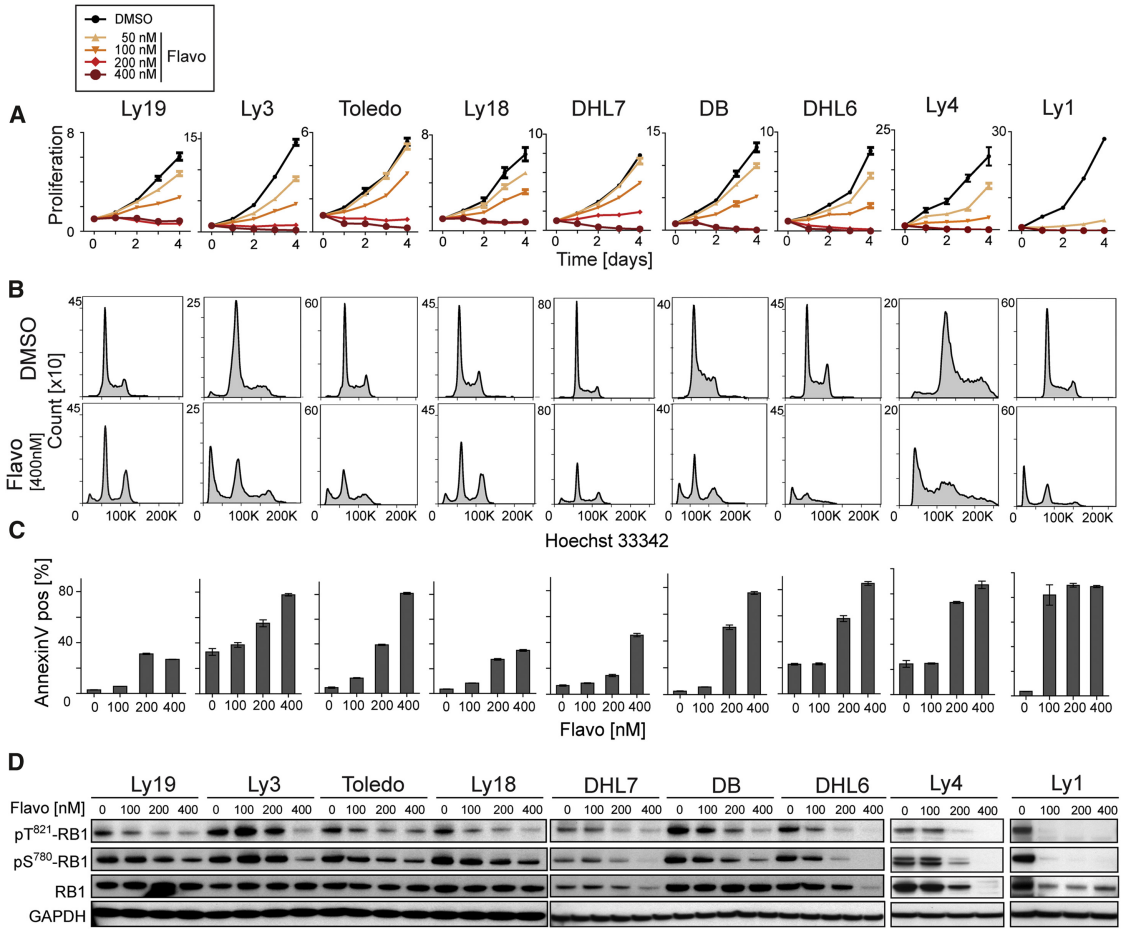

Figure 7. Targeting Deregulated Cell Cycle with a Pan-CDK Inhibitor

DLBCL cell lines with decreased or absent p53 activity and CNAs of *CDKN2A*, *CCND3*, *CDK4*, *CDK6*, *CDK2*, and/or copy loss of *RB1* were treated with the pan-CDK inhibitor, flavopiridol, which blocks CDK4/6, CDK2, and CDK1 (and CDK9).

(A) Proliferation following flavopiridol treatment (50–400 nM) for 1–4 days. DLBCL cell lines names at top.

(B) Cell cycle analysis following 72 hr flavopiridol treatment (400 nM) (DMSO control).

(C) Apoptosis (Annexin V staining) following 72 hr flavopiridol treatment (100–400 nM).

(D) RB1 phosphorylation at CDK4/6 and CDK2-specific sites (pS870 and pT821, respectively) following 24 hr flavopiridol treatment (100–400 nM). (Note that Rb is itself an E2F target; Knudsen and Knudsen, 2008.)

Error bars show the SD of triplicates. See also Figure S4.

increased E2F transcriptional activity underscoring the functional consequences of these genetic alterations.

The p53 and cell cycle component CNAs occur together in a comprehensive "complex" pattern in 66% of the primary DLBCLs; the remaining tumors have only rare CNAs. Gene set enrichment analysis revealed that DLBCLs with "complex" CNAs had significantly less abundant expression of p53 target genes, directly linking their genetic signature of p53 deficiency with decreased p53 activity. In addition, these "complex" tumors exhibited enrichment of E2F targets by GSEA and increased cellular proliferation by Ki67 immunostaining. Most importantly, the "complex" CNA pattern is highly predictive for outcome in R-CHOP treated DLBCL patients. These findings, which provide a mechanistic basis for previous observations regarding the prognostic significance of cellular proliferation in DLBCL (Broyde et al., 2009; Grogan et al., 1988; Salles et al., 2011), should be further validated in future DLBCL series.

The current study highlights the value of a comprehensive approach to identify CNA-defined alterations of p53 and cell cycle regulatory pathways, some of which have been characterized on an individual or selective basis and associated with outcome in earlier studies (Faber and Chiles, 2007; Jardin et al., 2010; Sánchez-Beato et al., 2003; Winter et al., 2010; Young et al., 2008). We find that a single CNA (17p13.1) targets several p53 modulators, multiple CNAs perturb p53 activity (1q23.3, 9p21.3, 12q15, 17p13.1, and 19q13.42) and a single CNA (12q15/*MDM2*, *CDK2*, and *CDK4*) modulates both p53 signaling and cell cycle progression. Because many of these CNAs are shared with additional nonhematologic malignancies (Figure 2), these findings may also be applicable to other tumor types. In fact, an array comparative genomic hybridization-defined "complex" pattern of copy gains and losses was recently associated with high mitotic counts and *TP53* alterations in breast cancer (reviewed in Kwei et al., 2010).

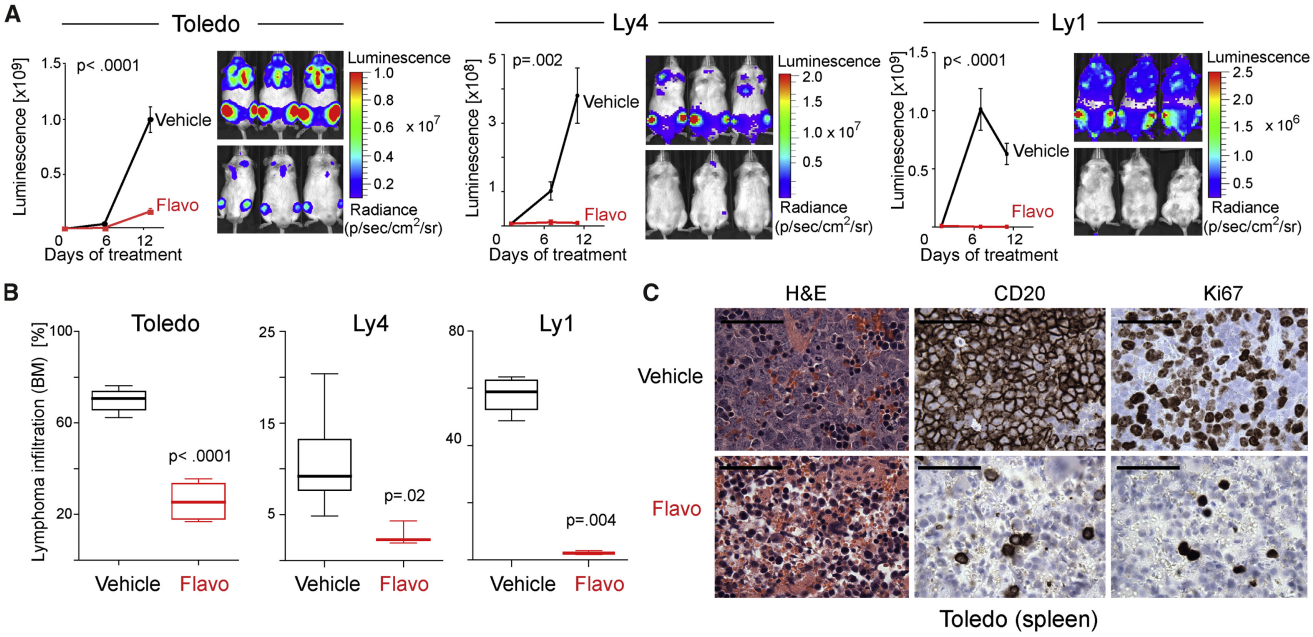

Figure 8. In Vivo Efficacy of a Pan-CDK Inhibitor in DLBCL Xenografts

(A) Bioluminescense of flavopiridol- or vehicle-treated NOD SCID Il2rγ^{null} (NSG) mice xenotransplanted with luciferized mCherry^{+} (Toledo, Ly4, or Ly1) DLBCL cells. Error bars show the SEM.

(B) Lymphoma infiltration in the bone marrow of NSG mice (in A) following flavopiridol or vehicle treatment. Single cell suspensions of bone marrow of tumor-bearing mice were evaluated for mCherry^{+} DLBCL cells by flow cytometry and visualized as Box-Plot (median, line; 25% and 75% quartile, box; whiskers, minimum to maximum). P values were obtained with a Mann-Whitney U test.

(C) Immunohistochemical analysis of lymphoma (Toledo) cell infiltration in spleens of vehicle- and flavopiridol-treated mice: H&E; anti-human CD20, and anti-Ki67 immunostaining. Scale bar represents 50 μm.

See also Figure S5.

Genomic Instability in the Subset of DLBCLs with Perturbed p53 Signaling and Cell Cycle Deregulation

In our DLBCL series, tumors with "complex" CNAs of p53 and cell cycle components also had significantly more of the additional recurrent CNAs, including focal and regional alterations and gains or losses of half or whole chromosomes (Figure S2A). The basis for the increased genomic instability in these "complex" DLBCLs remains to be defined but may be linked to the deficiencies in p53 signaling and perturbed cell cycle regulation. Numerical and structural chromosome instability (CIN) is better tolerated in a p53-deficient background and alterations of *TP53*, *MDM2*, *MDM4* (*MDMX*), the CDK2 partner, *CCNE1* (cyclin E1), and *RB1* all foster CIN (Hernando et al., 2004; Matijasevic et al., 2008; Shlien et al., 2008; Thompson et al., 2010; Wang et al., 2008). In the setting of hyperactive CDKs and DNA damage, cell cycle progression further increases genomic instability (Malumbres and Barbacid, 2009).

In addition to CNAs of the p53 apoptotic pathway, DLBCLs with the "complex" pattern exhibit alterations of other apoptotic members including *BCL2*/18q21.33, *FAS*/10q23.32, and *TNFRF10B*/8p21.3 (Figure S2A). CNAs of immune recognition molecules, including *HLA-B*, *HLA-C*, *MICA*, and *MICB* (6q21.33), *B2M* (15q21.1), *CD58*/1p13.1, and *TNFSF9* (19p13.3) also largely occur in DLBCLs with "complex" patterns (Figure S2A). These data highlight the importance of evaluating specific genetic alterations in the context of a more comprehensive assessment of CNAs and associated genomic instability.

Clinical Significance

The prognostic value of the perturbed p53 signaling/cell cycle deregulation signature prompted us to evaluate the activity of pan-CDK inhibitors in DLBCL. Following treatment, DLBCL cell lines with CNAs of p53 signaling and cell cycle components (with or without additional p53 mutations) exhibited decreased proliferation and RB1 phosphorylation and increased apoptosis in vitro and significantly reduced tumor growth in vivo. Therefore, prognostically significant, genetically driven cell cycle deregulation in DLBCL may be amenable to targeted treatment.

EXPERIMENTAL PROCEDURES

Patients and Primary Tumor Samples

High molecular weight DNA and total RNA were extracted from frozen biopsy specimens of newly diagnosed, previously untreated primary DLBCLs with ≥80% tumor involvement according to Institutional Review Board (IRB)-approved protocols from three institutions (Mayo Clinic, Brigham & Women Hospital, and Dana-Farber Cancer Institute). For one subset of patients, informed consent was obtained (Mayo Clinic). For other patients, a waiver to obtain informed consent was granted by the local IRBs because otherwise discarded tissue was used. The series included 72 DLBCLs from patients who were treated with a rituxan-containing, anthracycline-based combination chemotherapy regimen (R-CHOP-like) and had long-term follow up; 68 of these patients had available information on all clinical parameters in the IPI (Table S6).

HD-SNP Array Analysis and Expression Profiling

Primary DLBCL DNA samples and normal DNA specimens were profiled on Affymetrix HD-SNP arrays 6.0 (Supplemental Experimental Procedures). For

the detection of CN alterations, the SNP array 6.0 data was processed through a previously described analytical pipeline (Nature, 2008). Across-sample GISTIC analysis of the segmented data was carried out to identify statistically significant CNAs (Supplemental Experimental Procedures) (Beroukhim et al., 2007). Alteration regions with FDR q values below .25 were considered significant. Within each region, a peak (or peaks) was identified as the contiguous set (or sets) of loci with highest q values. To visualize the distribution of alterations across samples, we created a matrix with each entry indicating the presence/absence of an alteration (row) in a given sample (column).

RNA samples from 169 of the primary DLBCLs were transcriptionally profiled, and the data were processed using Affymetrix MAS5 summarization method (Supplemental Experimental Procedures).

Integrative Analysis

Cis-*Acting Alteration Signatures*

The genes within the peak (region) of each GISTIC-identified alteration were tested for an association between their expression (transcript abundance) and the presence/absence of the harboring alteration by a two-group t statistic with unequal variance. The *cis*-acting alteration signature for a given alteration was then defined as the set of within-peak (-region) transcripts with FDR q values $\leq$ .25.

Trans-*Acting Alteration Signatures*

The transcripts from genes, which were outside an alteration peak, were also evaluated for an association between their expression and the respective copy number alteration. The top 6,000 transcripts ranked by across-sample median absolute deviation (MAD) were used as the candidate list. The *trans*-acting alteration signature for an alteration was defined as the set of outside-peak transcripts with FDR q values $\leq$ .25 and fold change $\geq$ 1.3.

Pathway and TF Binding Site Enrichment Analysis

The global *cis*-acting signature, defined as the union of all of the individual *cis*-acting alteration signatures, was analyzed for pathway enrichment by testing the signature against curated gene sets from the MSigDB repository (C2 collection, version 2.5) (Supplemental Experimental Procedures). FDR-corrected q values were computed based on the hypergeometric distribution.

The global *trans*-acting signature was defined as the union of all *trans*-acting alteration signatures. The union of the global *cis*-acting and *trans*-acting signatures was then analyzed for enrichment of targets of specific TFs using the curated sets of TF targets in the MSigDB C3 collection (Supplemental Experimental Procedures). FDR-corrected q values were computed based on the hypergeometric distribution.

Xenograft Models

All animal studies were performed according to Dana-Farber Cancer Institute Institutional Animal Care and Use Committee-approved protocols.

ACCESSION NUMBERS

The Gene Expression Omnibus accession number for the HD-SNP 6.0 and gene expression data reported in this paper is GSE34171.

SUPPLEMENTAL INFORMATION

Supplemental Information includes seven tables, five figures, and Supplemental Experimental Procedures and can be found with this article online at http://dx.doi.org/10.1016/j.ccr.2012.07.014.

ACKNOWLEDGMENTS

This work was supported by NIH PO1CA092625. B.C. was supported by a grant from the German Research Foundation (DFG Ch 735/1-1).

Received: November 19, 2011
Revised: April 19, 2012
Accepted: July 24, 2012
Published: September 10, 2012

REFERENCES

Agger, K., Cloos, P.A.C., Rudkjaer, L., Williams, K., Andersen, G., Christensen, J., and Helin, K. (2009). The H3K27me3 demethylase JMJD3 contributes to the activation of the INK4A-ARF locus in response to oncogene- and stress-induced senescence. Genes Dev. *23*, 1171–1176.

Bea, S., Zettl, A., Wright, G., Salaverria, I., Jehn, P., Moreno, V., Burek, C., Ott, G., Puig, X., Yang, L., et al. (2005). Diffuse large B-cell lymphoma subgroups have distinct genetic profiles that influence tumor biology and improve gene-expression-based survival prediction. Blood *106*, 3183–3190.

Beaudry, V.G., Jiang, D., Dusek, R.L., Park, E.J., Knezevich, S., Ridd, K., Vogel, H., Bastian, B.C., and Attardi, L.D. (2010). Loss of the p53/p63 regulated desmosomal protein Perp promotes tumorigenesis. PLoS Genet. *6*, e1001168.

Bernal, F., Wade, M., Godes, M., Davis, T.N., Whitehead, D.G., Kung, A.L., Wahl, G.M., and Walensky, L.D. (2010). A stapled p53 helix overcomes HDMX-mediated suppression of p53. Cancer Cell *18*, 411–422.

Beroukhim, R., Getz, G., Nghiemphu, L., Barretina, J., Hsueh, T., Linhart, D., Vivanco, I., Lee, J.C., Huang, J.H., Alexander, S., et al. (2007). Assessing the significance of chromosomal aberrations in cancer: methodology and application to glioma. Proc. Natl. Acad. Sci. USA *104*, 20007–20012.

Beroukhim, R., Mermel, C.H., Porter, D., Wei, G., Raychaudhuri, S., Donovan, J., Barretina, J., Boehm, J.S., Dobson, J., Urashima, M., et al. (2010). The landscape of somatic copy-number alteration across human cancers. Nature *463*, 899–905.

Booman, M., Szuhai, K., Rosenwald, A., Hartmann, E., Kluin-Nelemans, H.C., de Jong, D., Schuuring, E., and Kluin, P.M. (2008). Genomic alterations and gene expression in primary diffuse large B-cell lymphomas of immune-privileged sites: the importance of apoptosis and immunomodulatory pathways. J. Pathol. *216*, 209–217.

Bourdon, J.-C., Renzing, J., Robertson, P.L., Fernandes, K.N., and Lane, D.P. (2002). Scotin, a novel p53-inducible proapoptotic protein located in the ER and the nuclear membrane. J. Cell Biol. *158*, 235–246.

Breunis, W.B., van Mirre, E., Bruin, M., Geissler, J., de Boer, M., Peters, M., Roos, D., de Haas, M., Koene, H.R., and Kuijpers, T.W. (2008). Copy number variation of the activating FCGR2C gene predisposes to idiopathic thrombocytopenic purpura. Blood *111*, 1029–1038.

Brooks, C.L., and Gu, W. (2006). p53 ubiquitination: Mdm2 and beyond. Mol. Cell *21*, 307–315.

Broyde, A., Boycov, O., Strenov, Y., Okon, E., Shpilberg, O., and Bairey, O. (2009). Role and prognostic significance of the Ki-67 index in non-Hodgkin's lymphoma. Am. J. Hematol. *84*, 338–343.

Calado, D.P., Zhang, B., Srinivasan, L., Sasaki, Y., Seagal, J., Unitt, C., Rodig, S., Kutok, J., Tarakhovsky, A., Schmidt-Supprian, M., and Rajewsky, K. (2010). Constitutive canonical NF-κB activation cooperates with disruption of BLIMP1 in the pathogenesis of activated B cell-like diffuse large cell lymphoma. Cancer Cell *18*, 580–589.

Camilleri-Broët, S., Cassard, L., Broët, P., Delmer, A., Le Touneau, A., Diebold, J., Fridman, W.H., Molina, T.J., and Sautès-Fridman, C. (2004). FcgammaRIIB is differentially expressed during B cell maturation and in B-cell lymphomas. Br. J. Haematol. *124*, 55–62.

Cancer Genome Atlas Research Network. (2008). Comprehensive genomic characterization defines human glioblastoma genes and core pathways. Nature *455*, 1061–1068.

Cancer Genome Atlas Research Network. (2011). Integrated genomic analyses of ovarian carcinoma. Nature *474*, 609–615.

Cato, M.H., Chintalapati, S.K., Yau, I.W., Omori, S.A., and Rickert, R.C. (2011). Cyclin D3 is selectively required for proliferative expansion of germinal center B cells. Mol. Cell. Biol. *31*, 127–137.

Challa-Malladi, M., Lieu, Y.K., Califano, O., Holmes, A.B., Bhagat, G., Murty, V.V., Dominguez-Sola, D., Pasqualucci, L., and Dalla-Favera, R. (2011). Combined genetic inactivation of β2-Microglobulin and CD58 reveals frequent escape from immune recognition in diffuse large B cell lymphoma. Cancer Cell *20*, 728–740.

Chen, J., and Kastan, M.B. (2010). 5′-3′-UTR interactions regulate p53 mRNA translation and provide a target for modulating p53 induction after DNA damage. Genes Dev. *24*, 2146–2156.

Chen, L., Monti, S., Juszczynski, P., Daley, J., Chen, W., Witzig, T.E., Habermann, T.M., Kutok, J.L., and Shipp, M.A. (2008). SYK-dependent tonic B-cell receptor signaling is a rational treatment target in diffuse large B-cell lymphoma. Blood *111*, 2230–2237.

Dornan, D., Bheddah, S., Newton, K., Ince, W., Frantz, G.D., Dowd, P., Koeppen, H., Dixit, V.M., and French, D.M. (2004). COP1, the negative regulator of p53, is overexpressed in breast and ovarian adenocarcinomas. Cancer Res. *64*, 7226–7230.

Faber, A.C., and Chiles, T.C. (2007). Inhibition of cyclin-dependent kinase-2 induces apoptosis in human diffuse large B-cell lymphomas. Cell Cycle *6*, 2982–2989.

Friedberg, J.W., and Fisher, R.I. (2008). Diffuse large B-cell lymphoma. Hematol. Oncol. Clin. North Am. *22*, 941–952, ix.

Fu, K., Weisenburger, D.D., Choi, W.W., Perry, K.D., Smith, L.M., Shi, X., Hans, C.P., Greiner, T.C., Bierman, P.J., Bociek, R.G., et al. (2008). Addition of rituximab to standard chemotherapy improves the survival of both the germinal center B-cell-like and non-germinal center B-cell-like subtypes of diffuse large B-cell lymphoma. J. Clin. Oncol. *26*, 4587–4594.

Grogan, T.M., Lippman, S.M., Spier, C.M., Slymen, D.J., Rybski, J.A., Rangel, C.S., Richter, L.C., and Miller, T.P. (1988). Independent prognostic significance of a nuclear proliferation antigen in diffuse large cell lymphomas as determined by the monoclonal antibody Ki-67. Blood *71*, 1157–1160.

Hernando, E., Nahlé, Z., Juan, G., Diaz-Rodriguez, E., Alaminos, M., Hemann, M., Michel, L., Mittal, V., Gerald, W., Benezra, R., et al. (2004). Rb inactivation promotes genomic instability by uncoupling cell cycle progression from mitotic control. Nature *430*, 797–802.

Infantino, S., Benz, B., Waldmann, T., Jung, M., Schneider, R., and Reth, M. (2010). Arginine methylation of the B cell antigen receptor promotes differentiation. J. Exp. Med. *207*, 711–719.

Jardin, F., Jais, J.-P., Molina, T.-J., Parmentier, F., Picquenot, J.-M., Ruminy, P., Tilly, H., Bastard, C., Salles, G.-A., Feugier, P., et al. (2010). Diffuse large B-cell lymphomas with CDKN2A deletion have a distinct gene expression signature and a poor prognosis under R-CHOP treatment: a GELA study. Blood *116*, 1092–1104.

Jordanova, E.S., Riemersma, S.A., Philippo, K., Schuuring, E., and Kluin, P.M. (2003). Beta2-microglobulin aberrations in diffuse large B-cell lymphoma of the testis and the central nervous system. Int. J. Cancer *103*, 393–398.

Kato, M., Sanada, M., Kato, I., Sato, Y., Takita, J., Takeuchi, K., Niwa, A., Chen, Y., Nakazaki, K., Nomoto, J., et al. (2009). Frequent inactivation of A20 in B-cell lymphomas. Nature *459*, 712–716.

Klein, U., and Dalla-Favera, R. (2008). Germinal centres: role in B-cell physiology and malignancy. Nat. Rev. Immunol. *8*, 22–33.

Knudsen, E.S., and Knudsen, K.E. (2008). Tailoring to RB: tumour suppressor status and therapeutic response. Nat. Rev. Cancer *8*, 714–724.

Kwei, K.A., Kung, Y., Salari, K., Holcomb, I.N., and Pollack, J.R. (2010). Genomic instability in breast cancer: pathogenesis and clinical implications. Mol. Oncol. *4*, 255–266.

Lapenna, S., and Giordano, A. (2009). Cell cycle kinases as therapeutic targets for cancer. Nat. Rev. Drug Discov. *8*, 547–566.

Lenz, G., and Staudt, L.M. (2010). Aggressive lymphomas. N. Engl. J. Med. *362*, 1417–1429.

Lenz, G., Wright, G., Dave, S.S., Xiao, W., Powell, J., Zhao, H., Xu, W., Tan, B., Goldschmidt, N., Iqbal, J., et al; Lymphoma/Leukemia Molecular Profiling Project. (2008a). Stromal gene signatures in large-B-cell lymphomas. N. Engl. J. Med. *359*, 2313–2323.

Lenz, G., Wright, G.W., Emre, N.C., Kohlhammer, H., Dave, S.S., Davis, R.E., Carty, S., Lam, L.T., Shaffer, A.L., Xiao, W., et al. (2008b). Molecular subtypes of diffuse large B-cell lymphoma arise by distinct genetic pathways. Proc. Natl. Acad. Sci. USA *105*, 13520–13525.

Leu, C.M., Davis, R.S., Gartland, L.A., Fine, W.D., and Cooper, M.D. (2005). FcRH1: an activation coreceptor on human B cells. Blood *105*, 1121–1126.

Lohr, J.G., Stojanov, P., Lawrence, M.S., Auclair, D., Chapuy, B., Sougnez, C., Cruz-Gordillo, P., Knoechel, B., Asmann, Y.W., Slager, S.L., et al. (2012). Discovery and prioritization of somatic mutations in diffuse large B-cell lymphoma (DLBCL) by whole-exome sequencing. Proc Natl Acad Sci USA *109*, 3879–3884.

Malumbres, M., and Barbacid, M. (2009). Cell cycle, CDKs and cancer: a changing paradigm. Nat. Rev. Cancer *9*, 153–166.

Mandelbaum, J., Bhagat, G., Tang, H., Mo, T., Brahmachary, M., Shen, Q., Chadburn, A., Rajewsky, K., Tarakhovsky, A., Pasqualucci, L., and Dalla-Favera, R. (2010). BLIMP1 is a tumor suppressor gene frequently disrupted in activated B cell-like diffuse large B cell lymphoma. Cancer Cell *18*, 568–579.

Matijasevic, Z., Krzywicka-Racka, A., Sluder, G., and Jones, S.N. (2008). MdmX regulates transformation and chromosomal stability in p53-deficient cells. Cell Cycle *7*, 2967–2973.

Middendorp, S., Xiao, Y., Song, J.Y., Peperzak, V., Krijger, P.H., Jacobs, H., and Borst, J. (2009). Mice deficient for CD137 ligand are predisposed to develop germinal center-derived B-cell lymphoma. Blood *114*, 2280–2289.

Monti, S., Savage, K.J., Kutok, J.L., Feuerhake, F., Kurtin, P., Mihm, M., Wu, B., Pasqualucci, L., Neuberg, D., Aguiar, R.C., et al. (2005). Molecular profiling of diffuse large B-cell lymphoma identifies robust subtypes including one characterized by host inflammatory response. Blood *105*, 1851–1861.

Morin, R.D., Mendez-Lago, M., Mungall, A.J., Goya, R., Mungall, K.L., Corbett, R.D., Johnson, N.A., Severson, T.M., Chiu, R., Field, M., et al. (2011). Frequent mutation of histone-modifying genes in non-Hodgkin lymphoma. Nature *476*, 298–303.

Nicholson, T.B., Chen, T., and Richard, S. (2009). The physiological and pathophysiological role of PRMT1-mediated protein arginine methylation. Pharmacol. Res. *60*, 466–474.

Ofir-Rosenfeld, Y., Boggs, K., Michael, D., Kastan, M.B., and Oren, M. (2008). Mdm2 regulates p53 mRNA translation through inhibitory interactions with ribosomal protein L26. Mol. Cell *32*, 180–189.

Pasqualucci, L., Compagno, M., Houldsworth, J., Monti, S., Grunn, A., Nandula, S.V., Aster, J.C., Murty, V.V., Shipp, M.A., and Dalla-Favera, R. (2006). Inactivation of the PRDM1/BLIMP1 gene in diffuse large B cell lymphoma. J. Exp. Med. *203*, 311–317.

Pasqualucci, L., Trifonov, V., Fabbri, G., Ma, J., Rossi, D., Chiarenza, A., Wells, V.A., Grunn, A., Messina, M., Elliot, O., et al. (2011). Analysis of the coding genome of diffuse large B-cell lymphoma. Nat. Genet. *43*, 830–837.

Polager, S., and Ginsberg, D. (2009). p53 and E2f: partners in life and death. Nat. Rev. Cancer *9*, 738–748.

Raulet, D.H. (2003). Roles of the NKG2D immunoreceptor and its ligands. Nat. Rev. Immunol. *3*, 781–790.

Salles, G., de Jong, D., Xie, W., Rosenwald, A., Chhanabhai, M., Gaulard, P., Klapper, W., Calaminici, M., Sander, B., Thorns, C., et al. (2011). Prognostic significance of immunohistochemical biomarkers in diffuse large B-cell lymphoma: a study from the Lunenburg Lymphoma Biomarker Consortium. Blood *117*, 7070–7078.

Sánchez-Beato, M., Sánchez-Aguilera, A., and Piris, M.A. (2003). Cell cycle deregulation in B-cell lymphomas. Blood *101*, 1220–1235.

Shangary, S., and Wang, S. (2008). Targeting the MDM2-p53 interaction for cancer therapy. Clin. Cancer Res. *14*, 5318–5324.

Shembade, N., Ma, A., and Harhaj, E.W. (2010). Inhibition of NF-kappaB signaling by A20 through disruption of ubiquitin enzyme complexes. Science *327*, 1135–1139.

Shipp, M., Harrington, D., Chairpersons, Anderson, J., Armitage, J., Bonadonna, G., Brittinger, G., Cabanillas, F., Canellos, G., Coiffier, B., Connors, J., et al. (1993). A predictive model for aggressive non-Hodgkin's lymphoma: The International NHL Prognostic Factors Project. N. Engl. J. Med. *329*, 987–994.

Shlien, A., Tabori, U., Marshall, C.R., Pienkowska, M., Feuk, L., Novokmet, A., Nanda, S., Druker, H., Scherer, S.W., and Malkin, D. (2008). Excessive genomic DNA copy number variation in the Li-Fraumeni cancer predisposition syndrome. Proc. Natl. Acad. Sci. USA *105*, 11264–11269.

Sola, S., Xavier, J.M., Santos, D.M., Aranha, M.M., Morgado, A.L., Jepsen, K., and Rodrigues, C.M.P. (2011). p53 interaction with JMJD3 results in its nuclear distribution during mouse neural stem cell differentiation. PLoS One *6*, e18421.

Stegh, A.H., and DePinho, R.A. (2011). Beyond effector caspase inhibition: Bcl2L12 neutralizes p53 signaling in glioblastoma. Cell Cycle *10*, 33–38.

Subramanian, A., Tamayo, P., Mootha, V.K., Mukherjee, S., Ebert, B.L., Gillette, M.A., Paulovich, A., Pomeroy, S.L., Golub, T.R., Lander, E.S., and Mesirov, J.P. (2005). Gene set enrichment analysis: a knowledge-based approach for interpreting genome-wide expression profiles. Proc. Natl. Acad. Sci. USA *102*, 15545–15550.

Takagi, M., Absalon, M.J., McLure, K.G., and Kastan, M.B. (2005). Regulation of p53 translation and induction after DNA damage by ribosomal protein L26 and nucleolin. Cell *123*, 49–63.

Thompson, S.L., Bakhoum, S.F., and Compton, D.A. (2010). Mechanisms of chromosomal instability. Curr. Biol. *20*, R285–R295.

Wang, P., Lushnikova, T., Odvody, J., Greiner, T.C., Jones, S.N., and Eischen, C.M. (2008). Elevated Mdm2 expression induces chromosomal instability and confers a survival and growth advantage to B cells. Oncogene *27*, 1590–1598.

Wilson, N.S., Dixit, V., and Ashkenazi, A. (2009). Death receptor signal transducers: nodes of coordination in immune signaling networks. Nat. Immunol. *10*, 348–355.

Winter, J.N., Li, S., Aurora, V., Variakojis, D., Nelson, B., Krajewska, M., Zhang, L., Habermann, T.M., Fisher, R.I., Macon, W.R., et al. (2010). Expression of p21 protein predicts clinical outcome in DLBCL patients older than 60 years treated with R-CHOP but not CHOP: a prospective ECOG and Southwest Oncology Group correlative study on E4494. Clin. Cancer Res. *16*, 2435–2442.

Yamagata, K., Daitoku, H., Takahashi, Y., Namiki, K., Hisatake, K., Kako, K., Mukai, H., Kasuya, Y., and Fukamizu, A. (2008). Arginine methylation of FOXO transcription factors inhibits their phosphorylation by Akt. Mol. Cell *32*, 221–231.

Young, K.H., Leroy, K., Møller, M.B., Colleoni, G.W.B., Sánchez-Beato, M., Kerbauy, F.R., Haioun, C., Eickhoff, J.C., Young, A.H., Gaulard, P., et al. (2008). Structural profiles of TP53 gene mutations predict clinical outcome in diffuse large B-cell lymphoma: an international collaborative study. Blood *112*, 3088–3098.

Cancer Cell
Article

Control of Tumor Bioenergetics and Survival Stress Signaling by Mitochondrial HSP90s

Young Chan Chae,[1] M. Cecilia Caino,[1] Sofia Lisanti,[1] Jagadish C. Ghosh,[1] Takehiko Dohi,[1] Nika N. Danial,[3] Jessie Villanueva,[2] Stefano Ferrero,[4] Valentina Vaira,[1,7] Luigi Santambrogio,[6] Silvano Bosari,[5] Lucia R. Languino,[1,8] Meenhard Herlyn,[2] and Dario C. Altieri[1,*]

[1]Prostate Cancer Discovery and Development Program
[2]Melanoma Research Center
The Wistar Institute, 3601 Spruce Street, Philadelphia, PA 19104, USA
[3]Dana-Farber Cancer Institute, Department of Cell Biology, Harvard Medical School, Boston, MA 02115, USA
[4]Department of Biomedical, Surgical and Dental Sciences, University of Milan Medical School and Division of Pathology
[5]Department of Clinical/Surgical Pathophysiology and Organ Transplant, University of Milan Medical School and Division of Pathology
[6]Department of Clinical/Surgical Pathophysiology and Organ Transplant, University of Milan Medical School and Division of Thoracic Surgery and Lung Transplantation
Fondazione IRCCS Cà Granda, Ospedale Maggiore Policlinico, Milan 20122, Italy
[7]Division of Pathology, Fondazione IRCCS Cà Granda, Ospedale Maggiore Policlinico, Milan 20135, Italy
[8]Department of Cancer Biology, Kimmel Cancer Center, Thomas Jefferson University, Philadelphia, PA 19107, USA
*Correspondence: daltieri@wistar.org
http://dx.doi.org/10.1016/j.ccr.2012.07.015

SUMMARY

Tumors successfully adapt to constantly changing intra- and extracellular environments, but the wirings of this process are still largely elusive. Here, we show that heat-shock-protein-90-directed protein folding in mitochondria, but not cytosol, maintains energy production in tumor cells. Interference with this process activates a signaling network that involves phosphorylation of nutrient-sensing AMP-activated kinase, inhibition of rapamycin-sensitive mTOR complex 1, induction of autophagy, and expression of an endoplasmic reticulum unfolded protein response. This signaling network confers a survival and proliferative advantage to genetically disparate tumors, and correlates with worse outcome in lung cancer patients. Therefore, mitochondrial heat shock protein 90s are adaptive regulators of tumor bioenergetics and tractable targets for cancer therapy.

INTRODUCTION

Heat shock protein-90 (HSP90) chaperones oversee protein-folding quality control in virtually every organism (Mayer, 2010). This process is essential for cellular homeostasis, buffering proteotoxic stress, and enabling cells to continuously adapt to changes in their internal and external milieus (Taipale et al., 2010). HSP90 plasticity has been traditionally linked to the diversity of its ''client proteins'', molecules that are implicated in multiple facets of cellular maintenance and require the chaperone ATPase activity for proper folding, maturation, and subcellular trafficking (Taipale et al., 2010). Successful cellular adaptation must also encompass fine-tuning of bioenergetics, nutrient sensing, and stress-response signaling, including autophagy (Yang et al., 2011), although a role of HSP90 in these pathways remains poorly defined. This may be important in cancer, where HSP90 chaperoning is universally exploited (Trepel et al., 2010), and it may help transformed cells thrive in unfavorable environments that are chronically depleted of oxygen and nutrients (Rodina et al., 2007).

Significance

Flexible adaptation to evolving environmental cues is a universal trait of human tumors, regardless of tissue of origin or genetic makeup, and it plays an important role in disease outcome. Generally considered a part of the cellular stress response, adaptive mechanisms influence cell metabolism, preserve proliferation, and promote cell survival. However, whether these pathways operate as an integrated signaling network that contributes to tumor maintenance has not been clearly delineated. The data presented here identify control of protein folding by mitochondrial, but not cytosolic, HSP90s as a global integrator of tumor bioenergetics, autophagy, and interorganelle stress-response signaling. Exploited to promote cell survival and cell proliferation in genetically disparate tumors, this adaptive network offers prime opportunities for cancer therapy.

Adding complexity to chaperone-directed protein homeostasis, or proteostasis, is the role of HSP90-like molecules compartmentalized in the endoplasmic reticulum (ER) (Richter et al., 2007) and mitochondria (Leskovar et al., 2008). The function of these specialized HSP90s in buffering the organelle protein-folding environment is beginning to emerge (Haynes and Ron, 2010), and deregulation of these pathways may contribute to human disease, including neurodegeneration (Gandhi et al., 2009) and cancer (Rodina et al., 2007). Specifically, HSP90 and its related chaperone, tumor necrosis factor receptor-associated protein-1 (TRAP-1), are abundantly present in mitochondria of tumor (though not most normal) cells (Kang et al., 2007), where they maintain organelle proteostasis (Siegelin et al., 2011) and antagonize mitochondrial permeability transition (Kang et al., 2007) mediated by the matrix immunophilin, cyclophilin D (CypD) (Green and Kroemer, 2004).

In this study, we asked whether HSP90-directed protein folding influences cellular energy production (Taipale et al., 2010), especially in tumors.

RESULTS

Regulation of Tumor Bioenergetics by Mitochondrial HSP90s

To begin exploring a role of mitochondrial chaperones in cellular energy production, we used Gamitrinib, a small-molecule inhibitor of HSP90 and TRAP-1 ATPase activity engineered to selectively accumulate in mitochondria (Kang et al., 2009). For these studies, we used 5 hr incubations with Gamitrinib, which neither reduce the viability of several independent tumor-cell types (Figure S1A available online) nor affect mitochondrial membrane potential (Figure S1B) but do create nonlethal proteotoxic stress in mitochondria, characterized by accumulation of misfolded and insoluble proteins (Siegelin et al., 2011).

Under these conditions, Gamitrinib inhibited ATP production in multiple tumor cell types in a dose-dependent manner (Figure 1A). Conversely, 17-allylamino demethoxygeldanamycin (17-AAG), which inhibits HSP90 ATPase activity in the cytosol (Trepel et al., 2010) but not in mitochondria (Kang et al., 2009), had no effect (Figure 1B). The effect of Gamitrinib on bioenergetics was selective for tumor cells, as FF2508 or MRC5 normal primary human fibroblasts were not affected (Figure 1C). Instead, Gamitrinib reduced glucose utilization (Figure 1D), extracellular lactate levels (Figure 1E), and oxygen consumption (Figure 1F), the latter a marker of impaired oxidative phosphorylation, in tumor cells. Supplementation of exogenous sodium pyruvate failed to rescue ATP production in Gamitrinib-treated tumor cells (Figure 1G). In addition, this response did not involve reactive oxygen species (ROS), which were unaffected by different concentrations of Gamitrinib (Figure 1H) for various time intervals (Figure 1I).

Small interfering RNA (siRNA) knockdown of TRAP-1 (Figure 1J), one of the HSP90 targets of Gamitrinib in mitochondria (Kang et al., 2009), similarly reduced ATP and lactate production in tumor cells (Figure 1J). A nontargeting siRNA had no effect (Figure 1J).

HSP90 Controls CypD Protein Folding and Hexokinase-II Recruitment to Tumor Mitochondria

We next asked how mitochondrial HSP90s controlled tumor bioenergetics. Mitochondrial proteotoxic stress induced by Gamitrinib (Siegelin et al., 2011) triggered concentration-dependent release of hexokinase-II (HK-II) from mitochondria, with concomitant accumulation in the cytosol (Figure 2A) HK-I expression and subcellular localization were not affected (Figure 2A). HK-II tethering to mitochondria is required for glycolysis (Vander Heiden et al., 2009) and for coupling glucose metabolism to oxidative phosphorylation. Consistent with this model, Gamitrinib-treated tumor cells exhibited decreased hexokinase activity, whereas 17-AAG had no effect (Figure 2B). siRNA knockdown of TRAP-1 gave similar results, with detachment of HK-II from tumor mitochondria (Figure 2C) and loss of hexokinase activity (Figure 2D).

In mitochondria, HSP90 binds the matrix peptidyl prolyl isomerase (PPIase), CypD (Kang et al., 2007), a component of the permeability transition pore (Green and Kroemer, 2004), which has been implicated in HK-II recruitment to the organelle outer membrane (Machida et al., 2006). Accordingly, siRNA knockdown of CypD released HK-II from mitochondria (Figure 2C) and induced loss of hexokinase activity in tumor cells (Figure 2D). Mitochondria isolated from CypD$^{-/-}$ mouse embryonic fibroblasts (MEFs) showed reduced content of HK-II compared to WT (CypD$^{+/+}$) MEFs (Figure 2E). However, transfection of these cells with a WT CypD cDNA restored binding of HK-II to mitochondria, whereas an H168Q CypD mutant defective in PPIase activity, or empty vector, had no effect (Figure 2F). As a control, the expression of voltage-dependent anion channel (VDAC) was not affected (Figure 2F). We next asked whether CypD retention of HK-II involved chaperone-directed protein folding. Inhibition of mitochondrial HSP90s by Gamitrinib rendered CypD insoluble at increasing detergent concentrations, which suggests protein misfolding and aggregation, compared to untreated cultures (Figure 2G). In contrast, the folding of another mitochondrial protein, COX-IV was indistinguishable in control or Gamitrinib-treated cells, and VDAC remained insoluble at all detergent concentrations used (Figure 2G).

Regulation of Energy-Sensing Pathways by Mitochondrial HSP90s

The downstream implications of defective HK-II-dependent bioenergetics were next investigated. First, siRNA silencing of the energy-sensing AMP-activated kinase (AMPK) (Mihaylova and Shaw, 2011) did not affect HK-II association with tumor mitochondria (Figure 3A) positioning its function downstream of HK-II-directed bioenergetics (Mihaylova and Shaw, 2011). Conversely, tumor cells treated with Gamitrinib, but not 17-AAG, exhibited concentration-dependent phosphorylation of AMPK (Figure 3B; Figure S2A). This response occurred within 30 min of Gamitrinib treatment, remained sustained for 9 hr (Figure 3C), and was quantitatively more robust than that induced by metformin, a known AMPK inducer (Figure 3D). Total AMPK levels were unaffected (Figures 3B–3D), and the combination of metformin plus Gamitrinib did not further stimulate AMPK phosphorylation (Figure 3D).

Silencing of AMPK (Figure S2B) or its main upstream activator, the serine/threonine kinase LKB1 (Mihaylova and Shaw, 2011) (Figure S2C), using multiple independent siRNA sequences suppressed AMPK phosphorylation mediated by Gamitrinib (Figures S2B and S2C). This response was selective for tumor cells, as FF2508 or MRC5 primary human fibroblasts did not activate AMPK in response to Gamitrinib, consistent with the absence

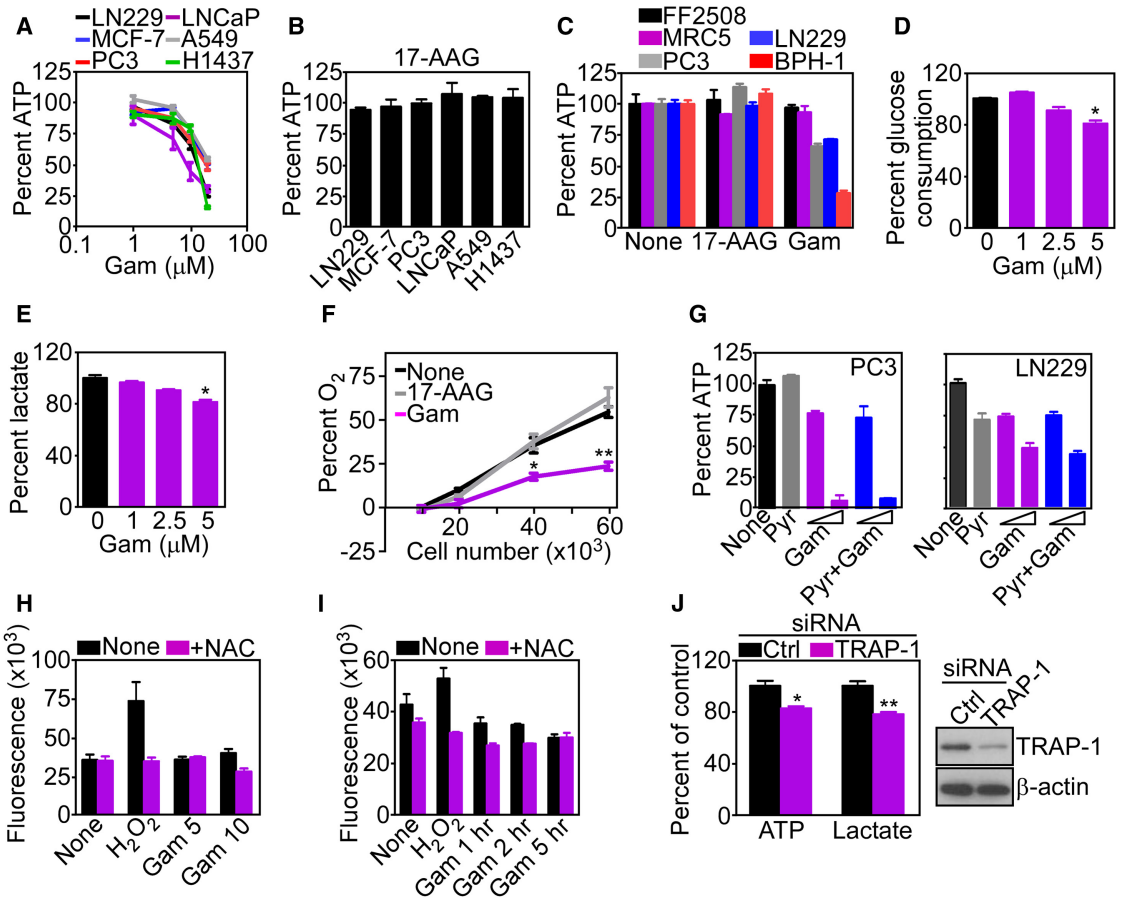

Figure 1. Mitochondrial HSP90 Regulation of Tumor Bioenergetics

(A) Breast (MCF-7), prostate (PC3, LNCaP), lung (A549, H1473), and brain (glioblastoma, LN229) tumor cell lines were treated with the indicated concentrations of Gamitrinib (Gam) for 5 hr and analyzed for ATP production. Mean ± SEM (n = 3).

(B) The indicated tumor cell lines were treated with 17-AAG (20 μM) for 5 hr and analyzed for ATP production. Mean ± SEM (n = 3).

(C) The indicated normal (FF2508, MRC5) or tumor (LN229, PC3, BPH-1) cell lines were incubated with 17-AAG or Gamitrinib (10 μM) for 5 hr and analyzed for ATP production. Mean ± SEM (n = 3).

(D and E) LN229 cells were treated with the indicated concentrations of Gamitrinib for 5 hr and analyzed for glucose consumption (D) or extracellular lactate content (E). Mean ± SEM (n = 3); *p = 0.015-0.022.

(F) LN229 cells were plated at the indicated number, treated with vehicle, Gamitrinib, or 17-AAG (5 μM), and analyzed for O_2 consumption by a fluorimetric assay. Mean ± SEM (n = 3), *p = 0.019; **p = 0.001.

(G) PC3 or LN229 cells were incubated with sodium pyruvate (Pyr, 1 mM) in the presence (5 or 10 μM, respectively) or absence (None) of Gamitrinib for 7 hr and analyzed for ATP production. Mean ± SD of replicates (n = 2).

(H) LN229 cells were labeled with the fluorescent dye H_2-DCFA (6 μM), treated with Gamitrinib (5–10 μM), and analyzed for changes in fluorescence expression in a luminometer, with or without the antioxidant *N*-acetyl-L-cysteine (10 mM, NAC). H_2O_2 (5 mM) was used as control. Mean ± SEM (n = 4).

(I) H_2-DCFA-labeled LN229 cells were treated with 10 μM Gamitrinib for the indicated time intervals and analyzed for changes in ROS production at the indicated time intervals with or without NAC. H_2O_2 was a control. Mean ± SEM (n = 3).

(J) LN229 transfected with control (Ctrl) or TRAP-1-directed siRNA were analyzed for changes in ATP production or extracellular lactate content (left) or TRAP-1 protein level (right). Mean ± SEM (n = 3); *p = 0.017; **p = 0.005.

See also Figure S1.

of TRAP-1 in normal mitochondria (Figure S2D) (Kang et al., 2007). In complementary studies, TRAP-1 knockdown in tumor cells using various siRNA sequences (Figure 3E) stimulated AMPK phosphorylation and induced detachment of HK-II, but not VDAC or COX-IV, from mitochondria (Figure 3E).

Downstream of AMPK activation, Gamitrinib treatment inhibited the rapamycin-sensitive mammalian target of rapamycin complex-1 (mTORC1) in tumor cells (Wullschleger et al., 2006), with loss of phosphorylation of mTOR and its downstream targets, p70S6 and 4EBP1 (Figures 3F and 3G). In these experiments, 17-AAG had no effect (Figure 3G), and total mTORC1 protein content was unchanged (Figures 3F and 3G). Consistent with a selectivity of this pathway for tumor cells, Gamitrinib treatment of nontransformed NIH 3T3 fibroblasts did not affect ATP production (Figure S2E), or AMPK or mTORC1 phosphorylation (Figure 3G). siRNA silencing of LKB1 (Figure S2F) or AMPK (Figure S2G) partially restored phosphorylation of mTOR, p70S6, and 4EBP1 in Gamitrinib-treated tumor cells (Figures S2F and

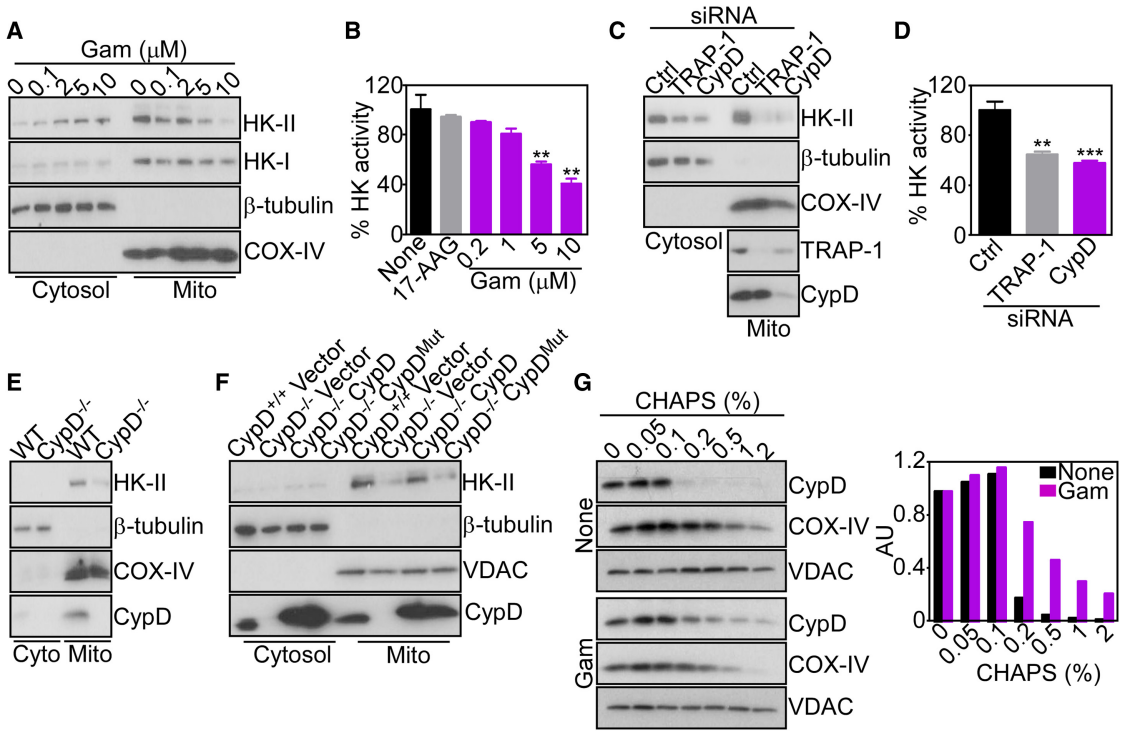

Figure 2. Mitochondrial HSP90 Control of CypD Folding and HK-II Recruitment

(A) LN229 cells were treated with Gamitrinib (Gam), and cytosolic or mitochondrial (Mito) fractions were analyzed after 5 hr by western blotting. COX-IV was a mitochondrial marker.

(B) LN229 cells were treated with 17-AAG (10 μM) or Gamitrinib (0.2–10 μM), and mitochondrial fractions were analyzed for hexokinase activity after 5 hr. Mean ± SD (n = 2); **p = 0.005–0.004.

(C) LN229 cells were transfected with control (Ctrl) or with CypD- or TRAP-1-directed siRNA, and isolated mitochondrial (Mito) or cytosol fractions were analyzed by western blotting after 48 hr.

(D) Mitochondrial fractions from LN229 cells transfected as in (C) were analyzed for hexokinase activity after 48 hr. Mean ± SD (n = 2); ***p = 0.0009; **p = 0.0024.

(E) Mitochondrial (Mito) or cytosol (Cyto) fractions from WT ($CypD^{+/+}$) or $CypD^{-/-}$ MEFs were analyzed by western blotting.

(F) $CypD^{+/+}$, $CypD^{-/-}$, or $CypD^{-/-}$ MEFs reconstituted with WT or PPIase-defective H168Q mutant CypD cDNA were fractionated in cytosol or mitochondrial (Mito) extracts, and analyzed by western blotting.

(G) LN229 cells were left untreated (None) or incubated with Gamitrinib (5 μM) and mixed with the indicated increasing concentrations of CHAPS. Detergent-insoluble proteins were analyzed by western blotting. The bar graph shows densitometric quantification of protein bands. AU, arbitrary units.

S2G). Conversely, knockdown of HK-II enhanced the effect of Gamitrinib, with increased AMPK phosphorylation and mTORC1 inhibition (Figure S2H).

Further supporting a role of defective bioenergetics in this response, exposure of tumor cells to the nonhydrolyzable glucose analog, 2-deoxy glucose (2-DG), which mimics energy starvation (Egan et al., 2011), reproduced the effect of Gamitrinib, with strong activation of AMPK and suppression of mTOR, p70S6, and 4EBP1 phosphorylation (Figure 3H).

Mitochondrial Proteotoxic Stress Activates Prosurvival Autophagy

The implication of mTORC1 inhibition by mitochondrial proteotoxic stress was next investigated. Consistent with an inhibitory role of mTORC1 on autophagy, and in agreement with recent observations (Siegelin et al., 2011), Gamitrinib strongly induced autophagy in tumor cells, with conversion of microtubule-associated protein light-chain-3 (LC3-II) to a lipidated form (Figure 4A) and appearance of a punctate fluorescence pattern of LC3-CFP staining in transfected cells (Figures S3A and S3B). This induction of autophagy required AMPK, as siRNA silencing of LKB1 (Figure 4B) or AMPK (Figure 4C) suppressed LC3-II conversion (Figures 4B and 4C) and autophagosome formation (Figures S3A and S3B) induced by Gamitrinib. As control, siRNA silencing of the essential autophagy gene, ATG5, produced similar results (Figure 4D; Figures S3A and S3B), consistent with recent observations (Siegelin et al., 2011).

We next asked whether autophagy activated by mitochondrial proteotoxic stress influenced tumor cell viability (Siegelin et al., 2011). Inhibition of phagosome formation by 3-methyadenine (3-MA) (Figure 4E), or siRNA knockdown of ATG5 (Figure 4F) (Siegelin et al., 2011) or LKB1 (Figure 4G), enhanced tumor cell killing mediated by suboptimal concentrations of Gamitrinib. Similarly, siRNA silencing of HK-II (Figure S3D) potentiated Gamitrinib-induced tumor cell death (Figure 4H), as characterized by increased Annexin V labeling, compared to control transfectants (Figure 4I). In contrast, the combination of 17-AAG plus 3-MA (Figure 4E), or 17-AAG plus siRNA silencing of LKB1 (Figure 4G) or HK-II (Figure 4H), did not decrease tumor cell viability compared to each treatment alone.

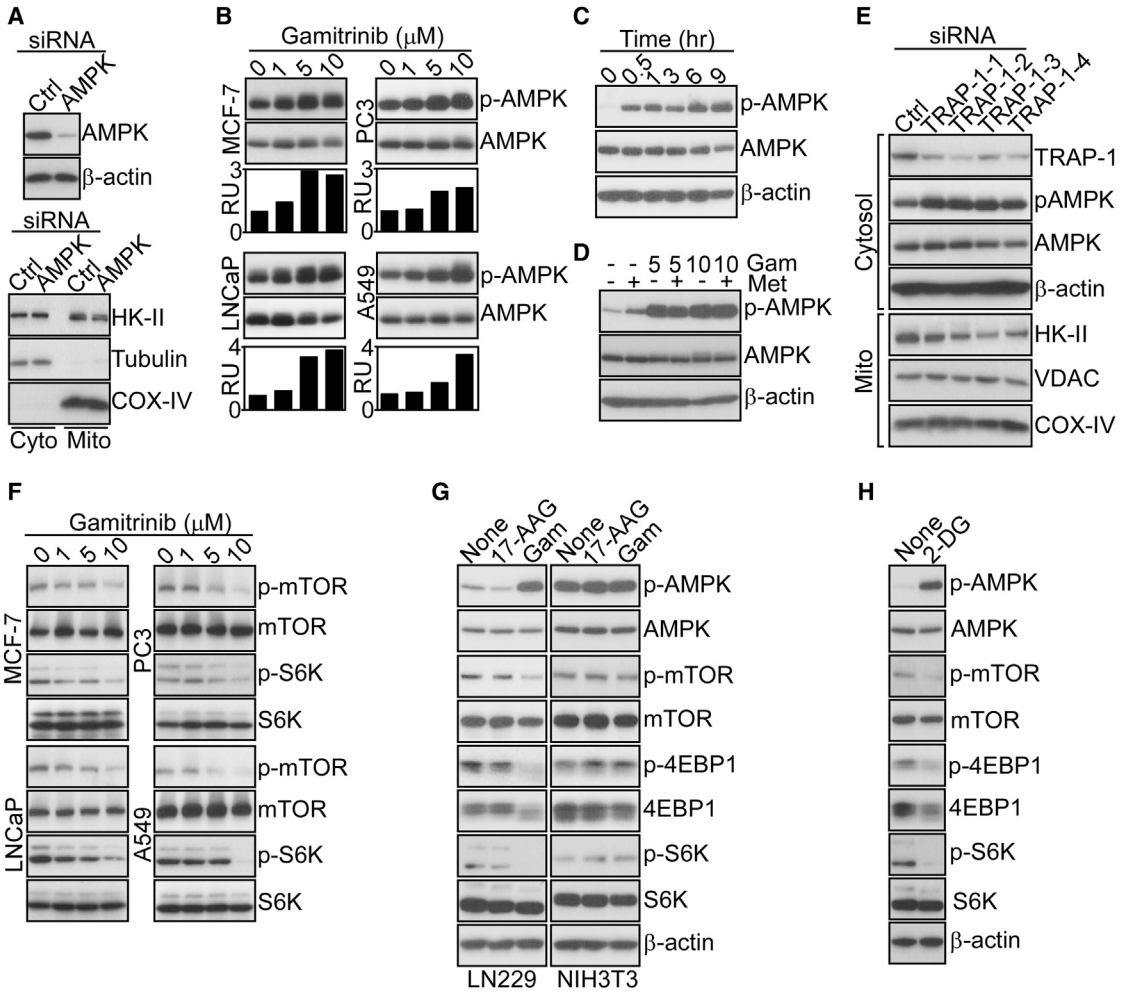

Figure 3. Modulation of AMPK and mTORC1 Signaling by Mitochondrial HSP90s

(A) LN229 cells were transfected with control (Ctrl) or AMPK-directed siRNA, and total cell extracts (top) or isolated cytosol (Cyto) or mitochondrial (Mito) fractions (bottom) were analyzed by western blotting.

(B) The various tumor cell lines were treated with the indicated concentrations of Gamitrinib, and analyzed by western blotting after 5 hr. The bar graphs show densitometric quantification of protein bands. RU, relative units.

(C) Gamitrinib-treated (10 μM) LN229 cells were analyzed at the indicated time intervals by western blotting.

(D) LN229 cells were treated with metformin (Met, 5 mM) in the presence or absence of Gamitrinib (Gam, 5–10 μM) and analyzed after 12 hr by western blotting.

(E) LN229 cells were transfected with control (Ctrl) or the indicated individual siRNA sequences against TRAP-1, and isolated cytosol or mitochondrial (Mito) fractions were analyzed by western blotting.

(F) The indicated tumor cell types were treated with increasing concentrations of Gamitrinib and analyzed after 12 hr by western blotting.

(G) Tumor (LN229) or normal (NIH 3T3) cell types were treated with Gamitrinib or 17-AAG (10 μM) and analyzed after 12 hr by western blotting.

(H) LN229 cells were treated with 2-DG (25 mM) and analyzed after 12 hr by western blotting.

See also Figure S2.

Metabolic Interorganelle ER Signaling by Mitochondrial HSP90s

Defective mitochondrial bioenergetics impair protein posttranslational modifications in the ER (Kaufman et al., 2002), which may trigger an unfolded protein response (UPR) (Hetz and Glimcher, 2009). Consistent with this model, tumor cells treated with Gamitrinib exhibited increased expression of inositol-requiring-1 (IRE-1) kinase (Figure 5A), an ER stress sensor (Hetz and Glimcher, 2009), and de novo mRNA splicing, i.e., activation, of its target, X-box protein-1 (XBP1) (Figure 5B). This was associated with activation of other ER UPR branches (Hetz and Glimcher, 2009), with activating transcription factor-6 (ATF-6)-mediated upregulation of the ER chaperone GRP78 (Figure 5C; Figure S4A), and PKR-like endoplasmic reticulum kinase (PERK) induction of transcription factors CCAAT-enhancer binding protein (C/EBPβ) and C/EBP homology protein (CHOP) (Figure 5C; Figures S4B and S4C) (Siegelin et al., 2011). Gamitrinib also induced transient phosphorylation of PERK-regulated eIF2α in tumor cells (Figure 5C). Upregulation of ER stress markers by Gamitrinib occurred within 1 hr of treatment (Figure S4A), and over a broad range of concentrations (Figure S4B), similar to the response induced by the ER stressor tunicamycin (Figure S4D).

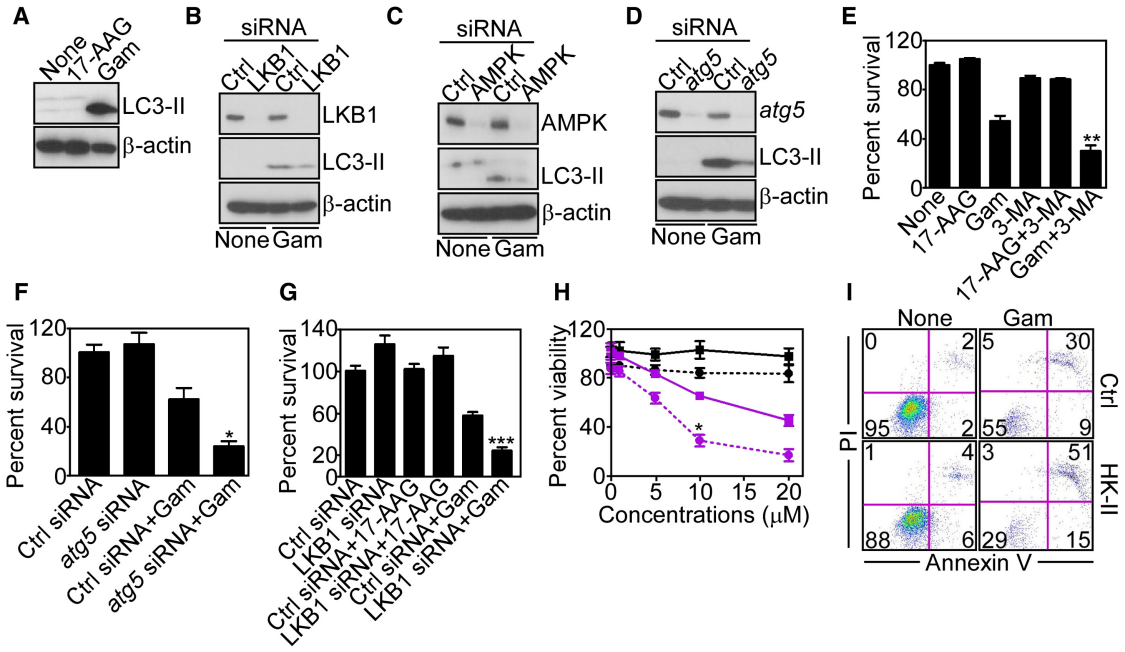

Figure 4. Mitochondrial Proteotoxic Stress Stimulates Autophagy

(A) LN229 cells treated with Gamitrinib or 17-AAG (10 μM) for 12 hr were analyzed by western blotting.

(B–D) LN229 cells were transfected with control (Ctrl), or with LKB1-, AMPK-, or ATG5-directed (B–D, respectively) siRNA, treated with vehicle or Gamitrinib (10 μM), and analyzed after 48 hr by western blotting.

(E) LN229 cells were treated with the inhibitor of phagosome formation, 3-MA, treated with Gamitrinib or 17-AAG (10 μM), and analyzed for cell viability by 3-(4,5-dimethylthiazol-2-YI)-2,5-diphenyltetrazolium bromide (MTT). Mean ± SD (n = 2); **p = 0.0072.

(F and G) LN229 cells were transfected with control siRNA (Ctrl) or with ATG5- or LKB1-directed siRNA (F and G, respectively), incubated with 17-AAG or Gamitrinib (10 μM) (G), and analyzed for cell viability by MTT. Mean ± SEM (n = 4). *p = 0.02; ***p < 0.0004.

(H) LN229 cells were transfected with control (squares) or HK-II-directed (circles) siRNA, treated with increasing concentrations of 17-AAG (black) or Gamitrinib (purple), and analyzed after 12 hr for cell viability by MTT. Mean ± SD (n = 2); *p = 0.02.

(I) LN229 cells were transfected with control (Ctrl) or HK-II-directed siRNA, treated with vehicle (None) or Gamitrinib, and analyzed for Annexin V and propidium iodide staining by multiparametric flow cytometry. The percentage of cells in each quadrant is indicated.

See also Figure S3.

Next, we asked whether this ER UPR involved de novo gene expression. Gamitrinib treatment resulted in time-dependent upregulation of CHOP, C/EBPβ, and GRP78 mRNA levels (Figure 5D). Similarly, exposure of tumor cells to Gamitrinib, 2-DG, or tunicamycin all resulted in transcriptional activation of IRE-1, ATF6, and PERK response elements in luciferase promoter analysis (Figures 5E and 5F). A minimal CHOP promoter region was also transcriptionally induced by Gamitrinib (Figure 5F).

A mechanistic link between Gamitrinib-induced ER UPR and defective mitochondrial bioenergetics was next investigated. First, exposure of tumor cells to the mitochondrial uncoupler carbonyl cyanide 3-chlorophenylhydrazone (CCCP) reproduced the effect of Gamitrinib, with time-dependent phosphorylation of AMPK (Figure S4E), upregulation of CHOP, C/EBPβ, and GRP78, inhibition of 4EBP1 phosphorylation, and stimulation of LC3-II conversion (Figure 5G). In contrast, incubation of tumor cells with inhibitory concentrations of the ROS scavenger *N*-acetyl-L-cysteine (NAC) did not affect Gamitrinib-induced phosphorylation of AMPK or its target acetyl-CoA carboxylase (ACC), or upregulation of ER stress markers (Figure 5H). Conversely, energy deprivation, or impaired N-linked glycosylation (Kurtoglu et al., 2007), caused by 2-DG mimicked the effect of Gamitrinib and resulted in concentration (Figure S4F)- and time (Figure S4G)-dependent upregulation of ER UPR in tumor cells. When combined with 2-DG, Gamitrinib maximally stimulated AMPK and eIF2α phosphorylation in tumor cells (Figure S4H). This resulted in complete translational repression, and ablation of GRP78, CHOP, or C/EBPβ levels (Figure S4H). Functionally, this was associated with enhanced tumor cell killing by suboptimal concentrations of Gamitrinib, compared to each agent alone (Figure S4I).

In parallel experiments, exposure of tumor cells to low-glucose-containing medium (5 mM) stimulated AMPK phosphorylation and increased the expression of CHOP, C/EBPβ, and GRP78 (Figure 5I). Supplementation of tumor cells with high-glucose-containing medium partially reversed this response and attenuated the expression of ER UPR markers and AMPK phosphorylation in the presence of Gamitrinib (Figure 5I). Similar to ATP production (Figure 1G), addition of exogenous sodium pyruvate did not modulate AMPK or ER UPR signaling by Gamitrinib (Figure 5J).

Cytoprotective Role of ER UPR Induced by Gamitrinib

We next mapped the requirements of Gamitrinib-induced ER UPR. First, siRNA knockdown of HK-II was insufficient, alone, to upregulate the expression of CHOP or GRP78, promote

AMPK phosphorylation, or stimulate LC3-II conversion in tumor cells (Figure 6A). However, the combination of HK-II knockdown plus Gamitrinib enhanced AMPK phosphorylation, ER UPR induction, and autophagy in tumor cells (Figure 6A). This pathway still depended on impaired tumor bioenergetics, as siRNA knockdown of AMPK (Figure 6B) or LKB1 (Figure 6C) attenuated Gamitrinib-induced phosphorylation of AMPK, ACC, and the upregulation of ER UPR markers (Figures 6B and 6C). Conversely, siRNA silencing of the ER UPR effector GRP78 (Figure 6D; Figure S5) did not affect phosphorylation of AMPK or mTORC1 kinases in the presence of Gamitrinib, positioning GRP78 induction downstream of impaired ATP production (Figure 1). Reciprocally, siRNA knockdown of the ER stress sensor IRE-1 did not significantly affect the induction of UPR markers by Gamitrinib (Figure 6E). In contrast, knockdown of PERK, alone or in combination with IRE-1 silencing, inhibited the expression of CHOP and C/EBPβ and abolished eIF2α phosphorylation induced by Gamitrinib, whereas GRP78 was not significantly affected, and no changes were observed in LC3 conversion (Figure 6E). In all silencing experiments, a nontargeting siRNA was ineffective (Figures 6A–6E).

Next, we asked whether components of this ER UPR influenced tumor cell functions. Silencing of GRP78 using multiple independent siRNA sequences inhibited tumor cell proliferation compared to control siRNA transfectants (Figure 6F). Similar results were obtained in different cell types (Figure 6G), indicating a general requirement of GRP78 for tumor cell proliferation. In addition, GRP78 knockdown decreased the viability of selected tumor cell types including prostate cancer PC3 or LNCaP cells (Figure 6H). In contrast, IRE-1 or PERK knockdown, alone or in combination, did not reduce tumor cell viability in the presence or absence of Gamitrinib (Figure 6I).

Chaperone-Regulated Bioenergetics Controls Tumor Maintenance

Next, we asked whether the signaling pathway controlled by mitochondrial HSP90s was important for tumor maintenance. In a first model, we looked at melanoma cells, where a V600E mutation of the BRAF oncogene results in ERK-mediated inhibitory phosphorylation of LKB1 and suppression of AMPK activation (Zheng et al., 2009). Accordingly, two BRAF mutant melanoma cell lines, which exhibited hyperphosphorylated ERK, failed to activate AMPK in response to Gamitrinib (Figure 7A; Figure S6A). Conversely, Gamitrinib induced AMPK phosphorylation in WT BRAF melanoma cells with low levels of phosphorylated ERK (Figure 7A; Figure S6A). 17-AAG had no effect on AMPK activation in WT or mutant BRAF melanoma cells (Figure 7A; Figure S6A). Similar to the data above, AMPK activation by mitochondrial stress activated autophagy in WT BRAF cells, whereas BRAF mutant cells did not increase autophagy in response to Gamitrinib (Figure 7B). Functionally, mutant BRAF melanoma cells exhibited increased sensitivity to Gamitrinib-induced cell death compared to WT BRAF melanoma cells (IC_{50} BRAF V600E, 1.95 ± 0.21; IC_{50} BRAF WT, 6 ± 1.4) (Figure 7C). This response was due to differential activation of compensatory autophagy, as siRNA knockdown of AMPK suppressed autophagy in WT BRAF cells (Figure 7D; Figure S6B) and enhanced their sensitivity to Gamitrinib-mediated killing (Figure 7E; Figure S6C). As control, an inhibitor of MEK, U0126, partially restored AMPK phosphorylation in mutant BRAF melanoma cells after Gamitrinib treatment (Figure S6D). To examine this pathway in a more disease-relevant model, we next reconstituted melanoma cell growth in 3-D spheroids embedded in a collagen matrix (Villanueva et al., 2010). In this system, low concentrations of Gamitrinib (1–3 μM) efficiently killed mutant BRAF melanoma cells, whereas WT BRAF spheroids were resistant to cell death (Figure 7F).

Mitochondrial HSP90-Directed Bioenergetics Influences Tumor Outcome

To determine whether mitochondrial HSP90-directed signaling occurred in vivo, we next examined a genetic model of prostate cancer in immunocompetent TRAMP (transgenic adenocarcinoma of the mouse prostate) mice treated systemically with Gamitrinib (Kang et al., 2011). In this model, Gamitrinib inhibited primary and metastatic prostate cancer growth, but did not affect prostatic intraepithelial neoplasia (PIN) (Kang et al., 2011). Here, Gamitrinib treatment was associated with increased expression of phosphorylated AMPK, induction of autophagy, i.e., LC3 conversion, and upregulation of GRP78 in PIN lesions, but not in normal prostate (Figure 8A). Prostate tissues from TRAMP mice treated with vehicle did not express these markers (Figure 8A).

We next looked at primary human tumor specimens, and we focused on a potential role of the ER stress chaperone GRP78 in disease progression in vivo. Except for lymphoma, GRP78 was strongly and uniformly upregulated in the tumor cell population of a large panel of genetically heterogeneous cancers, as shown by tissue microarray (TMA; Figure 8B; Figure S7A). Accordingly, GRP78 was abundantly expressed in non-small-cell lung cancer (NSCLC) patients (Table S1) with adenocarcinoma (AdCa) or squamous cell carcinoma (SCC) (Figures 8C and 8D), regardless of tumor stage (Figure S7B), or lymph node metastasis (Figure S7C). Conversely, GRP78 was undetectable in the normal epithelium of the lung (Figures 8C and 8D). When stratified for disease outcome, patients with lung AdCa expressing GRP78 had considerably shorter overall survival compared to those with low to undetectable GRP78 (Figure 8E).

Based on these results, we asked whether deregulated expression of GRP78 influenced cell proliferation and/or survival of lung cancer cells. siRNA silencing of GRP78 (Figure 8F) induced loss of viability of H1299 and A549 lung cancer cells, whereas H1457 and H1650 cells were only partially affected (Figure 8G). Similar to other tumor types (Figures 6F and 6G), silencing of GRP78 suppressed proliferation of all lung cancer cells tested (Figure 8H), whereas a nontargeting siRNA had no effect (Figures 8G and 8H).

DISCUSSION

In this study, we have shown that HSP90s compartmentalized in mitochondria (Kang et al., 2007) are essential regulators of bioenergetics in tumor cells but not normal cells. This pathway controls both glycolysis and oxidative phosphorylation and involves chaperone-dependent retention of HK-II (Vander Heiden et al., 2009) to the organelle outer membrane (Majewski et al., 2004). Interference with chaperone control of mitochondrial protein folding causes acute decrease in ATP production

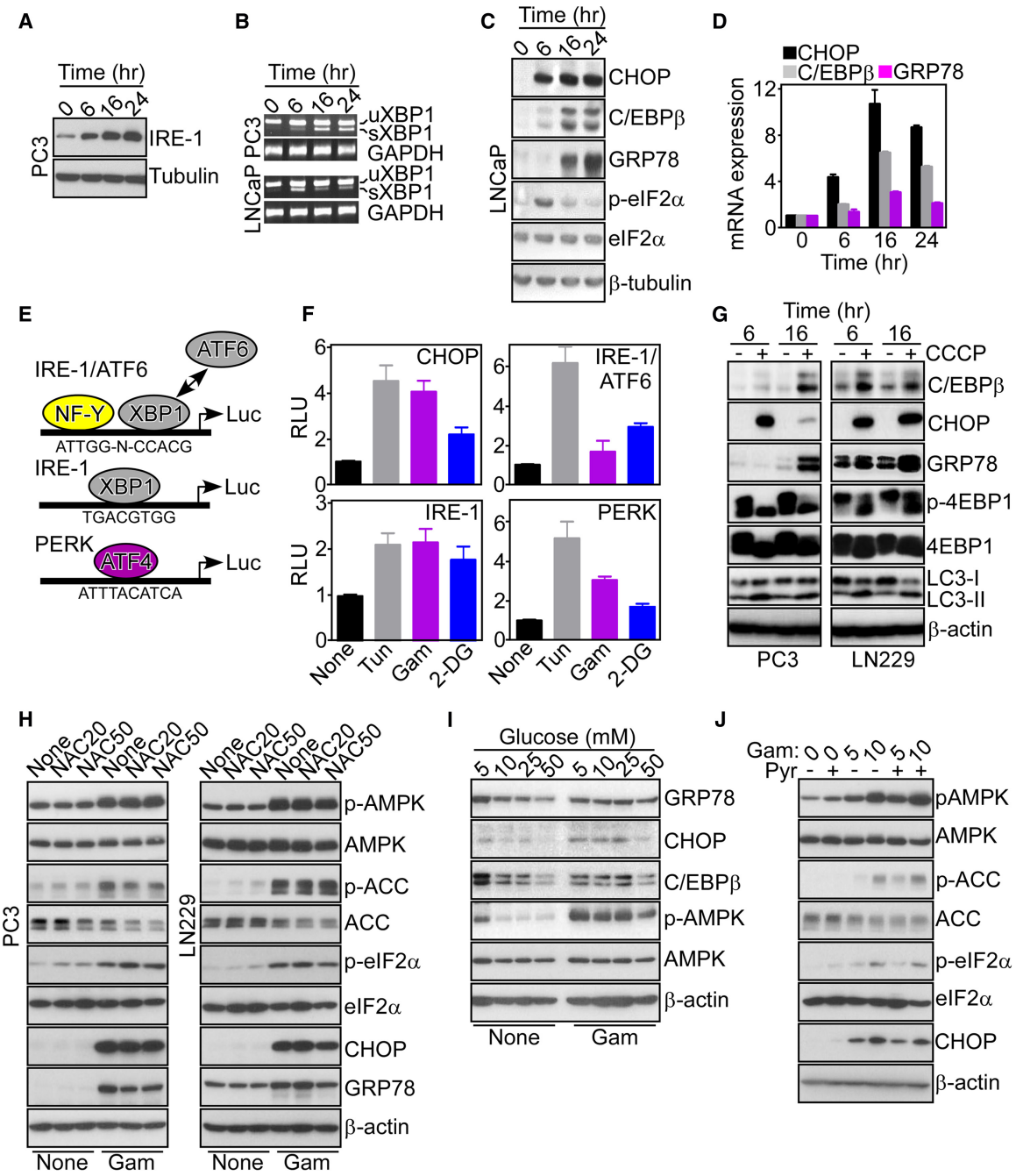

Figure 5. Regulation of ER UPR by Mitochondrial HSP90s

(A) PC3 cells were incubated with Gamitrinib (5 μM) and analyzed at the indicated time intervals by western blotting.

(B) Gamitrinib-treated tumor cells were harvested at the indicated time intervals, and total RNA was amplified with primers to detect spliced (s) or unspliced (u) XBP1 mRNA transcripts. GAPDH was used as a control.

(C) LNCaP cells were treated with Gamitrinib and analyzed at the indicated time intervals by western blotting.

(D) Gamitrinib-treated LNCaP cells were harvested at the indicated time intervals and analyzed for changes in CHOP, C/EBPβ, or GRP78 mRNA expression by quantitative PCR. Mean ± SEM of replicates of a representative experiment (n = 3).

(E) Schematic diagram of ER stress luciferase-promoter reporter constructs used in this study.

(F) PC3 cells were transfected with the indicated luciferase-promoter reporter constructs, or with a CHOP minimal promoter upstream of a luciferase gene, incubated with Gamitrinib (5 μM), tunicamycin (Tun, 2.5 μg/ml), or 2-DG (25 mM), and analyzed for changes in luciferase expression in a luminometer after 20 hr. Mean ± SEM (n = 4). None, untreated.

(G) PC3 cells were treated in the presence (+) or absence (−) of the mitochondrial uncoupler CCCP and analyzed after 6 or 16 hr by western blotting.

(H) The indicated tumor cell types were incubated without (None) or with 5 μM Gamitrinib in the presence or absence of the indicated concentrations of NAC (20 or 50 μM) and analyzed after 6 hr by western blotting.

and activation of an integrated signaling network, with phosphorylation of AMPK (Mihaylova and Shaw, 2011), inhibition of mTORC1 (Wullschleger et al., 2006), induction of autophagy (Yang et al., 2011), and stimulation of ER UPR (Hetz and Glimcher, 2009). Functionally, this pathway provides proliferative and cytoprotective compensatory signals for tumor cells, has been recapitulated in a genetic mouse model of prostate cancer in immunocompetent animals (Kang et al., 2011), and correlates with shortened overall survival in patients with lung adenocarcinoma.

CypD is the only known component of a mitochondrial permeability transition pore (Green and Kroemer, 2004) that is required for cell death triggered by certain stimuli, for instance, oxidative stress (Baines et al., 2005; Nakagawa et al., 2005). How this process is regulated is still a matter of debate, but recent evidence has pointed to chaperone-directed (re)folding of CypD as a potential mechanism to preserve mitochondrial integrity, and to antagonize apoptosis, selectively in tumor cells (Kang et al., 2007). The structural requirements of potential HSP90-CypD protein complexes in mitochondria (Kang et al., 2007) remain to be fully elucidated. However, complete suppression of chaperone ATPase activity with Gamitrinib (Kang et al., 2009) results in misfolding and aggregation of CypD (this study), culminating in acute permeability transition and CypD-dependent cell death (Kang et al., 2009). Conversely, titrating the extent of chaperone inhibition using suboptimal concentrations of Gamitrinib and shorter incubation times (Siegelin et al., 2011) uncovered additional functional roles of this pathway, and in particular a mechanism of CypD conformation-dependent retention of HK-II to the outer mitochondrial membrane. In this context, detachment of HK-II after nonlethal mitochondrial proteotoxic stress (Siegelin et al., 2011) is expected to lower an antiapoptotic threshold maintained by growth factor-Akt signaling (Robey and Hay, 2006), but, even more importantly, to impair aerobic glycolysis, the main energy source for tumor cells (Vander Heiden et al., 2009). Whether mitochondrial proteotoxic stress affects other pathways of ATP or biomass production in tumors remains to be determined. However, the inhibition of oxygen consumption observed here after Gamitrinib treatment, combined with the inability of exogenous pyruvate to restore ATP production under these conditions, suggest that organelle HSP90s may also contribute to oxidative phosphorylation. The details of this potential response are presently unknown, but it is intriguing that loss of HK-II (Vander Heiden et al., 2009) has been shown to shift tumor bioenergetics from aerobic glycolysis toward oxidative phosphorylation (Wolf et al., 2011), potentially rendering tumor cells especially sensitive to the pathway of mitochondrial proteotoxicity described here.

Consistent with current models of bioenergetics, loss of ATP production after mitochondrial proteotoxic stress resulted in downstream activation of an LKB1-AMPK signaling axis in tumor cells. These molecules participate in tumor suppression, and a growing number of cancers harbor LKB1-inactivating mutations (Hezel and Bardeesy, 2008). Here, however, activation of the LKB1-AMPK pathway was exploited for tumor cell survival via stimulation of autophagy (Mihaylova and Shaw, 2011). This may reflect release of mTORC1 inhibition on autophagy initiation (Gwinn et al., 2008; Inoki et al., 2003) and/or direct phosphorylation of the ULK-1-containing autophagy complex by AMPK (Egan et al., 2011). How common is the exploitation of LKB1-AMPK signaling for tumor cell survival in vivo remains to be determined. However, AMPK phosphorylation has been observed in hypoxic tumors deprived of nutrients (Laderoute et al., 2006). It was prominently induced in PIN lesions of TRAMP mice treated with therapeutic concentrations of Gamitrinib (Kang et al., 2011; this study). In addition, downstream activation of autophagy is being increasingly recognized as a major driver of tumor maintenance, potentially at later stages of disease progression (Yang et al., 2011). In melanoma, where AMPK can be differentially activated depending on the mutational status of the BRAF oncogene (Zheng et al., 2009), autophagy was a critical determinant of cell survival, making BRAF mutant cells especially sensitive to mitochondrial cell death initiated by Gamitrinib (Kang et al., 2007). This observation may have clinical relevance, as melanoma patients carrying a V600E BRAF mutation become invariably resistant to small-molecule BRAF inhibitors, pressing the need for alternative therapeutic targets to restore treatment responses in these settings.

ATP depletion results in insufficient energy available for protein posttranslational modifications (Kaufman et al., 2002), and in the case of mitochondrial proteotoxic stress, this triggered a canonical ER UPR (Hetz and Glimcher, 2009). This pathway was reproduced by pharmacologic uncoupling of mitochondrial membrane potential, in keeping with directional mitochondria-to-ER signaling, was partially reversed by high glucose, consistent with a causal role of defective ATP production in this process (Kaufman et al., 2002), and required LKB1-AMPK activation as part of bioenergetics signaling (Mihaylova and Shaw, 2011). The role of ER stress in cancer is complex, and prolonged activation of this pathway culminates with apoptosis contributed, at least in part, by transcriptional modulation of Bcl-2 proteins (Tabas and Ron, 2011). However, low-level, chronic ER stress may be beneficial for tumor growth (Ma and Hendershot, 2004), and the inducible ER chaperone GRP78 was identified here as an effector of tumor cell survival and proliferation during bioenergetics ER stress (Pfaffenbach and Lee, 2011). Cytoprotection by GRP78 may involve modulation of multiple antiapoptotic thresholds, including differential assembly of Bcl-2 homodimers (Zhou et al., 2011), and, as shown here, this pathway may become broadly exploited in genetically disparate cancers, correlating with shortened overall survival in patients with lung adenocarcinoma (this study), or prostate cancer (Tan et al., 2011). Regarding a potential role of other ER markers in disease outcome, high levels of eIF2α have been associated with improved survival in stage I, but not stages II–IV, NSCLC patients (He et al., 2011).

(I) LN229 cells were cultivated in the presence of the indicated increasing concentrations of glucose-containing medium without (None) or with Gamitrinib (5 μM) and analyzed by western blotting.
(J) LN229 cells were treated with the indicated concentrations of Gamitrinib in the presence (+) or absence (−) of sodium pyruvate (Pyr, 1 mM), and analyzed after 7 hr by western blotting.
See also Figure S4.

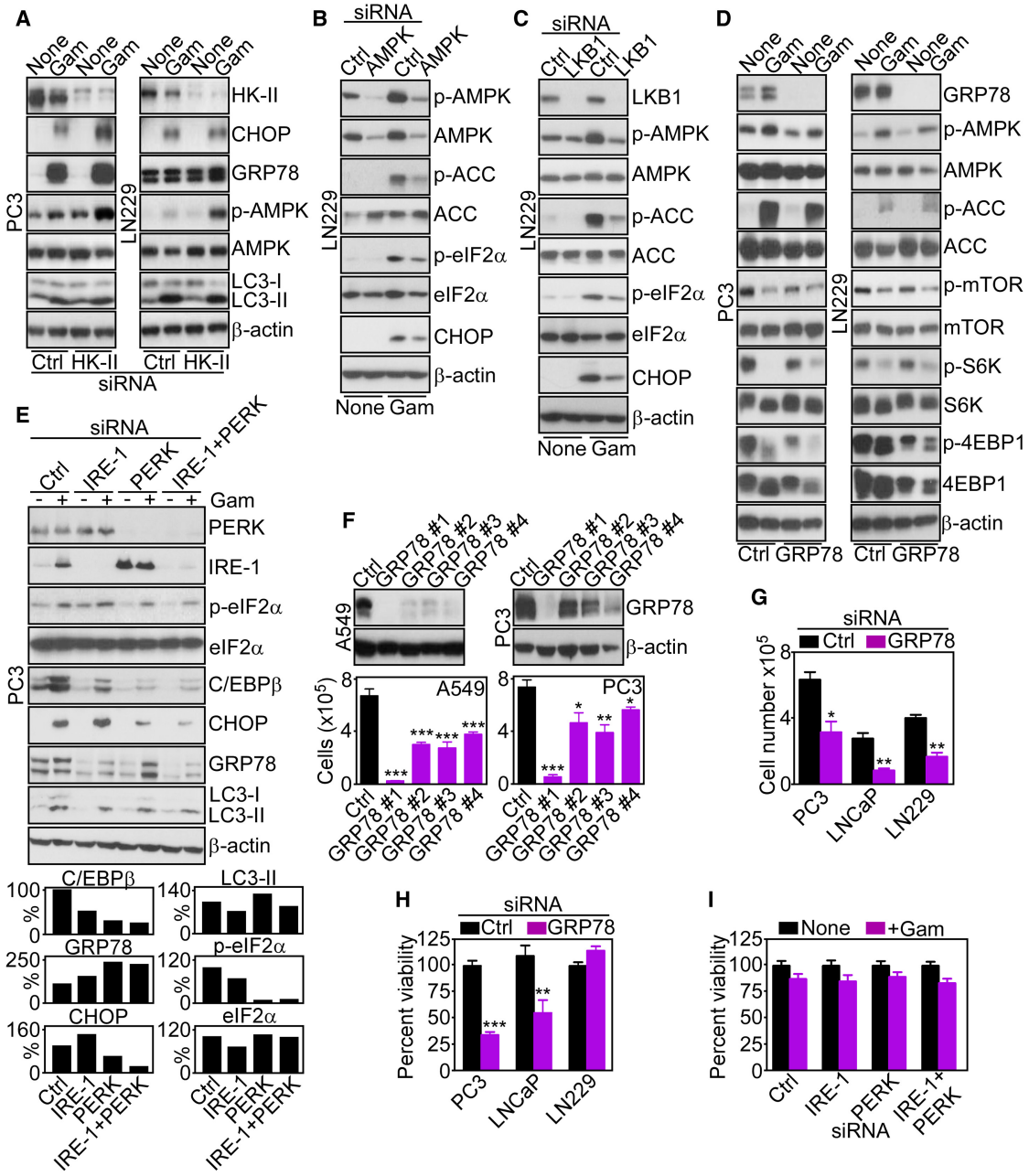

Figure 6. Functional Requirements of ER UPR Induced by Mitochondrial Proteotoxic Stress

(A–E) The indicated tumor cell lines were transfected with control siRNA (Ctrl), or with siRNA directed to HK-II (A), AMPK (B), LKB1 (C), GRP78 (D), or the ER stress sensors IRE-1 or PERK, alone or in combination (E), incubated in the presence or absence (None) of Gamitrinib (5 μM), and analyzed 24–48 hr after siRNA transfection by western blotting. The bar graphs in (E) show densitometric quantification of normalized C/EBPβ, CHOP, GRP78, LC3-II, or phosphorylated eIF2α bands in the presence of Gamitrinib. Basal eIF2α levels in the absence of Gamitrinib were also calculated.

(F) A549 or PC3 cells were transfected with control siRNA (Ctrl) or the indicated individual siRNA sequences to GRP78, and analyzed after 48 hr by western blotting. Bottom, siRNA-transfected cells as in the top images were analyzed for cell proliferation by direct cell counting. Mean ± SEM of three independent experiments. *$p < 0.05$; **$p < 0.01$; ***$p < 0.001$.

(G and H) The indicated tumor cell types were transfected with control siRNA (Ctrl) or GRP78-directed siRNA and analyzed for cell proliferation by direct cell counting (G) or cell viability by MTT (H). Mean ± SEM (n = 8 in [G] and 3 in [H]); *$p = 0.016$; **$p = 0.017–0.0055$; ***$p < 0.0001$.

(I) siRNA-transfected PC3 cells as in (E) were treated in the absence (None) or presence of 5 μM Gamitrinib and analyzed for cell viability by MTT. Mean ± SEM of replicates of a representative experiment from two independent determinations.

See also Figure S5.

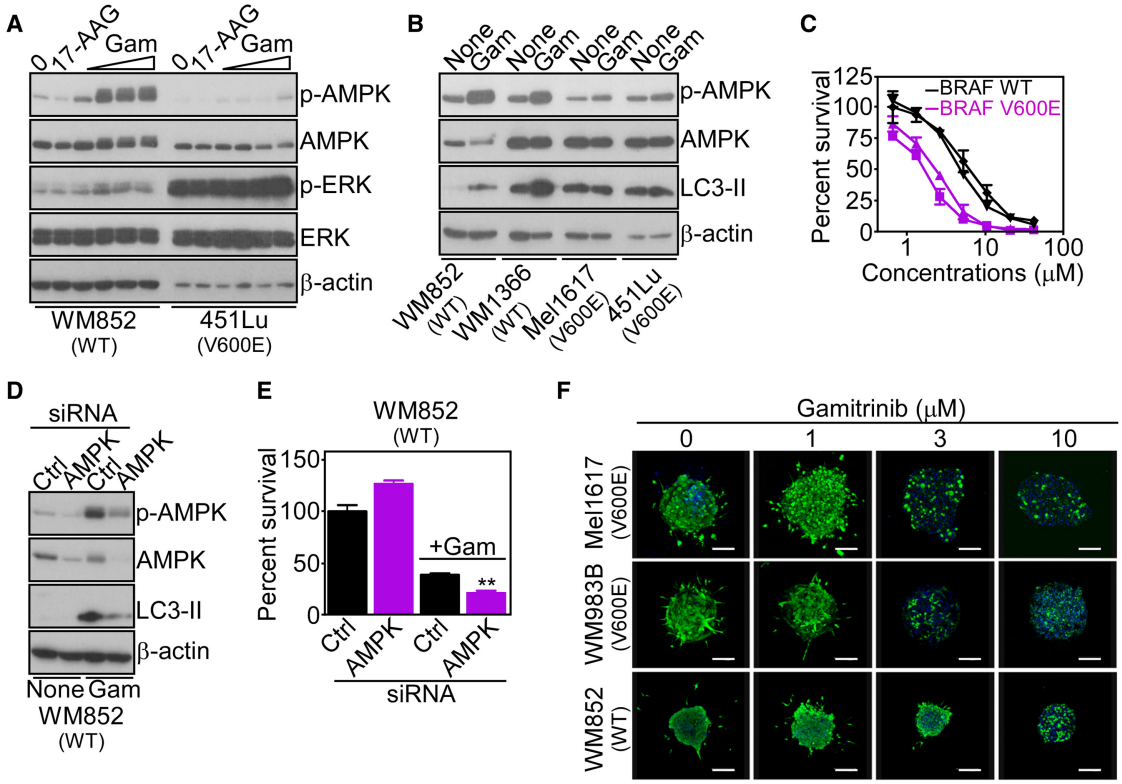

Figure 7. Regulation of Tumor Cell Survival by Mitochondrial Proteotoxic Stress

(A) WT or V600E mutant BRAF melanoma cell lines were treated with 17-AAG (10 μM) or Gamitrinib (1, 2.5, 5, or 10 μM) and analyzed after 5 hr by western blotting.

(B) The indicated melanoma cell types were incubated with Gamitrinib (5 μM) and analyzed after 9 hr by western blotting. None, untreated.

(C) WT (WM852, WM1366) or mutant BRAF (Me1617, 451Lu) melanoma cells were treated with Gamitrinib and analyzed after 16 hr for cell viability by MTT. Mean ± SD (n = 2).

(D) WM852 BRAF WT melanoma cells were transfected with control (Ctrl) or AMPK-directed siRNA, treated with Gamitrinib (5 μM), and analyzed by western blotting.

(E) WM852 melanoma cells transfected as in (D) were analyzed by MTT for Gamitrinib (10 μM)-mediated cell killing. Mean ± SEM (n = 3); **p = 0.002.

(F) Melanoma cells with the indicated BRAF genotype were grown as organotypic spheroids in 3D collagen-embedded matrices, incubated with the indicated concentrations of Gamitrinib, stained after 72 hr with calcein-AM (live cells; green) and Topro-3 (dead cells; blue), and analyzed by confocal laser scanning microscopy. Representative images were collected from one of two independent determinations.

See also Figure S6.

Together, the results presented here add complexity to HSP90 homeostasis (Taipale et al., 2010), uncovering a role of the mitochondrial pool(s) of these chaperones (Kang et al., 2007) in selective bioenergetics (Vander Heiden et al., 2009) and stress-response signaling (Hetz and Glimcher, 2009; Yang et al., 2011) in tumors. Although these mechanisms are critical for tumor growth, the pathophysiological context in which mitochondrial proteostasis (Siegelin et al., 2011) connects to bioenergetics and compensatory stress response in vivo remains to be fully elucidated. It may be speculated that the microenvironment of tumor growth, typically deprived of oxygen and nutrients, may produce a chronic degree of mitochondrial proteotoxic stress (Siegelin et al., 2011) that is further exacerbated by the higher biosynthetic needs of transformed cells and the unique structural environment of mitochondria (Haynes and Ron, 2010). In this context, the selective recruitment of HSP90s to tumor mitochondria (Kang et al., 2007) appears ideally poised to buffer organelle proteotoxic stress in general, and specifically to control the (re)folding of CypD (Green and Kroemer, 2004). In turn, this prevents permeability pore opening, especially against oxidative stimuli (Baines et al., 2005; Nakagawa et al., 2005), maintains ATP production via HK-II tethering (Vander Heiden et al., 2009), and connects to downstream survival mechanisms of autophagy (Yang et al., 2011) and GRP78 cytoprotection (Hetz and Glimcher, 2009; Yang et al., 2011). While this adaptive network promotes tumor maintenance in vivo, it may also offer tangible therapeutic prospects, as subcellular targeting of mitochondrial HSP90s is feasible and may selectively affect tumor cells, but not normal tissues (Kang et al., 2009).

EXPERIMENTAL PROCEDURES

Mitochondrial Protein Folding

Mitochondrial protein folding assays were performed as described (Moisoi et al., 2009). Briefly, mitochondrial fractions were isolated from vehicle or Gamitrinib-treated LN229 cells (5 μM for 12 hr) and suspended in equal volume of mitochondrial fractionation buffer containing increasing concentrations of CHAPS (0, 0.05, 0.1, 0.2, 0.5, 1, or 2%). Samples were incubated for 20 min on ice, and detergent-insoluble protein aggregates were

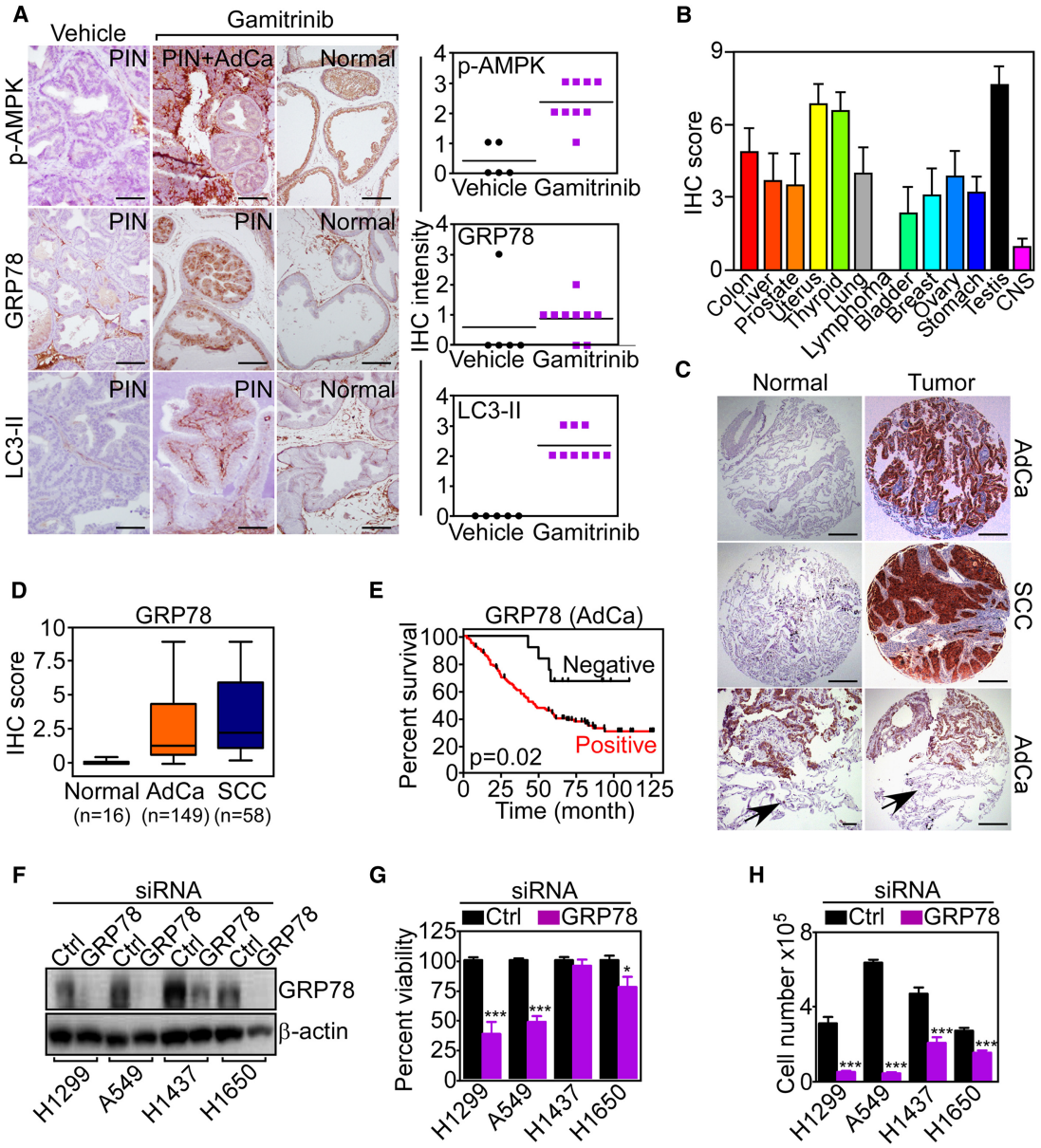

Figure 8. Activation of Mitochondrial Bioenergetics Signaling during Tumor Progression In Vivo

(A) Prostate samples from TRAMP mice treated systemically with vehicle or Gamitrinib were analyzed by immunohistochemistry with antibodies to phosphorylated AMPK (p-AMPK), GRP78, or LC3-II. The histological diagnosis of each prostate tissue section is indicated. Right: quantification of staining intensity for each condition. Scale bars, 50 μm.

(B) Expression of GRP78 in a universal tumor microarray was quantified by an immunohistochemistry (IHC) score. Each bar quantifies expression in the indicated tumor sites. CNS, central nervous system. Mean ± SEM of IHC score in each individual TMA core (n = 7).

(C) Immunohistochemical reactivity of GRP78 expression in a representative NSCLC-TMA. The bottom images show areas of normal lung parenchyma negative for GRP78 expression (arrows) adjacent to GRP78-positive lung cancer. Scale bars, 50 μm and 10 μm (bottom left).

(D) Summary of GRP78 expression in NSCLC or normal lung examined in this study. The number of cases for each histologic condition is indicated. In this series, 13 cases (6%) were not evaluable and 17 cases (8%) were negative for GRP78 expression. Bars correspond to median expression values of IHC scores with interquartile range. AdCa, adenocarcinoma; SCC, squamous cell carcinoma; IHC, immunohistochemistry. The statistical analysis for GRP78 expression in the various cohorts (t test) is as follows: NSCLC versus normal, $p = 1.37 \times 10^{-32}$; AdCa versus normal, $p = 1.49 \times 10^{-21}$; SCC versus normal, $p = 3.9 \times 10^{-13}$; AdCa versus SCC, p = 0.051.

(E) Patients with diagnosis of lung adenocarcinoma (AdCa) with no expression (negative) or high expression (positive) of GRP78 were analyzed for overall survival by the Kaplan-Meier method.

(F) The indicated lung adenocarcinoma cell types were transfected with control (Ctrl) or GRP78-directed siRNA and analyzed by western blotting.

(G and H) The indicated lung cancer cell lines were transfected as in (F) and analyzed for cell viability by MTT (G) or cell proliferation by direct cell counting (H). Mean ± SEM (n = 6). *p = 0.035; ***p = 0.0001–0.0002.

See also Figure S7 and Table S1.

isolated by centrifugation (20,000 × *g*) for 20 min and processed for further analysis.

Glucose and Lactate Determination

Glucose concentrations in cell culture media were determined using a glucose kit (Sigma-Aldrich). Briefly, 2×10^6 cells were seeded in 10 cm tissue-culture dishes for 48 hr and mixed with DMEM in the presence of Gamitrinib or 17-AAG (0–20 μM) for 4 hr; 200 μl aliquots of culture medium were then incubated with 1 ml assay mixture containing 1.5 mM NAD, 1 mM ATP, 1 U/ml HK, and 1 U/ml glucose-6-phosphate dehydrogenase (G6PDH). The glucose concentration was determined by measuring the amount of NAD reduced to NADH by G6PDH, and quantified spectrophotometrically at 340 nm wavelength. Extracellular lactate was measured by a colorimetric assay kit (Abcam). For these experiments, culture medium was replaced with DMEM containing vehicle (DMSO) or Gamitrinib (5 μM) for 5 hr. Changes in lactate concentrations were measured by analysis of lactate-dependent conversion of NADP to NADPH in the presence of excess lactate dehydrogenase (LDH) and were quantified by absorbance at 450 nm. All assays were performed at 25°C under conditions of linear lactate-limited NADPH formation.

Oxygen Consumption

Treated tumor cells were analyzed using a fluorescence oxygen-sensitive-probe-based oxygen measuring kit (Luxcel Bioscience). For these experiments, LN229 cells were plated at increasing cell density ($10–60 \times 10^4$/ml) on black-body, clear-bottom 96-well plates. The culture medium was replaced with 150 μl of phenol-free DMEM containing 10% fetal bovine serum in the presence of 17-AAG or Gamitrinib (10 μM). Cells were further incubated with an oxygen-sensing probe (10 pmol/well), and 100 μl of heavy mineral oil was added to each well to seal the samples from ambient oxygen. After 2 hr incubation at 37°C, oxygen consumption was determined by quantifying the probe fluorescence signal in each well using a plate reader (Beckman Coulter) with excitation and emission wavelengths at 370 nm and 625 nm, respectively.

ATP Measurement

Intracellular ATP concentrations were determined by a luciferin–luciferase method (Biochain) in a microplate luminometer (Beckman Coulter) against standard ATP solutions used as reference. In some experiments, PC3 or LN229 cells were incubated with sodium pyruvate (1 mM) for 7 hr in the presence of vehicle or Gamitrinib before determination of ATP production.

HK Activity

HK activity was measured as the total glucose-phosphorylating activity using a standard G6PDH-coupled assay kit (BioVision). Briefly, mitochondria isolated from Gamitrinib- or 17-AAG-treated LN229 cells, or cultures transfected with various siRNAs, were homogenized in cold PBS and then centrifuged at 1000 × *g* for 10 min at 4°C. HK activity was determined by analysis of G6PDH-dependent conversion of NADP to NADPH in the presence of excess G6PDH and 2 mM glucose, followed by quantification of absorbance at 450 nm. All assays were performed at 25°C under conditions of linear HK-limited NADPH formation.

Genetic Model of Prostate Cancer

All experiments involving vertebrate animals were approved by an Institutional Animal Care and Use Committee at the University of Massachusetts Medical School and The Wistar Institute. Activation of mitochondrial HSP90 signaling was investigated in immunocompetent TRAMP mice, as described (Kang et al., 2011).

Patient Samples

A series of 217 consecutive patients surgically treated for non-small-cell lung cancer (NSCLC) at Fondazione IRCCS Cà Granda Hospital (Milan, Italy) between 2000 and 2004 was available for this study. Informed consent was obtained from all patients enrolled, and the study was approved by an Institutional Review Board of the Fondazione IRCCS Cà Granda, Milan, Italy. Representative tissue blocks from consenting patients with various cancer diagnoses were used under IRB approval to construct the cancer universal TMA (CaU-TMA) and NSCLC TMAs. For the NSCLC-TMAs, four cores of each patient were included in the blocks, along with 16 cores of nonneoplastic lung parenchyma.

Statistical Analysis

Data were analyzed by means of two-sided unpaired t tests using a GraphPad software package (Prism 4.0) for Windows. For analysis of patient samples, groups were compared using the Wilcoxon signed-rank or Student's t test as univariate statistics. For overall survival analysis, the Kaplan-Meyer method was used. Patients negative for GRP78 (immunoreactivity score <0.25) were plotted separately from GRP78-positive cases (score ≥0.25), and the two-sided log-rank test was used to compare the two curves. Data are expressed as the mean ± SD or mean ± SEM of multiple independent experiments. A p value of ≤0.05 was considered statistically significant.

SUPPLEMENTAL INFORMATION

Supplemental Information includes seven figures, one table, and Supplemental Experimental Procedures and can be found with this article online at http://dx.doi.org/10.1016/j.ccr.2012.07.015.

ACKNOWLEDGMENTS

We thank Drs. Winklhofer and Fafournoux for providing luciferase reporter constructs and James Hayden for assistance with confocal microscopy. This work was supported by National Institutes of Health (NIH) Grants CA140043, CA78810, HL54131, and CA118005 (to D.C.A.) and Fondazione Cariplo (to S.B.). Support for Core Facilities utilized in this study was provided by Cancer Center Support Grant (CCSG) CA010815 to The Wistar Institute.

Y.C.C., M.C.C., S.L., J.C.G., T.D., and J.V. designed and carried out experiments. N.N.D. provided CypD knockout MEFs. L.S. provided clinical follow-up data. V.V., S.F., and S.B. provided pathological evaluation of the patient series and analysis of patient data. Y.C.C., M.C.C., S.L., N.D.D., J.V., M.H., L.R.L., S.B., and D.C.A. analyzed results. Y.C.C., M.C.C., S.L., and D.C.A. wrote the manuscript.

Received: October 21, 2011
Revised: April 23, 2012
Accepted: July 24, 2012
Published: September 10, 2012

REFERENCES

Baines, C.P., Kaiser, R.A., Purcell, N.H., Blair, N.S., Osinska, H., Hambleton, M.A., Brunskill, E.W., Sayen, M.R., Gottlieb, R.A., Dorn, G.W., et al. (2005). Loss of cyclophilin D reveals a critical role for mitochondrial permeability transition in cell death. Nature *434*, 658–662.

Egan, D.F., Shackelford, D.B., Mihaylova, M.M., Gelino, S., Kohnz, R.A., Mair, W., Vasquez, D.S., Joshi, A., Gwinn, D.M., Taylor, R., et al. (2011). Phosphorylation of ULK1 (hATG1) by AMP-activated protein kinase connects energy sensing to mitophagy. Science *331*, 456–461.

Gandhi, S., Wood-Kaczmar, A., Yao, Z., Plun-Favreau, H., Deas, E., Klupsch, K., Downward, J., Latchman, D.S., Tabrizi, S.J., Wood, N.W., et al. (2009). PINK1-associated Parkinson's disease is caused by neuronal vulnerability to calcium-induced cell death. Mol. Cell *33*, 627–638.

Green, D.R., and Kroemer, G. (2004). The pathophysiology of mitochondrial cell death. Science *305*, 626–629.

Gwinn, D.M., Shackelford, D.B., Egan, D.F., Mihaylova, M.M., Mery, A., Vasquez, D.S., Turk, B.E., and Shaw, R.J. (2008). AMPK phosphorylation of raptor mediates a metabolic checkpoint. Mol. Cell *30*, 214–226.

Haynes, C.M., and Ron, D. (2010). The mitochondrial UPR—protecting organelle protein homeostasis. J. Cell Sci. *123*, 3849–3855.

He, Y., Correa, A.M., Raso, M.G., Hofstetter, W.L., Fang, B., Behrens, C., Roth, J.A., Zhou, Y., Yu, L., Wistuba, I.I., et al. (2011). The role of PKR/eIF2α signaling pathway in prognosis of non-small cell lung cancer. PLoS ONE *6*, e24855.

Hetz, C., and Glimcher, L.H. (2009). Fine-tuning of the unfolded protein response: assembling the IRE1α interactome. Mol. Cell *35*, 551–561.

Hezel, A.F., and Bardeesy, N. (2008). LKB1; linking cell structure and tumor suppression. Oncogene *27*, 6908–6919.

Inoki, K., Zhu, T., and Guan, K.L. (2003). TSC2 mediates cellular energy response to control cell growth and survival. Cell *115*, 577–590.

Kang, B.H., Plescia, J., Dohi, T., Rosa, J., Doxsey, S.J., and Altieri, D.C. (2007). Regulation of tumor cell mitochondrial homeostasis by an organelle-specific Hsp90 chaperone network. Cell *131*, 257–270.

Kang, B.H., Plescia, J., Song, H.Y., Meli, M., Colombo, G., Beebe, K., Scroggins, B., Neckers, L., and Altieri, D.C. (2009). Combinatorial drug design targeting multiple cancer signaling networks controlled by mitochondrial Hsp90. J. Clin. Invest. *119*, 454–464.

Kang, B.H., Tavecchio, M., Goel, H.L., Hsieh, C.C., Garlick, D.S., Raskett, C.M., Lian, J.B., Stein, G.S., Languino, L.R., and Altieri, D.C. (2011). Targeted inhibition of mitochondrial Hsp90 suppresses localised and metastatic prostate cancer growth in a genetic mouse model of disease. Br. J. Cancer *104*, 629–634.

Kaufman, R.J., Scheuner, D., Schröder, M., Shen, X., Lee, K., Liu, C.Y., and Arnold, S.M. (2002). The unfolded protein response in nutrient sensing and differentiation. Nat. Rev. Mol. Cell Biol. *3*, 411–421.

Kurtoglu, M., Gao, N., Shang, J., Maher, J.C., Lehrman, M.A., Wangpaichitr, M., Savaraj, N., Lane, A.N., and Lampidis, T.J. (2007). Under normoxia, 2-deoxy-D-glucose elicits cell death in select tumor types not by inhibition of glycolysis but by interfering with N-linked glycosylation. Mol. Cancer Ther. *6*, 3049–3058.

Laderoute, K.R., Amin, K., Calaoagan, J.M., Knapp, M., Le, T., Orduna, J., Foretz, M., and Viollet, B. (2006). 5′-AMP-activated protein kinase (AMPK) is induced by low-oxygen and glucose deprivation conditions found in solid-tumor microenvironments. Mol. Cell. Biol. *26*, 5336–5347.

Leskovar, A., Wegele, H., Werbeck, N.D., Buchner, J., and Reinstein, J. (2008). The ATPase cycle of the mitochondrial Hsp90 analog Trap1. J. Biol. Chem. *283*, 11677–11688.

Ma, Y., and Hendershot, L.M. (2004). The role of the unfolded protein response in tumour development: friend or foe? Nat. Rev. Cancer *4*, 966–977.

Machida, K., Ohta, Y., and Osada, H. (2006). Suppression of apoptosis by cyclophilin D via stabilization of hexokinase II mitochondrial binding in cancer cells. J. Biol. Chem. *281*, 14314–14320.

Majewski, N., Nogueira, V., Bhaskar, P., Coy, P.E., Skeen, J.E., Gottlob, K., Chandel, N.S., Thompson, C.B., Robey, R.B., and Hay, N. (2004). Hexokinase-mitochondria interaction mediated by Akt is required to inhibit apoptosis in the presence or absence of Bax and Bak. Mol. Cell *16*, 819–830.

Mayer, M.P. (2010). Gymnastics of molecular chaperones. Mol. Cell *39*, 321–331.

Mihaylova, M.M., and Shaw, R.J. (2011). The AMPK signalling pathway coordinates cell growth, autophagy and metabolism. Nat. Cell Biol. *13*, 1016–1023.

Moisoi, N., Klupsch, K., Fedele, V., East, P., Sharma, S., Renton, A., Plun-Favreau, H., Edwards, R.E., Teismann, P., Esposti, M.D., et al. (2009). Mitochondrial dysfunction triggered by loss of HtrA2 results in the activation of a brain-specific transcriptional stress response. Cell Death Differ. *16*, 449–464.

Nakagawa, T., Shimizu, S., Watanabe, T., Yamaguchi, O., Otsu, K., Yamagata, H., Inohara, H., Kubo, T., and Tsujimoto, Y. (2005). Cyclophilin D-dependent mitochondrial permeability transition regulates some necrotic but not apoptotic cell death. Nature *434*, 652–658.

Pfaffenbach, K.T., and Lee, A.S. (2011). The critical role of GRP78 in physiologic and pathologic stress. Curr. Opin. Cell Biol. *23*, 150–156.

Richter, K., Reinstein, J., and Buchner, J. (2007). A Grp on the Hsp90 mechanism. Mol. Cell *28*, 177–179.

Robey, R.B., and Hay, N. (2006). Mitochondrial hexokinases, novel mediators of the antiapoptotic effects of growth factors and Akt. Oncogene *25*, 4683–4696.

Rodina, A., Vilenchik, M., Moulick, K., Aguirre, J., Kim, J., Chiang, A., Litz, J., Clement, C.C., Kang, Y., She, Y., et al. (2007). Selective compounds define Hsp90 as a major inhibitor of apoptosis in small-cell lung cancer. Nat. Chem. Biol. *3*, 498–507.

Siegelin, M.D., Dohi, T., Raskett, C.M., Orlowski, G.M., Powers, C.M., Gilbert, C.A., Ross, A.H., Plescia, J., and Altieri, D.C. (2011). Exploiting the mitochondrial unfolded protein response for cancer therapy in mice and human cells. J. Clin. Invest. *121*, 1349–1360.

Tabas, I., and Ron, D. (2011). Integrating the mechanisms of apoptosis induced by endoplasmic reticulum stress. Nat. Cell Biol. *13*, 184–190.

Taipale, M., Jarosz, D.F., and Lindquist, S. (2010). HSP90 at the hub of protein homeostasis: emerging mechanistic insights. Nat. Rev. Mol. Cell Biol. *11*, 515–528.

Tan, S.S., Ahmad, I., Bennett, H.L., Singh, L., Nixon, C., Seywright, M., Barnetson, R.J., Edwards, J., and Leung, H.Y. (2011). GRP78 up-regulation is associated with androgen receptor status, Hsp70-Hsp90 client proteins and castrate-resistant prostate cancer. J. Pathol. *223*, 81–87.

Trepel, J., Mollapour, M., Giaccone, G., and Neckers, L. (2010). Targeting the dynamic HSP90 complex in cancer. Nat. Rev. Cancer *10*, 537–549.

Vander Heiden, M.G., Cantley, L.C., and Thompson, C.B. (2009). Understanding the Warburg effect: the metabolic requirements of cell proliferation. Science *324*, 1029–1033.

Villanueva, J., Vultur, A., Lee, J.T., Somasundaram, R., Fukunaga-Kalabis, M., Cipolla, A.K., Wubbenhorst, B., Xu, X., Gimotty, P.A., Kee, D., et al. (2010). Acquired resistance to BRAF inhibitors mediated by a RAF kinase switch in melanoma can be overcome by cotargeting MEK and IGF-1R/PI3K. Cancer Cell *18*, 683–695.

Wolf, A., Agnihotri, S., Micallef, J., Mukherjee, J., Sabha, N., Cairns, R., Hawkins, C., and Guha, A. (2011). Hexokinase 2 is a key mediator of aerobic glycolysis and promotes tumor growth in human glioblastoma multiforme. J. Exp. Med. *208*, 313–326.

Wullschleger, S., Loewith, R., and Hall, M.N. (2006). TOR signaling in growth and metabolism. Cell *124*, 471–484.

Yang, S., Wang, X., Contino, G., Liesa, M., Sahin, E., Ying, H., Bause, A., Li, Y., Stommel, J.M., Dell'antonio, G., et al. (2011). Pancreatic cancers require autophagy for tumor growth. Genes Dev. *25*, 717–729.

Zheng, B., Jeong, J.H., Asara, J.M., Yuan, Y.Y., Granter, S.R., Chin, L., and Cantley, L.C. (2009). Oncogenic B-RAF negatively regulates the tumor suppressor LKB1 to promote melanoma cell proliferation. Mol. Cell *33*, 237–247.

Zhou, H., Zhang, Y., Fu, Y., Chan, L., and Lee, A.S. (2011). Novel mechanism of anti-apoptotic function of 78-kDa glucose-regulated protein (GRP78): endocrine resistance factor in breast cancer, through release of B-cell lymphoma 2 (BCL-2) from BCL-2-interacting killer (BIK). J. Biol. Chem. *286*, 25687–25696.

Cancer Cell
Article

Suppression of Acquired Docetaxel Resistance in Prostate Cancer through Depletion of Notch- and Hedgehog-Dependent Tumor-Initiating Cells

Josep Domingo-Domenech,[1,6,*] Samuel J. Vidal,[1] Veronica Rodriguez-Bravo,[1,5] Mireia Castillo-Martin,[1,6] S. Aidan Quinn,[1] Ruth Rodriguez-Barrueco,[1] Dennis M. Bonal,[1,6] Elizabeth Charytonowicz,[1,6] Nataliya Gladoun,[1,6] Janis de la Iglesia-Vicente,[1,6] Daniel P. Petrylak,[1,2] Mitchell C. Benson,[1,3] Jose M. Silva,[1,4] and Carlos Cordon-Cardo[1,3,4,6,*]

[1]Herbert Irving Comprehensive Cancer Center
[2]Department of Medicine, Division of Hematology/Oncology
[3]Department of Urology
[4]Department of Pathology and Cell Biology
Columbia University College of Physicians and Surgeons, Columbia University, New York, NY 10032, USA
[5]Present address: Molecular Biology Program, Memorial Sloan-Kettering Cancer Center, New York, NY 10065, USA
[6]Present address: Department of Pathology, Mount Sinai School of Medicine, New York, NY 10029, USA
*Correspondence: josep.domingo-domenech@mssm.edu (J.D.-D.), carlos.cordon-cardo@mssm.edu (C.C.-C.)
http://dx.doi.org/10.1016/j.ccr.2012.07.016

SUMMARY

Acquired resistance to Docetaxel precedes fatality in hormone-refractory prostate cancer (HRPC). However, strategies that target Docetaxel resistant cells remain elusive. Using in vitro and in vivo models, we identified a subpopulation of cells that survive Docetaxel exposure. This subpopulation lacks differentiation markers and HLA class I (HLAI) antigens, while overexpressing the Notch and Hedgehog signaling pathways. These cells were found in prostate cancer tissues and were related to tumor aggressiveness and poor patient prognosis. Notably, targeting Notch and Hedgehog signaling depleted this population through inhibition of the survival molecules AKT and Bcl-2, suggesting a therapeutic strategy for abrogating Docetaxel resistance in HRPC. Finally, these cells exhibited potent tumor-initiating capacity, establishing a link between chemotherapy resistance and tumor progression.

INTRODUCTION

Prostate cancer is the most common cancer diagnosis and second leading cause of cancer-related death in men (Jemal et al., 2011). Despite the availability of local treatment, many patients relapse after primary therapy. Initially, relapsed prostate cancer patients have a hormone-dependent disease that responds to androgen withdrawal. However, despite hormonal manipulations prostate cancer progresses to a hormone refractory state (Pound et al., 1999). Docetaxel is a taxane antimitotic agent currently used as the standard therapy for patients with hormone-refractory prostate cancer (HRPC) (Petrylak et al., 2004; Tannock et al., 2004). However, patients treated with this agent inexorably experience disease progression, and because limited effective therapies exist in this context, acquired resistance to Docetaxel is commonly fatal. Presently, the main identified mechanisms of acquired resistance relate to the expression of β-tubulin isoforms/mutations and the activation of drug efflux pumps, among others (Mahon et al., 2011; Seruga et al., 2011). Unfortunately, in spite of these advances, treatment of Docetaxel-resistant patients remains a critical clinical challenge. In this study, we sought to identify a therapeutic strategy to abrogate acquired resistance to Docetaxel in HRPC.

Significance

Acquisition of chemotherapy resistance is a devastating and widespread phenomenon in clinical oncology. Although Docetaxel improves survival in HRPC, patients who initially respond acquire resistance, and this event precedes therapeutic stalemate and death. This study identified a subpopulation of prostate cancer cells that contribute to Docetaxel resistance. The molecular characterization of this subpopulation culminated in an in vivo model in which a combination strategy using Docetaxel with Notch and Hedgehog inhibitors abrogated the acquisition of Docetaxel resistance. These findings provide the rationale for a therapeutic strategy in a currently intractable clinical challenge.

RESULTS

Docetaxel-Resistant Prostate Cancer Cells Lack Differentiation Markers and Show Upregulation of the Notch and Hedgehog Signaling Pathways

To study the phenomenon of relapse following Docetaxel therapy, we generated in vitro chemoresistance models using the well-established HRPC cell lines DU145 and 22Rv1. Drug-resistant cells were established by exposure to increasing concentrations of Docetaxel, and resistance was validated by cell viability, colony formation, annexin V, and poly-(ADP-ribose) polymerase (PARP) cleavage assays (Figures S1A–S1D available online). Gene expression profiling using oligonucleotide microarrays was performed to compare the sensitive parental cells (DU145/22Rv1) with the Docetaxel-resistant cells (DU145-DR/22Rv1-DR). This analysis revealed 1,245 deregulated genes in DU145-DR and 990 deregulated genes in 22Rv1-DR, of which 247 overlapped (Figure 1A). Of these overlapping genes, 29.5% were consistently upregulated and 70.5% were consistently downregulated. Gene Ontology (GO) analysis of these 247 genes revealed that, besides expected changes in biological processes, such as cell proliferation, cell death, and drug response, other categories, including cell differentiation, antigen presentation, and developmental/stemness pathways were significantly represented (Figure 1B).

Regarding differentiation, we focused on the expression of the low molecular weight cytokeratins (CKs) 18 and 19, because these epithelial markers are specifically expressed in normal luminal human prostate cells and prostate cancer (Ali and Epstein, 2008). We also analyzed prostate-related biomarkers, including the androgen receptor (AR), prostate-specific antigen (PSA), and prostate-specific membrane antigen (PSMA). We observed that DU145-DR and 22Rv1-DR showed a dramatic decrease in mRNA (Figure 1C) and protein levels of CK18 and CK19 (Figures 1D and 1E). 22Rv1, which expresses prostate-related differentiation markers, showed a decrease in mRNA and protein levels of PSMA and PSA, as well as a decrease in AR protein expression in Docetaxel-resistant cells (Figure 1D). Because loss of luminal markers could indicate a possible shift to a basal phenotype, we analyzed the expression of high molecular weight CKs and the prostate basal markers CD44 and p63. High molecular weight CKs (CK5 and CK14) and p63 remained undetectable in the drug-resistant cells as well as in their respective parental cells (Figures 1C and 1D). CD44 mRNA and protein levels were increased in DU145-DR and decreased in 22RV1-DR relative to their parental lines, indicating a cell line-dependent effect (Figures 1C and 1D). Therefore, the decrease in luminal differentiation and prostate-specific markers was not associated with a consistent shift to a basal phenotype. Further, Docetaxel-resistant cells did not express other lineage markers (Figure S1E). Finally, Docetaxel-resistant cells showed a strong downregulation of the mRNA level of HLAI antigens A, B, C, E, F, and G (Figure 1C), which was confirmed with a pan-HLAI antibody by immunoblotting (Figure 1D) and immunofluorescence (Figure 1E).

Regarding the developmental/stemness category, we observed that Docetaxel-resistant cells showed a marked upregulation of the Notch and Hedgehog signaling pathways. There was increased *NOTCH2* and *HES1* mRNA levels (Figure 1C), which was associated with increased cleaved Notch2 and Hes1 protein expression (Figure 1D) and cleaved Notch2 localization within the nucleus, where it exerts its activity (Figure 1E). Moreover, resistant cells showed reduced expression of the Hedgehog receptor Patched, which normally inhibits the activity of Smo, a positive regulator of the Hedgehog pathway (Figures 1C and 1D). This was associated with increased protein levels and nuclear localization of the transcription factors Gli1 and Gli2 (Figures 1D and 1E), consistent with Hedgehog pathway activation. In summary, Docetaxel-resistant HRPC cells displayed a phenotype characterized by loss of epithelial differentiation markers, prostate-specific antigens, and antigen presentation molecules, as well as an increase in the Notch and Hedgehog developmental signaling pathways.

Primary and Metastatic Prostate Cancer Tissues Contain Cells that Display the Docetaxel Resistance Phenotype and Associate with Tumor Aggressiveness

We next investigated whether cells with the identified Docetaxel-resistant phenotype were detectable in human prostate cancer tissue samples. We analyzed paraffin embedded tissues from 31 untreated primary prostate tumors from patients who had undergone radical prostatectomy and 36 metastatic prostate cancer tissue samples from untreated or Docetaxel-treated patients. Immunofluorescence-based double staining revealed that all prostate cancer tumors had a small subpopulation of CK-negative (CK^-) tumor cells that displayed the Docetaxel-resistant phenotype observed in our in vitro models. $CK18^-$/$CK19^-$ cells were mainly HLAI-negative ($HLAI^-$) (98.5% ± 1.1%) and displayed nuclear expression of cleaved Notch2 (72.8% ± 15.1%), Gli1 (67.5% ± 17.3%) and Gli2 (67% ± 17.3%), whereas CK-positive (CK^+) cells were HLAI-positive ($HLAI^+$, 99.6% ± 0.3%) and showed significantly lower nuclear expression of developmental transcription factors ($p < 0.0001$, Figure 2A). Moreover, CK^- tumor cells lacked expression of nuclear AR, whereas CK^+ cells displayed nuclear AR in 71.8% ± 14.3% of the cells ($p < 0.0001$; Figure 2B). Further, CK^- cells did not express high molecular weight CK5 and CK14, or p63 (Figure S2A). Finally, CK^- cells did not exhibit morphological criteria of necrosis (Figure S2B), and a subset expressed the proliferative marker Ki67 (Figure S2C).

Quantitative analysis revealed that in 31 primary tumors CK^- cells accounted for a mean of 1.3% ± 0.94% of the total tumor cell population, whereas in the 36 metastatic prostate tissues this cell population accounted for 3.2% ± 2.2% (Table S1). Therefore, specimens from advanced disease exhibited a higher percentage of CK^- cells ($p < 0.0001$). Notably, 14 out of the 36 metastatic prostate cancer samples analyzed belonged to patients who had been previously treated with Docetaxel and had the highest percentage of CK^- cells (5.2% ± 2.1%), whereas tumors of the other 22 untreated patients had a lower percentage of CK^- cells (1.8% ± 1.4%; $p < 0.0001$; Figure 2C). Thus, cells with the Docetaxel-resistant phenotype were more abundant in metastatic tumors and after chemotherapy treatment.

Next, we investigated if this subpopulation had prognostic significance in primary prostate cancer. Quantitative analysis performed in the 31 primary prostate tumor samples showed that the percentage of the CK^- cells was significantly related to established clinicopathologic prognostic factors like tumor

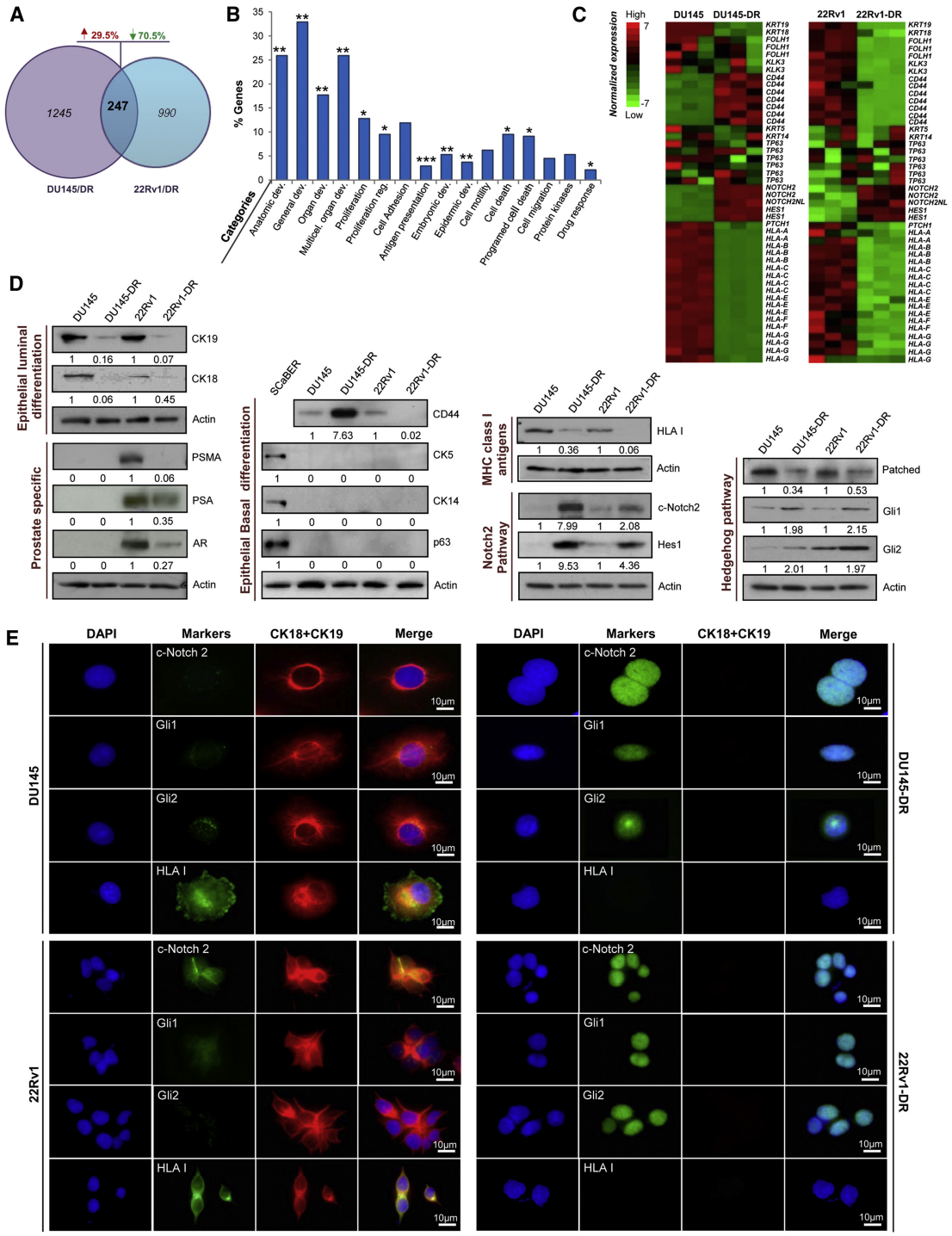

Figure 1. Phenotypical Characterization of Docetaxel-Resistant Cells

(A) Genes with at least 1.8-fold increase (↑) or decrease (↓) in transcript expression comparing parental and Docetaxel-resistant cells.

(B) Gene ontology categories of overlapping genes. Categories with statistical significance ($p \leq 0.01$) are represented. *GO categories related to cell proliferation, cell death, and response to drugs. **GO categories related to developmental processes. ***GO category related to antigen presentation.

(C) Heatmap illustrates epithelial differentiation, prostate specific, HLAI, and developmental (Notch and Hedgehog) gene expression of parental and Docetaxel-resistant cells.

(D) Immunoblotting and quantification of parental and Docetaxel-resistant cells for indicated proteins. SCaBER was used as a positive control for high molecular weight cytokeratins and p63.

(E) Immunofluorescent staining of parental and Docetaxel-resistant cells for indicated proteins.

See also Figure S1.

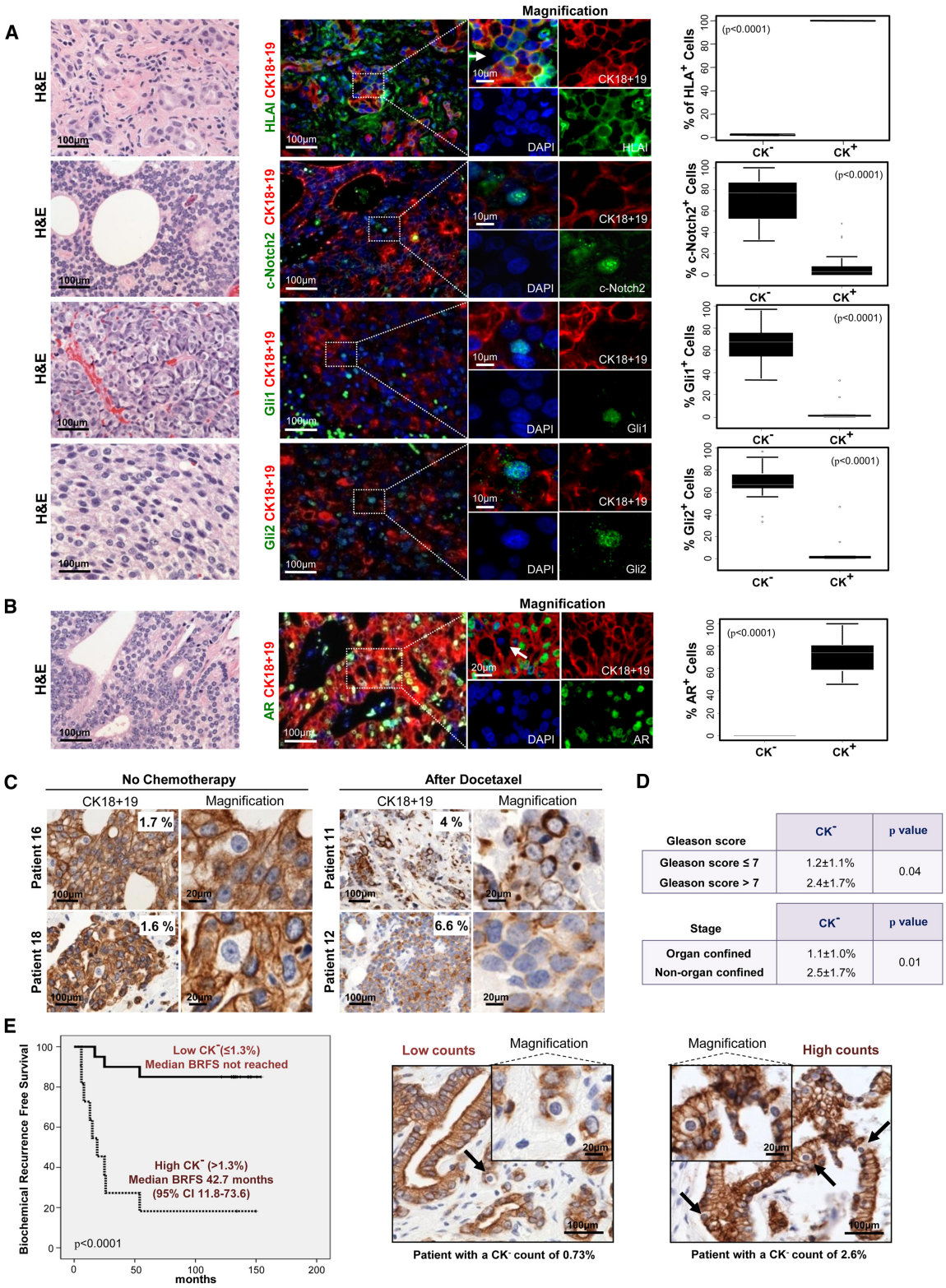

Figure 2. Docetaxel-Resistant Cells Are Present in Prostate Cancer Tissue Samples and Associate with Tumor Aggressiveness

(A and B) Hematoxylin and eosin (H&E) and immunofluorescent staining analyses of prostate cancer metastases for indicated proteins. White arrows point to CK^- cells. Corresponding box plots show protein expression in CK^- and CK^+ cells, including (from top) upper outliers, maximum (excluding outliers), upper quartile, median, lower quartile, minimum (excluding outliers), and lower outliers.

(C) CK18 and CK19 immunohistochemistry of clinical metastatic prostate cancer tissues nontreated and treated with Docetaxel.

grade (Gleason score) and pathological disease stage (Figure 2D). Further, patients with a high percentage of CK$^-$ cells had a shorter time to biochemical (PSA) relapse than did patients with a low percentage of CK$^-$cells ($p < 0.0001$; Figure 2E). In summary, cells displaying the Docetaxel-resistance phenotype were detectable in primary and metastatic prostate cancer tissue samples, increased in number after chemotherapy, and their abundance was associated with tumor aggressiveness and clinical prognosis.

A Subpopulation of Prostate Cancer Cells Exhibits the Docetaxel Resistance Phenotype and Survives Docetaxel Exposure

We next investigated whether the changes observed during the acquisition of Docetaxel resistance were the result of transition of sensitive cells toward a resistant phenotype or if chemotherapy had selected for a subpopulation of intrinsically Docetaxel-resistant cells (Figure 3A). Because both DU145-DR and 22Rv1-DR cells displayed downregulation of CK19 and CK18, we chose these markers to determine if CK$^-$ cells were present in the parental cell lines before any treatment. Immunofluorescence and flow cytometry revealed a small CK$^-$ subpopulation in both DU145 and 22Rv1 parental cells (Figure 3B).

We next investigated if this subpopulation could contribute to the acquisition of Docetaxel resistance. To test this hypothesis we designed a strategy to track the behavior of CK$^-$ cells under chemotherapy. We cloned a region of the CK19 promoter into a GFP vector, creating a reporter system for the expression of CK19 under different experimental conditions (Tripathi et al., 2005). DU145 and 22Rv1 parental cells were transfected with the pCK19-GFP construct and selected to establish stable cell lines named DU145-pCK19-GFP and 22Rv1-pCK19-GFP. Coexpression of CK19 and GFP was validated by immunofluorescence (Figure S3A), and PCR confirmed stable integration of the construct (data not shown).

We then tested whether CK19/GFP$^-$ cells survived Docetaxel exposure and were responsible for acquired chemoresistance (Figure 3C). Analysis of DU145-pCK19-GFP cells by flow cytometry showed that CK19/GFP$^+$ cells were a majority (87.5% ± 10.4%) of the total population before any treatment. However, the viable CK19/GFP$^+$ population was reduced to 28.3% ± 10.6% after exposure to 10 nM Docetaxel for 72 hr. In contrast, the viable CK19/GFP$^-$ population increased from 4.4% ± 4.3% to 73.1% ± 10.2%. Similar results were observed in 22Rv1-pCK19-GFP cells after exposure to 50 nM Docetaxel, with viable CK19/GFP$^-$ cells increasing from 8.5% ± 3.5% to 78.6% ± 4.1%, whereas viable CK19/GFP$^+$ cells decreased from 85.0% ± 2.0% to 19.3% ± 3.4%. Further, colony formation assays showed that only CK19/GFP$^-$ cells formed colonies after exposure to Docetaxel (Figure 3D). Next, we analyzed the behavior of DU145-pCK19-GFP and 22Rv1-pCK19-GFP in the presence of Docetaxel by live imaging. We observed that CK19/GFP$^-$ cells were able to divide and exit mitosis under therapy, whereas CK19/GFP$^+$ cells died after mitotic arrest (Figure 3E; Figure S3B; Movies S1 and S2). Finally, we characterized the CK19/GFP$^-$ and CK19/GFP$^+$ populations of DU145-pCK19-GFP and 22Rv1-pCK19-GFP, both under control and Docetaxel-treated conditions (Figure 3F). Immunoblots confirmed that CK19/GFP$^-$ cells exhibited the Docetaxel-resistance markers, namely, reduced CK18, CK19, HLAI, Patched, AR, PSMA, and PSA expression, as well as upregulation of cleaved Notch2, Hes1, Gli1, and Gli2. Moreover, unsorted cells treated with Docetaxel underwent the expected reduction in differentiation markers and an increase in developmental signaling pathways.

We also observed that CK19/GFP$^-$ cells exhibited a multidrug resistance phenotype. Indeed, CK19/GFP$^-$ cells from DU145-pCK19-GFP and 22Rv1-pCK19-GFP treated with DNA damaging agents (Mitoxantrone and Cisplatin) and other antimitotic agents (Vinorelbine) formed colonies, whereas CK19/GFP$^+$ cells failed to do so (Figure 3G).

Combined Notch and Hedgehog Signaling Inhibition Depletes Docetaxel-Resistant Prostate Cancer Cells

Given our findings that CK19$^-$ cells mediate acquired Docetaxel resistance in vitro and that these cells were more abundant in prostate cancer patients treated with Docetaxel, we investigated whether these cells could be targeted to inhibit acquired resistance to Docetaxel. The upregulation of Notch and Hedgehog signaling in DU145-DR and 22Rv1-DR (Figure 1) prompted us to investigate the role of these pathways in the survival of CK$^-$ cells. We used shRNAs to knock down genes critical for Notch and Hedgehog signaling in DU145-pCK19-GFP and 22Rv1-pCK19-GFP. ShRNAs against *NOTCH2*, *GLI1*, and *GLI2* were used in biological replicates conferring a 90% reduction in protein levels (Figure S4A). *NOTCH2* knockdown reduced the mRNA levels of the Notch target genes *HES1* and *HEY1*, and *GLI1* and *GLI2* knockdown reduced the mRNA levels of the Hedgehog target gene *SMO*, confirming that knockdown of these genes disrupted Notch and Hedgehog signaling (Figure S4B).

We then analyzed the effects of Notch and Hedghehog knockdown on CK19$^-$ cells. Colony formation assays of GFP$^-$ and GFP$^+$ sorted DU145-pCK19-GFP and 22Rv1-pCK19-GFP cells expressing shRNAs against *NOTCH2*, *GLI1*, and *GLI2* revealed that individual knockdown of Notch or Hedgehog signaling did not have an effect on the colony formation of CK19/GFP$^-$ or CK19/GFP$^+$ cells (Figure 4A; Figure S4C). In contrast, concomitant knockdown of both pathways dramatically abrogated the ability of CK19/GFP$^-$ cells to form colonies, whereas CK19/GFP$^+$ cells were unaffected (Figure 4A; Figure S4C). These results indicate that both Notch and Hedgehog signaling pathways in combination are required for the maintenance of cells displaying the Docetaxel-resistant phenotype.

We further validated these findings using the chemical inhibitors Cyclopamine and GDC-0449, Hedgehog pathway antagonists that act at the level of Smo (Chen et al., 2002; Karhadkar et al., 2004; Robarge et al., 2009; Taipale et al., 2000), and DBZ and Compound E, gamma-secretase inhibitors that block

(D) Association between the percentage of CK$^-$ cells with Gleason Score and pathological stage in primary prostate cancer tissues.
(E) Kaplan-Meier analysis of biochemical recurrence free survival of primary prostate cancer patients (n = 31) with low CK$^-$ content (≤1.3%) compared to high CK$^-$ content (>1.3%). Representative samples with low and high percentage of CK$^-$ cells. Black arrows point to CK$^-$ cells. Data is represented as means ± SD. See also Figure S2 and Table S1.

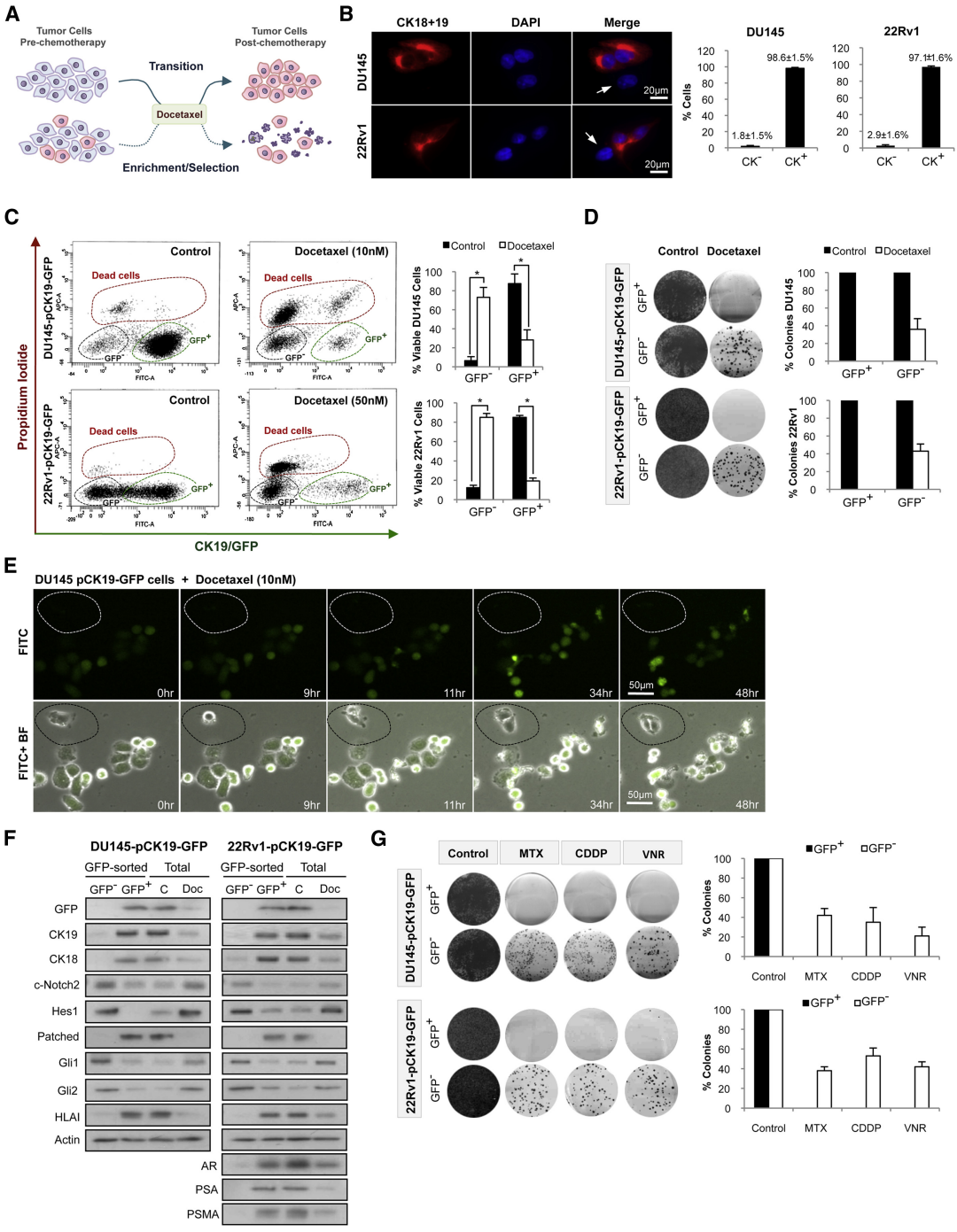

Figure 3. Docetaxel Exposure Selects for Pre-Existing Resistant Prostate Cancer Cells

(A) Working hypotheses; transition versus enrichment-selection induced by Docetaxel.

(B) Immunofluorescence and flow cytometry quantification of CK18 and CK19 expression in DU145 and 22Rv1. White arrows point to cells with a CK^{-} phenotype.

(C) Flow cytometry analysis of DU145-pCK19-GFP and 22Rv1-pCK19-GFP treated with Docetaxel (72 hr).

(D) Colony formation assay and quantification of sorted DU145-pCK19-GFP and 22Rv1-pCK19-GFP cells cultured with Docetaxel, 10 and 50 nM respectively, for 72 hr, or DMSO.

(E) Time-lapse microscopy of DU145-pCK19-GFP treated with Docetaxel. Dotted area shows a CK19/GFP^{-} cell.

(F) Immunoblots of GFP and Docetaxel-resistance markers in DU145-pCK19-GFP and 22Rv1-pCK19-GFP sorted cells, as well as in unsorted DU145-pCK19-GFP and 22Rv1-pCK19-GFP cells exposed to Docetaxel (72 hr) at the same concentrations as in (D).

(G) Colony formation assays and quantification of DU145-pCK19-GFP and 22Rv1-pCK19-GFP sorted cells cultured with or without Mitoxantrone 125 and 500 nM, Cisplatin 5 and 2.5 μM, and Vinorelbine 500 and 750 nM, respectively (all 72 hr). Data is represented as means ± SD of triplicate experiments. *$p < 0.0001$. See also Figure S3 and Movies S1 and S2.

proteolytic processing of Notch (Seiffert et al., 2000; van Es et al., 2005). Quantitative RT-PCR of pathway target genes confirmed that these pharmacological inhibitors were targeting their respective pathways (Figure S4D). Flow cytometry analysis of DU145-pCK19-GFP and 22Rv1-pCK19-GFP cells treated with a combination of Notch and Hedgehog inhibitors showed a significant loss in cell viability of CK19/GFP$^-$ cells and no effect on CK19/GFP$^+$ cells (Figure 4B). The decrease in CK19/GFP$^-$ cell viability was due to the induction of an apoptotic response, as demonstrated by Caspase-3 and PARP cleavage (Figure 4C; Figure S4E). Finally, as observed in the genetic knockdown studies, colony formation assays confirmed that combined pharmacological inhibition of Notch and Hedgehog signaling selectively depleted CK19/GFP$^-$ cells (Figure 4D; Figure S4F).

These results indicated that combined Notch and Hedgehog inhibition could target CK19$^-$ Docetaxel-resistant cells. Therefore, we hypothesized that a combination strategy of Docetaxel plus developmental pathway inhibitors could ablate both CK$^+$ and CK$^-$ compartments. Indeed, flow cytometry analysis of DU145-pCK19-GFP and 22Rv1-pCK19-GFP revealed that triple combinations of Cyclopamine and DBZ with Docetaxel reduced the viability of both CK19/GFP$^-$ and CK19/GFP$^+$ cells (Figure 4E). As expected, triple combination completely ablated the colony formation capacity of both DU145 and 22Rv1 parental cell lines (Figure 4F).

Abrogation of Acquired Docetaxel Resistance In Vivo through Notch and Hedgehog Signaling Inhibition

We next evaluated the effects of this combination strategy in vivo. For these experiments dexamethasone was used as a coadjuvant therapy to reduce the gut toxicity of gamma-secretase inhibitors (Real et al., 2009). NOD/SCID mice bearing DU145 and 22Rv1 xenografts were treated with dexamethasone alone, dual combinations (e.g., dexamethasone plus Docetaxel), triple combinations (e.g., dexamethasone plus Docetaxel plus DBZ), or a quadruple combination (dexamethasone plus Docetaxel plus Cyclopamine plus DBZ). Xenografts treated with dexamethasone and Docetaxel temporarily stabilized tumor volume before progression. Remarkably, mice treated with the quadruple combination showed a robust inhibition of tumor growth during the course of the experiment (15 weeks), compared to mice under the other combination regimes, therefore mirroring our in vitro results (Figure 5A). Inhibitory effects of the drugs on their respective signaling pathways was confirmed by testing the mRNA levels of Notch and Hedgehog pathway genes in tumor cells obtained from xenografts 4 hr after drug administration (Figure 5B). Moreover, in agreement with our in vitro and human sample results, Docetaxel treatment of DU145 and 22Rv1 xenografts enriched for CK$^-$ cells, and xenografts treated with the quadruple combination displayed a lower percentage of CK$^-$ cells in comparison to Docetaxel-treated animals (Figure 5C). To control for possible drug toxicity associated with the quadruple combination, we substituted Docetaxel for Etoposide, a chemotherapy agent with minor efficacy in prostate cancer (Figure S5A). Whereas similar toxicity (% body weight reduction) was observed (Figure S5B), there was no significant delay in tumor growth (Figure S5C), indicating that the efficacy of the quadruple therapy was not a result of drug toxicity. These results indicated that CK$^-$ Docetaxel-resistant cells were critically dependent on Notch and Hedgehog signaling, giving the rationale for an efficacious combination strategy.

Notch and Hedgehog Signaling Regulate Survival Molecules in Docetaxel-Resistant Cells

Our studies suggested that Notch and Hedgehog signaling were critical regulators of acquired Docetaxel resistance (Figures 4 and 5). In order to elucidate the molecular mechanisms underlying these observations, we investigated the downstream effectors of Notch and Hedgehog signaling in CK19/GFP$^-$ Docetaxel-resistant cells. Notch signaling can activate the prosurvival PI3K/AKT signaling pathway (Meurette et al., 2009; Palomero et al., 2007), whereas Hedgehog signaling can upregulate the antiapoptotic molecule Bcl-2 (Dierks et al., 2007; Singh et al., 2010). Therefore, we speculated that Notch and Hedgehog signaling may regulate CK19/GFP$^-$ Docetaxel-resistant cells through prosurvival and antiapoptotic mechanisms, respectively.

We first examined AKT phosphorylation (Ser473) and Bcl-2 expression in the CK19/GFP$^-$ and CK19/GFP$^+$ populations of DU145-pCK19-GFP and 22Rv1-pCK19-GFP. Immunoblots revealed that in both cell lines the CK19/GFP$^-$ compartment displayed increased levels of p-AKT (Ser473) and Bcl-2 (Figure 6A). To assess whether these survival molecules were indeed regulated by Notch and Hedgehog signaling in CK19/GFP$^-$ cells, we performed experiments using chemical inhibitors of Notch and Hedgehog signaling. Immunoblots showed that inhibition of Notch signaling and inhibition of Hedgehog signaling significantly reduced p-AKT (Ser473) and Bcl-2 levels, respectively (Figure 6B; Figure S6A).

To determine whether the activity of these downstream effectors was necessary for CK19/GFP$^-$ cell survival, we tested the combined effects of LY294002, a selective inhibitor of the PI3K/AKT pathway (Vlahos et al., 1994), and ABT-737, an inhibitor of the Bcl-2 family members (Oltersdorf et al., 2005). These studies revealed that combined, but not individual, PI3K/AKT and Bcl-2 inhibition induced apoptosis (Figure 6C) and reduced colony formation (Figure 6D) in CK19/GFP$^-$ cells, recapitulating the effect observed with Notch and Hedgehog inhibitors (see Figure 4). To further validate the role of Notch and Hedgehog signaling in CK19/GFP$^-$ cells through PI3K/AKT and Bcl-2, we performed rescue experiments. As expected, combined inhibition of Notch and Hedgehog signaling reduced the viability and colony formation of CK19/GFP$^-$ cells, whereas overexpression of either a constitutively active myristoylated form of AKT (MYR-AKT) or Bcl-2 reduced the inhibitory effect of these inhibitors (Figures 6E and 6F). Interestingly, we further observed that overexpression of either MYR-AKT or Bcl-2 in the CK19/GFP$^+$ populations of DU145-pCK19-GFP and 22Rv1-pCK19-GFP was sufficient to confer a multidrug resistant phenotype in these previously sensitive cells (Figure 6G). This data was consistent with previous reports that overexpression of these molecules contributes to resistance to an array of chemotherapeutics (Pommier et al., 2004).

Next, we assessed the expression of drug efflux mechanisms in CK19/GFP$^-$ cells. Current evidence suggests that the taxane chemotherapeutics are substrates for p-Glycoprotein/ABCB1 (Gottesman et al., 2002). We observed that P-gp/ABCB1 was elevated in the CK19/GFP$^-$ population of 22Rv1-pCK19-GFP but not DU145-pCK19-GFP (Figure S6B). Consistent with these

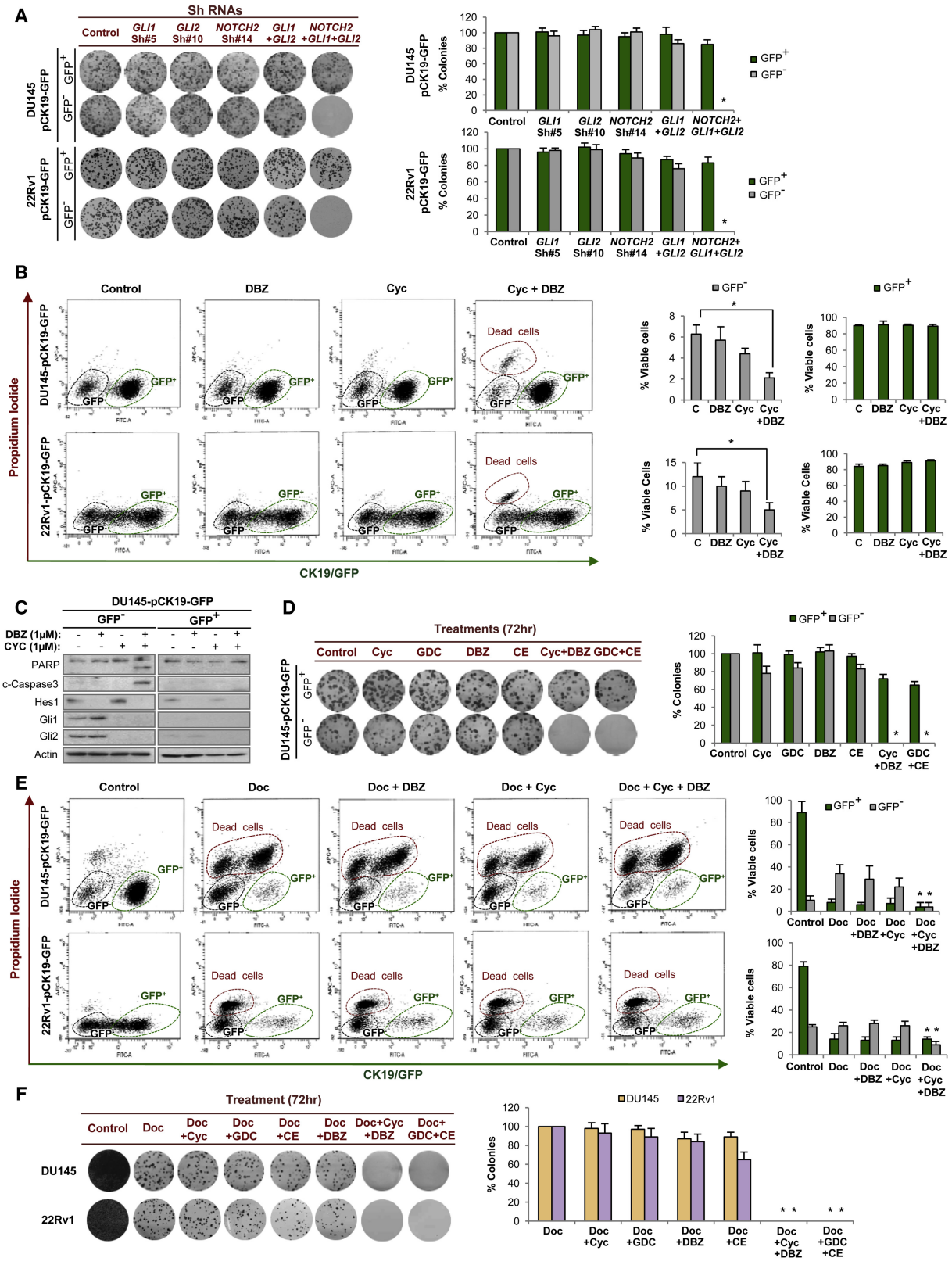

Figure 4. Docetaxel-Resistant Prostate Cancer Cells Are Dependent on Notch and Hedgehog Signaling

(A) Colony formation assay and quantification of DU145-pCK19-GFP- and 22Rv1-pCK19-GFP-sorted cells expressing shRNAs against *GLI1*, *GLI2*, and *NOTCH2* alone, as well as double (*GLI1* and *GLI2*) and triple knockdowns.

results, 22Rv1, but not DU145, exhibited a side population using a Hoechst 33342 assay (Figure S6C). Finally, we observed that Notch and Hedgehog signaling did not regulate *ABCB1* mRNA in 22Rv1-pCK19-GFP$^-$ cells (Figure S6D). Thus, expression of this drug efflux molecule was not a consistent feature of CK19/GFP$^-$ cells. Taken together, these data suggest that Notch and Hedgehog signaling regulate the activation of AKT and expression of Bcl-2, respectively, to promote survival and multidrug resistance in a P-gp/ABCB1 drug efflux independent mechanism.

Docetaxel-Resistant Prostate Cancer Cells Have Potent Tumor-Initiating Capacity

A number of studies have shown that tumor-initiating cells (T-ICs) may preferentially survive exposure to chemotherapy, providing an attractive rationale for relapse following initial tumor shrinkage with standard therapy (Corbin et al., 2011; Ishikawa et al., 2007; Lonardo et al., 2011; Todaro et al., 2007; Yu et al., 2007). Having demonstrated that CK$^-$ cells survive Docetaxel exposure in vitro and in vivo, we investigated the tumor-initiating capacity of these cells. Because efficient xenotransplantation is a major criterion for the validation of a T-IC-enriched compartment (Dalerba et al., 2007; Vermeulen et al., 2008; Visvader and Lindeman, 2008), we performed serial dilution tumor initiation assays using the Docetaxel-resistant models. Interestingly, DU145-DR and 22Rv1-DR had higher tumor-initiating capacity than did their parental sensitive cells when injected into NOD/SCID IL-2 receptor gamma chain null (NSG) mice (Figure 7A). These results indicate that DU145 and 22Rv1 Docetaxel-resistant cells display 15.8- and 22.4-fold higher tumor-initiating capacity than did their parental cells, respectively.

One feature of the Docetaxel-resistance phenotype was lack of HLAI expression (Figures 1 and 2). Therefore, we reasoned that viable CK$^-$ Docetaxel-resistant cells could be isolated from bulk populations using HLAI expression as a cell surface marker. Indeed, double marker flow cytometry analysis revealed that HLAI negativity closely overlapped with the CK$^-$ population both in cell lines (Figure S7A) and primary prostate cancers (Figure S7B). Thus, viable CK$^-$ and CK$^+$ subpopulations could be isolated by flow cytometry using HLAI expression.

We next used HLAI as a cell surface marker to perform limiting dilution tumor initiation assays in NSG mice. These studies revealed that in both DU145 and 22Rv1 the HLAI$^-$ compartment was at least 2,000-fold more tumorigenic than the HLAI-positive compartment (Figure 7B). Furthermore, primary xenografts formed from HLAI$^-$/CK$^-$ cells recapitulated the phenotypic heterogeneity of the parental cell lines with an HLAI$^+$/CK$^+$ phenotype in the majority of the tumor cells, as well as a small HLAI$^-$/CK$^-$ population that expressed nuclear cleaved Notch2, Gli1, and Gli2, and lacked nuclear AR (Figure 7C; Figure S7C). Further, HLAI$^-$ cells isolated from primary xenografts serially engrafted into secondary recipients, whereas HLAI$^+$ cells rarely engrafted (Figure 7B). Thus, in both DU145 and 22Rv1, the tumor-initiating capacity of HLAI$^-$ cells was ~2,000-fold higher than HLAI$^+$ cells. Moreover, we used complement-mediated lysis as an alternative method to show the presence of an HLAI$^-$ cell compartment with high tumor-initiating capacity in the parental cells. Incubation of DU145 and 22Rv1 parental cells with HLAI antibody and complement induced a robust depletion of HLAI$^+$ cells, whereas HLAI$^-$ cells remained viable (Figure S7D). The surviving HLAI$^-$ population exhibited a higher tumor-initiating capacity in comparison to the noncomplement depleted cells (Figure S7E).

To investigate the tumorigenic capacity of the identified prostate T-IC population in fresh tumors, we used primary prostate cancer tissue samples. We confirmed histologically the presence of adenocarcinoma in the processed tissue in 30 patients (Table S2). Overall, the injection of cells from 4 out of the 30 (13.3%) confirmed individual prostate cancer samples generated tumor xenografts after a median follow-up time of 55.6 weeks (range 37.3–62.0) in NOD/SCID mice. Among these four patient samples, the HLAI$^-$ cells displayed 336-fold higher tumorigenic potential compared to the HLAI$^+$ cells (Figure 7D). Moreover, in a subanalysis using HLAI-sorted cells from primary xenografts injected into NSG mice, HLAI$^-$ cells continued to form tumors efficiently, whereas HLAI$^+$ cells failed to engraft, indicating that tumor initiation of HLAI$^-$ cells was independent of a remnant host immune response (Figure S7F). Immunohistochemistry of tumors derived from HLAI$^-$ cells showed that they faithfully reproduced the phenotype of the primary prostate tumor with the expression of epithelial- and prostate-related markers (CKs and AR) as well as HLAI antigens in the majority of tumor cells, in addition to a small HLAI$^-$/CK$^-$ compartment characterized by lack of AR and expression of nuclear cleaved Notch2, Gli1, and Gli2 (Figure 7E; Figure S7G). Because of the long latency of the generated prostate cancer xenografts, we confirmed their identity by short tandem repeat DNA fingerprinting (data not shown). Further, HLAI$^-$ cells isolated from primary xenografts serially engrafted into secondary recipients, whereas HLAI$^+$ cells failed to engraft (Figure 7D). Taken together, these results suggest that the HLAI$^-$ subpopulation is highly enriched in T-ICs that sustain serial xenotransplantation and reproduce the phenotypic heterogeneity of the primary tumor.

Finally, given that our previous data suggested that Notch and Hedgehog signaling were required to sustain the viability of CK$^-$/HLAI$^-$ cells, we assessed whether inhibition of these pathways

(B) Flow cytometry analysis of DU145-pCK19-GFP and 22Rv1-pCK19-GFP treated with Cyclopamine (1 μM) and/or DBZ (1 μM, both 48 hr).
(C) Immunoblots of indicated proteins in DU145-pCK19-GFP cells treated with the same conditions as (B).
(D) Colony formation assay and quantification of DU145-pCK19-GFP-sorted cells exposed for 72 hr to Cyclopamine, GDC-0449, DBZ, and Compound E (all 1 μM), alone or in combination (Cyc+DBZ or GDC+CE).
(E) Flow cytometry analysis after Docetaxel (48 hr) alone or in combination with Cyclopamine and/or DBZ (both 1 μM). DU145-pCK19-GFP and 22Rv1-pCK19-GFP cells were treated with 10 and 50 nM Docetaxel, respectively.
(F) Colony formation assay and quantification of parental DU145 and 22Rv1 cells exposed for 72 hr to Docetaxel (10 and 50 nM, respectively) alone or in combination with Notch inhibitors (CE or DBZ, both 1 μM) and/or Hedgehog inhibitors (Cyclopamine or GDC-0449, both 1 μM). Data are represented as means ± SD of triplicate experiments. *$p < 0.05$.
See also Figure S4.

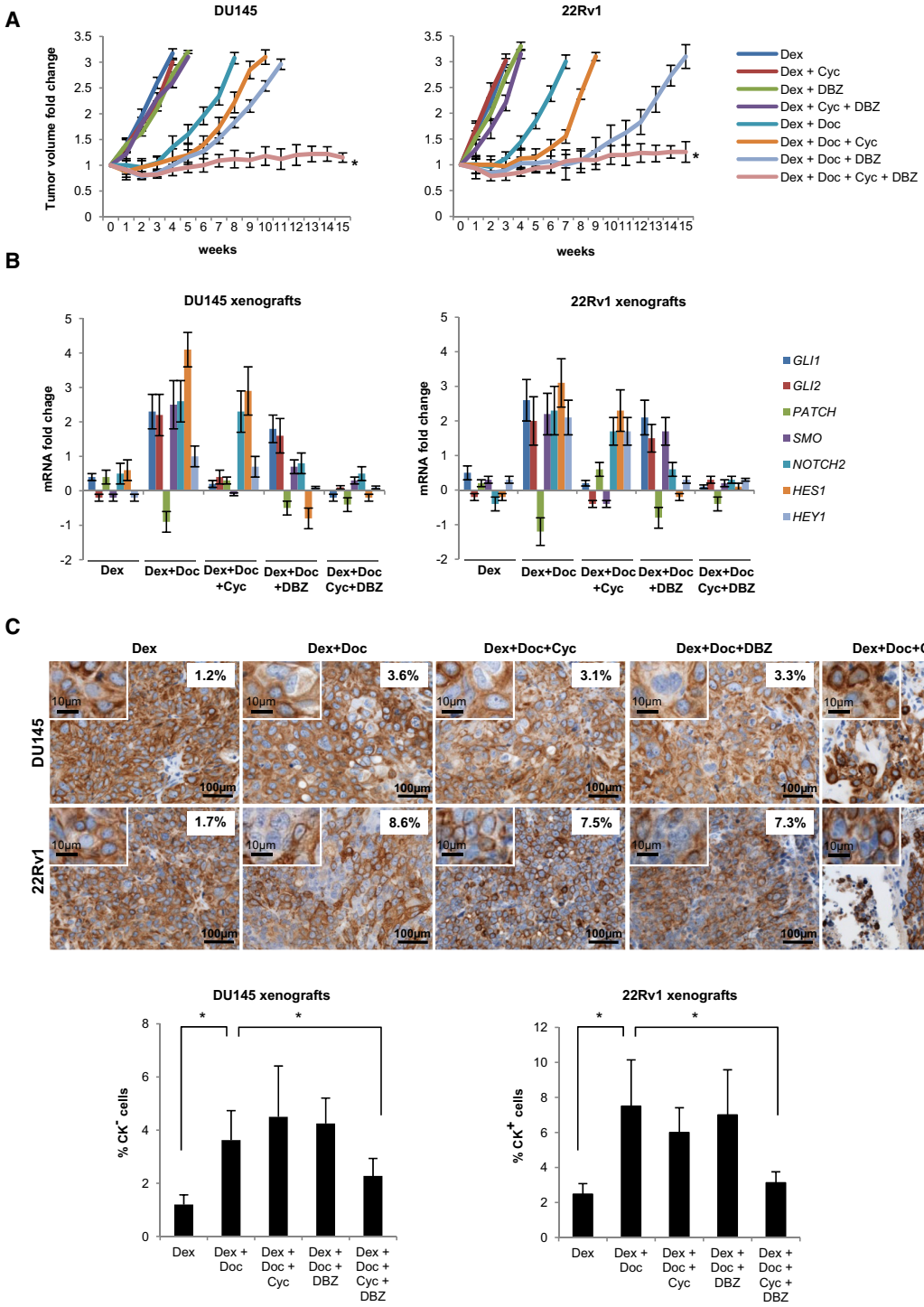

Figure 5. Notch and Hedgehog Inhibition Abrogates the Acquisition of Docetaxel Resistance

(A) Changes in tumor volume of DU145 and 22RV1 xenografts treated with Dexamethasone alone, double combinations, triple combinations, and quadruple combination. Dose schedules were Dexamethasone (15 mg/kg/i.p. daily), Docetaxel (10 mg/kg/i.p. once a week for 3 weeks every 4 weeks), DBZ (10 μM/kg/ip daily for 15 days every 4 weeks), and Cyclopamine (50 μg/kg/sc daily).

(B) Quantitative RT-PCR of Notch and Hedgehog target genes in DU145 and 22RV1 xenografts obtained from mice treated with the same drugs and concentrations as in (A). Bars represent fold change in mRNA levels relative to vehicle (control).

(C) Microphotographs illustrate the expression of low molecular weight cytokeratins (CK18 and CK19) in DU145 and 22RV1 prostate cancer tumor xenografts in NOD/SCID mice treated for 4 weeks with the same drugs as in (A). Magnifications illustrate CK^- cells. Histogram represents the percentage of CK^- cells detected in DU145 and 22RV1 xenografts for each treatment arm. Four xenografts for each treatment group where analyzed. Data is represented as means ± SD. *$p < 0.05$. See also Figure S5.

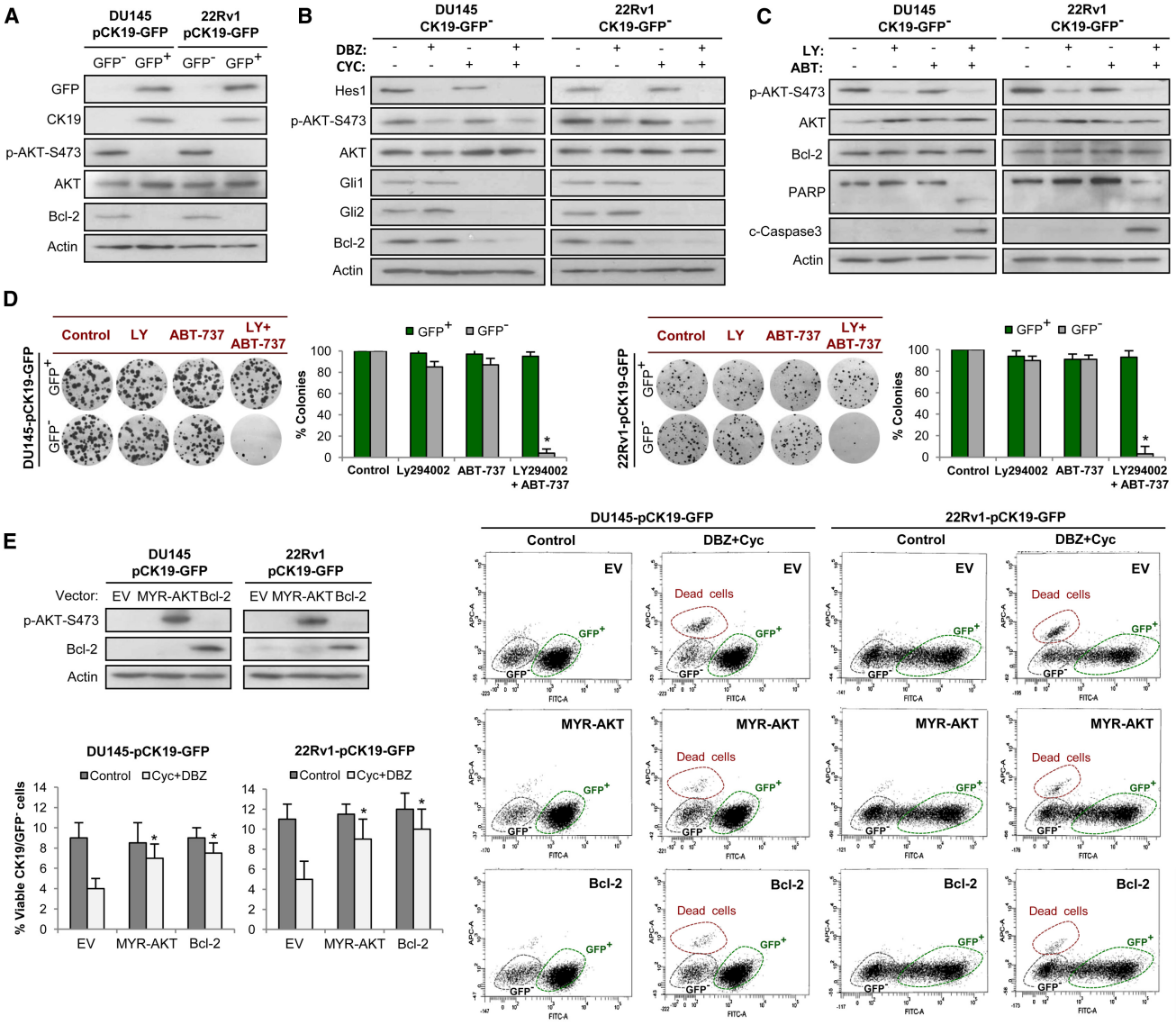
A
DU145 pCK19-GFP
22Rv1 pCK19-GFP
GFP- GFP+ GFP- GFP+
GFP
CK19
p-AKT-S473
AKT
Bcl-2
Actin
B
DU145 CK19-GFP-
22Rv1 CK19-GFP-
DBZ:
CYC:
Hes1
p-AKT-S473
AKT
Gli1
Gli2
Bcl-2
Actin
C
DU145 CK19-GFP-
22Rv1 CK19-GFP-
LY:
ABT:
p-AKT-S473
AKT
Bcl-2
PARP
c-Caspase3
Actin
D
Control
LY
ABT-737
LY+ ABT-737
DU145-pCK19-GFP
22Rv1-pCK19-GFP
GFP+
GFP-
% Colonies
Control
Ly294002
ABT-737
LY294002 + ABT-737
E
DU145 pCK19-GFP
22Rv1 pCK19-GFP
Vector:
EV
MYR-AKT
Bcl-2
p-AKT-S473
Bcl-2
Actin
DU145-pCK19-GFP
22Rv1-pCK19-GFP
Control
Cyc+DBZ
% Viable CK19/GFP- cells
EV
MYR-AKT
Bcl-2
DU145-pCK19-GFP
22Rv1-pCK19-GFP
Control
DBZ+Cyc
EV
MYR-AKT
Bcl-2
Dead cells
GFP+
GFP-
APC-A
FITC-A
F
DU145-pCK19-GFP-
22Rv1-pCK19-GFP-
Treatments (72hr)
Control
Cyc+DBZ
GDC+CE
EV
MYR-AKT
Bcl-2
GFP-
% Colonies
EV
MYR-AKT
Bcl-2
G
DU145-pCK19-GFP+
22Rv1-pCK19-GFP+
Treatments (72hr)
Control
Doc
MTX
CDDP
VNR
EV
MYR-AKT
BCL2
GFP+
% Colonies
Control
Doc
MTX
CDDP
VNR

could reduce the tumor-initiating capacity of these cells. We injected 100 HLAI$^-$-sorted cells from human prostate cancer xenografts #5, #9, and #12 subcutaneously into NSG mice, which were treated with vehicle solution, dexamethasone alone, dual drug combinations (e.g., dexamethasone plus Cyclopamine), or triple drug combination (dexamethasone plus Cyclopamine and DBZ). Mice treated with the combination of Notch and Hedgehog inhibitors showed a significant ($p < 0.0001$) reduction in tumor incidence when compared to mice treated with vehicle solution (DMSO) or each inhibitor alone (Figure 7F).

DISCUSSION

Here, we identify a population of prostate cancer cells, existing both in cell lines and patient samples, which exhibits resistance to Docetaxel, an undifferentiated phenotype, dependence on combined Notch and Hedgehog signaling, and high tumor-initiating capacity. Overall, our results have important implications for clinical oncology and prostate cancer biology.

Using two independent HRPC cell models, we identified a Docetaxel-resistance phenotype characterized by absence of epithelial differentiation markers and HLAI antigens, as well as activation of developmental pathways. Interestingly, in agreement with our data a previous study reported that treatment of a breast cancer cell line xenograft with an anthracycline resulted in the loss of CKs and other differentiation markers (Yu et al., 2007). In vitro studies revealed that the Docetaxel-resistance phenotype corresponds to a small, intrinsically multidrug resistant subpopulation present in unselected HRPC cells. We identified a small subpopulation of cells that exhibited the Docetaxel-resistance phenotype in all primary and metastatic clinical prostate cancer samples studied, and this cell population was significantly higher in metastatic patients treated with Docetaxel than in untreated patients. Further, the abundance of cells exhibiting the Docetaxel-resistance phenotype was higher in metastatic than primary samples, and in primary untreated samples its percentage was associated with canonical prognostic factors and time to biochemical relapse. Thus, the Docetaxel-resistance phenotype was consistently identified in prostate cancer as a small subpopulation, which is associated with both Docetaxel resistance and canonical prognostic parameters.

Most importantly, although resistance to Docetaxel in HRPC has been a subject of considerable interest, the development of therapeutic strategies that target Docetaxel-resistant cells has remained an elusive challenge in clinical oncology (Mahon et al., 2011; Seruga et al., 2011). Interestingly, Notch and Hedgehog signaling have been implicated in the self-renewal and differentiation of progenitor cells as well as prostate cancer tumorigenesis (Karhadkar et al., 2004; Katoh, 2007; Leong and Gao, 2008; Wang et al., 2006). The upregulation of Notch and Hedgehog signaling in our in vitro models prompted us to evaluate the role of these pathways in Docetaxel resistance in HRPC. These studies resulted in a combination strategy that abrogated tumor regrowth after Docetaxel administration in vivo. These data corroborate previous studies in other tumor types, which have found a link between activation of developmental pathways and chemotherapy resistance (Lonardo et al., 2011; Meng et al., 2009; Steg et al., 2012). Mechanistically, Notch and Hedgehog signaling regulated canonical survival molecules with well-documented roles in chemotherapy resistance (Pommier et al., 2004). These results were consistent with previous reports that Notch and Hedgehog signaling regulate canonical survival pathways in other tumor types (Dierks et al., 2007; Meurette et al., 2009; Palomero et al., 2007; Singh et al., 2010). In summary, given the limited capacity of Docetaxel to control HRPC, a widespread and fatal disease, this work lays the foundation for a promising therapeutic strategy.

Further, the identified Docetaxel-resistance phenotype enabled us to validate a bona fide T-IC population on the basis of HLAI expression in both HRPC cell lines and primary prostate clinical samples. The T-IC hypothesis posits that tumors are hierarchically organized with a distinct compartment endowed with the capacity to self-renew and generate the diversity of cells that comprise the tumor, and the gold standard for testing this hypothesis is a serial xenotransplantation assay from freshly resected human materials (Visvader and Lindeman, 2008; Zhou et al., 2009). Here, we provided evidence that a subpopulation of cells, which exhibits the Docetaxel-resistance phenotype in cell lines and prostate cancer tissues, satisfied the T-IC criteria. These results corroborate a growing body of evidence (Corbin et al., 2011; Ishikawa et al., 2007; Lonardo et al., 2011; Todaro et al., 2007; Yu et al., 2007) that T-ICs may contribute to disease progression by participating in chemotherapy resistance.

In conclusion, a common and devastating phenomenon in clinical oncology is tumor relapse following initial success with cytotoxic therapies. We provide evidence that inhibition of Notch and Hedgehog signaling in HRPC depletes a subpopulation of cells responsible for acquired Docetaxel resistance and tumor initiation, laying the foundation for a promising therapeutic strategy.

Figure 6. Notch and Hedgehog Signaling Regulate Survival Molecules in Docetaxel-Resistant Cells

(A) Immunoblots of indicated proteins in CK19/GFP$^-$ and CK19/GFP$^+$ sorted cells from DU145-pCK19-GFP and 22Rv1-pCK19-GFP.

(B) Immunoblots of indicated proteins in DU145-pCK19-GFP$^-$ and 22Rv1-pCK19-GFP$^-$ cells exposed for 72 hr to DBZ and/or Cyclopamine (both 1 μM).

(C) Immunoblots of indicated proteins in DU145-pCK19-GFP$^-$ and 22Rv1-pCK19-GFP$^-$ cells exposed for 72 hr to LY294002 (50 μM) and/or ABT-737 (10 μM).

(D) Colony formation assay and quantification of colonies derived from GFP$^-$ and GFP$^+$ cells exposed to the same drugs and concentrations as in (C).

(E) Flow cytometry analysis after 48 hr administration of Cyclopamine (1 μM) and/or DBZ (1 μM) of DU145-pCK19-GFP and 22Rv1-pCK19-GFP cells stably transfected with empty vector (EV), MYR-AKT and *BCL2*. Immunoblots illustrate the overexpression levels of pAKT (Ser-473) and Bcl-2.

(F) Colony formation assay and quantification of DU145-pCK19-GFP- and 22Rv1-pCK19-GFP-sorted cells stably transfected with empty vector (EV), MYR-AKT, or *BCL2* and exposed for 72 hr to Cyclopamine (Cyc), GDC-0449 (GDC), DBZ, and Compound-E (CE, all 1 μM), alone or in combination.

(G) Colony formation assays and quantifications of GFP$^+$-sorted DU145-pCK19-GFP and 22Rv1-pCK19-GFP stably transfected with EV, MYR-AKT, or *BCL2* and treated for 72 hr with Mitoxantrone 125 and 500 nM, Cisplatin 5 and 2.5 μM, and Vinorelbine 500 and 750 nM, respectively. Data is represented as means ± SD of three independent experiments. *$p < 0.05$.

See also Figure S6.

A

Cell Type	Cell dose	Tumor Incidence	T-IC frequency (95% CI)	Latency (weeks)	Cell Type	Cell dose	Tumor Incidence	T-IC frequency (95% CI)	Latency (weeks)
DU145	10 100 1000	1/24 7/24 24/24	1/237 (1/144-1/390)	21.3 15.9±1.2 11.9±1.7	22Rv1	10 100 1000	2/24 8/24 24/24	1/202 (1/121-1/338)	23.9±0.2 15.1±1.9 10.5±0.6
DU145-DR	10 100 1000	16/24* 23/24* 24/24	1/15 (1/9-1/27)	17.3±2.5* 10.7±1.3* 7.3±0.8*	22Rv1-DR	10 100 1000	16/24* 24/24* 24/24	1/9 (1/5-1/15)	15.8±1.0* 11.4±0.6* 7.2±0.7*

B

Cell Type	Cell dose	1ary Tumor Incidence	T-IC frequency (95% CI)	Latency (weeks)	2aryTumor Incidence	T-IC frequency (95% CI)	Latency (weeks)
DU145 HLAI+	10 100 1000 10000	0/24 0/24 3/24 6/24	1/2.5x10⁴ (1/1.3x10⁴-1/5 .0x10⁴)	- - 21.4±1.2 17.8±0.6	0/24 0/24 4/24 7/24	1/2.0x10⁴ (1/1.1x10⁴-1/3 .7x10⁴)	- - 19.3±1.1 18.0±2.2
DU145 HLAI-	10 100 1000 10000	15/24* 24/24* 24/24* 24/24*	1/10 (1/6-1/17)	18.9±1.7 12.8±1.8 9.9±1.4* 4.9±0.5*	16/24 24/24 24/24* 24/24*	1/9 (1/5-1/15)	19.2±1.9* 11.4±0.9* 9.5±0.5* 4.9±0.6*
22Rv1 HLAI+	10 100 1000 10000	0/24 0/24 1/24 5/24	1/4.0x10⁴ (1/1.7x10⁴-1/8 .9x10⁴)	- - 21.1 16.7±1.9	0/24 0/24 2/24 6/24	1/2.9x10⁴ (1/1.4x10⁴-1/5 .9x10⁴)	- - 21.4±3.9 16.8±2.7
22Rv1 HLAI-	10 100 1000 10000	21/24* 24/24* 24/24* 24/24*	1/5 (1/3-1/8)	17.0±1.6 10.5±1.3 8.7±1.3* 3.9±0.8*	20/24* 24/24* 24/24* 24/24*	1/6 (1/3-1/9)	14.9±1.4 10.9±1.2 8.8±0.7* 4.2±0.7*

C

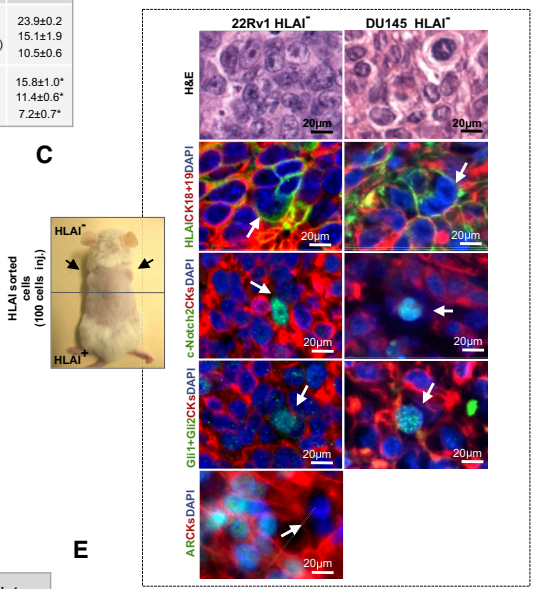

D

Patient	Tumor stage	Gleason	Cell type	Cell dose	1ary tumor incidence	T-IC frequency (95% CI)	Latency (weeks)	2ary tumor incidence	T-IC frequency (95% CI)	Latency (weeks)
#5	pT2c,pN0	7(3+4)	HLAI+	10 100 1000	0/8 0/8 3/8	1/2.4x10³ (1/0.8x10³ - 1/7.4x10³)	- - 26.8±4.0	0/8 0/8 0/8		- - -
			HLAI-	10 100 1000	5/8* 8/8* 8/8*	1/10 (1/4-1/25)	34.4±5.2 24.1±6.8 12.6±3.9	6/8 8/8 8/8	1/7 (1/3-1/17)	22.8±4.8 19.9±2.7 13.8±2.8
#9	pT2c,pN0	7(3+4)	HLAI+	10 100 1000	0/8 0/8 1/8	1/8.4x10³ (1/1.2x10³ - 1/5.9x10⁴)	- - 22.4	0/8 0/8 0/8		- - -
			HLAI-	10 100 1000	5/8* 8/8* 8/8*	1/10 (1/4-1/25)	30.8±6.0 16.1±4.5 10.8±1.5	6/8* 8/8* 8/8*	1/7 (1/3-1/17)	26.0±3.4 15.1±3.3 10.3±1.5
#12	pT2c,pN0	7(4+3)	HLAI+	10 100 1000	0/8 0/8 0/8		- - -	0/8 0/8 0/8		- - -
			HLAI-	10 100 1000	3/8* 7/8* 8/8*	1/37 (1/16-1/82)	36.3±4.5 21.5±5.8 12.6±3.6	4/8* 8/8* 8/8*	1/14 (1/5-1/37)	35.3±3.7 20.3±4.5 16.6±2.5
#24	pT2c,pN0	7(3+4)	HLAI+	10 100 1000	0/8 0/8 0/8		- - -	0/8 0/8 0/8		- - -
			HLAI-	10 100 1000	2/8* 7/8* 8/8*	1/44 (1/20-1/96)	43.0±4.2 32.5±7.4 25.7±7.9	3/8* 7/8* 8/8*	1/37 (1/16-1/82)	45.4±3.5 40.5±8.4 31.9±9.8
ALL	-	-	HLAI+	10 100 1000	0/32 0/32 4/32	1/8.4x10³ (1/3.1x10³- 1/2.2x10⁴)	- - -	0/8 0/8 0/8		- - -
			HLAI-	10 100 1000	15/32* 30/32* 32/32*	1/25 (16-39)	43.0±4.2 32.5±7.4 25.7±7.9	17/32* 31/32* 32/32*	1/16 (1/10-1/26)	45.4±3.5 40.5±8.4 31.9±9.8

E

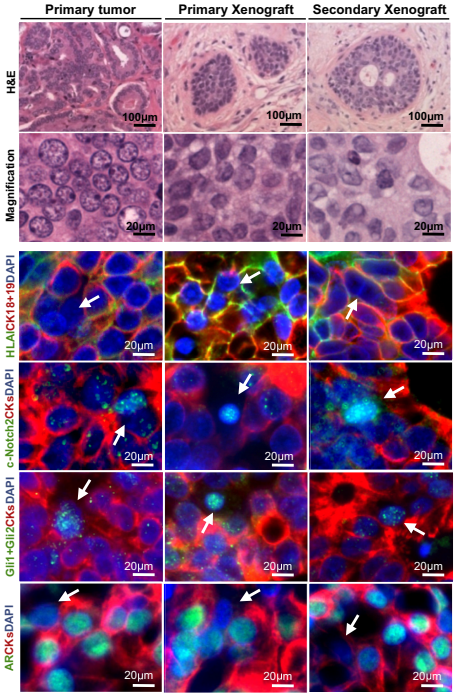

F

Patient	Treatment	Tumor Incidence	Latency (weeks)	Patient	Treatment	Tumor Incidence	Latency (weeks)
#5	Vehicle (DMSO)	8/8	19.0±1.9	#12	Vehicle (DMSO)	8/8	16.1±2.6
	Dexamethasone	8/8	18.3±2.2		Dexamethasone	8/8	17.5±2.3
	Dex+DBZ	7/8	20.3±1.3		Dex+DBZ	7/8	20.9±1.8
	Dex+Cyc	6/8	21.4±1.4		Dex+Cyc	6/8	21.7±2.4
	Dex+DBZ+Cyc	0/8	-		Dex+DBZ+Cyc	1/8	21.8
#9	Vehicle (DMSO)	8/8	12.6±3.5	ALL	Vehicle (DMSO)	24/24 (100%)	16.0±3.2
	Dexamethasone	8/8	11.9±1.8		Dexamethasone	24/24 (100%)	15.9±3.5
	Dex+DBZ	6/8	13.1±2.1		Dex+DBZ	20/24 (83%)	18.1±4.3
	Dex+Cyc	6/8	13.9±2.1		Dex+Cyc	18/24 (75%)	19.0±4.1
	Dex+DBZ+Cyc	1/8	22.7		Dex+DBZ+Cyc	2/24 (8.3%)*	22.2±0.6

Figure 7. Docetaxel-Resistant Prostate Cancer Cells Have High Tumor-Initiating Capacity

(A) Tumor incidence, T-IC frequency, and latencies 36 weeks after injection of limiting dilutions of parental and Docetaxel-resistant cells.

(B) Tumor incidence, T-IC frequency, and latencies 38 weeks after injection of limiting dilutions of DU145 and 22RV1 HLAI-sorted cells.

(C) Image of a mouse bearing tumors after injection of DU145 HLAI$^-$ cells in the upper flanks and HLAI$^+$ cells in the lower flanks. H&E and immunofluorescence of indicated proteins in representative tumor xenografts generated from DU145 and 22RV1 HLAI$^-$ cells. White arrows point to CK$^-$ cells with positive nuclear staining of transcription factors and lack of HLAI and AR.

(D) Table summarizes prostate cancer patients' clinicopathological characteristics, tumor incidence, T-IC frequency, and latencies after 61 weeks of injection of limiting dilutions of HLAI-sorted cells from fresh human prostate cancer samples.

EXPERIMENTAL PROCEDURES

Additional experimental procedures are described in detail in the Supplemental Experimental Procedures.

Generation of Acquired Docetaxel-Resistant Prostate Cancer Cell Models

Human HRPC cell lines, DU-145 and 22RV1, were obtained from American Type Culture Collection (ATCC) and maintained in RPMI 1640 medium (GIBCO) supplemented with 10% FBS without antibiotics. Docetaxel-resistant clones, DU-145-DR and 22RV1-DR, were selected by culturing cells with Docetaxel in a dose-escalation manner using 72 hr exposures. Initial culture was at 5 nM Docetaxel for DU145 and 25 nM for 22RV1. After sensitive clones were no longer present and surviving DU-145 and 22RV1 cells repopulated the flask, the concentration of Docetaxel was increased to 10, 25, 50, 100, and 250 nM. 22RV1-DR cells were further exposed to 500 nM. The process of acquired drug resistance took 9 months for DU-145-DR and 6.5 months for 22RV1-DR. In parallel, parental DU-145 and 22RV1 cells were exposed to DMSO (vehicle solution) in the same dose-escalation manner. Cell viability, apoptosis, immunoblotting, immunofluorescence, and quantitative RT-PCR assays are described in the Supplemental Experimental Procedures.

cDNA Microarray Analysis

22RV1, 22RV1-DR, DU-145, and DU-145-DR gene expression profiles were analyzed. Total RNA from each sample was isolated by Tryzol (Invitrogen, Carlsbad, CA, USA) and purified by RNeasy mini kit and RNase-free DNase set (Qiagen, Venlo, The Netherlands) in accordance with the manufacturer's protocols. RNA quality of all samples was tested by RNA electrophoresis and RNA LabChip analysis (Agilent, Santa Clara, CA, USA) to ensure RNA integrity. Samples were prepared for analysis with Affymetrix Human U133 arrays in accordance with the manufacturer's instructions. Gene expression levels of samples were normalized and analyzed with Microarray Suite, MicroDB, and Data Mining tool software (Affymetrix, Santa Clara, CA, USA). The absolute call (present, marginal, or absent) and average difference of 22,215 expressions in a sample, and the absolute call difference, fold change, average difference of gene expression between two or three samples were normalized and identified using this software package. Statistical analysis of the mean expression average difference of genes change was done using a t test between Docetaxel-sensitive and Docetaxel-resistant samples. Genes that were not annotated or not easily classified were excluded from the functional clustering analysis.

Gene Ontology Analysis

Genes differentially expressed in the Docetaxel-resistant cells compared to the parental-sensitive cells generated a list of commonly deregulated transcripts. This list was assessed by the DAVID Bioinformatics Resources, a web-based statistical hypergeometric test applied for enrichment analysis of gene ontology (GO) categories, which include biological process, molecular function, and cellular component (http://david.adcc.ncifcrf.gov/). GO categories enriched on the highest hierarchical level (≥ level 5) at statistical significance ($p < 0.01$) were taken into consideration.

Generation of the pCK19-GFP Reporter Plasmid

CK19 gene promoter region was amplified from genomic DNA of DU145 cells by PCR with specific primer sets (Fw 5′-AACGCATGCTTTGGGGGGATG-3′and Rv 5′-TCCCCCTTTACTCGGCCCCCAC-3′) as described previously (Tripathi et al., 2005). Briefly, a region of 1,768 bp corresponding to human Cytokeratin 19 promoter was amplified. The promoter region includes 1,142 bp of the 5′ UTR region, 480 bp belonging to Exon 1, and 146 bp belonging to Intron 1. The PCR products were digested with *Ase I* and *Hind III* and cloned into pEGFPN1 vector (Clontech, Mountain View, CA, USA) previously digested with the same enzymes. As a result, the CMV promoter was removed from the original vector and the GFP expression was under control of the CK19 promoter. The final construct was confirmed by digestion and sequencing analysis. DU145 and 22Rv1 cells were transfected with pCK19-GFP construct using Lipofectamine Plus 2000 (Invitrogen). After 24 hr, medium was replaced with fresh medium and stably expressing cells selected in the presence of G418 (Invitrogen). Positive clones were confirmed by direct microscopy and immunofluorescence and also by PCR amplification of GFP coding region using specific primers (Fw 5′-TTCCTGCGTTATCCCCTGATTC-3′ and Rv 5′-GCTCCTCCGGCCCTTGCTCACCAT-3′). Notch and Hedgehog genetic (shRNA) and chemical inhibition experiments are described in the Supplemental Experimental Procedures.

Live Cell Imaging

Time-lapse videomicroscopy was used to assess Docetaxel sensitivity of DU145-pCK19-GFP and 22Rv1-pCK19-GFP cells. Cells growing in 6-well plates at low confluence were placed in the stage inside an incubator chamber at 37°C, 50% humidity and in an atmosphere of 5% CO_2. Unattended time-lapse movies of randomly chosen GFP^+ and GFP^- DU145 and 22Rv1 cells were performed with a Nikon Eclipse T*i* inverted microscope. NIS Elements AR (Nikon, Tokyo, Japan) software was used to collect and process data. Imaging was performed using a 10× objective, and images were captured using 200-ms exposure times for GFP and 20-ms for bright field every 30 min.

Human Prostate Cancer Tissue Samples

Formalin-fixed paraffin-embedded human primary (n = 31) and metastatic (n = 36) prostate cancer tissue samples were provided by the tumor bank of Columbia University Medical Center. Fresh primary prostate tumor tissue samples (n = 30) were obtained from patients who had undergone surgical procedures at Columbia University Medical Center. All samples were collected under informed consent and supervision of the Columbia University Medical Center Institutional Review Board, and all studies using these samples were approved by the Columbia University Medical Center Institutional Review Board. Tissue sections with cancer were selected by reviewing hematoxylin and eosin (H&E) stained slides. Immunohistochemistry and immunofluorescent analyses are described in the Supplemental Experimental Procedures.

Mouse Procedures

All animal experiments were approved by the Institutional Animal Care and Use Committee (IACUC) at Columbia University. Animal use and care was in strict compliance with institutional guidelines and all experiments conformed to the relevant regulatory standards established by Columbia University. Xenograft experiments were performed with 5- to 6-week-old NOD.Cg-Prkdc^{scid} IL2rg^{tm1Wjl} (NSG) and NOD.CB17-Prkdc^{scid} (NOD/SCID) mice obtained from Jackson Laboratories. In vivo effects of the combination of Docetaxel with Notch and Hedgehog pathway inhibitors and assessment of tumor initiating capacity are described in the Supplemental Experimental Procedures.

Statistical Analyses

Statistical analysis was carried out with SPSS version 19.0 (SPSS, Inc., Chicago, IL, USA). Experimental data is expressed as means ± SD and analyzed by Student's t test. Association between the percentage of CK^- cells and biochemical (PSA) disease recurrence was analyzed by the Kaplan-Meier method, and curves were compared by the log-rank test. All the statistical tests were conducted at the two-sided 0.05 level of significance.

(E) H&E and immunofluorescence analysis of indicated proteins in human tumors and primary and secondary xenografts generated from $HLAI^-$ cells. Patient 9 is represented. White arrows point to CK^- cells with nuclear expression of transcription factors and lack of HLAI and AR.
(F) Tumor incidence and latencies 24 weeks after injection of 100 $HLAI^-$-sorted cells from prostate cancer xenografts treated with DMSO, Dexamethasone 15 mg/kg/i.p. daily, Cyclopamine 50 μg/kg/sc daily plus dexamethasone, DBZ 10 μM/kg/i.p. daily for 15 days every 4 weeks plus Dexamethasone, or with triple combination. Data is represented as means ± SD. *$p < 0.05$.
See also Figure S7 and Table S2.

ACCESSION NUMBERS

Microarray data have been deposited at GEO with the accession number GSE36135.

SUPPLEMENTAL INFORMATION

Supplemental Information includes seven figures, two tables, Supplemental Experimental Procedures, and two movies and can be found with this article online at http://dx.doi.org/10.1016/j.ccr.2012.07.016.

ACKNOWLEDGMENTS

We thank the Flow Cytometry Shared Resource, Molecular Pathology Shared Resource, Department of Pathology, and Drs. Donna Farber and Damian Turner at Columbia University, as well as Dr. Ruth Kornreich and Edith Gould from Mount Sinai School of Medicine. Finally, we thank the TJ Martell Foundation for its support.

Received: February 13, 2012
Revised: May 29, 2012
Accepted: July 27, 2012
Published: September 10, 2012

REFERENCES

Ali, T.Z., and Epstein, J.I. (2008). False positive labeling of prostate cancer with high molecular weight cytokeratin: p63 a more specific immunomarker for basal cells. Am. J. Surg. Pathol. *32*, 1890–1895.

Chen, J.K., Taipale, J., Cooper, M.K., and Beachy, P.A. (2002). Inhibition of Hedgehog signaling by direct binding of cyclopamine to Smoothened. Genes Dev. *16*, 2743–2748.

Corbin, A.S., Agarwal, A., Loriaux, M., Cortes, J., Deininger, M.W., and Druker, B.J. (2011). Human chronic myeloid leukemia stem cells are insensitive to imatinib despite inhibition of BCR-ABL activity. J. Clin. Invest. *121*, 396–409.

Dalerba, P., Cho, R.W., and Clarke, M.F. (2007). Cancer stem cells: models and concepts. Annu. Rev. Med. *58*, 267–284.

Dierks, C., Grbic, J., Zirlik, K., Beigi, R., Englund, N.P., Guo, G.R., Veelken, H., Engelhardt, M., Mertelsmann, R., Kelleher, J.F., et al. (2007). Essential role of stromally induced hedgehog signaling in B-cell malignancies. Nat. Med. *13*, 944–951.

Gottesman, M.M., Fojo, T., and Bates, S.E. (2002). Multidrug resistance in cancer: role of ATP-dependent transporters. Nat. Rev. Cancer *2*, 48–58.

Ishikawa, F., Yoshida, S., Saito, Y., Hijikata, A., Kitamura, H., Tanaka, S., Nakamura, R., Tanaka, T., Tomiyama, H., Saito, N., et al. (2007). Chemotherapy-resistant human AML stem cells home to and engraft within the bone-marrow endosteal region. Nat. Biotechnol. *25*, 1315–1321.

Jemal, A., Bray, F., Center, M.M., Ferlay, J., Ward, E., and Forman, D. (2011). Global cancer statistics. CA Cancer J. Clin. *61*, 69–90.

Karhadkar, S.S., Bova, G.S., Abdallah, N., Dhara, S., Gardner, D., Maitra, A., Isaacs, J.T., Berman, D.M., and Beachy, P.A. (2004). Hedgehog signalling in prostate regeneration, neoplasia and metastasis. Nature *431*, 707–712.

Katoh, M. (2007). Networking of WNT, FGF, Notch, BMP, and Hedgehog signaling pathways during carcinogenesis. Stem Cell Rev. *3*, 30–38.

Leong, K.G., and Gao, W.Q. (2008). The Notch pathway in prostate development and cancer. Differentiation *76*, 699–716.

Lonardo, E., Hermann, P.C., Mueller, M.T., Huber, S., Balic, A., Miranda-Lorenzo, I., Zagorac, S., Alcala, S., Rodriguez-Arabaolaza, I., Ramirez, J.C., et al. (2011). Nodal/Activin signaling drives self-renewal and tumorigenicity of pancreatic cancer stem cells and provides a target for combined drug therapy. Cell Stem Cell *9*, 433–446.

Mahon, K.L., Henshall, S.M., Sutherland, R.L., and Horvath, L.G. (2011). Pathways of chemotherapy resistance in castration-resistant prostate cancer. Endocr. Relat. Cancer *18*, R103–R123.

Meng, R.D., Shelton, C.C., Li, Y.M., Qin, L.X., Notterman, D., Paty, P.B., and Schwartz, G.K. (2009). gamma-Secretase inhibitors abrogate oxaliplatin-induced activation of the Notch-1 signaling pathway in colon cancer cells resulting in enhanced chemosensitivity. Cancer Res. *69*, 573–582.

Meurette, O., Stylianou, S., Rock, R., Collu, G.M., Gilmore, A.P., and Brennan, K. (2009). Notch activation induces Akt signaling via an autocrine loop to prevent apoptosis in breast epithelial cells. Cancer Res. *69*, 5015–5022.

Oltersdorf, T., Elmore, S.W., Shoemaker, A.R., Armstrong, R.C., Augeri, D.J., Belli, B.A., Bruncko, M., Deckwerth, T.L., Dinges, J., Hajduk, P.J., et al. (2005). An inhibitor of Bcl-2 family proteins induces regression of solid tumours. Nature *435*, 677–681.

Palomero, T., Sulis, M.L., Cortina, M., Real, P.J., Barnes, K., Ciofani, M., Caparros, E., Buteau, J., Brown, K., Perkins, S.L., et al. (2007). Mutational loss of PTEN induces resistance to NOTCH1 inhibition in T-cell leukemia. Nat. Med. *13*, 1203–1210.

Petrylak, D.P., Tangen, C.M., Hussain, M.H., Lara, P.N., Jr., Jones, J.A., Taplin, M.E., Burch, P.A., Berry, D., Moinpour, C., Kohli, M., et al. (2004). Docetaxel and estramustine compared with mitoxantrone and prednisone for advanced refractory prostate cancer. N. Engl. J. Med. *351*, 1513–1520.

Pommier, Y., Sordet, O., Antony, S., Hayward, R.L., and Kohn, K.W. (2004). Apoptosis defects and chemotherapy resistance: molecular interaction maps and networks. Oncogene *23*, 2934–2949.

Pound, C.R., Partin, A.W., Eisenberger, M.A., Chan, D.W., Pearson, J.D., and Walsh, P.C. (1999). Natural history of progression after PSA elevation following radical prostatectomy. JAMA *281*, 1591–1597.

Real, P.J., Tosello, V., Palomero, T., Castillo, M., Hernando, E., de Stanchina, E., Sulis, M.L., Barnes, K., Sawai, C., Homminga, I., et al. (2009). Gamma-secretase inhibitors reverse glucocorticoid resistance in T cell acute lymphoblastic leukemia. Nat. Med. *15*, 50–58.

Robarge, K.D., Brunton, S.A., Castanedo, G.M., Cui, Y., Dina, M.S., Goldsmith, R., Gould, S.E., Guichert, O., Gunzner, J.L., Halladay, J., et al. (2009). GDC-0449-a potent inhibitor of the hedgehog pathway. Bioorg. Med. Chem. Lett. *19*, 5576–5581.

Seiffert, D., Bradley, J.D., Rominger, C.M., Rominger, D.H., Yang, F., Meredith, J.E., Jr., Wang, Q., Roach, A.H., Thompson, L.A., Spitz, S.M., et al. (2000). Presenilin-1 and -2 are molecular targets for gamma-secretase inhibitors. J. Biol. Chem. *275*, 34086–34091.

Seruga, B., Ocana, A., and Tannock, I.F. (2011). Drug resistance in metastatic castration-resistant prostate cancer. Nat. Rev. Clin. Oncol *8*, 12–23.

Singh, R.R., Kim, J.E., Davuluri, Y., Drakos, E., Cho-Vega, J.H., Amin, H.M., and Vega, F. (2010). Hedgehog signaling pathway is activated in diffuse large B-cell lymphoma and contributes to tumor cell survival and proliferation. Leukemia *24*, 1025–1036.

Steg, A.D., Bevis, K.S., Katre, A.A., Ziebarth, A., Dobbin, Z.C., Alvarez, R.D., Zhang, K., Conner, M., and Landen, C.N. (2012). Stem cell pathways contribute to clinical chemoresistance in ovarian cancer. Clin. Cancer Res. *18*, 869–881.

Taipale, J., Chen, J.K., Cooper, M.K., Wang, B., Mann, R.K., Milenkovic, L., Scott, M.P., and Beachy, P.A. (2000). Effects of oncogenic mutations in Smoothened and Patched can be reversed by cyclopamine. Nature *406*, 1005–1009.

Tannock, I.F., de Wit, R., Berry, W.R., Horti, J., Pluzanska, A., Chi, K.N., Oudard, S., Théodore, C., James, N.D., Turesson, I., et al; TAX 327 Investigators. (2004). Docetaxel plus prednisone or mitoxantrone plus prednisone for advanced prostate cancer. N. Engl. J. Med. *351*, 1502–1512.

Todaro, M., Alea, M.P., Di Stefano, A.B., Cammareri, P., Vermeulen, L., Iovino, F., Tripodo, C., Russo, A., Gulotta, G., Medema, J.P., and Stassi, G. (2007). Colon cancer stem cells dictate tumor growth and resist cell death by production of interleukin-4. Cell Stem Cell *1*, 389–402.

Tripathi, M.K., Misra, S., and Chaudhuri, G. (2005). Negative regulation of the expressions of cytokeratins 8 and 19 by SLUG repressor protein in human breast cells. Biochem. Biophys. Res. Commun. *329*, 508–515.

van Es, J.H., van Gijn, M.E., Riccio, O., van den Born, M., Vooijs, M., Begthel, H., Cozijnsen, M., Robine, S., Winton, D.J., Radtke, F., and Clevers, H. (2005). Notch/gamma-secretase inhibition turns proliferative cells in intestinal crypts and adenomas into goblet cells. Nature *435*, 959–963.

Vermeulen, L., Sprick, M.R., Kemper, K., Stassi, G., and Medema, J.P. (2008). Cancer stem cells—old concepts, new insights. Cell Death Differ. *15*, 947–958.

Visvader, J.E., and Lindeman, G.J. (2008). Cancer stem cells in solid tumours: accumulating evidence and unresolved questions. Nat. Rev. Cancer *8*, 755–768.

Vlahos, C.J., Matter, W.F., Hui, K.Y., and Brown, R.F. (1994). A specific inhibitor of phosphatidylinositol 3-kinase, 2-(4-morpholinyl)-8-phenyl-4H-1-benzopyran-4-one (LY294002). J. Biol. Chem. *269*, 5241–5248.

Wang, X.D., Leow, C.C., Zha, J., Tang, Z., Modrusan, Z., Radtke, F., Aguet, M., de Sauvage, F.J., and Gao, W.Q. (2006). Notch signaling is required for normal prostatic epithelial cell proliferation and differentiation. Dev. Biol. *290*, 66–80.

Yu, F., Yao, H., Zhu, P., Zhang, X., Pan, Q., Gong, C., Huang, Y., Hu, X., Su, F., Lieberman, J., and Song, E. (2007). let-7 regulates self renewal and tumorigenicity of breast cancer cells. Cell *131*, 1109–1123.

Zhou, B.B., Zhang, H., Damelin, M., Geles, K.G., Grindley, J.C., and Dirks, P.B. (2009). Tumour-initiating cells: challenges and opportunities for anticancer drug discovery. Nat. Rev. Drug Discov. *8*, 806–823.

Cancer Cell
Article

TGF-β-miR-34a-CCL22 Signaling-Induced Treg Cell Recruitment Promotes Venous Metastases of HBV-Positive Hepatocellular Carcinoma

Pengyuan Yang,[1,5] Qi-Jing Li,[2] Yuxiong Feng,[3] Yun Zhang,[1] Geoffrey J. Markowitz,[1] Shanglei Ning,[1] Yuezhen Deng,[3] Jiangsha Zhao,[3] Shan Jiang,[2] Yunfei Yuan,[6] Hong-Yang Wang,[4] Shu-Qun Cheng,[4] Dong Xie,[3,*] and Xiao-Fan Wang[1,*]
[1]Department of Pharmacology and Cancer Biology
[2]Department of Immunology
Duke University Medical Center, Durham, NC 27710, USA
[3]Laboratory of Molecular Oncology, Institute for Nutritional Sciences, Shanghai Institutes of Biological Sciences, Shanghai 200031, China
[4]The Eastern Hepatobiliary Surgery Hospital
[5]Department of Pharmacology and School of Pharmacy
Second Military Medical University, Shanghai 200433, China
[6]Department of Hepatobiliary Surgery, Sun Yat-sen University Cancer Center, Guangzhou 510060, China
*Correspondence: dxie@sibs.ac.cn (D.X.), wang0011@mc.duke.edu (X.-F.W.)
http://dx.doi.org/10.1016/j.ccr.2012.07.023

SUMMARY

Portal vein tumor thrombus (PVTT) is strongly correlated to a poor prognosis for patients with hepatocellular carcinoma (HCC). In this study, we uncovered a causative link between hepatitis B virus (HBV) infection and development of PVTT. Mechanistically, elevated TGF-β activity, associated with the persistent presence of HBV in the liver tissue, suppresses the expression of microRNA-34a, leading to enhanced production of chemokine CCL22, which recruits regulatory T (Treg) cells to facilitate immune escape. These findings strongly suggest that HBV infection and activity of the TGF-β-miR-34a-CCL22 axis serve as potent etiological factors to predispose HCC patients for the development of PVTT, possibly through the creation of an immune-subversive microenvironment to favor colonization of disseminated HCC cells in the portal venous system.

INTRODUCTION

Hepatocellular carcinoma (HCC) is one of the major health problems worldwide (Parkin et al., 2005). Since HCC is often diagnosed at an advanced stage, a large proportion of HCC patients display symptoms of intrahepatic metastases or postsurgical recurrence (Portolani et al., 2006), with a 5 year survival rate of around only 30%–40%. In about a third of those instances, metastatic tumors colonize the major branches of the portal vein with the clinical symptom termed portal vein tumor thrombus (PVTT) (Chambers et al., 2002), although the mechanism underlying the formation of PVTT remains largely unknown. Interestingly, almost all of the reported PVTT cases in the literature have been from developing countries, suggesting that this particular pathological symptom may not be common in HCC patients in developed countries.

The development of HCC is believed to be associated with hepatitis B virus (HBV) and hepatitis C virus (HCV) infection, carcinogen/toxin exposure, and/or genetic factors. Among these suspected etiological factors, HBV infection accounts for more than 60% of the total liver cancer in developing countries and less than a quarter of cases in developed countries (Jemal et al., 2011). The HBV-initiated tumorigenic process often follows from or accompanies long-term symptoms of chronic hepatitis, inflammation, and cirrhosis. The HBV infection-triggered inflammatory and/or fibrotic process, with extensive involvement of cytokine/chemokine production/activation and leukocytes infiltration, is believed to create a microenvironment that favors

Significance

Immune surveillance imposed by a functionally active immune system represents a critical barrier to prevent disseminated tumor cells from forming metastasis. Tumor cells need to acquire specific activities to breach this barrier to successfully colonize a new tissue microenvironment. Emerging evidence also indicates that specific pathways are activated and utilized by tumors initiated by different etiological factors. In this regard, the findings presented here support the notion that HCC initiated by HBV infection could acquire the ability to recruit immune-suppressive Treg cells via activation of the TGF-β signaling pathway, consequently promoting the formation of a particular type of intrahepatic metastasis. Meanwhile, identification of components of this pathway also provides potential therapeutic targets for the treatment of this deadly disease.

the development of HCC. Consistent with an important role for HBV in HCC, persistent presence of HBV DNA in the serum of infected individuals is found to be a strong indicator for the development of HCC (Chen et al., 2006). Moreover, HCC patients with high levels of serum HBV DNA have a poor prognosis, including risks of death, metastasis, and recurrence following surgery (Chen et al., 2009). However, it remains unclear whether the HBV-initiated pathological process plays a specific role in late stages of HCC progression such as formation of PVTT.

The cytokine transforming growth factor β (TGF-β) is known to be a multifunctional factor that plays critical roles in various aspects of liver pathogenesis, including chronic HBV/HCV infection (Marotta et al., 2004), cirrhosis (Matsuzaki, 2009), and tumorigenesis (Massagué, 2008). Mounting evidence indicates that one efficacious mechanism by which TGF-β promotes tumor progression and metastasis is through repression of immune surveillance within the tumor microenvironment (Bierie and Moses, 2006; Massagué, 2008; Schmierer and Hill, 2007): TGF-β can attract several types of innate and adaptive immune cells to the tumor sites, enhance production of various cytokines/chemokines, and alter the functional differentiation program of those cells consequently promoting tumor growth, invasion, and metastasis (Massagué, 2008).

Within the tumor microenvironment, FoxP3-expressing regulatory T (Treg) cells, which normally function as a dominant inhibitory component in the immune system to actively maintain self-tolerance and immune homeostasis through suppression of various immune responses, have been demonstrated to be coopted by tumor cells to escape immune surveillance (Mailloux and Young, 2010). Treg cells are frequently found to accumulate within the tumor mass and ascites (Quezada et al., 2006). A number of chemokines, including CCL22, which is also termed macrophage-derived chemokine (MDC) and originally found to be secreted by macrophages and dendritic cells upon stimulation with microbial products, have been shown to recruit Treg cells to modulate the immune response during the tumorigenic process (Curiel et al., 2004). Although TGF-β has been found to regulate the development of natural Treg cells in the thymus during negative selection (Ouyang et al., 2010) and the extrathymical conversion of conventional T cells into suppressive inducible Treg cells (Chen et al., 2003), it is unclear whether TGF-β contributes to the accumulation of natural Treg cells within the tumor microenvironment.

MicroRNAs (miRNAs) are small noncoding RNAs of ~22 nucleotides that negatively regulate gene expression by blocking protein translation and promoting degradation of the target messenger RNA (Bartel, 2004). Changes in the expression profiles of miRNAs have been linked to the development of various types of human diseases, including cancer (Lujambio and Lowe, 2012). MicroRNAs can act as oncogenic promoters or tumor suppressors, depending on the functional nature of their specific target genes within a specific cell or tissue type (Esquela-Kerscher and Slack, 2006; Nicoloso et al., 2009). In the context of HCC, recent reports indicate that alterations in the expression levels of specific miRNAs are closely associated with specific stages of the disease process, including intrahepatic metastasis (Ding et al., 2010; Xiong et al., 2010). However, those studies did not elucidate the specific roles of any those miRNAs in the progression of HCC to venous metastasis. In this study, we explored the possibility that specific miRNAs could act as mediators of changes in the tumor microenvironment during HCC progression and whether there was a potential link between HBV status as an etiological factor and development of HCC-PVTT.

Table 1. Clinical Characteristics of HCC patients with or without PVTT

Clinical Characteristics		HCC without PVTT (n = 54)	HCC with PVTT (n = 234)
Age	Mean ± SD	55.89 ± 10.25	48.08 ± 9.43
Gender	Male/Female	43/11	211/23
Hepatitis virus	$HBsAg^+$	41	209
	$HBsAg^-$	12	2
	$HCVAb^+$	0	3
	$HBsAg^+$ $HCVAb^+$	0	0
	Unknown	1	20
Tumor number	1	46	214
	≥2	8	20
Median survival	Days	964	263
AFP (ng/ml)	<20	27	37
	≥20	27	197
Distant metastasis[a]	Met/Total cases	3/54	66/234

Tumor number indicates number of primary tumor mass detected at the time of surgical operation. AFP, α-fetal protein in the serum.
[a]Distant metastasis includes metastases to lung, bone, brain, abdominal lymph nodes, adrenal gland, and abdominal wall.

RESULTS

HBV Infection Status and TGF-β Signaling Activity Are Positively Associated with PVTT Development in HCC Patients

To investigate whether there is an etiological basis for the development of PVTT, we analyzed the clinical data of 288 HCC patients who received treatment in the Shanghai Eastern Hepatobiliary Surgery Hospital and Guangzhou Sun Yat-sen University Cancer Center in China (Table 1). Among those patients, 234 developed PVTT with a poor prognosis in comparison to the 54 patients who were negative for symptoms associated with PVTT (Figure 1A). Within the PVTT positive group, the prognosis of the patients showed a clear correlation with the types of PVTT development (Shi et al., 2010) as measured by the presence of tumor lesions in different segments of the portal venous system (Figure 1B).

In contrast to developed countries, HBV infection is the major causative factor of HCC in China and other developing countries with HBV positive (HBV^+) status accounting for as much as 80% of all HCC cases. In our patient cohort, 89% of the 234 HCC patients with PVTT who were examined for their HBV status were HBV^+, but only 68% of 60 HCC patients without PVTT are HBV^+ (Figure 1C). This indicates that HBV infection status is strongly associated with the development of PVTT, which was not noted previously likely because PVTT has not been reported as a major pathological feature of HCC patients in developed countries. Consistent with a poorer prognosis of HCC patients

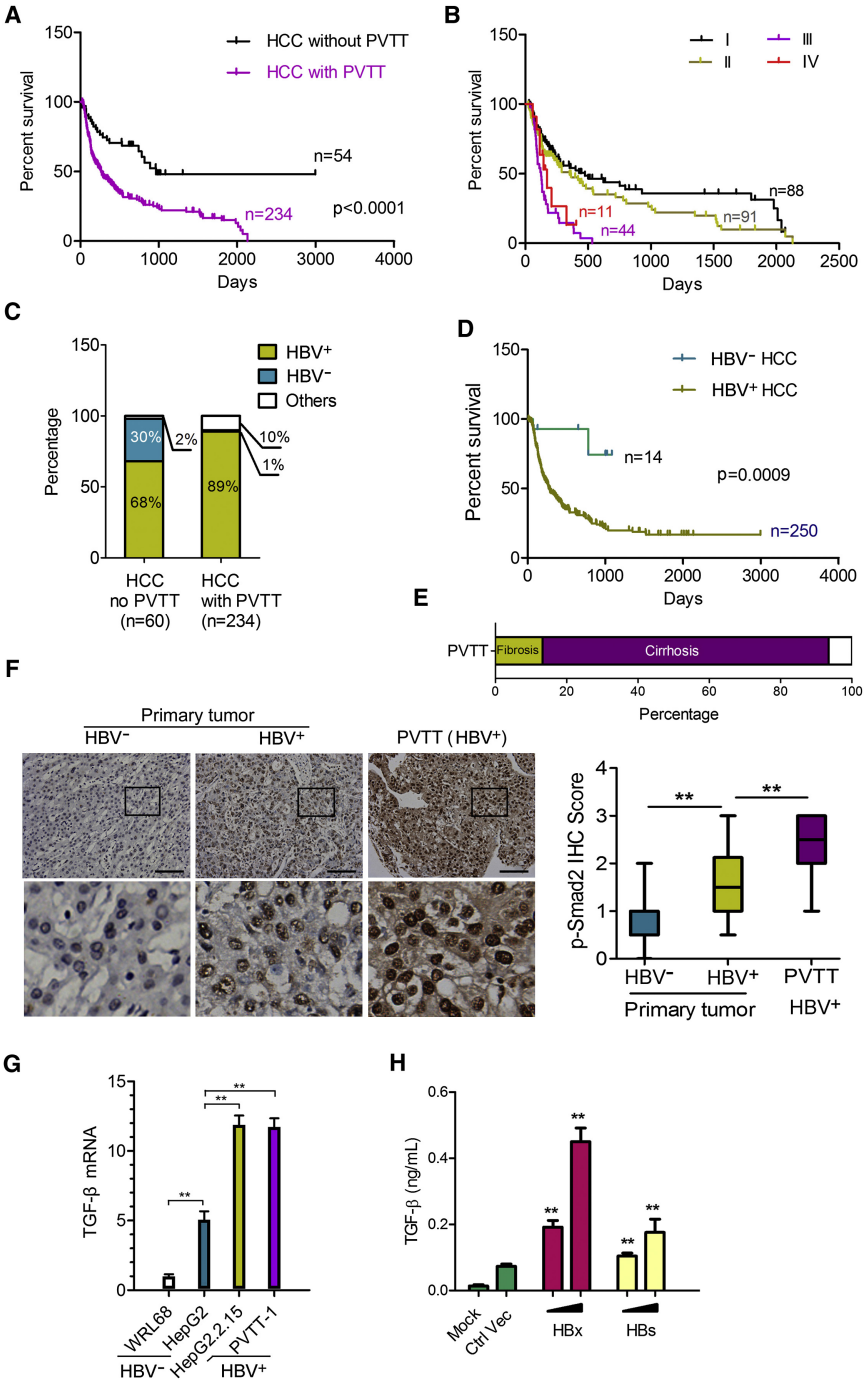

Figure 1. HBV Infection Status and TGF-β Signaling Activity Are Associated with Development of PVTT in Human HCC Patients

(A) Kaplan-Meier survival curves of HCC patients with PVTT in comparison with those without PVTT detected at the time of surgical operation. Clinical characteristics of those patients are presented in Table 1.

(B) Kaplan-Meier survival curves of HCC patients shown in Table 1 with different degree of PVTT development based on the extent of venous tumor thrombus formation. Type I: Tumor thrombi involving segmental branches of the portal vein or above; Type II: Tumor thrombi involving right/left portal vein; Type III: Tumor thrombi involving the main portal vein trunk; Type IV: Tumor thrombi involving the superior mesenteric vein.

(C) Percentage of HBV infection in HCC patients with PVTT compared with those without PVTT. "Others" in the PVTT group include 3 HCV^+ patients and 20 patients without the information of their hepatitis viral infection status. "Others" in the HCC without PVTT group include one HCC patient without information of hepatitis viral infection status, as well as six additional patients who were HBV^- that were not a part of the original set of the 288 patients analyzed in (A) and (B).

(D) Kaplan-Meier survival curves of HBV^+ verses HBV^- patients with HCC. The HBV^+ group includes 41 HCC patients without PVTT and 209 HCC patients with PVTT; The HBV^- group includes 12 HCC patients without PVTT and 2 HCC patients with PVTT. Thirty of the 294 patients displayed in (C) were excluded from this analysis due to the lack of specific information: 6 HBV^- patients without PVTT lacked survival information, 21 patients lacked hepatitis viral infection status, and 3 HCV^+ HCC patients.

(E) Rate of occurrence of pathological symptoms associated with liver cirrhosis or fibrosis in the 234 HCC patients with PVTT shown in Table 1.

(F) IHC of phosphorylated Smad2 in HCC samples. Left: Representative images showing different intensities of nuclear staining of pSmad2. Scale bars, 100μm. Lower panels represent magnified pictures (5×) of boxed area in the corresponding upper panels. Right: Box plot graph showing the quantitative evaluation of pSmad2 staining intensity from a tissue microarray. Plot of a box-plot (25%–75%) with whiskers to minimal and maximal of all the score data was used. The statistical differences between the three groups were analyzed by one-way analysis of variance. $^{**}p < 0.01$.

(G) TGF-β expression levels in four different liver cell lines. Relative TGF-β1 mRNA level was measured by qRT-PCR and normalized to β-actin. $^{**}p < 0.01$, n = 3.

(H) 10^5 HepG2 cells were transfected with 0.5 μg and 1 μg HBx or HBs expression construct, respectively. Twenty-four hr later, relative amounts of TGF-β1 secreted into the culture media were determined by ELISA. $^{**}p < 0.01$ versus control vector group, n = 3. All error bars indicate mean ± SD.

See also Figure S1.

who develop PVTT, HBV^+ patients showed a much worse prognosis than HBV negative (HBV^-) patients (Figure 1D). Taken together, the clinical data on our patients strongly support the notion that HBV infection is a potent etiological factor predisposing HCC patients to develop PVTT with a poor prognosis of the disease.

To investigate possible mechanisms underlying the observed link between positive HBV status and the development of PVTT, we conducted further analysis on the pathological characteristics of the 234 PVTT patients whose clinical history was recorded in more detail. It has been well established that chronic HBV infection is associated with induction of inflammation, fibrosis,

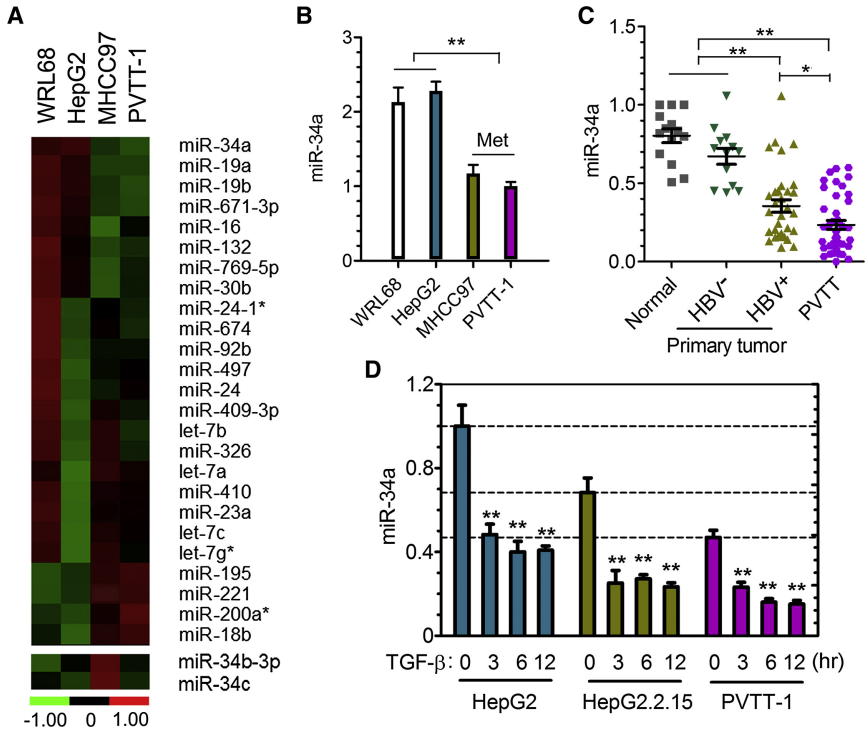

Figure 2. Reduced Expression of miR-34a Is Correlated with HBV-Positive HCC-PVTT and Regulated by TGF-β

(A) Heat map of a partial list of miRNAs, which expression levels differ among the indicated four liver cell lines as determined using an RT-PCR-based miRNA expression array.

(B) The relative level of miR-34a of indicated cell lines was measured by qRT-PCR and normalized to the level of U6. n = 3. **p < 0.01 calculated by Student's t test.

(C) The relative level of miR-34a in 26 PVTT tissue samples (all HBV$^+$), 30 primary tumor tissue samples (17 HBV$^+$ and 13 HBV$^-$), and 14 normal liver tissues distal to tumor regions was determined by qRT-PCR and normalized to U6. **p < 0.01 calculated by Student's t test.

(D) The relative level of miR-34a in different cell lines mock-treated or treated with TGF-β1 for indicated time points was measured by qRT-PCR and normalized to U6. n = 3. **p < 0.01 calculated by Student's t test.

All error bars indicate mean ± SD. See also Table S1 and Figure S2.

or even cirrhosis prior to the development of HCC. Indeed, 219 patients were recorded to have liver cirrhosis or their tumors were found to display pathological features of inflammation and fibrosis at the time of surgery (Figure 1E). Since TGF-β is among the most potent cytokines linked to liver inflammation, fibrosis, and cirrhosis (Bissell, 2001), we next determined the level of TGF-β signaling activity by measuring the status of Smad2 phosphorylation in the nucleus using tissue microarrays prepared from some of the 294 HCC patient samples. Strong nuclear p-Smad2 staining, with a score of immunohistochemistry (IHC) intensity over 2 (++), was detected in 11 of 16 PVTT tumor specimens and 22 of 66 HBV$^+$ primary HCC tumor samples. In contrast, seven of ten HBV$^-$ HCC tumor samples showed very low p-Smad2 levels with a score of IHC intensity less than 1 (+) (Figure 1F). Consistent with the IHC results, the levels of p-Smad2 determined by western blot from fresh tumor tissues were also found to be significantly higher in HBV$^+$ HCC primary and PVTT tissue samples compared with those of HBV$^-$ tumors (Figure S1 available online). These data indicate that high levels of TGF-β signaling activity are strongly associated with the development of HBV$^+$ primary HCC and PVTT.

We also measured the expression of TGF-β1, the main isoform of the TGF-β family, in several liver cell lines, including WRL68 (nontumorigenic and HBV$^-$), HepG2 (HBV$^-$ liver tumor cells), HepG2.2.15 (HepG2-derivative with integration of the HBV genome) (Delaney and Isom, 1998), and PVTT-1 (established from a PVTT biopsy sample of a HBV$^+$ HCC patient). As shown in Figure 1G, TGF-β1 expression is much higher in HBV$^+$ than in HBV$^-$ cell lines, providing support to the notion that TGF-β may play a role in the progression of HBV-initiated HCC to PVTT. To test whether HBV could have a more direct effect on the expression of TGF-β, we transiently transfected HepG2 cells with two HBV-encoded genes, HBx and HBs, that have been reported to play functional roles in HBV-associated carcinogenesis (Lupberger and Hildt, 2007). Interestingly, transient expression of these genes leads to increased TGF-β1 levels in the cell supernatants within 24 hr in a dose-dependent manner (Figure 1H). These results suggest that the presence of HBV encoded genes could have a direct influence on TGF-β expression in liver cancer cells.

Expression of miR-34a Is Inversely Correlated with Metastatic Potential in HBV$^+$ HCC and Subject to Negative Regulation by TGF-β

We then screened WRL68, HepG2, PVTT-1, and MHCC97 cell lines using a quantitative RT-PCR (qRT-PCR)-based miRNA-array strategy to identify miRNAs that may be functionally linked to HCC metastases. MHCC97 is a HBV$^+$ cell line that acquired metastatic capacity through passages in nude mice (Tian et al., 1999). As shown in Figure 2A and Table S1, the expression of a group of miRNAs displays significant differences among these four cell lines. The miR-34a, but not its family members miR-34b/c, level is significantly lower in both HBV$^+$ PVTT-1 and MHCC97 lines with high metastatic potential than in the other two cell lines (Figure 2B). We selected miR34a for further investigation because it is a well-established tumor suppressor (He et al., 2007), and it was 1 of the 20-miRNA signature for prediction of developing HCC venous metastasis and poor prognosis when its expression is reduced in primary HCC tumors at the time of diagnosis (Budhu et al., 2008).

We next determined whether this suppressed miR-34a expression represents a general pattern in HCC patients with different HBV and PVTT status. We selected clinical samples from the original 294 patients shown in Figure 1C based on the initial evaluation of quality of RNA extracted from the tissue specimen and analyzed the expression of miR-34a using qPCR

from 26 PVTT tissue samples (all were HBV$^+$), 30 primary tumor tissue samples (17 HBV$^+$ and 13 HBV$^-$), and 14 normal liver tissues derived from areas distal to tumor lesions. As shown in Figure 2C, the level of miR-34a was significantly lower in a large fraction of the HBV$^+$ primary and PVTT tumor samples than that of the HBV$^-$ primary tumor or normal liver tissues. Together these data suggest that reduction in miR-34a expression is frequently associated with HBV-initiated HCC during the disease progression toward the development of PVTT.

To determine whether TGF-β could have a direct role in regulating miR-34a expression, we treated three HCC cell lines with TGF-β and measured the levels of miR-34a at various time points. TGF-β induced a rapid and robust reduction of mature miR-34a in all of these cell lines, even though the basal level of this miRNA in PVTT-1 cells was already very low (Figure 2D). Interestingly, the basal level of miR-34a in the HBV$^+$ HepG2.2.15 cells was also reduced in comparison to their parental HepG2 cells, indicating that presence of the HBV genome could lead to suppression of miR-34a expression (Figure 2D), possibly through the autocrine action of TGF-β1 produced by the same cells (Figure 1G). To test this possibility, we treated HepG2.2.15 cells with SB431542, an inhibitor of the type I TGF-β receptor kinase and found an increase in the level of miR-34a after blocking autocrine TGF-β signaling activity (Figure S2). Taken together with data shown in Figure 1, these results indicate that reduction in miR-34a expression in HBV$^+$ HCC primary and PVTT tumor samples could be directly linked to the high level of TGF-β signaling activity.

The Primary Target of miR-34a in PVTT Cells Is the Chemokine Gene *CCL22*

We initially speculated that previously reported targeting CDK4, CCNE2, and MET by the miR-34a/b/c family (He et al., 2007) could be the potential mechanism underlying the association between the reduced miR-34a expression and HCC-PVTT development. However, we did not observe an inhibitory effect on cell viability and proliferation, or any difference in cell migration when miR-34a mimic oligos were transfected into PVTT-1 cells (Figures S3A–S3C). Moreover, there were only slight negative effects observed on messenger RNA (mRNA) levels of these three reported target genes with the presence of high-level miR-34a in those cells (Figure S3D). Ectopic expression of miR-34a also did not affect the growth of PVTT-1 tumors in vivo (Figures S3E–S3G). These negative results strongly suggest that should miR-34a have a tumor-suppressive effect on the development of HCC-PVTT, it likely acts through a cell nonautonomous mechanism.

One possible cell nonautonomous route for miR-34a to execute its tumor-suppressive function is to impact the tumor microenvironment by regulating the production of secreted proteins. To test this hypothesis, we developed a qPCR-based assay (Figure S3H) to investigate the potential effect of this miRNA on the expression of cytokines, chemokines, and their receptors in PVTT-1 cells and identified the chemokine CCL22 as the most significantly downregulated molecule upon miR-34a overexpression (Figure 3A). In parallel, we employed established bioinformatic procedures to predict putative miR-34a target genes and identified CCL22 among the top hits associated with tumor metastasis. There are three putative miR-34a targeting sequences present in the 3′ untranslated region (UTR) of the human *CCL22* (Figure 3B), two of which were also found in the murine *Ccl22* (data not shown). To determine if miR-34a affect the expression of CCL22 through these putative targeting elements, we employed a luciferase reporter carrying these elements. A control construct was also generated in which the three putative miR-34a targeting sequences were mutated. As shown in Figure 3C, expression of the miR-34a mimic oligos significantly suppressed the luciferase activity of the wild-type reporter in a dose-dependent manner but had minimal effect on the mutant reporter, supporting the notion that CCL22 is a bona fide target of miR-34a.

To further validate CCL22 as a legitimate target of miR-34a, we examined the expression of the endogenous CCL22 when miR-34a expression was manipulated. As shown in Figure 3D, ectopic expression of miR-34a significantly reduced CCL22 mRNA level. Interestingly, overexpression of miR-34b/c was much less potent in reducing the expression of CCL22 (Figure S3I), even though they share the same seed targeting sequence as miR-34a. Corresponding to a reduction in the level of CCL22 mRNA, the secretion of CCL22 protein was also drastically diminished with miR-34a ectopic expression (Figure 3E). Reciprocally, introduction of antisense (AS)-miR-34a oligos into the PVTT-1 cells was accompanied by an increase in CCL22 production in a dose-dependent manner (Figure 3F). To examine this further, we also transfected the AS-miR-34a oligos into HepG2 cells, which have a relatively higher basal level of miR-34a compared to that of PVTT-1 cells (Figure 2B), and detected an increase in the level of CCL22 mRNA (Figure S3J). Taken together, these data suggest that the expression of miR-34a and CCL22 is inversely correlated, most likely through the direct targeting of the CCL22 gene by miR-34a.

An Inverse Relationship between the CCL22 Level and the miR-34a Level Is Observed in HBV$^+$ HCC Tumor Samples

We next determined the expression pattern of CCL22 in four cell lines with different HBV status. As shown in Figure 4A, higher protein levels of CCL22 were detected in HBV$^+$ (miR-34a low), HepG2.2.15, and PVTT-1 cells than in HBV$^-$(miR-34a high), WRL68, and HepG2 cells. We then measured mRNA levels of CCL22 by qPCR using the same set of tissue samples shown in Figure 2C and found that CCL22 mRNA level was significantly increased in the group of HBV$^+$ primary tumors and further elevated in PVTT samples (Figure 4B). Importantly, the CCL22 mRNA level is inversely associated with the miR-34a level in HBV$^+$ primary tumor and PVTT tumors when the values for each individual patient were plotted (Figure 4C). In contrast, such association is not observed in HBV$^-$ tumor samples or normal liver tissues (Figure 4C). Again, these clinical data provide strong support for our hypothesis that the elevation in CCL22 is likely the result of reduced expression of miR-34a with a close association with the positive status of HBV as the etiological factor in the development of PVTT.

Reduced miR-34a Expression Is Correlated with Enhanced Recruitment of Treg Cells

CCL22 has been implicated in the tumorigenic process by binding to its receptor CCR4 on the surface of Treg cells,

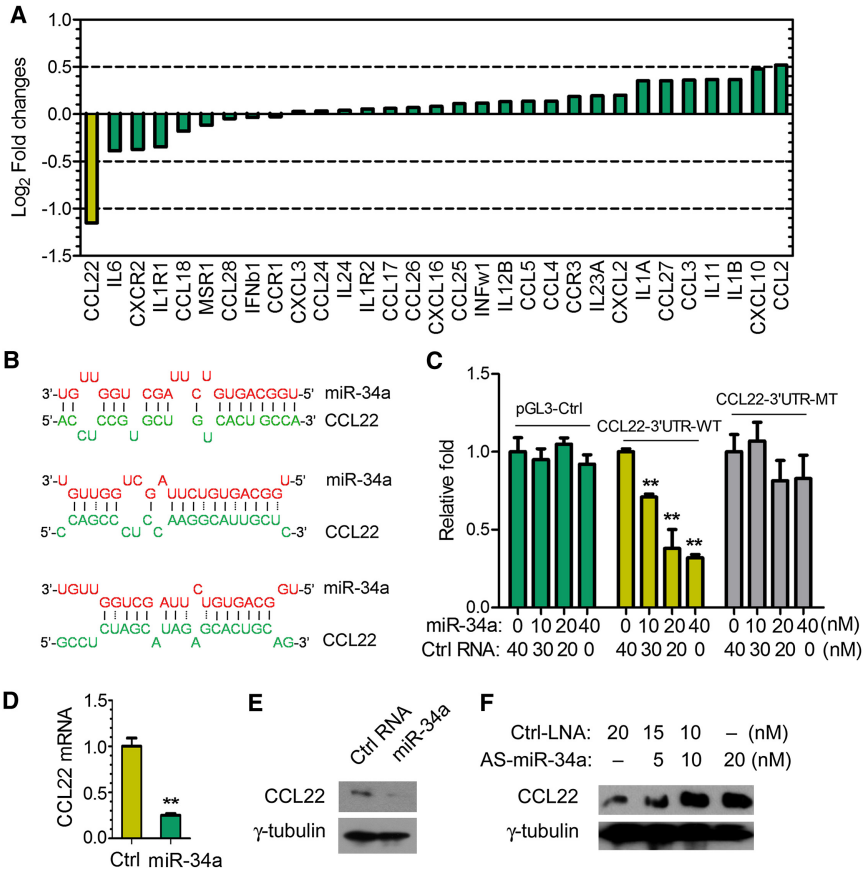

Figure 3. The Chemokine CCL22 Is a Bona Fide Target of miR-34a

(A) PVTT-1 cells were transfected with 80 nM of pre-miR-34a mimetic oligos, and a RT-PCR-based expression array was carried out to determine the expression profile of 94 cytokines, chemokines, and their receptors 6 hr later. The expression pattern for 31 out of the 94 genes is presented as representatives.

(B) Putative miR-34a binding sites in the 3′ UTR of human *CCL22*.

(C) HEK293T cells were transiently transfected with pre-miR-34a mimetic or control oligos together with the pGL3 control plasmid, a modified pGL3 plasmid containing the wild-type CCL22 3′ UTR, or a mutant CCL22 3′ UTR with all three putative target sequences mutated. Pre-miR-34a mimetic or control oligos were added at the indicated concentrations and the luciferase activity was analyzed 24 hr later. Data are presented as relative firefly luciferase units normalized with the value of renilla luciferase. N = 3. $^{**}p < 0.01$ (Student's t test).

(D) PVTT-1 cells were transfected with 80 nM of pre-miR-34a mimetic oligos, and the CCL22 mRNA level was determined by qPCR 48 hr later and normalized to GAPDH. $^{**}p < 0.01$ (Student's t test).

(E) PVTT-1 cells were treated as in (D), and CCL22 protein level in culture media was determined by western blot. γ-tubulin in corresponding cell lysates was used as a loading control. n = 3.

(F) PVTT-1 cells were transfected with AS-miR-34a or control oligos at the indicated concentrations, and the CCL22 level in culture media was determined by western blot 48 hr later. γ-tubulin in corresponding cell lysates was used as a loading control. n = 3. All error bars indicate mean ± SD. See also Figure S3.

consequently recruiting those immunosuppressive cells to the tumor microenvironment and promoting tumor cell escape from immune surveillance. Thus, miR-34a may exert its cell nonautonomous tumor-suppressive effect by regulating CCL22 expression and recruitment of Treg cells. To test this hypothesis, we examined the ability of culture media from PVTT-1 cells treated with different concentrations of AS-miR-34a oligos to mobilize $CD4^+CD25^+$ cells freshly isolated from healthy donors, the majority of which were $FoxP3^+$ Treg cells (Figure S4A). As shown in Figure 5A, inhibition of miR-34a correlates with increase in the migratory activity of the Treg cells. Furthermore, antihuman CCL22 neutralizing antibody significantly inhibited the enhanced Treg cell migratory activity, indicating that miR-34a inhibitor-induced Treg cell migration is dependent on the production of CCL22.

To investigate the role of miR-34a in regulating Treg cell migration in vivo, we inoculated PVTT-1 cells with or without ectopic expression of miR-34a into nude mice to form tumors and transferred freshly isolated $CD4^+CD25^+$ human Treg cells into those mice via tail vein injection 14 days later. Together with determination of the expression status of CCL22 (Figure 5B), the accumulation of human Treg cells inside the PVTT tumors was assessed 48 hr later. As shown in Figures 5C and S4B, miR-34a ectopic expression in PVTT-1 cells significantly decreased accumulation of $CD4^+CD25^+$ Treg cells, but not $CD4^+CD25^-$ T cells inside the tumor.

To investigate whether there is a link between the expression of miR34a and the level of Treg cells present in clinical samples, we determined the expression profile of FoxP3, which is expressed primarily if not exclusively in Treg cells, in the same set of tissue specimen used in experiments presented in Figures 2C and 4B. We observed higher levels of FoxP3 mRNA in HBV^+ primary and PVTT tumor tissues (Figure 5D), indicating a greater accumulation of Treg cells in HBV^+ primary and PVTT tumor tissues. Indeed, this postulation is supported by immunohistochemical staining of a subset of the tumor specimens (Figure 5E). Again, analyzed at the individual patient level, the increase of FoxP3 mRNA inside the tumor mass is strongly associated with the decrease of miR-34a level in HBV^+ primary and PVTT tumors (Figure 5F). Together these results provide strong support to the notion that the suppression of miR-34a in HBV^+ primary and PVTT tumor cells leads to elevated production of CCL22 in the tumor microenvironment, which in turn augments the recruitment of Treg cells and immune suppression.

TGF-β Induces CCL22 Production via Suppression of miR-34a

We then tested whether TGF-β could affect CCL22 expression. As shown in Figure 6A, CCL22 production by PVTT-1 cells was increased following TGF-β treatment in a time-dependent manner. To determine whether TGF-β exerts its effect via the canonical signaling pathway, we added SB431542 to the

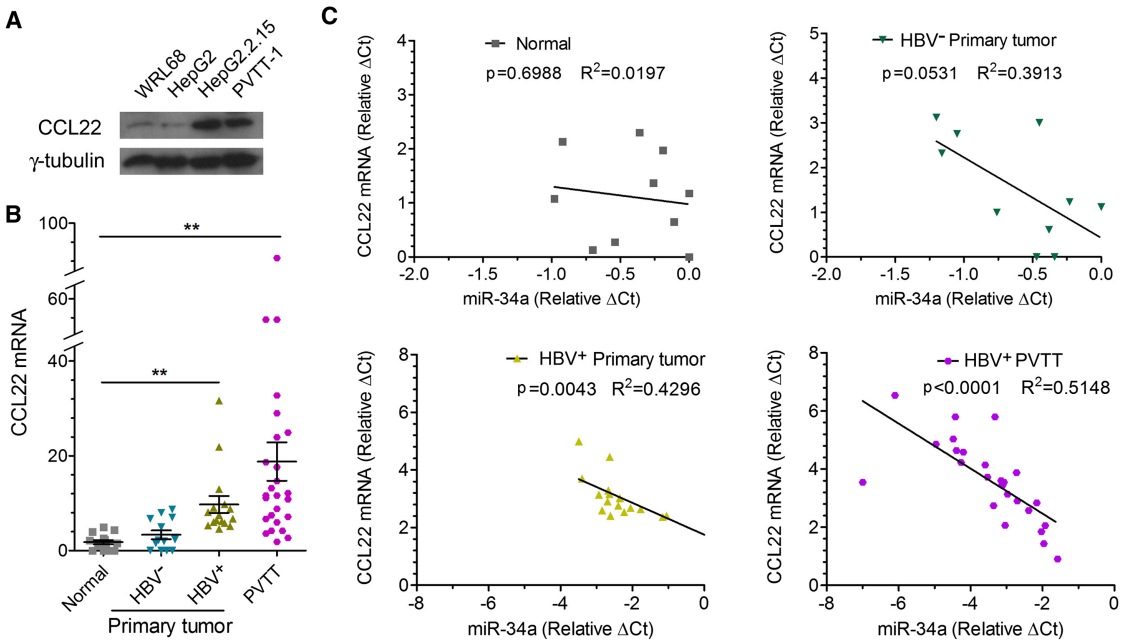

Figure 4. CCL22 Upregulation in PVTT Is Associated with Downregulation of miR-34a

(A) The CCL22 protein level in indicated liver cell lines was determined by western blot. γ-tubulin was used as a loading control.

(B) Tissue specimens from the same set of patients as in Figure 2C were examined for the mRNA level of CCL22 by qRT-PCR and normalized to that of β-actin (CCL22 mRNA was undetectable in four normal liver tissues and two HBV$^-$ HCC primary tumor tissues). *p < 0.05, **p < 0.01 (Student's t test). Mean ± SD.

(C) Clinical samples from the same set of specimen as in Figures 2C and 4B were analyzed in the four groups as indicated (CCL22 mRNA was undetectable in four normal liver tissues and two HBV$^-$ HCC primary tumor tissues). The correlation between miR-34a and CCL22 expression for each individual was assessed by linear regression.

PVTT-1 cells in the presence or absence of TGF-β. SB431542 completely blocked the ability of TGF-β to suppress miR-34a or to induce CCL22 expression (Figure 6B). We also observed that forced miR-34a elevation dose-dependently blocked the ability of TGF-β to induce the expression of CCL22 in PVTT-1 cells (Figure 6C), suggesting that the effect of TGF-β on CCL22 expression was predominantly mediated by downregulation of miR-34a. The functional relationship between miR-34a and TGF-β observed here is similar to the previous reported inhibition of TGF-β-induced epithelial-mesenchymal transition by ectopic miR-34a expression (Siemens et al., 2011).

We next investigated the role of this TGF-β-miR-34a-CCL22 pathway on Treg cell migration. Culture media from PVTT-1 cells treated with different concentrations of miR-34a mimic oligos were tested for their capacity to mobilize freshly isolated human CD4$^+$CD25$^+$ Treg cells. Consistent with the enhanced CCL22 production, Treg cell migratory activity was correspondingly increased upon exposure to supernatant derived from PVTT-1 cells treated with TGF-β (Figure 6D). On the other hand, transfection of miR-34a mimic oligos into the PVTT-1 cells blocked the effect of TGF-β-induced CCL22 expression and Treg cell migration in a dose-dependent manner (Figure 6D).

The Suppressive Function of miR-34a on Tumor Growth and Metastasis Is Mediated by CCL22

The miR-34a-CCL22-Treg link demonstrated above provides us with a plausible explanation for why miR-34a has little impact on xenograft tumor formation by human PVTT-1 cells in athymic nude mice (Figures S3F and S3G); the hosts have no T cells (including Tregs) and exhibit little cellular immunity. The use of murine model systems in which liver tumorigenesis can be induced by gene manipulation or chemicals has very limited application or relevance for our purpose since HBV is not an etiological factor for the initiation of liver tumor formation in those established models. Nevertheless, we have adopted a model by employing a murine liver tumor cell line, Hepa1-6, originally derived from the C57BL/6J mouse strain that is immune-competent with fully functional T cell lineages. Consistent with what is shown in Figures S3F and S3G, we found that miR-34a overexpression has minimal effect on Hepa1-6 tumor growth in nude mice (Figure 7A), even though tumors derived from Hepa1-6 cells express a low level of CCL22, which was reduced by the ectopic expression of miR-34a (Figure 7B). In order to test the full potential of CCL22 to promote tumor metastasis in the context of an immune-competent host, we engineered ectopic expression in Hepa1-6 cells of the mouse CCL22 open reading frame (ORF) without its 3′ UTR so that it cannot be targeted by miR-34a. Indeed, overexpression of CCL22 was not affected by the coexpression of miR-34a (Figure 7B). Subsequently, these four populations of Hepa1-6 cells were inoculated subcutaneously into C57BL/6J mice, and tumor growth was followed for 21 days. As shown in Figure 7C, Hepa1-6 tumor growth was significantly suppressed by miR-34a overexpression in immune-competent mice in comparison to that of the vector control. In contrast, CCL22 overproduction appeared to have a dramatic positive effect on tumor growth. Importantly, miR-34a-induced tumor

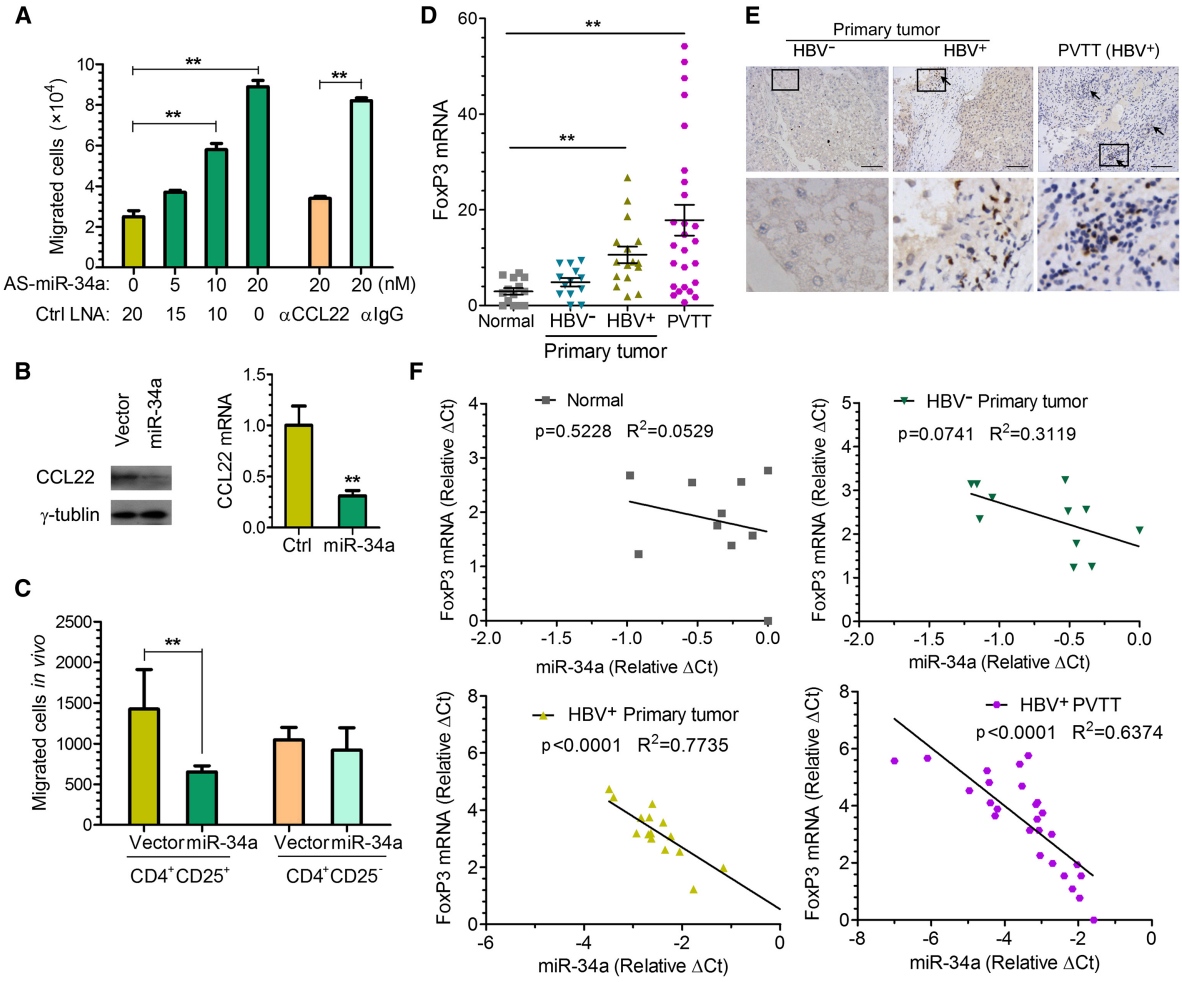

Figure 5. The miR-34a-CCL22 Pathway Regulates CD4$^+$CD25$^+$ Treg Cell Recruitment into the Tumor Microenvironment

(A) 1 × 10^5 human CD4$^+$CD25$^+$ Treg cells were tested by transwell assay for their migration toward culture media of PVTT-1 cells harvested 24 hr after the cells were transfected with different amounts of AS-miR-34a or control oligos as indicated. CCL22 neutralizing or control antibody was added to the culture media of AS-miR-34a oligos transfected PVTT-1 cells to determine the effect on Treg cell migration. Four hours after plating of the T cells in the upper chamber, migrated Treg cells were quantified by Cell Counter analysis (n = 3, mean ± SD). **p < 0.01 (Student's t test).

(B) CCL22 protein (left panel) or mRNA (right panel) level in xenograft tumors tissue samples derived from indicated PVTT-1 cells in nude mice was determined. γ-tubulin was used as a loading control for the western blot, and mRNA level of CCL22 was normalized to that of GAPDH. n = 4.

(C) Freshly isolated human CD4$^+$CD25$^+$ or CD4$^+$CD25$^-$ T cells were injected via the tail vein into nude mice with xenograft tumors formed by PVTT-1 cells ectopically expressing the vector control or miR-34a as indicated, and tumors were extracted 48 hr later. Fluorescence-activated cell sorting was used to quantify the number of T cells within 1 × 10^8 total cells from each tumor. n = 4, mean ± SD **p < 0.01 (Student's t test).

(D) The mRNA level of FoxP3 in HBV$^+$ HCC primary and PVTT samples from the same set of patients as in Figures 2C and 4B was measured by qRT-PCR and normalized to that of β-actin (FoxP3 mRNA was undetectable in four normal liver tissues and two HBV$^-$ HCC primary tumor tissues). *p < 0.05, **p < 0.01 (Student's t test).

(E) Treg cell accumulation in HCC primary and PVTT samples was determined by immunohistochemistry staining using an anti-FoxP3 antibody. Representative images from one set of the samples are shown. Arrows indicate FoxP3$^+$ Treg cells stained in dark brown color. Scale bars, 100 μm. Lower panel represents magnified views (5×) indicated by boxes in the upper panel.

(F) Clinical samples from the same set of patients as in Figures 2C and 5D were analyzed in four groups as indicated (FoxP3 mRNA was undetectable in four normal liver tissues and two HBV$^-$ HCC primary tumor tissues). The correlation between miR-34a and FoxP3 expression for each individual was assessed by linear regression. All error bars indicate mean ± SD.

See also Figure S4.

suppression was largely eliminated upon the overexpression of the nontargetable CCL22 (Figure 7C), strongly suggesting that the tumor-suppressive effect of miR-34a was mediated by reducing the production of CCL22 as its predominant target. To further investigate the mechanism by which miR-34a and CCL22 exert their effects on the growth of Hepa1-6 cells in their syngeneic and immune-competent hosts, we quantified the number of Treg cells infiltrated into the tumor mass formed by the four types of cells. Consistent with the role of CCL22 as a chemoattractant predominantly for Treg cells, the number of

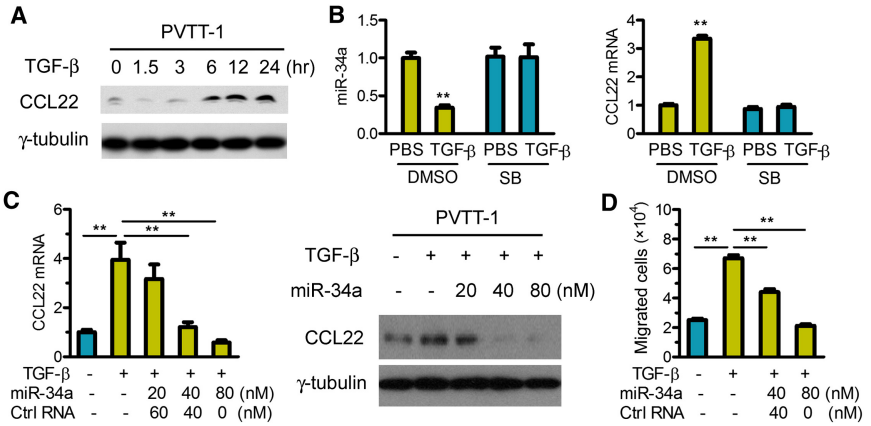

Figure 6. TGF-β Positively Regulates the Production of CCL22 and Treg Cell Migration via Repression of miR-34a in PVTT-1 Cells

(A) Time course of TGF-β-induced CCL22 production detected in the culture media of PVTT-1 cells. CCL22 was detected by western blot and γ-tubulin in corresponding cell lysate was used as a loading control.

(B) PVTT-1 cells were pretreated with the control solvent (DMSO) or SB431542 (SB) at 20 μM for 30 min and then treated with TGF-β1 for 12 hr. The expression of miR-34a (left panel) and of CCL22 mRNA (right panel) were measured by qRT-PCR and normalized to U6 or GAPDH, respectively (n = 3, mean ± SD). **p < 0.01 (Student's t test).

(C) PVTT-1 cells were pretreated with various doses of pre-miR-34a mimetic or control oligos for 24 hr before TGF-β1 treatment for another 12 hr, as indicated. The level of CCL22 mRNA was measured by qRT-PCR and normalized to GAPDH (left panel). CCL22 protein was detected by western blot and γ-tubulin was used as a loading control (right panel).

(D) The same transwell assay as in Figure 5A was conducted with supernatants from PVTT-1 cells first transfected with pre-miR-34a or control oligos and 24 hr later treated with TGF-β1 for another 24 hr. (n = 3, mean ± SD). **p < 0.01 (Student's t test). All error bars indicate mean ± SD.

$CD4^+CD25^+FoxP3^+$ cells detected in tumors correlated with the level of CCL22 produced by each population of Hepa1-6 cells (Figure 7D).

Using the same set of four populations of Hepa1-6 cells, we assessed the effects of miR-34a and CCL22 on metastatic potential following a well-established protocol (Bao et al., 2004; Feng et al., 2011). The different batch of Hepa1-6 cells carrying a luciferase reporter was inoculated intrasplenically into C57BL/6J mice. After 21 days, luciferase signals derived from abdominal metastatic growth were measured by the Xenogen IVIS Lumina system (Caliper, Hopkinton, MA, USA). As shown in Figures 7E–7G, ectopic miR-34a expression significantly reduced metastatic growth. In contrast, CCL22 had a potent effect in boosting the growth of Hepa1-6 cells inside the mouse liver and abdomen, completely overcoming any inhibitory effect by miR-34a (Figures 7E–7G).

To provide further support for the role of miR-34a in promoting tumor metastasis using a different immune-competent mouse model and to assess whether this miR-34a-CCL22-Treg pathway can function in a different tumor context, we employed a well-established mouse model of lung metastasis by 4T1 murine mammary tumor cells in their syngeneic hosts of the BALB/c background (Morecki et al., 1998). We first determined that miR-34a overexpression has the same negative effect on CCL22 production in 4T1 cells as in human PVTT-1 cells (Figure S5A). We then inoculated 2×10^4 4T1 cells with or without miR-34a overexpression into the mammary fat pad of female BALB/c mice. Consistent with the results shown in Figure 7C, the size of tumors from 4T1 cells ectopically expressing miR-34a was smaller than that of control cells after 21 days of growth (Figure S5B). To test if Treg cells were differentially recruited to the 4T1 tumors upon manipulation of tumor miR-34a levels, we quantified the number of $CD4^+CD25^+FoxP3^+$ Treg cells inside the tumor mass of the collected primary tumor tissue. A significant reduction in the number of Treg cells was observed from tumors derived from 4T1 cells with ectopic miR-34a expression (Figure S5B). To gain further insight using this system, we repeated these experiments by implanting 5×10^4 4T1 cells. Seven or fourteen days postimplantation, mice were subjected to imaging analysis to quantify the metastatic tumor mass in the lung. As shown in Figure S5C, ectopic miR-34a expression completely blocked the formation of lung metastases by the 4T1 cells, likely through the reduction of CCL22. Taken together, our results from both liver and mammary tumor models demonstrate the potent antimetastatic effect of miR-34a, which is mediated primarily by suppressing Treg cell recruitment via inhibition of CCL22 production.

DISCUSSION

The presence of PVTT in patients with HCC is one of the most significant factors for a poor prognosis in developing countries (Lin et al., 2011; Shi et al., 2010). Once PVTT is formed, the tumor cells may spread along the portal vein, leading to extensive bilobar intrahepatic metastasis. Portal vein obstruction also causes further deterioration in liver function often resulting in liver failure. In addition, PVTT-induced portal hypertension can cause intractable ascites and esophageal variceal bleeding. The symptoms associated with PVTT present a major challenge for the treatment of HCC in such patients. Despite its clinical importance, however, the mechanism associated with the pathogenesis of PVTT remains largely unclear.

In the current study, we extensively investigated the risk factors and mechanism underlying the development of this important intrahepatic metastasis. Consistent with a previous report (Takizawa et al., 2007), PVTT also strongly correlates with poor prognosis in our cohort of HCC patients. Importantly, we uncovered a link between the development of PVTT and positive HBV infection status, as well as a high level of TGF-β signaling activity. Compared with a rate of 14.3% of PVTT metastasis in HBV^- HCC patients, a much higher rate of 82.5% of PVTT development was found among HBV^+ patients. Thus, our findings strongly suggest that HCC initiated by HBV infection predisposes those patients for development of PVTT, which in turn accounts for the high mortality rate for HCC patients in the developing countries, such as China (Jemal

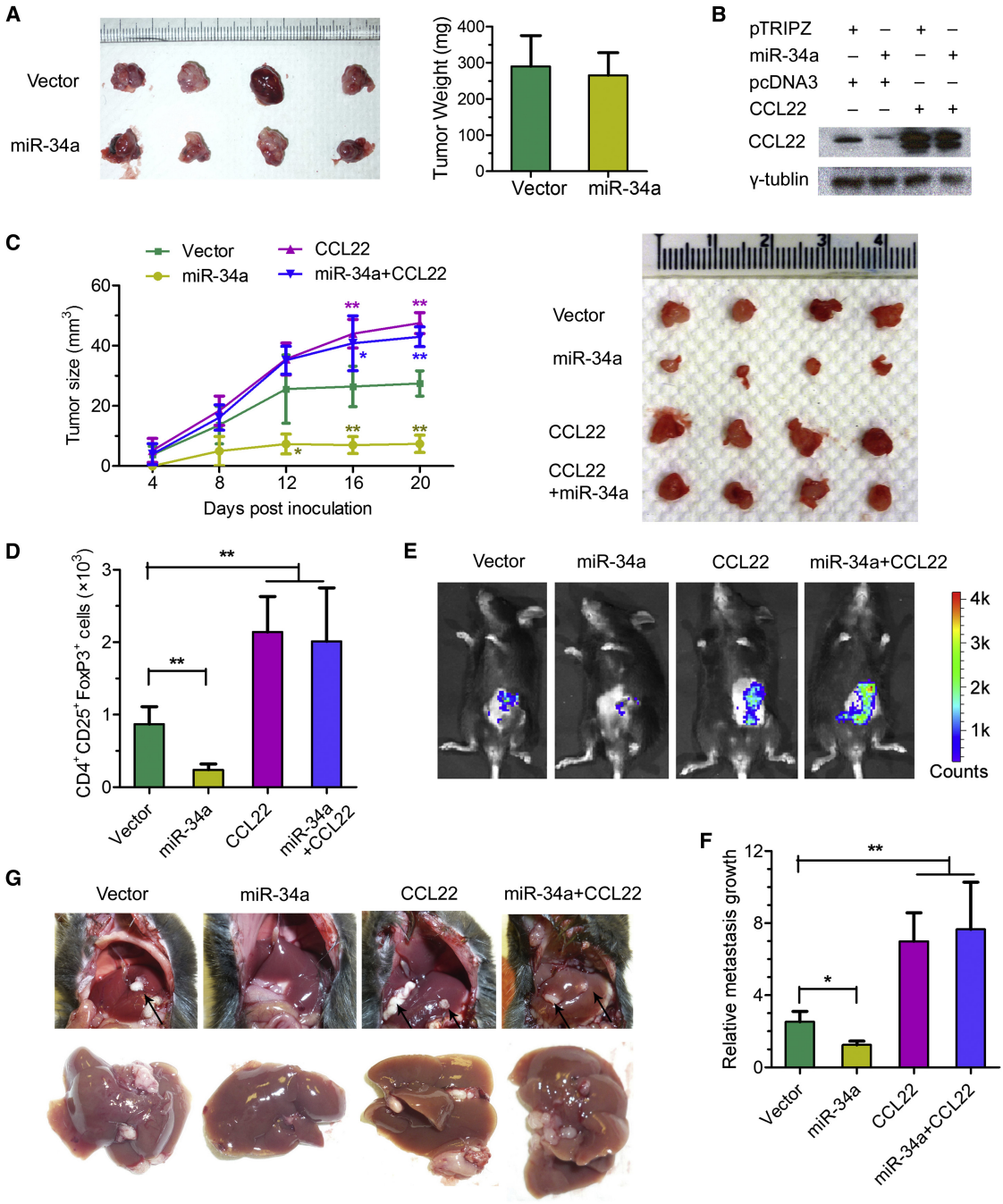

Figure 7. Impact of miR-34a and CCL22 on Tumor Growth and Metastasis Associated with Treg Cell Recruitment to the Tumor Microenvironment

(A) 5 × 10^5 pTRIPZ-miR-34a or pTRIPZ-mock stably transfected Hepa1-6 cells were subcutaneously injected into 6-week-old nude mice. Three weeks later, tumors derived from indicated cells were isolated and shown in the left panel with the plot of their weight displayed in the right panel. n = 4.

(B) pTRIPZ-miR-34a or pTRIPZ-mock together with pcDNA3-CCL22-ORF or pcDNA3 vector as indicated were stably transfected into Hepa1-6 cells to generate population of cells. 2 × 10^6 of each population of those cells were subcutaneously injected into 6-week-old male C57BL/6J mice. The animals were administered Doxcycline 2 μg/mouse by gavage every 2 days. After 21 days, CCL22 in tumor tissues was detected by western blot, and γ-tubulin was used as a loading control.

(C) The tumor growth curves (left panel) for the same four populations of stably transfected Hepa1-6 cells as described in (B) were measured, and the tumors isolated 21 days after inoculation are shown in the right panel. **p < 0.01 (Student's t test). n = 4 per experimental group; experiment repeated three times.

(D) Treg cells were quantified in tumors grown from the four populations of Hepa1-6 cells in C57BL/6J mice. The number of Treg cells from 50 mg of tumor tissue derived from indicated cells was determined via cell counting by flow cytometry.

(E) The same four Hepa1-6 populations as described in (B) coexpressing a luciferase reporter were introduced into the C57BL/6J mice via intrasplenic injection. After 21 days, luciferase signals derived from abdominal metastatic tumor growth, as shown in the representative images, were determined by the Xenogen IVIS Lumina system.

et al., 2011), where a large population has been exposed to HBV infection and become chronic carriers of the virus (Han, 2009).

Consequently, HCC should be stratified to at least two major categories based on the pathological nature of the likely initiating step of tumorigenesis associated with the dominant etiological factor: HBV (possibly HCV as well) infection versus other causes such as toxin exposure or alcoholism-induced cirrhosis. One protein encoded by the HBV genome, HBx, has been well established to play a critical role in HBV-associated liver pathogenesis, including tumorigenesis by functioning as an oncogene (Benhenda et al., 2009; Kew, 2011). Together with inactivation of p53 and activation of the Wnt pathway commonly detected in HCC (Ding et al., 2005; Feitelson and Duan, 1997), HBx and possibly other HBV-encoded proteins could act as the drivers for HCC initiation and progression. In the meantime, pathological changes associated with the HBV-initiated tumorigenic process, both cell autonomous and nonautonomous, that predispose patients to the development of PVTT could be distinct from those genetic and epigenetic alterations in hepatocytes and their microenvironment induced by etiological factors other than HBV (Herceg and Paliwal, 2011). In this regard, treatment options should be developed that tailor to the specific molecular nature of HCC pathogenesis associated with HBV to improve the prognosis of those patients.

The full spectrum of pathological factors that contribute to the development of PVTT of HBV^+ HCC patients remain to be adequately elucidated, mainly because the lack of a suitable mouse model system that could faithfully and more completely mimic the pathological process of tumor thrombosis formation in human HCC patients since HBV is incapable of infecting mouse hepatocytes. Nevertheless, our discovery of the TGF-β-miR-34a-CCL22 pathway, which could render the microenvironment of liver tissue around the portal venous system immunosuppressive to favor the colonization and expansion of HCC cells disseminated from the primary tumor site, represents a major step toward addressing this critical question. Following HBV infection and during subsequent pathological processes, such as inflammation and/or fibrosis, a change in the liver microenvironment may begin with a significant increase in the activity of TGF-β signaling, which in turn suppresses the expression of miR-34a, resulting in the enhanced production of the chemokine CCL22 and recruitment of Treg cells. The potent immunesuppressive activity of Treg cells causes subversion of immune responses against tumor cells escaped from the primary tumor, leading to the development of intrahepatic venous metastasis. In this regard, CCL22, a secreted molecule capable of acting on both tumor and immune cells, could be considered as a potential therapeutic target for the development of an effective treatment for this disease.

The paradoxical results from the different phenotypes of miR-34a overexpressing tumor cells in immune-compromised nude mice and in immune-competent C57BL/6J and BALB/c mice provided the key evidence that this miR-34a-CCL22 pathway plays a central role in modulating the tumor immune microenvironment. A wealth of evidence suggests that Treg cells, especially $CD4^+CD25^+$ Treg cells, act to sustain self-tolerance and immune homeostasis by suppressing a wide variety of physiological and pathological immune responses against self and nonself, as well as quasi self-tumor antigens (Sakaguchi, 2004; Shevach, 2002). However, how these naturally arising Treg cells are recruited into the tumor microenvironment to negatively control immune tumor surveillance has remained largely unknown. Several studies indicated that TGF-β could induce naive T cell differentiation into Treg cells (Liu et al., 2008), consistent with the close association in expression profiles of TGF-β and Treg cell marker FoxP3 in multiple types of human tumors. However, this function for TGF-β signaling in regulating the development of natural Treg cells cannot adequately explain the observed recruitment of Treg cells into tumor microenvironment, which is particularly important for tumor progression and metastasis. In this regard, our findings provide the critical experimental evidence on the important roles of TGF-β and cytokines/chemokines induced by TGF-β in the creation of a favorable microenvironment for tumor metastasis through regulation of Treg cell recruitment.

EXPERIMENTAL PROCEDURES

Patients and Tissue Samples

Clinical samples were obtained from 294 HCC patients treated at the Shanghai Eastern Hepatobiliary Surgery Hospital and Guangzhou Sun Yat-sen University Cancer Center in China. Among those patients, 234 were diagnosed with developed PVTT and 60 were negative for symptoms associated with PVTT. Within the PVTT positive group, the types of PVTT development as measured by the presence of tumor lesions in different segments of the portal venous system (Shi et al., 2010). All of the samples and associated clinical information were collected with informed consent of patients and all of the experiments were approved by the Internal Review and Ethics Boards of the Shanghai Eastern Hepatobiliary Surgery Hospital and Guangzhou Sun Yat-sen University Cancer Center, respectively.

Cell Culture

HepG2, Hepa1-6, and WRL68 cells were obtained from the American Type Culture Collection and cultured under standard conditions. PVTT-1 cells have been described previously (Wang et al., 2010). MHCC97 cells were obtained from Dr. Z. Tang. 4T1 cells were obtained from Dr. R.A. Weinberg. $CD4^+CD25^+$ T cells and $CD4^+CD25^-$ T cells were separately purified with Dynabeads Regulatory $CD4^+CD25^+$ T cell kits (Invitrogen, Grand Island, NY, USA) from human blood (Gulf Coast Regional Blood Center, Houston, USA).

Reagents and Plasmids

AS-miR-34a and scramble control locked nucleic acid oligonucleotides were purchased from Exiqon (Vedbaek, Denmark). Pre-miR-34a mimic processor and scramble control oligonucleotides were purchased from Ambion (Grand Island, NY, USA). The miR-34a and miR-34b/c expression vectors were constructed using TRIPZ lentiviral system from Thermo Scientific Open Biosystems (Lafayette, CO, USA).

(F) Luciferase signal levels from the four groups of mice shown in (E) was normalized to that of control mice without tumor growth and computed as the values for relative metastatic growth by each of the indicated Hepa1-6 cell populations. *$p < 0.05$, **$p < 0.01$ (Student's t test). n = 4 per experimental group; experiment repeated three times.

(G) Representative images showing the formation of tumor metastases in the mouse liver by each of the indicated Hepa1-6 populations. Arrows indicate metastatic tumors in the mouse liver.

All error bars indicate mean ± SD. See also Figure S5.

miRNA Detection

Total RNA, inclusive of the small RNA fraction, was extracted from cultured cells with a mirVana miRNA Isolation Kit (Ambion). RT-PCR-based array for detection of mature miRs and U6 was achieved with gene-specific primers.

Animal Studies

All research involving animals complied with protocols approved by the Duke University Animal Care and Use Committee. The in vivo migration assays were measured following an established method (Curiel et al., 2004). For spontaneous metastasis assays, the metastatic formation was monitored by the appearance of luciferase activities by imaging apparatus of IVIS systems (Caliper).

MTT and BrdU Assays

In vitro cell viability was measured by MTT assay following established protocols (Feng et al., 2011). A bromodeoxyuridine (BrdU) incorporation assay was conducted according to the manufacturer's instruction (BD PharMingen, San Diego, CA, USA).

Immunoblots

Cell lysates and supernatants were resolved by electrophoresis, transferred to a polyvinylidene floride membrane, and probed with antibodies against γ-tubulin (Santa Cruz Biotechnology, Santa Cruz, CA, USA) or CCL22 (R&D Systems, Minneapolis).

Immunohistochemistry

Detection of phospho-Smad2 (Cell Signaling Technology, Danvers, MA, USA) and FoxP3 (Abcam, Cambridge, MA, USA) was performed on 5 μm paraffin sections of tissue samples with the indicated antibodies, using Vectastain Elite ABC kits (Vector, Burlingame, CA, USA) and ImmPACT DAB Substrate (Vector). For pSmad2, the score was evaluated as four levels from 0 (−), 1(+), to 2(++), 3(+++).

Fluorescence-Activated Cell Sorting

Cells were stained with monoclonal antibodies and analyzed on a FACSCanto (Becton Dickinson, Franklin Lakes, NJ, USA). Antibodies were mouse antihuman CD4-APC (Biolegend, San Diego, CA, USA), mouse antihuman CD25-PE (Biolegend), mouse antihuman FoxP3-PB (Biolegend), PB antimouse CD4 (eBioscience, San Diego, CA, USA), PE antimouse CD25 (eBioscience), and PE-Cy5 antimouse/rat Foxp3 (eBioscience).

Migration Assay

Cell migration was assessed as described (Curiel et al., 2004) using $CD4^+CD25^+$ Treg cells. PVTT-1 tumor cell supernatants were added to the lower chamber. Antibody against CCL22 and control IgG were obtained from R&D Systems.

Statistical Analyses

Data are presented as mean ± SD. Student's t test was used for comparisons.

SUPPLEMENTAL INFORMATION

Supplemental Information includes five figures, one table, and Supplemental Experimental Procedures and can be found with this article online at http://dx.doi.org/10.1016/j.ccr.2012.07.023.

ACKNOWLEDGMENTS

We wish to thank J. Lee and I. Liu for help with the use of the 4T1/BALB/c mouse model; L. Su and J. Gao for Treg cell purification and IHC for Foxp3; X. Cao for advice on tumor immunology; L. He for providing the miR-34b/c plasmid; Y. Gao in the Duke University Light Microscopy Core Facility for imaging experiments; and the CCIF and Cell Sorting Facility of Duke Cancer Institute for animal care and cell sorting experiments, respectively. Q.-J.L. is a Whitehead Family Foundation Scholar, and the research reported in this publication was supported by the Research Scholar Grant RSG-10-157-01-LIB from the American Cancer Society to Q.-J.L., Ministry of Science and Technology Key Program of China 2012ZX10002009-017, National Basic Research Program of China 2010CB912102 to D.X., and the National Cancer Institute of the National Institutes of Health under award number CA151541 to X.-F.W.

Received: December 12, 2011
Revised: May 29, 2012
Accepted: July 31, 2012
Published: September 10, 2012

REFERENCES

Bao, S., Ouyang, G., Bai, X., Huang, Z., Ma, C., Liu, M., Shao, R., Anderson, R.M., Rich, J.N., and Wang, X.F. (2004). Periostin potently promotes metastatic growth of colon cancer by augmenting cell survival via the Akt/PKB pathway. Cancer Cell *5*, 329–339.

Bartel, D.P. (2004). MicroRNAs: genomics, biogenesis, mechanism, and function. Cell *116*, 281–297.

Benhenda, S., Cougot, D., Buendia, M.A., and Neuveut, C. (2009). Hepatitis B virus X protein molecular functions and its role in virus life cycle and pathogenesis. Adv. Cancer Res. *103*, 75–109.

Bierie, B., and Moses, H.L. (2006). Tumour microenvironment: TGFbeta: the molecular Jekyll and Hyde of cancer. Nat. Rev. Cancer *6*, 506–520.

Bissell, D.M. (2001). Chronic liver injury, TGF-beta, and cancer. Exp. Mol. Med. *33*, 179–190.

Budhu, A., Jia, H.L., Forgues, M., Liu, C.G., Goldstein, D., Lam, A., Zanetti, K.A., Ye, Q.H., Qin, L.X., Croce, C.M., et al. (2008). Identification of metastasis-related microRNAs in hepatocellular carcinoma. Hepatology *47*, 897–907.

Chambers, A.F., Groom, A.C., and MacDonald, I.C. (2002). Dissemination and growth of cancer cells in metastatic sites. Nat. Rev. Cancer *2*, 563–572.

Chen, C.J., Yang, H.I., Su, J., Jen, C.L., You, S.L., Lu, S.N., Huang, G.T., and Iloeje, U.H.; REVEAL-HBV Study Group. (2006). Risk of hepatocellular carcinoma across a biological gradient of serum hepatitis B virus DNA level. JAMA *295*, 65–73.

Chen, C.J., Yang, H.I., and Iloeje, U.H.; REVEAL-HBV Study Group. (2009). Hepatitis B virus DNA levels and outcomes in chronic hepatitis B. Hepatology *49* (5, Suppl), S72–S84.

Chen, W., Jin, W., Hardegen, N., Lei, K.J., Li, L., Marinos, N., McGrady, G., and Wahl, S.M. (2003). Conversion of peripheral CD4+CD25- naive T cells to CD4+CD25+ regulatory T cells by TGF-beta induction of transcription factor Foxp3. J. Exp. Med. *198*, 1875–1886.

Curiel, T.J., Coukos, G., Zou, L., Alvarez, X., Cheng, P., Mottram, P., Evdemon-Hogan, M., Conejo-Garcia, J.R., Zhang, L., Burow, M., et al. (2004). Specific recruitment of regulatory T cells in ovarian carcinoma fosters immune privilege and predicts reduced survival. Nat. Med. *10*, 942–949.

Delaney, W.E., 4th, and Isom, H.C. (1998). Hepatitis B virus replication in human HepG2 cells mediated by hepatitis B virus recombinant baculovirus. Hepatology *28*, 1134–1146.

Ding, J., Huang, S., Wu, S., Zhao, Y., Liang, L., Yan, M., Ge, C., Yao, J., Chen, T., Wan, D., et al. (2010). Gain of miR-151 on chromosome 8q24.3 facilitates tumour cell migration and spreading through downregulating RhoGDIA. Nat. Cell Biol. *12*, 390–399.

Ding, Q., Xia, W., Liu, J.C., Yang, J.Y., Lee, D.F., Xia, J., Bartholomeusz, G., Li, Y., Pan, Y., Li, Z., et al. (2005). Erk associates with and primes GSK-3beta for its inactivation resulting in upregulation of beta-catenin. Mol. Cell *19*, 159–170.

Esquela-Kerscher, A., and Slack, F.J. (2006). Oncomirs - microRNAs with a role in cancer. Nat. Rev. Cancer *6*, 259–269.

Feitelson, M.A., and Duan, L.X. (1997). Hepatitis B virus X antigen in the pathogenesis of chronic infections and the development of hepatocellular carcinoma. Am. J. Pathol. *150*, 1141–1157.

Feng, Y.X., Wang, T., Deng, Y.Z., Yang, P., Li, J.J., Guan, D.X., Yao, F., Zhu, Y.Q., Qin, Y., Wang, H., et al. (2011). Sorafenib suppresses postsurgical recurrence and metastasis of hepatocellular carcinoma in an orthotopic mouse model. Hepatology *53*, 483–492.

Han, Z. (2009). Recent progress in genomic [corrected] research of liver cancer. Sci. China C. Life Sci. *52*, 24–30.

He, L., He, X., Lim, L.P., de Stanchina, E., Xuan, Z., Liang, Y., Xue, W., Zender, L., Magnus, J., Ridzon, D., et al. (2007). A microRNA component of the p53 tumour suppressor network. Nature *447*, 1130–1134.

Herceg, Z., and Paliwal, A. (2011). Epigenetic mechanisms in hepatocellular carcinoma: how environmental factors influence the epigenome. Mutat. Res. *727*, 55–61.

Jemal, A., Bray, F., Center, M.M., Ferlay, J., Ward, E., and Forman, D. (2011). Global cancer statistics. CA Cancer J. Clin. *61*, 69–90.

Kew, M.C. (2011). Hepatitis B virus x protein in the pathogenesis of hepatitis B virus-induced hepatocellular carcinoma. J. Gastroenterol. Hepatol. *26* (*Suppl 1*), 144–152.

Lin, D.X., Zhang, Q.Y., Li, X., Ye, Q.W., Lin, F., and Li, L.L. (2011). An aggressive approach leads to improved survival in hepatocellular carcinoma patients with portal vein tumor thrombus. J. Cancer Res. Clin. Oncol. *137*, 139–149.

Liu, Y., Zhang, P., Li, J., Kulkarni, A.B., Perruche, S., and Chen, W. (2008). A critical function for TGF-beta signaling in the development of natural CD4+ CD25+Foxp3+ regulatory T cells. Nat. Immunol. *9*, 632–640.

Lujambio, A., and Lowe, S.W. (2012). The microcosmos of cancer. Nature *482*, 347–355.

Lupberger, J., and Hildt, E. (2007). Hepatitis B virus-induced oncogenesis. World J. Gastroenterol. *13*, 74–81.

Mailloux, A.W., and Young, M.R. (2010). Regulatory T-cell trafficking: from thymic development to tumor-induced immune suppression. Crit. Rev. Immunol. *30*, 435–447.

Marotta, F., Vangieri, B., Cecere, A., and Gattoni, A. (2004). The pathogenesis of hepatocellular carcinoma is multifactorial event. Novel immunological treatment in prospect. Clin. Ter. *155*, 187–199.

Massagué, J. (2008). TGFbeta in Cancer. Cell *134*, 215–230.

Matsuzaki, K. (2009). Modulation of TGF-beta signaling during progression of chronic liver diseases. Front. Biosci. *14*, 2923–2934.

Morecki, S., Yacovlev, L., and Slavin, S. (1998). Effect of indomethacin on tumorigenicity and immunity induction in a murine model of mammary carcinoma. Int. J. Cancer *75*, 894–899.

Nicoloso, M.S., Spizzo, R., Shimizu, M., Rossi, S., and Calin, G.A. (2009). MicroRNAs—the micro steering wheel of tumour metastases. Nat. Rev. Cancer *9*, 293–302.

Ouyang, W., Beckett, O., Ma, Q., and Li, M.O. (2010). Transforming growth factor-beta signaling curbs thymic negative selection promoting regulatory T cell development. Immunity *32*, 642–653.

Parkin, D.M., Bray, F., Ferlay, J., and Pisani, P. (2005). Global cancer statistics, 2002. CA Cancer J. Clin. *55*, 74–108.

Portolani, N., Coniglio, A., Ghidoni, S., Giovanelli, M., Benetti, A., Tiberio, G.A., and Giulini, S.M. (2006). Early and late recurrence after liver resection for hepatocellular carcinoma: prognostic and therapeutic implications. Ann. Surg. *243*, 229–235.

Quezada, S.A., Peggs, K.S., Curran, M.A., and Allison, J.P. (2006). CTLA4 blockade and GM-CSF combination immunotherapy alters the intratumor balance of effector and regulatory T cells. J. Clin. Invest. *116*, 1935–1945.

Sakaguchi, S. (2004). Naturally arising CD4+ regulatory t cells for immunologic self-tolerance and negative control of immune responses. Annu. Rev. Immunol. *22*, 531–562.

Schmierer, B., and Hill, C.S. (2007). TGFbeta-SMAD signal transduction: molecular specificity and functional flexibility. Nat. Rev. Mol. Cell Biol. *8*, 970–982.

Shevach, E.M. (2002). CD4+ CD25+ suppressor T cells: more questions than answers. Nat. Rev. Immunol. *2*, 389–400.

Shi, J., Lai, E.C., Li, N., Guo, W.X., Xue, J., Lau, W.Y., Wu, M.C., and Cheng, S.Q. (2010). Surgical treatment of hepatocellular carcinoma with portal vein tumor thrombus. Ann. Surg. Oncol. *17*, 2073–2080.

Siemens, H., Jackstadt, R., Hünten, S., Kaller, M., Menssen, A., Götz, U., and Hermeking, H. (2011). miR-34 and SNAIL form a double-negative feedback loop to regulate epithelial-mesenchymal transitions. Cell Cycle *10*, 4256–4271.

Takizawa, D., Kakizaki, S., Sohara, N., Sato, K., Takagi, H., Arai, H., Katakai, K., Kojima, A., Matsuzaki, Y., and Mori, M. (2007). Hepatocellular carcinoma with portal vein tumor thrombosis: clinical characteristics, prognosis, and patient survival analysis. Dig. Dis. Sci. *52*, 3290–3295.

Tian, J., Tang, Z.Y., Ye, S.L., Liu, Y.K., Lin, Z.Y., Chen, J., and Xue, Q. (1999). New human hepatocellular carcinoma (HCC) cell line with highly metastatic potential (MHCC97) and its expressions of the factors associated with metastasis. Br. J. Cancer *81*, 814–821.

Wang, T., Hu, H.S., Feng, Y.X., Shi, J., Li, N., Guo, W.X., Xue, J., Xie, D., Liu, S.R., Wu, M.C., and Cheng, S.Q. (2010). Characterisation of a novel cell line (CSQT-2) with high metastatic activity derived from portal vein tumour thrombus of hepatocellular carcinoma. Br. J. Cancer *102*, 1618–1626.

Xiong, Y., Fang, J.H., Yun, J.P., Yang, J., Zhang, Y., Jia, W.H., and Zhuang, S.M. (2010). Effects of microRNA-29 on apoptosis, tumorigenicity, and prognosis of hepatocellular carcinoma. Hepatology *51*, 836–845.

Cancer Cell
Article

EGF Receptor Is Required for KRAS-Induced Pancreatic Tumorigenesis

Christine M. Ardito,[1,11] Barbara M. Grüner,[2,11] Kenneth K. Takeuchi,[3] Clara Lubeseder-Martellato,[2] Nicole Teichmann,[2] Pawel K. Mazur,[4] Kathleen E. DelGiorno,[1,3] Eileen S. Carpenter,[1] Christopher J. Halbrook,[1,3] Jason C. Hall,[1,3] Debjani Pal,[1] Thomas Briel,[2] Alexander Herner,[2] Marija Trajkovic-Arsic,[2] Bence Sipos,[5] Geou-Yarh Liou,[3] Peter Storz,[3] Nicole R. Murray,[3] David W. Threadgill,[6] Maria Sibilia,[7] M. Kay Washington,[8] Carole L. Wilson,[9] Roland M. Schmid,[2] Elaine W. Raines,[9] Howard C. Crawford,[1,3,10,*] and Jens T. Siveke[2,*]

[1]Department of Pharmacological Sciences, Stony Brook University, Stony Brook, NY 11794, USA
[2]II. Medizinische Klinik, Klinikum rechts der Isar, Technische Universität München, Munich 81675, Germany
[3]Department of Cancer Biology, Mayo Clinic, Jacksonville, FL 32224, USA
[4]Department of Pediatrics and Department of Genetics, Stanford University, Stanford, CA 94305, USA
[5]Department of Pathology, University Hospital Tübingen, Tübingen D-72076, Germany
[6]Department of Genetics, North Carolina State University, Raleigh, NC 27599, USA
[7]Institute for Cancer Research, Department of Medicine I, Comprehensive Cancer Center, Medical University of Vienna, Vienna A-1090, Austria
[8]Department of Pathology, Vanderbilt University Medical Center, Nashville, TN 37232, USA
[9]Department of Pathology, University of Washington, Seattle, WA 98195, USA
[10]Department of Research, Veterans Affairs Medical Center, Northport, NY 11768, USA
[11]These authors contributed equally to this work
*Correspondence: crawford.howard@mayo.edu (H.C.C.), jens.siveke@lrz.tu-muenchen.de (J.T.S.)
http://dx.doi.org/10.1016/j.ccr.2012.07.024

SUMMARY

Initiation of pancreatic ductal adenocarcinoma (PDA) is definitively linked to activating mutations in the *KRAS* oncogene. However, PDA mouse models show that mutant *Kras* expression early in development gives rise to a normal pancreas, with tumors forming only after a long latency or pancreatitis induction. Here, we show that oncogenic KRAS upregulates endogenous EGFR expression and activation, the latter being dependent on the EGFR ligand sheddase, ADAM17. Genetic ablation or pharmacological inhibition of EGFR or ADAM17 effectively eliminates KRAS-driven tumorigenesis in vivo. Without EGFR activity, active RAS levels are not sufficient to induce robust MEK/ERK activity, a requirement for epithelial transformation.

INTRODUCTION

Pancreatic ductal adenocarcinoma (PDA) is almost universally fatal, but its remarkable genetic homogeneity has aided greatly in our understanding of its genesis and progression. Most PDA samples harbor oncogenic mutations in the *KRAS* gene, from early pancreatic intraepithelial neoplasia (PanIN) to PDA, marking mutant *KRAS* as the most prominent PDA initiating gene. Pancreas-specific mutant *Kras* expression in mice results in mouse PanIN (mPanIN) formation, eventually leading to PDA. Strikingly, even with universal expression of mutant *Kras* in early organogenesis, the pancreas develops normally, giving rise to a functional, tumor-free pancreas with preneoplastic lesions and mPanINs forming stochastically only after several weeks (Hingorani et al., 2003). Consistent with this, oncogenic *KRAS* mutations are found in human pancreata with no signs of PDA (Lüttges et al., 1999). Together, these observations suggest that expression of mutant *Kras* requires ill-defined secondary events to initiate pancreatic tumorigenesis.

The ductal nature of PanIN and PDA suggests their derivation via transformation of normal duct epithelium or of progenitor cells capable of assuming a ductal morphology. Confounding this hypothesis, $Kras^{G12D}$ expression directed to specific cellular compartments has shown that duct, islet, and acinar cells can all

Significance

The almost universal lethality of PDA has led to the intense study of genetic mutations responsible for its formation and progression. The most common oncogenic mutations associated with all PDA stages are found in the *KRAS* gene, suggesting it as the primary initiator of pancreatic neoplasia. However, mutant *Kras* expression throughout the mouse pancreatic parenchyma shows that the oncogene remains largely indolent until secondary events, such as pancreatitis, unlock its transforming potential. We find KRAS requires an inside-outside-in signaling axis that involves ligand-dependent EGFR activation to initiate the signal transduction and cell biological changes that link PDA and pancreatitis.

give rise to mPanIN lesions (Gidekel Friedlander et al., 2009), but expression in the adult acinar or islet cell compartments requires pancreatitis induction (Carrière et al., 2009; Gidekel Friedlander et al., 2009; Guerra et al., 2007). This acquired sensitivity to transformation is attributed to acinar cell transdifferentiation to metaplastic ducts, which have progenitor-like characteristics (Miyamoto et al., 2003; Sharma et al., 1999) that may make them more susceptible to KRAS-induced oncogenesis. Consistent with this hypothesis, Hebrok and colleagues have shown that $KRAS^{G12D}$ expression hijacks the regeneration process after tissue damage, promoting the metaplasia-to-PanIN transition (Morris et al., 2010).

Aberrant signal transduction pathways that control acinar-to-ductal metaplasia (ADM) are under intense study. Examination of chronic pancreatitis (CP) and PDA patient samples has shown an upregulation of epidermal growth factor receptor (EGFR, ERBB1) (Fjällskog et al., 2003; Korc et al., 1994; Tobita et al., 2003) and several of its ligands (Kobrin et al., 1994; Zhu et al., 2000). The relevance of this correlation is bolstered by the induction of metaplasia and desmoplasia in vivo by transgenic EGFR ligand overexpression (Means et al., 2003; Sandgren et al., 1990). In vitro, treatment of acinar cell explants with EGFR ligands, such as transforming growth factor alpha (TGFA), results in ADM (De Lisle and Logsdon, 1990; Means et al., 2005). Lineage tracing experiments confirm that metaplastic ducts arise in part from acinar cell transdifferentiation in response to tissue injury (Strobel et al., 2007), supporting a physiological relevance to acinar cell transdifferentiation. However, it is not known whether endogenous ligand activation of EGFR plays a role in ADM in pancreatic disease.

Taking advantage of the reproducible kinetics of tumor formation in PDA mouse models, we set out to address the contribution of EGFR activity to disease progression using genetic and pharmacological approaches.

RESULTS

EGFR Pathway Upregulation Precedes Tumorigenesis in $Kras^{G12D}$ Mice

EGFR is upregulated in PDA and PDA mouse models (Fjällskog et al., 2003; Korc et al., 1994; Tobita et al., 2003; Figure S1 available online), although its function primarily has been associated with enhanced proliferation and invasiveness (Jaganathan et al., 2010; Larbouret et al., 2007; Pino et al., 2006; Zhao et al., 2010). To better dissect the role of EGFR in PDA progression, we tested if EGFR was activated in the $Kras^{LSL\text{-}G12D/+}$;$Ptf1a^{Cre/+}$ mouse model (referred to hereinafter as $Kras^{G12D}$), which reproducibly shows metaplasia and mPanIN formation beginning at ~8 weeks of age, with progression to PDA at ~1 year (Hingorani et al., 2003). Immunohistochemistry (IHC) for active EGFR (pY1068) was undetectable in wild-type pancreata but easily detectable in acinar areas prior to mPanIN formation in 30-day-old $Kras^{G12D}$ mice and in mPanINs in 3-month-old $Kras^{G12D}$ mice (Figure 1A). To test if EGFR itself was upregulated, we used quantitative real-time PCR (qRT-PCR) to analyze mRNA isolated from 6-week-old $Kras^{G12D}$ pancreata, an age prior to the formation of significant metaplasia or neoplasia. Transcripts for both EGFR and TGFA, an EGFR ligand, were consistently upregulated ~2-fold (Figure 1B). Amphiregulin (AREG), another EGFR ligand, was also upregulated relative to wild-type controls, which had undetectable AREG levels (data not shown). Immunofluorescence staining (IF) for total EGFR showed upregulation in discrete acinar cell clusters in $Kras^{G12D}$ pancreata (Figure 1C), becoming very prominent in larger acinar clusters, especially near areas of metaplasia and mPanIN, and was particularly high in metaplasia and mPanINs. Thus, EGFR pathway upregulation is a very early event in pancreatic tumorigenesis. Moreover, the stochasticity of EGFR overexpression in acini prior to mPanIN formation reflected the pattern of eventual tumor formation, suggesting a role for EGFR signaling in transformation of the acinar cell compartment.

To test if acinar cell EGFR activation coincided with ductal transdifferentiation, we examined primary acinar cell explants isolated from $Kras^{G12D}$ mice, which spontaneously transdifferentiate into duct cells when embedded in fibrillar collagen. On Day 1 of culture, active pY1068 EGFR was undetectable (Figure 1D) but was strongly positive by Day 3, as transdifferentiation took place. Activation correlated with increased EGFR expression, as determined by qRT-PCR (Figure 1E). Thus, EGFR upregulation and activation is initiated by KRAS in vitro and in vivo in a manner consistent with its involvement in preneoplastic duct formation.

Inhibition of EGFR Limits Pancreatic Tumorigenesis but Not Progression

To test if EGFR activity is required for pancreatic preneoplastic lesion formation, we examined the effects of pharmacological EGFR inhibition in a highly aggressive PDA model. $Kras^{LSL\text{-}G12D/+}$;$Ptf1a^{Cre/+}$;$Trp53^{fl/fl}$ mice, referred to as $Kras^{G12D}$;$p53^{KO}$, develop invasive PDA at 4–6 weeks of age (Bardeesy et al., 2006). Starting at 1 week of age, $Kras^{G12D}$;$p53^{KO}$ mice were treated daily with either cetuximab, a monoclonal antibody that blocks ligand interaction with the receptor; erlotinib, a small molecule EGFR tyrosine kinase inhibitor; or vehicle for 3 weeks. Histological examination showed substantial areas of normal, nontransformed tissue with either treatment, and a significantly reduced number of $CK19^{+}$ ductal lesions compared to control (Figures 2A–2C).

Retention of substantial areas of normal tissue with EGFR inhibition supported a role for EGFR signaling in tumor initiation. To test this possibility definitively, we mated $Kras^{G12D}$;$p53^{KO}$ mice with conditional *Egfr* knockout mice (Lee and Threadgill, 2009; Natarajan et al., 2007). Mice with EGFR ablated from the pancreas ($Egfr^{fl/fl}$;$Ptf1a^{Cre/+}$, referred to as $Egfr^{KO}$) were viable and showed no gross pancreatic abnormalities. Consistent with the inhibitor experiments, $Kras^{G12D}$;$p53^{KO}$;$Egfr^{KO}$ pancreata retained substantial areas of normal acinar tissue, whereas age-matched $Kras^{G12D}$;$p53^{KO}$ pancreata were completely replaced by tumorous tissue (Figures 2D and 2E). IHC for EGFR confirmed that ~50% of mPanINs that formed in these mice were EGFR negative (Figure S2A), with the other half likely a product of incomplete recombination of the *Egfr* locus. To gain insight into the escape from EGFR dependency, we established cell lines from $Kras^{G12D}$;$p53^{KO}$;$Egfr^{KO}$ pancreata. Confirming EGFR loss by western blot, we assessed other signaling and differentiation changes compared to EGFR wild-type controls. Two pathways in particular showed consistent upregulation and activation in the absence of EGFR: the Notch pathway and MET, both of

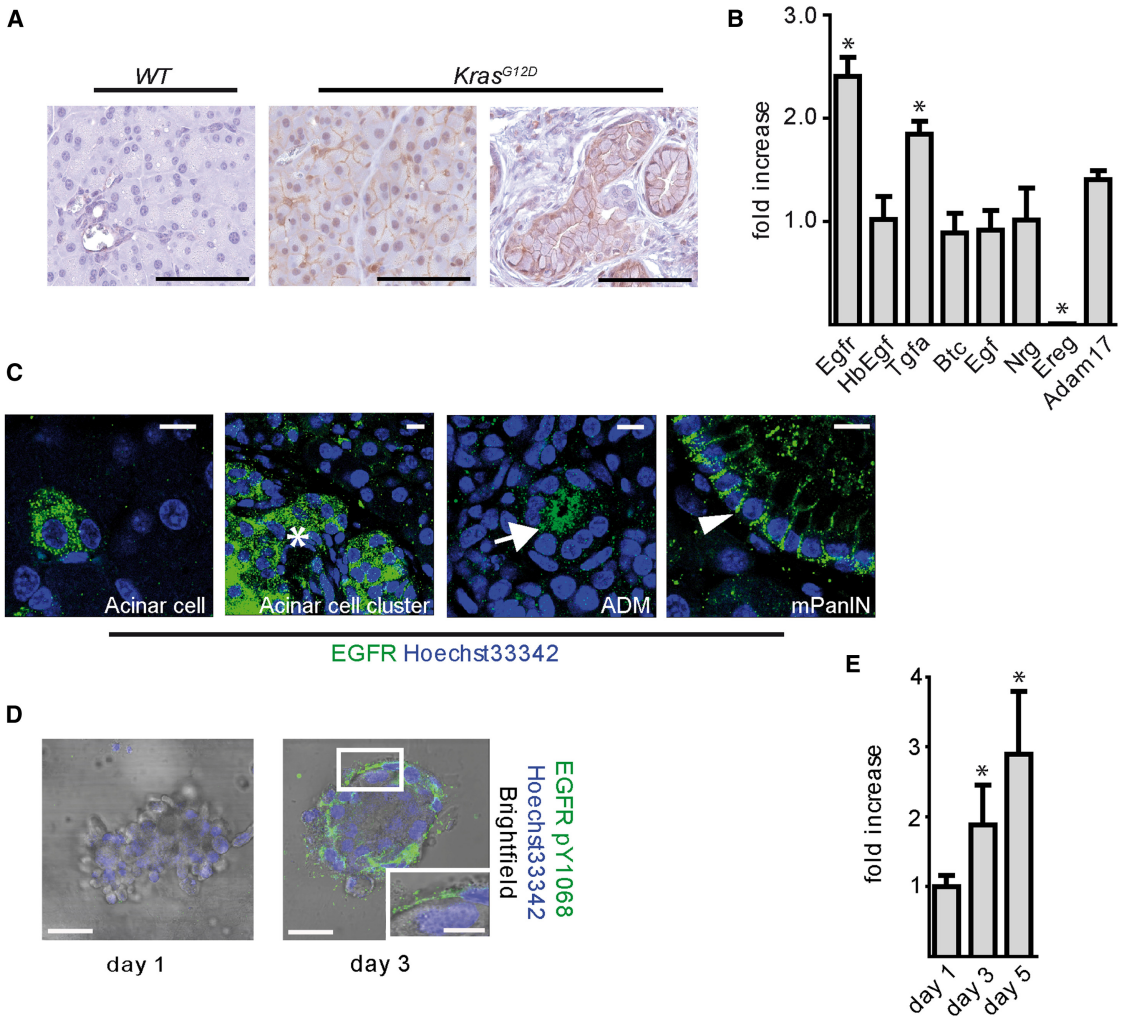

Figure 1. EGFR Signaling during mPanIN Development

(A) IHC for EGFR pY1068 in wild-type and $Kras^{G12D}$ pancreata. Scale bars, 50 μm.

(B) qRT-PCR analysis for *Egfr*, its ligands, and *Adam17*. Error bars, ± SEM. *p < 0.05, n = 3.

(C) Confocal IF staining for total EGFR in distinct single acinar cells, acinar cell clusters (asterisk), ADM (arrow), and mPanINs (arrowhead) of $Kras^{G12D}$ pancreata. Scale bars, 10 μm.

(D and E) Panels show (D) IF for EGFR pY1068 and (E) qRT-PCR analysis of *Egfr* in $Kras^{G12D}$ acinar cell explants. Scale bars, 10 μm for micrographs, 50 μm for inset. Error bars, ±SEM; *p < 0.05, n = 3.

See also Figure S1.

which have been implicated in pancreatic tumor progression (Figure S2B), most notably in the ADM process (Means et al., 2005; Miyamoto et al., 2003).

EGFR inhibition has been shown to be minimally effective in PDA patients. To test if the $Kras^{G12D};p53^{KO}$ model reflected the clinical data, we treated mice with magnetic resonance imaging (MRI)-detectable advanced PDA with gemcitabine or erlotinib plus gemcitabine. Combination-treated mice showed no significant difference in life span compared to mice with gemcitabine treatment alone (Figure 2F) and showed no reduction in tumor burden by MRI, consistent with independence from EGFR after progression to PDA.

EGFR inhibition most clearly affected pancreatic tumorigenesis, leading us to explore its effects more thoroughly in the slower-progressing $Kras^{LSL\text{-}G12D/+}$ model. Tumor burden of $Kras^{G12D}$ and *Egfr* knockout $Kras^{G12D}$ mice ($Kras^{G12D};Egfr^{KO}$) was assessed at various ages by relative pancreatic mass, histology, loss of normal acinar (amylase$^+$) tissue, and appearance of MUC5AC$^+$ ductal lesions (Figures 3A–3C, S3A, and S3B). By all criteria, *Egfr* ablation almost completely blocked tumorigenesis. Unlike $Kras^{G12D};p53^{KO};EgfrR^{KO}$ mice, all metaplasia and mPanIN that formed in $Kras^{G12D};Egfr^{KO}$ mice were EGFR positive (Figure S3D), suggesting incomplete recombination of the *Egfr* locus and reinforcing the need for EGFR in tumorigenesis. These data also suggested that p53 inactivation itself allows for escape from EGFR dependency. The tumorigenesis block was not due to a failure to recombine the silenced $Kras^{G12D}$ allele (Figure S3E).

Coordinated upregulation of *Tgfa*, *Areg*, and *Egfr* in $Kras^{G12D}$ pancreata, together with the effectiveness of cetuximab,

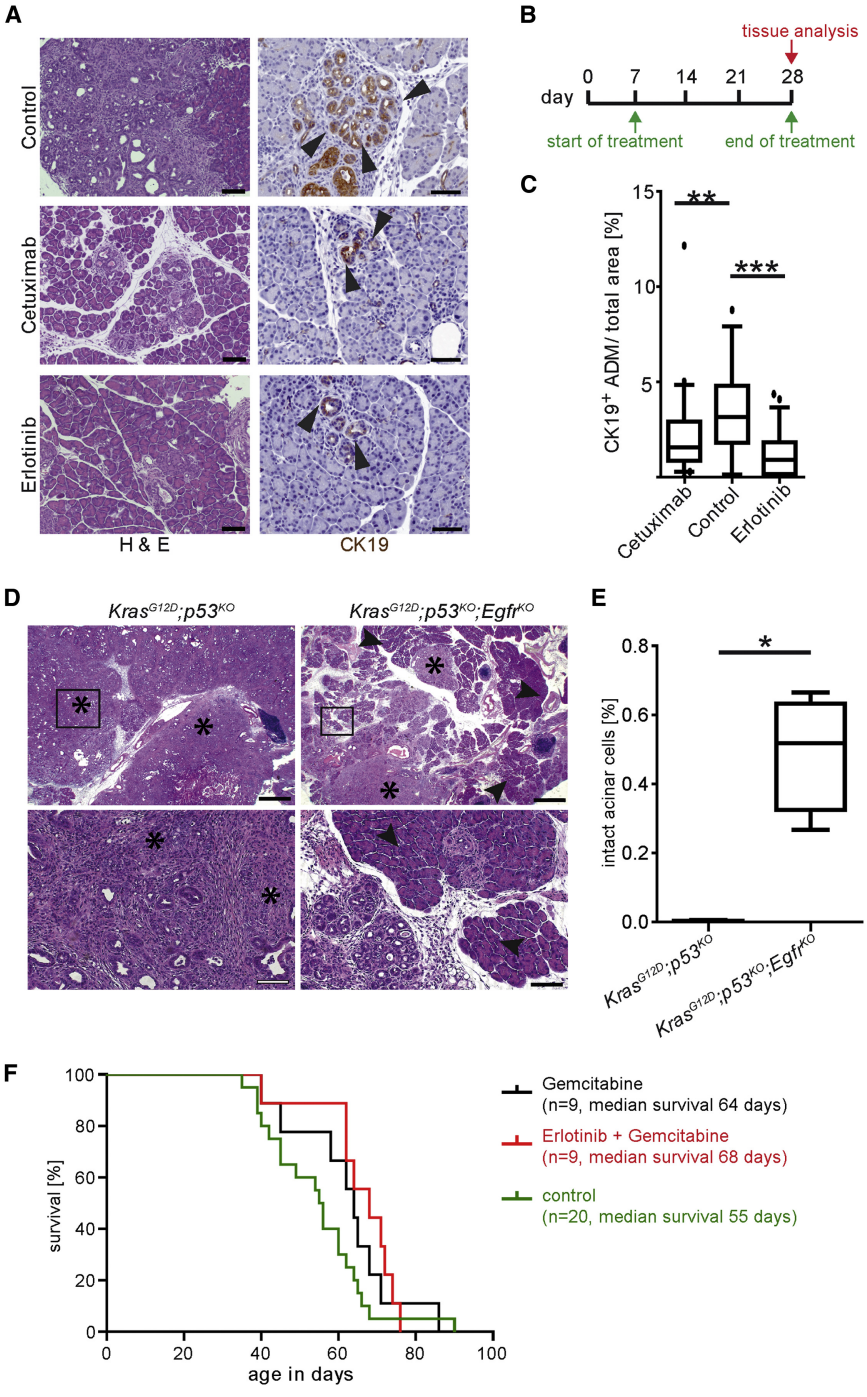

Figure 2. Inhibition of EGFR Signaling Blocks KRAS-Driven Tumorigenesis but Not PDA Progression

(A) Hematoxylin and eosin staining (H&E) and CK19 IHC of 4-week-old $Kras^{G12D};p53^{KO}$ control, cetuximab-treated, and erlotinib-treated pancreata. Arrowheads indicate $CK19^{+}$ structures. Scale bars, 100 μm for H&E and 50 μm for CK19 panels.

(B) Schematic of cetuximab and erlotinib treatment protocols.

(C) Quantitation of $CK19^{+}$ structures (n = 3; **p < 0.01; ***p < 0.001).

(D) Histology of 9-week-old $Kras^{G12D};p53^{KO}$ and $Kras^{G12D};p53^{KO};Egfr^{KO}$ pancreata. Asterisks indicate areas of invasive PDA. Arrowheads highlight areas of normal acinar tissue. Scale bars, 200 μm for upper panels and 50 μm for lower panels.

(E) Quantitation of normal acinar area in $Kras^{G12D};p53^{KO}$ and $Kras^{G12D};p53^{KO};Egfr^{KO}$ pancreata.

(F) Kaplan–Meier curve depicting survival of $Kras^{G12D};p53^{KO}$ mice treated with gemcitabine or erlotinib plus gemcitabine after progression to PDA.

See also Figure S2.

suggested that receptor ligation is a necessary step in pancreatic tumorigenesis. EGFR ligands are generally shed from the cell surface by metalloproteinase "sheddases" but can also activate receptor in their membrane-bound forms in a juxtacrine manner (Singh and Harris, 2005). TGFA and AREG share a common primary sheddase in ADAM17 (Sahin et al., 2004). To test if EGFR ligand shedding was necessary for tumorigenesis, we crossed a conditional *Adam17* knockout mouse line ($Adam17^{\Delta Ex5/\Delta Ex5}$) into the $Kras^{G12D}$ background ($Kras^{G12D};Adam17^{KO}$). Pancreas-specific *Adam17* knockout mice ($Adam17^{\Delta Ex5/\Delta Ex5};Ptf1a^{Cre/+}$, referred to as $Adam17^{KO}$) were viable and showed no gross pancreatic abnormalities. To assess tumor formation in the $Kras^{G12D};Adam17^{KO}$ background, we aged mice and examined their pancreata for tumor development. Indeed, $Kras^{G12D};Adam17^{KO}$ mice phenocopied $Kras^{G12D};Egfr^{KO}$ mice, showing a similar degree of protection from tumorigenesis (Figures 3A–3C, S3A, and S3C), with no effect on $Kras^{G12D}$ recombination (Figure S3E). These results are consistent with EGFR activation by ADAM17-dependent ligand shedding being a necessary step in KRAS-driven pancreatic tumorigenesis.

Pancreatitis-Associated Tumorigenesis Requires EGFR and ADAM17

Oncogenic *Kras* expression confined to acinar or islet cell compartments, requires pancreatitis for PDA formation (Gidekel Friedlander et al., 2009; Guerra et al., 2007). EGFR overexpression in $Kras^{G12D}$ acinar cells suggested that EGFR ablation blocks transformation of this cellular compartment. To test if EGFR activity is required for pancreatitis-dependent, acinar cell-derived tumorigenesis, we treated 30-day-old $Kras^{G12D}$, $Kras^{G12D};Egfr^{KO}$, and $Kras^{G12D};Adam17^{KO}$ mice with 250 μg/kg cerulein, a known inducer of pancreatic damage, daily for 5 days, followed by 7 days recovery. With cerulein treatment, $Kras^{G12D}$ mice showed an almost complete replacement of normal pancreatic tissue with fibrotic, inflamed tissue and the

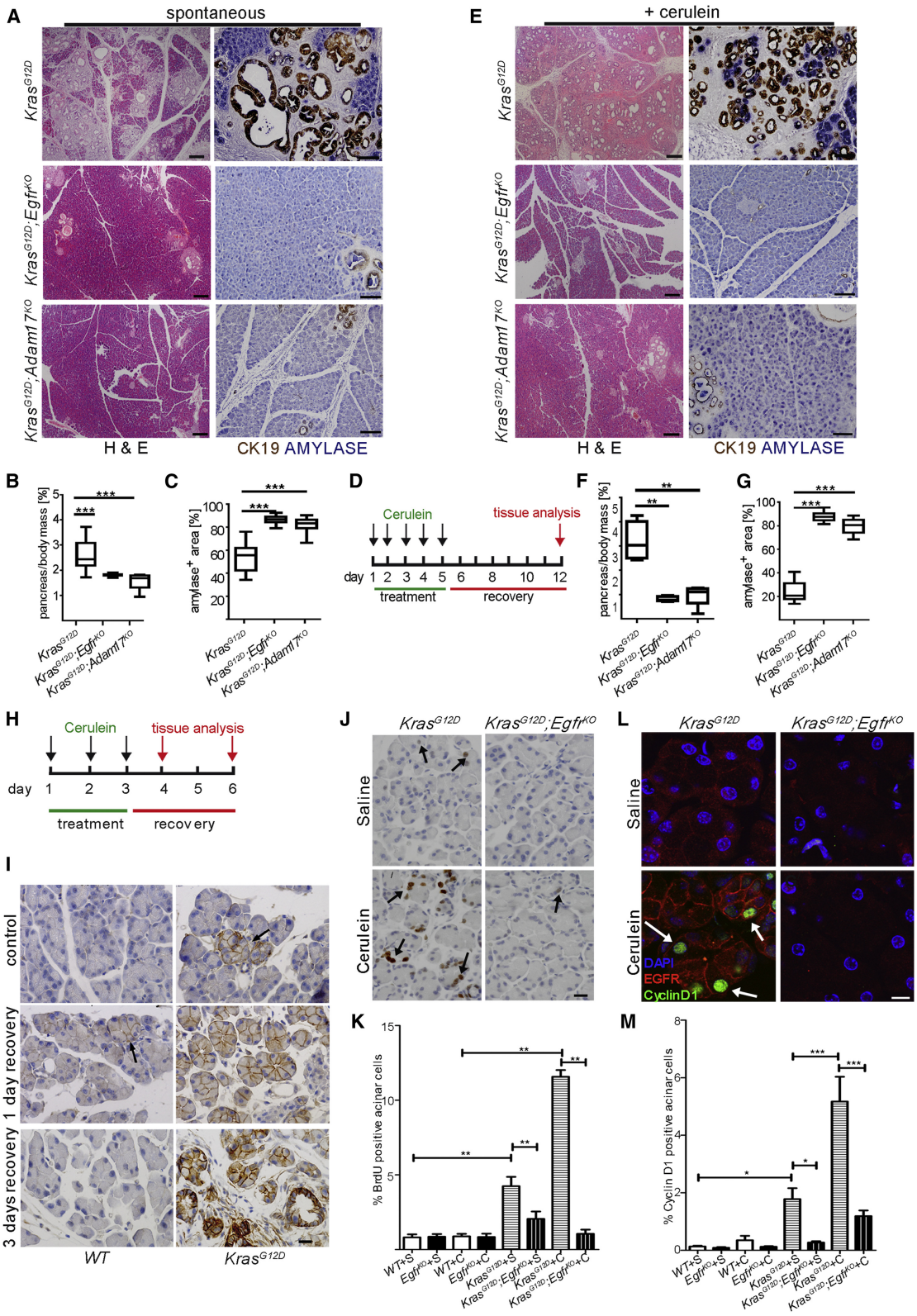

Figure 3. Genetic Ablation of EGFR Activity Prevents KRAS-Driven PDA Development

(A–G) Panels show (A–C) spontaneous and (D–G) cerulein-induced mPanIN formation in $Kras^{G12D}$;$Egfr^{KO}$ and $Kras^{G12D}$;$Adam17^{KO}$ mice compared to $Kras^{G12D}$ controls, shown by H&E (left panels; scale bars, 200 μm) and dual IHC for CK19 (brown) and amylase (blue) (right panels; scale bars, 100 μm). Quantitation of pancreas-to-body weight ratios in (B) and (F) and amylase-positive area in (C) and (G) (n > 6; **p < 0.01; ***p < 0.001) compared to control.

majority of epithelia replaced by metaplasia and mPanIN. Both $Kras^{G12D}$;$Egfr^{KO}$ and $Kras^{G12D}$;$Adam17^{KO}$ mice were almost completely protected from this dramatic transition (Figures 3D–3G).

Noting the earlier correlation between the patterns of EGFR overexpression and spontaneous tumor formation, we tested if cerulein treatment affected EGFR expression. Using a truncated cerulein treatment protocol (Figure 3H), we examined EGFR expression prior to rampant epithelial morphogenesis (Figure 3I). In 34-day-old saline-treated controls, EGFR was minimally expressed in wild-type pancreata. As noted previously, in $Kras^{G12D}$ controls, EGFR was elevated in discrete acinar clusters (1.3% of acinar cells). In contrast, 3 days of cerulein treatment in wild-type mice induced EGFR in discrete acini (<1% of total) after 1 day recovery, which returned to baseline levels with 3 days recovery. It is striking that cerulein treatment of $Kras^{G12D}$ mice induced very high EGFR expression in 73% of acinar cells with 1 day recovery, which was sustained after 3 days recovery and elevated further in metaplasia that had begun to form. Once again, EGFR overexpression in acinar cells reflected the pattern of the eventual tumor formation in this model.

The striking upregulation of EGFR in acinar cells suggested that this cellular compartment is prominently affected by its activity. Besides inducing acinar cell transdifferentiation, EGFR is known to both protect cells from apoptotic cell death and to induce proliferation. Cleaved caspase-3 IHC showed no significant upregulation of apoptosis in 6-week-old $Kras^{G12D}$ pancreata (data not shown). In contrast, proliferation, as measured by BrdU incorporation, increased ~4-fold in $Kras^{G12D}$ acinar cells compared to wild-type, with this increase reduced by half in $Kras^{G12D}$;$Egfr^{KO}$ acinar cells (Figures 3J and 3K). This difference was exaggerated in cerulein-treated mice, where >10% of acinar cells in $Kras^{G12D}$ mice incorporated BrdU, with no increase under the same conditions in $Kras^{G12D}$;$Egfr^{KO}$ pancreata. Consistent with this, CyclinD1 was upregulated in acinar cells of $Kras^{G12D}$ and cerulein-treated $Kras^{G12D}$ mice but remained unchanged in $Kras^{G12D}$;$Egfr^{KO}$ pancreata with or without cerulein (Figures 3L and 3M).

EGFR Activity Is Required for Metaplastic Duct Formation

The dependency of acinar-cell-derived pancreatic tumorigenesis on pancreatitis has been attributed to the need for ADM prior to transformation (Gidekel Friedlander et al., 2009). Chronic activation of EGFR is sufficient to induce ADM in vitro (De Lisle and Logsdon, 1990) and in vivo (Sandgren et al., 1990). To test if EGFR signaling is necessary for this process, we used several in vivo and in vitro models of ADM. Chronic overexpression of the EGFR ligand TGFA in the *Ela-Tgfa* transgenic model induces substantial ductal metaplasia and fibrosis after several weeks of transgene expression (Sandgren et al., 1990). Ablation of either *Egfr* or *Adam17* effectively eliminated TGFA-induced metaplasia in vivo even at 1 year of age (Figure S3F), reinforcing the necessity for ligand shedding in the ADM process.

Turning to metaplasia associated with experimental pancreatitis, we used a cerulein treatment protocol that produced a chronic pancreatitis-like phenotype in wild-type mice, marked by replacement of acinar tissue with metaplastic ducts and a reactive and inflamed stroma (Figure S3G). Both $Egfr^{KO}$ and $Adam17^{KO}$ mice were strongly protected from most aspects of pancreatitis, including ADM and the parallel stromal response. Quantitation of inflammatory cell infiltration into the damaged tissue confirmed a significant loss of this response (Figures S3H and S3I). Protein arrays revealed that several cytokines were significantly lower in cerulein-treated $Egfr^{KO}$ pancreata compared to wild-type, including RANTES, IL16, CXCL13, and IL23 (data not shown). However, the common expression of each of these factors by reactive inflammatory and other stromal cells suggested that these lower levels were possibly a secondary effect of the reduction in inflammatory infiltrates. Two proinflammatory proteins that were definitively produced by the metaplastic epithelia, as well as the stroma, were COX-1 and COX-2 (Figure S3J), suggesting that the inability of $Egfr^{KO}$ pancreata to form metaplastic ducts contributes to the reduced inflammatory response.

The block in the pancreatitis phenotype was not due to gross loss of cerulein-induced signal transduction. When treated with cerulein to induce acute pancreatitis, mice of all genotypes showed a gain of pancreatic wet weight associated with edema, increased serum amylase levels, areas of tissue necrosis, and induction of acinar cell SOX9 expression (Figures S3K–S3N).

We then tested if in vitro ADM required EGFR activation. In vitro ADM in collagen-embedded acinar cell explants is usually induced by the addition of ectopic EGFR ligand. To simulate the in vivo animal models more closely, and to bypass direct EGFR stimulation, we chose to induce in vitro ADM either by expression of $Kras^{G12D}$ or by addition of low concentrations of cerulein into the culture medium.

Acinar cell explants derived from $Kras^{G12D}$ mice transdifferentiated spontaneously in culture within 3 days, as determined by coimmunofluorescence for the acinar and duct cell markers, amylase and CK19, respectively. This transition was almost entirely absent in explants derived from $Kras^{G12D}$;$Egfr^{KO}$ mice (Figures 4A and 4B), arresting at a nestin-positive intermediate stage (Miyamoto et al., 2003) (Figures S4A and S4B).

(H) Truncated cerulein treatment protocol for analysis of premetaplastic signaling.
(I) EGFR IHC in saline-treated (control) and cerulein treated WT (left panels) and $Kras^{G12D}$ (right panels) pancreata with 1 day and 3 days recovery. Arrows indicate focal areas of high EGFR expression. n = 3, scale bars = 20 μm.
(J) BrdU incorporation measured by IHC in acinar cells of saline or cerulein-treated $Kras^{G12D}$ and $Kras^{G12D}$;$Egfr^{KO}$ pancreata with 3 days recovery. Arrows indicate positive acinar nuclei. Scale bar, 20 μm.
(K) Counts of $BrdU^{+}$ acinar cells; n = 3; $^{**}p < 0.01$.
(L) Co-IF for CyclinD1 (green) and EGFR (red) in saline or cerulein-treated $Kras^{G12D}$ and $Kras^{G12D}$;$Egfr^{KO}$. Arrows indicate some positive acinar nuclei. Scale bar, 10 μm.
(M) Quantitation of CyclinD1 expression. $^{*}p < 0.05$; $^{***}p < 0.001$; all other differences were not significant, n = 3.
Error bars in all panels, ± SEM. See also Figure S3.

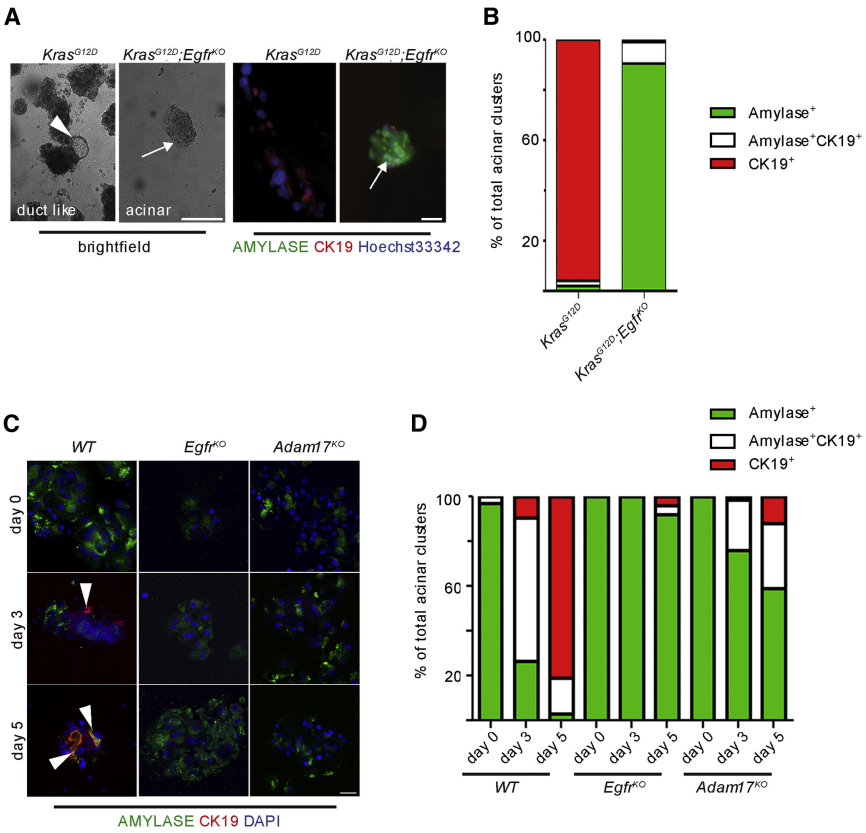

Figure 4. EGFR Signaling Is Required for Acinar Transdifferentiation in Three-Dimensional Primary Culture

(A) Light microscopy (left panels) and co-IF for amylase (green) and CK19 (red, right panels) in $Kras^{G12D}$ and $Kras^{G12D};Egfr^{KO}$ acinar cell explants after 3 days in three-dimensional collagen culture. Arrowhead indicates area of ductal morphology in $Kras^{G12D}$ explants, compared to maintained acinar cell morphology and amylase expression in $Kras^{G12D};Egfr^{KO}$ explants (arrows). Scale bars, 20 μm.

(B) Quantitation of amylase and CK19 positive acinar clusters on Day 3 of culture.

(C) Co-IF for amylase (green) and CK19 (red) in cerulein-treated WT (left panels), $Egfr^{KO}$ (middle panels), and $Adam17^{KO}$ acinar cell explants (right panels). Arrowheads indicate $CK19^{+}$ cells. Scale bars, 20 μm.

(D) Quantitation of amylase and CK19 positive acinar clusters in cerulein-treated explant cultures.

See also Figure S4.

We found also that treatment of wild-type acinar cell explants with cerulein induced ADM within 5 days (Figure 4C). Both $Egfr^{KO}$ and $Adam17^{KO}$ explants were strongly resistant to this effect, although $Egfr^{KO}$ explants were more so (Figures 4C and 4D), indicating possible compensation from other sheddases. Like $KRAS^{G12D}$ (Figure 1C), cerulein also induced EGFR activation, in an ADAM17-dependent manner (Figure S4C). We then examined expression of the EGFR ligands and ADAM17 substrates TGFA and AREG in acinar explants. While AREG was not detected (data not shown), TGFA was induced by the third day of cerulein treatment (Figure S4D), independent of genotype, confirming that the mutant acinar cells remain cerulein responsive. Finally, because ADAM17 is known to shed several bioactive cell surface molecules, we confirmed that the $Adam17^{KO}$ ADM blockade did not require shedding of other substrates by rescuing the wild-type phenotype with addition of TGFA to the culture medium (Figure S4E).

The dependency of pancreatitis-associated and in vitro ADM upon acinar cell EGFR and ADAM17 led us to test the relevance of these findings to human disease. Expression of components of the EGFR pathway in human CP, including active EGFR (pY1068), ADAM17, TGFA, and AREG was determined by IHC (Figure S4F). Regardless of CP type (alcoholic, familial, or spontaneous), active EGFR, ADAM17, and TGFA were consistently upregulated, particularly in acinar cells adjacent to inflamed and fibrotic stroma in 10/10 CP samples. AREG was consistently expressed in ductal metaplasia adjacent to nonexpressing acinar cells. Thus, activation of the EGFR circuitry in vivo and in vitro is reflected in human CP.

EGFR-Dependent ERK Activation Is Required for Pancreatic Tumorigenesis

Initially, we hypothesized that EGFR was responsible for activation of some of the pathways that have been shown to be important for pancreatic tumorigenesis, including STAT3 and RAC1. Contrary to these possibilities, we observed substantial pSTAT3 in $Kras^{G12D};Egfr^{KO}$ pancreata comparable to $Kras^{G12D}$ tissue (Figure S5A). We also saw no change in active RAC pulldown experiments (data not shown). Recent data suggesting that RAS activation must reach a minimum threshold in order to transform the pancreas (Ji et al., 2009) led us to examine if EGFR and ADAM17 inhibition or ablation is consistent with this model by examining downstream effectors of RAS, including PI3K/AKT (pAKT) and MAPK (pERK1/2). $Kras^{G12D};Egfr^{KO}$ mice showed no diminution of active AKT compared to control $Kras^{G12D}$ mice (Figure 5A), suggesting no difference in PI3K activity. In contrast, we observed ~2-fold lower levels of pERK in 3-month-old $Kras^{G12D};Egfr^{KO}$ pancreatic lysates (Figure 5A). Since this difference may be an indirect effect of enhanced pERK levels in tumors that form only in $Kras^{G12D}$ controls, we confirmed a similar loss of pERK in 4-week-old pancreatic lysates prior to substantial transformation (Figure 5A, lower panel). IHC for pERK in 4-week-old $Kras^{G12D}$ mice revealed several positive isolated acinar regions (0.8% of total), whereas in $Kras^{G12D};Egfr^{KO}$ mice, pERK was limited to stromal cells (Figure 5B). ERK activation was also clearly detectable in 88% of acinar cell clusters in wild-type cerulein-treated acinar explants, compared to 4.2% and 10.8% in $Egfr^{KO}$ and $Adam17^{KO}$ explants, respectively (Figure 5C).

KRAS oncogenic mutations are dominant, usually only affecting a single allele. Thus, approximately half the KRAS protein expressed is wild-type and turns over guanosine triphosphate (GTP) at a rapid rate, thus inactivating signaling. Active EGFR

is known to relocalize wild-type KRAS to the plasma membrane via Grb2/Sos where it is activated (Basu et al., 1994; Gale et al., 1993). Consistent with this, coimmunoprecipitation and coimmunofluorescence experiments showed clear interaction and colocalization of KRAS and EGFR in $Kras^{G12D}$-expressing tumor cell lines and acinar explants (Figures S5B and S5C). Using isolated acinar cells from wild-type, $Kras^{G12D}$, $Kras^{G12D}$;$Egfr^{KO}$ and $Kras^{G12D}$;$ADAM17^{KO}$ mice, we found an upregulation of both total and active RAS in $Kras^{G12D}$ acinar cells (Figure 5D), consistent with previous reports (Ji et al., 2009). However, in $Kras^{G12D}$;$Egfr^{KO}$ and $Kras^{G12D}$;$ADAM17^{KO}$ cells, active RAS was reduced by more than 50%, while the upregulation of total RAS remained, leaving the active/total RAS ratios an average of 55% and 45% lower than $Kras^{G12D}$ cells, respectively.

We next tested if EGFR activity was required for maintenance of ERK activity when *Kras* is mutated. Treatment of isolated $Kras^{G12D}$ acinar cells with erlotinib reduced the active RAS/total RAS ratio by an average of 39.8% compared to control, with no effect on total RAS expression (Figure 5E). We then treated $Kras^{G12D}$ mice with cerulein to induce rampant transformation (Figure 3D) then treated acutely with erlotinib by oral gavage 12, 6, and 2 hr prior to tissue harvest. Compared to vehicle, erlotinib treatment reduced pERK levels by an average of 46% (Figure 5F). Treated pancreata showed an obvious reduction of pERK IHC, especially in isolated mPanINs (Figure 5G). Unlike our observations in $Egfr^{KO}$ mice, acute erlotinib treatment dramatically reduced pAKT staining in mPanINs (Figure 5G), suggesting an acute effect on PI3K signaling that is apparently compensated for under conditions of chronic inhibition. Consistent with the knockout mice, no alteration in pSTAT3 was observed (Figure 5G). Erlotinib-treated pancreata also showed a dramatic ~4-fold upregulation of cleaved caspase-3 IHC-positive cells (Figure 5H) and a significant decrease in CyclinD1 expression (Figure 5I), indicating that EGFR activity is critical for survival and proliferation of metaplastic and mPanIN epithelia. EGFR dependency is also demonstrable in human PDA cell lines, with both RAS and ERK activity responsive to EGFR inhibition and activation, even in *KRAS* mutant cells (Figure S5D). We also found upregulation of pERK IHC in acinar cells of human CP samples (Figure S5E), consistent with a role in ADM in human disease.

We have shown that EGFR is required for ADM and ERK activation and that EGFR and pERK are upregulated in acinar cells in human CP. To test if ERK activation is involved in ADM in vitro and pancreatic tumorigenesis in vivo, we used the allosteric MEK1/2 inhibitor BAY 86-9766 (Iverson et al., 2009). BAY 86-9766 treatment of $Kras^{G12D}$ acinar explants strongly blocked transdifferentiation (Figures 6A and 6B). We then treated 6-week-old $Kras^{G12D}$ mice with cerulein to induce pancreatitis. Concomitant with pancreatitis induction and continuing for 3 weeks after, mice were treated daily with 25 mg/kg BAY86-9766 or vehicle by oral gavage (Figure 6C). As expected, pERK levels in BAY86-9766-treated pancreata were reduced (Figure 6D) and vehicle-treated $Kras^{G12D}$ mice developed fibrotic, inflamed tissue, with the majority of epithelia replaced by metaplasia and mPanIN. In contrast, BAY86-9766-treated mice retained mostly phenotypically normal tissue with only rare $MUC5AC^{+}$ mPanINs (Figures 6E and 6F).

DISCUSSION

The reproducible tumor onset and progression in the $Kras^{G12D}$ PDA model has allowed us to explore how EGFR affects the transition of normal epithelia to neoplastic lesions. We find that KRAS upregulates EGFR in distinct, phenotypically normal acinar clusters prior to formation of metaplasia and mPanINs. Acinar cell upregulation of EGFR is rapid in cerulein-induced pancreatitis, with $KRAS^{G12D}$ activity able to sustain the elevated expression. Most important, blocking EGFR activity effectively eliminates KRAS-initiated pancreatic tumorigenesis, with or without pancreatitis induction, due to its critical role in amplifying ERK activation within the pancreas. Furthermore, EGFR is critical for acinar cell proliferation and its stimulation of MEK is necessary for transdifferentiation of transformation-resistant acinar cells to a transformation-sensitive, progenitor cell-like, metaplastic duct cell. Thus, we propose that EGFR's major role in pancreatic tumorigenesis lies in its control of the differentiation of neoplastic precursors and, after tumor initiation, maintenance of ERK activity.

EGFR has been implicated in the pathogenesis of several epithelial cancers (Normanno et al., 2006). Inappropriate EGFR activation results from mutation of the receptor or overexpression of its ligands and their ADAM sheddases. Its contributions in *RAS*-mutated tumors are presumed to be through activation of complementary oncogenic pathways, as its abilities to activate the RAS pathway would be redundant. Nonetheless, upregulation of EGFR, its ligands, and ADAM17 have been reported in PDA (Friess et al., 1996; Ringel et al., 2006), consistent with their importance in these usually *Kras* mutant cancers. Several studies show that constitutive RAS signaling is not sufficient to compensate for EGFR activity. EGFR is necessary for the growth (Dlugosz et al., 1997) and survival (Sibilia et al., 2000) of RAS-initiated cutaneous squamous cell carcinoma and maintains the stem-cell-like nature of transformed keratinocytes (Hansen et al., 2000). In H-RAS initiated melanoma, an EGFR autocrine loop is required for tumor cell maintenance and survival (Bardeesy et al., 2005). In PDA cell lines, the unique activities of EGFR promote cell proliferation and invasion even when *KRAS* is mutated (Jaganathan et al., 2010; Larbouret et al., 2007; Pino et al., 2006; Zhao et al., 2010). Overall, the majority of studies support models where EGFR in *RAS*-mutated tumors is generally involved in posttransformation functions. Two studies provide notable exceptions where, in vitro, RAS transformation of otherwise normal immortalized cells requires EGFR activity (Gangarosa et al., 1997; Sibilia et al., 2000). In addition, concomitant pancreatic activation of oncogenic KRAS and EGFR signaling leads to accelerated formation of high-grade preneoplastic lesions and PDA (Siveke et al., 2007). Our data support a model where endogenous EGFR signaling is required to maintain the critical threshold of RAS activity required for tumorigenesis (Ji et al., 2009). Based on numerous experimental approaches, loss of EGFR signaling resulted in an ~50% drop in active RAS, consistent with continual stimulation of GTP loading of the highly catalytically active wild-type RAS proteins, although we cannot eliminate the possibility that it is required for the occasional reactivation of the catalytically impaired mutant KRAS.

Much has been made recently of experimental pancreatitis being required for transformation of oncogenic KRAS expressing

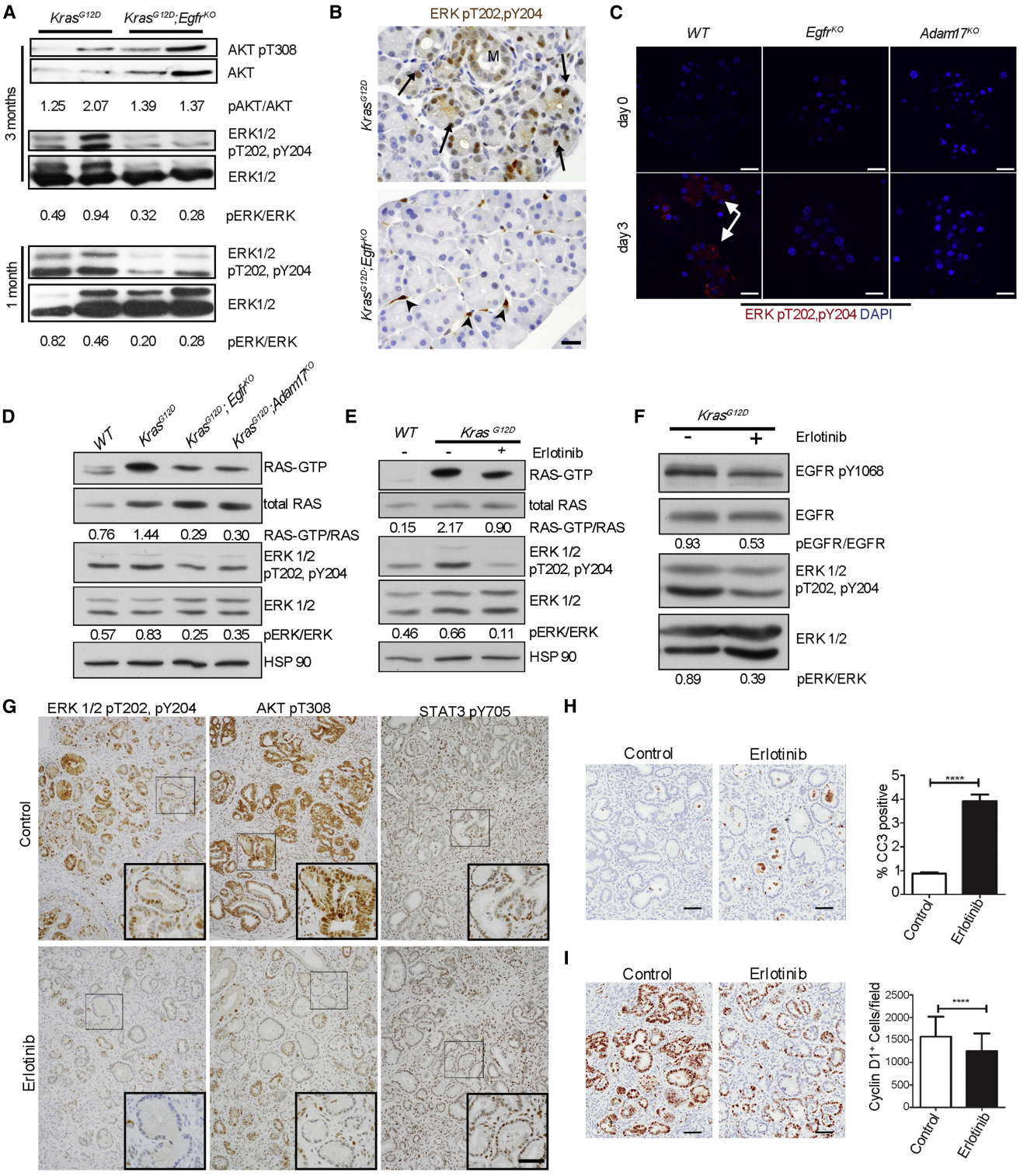

Figure 5. Endogenous EGFR Is Required for Robust Activation of RAS and ERK

(A) Western blot analysis of whole pancreatic lysates for active pAKT and pERK in $Kras^{G12D}$ and $Kras^{G12D}$;$Egfr^{KO}$ mice, at 3 months (upper and middle panels) and pERK at 1 month of age (lower panels). Numbers indicate densitometric quantitation of pERK/total ERK and pAKT/AKT ratios of representative blots shown; n = 4.

(B) IHC for active pERK in 6-week-old $Kras^{G12D}$ and $Kras^{G12D}$;$Egfr^{KO}$ pancreata. Arrows indicate areas of focal acinar cell staining. Metaplasia is indicated with an M. Arrowheads indicate stromal cell staining. Micrographs are representative of six mice. Scale bar, 20 μm.

(C) IF staining for active pERK in acinar cell explants of cerulein treated wild-type (WT), $Egfr^{KO}$, and $Adam17^{KO}$ explants at 0 and 3 days of culture. Arrows indicate areas of positive staining. Scale bar, 20 μm.

acinar cells (Carrière et al., 2009; Gidekel Friedlander et al., 2009; Guerra et al., 2007, 2011). In this model, cerulein induces intracellular activation of digestive enzymes, leading to cellular stress and necrosis. Necrosis attracts inflammatory cells, which cooperate with oncogenic KRAS in the epithelia to induce tumor formation by overcoming cellular senescence (Guerra et al., 2011; Lee and Bar-Sagi, 2010). While this provides a satisfying connection between PDA and one of its primary risk factors, our data show that KRAS and cerulein induce transdifferentiation of acinar cells in vitro by inducing EGFR expression and ADAM17-dependent activation, demonstrating that the earliest steps in this program are initiated cell autonomously. Even so, since parenchymal EGFR ablation also dampens the stromal response, definitive separation of epithelial and stromal contributions to tumorigenesis is complicated. EGFR is known to influence the expression of inflammatory cytokines (Mascia et al., 2010; Monick et al., 2005), and expression of the proinflammatory COX proteins in metaplastic ducts suggests that reactive epithelia promote the host response. Unlike EGFR or pERK activity, however, we did not find COX upregulation in acinar cells, suggesting that this is not direct control of gene expression by EGFR signaling but is inherent to the metaplastic duct phenotype.

The role of EGFR as a therapeutic target in PDA is complex. In unselected metastatic PDA patients, anti-EGFR therapy has only a modest survival effect; however, subgroups of patients and defined molecular subtypes respond to EGFR targeting (Collisson et al., 2011; Jimeno et al., 2008; Moore et al., 2007). In our study, EGFR-negative PDA developed in $Kras^{G12D};p53^{KO};Egfr^{KO}$ mice, albeit with reduced efficiency. In addition, $Kras^{G12D};p53^{KO}$ mice showed no additional survival advantage with erlotinib treatment, indicating that development and progression to PDA can be EGFR independent in a p53 null setting. While we have some indication of what may be compensating for EGFR loss, such as MET activation, this activity was detectable in only a minority of EGFR negative tumors, possibly suggesting multiple routes for bypassing EGFR deficiency. Defining the underlying molecular cues and defining the role of p53 inactivation as a potential contraindication of responsiveness to EGFR inhibition are important issues to be resolved.

In summary, we have identified a critical role for EGFR in KRAS's reprogramming of the pancreatic epithelia en route to tumorigenesis. EGFR activation in this context requires ADAM17 and results in a substantial amplification of MEK signaling. The ADAM17/EGFR/MEK signaling axis is critical for some of the fundamental pathologies associated with PDA risk, such as formation of metaplastic ducts in pancreatitis, suggesting that there may be benefit in targeting the pathway in these at-risk patients to restore homeostasis and thereby reduce the chance of tumorigenesis.

EXPERIMENTAL PROCEDURES

Mice

$Kras^{LSL-G12D/+}$, $Ptf1a^{Cre/+}$, *Ela-Tgfa*, $Trp53^{fl/fl}$, $Adam17^{\Delta Ex5/\Delta Ex5}$, and $Egfr^{fl/fl}$ strains have been described elsewhere (Hingorani et al., 2003; Kawaguchi et al., 2002; Lee and Threadgill, 2009; Marino et al., 2000; Natarajan et al., 2007; Sandgren et al., 1990; Siveke et al., 2007; Tang et al., 2011). Experiments were conducted in accordance with the Office of Laboratory Animal Welfare and the German Federal Animal Protection Laws and were approved by the Institutional Animal Care and Use Committees of the Technische Universität München, Stony Brook University, and the Mayo Clinic.

Histology, IHC, IF, and Western Blot

Distribution and the use of all human samples were approved by the Institutional Review Boards of Vanderbilt University Medical Center and the Mayo Clinic. IHC was performed on a Ventana XT (Tucson, AZ, USA) autostainer or as previously described (Siveke et al., 2007). For total EGFR and phospho-ERK IHC, mice were anesthetized and perfused with 4% paraformaldehyde. All IHC was counterstained with hematoxylin except amylase/CK19 dual IHC. Quantitation of amylase-positive area was performed on singly DAB-stained sections using Olympus cellSens Dimension software. Quantitation represents the average of 15–20 20× fields of view from three mice of each genotype, treatment regimen, or time point, as indicated. IF and western blot were performed according to standard protocols (Siveke et al., 2007). Confocal IF images were collected on a Leica SP2 or a Ziess-LSM-510 Meta confocal microscope at consistent gain and offset. Antibodies are described in the Supplemental Experimental Procedures.

RAS Activity Assay

GST-Raf-1-RBD fusion protein was prepared by modifying procedures published elsewhere (Castro et al., 2005). Details of cell preparation and protocol modifications are found in the Supplemental Experimental Procedures.

Quantitative RT-PCR

RT-PCR was performed as previously described (Siveke et al., 2007). For protocol details, see the Supplemental Experimental Procedures.

Preparation of Pancreatic Epithelial Explants Culture

Pancreatic epithelial explants were as described previously (Heid et al., 2011). Either recombinant human TGF-α (rh TGFα, R&D Systems; final concentration, 50 ng/ml) or cerulein (American Peptide Company; final concentration, 2.6 pM) was added as indicated. For MEK inhibition, BAY 86-9766 (provided by Bayer Schering) was added at indicated concentrations.

For each genotype, experiments with acinar epithelial explants were performed with the following numbers of mice: *WT*, n = 15; $Egfr^{KO}$, n = 5; $Adam17^{KO}$, n = 10; $Kras^{G12D}$, n = 7; $Kras^{G12D};Egfr^{KO}$, n = 10; *WT* plus BAY 86-9766, n = 3; and $Kras^{G12D}$ plus BAY 86-9766, n = 3. For quantification, acinar explants were seeded in triplicate and cell clusters were counted from at least three optical fields per well.

(D) Active RAS pulldown assays from lysates of isolated primary acinar cells from WT, $Kras^{G12D}$, $Kras^{G12D};Egfr^{KO}$, and $Kras^{G12D};Adam17^{KO}$ mice. Numbers indicate densitometric quantitation of the ratio of GTP-bound and total RAS of representative blots shown. Western blots show concomitant relative ERK activity (pERK/ERK) in these lysates; n = 3.
(E) GTP-bound RAS/total RAS and pERK/total ERK ratios in isolated acinar cells treated with erlotinib for 6 hr. Numbers indicate quantitation of representative blots shown. n = 3.
(F) $Kras^{G12D}$ mice were treated with cerulein as in Figure 3D to induce uniform tumorigenesis and then treated with vehicle or 100 mg/kg erlotinib 12, 6, and 2 hr before sacrifice. Shown are western blots of pY1068 and total EGFR and pERK and total ERK. Numbers indicate ratios of representative blots shown; n = 3.
(G) IHC for active pERK, pAKT, and pSTAT3 in vehicle or erlotinib-treated mice described in (F). Scale bar, 100 μm for primary micrographs and 50 μm for insets.
(H and I) IHC and quantitation for (H) cleaved caspase-3 (CC3) and (I) CyclinD1 in vehicle or erlotinib-treated mice described in (F). Scale bars, 50 μm. Error bars, ± SEM.
See also Figure S5.

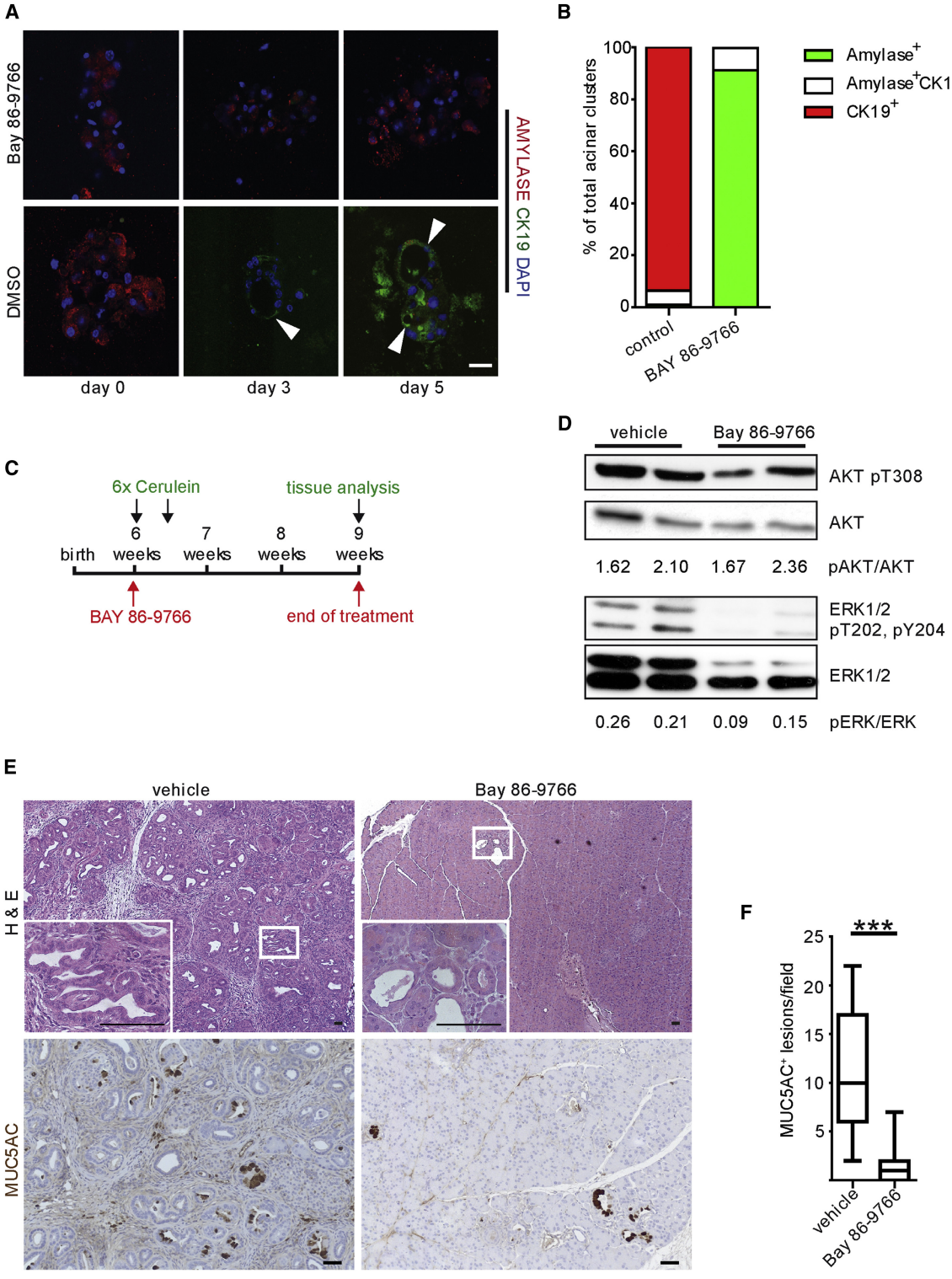

Figure 6. ERK Activity Is Critical for Metaplasia and Neoplasia

(A) Co-IF for amylase and CK19 in acinar cell explants of $Kras^{G12D}$ mice treated with either the MEK inhibitor BAY 86-9766 or vehicle. Arrowheads point to $CK19^+$ duct-like structures. Scale bar, 20 μm.

(B) Quantitation of $amylase^+$ and $CK19^+$ cell clusters is representative of at least three independent experiments per treatment.

(C) Schematic illustration of pancreatitis induction in $Kras^{G12D}$ mice with a BAY 86-9766 treatment regimen. In 6-week-old $Kras^{G12D}$ mice pancreatitis was induced by six hourly injections with 50 μg/kg cerulein on 2 consecutive days. Mice were treated either with a daily oral dose of BAY 86-9766 or vehicle, 6 days/week for 3 consecutive weeks, beginning on the first day of cerulein treatment.

Cerulein Treatments

To induce a CP-like phenotype, 250 μg/kg cerulein injections twice daily were administered intraperitoneally (i.p.) for 3 weeks, with 24 hr recovery. $Kras^{G12D}$ and knockout derivatives were treated with 250 μg/kg cerulein once daily for 5 consecutive days and allowed to recover for 1 week before tissue harvesting. For examining EGFR protein induction, one daily 250 μg/kg dose was administered i.p. for 3 days, with 1 or 3 days of recovery, as indicated.

In Vivo Inhibition of MEK in Pancreatitis-Induced Tumors

Six-week-old $Kras^{G12D}$ mice were treated to induce pancreatitis, as described previously (Morris et al., 2010). On Day 1 postcerulein injection, mice received a single daily dose of 25 mg/kg BAY 86-9766 or vehicle by oral gavage, 6 days/week for 3 weeks.

In Vivo Treatment of $Kras^{G12D};p53^{KO}$ Mice with Erlotinib or Cetuximab

Seven-day-old $Kras^{G12D};p53^{KO}$ mice were injected i.p. with either cetuximab (twice per week, 2 mg/kg), erlotinib (daily, 25 mg/kg), or vehicle (daily) for 3 weeks and sacrificed at 28 days of age. To assess efficacy of gemcitabine alone and in combination with erlotinib, mice with detectable tumor burden by MRI, determined by a clinical 1.5 T MRI device, were treated daily with gemcitabine i.p. (120 mg/kg, four doses every third day) or gemcitabine i.p. (100 mg/kg, four doses every third day) in combination with erlotinib (daily, 50 mg/kg) by oral gavage. Tumor burden was monitored by MRI. For acute erlotinib treatment, $Kras^{G12D}$ were treated with five daily doses of 250 μg/kg cerulein, allowed to recover for 1 week, and then treated with 100 mg/kg erlotinib 12, 6, and 2 hr before sacrifice and tissue harvest.

Statistical Analysis

Statistical analyses were performed using the Mann–Whitney test for nonnormally distributed, unpaired data. Tumor burden was compared between strains using one-way analysis of variance. With all box plots, the bottom and top of the box are the 25th and 75th percentile and the central line is the median of the data. The whiskers represent maximum and minimum values, with the remaining dots being outliers.

SUPPLEMENTAL INFORMATION

Supplemental Information includes five figures and Supplemental Experimental Procedures and can be found with this article online at http://dx.doi.org/10.1016/j.ccr.2012.07.024.

ACKNOWLEDGMENTS

This work was supported by a VA Merit Award, the Knapp Chair for Pancreatic Cancer Research, and National Institutes of Health (NIH) Grants R01CA159222 and R03CA129579 to H.C.C.; NIH Grants P01HL018645 and R01HL067267 to E.W.R.; a pilot and feasibility award from the University of Washington Nutrition and Obesity Center, Grant DK035816 to C.L.W.; grants from the Austrian Science Fund ([FWF] W1212), the EC Program (LSHC-CT-2006-037731), and the GEN-AU Program "Austromouse" (GZ200.147/1-VI/1a/2006 and 820966) to M.S.; Grants R01CA092479 and P50CA106991 to D.W.T.; Grant R01CA140290 to N.R.M.; Grant R01CA140182 to P.S.; Grant P50CA102701 to the Mayo Clinic Pancreatic Cancer SPORE; Grant P50CA095103 for the Vanderbilt University Medical Center GI Spore Tissue Core; Deutsche Krebshilfe (Grant 109992 to J.T.S.), the German Federal Ministry of Education and Research (National Genomic Research Network [NGFN-Plus], 01GS08115 to J.T.S. and R.M.S.); and the German Research Foundation (SFB824/C4 to J.T.S.). TROMAIII antibody, developed by Rolf Kemmler, was obtained from the Developmental Studies Hybridoma Bank, developed under the auspices of the National Institute of Child Health and Human Development, and maintained by The University of Iowa, Department of Biology, Iowa City, IA.

Received: February 8, 2012
Revised: May 16, 2012
Accepted: July 31, 2012
Published: September 10, 2012

REFERENCES

Bardeesy, N., Kim, M., Xu, J., Kim, R.S., Shen, Q., Bosenberg, M.W., Wong, W.H., and Chin, L. (2005). Role of epidermal growth factor receptor signaling in RAS-driven melanoma. Mol. Cell. Biol. *25*, 4176–4188.

Bardeesy, N., Aguirre, A.J., Chu, G.C., Cheng, K.H., Lopez, L.V., Hezel, A.F., Feng, B., Brennan, C., Weissleder, R., Mahmood, U., et al. (2006). Both p16(Ink4a) and the p19(Arf)-p53 pathway constrain progression of pancreatic adenocarcinoma in the mouse. Proc. Natl. Acad. Sci. USA *103*, 5947–5952.

Basu, T., Warne, P.H., and Downward, J. (1994). Role of Shc in the activation of Ras in response to epidermal growth factor and nerve growth factor. Oncogene *9*, 3483–3491.

Carrière, C., Young, A.L., Gunn, J.R., Longnecker, D.S., and Korc, M. (2009). Acute pancreatitis markedly accelerates pancreatic cancer progression in mice expressing oncogenic Kras. Biochem. Biophys. Res. Commun. *382*, 561–565.

Castro, A.F., Rebhun, J.F., and Quilliam, L.A. (2005). Measuring Ras-family GTP levels in vivo—running hot and cold. Methods *37*, 190–196.

Collisson, E.A., Sadanandam, A., Olson, P., Gibb, W.J., Truitt, M., Gu, S., Cooc, J., Weinkle, J., Kim, G.E., Jakkula, L., et al. (2011). Subtypes of pancreatic ductal adenocarcinoma and their differing responses to therapy. Nat. Med. *17*, 500–503.

De Lisle, R.C., and Logsdon, C.D. (1990). Pancreatic acinar cells in culture: expression of acinar and ductal antigens in a growth-related manner. Eur. J. Cell Biol. *51*, 64–75.

Dlugosz, A.A., Hansen, L., Cheng, C., Alexander, N., Denning, M.F., Threadgill, D.W., Magnuson, T., Coffey, R.J., Jr., and Yuspa, S.H. (1997). Targeted disruption of the epidermal growth factor receptor impairs growth of squamous papillomas expressing the v-ras(Ha) oncogene but does not block in vitro keratinocyte responses to oncogenic ras. Cancer Res. *57*, 3180–3188.

Fjällskog, M.L., Lejonklou, M.H., Oberg, K.E., Eriksson, B.K., and Janson, E.T. (2003). Expression of molecular targets for tyrosine kinase receptor antagonists in malignant endocrine pancreatic tumors. Clin. Cancer Res. *9*, 1469–1473.

Friess, H., Berberat, P., Schilling, M., Kunz, J., Korc, M., and Büchler, M.W. (1996). Pancreatic cancer: the potential clinical relevance of alterations in growth factors and their receptors. J. Mol. Med. *74*, 35–42.

Gale, N.W., Kaplan, S., Lowenstein, E.J., Schlessinger, J., and Bar-Sagi, D. (1993). Grb2 mediates the EGF-dependent activation of guanine nucleotide exchange on Ras. Nature *363*, 88–92.

Gangarosa, L.M., Sizemore, N., Graves-Deal, R., Oldham, S.M., Der, C.J., and Coffey, R.J. (1997). A raf-independent epidermal growth factor receptor autocrine loop is necessary for Ras transformation of rat intestinal epithelial cells. J. Biol. Chem. *272*, 18926–18931.

Gidekel Friedlander, S.Y., Chu, G.C., Snyder, E.L., Girnius, N., Dibelius, G., Crowley, D., Vasile, E., DePinho, R.A., and Jacks, T. (2009). Context-dependent transformation of adult pancreatic cells by oncogenic K-Ras. Cancer Cell *16*, 379–389.

Guerra, C., Schuhmacher, A.J., Cañamero, M., Grippo, P.J., Verdaguer, L., Pérez-Gallego, L., Dubus, P., Sandgren, E.P., and Barbacid, M. (2007).

(D) Western blot analysis for active pERK and pAKT in control and BAY 86-9766-treated mice. Numbers indicate quantitation of ratios of blots shown, as indicated.
(E) Histological analysis and IHC for the PanIN marker MUC5AC in vehicle and BAY 86-9766-treated mice (inset, n = 3). Scale bars, 50 μm.
(F) Quantitation of $MUC5AC^{+}$ lesions in BAY 86-9766-treated mice compared to controls (***$p < 0.001$).

Chronic pancreatitis is essential for induction of pancreatic ductal adenocarcinoma by K-Ras oncogenes in adult mice. Cancer Cell *11*, 291–302.

Guerra, C., Collado, M., Navas, C., Schuhmacher, A.J., Hernández-Porras, I., Cañamero, M., Rodriguez-Justo, M., Serrano, M., and Barbacid, M. (2011). Pancreatitis-induced inflammation contributes to pancreatic cancer by inhibiting oncogene-induced senescence. Cancer Cell *19*, 728–739.

Hansen, L.A., Woodson, R.L., 2nd, Holbus, S., Strain, K., Lo, Y.C., and Yuspa, S.H. (2000). The epidermal growth factor receptor is required to maintain the proliferative population in the basal compartment of epidermal tumors. Cancer Res. *60*, 3328–3332.

Heid, I., Lubeseder-Martellato, C., Sipos, B., Mazur, P.K., Lesina, M., Schmid, R.M., and Siveke, J.T. (2011). Early requirement of Rac1 in a mouse model of pancreatic cancer. Gastroenterology *141*, 719–730.

Hingorani, S.R., Petricoin, E.F., Maitra, A., Rajapakse, V., King, C., Jacobetz, M.A., Ross, S., Conrads, T.P., Veenstra, T.D., Hitt, B.A., et al. (2003). Preinvasive and invasive ductal pancreatic cancer and its early detection in the mouse. Cancer Cell *4*, 437–450.

Iverson, C., Larson, G., Lai, C., Yeh, L.T., Dadson, C., Weingarten, P., Appleby, T., Vo, T., Maderna, A., Vernier, J.M., et al. (2009). RDEA119/BAY 869766: a potent, selective, allosteric inhibitor of MEK1/2 for the treatment of cancer. Cancer Res. *69*, 6839–6847.

Jaganathan, S., Yue, P., and Turkson, J. (2010). Enhanced sensitivity of pancreatic cancer cells to concurrent inhibition of aberrant signal transducer and activator of transcription 3 and epidermal growth factor receptor or Src. J. Pharmacol. Exp. Ther. *333*, 373–381.

Ji, B., Tsou, L., Wang, H., Gaiser, S., Chang, D.Z., Daniluk, J., Bi, Y., Grote, T., Longnecker, D.S., and Logsdon, C.D. (2009). Ras activity levels control the development of pancreatic diseases. Gastroenterology *137*, 1072–1082.

Jimeno, A., Tan, A.C., Coffa, J., Rajeshkumar, N.V., Kulesza, P., Rubio-Viqueira, B., Wheelhouse, J., Diosdado, B., Messersmith, W.A., Iacobuzio-Donahue, C., et al. (2008). Coordinated epidermal growth factor receptor pathway gene overexpression predicts epidermal growth factor receptor inhibitor sensitivity in pancreatic cancer. Cancer Res. *68*, 2841–2849.

Kawaguchi, Y., Cooper, B., Gannon, M., Ray, M., MacDonald, R.J., and Wright, C.V. (2002). The role of the transcriptional regulator Ptf1a in converting intestinal to pancreatic progenitors. Nat. Genet. *32*, 128–134.

Kobrin, M.S., Funatomi, H., Friess, H., Buchler, M.W., Stathis, P., and Korc, M. (1994). Induction and expression of heparin-binding EGF-like growth factor in human pancreatic cancer. Biochem. Biophys. Res. Commun. *202*, 1705–1709.

Korc, M., Friess, H., Yamanaka, Y., Kobrin, M.S., Buchler, M., and Beger, H.G. (1994). Chronic pancreatitis is associated with increased concentrations of epidermal growth factor receptor, transforming growth factor alpha, and phospholipase C gamma. Gut *35*, 1468–1473.

Larbouret, C., Robert, B., Navarro-Teulon, I., Thèzenas, S., Ladjemi, M.Z., Morisseau, S., Campigna, E., Bibeau, F., Mach, J.P., Pèlegrin, A., and Azria, D. (2007). In vivo therapeutic synergism of anti-epidermal growth factor receptor and anti-HER2 monoclonal antibodies against pancreatic carcinomas. Clin. Cancer Res. *13*, 3356–3362.

Lee, K.E., and Bar-Sagi, D. (2010). Oncogenic KRas suppresses inflammation-associated senescence of pancreatic ductal cells. Cancer Cell *18*, 448–458.

Lee, T.C., and Threadgill, D.W. (2009). Generation and validation of mice carrying a conditional allele of the epidermal growth factor receptor. Genesis *47*, 85–92.

Lüttges, J., Reinecke-Lüthge, A., Möllmann, B., Menke, M.A., Clemens, A., Klimpfinger, M., Sipos, B., and Klöppel, G. (1999). Duct changes and K-ras mutations in the disease-free pancreas: analysis of type, age relation and spatial distribution. Virchows Arch. *435*, 461–468.

Marino, S., Vooijs, M., van Der Gulden, H., Jonkers, J., and Berns, A. (2000). Induction of medulloblastomas in p53-null mutant mice by somatic inactivation of Rb in the external granular layer cells of the cerebellum. Genes Dev. *14*, 994–1004.

Mascia, F., Cataisson, C., Lee, T.C., Threadgill, D., Mariani, V., Amerio, P., Chandrasekhara, C., Souto Adeva, G., Girolomoni, G., Yuspa, S.H., and Pastore, S. (2010). EGFR regulates the expression of keratinocyte-derived granulocyte/macrophage colony-stimulating factor in vitro and in vivo. J. Invest. Dermatol. *130*, 682–693.

Means, A.L., Ray, K.C., Singh, A.B., Washington, M.K., Whitehead, R.H., Harris, R.C., Jr., Wright, C.V., Coffey, R.J., Jr., and Leach, S.D. (2003). Overexpression of heparin-binding EGF-like growth factor in mouse pancreas results in fibrosis and epithelial metaplasia. Gastroenterology *124*, 1020–1036.

Means, A.L., Meszoely, I.M., Suzuki, K., Miyamoto, Y., Rustgi, A.K., Coffey, R.J., Jr., Wright, C.V., Stoffers, D.A., and Leach, S.D. (2005). Pancreatic epithelial plasticity mediated by acinar cell transdifferentiation and generation of nestin-positive intermediates. Development *132*, 3767–3776.

Miyamoto, Y., Maitra, A., Ghosh, B., Zechner, U., Argani, P., Iacobuzio-Donahue, C.A., Sriuranpong, V., Iso, T., Meszoely, I.M., Wolfe, M.S., et al. (2003). Notch mediates TGF alpha-induced changes in epithelial differentiation during pancreatic tumorigenesis. Cancer Cell *3*, 565–576.

Monick, M.M., Cameron, K., Staber, J., Powers, L.S., Yarovinsky, T.O., Koland, J.G., and Hunninghake, G.W. (2005). Activation of the epidermal growth factor receptor by respiratory syncytial virus results in increased inflammation and delayed apoptosis. J. Biol. Chem. *280*, 2147–2158.

Moore, M.J., Goldstein, D., Hamm, J., Figer, A., Hecht, J.R., Gallinger, S., Au, H.J., Murawa, P., Walde, D., Wolff, R.A., et al.; National Cancer Institute of Canada Clinical Trials Group. (2007). Erlotinib plus gemcitabine compared with gemcitabine alone in patients with advanced pancreatic cancer: a phase III trial of the National Cancer Institute of Canada Clinical Trials Group. J. Clin. Oncol. *25*, 1960–1966.

Morris, J.P., 4th, Cano, D.A., Sekine, S., Wang, S.C., and Hebrok, M. (2010). Beta-catenin blocks Kras-dependent reprogramming of acini into pancreatic cancer precursor lesions in mice. J. Clin. Invest. *120*, 508–520.

Natarajan, A., Wagner, B., and Sibilia, M. (2007). The EGF receptor is required for efficient liver regeneration. Proc. Natl. Acad. Sci. USA *104*, 17081–17086.

Normanno, N., De Luca, A., Bianco, C., Strizzi, L., Mancino, M., Maiello, M.R., Carotenuto, A., De Feo, G., Caponigro, F., and Salomon, D.S. (2006). Epidermal growth factor receptor (EGFR) signaling in cancer. Gene *366*, 2–16.

Pino, M.S., Shrader, M., Baker, C.H., Cognetti, F., Xiong, H.Q., Abbruzzese, J.L., and McConkey, D.J. (2006). Transforming growth factor alpha expression drives constitutive epidermal growth factor receptor pathway activation and sensitivity to gefitinib (Iressa) in human pancreatic cancer cell lines. Cancer Res. *66*, 3802–3812.

Ringel, J., Jesnowski, R., Moniaux, N., Lüttges, J., Ringel, J., Choudhury, A., Batra, S.K., Klöppel, G., and Löhr, M. (2006). Aberrant expression of a disintegrin and metalloproteinase 17/tumor necrosis factor-alpha converting enzyme increases the malignant potential in human pancreatic ductal adenocarcinoma. Cancer Res. *66*, 9045–9053.

Sahin, U., Weskamp, G., Kelly, K., Zhou, H.M., Higashiyama, S., Peschon, J., Hartmann, D., Saftig, P., and Blobel, C.P. (2004). Distinct roles for ADAM10 and ADAM17 in ectodomain shedding of six EGFR ligands. J. Cell Biol. *164*, 769–779.

Sandgren, E.P., Luetteke, N.C., Palmiter, R.D., Brinster, R.L., and Lee, D.C. (1990). Overexpression of TGF alpha in transgenic mice: induction of epithelial hyperplasia, pancreatic metaplasia, and carcinoma of the breast. Cell *61*, 1121–1135.

Sharma, A., Zangen, D.H., Reitz, P., Taneja, M., Lissauer, M.E., Miller, C.P., Weir, G.C., Habener, J.F., and Bonner-Weir, S. (1999). The homeodomain protein IDX-1 increases after an early burst of proliferation during pancreatic regeneration. Diabetes *48*, 507–513.

Sibilia, M., Fleischmann, A., Behrens, A., Stingl, L., Carroll, J., Watt, F.M., Schlessinger, J., and Wagner, E.F. (2000). The EGF receptor provides an essential survival signal for SOS-dependent skin tumor development. Cell *102*, 211–220.

Singh, A.B., and Harris, R.C. (2005). Autocrine, paracrine and juxtacrine signaling by EGFR ligands. Cell. Signal. *17*, 1183–1193.

Siveke, J.T., Einwächter, H., Sipos, B., Lubeseder-Martellato, C., Klöppel, G., and Schmid, R.M. (2007). Concomitant pancreatic activation of Kras(G12D) and Tgfa results in cystic papillary neoplasms reminiscent of human IPMN. Cancer Cell *12*, 266–279.

Strobel, O., Dor, Y., Alsina, J., Stirman, A., Lauwers, G., Trainor, A., Castillo, C.F., Warshaw, A.L., and Thayer, S.P. (2007). In vivo lineage tracing defines the role of acinar-to-ductal transdifferentiation in inflammatory ductal metaplasia. Gastroenterology *133*, 1999–2009.

Tang, J., Zarbock, A., Gomez, I., Wilson, C.L., Lefort, C.T., Stadtmann, A., Bell, B., Huang, L.C., Ley, K., and Raines, E.W. (2011). Adam17-dependent shedding limits early neutrophil influx but does not alter early monocyte recruitment to inflammatory sites. Blood *118*, 786–794.

Tobita, K., Kijima, H., Dowaki, S., Kashiwagi, H., Ohtani, Y., Oida, Y., Yamazaki, H., Nakamura, M., Ueyama, Y., Tanaka, M., et al. (2003). Epidermal growth factor receptor expression in human pancreatic cancer: Significance for liver metastasis. Int. J. Mol. Med. *11*, 305–309.

Zhao, S., Wang, Y., Cao, L., Ouellette, M.M., and Freeman, J.W. (2010). Expression of oncogenic K-ras and loss of Smad4 cooperate to induce the expression of EGFR and to promote invasion of immortalized human pancreas ductal cells. Int. J. Cancer *127*, 2076–2087.

Zhu, Z., Kleeff, J., Friess, H., Wang, L., Zimmermann, A., Yarden, Y., Büchler, M.W., and Korc, M. (2000). Epiregulin is Up-regulated in pancreatic cancer and stimulates pancreatic cancer cell growth. Biochem. Biophys. Res. Commun. *273*, 1019–1024.

Cancer Cell
Article

EGF Receptor Signaling Is Essential for K-*Ras* Oncogene-Driven Pancreatic Ductal Adenocarcinoma

Carolina Navas,[1] Isabel Hernández-Porras,[1] Alberto J. Schuhmacher,[1,3] Maria Sibilia,[2] Carmen Guerra,[1,*] and Mariano Barbacid[1,*]
[1]Molecular Oncology Programme, Centro Nacional de Investigaciones Oncológicas (CNIO), E-28029 Madrid, Spain
[2]Institute of Cancer Research, Department of Medicine I, Comprehensive Cancer Center, Medical University of Vienna, Borschkegasse 8a, A1090 Vienna, Austria
[3]Present address: Cancer Biology and Genetics Program, Memorial Sloan-Kettering Cancer Center, New York, NY 10021, USA
*Correspondence: mcguerra@cnio.es (C.G.), mbarbacid@cnio.es (M.B.)
http://dx.doi.org/10.1016/j.ccr.2012.08.001

SUMMARY

Clinical evidence indicates that mutation/activation of EGF receptors (EGFRs) is mutually exclusive with the presence of K-*RAS* oncogenes in lung and colon tumors. We have validated these observations using genetically engineered mouse models. However, development of pancreatic ductal adenocarcinomas driven by K-*Ras* oncogenes are totally dependent on EGFR signaling. Similar results were obtained using human pancreatic tumor cell lines. EGFRs were also essential even in the context of pancreatic injury and absence of p16Ink4a/p19Arf. Only loss of p53 made pancreatic tumors independent of EGFR signaling. Additional inhibition of PI3K and STAT3 effectively prevented proliferation of explants derived from these p53-defective pancreatic tumors. These findings may provide the bases for more rational approaches to treat pancreatic tumors in the clinic.

INTRODUCTION

Patients with pancreatic ductal adenocarcinoma (PDAC) have an average survival of less than a year with fewer than 5% surviving more than 5 years (Vincent et al., 2011). Current standard of care for PDAC patients is Gemcitabine, a nucleoside analog that only prolongs survival for few weeks (Burris et al., 1997; Li et al., 2004). Hence, there is an urgent medical need to find more effective therapeutic approaches to treat this deadly disease (Hidalgo, 2010).

PDAC is likely to stem from a process known as acinar to ductal metaplasia that involves either transdifferentiation of adult acinar cells or misdifferentiation of their progenitors into ductal-like cells. These cells can subsequently progress into malignant adenocarcinoma through a series of histopathological lesions known as pancreatic intraepithelial neoplasias (PanINs) (Maitra and Hruban, 2008). Early pancreatic lesions including low-grade PanINs already carry mutations in K-*RAS* oncogenes, along with loss or inactivation of the *P16INK4a* tumor suppressor (Kanda et al., 2012). High-grade lesions develop upon accumulation of further mutational events, mainly involving inactivation of other tumor suppressors such as *TP53*, *SMAD4*, or *BRCA2* (Hong et al., 2011). Exome sequencing analysis of PDAC genomes has revealed an incredibly complex pattern of mutations affecting as many as 12 different signaling pathways (Jones et al., 2008). In a recent study describing the exomic sequence of different areas of a single PDAC tumor, Campbell et al. (2010) have illustrated the perverse molecular evolution of these tumors even before they spread to other organs.

In 2007, a clinical trial combining Gemcitabine with the EGFR inhibitor, Erlotinib, reported some responses in a limited number of PDAC patients (Moore et al., 2007). Yet, the overall results were not sufficiently significant for the FDA to recommend the

Significance

Previous clinical studies have suggested a therapeutic benefit of Erlotinib, an EGFR inhibitor, in pancreatic ductal adenocarcinoma patients. Here, we show that these observations may have a mechanistic base. EGFRs are expressed during pancreatic injury and in preneoplastic PanIN lesions. Loss of p53, but not of p16INK4a/p19ARF tumor suppressors, relieved the need of tumor cells to maintain EGFR signaling. Yet, loss of EGFRs increased tumor latency and survival. Tumor explants lacking p53 and EGFRs were sensitive to the combined inhibition of PI3K and STAT3. Thus, successful treatment of advanced human pancreatic tumors may require inhibition of at least four distinct signaling cascades including those driven by K-RAS, EGFRs, PI3K, and STAT3.

combination of these two drugs as standard of care. These observations are intriguing because the EGFR is known to signal upstream of K-RAS and hence, its inhibition should have little or no effect on downstream K-RAS-driven oncogenic signals (Yarden and Sliwkowski, 2001). Indeed, in nonsmall lung adenocarcinoma (NSCLC) mutations in *EGFR* and in K-*RAS* are mutually exclusive (Shigematsu et al., 2005). Likewise, a large clinical trial carried out in patients with advanced colorectal carcinomas (CRC) has determined that patients carrying tumors with K-*RAS* mutations do not benefit from treatment with Cetuximab, a monoclonal antibody that blocks EGFR signaling (Karapetis et al., 2008). In spite of these odds, we decided to interrogate by genetic means whether EGFRs might play a role in K-*Ras* oncogene-driven PDAC using a well-characterized genetically engineered mouse (GEM) model for this disease (Guerra et al., 2007, 2011).

RESULTS

Acinar to Ductal Metaplasia Requires EGFR Signaling Even in the Presence of K-*Ras* Oncogenes

Pancreatic acinar to ductal metaplasia is a precursor of the preneoplastic PanIN lesions that eventually lead to PDAC development (Parsa et al., 1985). In normal mice, generation of acinar to ductal metaplasia is largely dependent on activation of EGFRs (Means et al., 2005). Because EGFRs signal through the Ras pathway, we examined whether expression of a constitutive active K-Ras oncoprotein could bypass the requirement for EGFR activity during the generation of metaplasia. Pancreatic cell explants obtained from K-*Ras*$^{+/LSLG12Vgeo}$;*Elas*-tTA/*tetO*-Cre mice (from now on *ElasK-Ras*^{G12V}) in which the K-*Ras*^{G12V} oncogene is selectively expressed in acinar cells, efficiently transdifferentiated into metaplastic ductal-like cells leading to the generation of 5- to 10-fold more metaplastic structures than those not expressing the oncogene (Figure S1A available online). Yet, K-Ras^{G12V}-driven metaplasia was still largely dependent on activation of EGFRs because addition of their cognate ligands EGF or TGFα, effectively increased the number of metaplastic figures (Figure S1B). Ablation of *Egfr* alleles significantly reduced, but did not eliminate the ability of acinar cell explants to generate metaplastic structures (Figures S1B–S1D). These observations suggest that EGF and TGFα may contribute to acinar to ductal metaplasia by activating additional receptors, at least in vitro. Pancreatic acinar cells also expressed high levels of amphiregulin, but not of other members of the EGFR family of ligands (Figure S1E).

Human and Mouse Pancreatic Lesions Express Abundant EGFRs

Mouse acinar cells did not express detectable levels of EGFRs regardless of whether they expressed a K-*Ras* oncogene or not (Figure 1A). In contrast, PanINs, regardless of their grade, were decorated with high levels of the receptor (Figure 1A) (Ueda et al., 2004; Hingorani et al., 2005). Elevated expression of EGFRs was maintained during tumor progression including well-differentiated glandular structures within PDAC tumors (Figure 1A). However, expression levels decreased in poorly differentiated tumor cells (Figure 1B) (Ueda et al., 2004; Hingorani et al., 2005). Human normal pancreata also displayed undetectable levels of EGFRs (Figure 1C). However, morphologically normal acinar cells of pancreatitis patients expressed significant levels of EGFRs in a manner highly reminiscent of the result obtained in pancreata derived from mice exposed to caerulein (Figures 1B and 1C).

These observations are in agreement with an early study describing overexpression of EGFRs in patients with chronic pancreatitis (Korc et al., 1994). We also observed that metaplasias present in pancreatitis biopsies displayed elevated levels of EGFRs (Figure 1C). Low-grade and high-grade PanINs present in human PDAC tumors also expressed high levels of EGFRs (Figure 1C). Interestingly, their pattern of expression in tumored areas closely resembled that observed in mouse PDACs (Figure 1B). Whereas well-differentiated tumor glands were uniformly decorated with EGFR antibodies, less-differentiated glands expressed significantly lower levels of the receptors (Figure 1C). Finally, metastatic cells localized in a regional lymph node retained detectable, albeit somewhat attenuated levels of EGFRs (Figure 1C). These observations indicate that induction of EGFRs in acinar cells of injured pancreata as well as in PanIN and PDAC lesions is a common event in mouse and human pancreatic tissues.

EGFRs Are Essential for the Generation of K-*Ras* Oncogene-Driven PanIN Lesions

To determine whether development of PanIN lesions and PDAC tumors require EGFR signaling, we generated *ElasK-Ras*^{G12V}; *Egfr*$^{+/+}$ and *ElasK-Ras*^{G12V}; *Egfr* $^{lox/lox}$ strains and analyzed their pancreata at 1 year of age. These mice were not exposed to doxycycline to allow expression of the *Elastase*-driven Cre recombinase during late embryonic development (E16.5). Cre-mediated recombination allowed concomitant expression of the resident K-*Ras*^{G12V} oncogene and ablation of the floxed *Egfr* alleles in acinar cells (Figure S2A). As illustrated in Figure 2A, control *ElasK-Ras*^{G12V};*Egfr*$^{+/+}$ littermates (12 out of 13 animals, 92%) exhibited abundant low- and high-grade PanIN lesions (average of 16 and 5 lesions per pancreata, respectively). Moreover, three animals (23%) displayed sizable PDAC tumors. Animals heterozygous for the *Egfr* locus also harbored low- and high-grade PanIN lesions albeit at reduced numbers (average of 5 and 2.5 lesions per pancreata, respectively). Likewise, only one out of ten heterozygous mice carried a PDAC tumor (Figure 2A).

In contrast, careful analysis of serial sections of pancreata from 1-year-old *ElasK-Ras*^{G12V}; *Egfr* $^{lox/lox}$ animals (n = 24) only revealed the presence of a limited number of PanIN lesions (ten low-grade and two high-grade PanINs) in eight mice. More importantly, all of these lesions expressed EGFRs due to incomplete recombination of the floxed *Egfr* alleles (Figures S2B and S2C). Similar results were obtained in older mice sacrificed at 2 years of age (data not shown). These observations indicate that EGFRs are essential for the induction of PanINs and PDAC by K-*Ras* oncogenes.

Adult Mice Also Require EGFR Signaling for PDAC Development

To exclude the possibility that these observations were due to developmental defects in acinar cells lacking EGFRs during embryonic development, we exposed *ElasK-Ras*^{G12V};*Egfr*$^{+/+}$

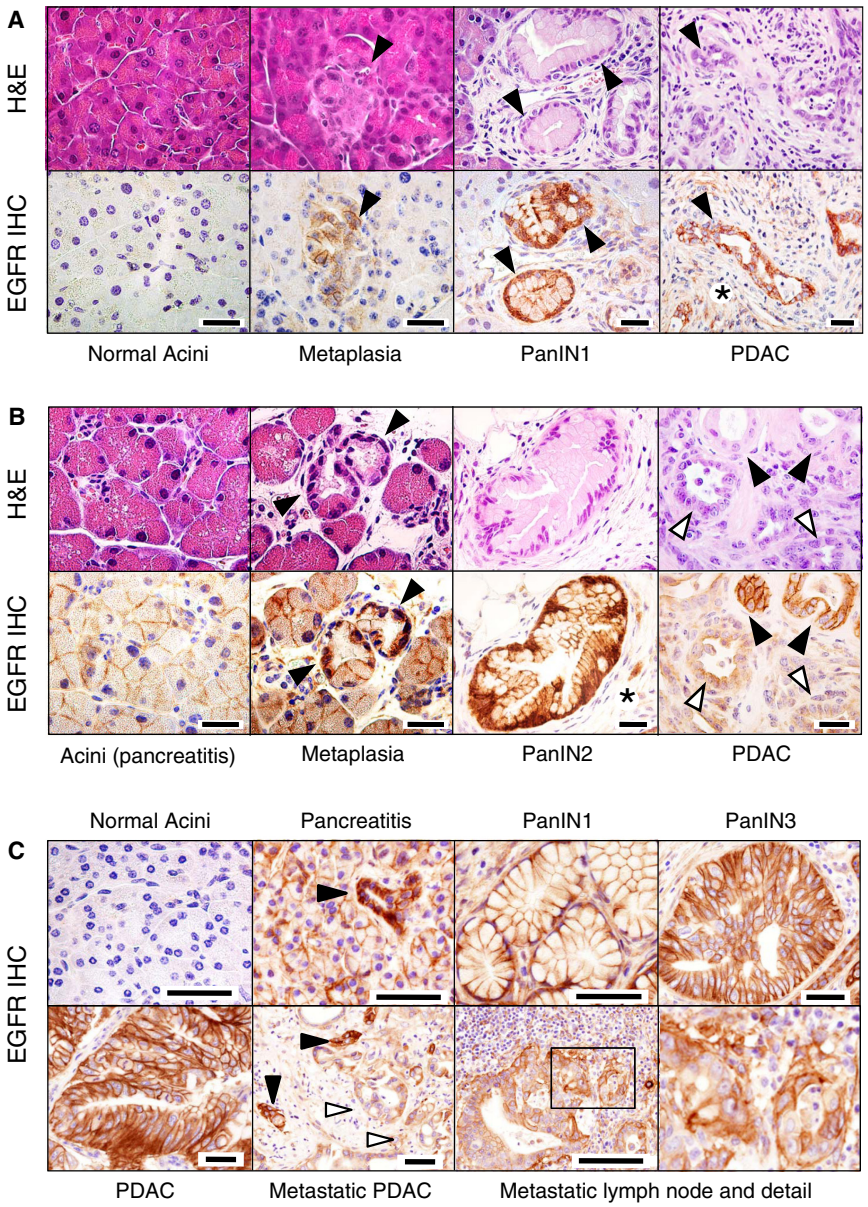

Figure 1. Expression of EGFR in Pancreas of *ElasK-Ras*^{G12V} Mice and of Patients with Pancreatitis and PDAC

(A) Serial paraffin sections obtained from *ElasK-Ras*^{G12V} mice not exposed to doxycycline depicting normal acini, acinar to ductal metaplasia, PanIN1, and PDAC were stained with hematoxylin and eosin (H&E) or with antibodies against the EGFR (EGFR IHC). Lesions are indicated by solid arrowheads. Asterisk indicates stroma cells positive for EGFR immunostaining. Scale bars represent 20 μm.

(B) Serial paraffin sections obtained from *ElasK-Ras*^{G12V} mice exposed to doxycycline from conception to P60 and to caerulein from P90 to P180 depicting acini, acinar to ductal metaplasia, PanIN2 and PDAC were stained with H&E or with antibodies against the EGFR (EGFR IHC). Lesions are indicated by solid arrowheads. Open arrowheads indicate less-differentiated glands within a PDAC. Asterisk indicates stroma cells positive for EGFR expression. Scale bars represent 20 μm.

(C) EGFR IHC of human pancreatic biopsies depicting normal pancreata, pancreata from patients with pancreatitis, PanIN lesions (PanIN1 and PanIN3), nonmetastatic PDAC and a metastatic lymph node with amplified detail. Lesions are indicated by solid arrowheads. Open arrowheads indicate less-differentiated glands within the metastatic PDAC. Scale bars represent 50 μm. See also Figure S1.

and *ElasK-Ras*^{G12V};*Egfr*$^{lox/lox}$ littermates to doxycycline from conception until adulthood (8 weeks of age) to prevent expression of the Cre recombinase. As previously reported, induction of PanIN lesions in these mice requires a pancreatic insult (Guerra et al., 2007). Analysis of 14-month-old *ElasK-Ras*^{G12V};*Egfr*$^{lox/lox}$ mice (n = 14) treated with caerulein for 3 months (P90–P180), that is, 1 year after turning on expression of the resident K-*Ras*^{G12V} oncogene, revealed complete absence of EGFR positive low- and high-grade PanIN lesions or PDAC tumors (Figure 2B). Only three mice carried PanIN lesions, all of which expressed EGFRs (data not shown). Mice examined at 2 years of age displayed a total of nine low-grade and three high-grade PanIN lesions in three out of the seven mice analyzed, all of which retained EGFR expression (data not shown).

As summarized in Figure 2B, control *ElasK-Ras*^{G12V};*Egfr*$^{+/+}$ littermates exhibited the expected number of lesions (Guerra et al., 2011). All mice (n = 13) developed low-grade PanINs (average of 18 lesions per pancreata) and more than 90% (12 out of 13) displayed high-grade PanINs (average of 16 lesions per pancreata). Only one mouse out of 13 (8%) had a full-blown PDAC tumor (Figure 2B). Ablation of a single *Egfr* allele yielded similar results regarding the number of mice affected (80% of the animals carried PanIN lesions and 10% a PDAC tumor). However, the average number of lesions per pancreata was significantly lower (Figure 2B). These observations strongly support the concept that initiation of PDAC tumors requires at least two independent signaling inputs mediated by the EGFR and the K-Ras oncoprotein.

EGFRs Cooperate with Resident K-*Ras* Oncogenes by Activating AKT and STAT3 Signaling Pathways

In an attempt to shed light on the mechanism by which the EGFR cooperate with the resident K-Ras^{G12V} oncoprotein to induce pancreatic lesions, we examined the status of AKT, a well-known downstream effector of the PI3K/AKT survival pathway and STAT3, a mediator of inflammatory cytokines that has been recently implicated in PDAC development (Corcoran et al., 2011; Fukuda et al., 2011; Lesina et al., 2011). As illustrated in Figure S2D, pancreata of untreated *ElasK-Ras*^{G12V} mice display acinar cells that do not express either EGFR or detectable levels

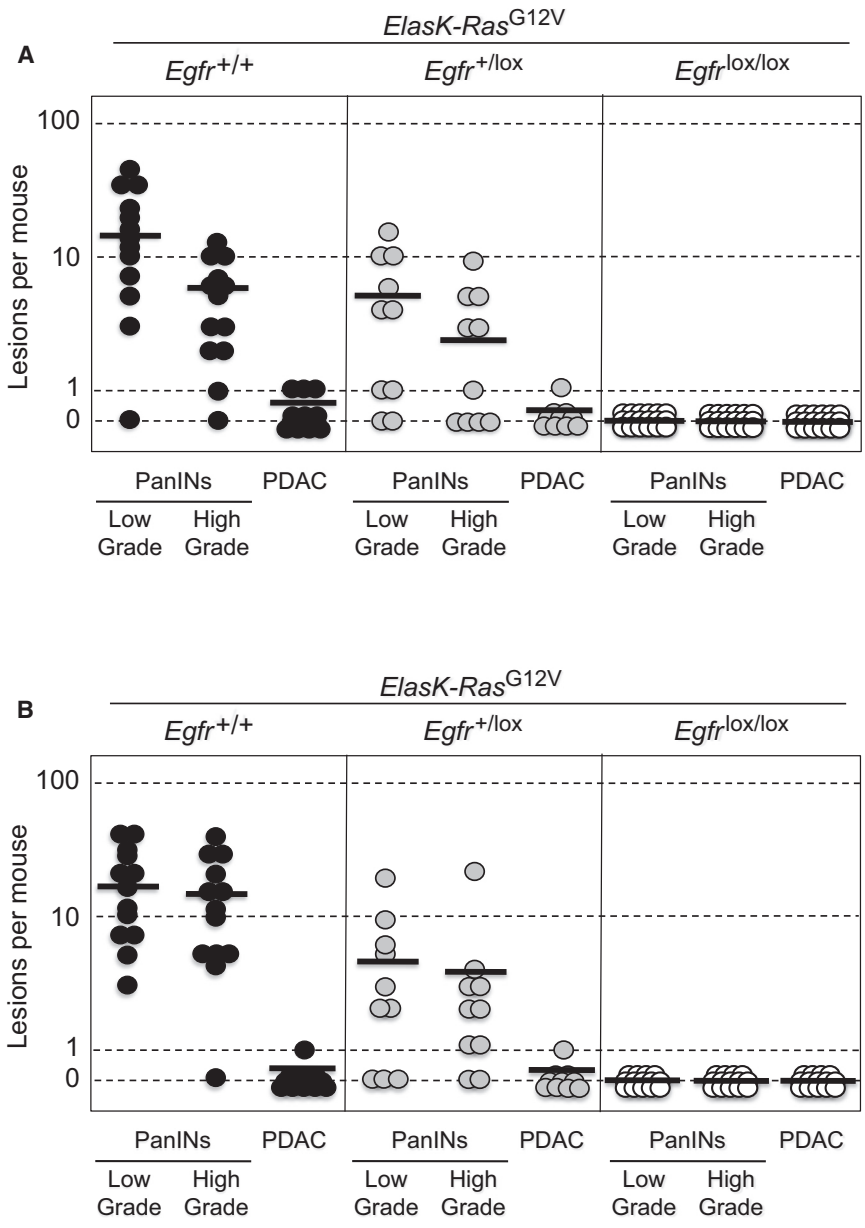

Figure 2. Induction of PanINs and PDAC Tumors by an Endogenous K-*Ras*^{G12V} Oncogene Requires Expression of the EGFR

(A) Number of low- and high-grade PanINs and PDACs per mouse in untreated, 1-year-old *ElasK-Ras*^{G12V} mice carrying the indicated *Egfr* alleles. *ElasK-Ras*^{G12V};*Egfr*$^{+/+}$ (solid circles), *ElasK-Ras*^{G12V};*Egfr*$^{+/lox}$ (gray circles), and *ElasK-Ras*^{G12V};*Egfr*$^{lox/lox}$ (open circles) mice. In these mice, Cre recombinase-mediated expression of the endogenous K-*Ras*^{G12V} oncogene and ablation of the conditional *Egfr*^{lox} alleles took place in a percentage (30%) of acinar cells during late embryonic development.

(B) Number of low- and high-grade PanINs and PDACs per mouse in 14-month-old *ElasK-Ras*^{G12V} mice carrying the indicated *Egfr* alleles. *ElasK-Ras*^{G12V};*Egfr*$^{+/+}$ (solid circles), *ElasK-Ras*^{G12V};*Egfr*$^{+/lox}$ (gray circles), and *ElasK-Ras*^{G12V};*Egfr*$^{lox/lox}$ (open circles) mice. These mice were exposed to doxycycline from conception to P60, a time at which Cre recombinase-mediated expression led to the concomitant activation of the resident K-*Ras*^{G12V} oncogene and ablation of the conditional *Egfr*^{lox} alleles in acinar cells. Mice were subsequently treated with caerulein from P90 to P180.

Horizontal bars indicate the average number of lesions per mouse for each genotype. See also Figure S2.

of phosphorylated AKT or STAT3. Thus indicating that expression of the resident K-Ras^{G12V} oncoprotein does not activate these pathways, at least in this cellular context. In contrast, pancreata of *ElasK-Ras*^{G12V} mice treated with caerulein for 3 months exhibit uniform expression of EGFRs along with nuclear phospho-AKT and phospho-STAT3 proteins through the entire pancreas. Since K-Ras^{G12V} expression in these mice only takes place in about 30% of their acinar cells, activation of the EGFR/AKT/STAT3 axis must be independent of K-*Ras* oncogene signaling (Guerra et al., 2007, 2011). As expected, pancreatic lesions including metaplasias and PanINs, also display activated phospho-AKT and phophop-STAT3 molecules in response to EGFR expression, suggesting that activation of the PI3K/AKT and STAT3 signaling pathways play a role in the induction of these lesions (Figure S2E). Finally, the presence of nuclear phospho-AKT and phospho-STAT3 in PDAC tumors also suggests that activation of these effector molecules might be required for tumor progression (data not shown).

Human Pancreatic Ductal Tumor Cell Lines Are Dependent on EGFR Signaling Regardless of the Presence of K-*RAS* Oncogenes

Next, we interrogated whether cell lines derived from human PDACs also depend on EGFR signaling for proliferation. We selected eight well-characterized tumor cell lines with different pattern of mutations. Six of them, AsPc1, CFPAC, IMIMPC-2, MIAPaCa, PANC1, and SKPC, harbor K-*RAS* oncogenes along with inactivation of *P16INK4a* and *TP53* tumors suppressor genes (Table 1). CFPAC and SKPC cells also have a deleted *SMAD4* locus. The remaining pancreatic tumor cell lines BxPc3 and T3M4, carry a wild-type K-*RAS* locus. Yet, they also have mutated or silenced *P16INK4a* and *TP53* loci and one of them, BxPc3, a mutated *SMAD4* locus (Table 1). Knockdown of EGFRs using two independent shRNAs efficiently inhibited proliferation (>70%) of AsPc1, BxPc3, MIAPaCa, and T3M4 cells. Two cell lines, PANC1 and IMIMPC-2, were only partially inhibited whereas the remaining cell lines, CFPAC and SKPC, were resistant (Table 1). Thus, the effect of EGFR signaling on proliferation appears to be independent of the presence of K-*RAS* oncogenes. Knockdown of EGFR expression only inhibited the PI3K pathway, as determined by

Table 1. Human Pancreatic Ductal Adenocarcinoma Cell Lines Are Sensitive to Inhibition of EGFR and MEK Signaling

	Mutation				*EGFR* Knockdown	Treatment			
						Erlotinib		PD325901	
Tumor	*K-RAS*	*P16INK4a*	*TP53*	*SMAD4*	% Inhibition	IC_{50}	IC_{90}	IC_{50}	IC_{90}
AsPc1	G12D	Frameshift	Frameshift	WT	72.3	>200.0 μM	>200 μM	190.0 μM	>200 μM
CFPAC	G12V	Methylated	Mutation	Deletion	5.2	20.0 μM	>200 μM	22.5 μM	>200 μM
IMIMPC-2	G12D	Deletion	Mutation	WT	32.5	>200.0 μM	>200 μM	0.8 μM	>200 μM
MIAPaCa	G12C	Deletion	Mutation	WT	97.0	66.8 μM	>200 μM	8.5 μM	>200 μM
PANC1	G12D	Deletion	Mutation	WT	59.9	>200.0 μM	>200 μM	>200.0 μM	>200 μM
SKPC	G12V	Methylated	Mutation	Deletion	08.7	70.0 μM	>200 μM	0.5 μM	>200 μM
BxPc3	WT	Mutation	Mutation	Mutation	81.0	23.5 μM	>200 μM	0.3 μM	>200 μM
T3M4	WT	Methylated	Mutation	WT	90.1	12.2 μM	>200 μM	0.1 μM	>200 μM

WT, wild-type. See also Figure S3.

phosphorylation of AKT, in those cells carrying a wild-type K-*RAS* locus (Figure S3).

Five of these tumor cell lines, including K-*RAS* oncogene-positive CFPAC, MiaPaCa and SKPC cells, and K-*RAS* oncogene-negative BxPc3 and T3M4 cells were partially sensitive to Erlotinib (Table 1). Erlotinib treatment did not result in complete inhibition of cell proliferation (IC_{90}) even at concentrations as high as 200 μM. The SKPC cell line, whereas partially sensitive to Erlotinib, was refractory to EGFR knockdown (Table 1). This discrepancy might be explained by either the inability of the shRNAs to effectively knockdown the high levels of EGFRs present in this cell line or to the off-target effect of Erlotinib on related tyrosine protein kinase receptors (Figure S3). We also examined the effect of directly inhibiting the RAS pathway by using the MEK inhibitor, PD325901. Four cell lines carrying K-*RAS* oncogenes, CFPAC, IMIMPC-2, MiaPaCa, and SKPC cells were sensitive to this inhibitor. Interestingly, the BxPc3 and T3M4 cell lines that have a wild-type K-*RAS* locus, were also highly sensitive to the MEK inhibitor, suggesting that these cells may have activated their RAS pathway by mechanisms other than mutating their K-*RAS* locus (Table 1). Finally, AsPc1 and PANC1 cells were resistant to MEK inhibition in spite of carrying K-*RAS* oncogenes, suggesting that in these cells K-*RAS* oncogenes may no longer play an essential role in maintaining their proliferative properties (Table 1).

K-RAS^{G12V}-Driven Lung and Intestinal Tumors Do Not Require EGFR Signaling

The above results, taken together, indicate that proliferation of pancreatic ductal tumor cells have a dual requirement for EGFR and K-RAS signaling. These observations are at odds with extensive clinical data in human NSCLCs, in which oncogenic mutations in the *EGFR* and K-*RAS* loci are mutually exclusive (Shigematsu et al., 2005). Likewise, CRC patients carrying K-*RAS* oncogenes do not benefit from treatments involving inhibition of EGFR signaling (Karapetis et al., 2008). To determine whether the results described above only occur in the context of mouse tumor models or are an intrinsic property of pancreatic tumors, we ablated the *Egfr* locus in two well-characterized GEM models of lung and intestinal tumors induced by the same endogenous K-*Ras*^{G12V} oncogene used to initiate pancreatic lesions. In these models, expression of the resident K-*Ras*^{G12V} oncogene is mediated by activation of an ubiquitously expressed Cre-ERT2 inducible recombinase knocked-in at the locus encoding the large subunit of RNA polymerase II (*RERT* strain; see Guerra et al., 2003). For the lung model, *RERT;K-Ras*^{G12V};*Egfr*$^{+/+}$ (n = 17), *RERT;K-Ras*^{G12V};*Egfr*$^{+/lox}$ (n = 13), and *RERT;K-Ras*^{G12V};*Egfr*$^{lox/lox}$ (n = 25) littermates were treated at weaning with a single dose of 4-hydroxy-tamoxifen (4OHT) (Guerra et al., 2003; Puyol et al., 2010). As illustrated in Figure 3A, all mice died of lung tumors between 63 and 72 weeks of age. Mice displayed similar number of adenomas (average of 15 per mouse) and adenocarcinomas (average of three per mouse) regardless of genotype. None of the tumors analyzed expressed EGFRs by IHC analysis (Figure 3B). Moreover, PCR analysis of tumor DNA only revealed recombined *Egfr null* alleles (data not shown), thus indicating that tumor development had occurred in the absence of EGFRs.

Similar results were obtained in a GEM model of intestinal tumors. *RERT;K-Ras*^{G12V};*Apc*$^{lox/lox}$;*Egfr*$^{lox/lox}$ mice (n = 16) along with control *RERT;K-Ras*^{G12V};*Apc*$^{lox/lox}$;*Egfr*$^{+/lox}$ (n = 17) and *RERT;K-Ras*^{G12V};*Apc*$^{lox/lox}$;*Egfr*$^{+/+}$ (n = 7) littermates were treated at weaning for 2 weeks (3 days per week) with 4OHT. These mice displayed similar tumor burden including adenomas and adenocarcinomas (data not shown) and did not survive beyond 20 weeks of age (Figure 3C). As expected, tumor cells, regardless of genotype, failed to express EGFRs (Figure 3D). These results, taken together, indicate that the requirement of EGFR signaling for the onset of neoplastic pancreatic lesions driven by K-*Ras* oncogenes is unique to this tumor type. Moreover, the similarity between the results obtained in clinical trials and in mouse models of lung and intestinal cancer reinforces the concept that GEM tumor models faithfully reproduce those events observed in cancer patients.

Loss of Senescence Does Not Override the Need for EGFR Signaling during PanIN and PDAC Development

The EGFR is known to promote survival signals that might be essential to overcome the oncogene-induced senescence characteristic of the early stages of pancreatic tumor development (Collado et al., 2005; Guerra et al., 2011). Indeed, most human PDACs carry a mutated or silenced *P16INK4a/P14ARF* locus, an event likely to override senescence (Hong et al., 2011). Thus, we reasoned that ablation of the p16INK4A/p19ARF tumor suppressors (from now on p16/p19), might bypass the requirement for EGFR signaling during tumor

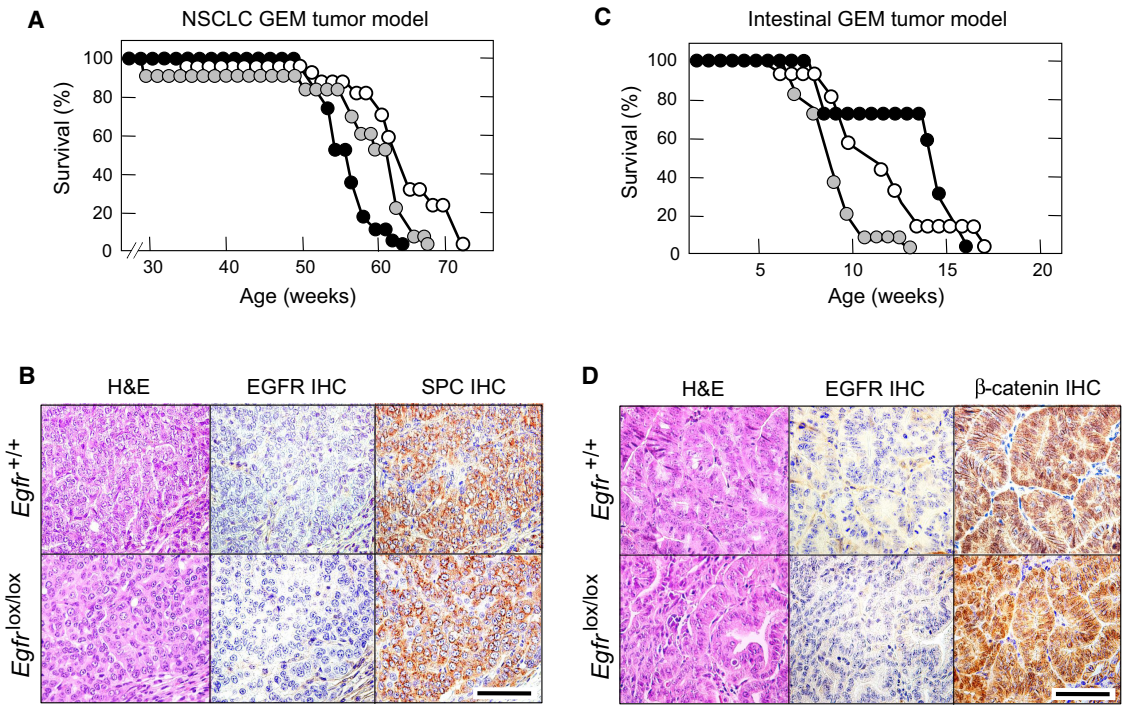

Figure 3. Ablation of EGFRs Has No Effect on K-*Ras*^{G12V}-Driven Lung and Intestinal Tumors

(A) Survival of *RERT;K-Ras*^{G12V};*Egfr*$^{+/+}$ (solid circles), *RERT;K-Ras*^{G12V};*Egfr*$^{+/lox}$ (gray circles), and *RERT;K-Ras*^{G12V};*Egfr*$^{lox/lox}$ (open circles) mice treated with a single injection of 4OHT at P21 to induce NSCLCs.

(B) H&E staining and EGFR and pro-surfactant protein C (SPC) immunostaining (IHC) of consecutive paraffin sections showing representative adenocarcinoma lesions from 9-month-old *RERTK-Ras*^{G12V} mice carrying either (top) wild-type *Egfr* or (bottom) conditional *Egfr* alleles. Scale bar represents 50 μm.

(C) Survival of *RERT;K-Ras*^{G12V};*Apc*$^{lox/lox}$;*Egfr*$^{+/+}$ (solid circles), *RERT;K-Ras*^{G12V};*Apc*$^{lox/lox}$;*Egfr*$^{+/lox}$ (gray circles), and *RERT;K-Ras*^{G12V};*Apc*$^{lox/lox}$;*Egfr*$^{lox/lox}$ (open circles) mice treated with 4OHT (3 days per week, for 2 weeks) at P21 to induce intestinal tumors.

(D) H&E staining and EGFR and β-catenin immunostaining (IHC) of consecutive paraffin sections showing representative intestinal tumor lesions from 2-month-old *RERT;K-Ras*^{G12V};*Apc*$^{lox/lox}$ mice carrying either (top) wild-type *Egfr* or (bottom) conditional *Egfr* alleles. Scale bar represents 50 μm.

initiation. Conditional floxed *p16/p19* alleles were introduced into *ElasK-Ras*^{G12V} mice carrying wild-type or floxed *Egfr* alleles and their pancreata examined at 16 weeks of age, before they displayed any obvious signs of overt tumor development. These mice were not exposed to doxycycline to allow expression of the resident K-*Ras*^{G12V} oncogene during late embryonic development (Guerra et al., 2007). As summarized in Figure 4A, six out of eight mice carrying wild-type EGFRs displayed abundant low- and high-grade lesions. Moreover, five animals had developed at least a PDAC tumor at this time. In contrast, none of the mice carrying *Egfr*$^{lox/lox}$ alleles (n = 6) displayed PanIN lesions or PDAC (Figure 4A).

Mice with the above genotypes were allowed to age. Littermates carrying wild-type *Egfr* alleles, either in homozygocity (n = 12) or heterozygocity (n = 30) succumbed to the disease before they reached 10 months of age (Figure 4B). Postmortem analysis revealed multiple lesions including invasive and metastatic PDAC as well as anaplastic carcinomas that metastasized to multiple organs (Aguirre et al., 2003; Guerra et al., 2011). As expected, none of the low-grade PanIN lesions contained senescent cells as determined by staining for β-galactosidase activity (data not shown). In contrast, *ElasK-Ras*^{G12V};*p16/p19*$^{lox/lox}$;*Egfr*$^{lox/lox}$ mice (n = 7) sacrificed at 1 year of age did not carry any PanIN lesion positive for EGFRs in spite of careful analysis of multiple serial sections (data not shown). Only four animals had a total of six low-grade and two high-grade PanIN "escaper" lesions positive for EGFRs (Figure 4C). Seventeen additional *ElasK-Ras*^{G12V};*p16/p19*$^{lox/lox}$;*Egfr*$^{lox/lox}$ mice were allowed to age beyond 1 year. All of them remained in good health condition at 80 weeks of age (Figure 4B). Histological examination of their pancreata at this time did not reveal any lesions (data not shown). These observations indicate that abrogation of senescence by inactivation of the *p16/p19* tumor suppressors does not relieve pancreatic tumor cells of their need for EGFR signaling.

Loss of p16/p19 tumor suppressors also accelerates tumor development in adult mice providing they have undergone chronic or temporary pancreatitis (Guerra et al., 2011). Analysis of pancreata of *ElasK-Ras*^{G12V};*p16/p19*$^{lox/lox}$;*Egfr*$^{lox/lox}$ mice (n = 7) 12 months after turning on K-Ras^{G12V} expression (8 months after completing caerulein treatment), also failed to reveal EGFR-negative PanIN lesions or PDAC tumors. Control *ElasK-Ras*^{G12V};*p16/p19*$^{lox/lox}$;*Egfr*$^{+/+}$ littermates (n = 10) died at the expected age (40 weeks of median survival) and displayed multiple PanIN lesions as well as PDACs, in some cases with perineural invasion, invasion of the intestinal wall and lymph node metastasis, as previously described (Guerra et al., 2011). These observations indicate that the requirement for EGFR

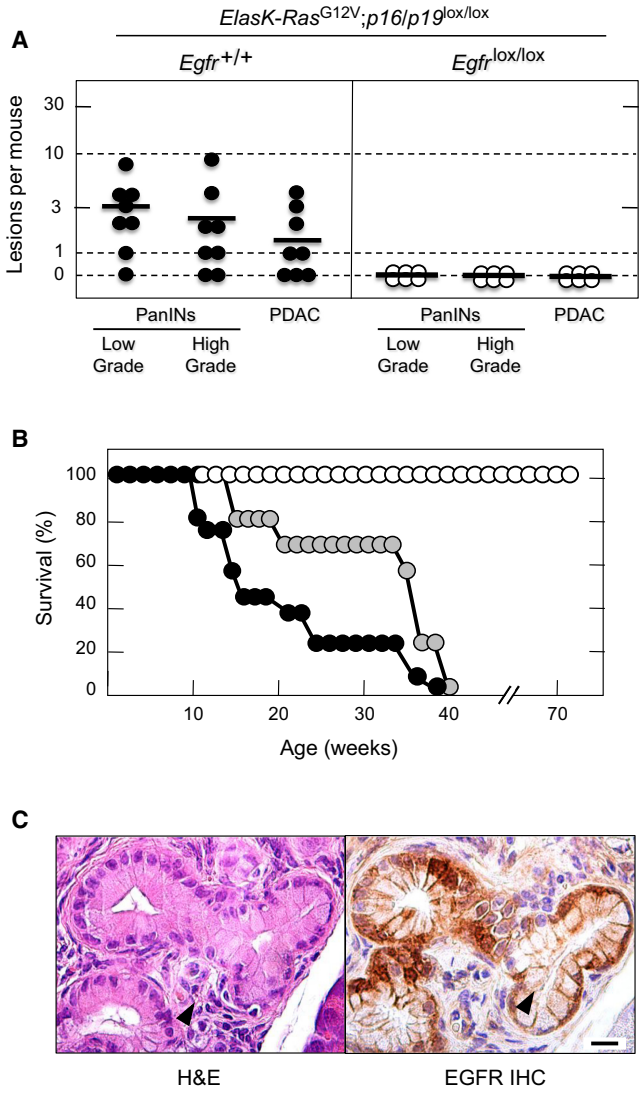

Figure 4. Loss of p16/p19 Tumor Suppressors Does Not Abrogate the Need for EGFR Expression during PanIN and PDAC Development

(A) Number of low- and high-grade PanINs and PDAC lesions per mouse in untreated, 16-week-old *ElasK-Ras*^{G12V};*p16/p19*$^{lox/lox}$ mice carrying either wild-type (solid circles) or conditional (open circles) *Egfr* alleles. In these mice, expression of a Cre recombinase in pancreatic acinar cells during late embryonic development results in the concomitant expression of the endogenous K-*Ras*^{G12V} oncogene and in the ablation of the conditional *p16/p19* and *Egfr* alleles. PanIN lesions positive for EGFR expression in *ElasK-Ras*^{G12V};*p16/p19*$^{lox/lox}$;*Egfr*$^{lox/lox}$ mice (see below) were not scored. Horizontal bars indicate the average number of lesions per mouse.

(B) Survival of untreated *ElasK-Ras*^{G12V};*p16/p19*$^{lox/lox}$; *Egfr* $^{+/+}$ (solid circles), *ElasK-Ras*^{G12V};*p16/p19*$^{lox/lox}$;*Egfr*$^{+/lox}$ (gray circles), and *ElasK-Ras*^{G12V};*p16/p19*$^{lox/lox}$;*Egfr*$^{lox/lox}$ (open circles) mice.

(C) H&E (left) and EGFR IHC (right) of consecutive paraffin sections showing an occasional PanIN lesion observed in *ElasK-Ras*^{G12V};*p16/p19*$^{lox/lox}$;*Egfr*$^{lox/lox}$ animals positive for EGFR expression (arrowhead). Scale bar represents 50 μm.

signaling during PanIN and PDAC development cannot be compensated by loss of the p16/p19 tumor suppressors even in the context of an inflammatory response induced by pancreatitis.

Loss of p53 Triggers Oncogenic Pathways Independent of EGFR Signaling

Human PDAC tumors harbor mutations in classical tumor suppressor genes such as *TP53*, *SMAD4*, or *BRCA2* (Hong et al., 2011). Likewise, mice expressing an endogenous K-*Ras* oncogene during embryonic development in the absence of a functional p53 protein develop aggressive PanINs and PDAC tumors that result in the death of the animals within their first 4 to 5 months of life (Hingorani et al., 2005; Guerra et al., 2007). Similar results have been obtained in the context of adult K-*Ras* oncogene expression followed by pancreatic damage (Guerra et al., 2011). To examine the effect of abrogating EGFR signaling in the absence of p53, we inserted conditional *p53*^{lox} alleles in the *ElasK-Ras*^{G12V} strain in the presence of wild-type or floxed *Egfr* alleles. Animals were sacrificed at 10 weeks of age before they showed signs of overt tumor development. As summarized in Figure 5A, control mice carrying wild-type *Egfr* alleles (n = 7) displayed abundant low- and high-grade lesions and PDAC, averaging ten high grade PanINs and four PDAC tumors per mouse. Interestingly, mice carrying conditional *Egfr* alleles (n = 5) also displayed neoplastic lesions but with reduced incidence (Figure 5A).

When we allowed these mice to age, all animals carrying wild-type *Egfr* alleles (n = 10) succumbed to pancreatic tumors around 20 weeks of age with a median survival of 12 weeks (Figure 5B). Similar results were obtained with heterozygous mice (n = 13) (Figure 5B). At the time of death or humane end point, these mice displayed multiple PanIN lesions and PDAC tumors including a lung metastasis in one of the animals. *ElasK-Ras*^{G12V};*p53*$^{lox/lox}$;*Egfr*$^{lox/lox}$ mice (n = 13) also developed low- and high-grade PanINs as well as PDAC tumors (Figure 5B). Moreover, three of these mice also had macroscopic metastasis at different locations such as peritoneum, diaphragm, liver, and lung (data not shown). However, mice in which the conditional *Egfr* alleles have been ablated died by 40 weeks of age and displayed a median survival 83% longer than that of littermates expressing EGFRs (22 versus 12 weeks) (Figure 5B). Similar results were obtained with mice that expressed the resident K-*Ras*^{G12V} oncogene during adulthood and were treated for 3 months with caerulein. Whereas *ElasK-Ras*^{G12V};*p53*$^{lox/lox}$;*Egfr*$^{lox/lox}$ animals (n = 26) died before reaching 60 weeks of age with a median survival of 38 weeks, control *ElasK-Ras*^{G12V};*p53*$^{lox/lox}$;*Egfr*$^{+/lox}$ mice (n = 8) were dead at 35 weeks of age with a median survival of 27 weeks (data not shown). Thus, ablation of EGFR signaling resulted in an increased survival time of 40%.

Tumor development in mice carrying conditional *Egfr* alleles was not due to incomplete recombination because the large majority of the PanIN lesions and PDAC tumors did not express EGFRs when analyzed by IHC (Figure S4A). Moreover, PCR analysis of DNA isolated from tumor cells also failed to reveal unrecombined *Egfr*^{lox} alleles in most lesions (data not shown). Finally, histopathological analysis of PanIN and PDAC tumors lacking p53 and EGFRs did not reveal significant differences with those present in control animals (Figure S4A). These observations, taken together, indicate that loss of p53 activates oncogenic pathways that bypass the requirement of EGFR signaling for tumor development.

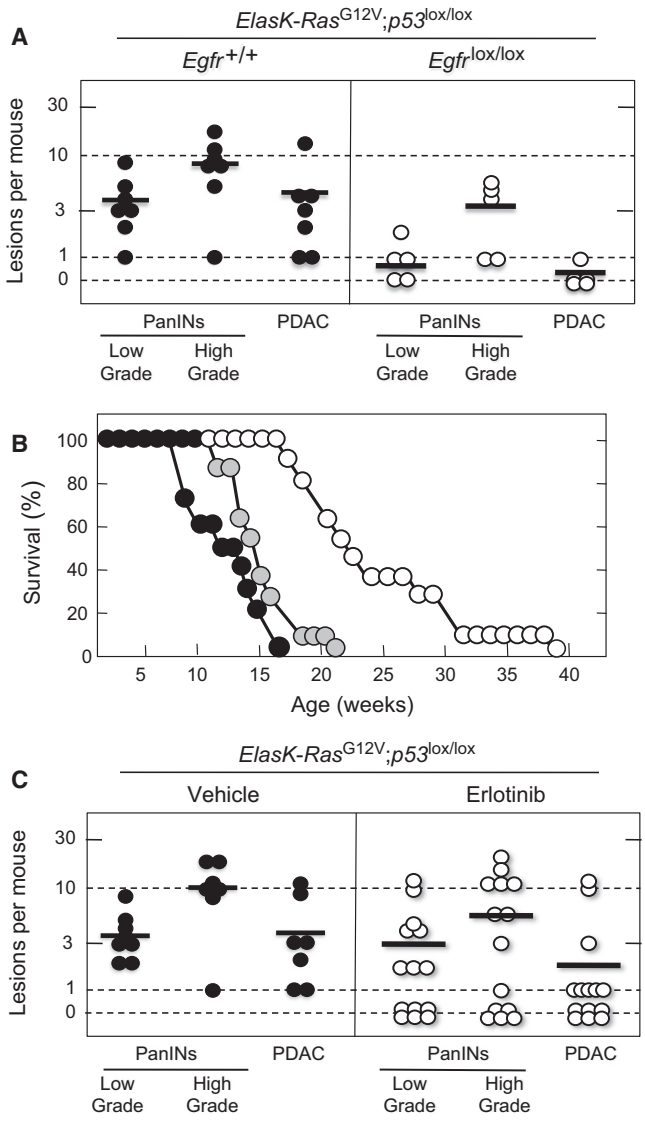

Figure 5. Loss of EGFRs Delays but Does Not Prevent PanIN and PDAC Development in the Absence of p53

(A) Number of low- and high-grade PanINs and PDACs per mouse in untreated, 10-week-old *ElasK-Ras*^{G12V};*p53*$^{lox/lox}$ mice carrying either wild-type (solid circles) or conditional (open circles) *Egfr* alleles. In these mice, expression of a Cre recombinase in pancreatic acinar cells during late embryonic development results in the concomitant expression of the endogenous K-*Ras*^{G12V} oncogene and in the ablation of the conditional *p53* and *Egfr* alleles. Horizontal bars indicate the average number of lesions per mouse.

(B) Survival of untreated *ElasK-Ras*^{G12V};*p53*$^{lox/lox}$;*Egfr*$^{+/+}$ (solid circles), *ElasK-Ras*^{G12V};*p53*$^{lox/lox}$;*Egfr*$^{+/lox}$ (gray circles), and *ElasK-Ras*^{G12V};*p53*$^{lox/lox}$;*Egfr*$^{lox/lox}$ (open circles) mice.

(C) Inhibition of EGFR signaling by Erlotinib treatment reduces the number of PanIN and PDAC lesions. Number of low- and high-grade PanINs and PDACs per mouse in 6-week-old *ElasK-Ras*^{G12V};*p53*$^{lox/lox}$ mice treated for 4 weeks with vehicle (solid circles) or Erlotinib (open circles). Horizontal bars indicate the average number of lesions per mouse. The decrease in the number of PDAC tumors in the Erlotinib-treated cohort was statistically significant ($p < 0.05$).

See also Figure S4.

Inhibition of EGFR Signaling with Erlotinib Interferes with PDAC Development In Vivo

Previous studies have shown that Gefitinib can slow down progression of pancreatic precursor lesions to PDAC (Mohammed et al., 2010). To determine whether EGFRs are required for the progression of PanIN lesions in a more aggressive GEM model, 6-week-old *ElasK-Ras*^{G12V};*p53*$^{lox/lox}$ mice were treated with either vehicle or Erlotinib (100 mg/Kg) for 4 weeks. A small group of mice (n = 3) analyzed at the start of the treatment revealed low- and high-grade PanINs in each of the animals. Moreover, two of the mice already carried small PDACs (Figure S4B). At the end of the 4-week treatment, all mice that received vehicle (n = 7) displayed a significant increase in the number of lesions (Figure 5C). In contrast, Erlotinib treatment led to disappearance of all lesions in three out of the 14 animals included in this cohort. Moreover, three additional Erlotinib-treated mice contained PanIN lesions but no PDAC tumors (Figure 5C). Overall, the Erlotinib-treated cohort had fewer lesions than the control group, indicating a limited but reproducible therapeutic effect of this EGFR inhibitor on PDAC development (Figure 5C).

IHC analysis of lesions in mice treated with Erlotinib for 4 weeks revealed robust inhibition of pAKT but not of pSTAT3 or pERK when compared with samples obtained from control mice treated with vehicle (Figure S4C). As an additional control, we examined the status of pAKT, pSTAT3 and pERK in *ElasK-Ras*^{G12V};*p53*$^{lox/lox}$ mice carrying either wild-type or conditional *Egfr* alleles. As expected, ablation of EGFR expression resulted in inhibition of pAKT but not of pSTAT3 or pERK (Figure S4D). Interestingly, full blown PDACs retained pAKT IHC (Figure S4E), a result confirmed by western blot analysis (Figure S5 and data not shown). These observations suggest that loss of p53 might activate the PI3K pathway by a mechanism independent of EGFR signaling.

EGFR Signaling Is Required for Proliferation of PDAC Tumor Cell Explants

Knockdown of EGFR expression effectively slowed proliferation of cell explants derived from PDAC tumors isolated from *ElasK-Ras*^{G12V} mice (Figure 6A). Similar results were obtained using explants from tumors obtained from *ElasK-Ras*^{G12V};*p16/p19*$^{lox/lox}$ and *ElasK-Ras*^{G12V};*p53*$^{lox/lox}$ animals (Figure 6A). These tumor explants, regardless of genotype, were also sensitive to Erlotinib (Figure 6B). As expected, Erlotinib had a cytostatic effect because inhibition required continuous exposure to the drug (data not shown). Knockdown of EGFRs in these tumor explants significantly inhibited phosphorylation of STAT3 (Figure S5). Phosphorylation of ERK proteins was also ameliorated by EGFR knockdown (Figure S5), possibly an indirect consequence of the limited proliferation of these cells in the absence of EGFRs (Figure 6A). Interestingly, phosphorylation of AKT, a marker for the activation of the PI3K/AKT survival pathway was downregulated in all explants except in those lacking p53 (Figure S5).

Cooperation between PI3K and STAT3 Signaling Pathways in the Absence of EGFRs

We reasoned that availability of mouse PDAC tumor explants lacking EGFRs and p53 may allow us to identify additional signaling pathways that contribute to tumor development.

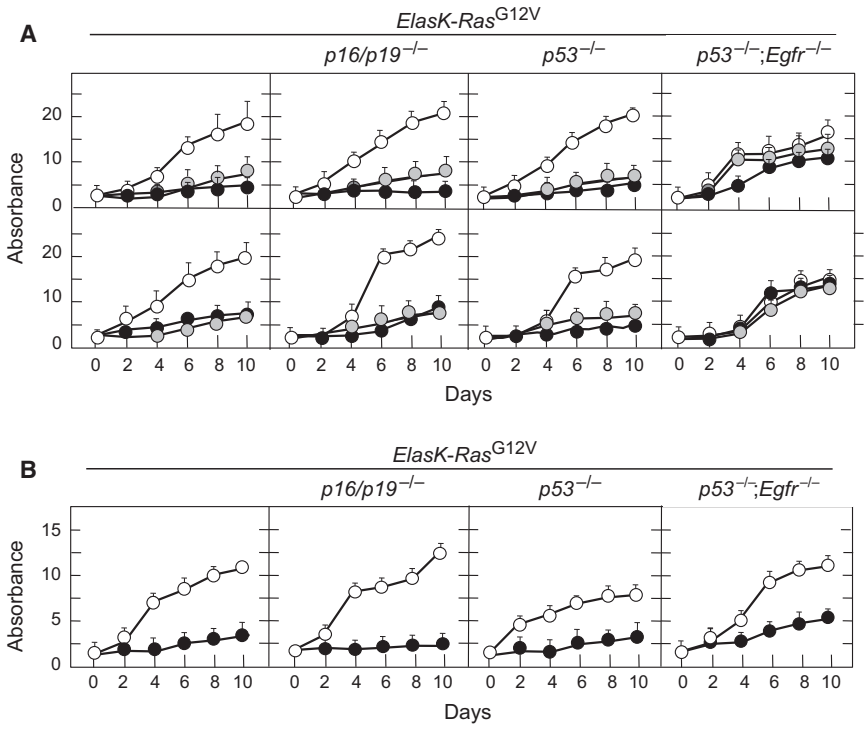

Figure 6. EGFR Expression Is Required for Proliferation of PDAC Tumor Explants In Vitro

(A) PDAC cell explants derived from tumors present in mice with the indicated genotypes were infected with lentiviral vectors expressing two independent shRNAs against the *Egfr* (solid and gray circles) or shRNA control (open circles). Results are the average of two experiments carried out with two independent cell explants done in triplicate. Errors bars mean SD.

(B) PDAC cell explants derived from tumors present in mice with the indicated genotypes were either untreated (open circles) or treated with Erlotinib (solid circles). Erlotinib was used at a final concentration of 50 μM, a concentration that corresponds with the average IC_{90} for these cell explants. Results are the average of two experiments carried out with two independent cell explants done in triplicate. Errors bars mean SD. See also Figure S5.

Unexpectedly, Erlotinib partially inhibited proliferation of PDAC explants from *ElasK-Ras*^{G12V};*p53*$^{lox/lox}$;*Egfr*$^{lox/lox}$ mice. These results are most likely due to off-target effects because shRNAs against the *Egfr* locus did not have any inhibitory effect on the proliferation rate of these cells (Figures 6A and 6B). As illustrated in Figure 7, inhibition of PI3K with ETP-46992 (Martínez González et al., 2012) a selective inhibitor for the p110α and δ catalytic subunits only induced partial inhibition (Figure S6). However, combination of this inhibitor with Erlotinib resulted in robust inhibition of these tumor cell explants even in the absence of EGFRs and p53 (Figure 7).

As indicated above, ablation or inhibition of EGFRs in *ElasK-Ras*^{G12V};*p53*$^{lox/lox}$ mice blocked AKT but not STAT3 phosphorylation (Figures S4C and S4D). Interestingly, knockdown of STAT3 expression did not inhibit proliferation of tumor cell explants, regardless of their genotype. However, addition of the PI3K inhibitor to the *Stat3* shRNA robustly inhibited proliferation of all tumor cell explants (Figure 7). These observations indicate that the STAT3 pathway also contributes to tumor development at least in the absence of p53. Moreover, in this context, PI3K may signal by pathways independent of AKT (Vogt and Hart, 2011). Thus, successful treatment of PDAC tumors in the clinic may require compound inhibition of at least four distinct signaling cascades including those driven by K-RAS, EGFR, PI3K, and STAT3.

DISCUSSION

Current dogma indicates that malignant progression of tumor cells selects against mutations in components of the same signaling pathway such as that driven by the EGFR and their downstream effectors, the RAS proteins. Indeed, clinical observations in NSCLCs, a tumor type that present frequent mutations in both *EGFR* and K-*RAS*, have indicated that they are mutually exclusive (Shigematsu et al., 2005). Similar results have been obtained in CRC patients. According to a large clinical trial, only patients containing nonmutated K-*RAS* genes benefit from treatment with EGFR inhibitors (Karapetis et al., 2008). This dogma, however, might not apply to PDAC tumors. Although *EGFR* mutations have been found in a very small percentage (<3%) of human pancreatic cancers, they can coexist with K-*RAS* mutations (Oliveira-Cunha et al., 2012). Moreover, as illustrated in this study, initiation of K-*Ras* oncogene-driven PanIN lesions and PDAC is absolutely dependent on EGFR signaling. This requirement is not abrogated even in the absence of the p16/p19 tumor suppressors, indicating that the absolute requirement for EGFR signaling in not involved in overcoming senescence. Only ablation of p53 overrules this requirement. Yet, neoplastic lesions lacking p53 take significantly longer to develop in the absence of EGFRs. Ongoing efforts to establish the mutational spectra of mouse PDAC exomic sequences might help us to identify those additional pathways activated by loss of p53.

Pancreatic injury results in the immediate induction of EGFR expression in acinar cells, leading to activation of the PI3K/AKT and STAT3 signaling pathways. EGFR expression, along with activation of AKT and STAT3, is maintained during PanIN progression to PDAC and only becomes attenuated in poorly differentiated glands of advanced PDAC tumors. The EGFR is also expressed in human biopsies obtained from patients suffering from pancreatitis and PDAC tumors, thus supporting the concept that GEM models faithfully reproduce PDAC development in an experimental setting. Previous studies have shown that overexpression of TGFα in the presence of a resident K-*Ras*^{G12D} oncogene accelerated progression of PanIN lesions to metastatic cancer and led to the development of cystic papillary lesions that resembled human intraductal papillary mucinous neoplasms (IPMN) (Siveke et al., 2007). These observations,

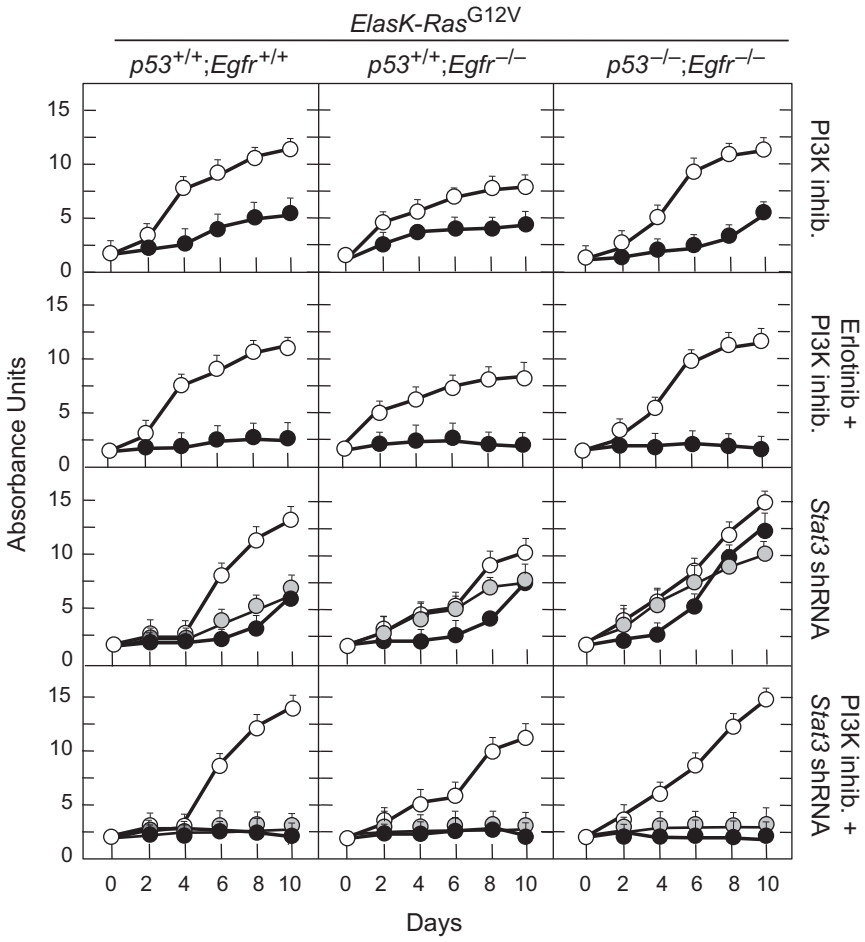

Figure 7. Loss of p53 Activates STAT3 and PI3K Pathways

PDAC cell explants derived from tumors present in mice with the indicated genotypes were treated with the indicated inhibitor(s) or infected with lentiviral vectors expressing two independent shRNA against *Stat3* (solid and gray circles). Control cells were either left untreated or infected with a shRNA control (open circles). Erlotinib was used at a final concentration of 50 μM, a concentration that corresponds with the average IC_{90} for these cell explants. ETP-46992, a selective PI3Kp110α and p110δ inhibitor, was used at a final concentration of 20 μM, a concentration that corresponds to the average IC_{90} for these tumor explants. Each graph represents the average of two experiments carried out with two independent cell explants. Each sample was carried out in triplicate. Errors bars mean SD. See also Figure S6.

taken together, suggest that upregulated expression of EGFRs leading to the activation of the PI3K/AKT and STAT3 pathways might be one of the early responses that predispose acinar cells to undergo neoplastic changes upon activation of K-*Ras* oncogenes. It is interesting to note that in acinar cells, activation of the PI3K/AKT pathway is mediated by induction of EGFRs and not by the resident K-*Ras* oncogenes. These observations may explain why, in spite of the presence of K-*Ras* oncogenes, EGFR signaling is essential to induce neoplastic lesions in pancreatic acinar cells.

Current GEM models of PDAC do not allow target ablation in existing tumors. Yet, our results demonstrating that expression of EGFRs are essential for the proliferation of tumor cell explants strongly suggest that EGFRs signaling is essential beyond the early stages of tumor development. Indeed, knockdown or pharmacological inhibition of EGFRs blocked proliferation of certain human pancreatic tumor cells lines. Likewise, EGFR inhibitors have been shown to limit progression of pancreatic lesions in mouse xenograft models (Ng et al., 2002; Durkin et al., 2006) as well as in K-*Ras* oncogene-driven GEM models (Mohammed et al., 2010; this study). These results suggest that clinical observations showing a limited beneficial effect of EGFR inhibitors in combination with Gemcitabine in patients with PDAC tumors need to be further explored (Moore et al., 2007).

Finally, our results using genetic as well as pharmacologic approaches, illustrate that blocking EGFR signaling only produces limited therapeutic benefit in the context of p53 inactivation, a mutation present in most human PDAC tumors. Availability of tumor cells lacking EGFRs and p53 has allowed us to demonstrate a synergistic activity between PI3K inhibitors and attenuation of STAT3 expression. These observations suggest that loss of TP53 might "reactivate" the PI3K/AKT and STAT3 signaling pathways by mechanisms independent of EGFR in human tumors. Further support for a key role of the EGFR/PI3K/AKT axis in PDAC development comes from preliminary studies in which ablation of the *Pten* tumor suppressor locus in *ElasK-Ras*^{G12V};*Egfr*$^{lox/lox}$ mice leads to efficient tumor development (C.N., I.H., C.G., and M.B., unpublished observations). Recent observations regarding a limited but significant tumor inhibitory effect by inhibitors of the Notch pathway (Plentz et al., 2009; Cook et al., 2012) may open the door to design therapeutic strategies in combination with PI3K and STAT3 inhibitors. Yet, to induce complete regression of aggressive PDAC tumors it will be necessary to unveil additional signaling pathways amenable to pharmacological inhibition. Recent progress in overcoming the stromal barrier characteristic of PDAC tumors (Olive et al., 2009; Von Hoff et al., 2011; Frese et al., 2012; Jacobetz et al., 2012; Provenzano et al., 2012) should facilitate testing these drug combinations in relevant GEM models of pancreatic cancer as a preliminary step prior to their use in a clinical setting.

EXPERIMENTAL PROCEDURES

Mice

The *ElasK-Ras*^{G12V} strain has been previously described (Guerra et al., 2007). In these mice, the *Elas*-tTA/*tetO*-Cre transgenes drive expression of the bacterial Cre recombinase from the *Elastase* promoter under the negative control of doxycycline (Tet-off system). Other strains of mice used in this study include *Egfr*^{lox}, *p16/p19*^{lox}, *p53*^{lox}, *Apc*^{lox}, and *RERT*. The original references

describing these strains appear in the Supplemental Experimental Procedures. All experiments were approved by the CNIO Ethical Committee and performed in accordance with the guidelines for Ethical Conduct in the Care and Use of Animals as stated in The International Guiding Principles for Biomedical Research involving Animals, developed by the Council for International Organizations of Medical Sciences (CIOMS).

Mouse Treatments

To prevent expression of the *Elastase*-driven Cre recombinase in *ElasK-Ras*^{G12V} mice, doxycycline (2 mg/ml; Sigma) was provided in the drinking water as a sucrose solution (5% w/v) to pregnant mothers from the time of conception and to their offspring until the time we activated expression of the resident K-*Ras*^{G12V} oncogene. Pancreatitis was induced by intraperitoneal injections of caerulein for 3 months (125 μg/Kg, 5 days per week; Sigma). For induction of NSCLC, *RERT;K-Ras*^{G12V} mice carrying wild-type or floxed *Egfr* alleles were treated at P21 with a single dose of 4OHT (0.5 mg/ml in oil). For intestinal tumors, *RERT;K-Ras*^{G12V};*Apc*$^{lox/lox}$ mice carrying wild-type or floxed *Egfr* alleles were treated 3 days per week for 2 weeks with 4OHT (0.5 mg/ml in oil) starting at P21. Erlotinib treatment was carried out in 6-week-old *ElasK-Ras*^{G12V};*p53*$^{lox/lox}$ mice by oral gavage (100 mg/Kg in 0.5% methylcellulose with 0.1% Tween80) for 4 weeks. Control mice received the same treatment without Erlotinib.

Histopathology and Immunohistochemistry

Specimens were fixed in 10% buffered formalin and embedded in paraffin. For histopathological analysis, pancreata were serially sectioned (3 μm thick) and every ten sections stained with hematoxylin and eosin (H&E). Remaining sections were kept for immunohistochemical studies with β-catenin (1:750, goat polyclonal; Santa Cruz Biotechnology, Sc-1496), pAKT (pS473) (1:175, rabbit monoclonal EP2109Y; Epitomics 2118-1), EGFR (1:100, rabbit monoclonal; Epitomics 1902-1), SPC (1:175, rabbit polyclonal; Millipore, AB3786), and pSTAT3 (Tyr705) (1:100, rabbit monoclonal D3A7; Cell Signaling Technology, 9145) antibodies. Following incubation with the primary antibodies, positive cells were visualized using 3,3-diaminobenzidine tetrahydrochloride plus (DAB+) as a chromogen. For human samples (see below), immunostaining for EGFRs was preformed as described above.

PDAC Cell Explants

To generate mouse PDAC explants, freshly isolated tumors were minced with sterile razor blades, digested with collagenase P (1.5 μg/ml) in Hanks' balanced salt solution (HBSS) for 30 min at 37°C, and cultured in DMEM with 10% of fetal bovine serum (FBS). After 48 hr, media was supplemented with Geneticin (75 μg/ml) to select for K-Ras^{G12V} expressing cells. All studies were done on cells cultivated for less than ten passages. Their corresponding genotypes were verified by PCR analysis.

Cell Culture and Inhibitor Treatments

Mouse embryonic fibroblasts (MEFs) were isolated from E13.5 embryos and propagated according to standard 3T3 protocols. Human tumor cell lines PANC1, MIAPaCa-2, SKPC, T3M4, were purchased from ATCC. BxPc3 was kindly provided by M. Hidalgo (CNIO). AsPc1, CFPAC, and IMIMPC-2 by F.X. Real (CNIO). These cell lines as well as the PDAC explants were seeded in 96-well plates at a density of 1,000 cells/well or 300 cells/well, respectively, and incubated for 24 hr in DMEM media supplemented with 10% FBS, 2 mM L-glutamine, 50 U/ml penicillin, and 50 μg/ml streptomycin (GIBCO-Invitrogen) before adding the corresponding inhibitor. Inhibitors, including EGFR inhibitor Erlotinib (LC laboratories), MEK inhibitor PD0325901 (Pfizer), and PI3K inhibitor ETP-46992 (CNIO) (Martínez González et al., 2012), were dissolved in DMSO to yield the appropriate final concentrations. Three sets of control wells were included on each plate, containing either medium without drug or medium with the same concentration of DMSO. Cells were exposed to inhibitors for 10 to 14 days. Fresh drug was added every 2 days. For shRNA knockdown assays, human or mouse tumor cells were infected with MISSION shRNAs (Sigma) directed against human *EGFR* (TRC0000121206 and TRC0000121203), mouse *Egfr* (TRCN0000055218 and TRCN0000055221), and mouse *Stat3* (TRCN0000071454 and TRCN0000071456) sequences. Non-Target shRNA Control vector (SHC002, Sigma) was used as a negative control. Cells were selected with puromycin (2 μg/ml) for 5 days before seeding and maintained in DMEM media supplemented with 10% FBS and puromycin. Proliferation rates were determined by the (4,5-dimethylthiazol-2-yl)-2,5-diphenyltetrazolium bromide (MTT) assay (Roche). The resulting absorbance was measured with a microplate reader at 544 nm (EnVision 2104 Multilabel Reader, Perkin Elmer, Waltham, MA). Results represent the average of three independent experiments in which all samples were assayed in triplicate.

Human Samples

Studies using human material were approved by the Ethics and Institutional Review Board of the Grupo Hospital de Madrid (CBBA/4 2008; REF: PI 275). All subjects gave informed consent.

SUPPLEMENTAL INFORMATION

Supplemental Information includes six figures and Supplemental Experimental Procedures and can be found with this article online at http://dx.doi.org/10.1016/j.ccr.2012.08.001.

ACKNOWLEDGMENTS

We thank Howard C. Crawford (Mayo Clinic, Jacksonville, FL) and Jens T. Siveke (Technical University, Munich) for sharing their results prior to publication. We also thank I. Agudo, I. Aragón, M.C. González, M. Lamparero, M. San Román, and R. Villar for excellent technical assistance. We value the excellent support provided by V. Alvarez, E. Gil, M. Gómez, P. González, and N. Matesanz with histopathology and M. Lozano with the laser-capture microscope. We thank J. Pastor and S. Martinez (CNIO) for providing a sample of the PI3K inhibitor, ETP-46992, E. Garcia, M. Hidalgo, and F.X. Real (CNIO) for human samples, and A. Means (Vanderbilt University Medical Centre, Nashville, TN) for help with acinar to ductal transdifferentiation protocols. Work was supported by grants from the European Research Council (ERC-AG/250297-RAS AHEAD), the EU-Framework Programme (LSHG-CT-2007-037665, HEALTH-F2-2010-259770, HEALTH-2010-260791), the Spanish Ministry of Science and Innovation (SAF2006-11773, CSD2007-00017), the Spanish Ministry of Economy and Competitiveness (SAF2011-30173), Autonomous Community of Madrid (GR/SAL/0587/2004, S2006/BIO-0232), and the Fundación de la Mutua Madrileña del Automóvil to M.B. and grants from Fondo de Investigación Sanitaria (PI042124, PI08-1623), Autonomous Community of Madrid (GR/SAL/0349/2004), and Fundación Ramón Areces (FRA 01-09-001) to C.G. M.S. acknowledges funding by the Doctoral Program "Inflammation and Immunity" DK W1212, the EC program LSHC-CT-2006-037731 (Growthstop), and the Austrian Federal Government's GEN-AU program "Austromouse" (GZ 200.147/1-VI/1a/2006 and 820966).

Received: February 22, 2012
Revised: May 8, 2012
Accepted: August 1, 2012
Published: September 10, 2012

REFERENCES

Aguirre, A.J., Bardeesy, N., Sinha, M., Lopez, L., Tuveson, D.A., Horner, J., Redston, M.S., and DePinho, R.A. (2003). Activated Kras and Ink4a/Arf deficiency cooperate to produce metastatic pancreatic ductal adenocarcinoma. Genes Dev. *17*, 3112–3126.

Burris, H.A., 3rd, Moore, M.J., Andersen, J., Green, M.R., Rothenberg, M.L., Modiano, M.R., Cripps, M.C., Portenoy, R.K., Storniolo, A.M., Tarassoff, P., et al. (1997). Improvements in survival and clinical benefit with gemcitabine as first-line therapy for patients with advanced pancreas cancer: a randomized trial. J. Clin. Oncol. *15*, 2403–2413.

Campbell, P.J., Yachida, S., Mudie, L.J., Stephens, P.J., Pleasance, E.D., Stebbings, L.A., Morsberger, L.A., Latimer, C., McLaren, S., Lin, M.L., et al. (2010). The patterns and dynamics of genomic instability in metastatic pancreatic cancer. Nature *467*, 1109–1113.

Collado, M., Gil, J., Efeyan, A., Guerra, C., Schuhmacher, A.J., Barradas, M., Benguría, A., Zaballos, A., Flores, J.M., Barbacid, M., et al. (2005). Tumour biology: senescence in premalignant tumours. Nature *436*, 642.

Cook, N., Frese, K.K., Bapiro, T.E., Jacobetz, M.A., Gopinathan, A., Miller, J.L., Rao, S.S., Demuth, T., Howat, W.J., Jodrell, D.I., and Tuveson, D.A. (2012). Gamma secretase inhibition promotes hypoxic necrosis in mouse pancreatic ductal adenocarcinoma. J. Exp. Med. *209*, 437–444.

Corcoran, R.B., Contino, G., Deshpande, V., Tzatsos, A., Conrad, C., Benes, C.H., Levy, D.E., Settleman, J., Engelman, J.A., and Bardeesy, N. (2011). STAT3 plays a critical role in KRAS-induced pancreatic tumorigenesis. Cancer Res. *71*, 5020–5029.

Durkin, A.J., Osborne, D.A., Yeatman, T.J., Rosemurgy, A.S., Armstrong, C., and Zervos, E.E. (2006). EGF receptor antagonism improves survival in a murine model of pancreatic adenocarcinoma. J. Surg. Res. *135*, 195–201.

Frese, K.K., Neesse, A., Cook, N., Bapiro, T.E., Lolkema, M.P., Jodrell, D.I., Tuveson, D.A., and Tuveson, D.A. (2012). nab-Paclitaxel potentiates gemcitabine activity by reducing cytidine deaminase levels in a mouse model of pancreatic cancer. Cancer Discov. *2*, 260–269.

Fukuda, A., Wang, S.C., Morris, J.P., 4th, Folias, A.E., Liou, A., Kim, G.E., Akira, S., Boucher, K.M., Firpo, M.A., Mulvihill, S.J., and Hebrok, M. (2011). Stat3 and MMP7 contribute to pancreatic ductal adenocarcinoma initiation and progression. Cancer Cell *19*, 441–455.

Guerra, C., Mijimolle, N., Dhawahir, A., Dubus, P., Barradas, M., Serrano, M., Campuzano, V., and Barbacid, M. (2003). Tumor induction by an endogenous K-ras oncogene is highly dependent on cellular context. Cancer Cell *4*, 111–120.

Guerra, C., Schuhmacher, A.J., Cañamero, M., Grippo, P.J., Verdaguer, L., Pérez-Gallego, L., Dubus, P., Sandgren, E.P., and Barbacid, M. (2007). Chronic pancreatitis is essential for induction of pancreatic ductal adenocarcinoma by K-Ras oncogenes in adult mice. Cancer Cell *11*, 291–302.

Guerra, C., Collado, M., Navas, C., Schuhmacher, A.J., Hernández-Porras, I., Cañamero, M., Rodriguez-Justo, M., Serrano, M., and Barbacid, M. (2011). Pancreatitis-induced inflammation contributes to pancreatic cancer by inhibiting oncogene-induced senescence. Cancer Cell *19*, 728–739.

Hidalgo, M. (2010). Pancreatic cancer. N. Engl. J. Med. *362*, 1605–1617.

Hingorani, S.R., Wang, L., Multani, A.S., Combs, C., Deramaudt, T.B., Hruban, R.H., Rustgi, A.K., Chang, S., and Tuveson, D.A. (2005). Trp53R172H and KrasG12D cooperate to promote chromosomal instability and widely metastatic pancreatic ductal adenocarcinoma in mice. Cancer Cell *7*, 469–483.

Hong, S.-M., Park, J.Y., Hruban, R.H., and Goggins, M. (2011). Molecular signatures of pancreatic cancer. Arch. Pathol. Lab. Med. *135*, 716–727.

Jacobetz, M.A., Chan, D.S., Neesse, A., Bapiro, T.E., Cook, N., Frese, K.K., Feig, C., Nakagawa, T., Caldwell, M.E., Zecchini, H.I., et al. (2012). Hyaluronan impairs vascular function and drug delivery in a mouse model of pancreatic cancer. Gut. http://dx.doi.org/10.1136/gutjnl-2012-302529, August 7, 2012.

Jones, S., Zhang, X., Parsons, D.W., Lin, J.C., Leary, R.J., Angenendt, P., Mankoo, P., Carter, H., Kamiyama, H., Jimeno, A., et al. (2008). Core signaling pathways in human pancreatic cancers revealed by global genomic analyses. Science *321*, 1801–1806.

Kanda, M., Matthaei, H., Wu, J., Hong, S.M., Yu, J., Borges, M., Hruban, R.H., Maitra, A., Kinzler, K., Vogelstein, B., and Goggins, M. (2012). Presence of somatic mutations in most early-stage pancreatic intraepithelial neoplasia. Gastroenterology *142*, 730–733, e9.

Karapetis, C.S., Khambata-Ford, S., Jonker, D.J., O'Callaghan, C.J., Tu, D., Tebbutt, N.C., Simes, R.J., Chalchal, H., Shapiro, J.D., Robitaille, S., et al. (2008). K-ras mutations and benefit from cetuximab in advanced colorectal cancer. N. Engl. J. Med. *359*, 1757–1765.

Korc, M., Friess, H., Yamanaka, Y., Kobrin, M.S., Buchler, M., and Beger, H.G. (1994). Chronic pancreatitis is associated with increased concentrations of epidermal growth factor receptor, transforming growth factor alpha, and phospholipase C gamma. Gut *35*, 1468–1473.

Lesina, M., Kurkowski, M.U., Ludes, K., Rose-John, S., Treiber, M., Klöppel, G., Yoshimura, A., Reindl, W., Sipos, B., Akira, S., et al. (2011). Stat3/Socs3 activation by IL-6 transsignaling promotes progression of pancreatic intraepithelial neoplasia and development of pancreatic cancer. Cancer Cell *19*, 456–469.

Li, D., Xie, K., Wolff, R., and Abbruzzese, J.L. (2004). Pancreatic cancer. Lancet *363*, 1049–1057.

Maitra, A., and Hruban, R.H. (2008). Pancreatic cancer. Annu. Rev. Pathol. *3*, 157–188.

Martínez González, S., Hernández, A.I., Varela, C., Lorenzo, M., Ramos-Lima, F., Cendón, E., Cebrián, D., Aguirre, E., Gomez-Casero, E., Albarrán, M.I., et al. (2012). Rapid identification of ETP-46992, orally bioavailable PI3K inhibitor, selective versus mTOR. Bioorg. Med. Chem. Lett. *22*, 5208–5214.

Means, A.L., Meszoely, I.M., Suzuki, K., Miyamoto, Y., Rustgi, A.K., Coffey, R.J., Jr., Wright, C.V., Stoffers, D.A., and Leach, S.D. (2005). Pancreatic epithelial plasticity mediated by acinar cell transdifferentiation and generation of nestin-positive intermediates. Development *132*, 3767–3776.

Mohammed, A., Janakiram, N.B., Li, Q., Madka, V., Ely, M., Lightfoot, S., Crawford, H., Steele, V.E., and Rao, C.V. (2010). The epidermal growth factor receptor inhibitor gefitinib prevents the progression of pancreatic lesions to carcinoma in a conditional LSL-KrasG12D/+ transgenic mouse model. Cancer Prev. Res. (Phila.) *3*, 1417–1426.

Moore, M.J., Goldstein, D., Hamm, J., Figer, A., Hecht, J.R., Gallinger, S., Au, H.J., Murawa, P., Walde, D., Wolff, R.A., et al; National Cancer Institute of Canada Clinical Trials Group. (2007). Erlotinib plus gemcitabine compared with gemcitabine alone in patients with advanced pancreatic cancer: a phase III trial of the National Cancer Institute of Canada Clinical Trials Group. J. Clin. Oncol. *25*, 1960–1966.

Ng, S.S., Tsao, M.S., Nicklee, T., and Hedley, D.W. (2002). Effects of the epidermal growth factor receptor inhibitor OSI-774, Tarceva, on downstream signaling pathways and apoptosis in human pancreatic adenocarcinoma. Mol. Cancer Ther. *1*, 777–783.

Olive, K.P., Jacobetz, M.A., Davidson, C.J., Gopinathan, A., McIntyre, D., Honess, D., Madhu, B., Goldgraben, M.A., Caldwell, M.E., Allard, D., et al. (2009). Inhibition of Hedgehog signaling enhances delivery of chemotherapy in a mouse model of pancreatic cancer. Science *324*, 1457–1461.

Oliveira-Cunha, M., Hadfield, K.D., Siriwardena, A.K., and Newman, W. (2012). EGFR and KRAS mutational analysis and their correlation to survival in pancreatic and periampullary cancer. Pancreas *41*, 428–434.

Parsa, I., Longnecker, D.S., Scarpelli, D.G., Pour, P., Reddy, J.K., and Lefkowitz, M. (1985). Ductal metaplasia of human exocrine pancreas and its association with carcinoma. Cancer Res. *45*, 1285–1290.

Plentz, R., Park, J.S., Rhim, A.D., Abravanel, D., Hezel, A.F., Sharma, S.V., Gurumurthy, S., Deshpande, V., Kenific, C., Settleman, J., et al. (2009). Inhibition of gamma-secretase activity inhibits tumor progression in a mouse model of pancreatic ductal adenocarcinoma. Gastroenterology *136*, 1741–1749.

Provenzano, P.P., Cuevas, C., Chang, A.E., Goel, V.K., Von Hoff, D.D., and Hingorani, S.R. (2012). Enzymatic targeting of the stroma ablates physical barriers to treatment of pancreatic ductal adenocarcinoma. Cancer Cell *21*, 418–429.

Puyol, M., Martín, A., Dubus, P., Mulero, F., Pizcueta, P., Khan, G., Guerra, C., Santamaría, D., and Barbacid, M. (2010). A synthetic lethal interaction between K-Ras oncogenes and Cdk4 unveils a therapeutic strategy for non-small cell lung carcinoma. Cancer Cell *18*, 63–73.

Shigematsu, H., Lin, L., Takahashi, T., Nomura, M., Suzuki, M., Wistuba, I.I., Fong, K.M., Lee, H., Toyooka, S., Shimizu, N., et al. (2005). Clinical and biological features associated with epidermal growth factor receptor gene mutations in lung cancers. J. Natl. Cancer Inst. *97*, 339–346.

Siveke, J.T., Einwächter, H., Sipos, B., Lubeseder-Martellato, C., Klöppel, G., and Schmid, R.M. (2007). Concomitant pancreatic activation of Kras(G12D) and TGFA results in cystic papillary neoplasms reminiscent of human IPMN. Cancer Cell *12*, 266–279.

Ueda, S., Ogata, S., Tsuda, H., Kawarabayashi, N., Kimura, M., Sugiura, Y., Tamai, S., Matsubara, O., Hatsuse, K., and Mochizuki, H. (2004). The correlation between cytoplasmic overexpression of epidermal growth factor receptor

and tumor aggressiveness: poor prognosis in patients with pancreatic ductal adenocarcinoma. Pancreas *29*, e1–e8.

Vincent, A., Herman, J., Schulick, R., Hruban, R.H., and Goggins, M. (2011). Pancreatic cancer. Lancet *378*, 607–620.

Vogt, P.K., and Hart, J.R. (2011). PI3K and STAT3: a new alliance. Cancer Discov. *1*, 481–486.

Von Hoff, D.D., Ramanathan, R.K., Borad, M.J., Laheru, D.A., Smith, L.S., Wood, T.E., Korn, R.L., Desai, N., Trieu, V., Iglesias, J.L., et al. (2011). Gemcitabine plus nab-paclitaxel is an active regimen in patients with advanced pancreatic cancer: a phase I/II trial. J. Clin. Oncol. *29*, 4548–4554.

Yarden, Y., and Sliwkowski, M.X. (2001). Untangling the ErbB signalling network. Nat. Rev. Mol. Cell Biol. *2*, 127–137.

Cancer Cell
Article

A "*Twist box*" Code of p53 Inactivation: *Twist box*:p53 Interaction Promotes p53 Degradation

Sara Piccinin,[1,5,*] Elena Tonin,[1,5] Sara Sessa,[1] Silvia Demontis,[1] Sabrina Rossi,[2] Lorenza Pecciarini,[3] Lucia Zanatta,[2] Flavia Pivetta,[1] Alessandra Grizzo,[1] Maura Sonego,[1] Camillo Rosano,[4] Angelo Paolo Dei Tos,[2] Claudio Doglioni,[3] and Roberta Maestro[1,*]

[1]Experimental Oncology 1, CRO National Cancer Institute, Aviano 33081, Italy
[2]Department of Pathology, Treviso General Hospital, Treviso 31100, Italy
[3]Department of Pathology, San Raffaele Scientific Institute, Milano 20132, Italy
[4]Nanotechnology Unit, IST National Cancer Institute, Genova 16132, Italy
[5]These authors contributed equally to the work
*Correspondence: spiccinin@cro.it (S.P.), maestro@cro.it (R.M.)
http://dx.doi.org/10.1016/j.ccr.2012.08.003

SUMMARY

Twist proteins have been shown to contribute to cancer development and progression by impinging on different regulatory pathways, but their mechanism of action is poorly defined. By investigating the role of Twist in sarcomas, we found that Twist1 acts as a mechanism alternative to *TP53* mutation and MDM2 overexpression to inactivate p53 in mesenchymal tumors. We provide evidence that Twist1 binds p53 C terminus through the *Twist box*. This interaction hinders key posttranslational modifications of p53 and facilitates its MDM2-mediated degradation. Our study suggests the existence of a *Twist box* code of p53 inactivation and provides the proof of principle that targeting the *Twist box*:p53 interaction might offer additional avenues for cancer treatment.

INTRODUCTION

Twist1 and Twist2 (collectively hereafter referred as "Twist") are closely related members of a family of bHLH transcription factors involved in gastrulation and mesoderm specification. Typically, Twist proteins regulate the expression of target genes by binding, as homo- or heterodimers, to E-box-containing promoters. Consistent with the role in tissue specification, the expression of *Twist1* in mouse embryo follows mesoderm induction and becomes negligible in adult mesenchymal tissues, except a population of quiescent mesodermal stem cells. *Twist2* is also involved in mesoderm development, but its activation occurs later than *Twist1* and is essentially restricted to the dermis (Barnes and Firulli, 2009; Castanon and Baylies, 2002; Qin et al., 2012; Tukel et al., 2010).

Twist proteins were first associated with cancer on the basis of their ability to promote the bypass of cellular safeguard programs. Both genes were isolated through a genetic screen for cDNAs capable of overriding Myc-induced apoptosis, and Twist1 was found to be overexpressed in rhabdomyosarcomas, where it was suggested to support oncogenic transformation and to inhibit myogenic differentiation (Maestro et al., 1999). Subsequently, de novo Twist1 activation was reported in several types of cancer including neuroblastomas (Valsesia-Wittmann et al., 2004) and carcinomas, where it was shown to contribute to metastatic progression through the induction of epithelial-mesenchymal transition (EMT) (Karreth and Tuveson, 2004; Yang et al., 2004). A role for Twist proteins in stemness has also recently emerged (Cakouros et al., 2010; Vesuna et al., 2009).

Significance

Although sarcomas are relatively rare tumors, their aggressive behavior, resistance to therapies, and often early-age onset make them one of the most challenging types of cancer. Intriguingly, despite clear evidence of attenuation of the p53 response, a large fraction of sarcomas retain wild-type *TP53*, indicating that mechanisms different from mutations account for p53 inactivation in these tumors. Here, we provide evidence that Twist1-induced destabilization of p53 represents an important strategy of attenuation of the p53 response in sarcomas. We show that Twist1 accumulates mostly in tumors that retain wild-type *TP53*. Moreover, we show that, by establishing direct interaction, Twist1 hinders key phosphorylations of p53 and facilitates its degradation. Thus, targeting the Twist1:p53 interaction might offer additional avenues for cancer treatment.

The different consequences of constitutive Twist expression suggest that these transcription factors may contribute to tumorigenesis and neoplastic progression through different routes. In particular, Twist1 has been demonstrated to bind the E-cadherin promoter to suppress its transcription, thus facilitating EMT and metastatic spreading of epithelial tumors (Karreth and Tuveson, 2004; Yang et al., 2004). Twist proteins have also been shown to suppress the transcription of p19ARF, thus attenuating oncogene-induced p53 response, and p16INK4a, thus allowing cancer cells to escape Rb-mediated cell cycle control (Ansieau et al., 2008; Feng et al., 2009; Kwok et al., 2007; Lee and Bar-Sagi, 2010; Li et al., 2009; Maestro et al., 1999; Shiota et al., 2008; Stasinopoulos et al., 2005; Valsesia-Wittmann et al., 2004; Vichalkovski et al., 2010). Moreover, Twist mediates mesenchymal stem cell self-renewal, and Twist1-induced EMT requires BMI1, thus linking EMT and stemness (Isenmann et al., 2009; Yang et al., 2010). Finally, it has been proposed that EMT and bypass of safeguard programs might represent two sides of the same coin (Ansieau et al., 2008). Overall, the emerging picture is that Twist proteins play important roles in cancer, but the fact that they intersect multiple different pathways makes it hard to dissect the mechanisms of action as EMT/metastasis factors and as primary oncogenic drivers.

Sarcomas represent a heterogeneous group of mesenchymal tumors that account for about 5% of adult and 10% of pediatric neoplasias. Sarcomas include over 60 histopathological categories and are broadly classified into two cytogenetic groups, complex and simple karyotype, and these latter are often characterized by reciprocal translocations or targeted amplifications (Borden et al., 2003; Fletcher et al., 2002; Helman and Meltzer, 2003). A large fraction of localized sarcomas, especially the simple karyotype ones, retain wild-type *TP53* but their p53 response is attenuated. Thus, other, still elusive, mechanisms are likely responsible for p53 inactivation in these tumors.

We reasoned that, being mesenchymal in nature, sarcomas offer the opportunity to discern the functions of Twist related to the induction of EMT, typically occurring in carcinomas, from those more specifically related to the interference with tumor-suppressive pathways. Thus, in the attempt to provide a better understanding on how Twist contribute to tumorigenesis, we sought to investigate the role of Twist in antagonizing p53, focusing on sarcomas as a tumor model.

RESULTS

Twist1 Is Overexpressed and Undergoes Copy-Number Gain in Sarcomas

To assess the oncogenic role of Twist in the context of mesenchymal tumors, 146 sarcomas and adjacent normal tissues were investigated by immunohistochemistry (IHC). With the exception of dermal fibroblasts, where scattered nuclear reactivity was observed, normal adult mesenchymal tissues were essentially negative for Twist1. In contrast, a strong and diffuse nuclear accumulation of Twist1 was observed in over 60% of soft-tissue sarcomas of different subtypes (Figure 1A; see Table S1 available online). Overexpression of Twist2 was uncommon in sarcomas (6/84 cases) and sarcoma cell lines (Figure S1A). Fluorescence in situ hybridization (FISH) analyses with a probe encompassing the *TWIST1* locus revealed that, in 9 of 19 (47%) Twist1 IHC$^+$ frozen samples, Twist1 accumulation was associated with *TWIST1* copy-number gain (Figure 1B; Table S2).

In light of the role of Twist1 in EMT, we then compared Twist1 expression pattern in sarcomas and carcinomas. In contrast to the widespread and robust accumulation detected in sarcomas, a weak-moderate nuclear expression of Twist1 was observed in 10%–30% of breast, colorectal, prostate, and lung carcinomas, often confined to the invasion front (Figure 1A; Table S3).

Twist1 Overexpression Serves as an Alternative Mechanism of p53 Inactivation during Sarcomagenesis

Because mutations of *TP53* are rare in sarcomas and Twist1 has been suggested to attenuate the p53 pathway (Ansieau et al., 2008; Feng et al., 2009; Kwok et al., 2007; Lee and Bar-Sagi, 2010; Li et al., 2009; Maestro et al., 1999; Shiota et al., 2008; Stasinopoulos et al., 2005; Valsesia-Wittmann et al., 2004; Vichalkovski et al., 2010), we asked whether the overexpression of Twist1 could account for p53 inactivation in sarcomas retaining wild-type *TP53*. We first focused on leiomyosarcomas (LMS), a sarcoma subtype that has one of the highest frequencies of *TP53* mutations (Dei Tos et al., 1996; Hall et al., 1997). In particular, we analyzed localized/nonmetastatic tumors because sarcomas may acquire p53 mutations that contribute to tumor aggressiveness during progression (Cordon-Cardo et al., 1994). Among the 35 LMS analyzed, overexpression (>25% positive cells) of p53, Twist1, Twist2, and MDM2 were found in 14, 15, three, and four cases, respectively (Table S4). *TP53* missense mutations were found in eight cases (Figure 1C), all displaying strong nuclear accumulation of p53; no mutation was detected in samples that were negative or with focal/patchy p53 immunostaining. Fourteen of 15 Twist1$^+$ cases retained wild-type *TP53*, the only exception being a case that was also positive for MDM2. Thus, although not reaching the conventional 5% level of statistical significance, probably in part because of the small sample size of these clinically rare tumors, the clustering of Twist1-positivity among p53 wild-type LMS suggests that overexpression of Twist1 may serve as a mechanism alternative to *TP53* mutations to inactivate the p53 response in these tumors. To corroborate the role of Twist1 in inhibiting p53, we then focused on liposarcomas (LS), which include well-differentiated (WD) and dedifferentiated (DD) LS, and myxoid/round cell (myxoid) LS. These LS display a simple karyotype and often retain the wild-type *TP53*. WD and the more aggressive DD LS, which are considered the same entity at different malignant stages, typically carry the amplification of the chromosome region harboring the *MDM2* locus (Fletcher et al., 2002), and their p53 is inactivated as a result of enhanced MDM2-mediated degradation. In contrast, the mechanism of inactivation of p53 in myxoid LS, which are negative for MDM2, remains unclear (Coindre et al., 2010; Mentzel and Fletcher, 1995). In a series of 24 LS, all molecularly confirmed to be *TP53* wild-type, we observed an inverse correlation between Twist1 and MDM2 overexpression: Twist1 was robustly overexpressed in 13 of 14 MDM2$^-$ myxoid LS, whereas only 2 of 10 MDM2$^+$ WD and DD LS expressed Twist1 ($p = 0.00049$) (Figures 1A and 1C). Thus, Twist1 and MDM2 appear to be essentially mutually exclusive in LS, supporting the notion that Twist1 may inactivate p53 in mesenchymal tumors.

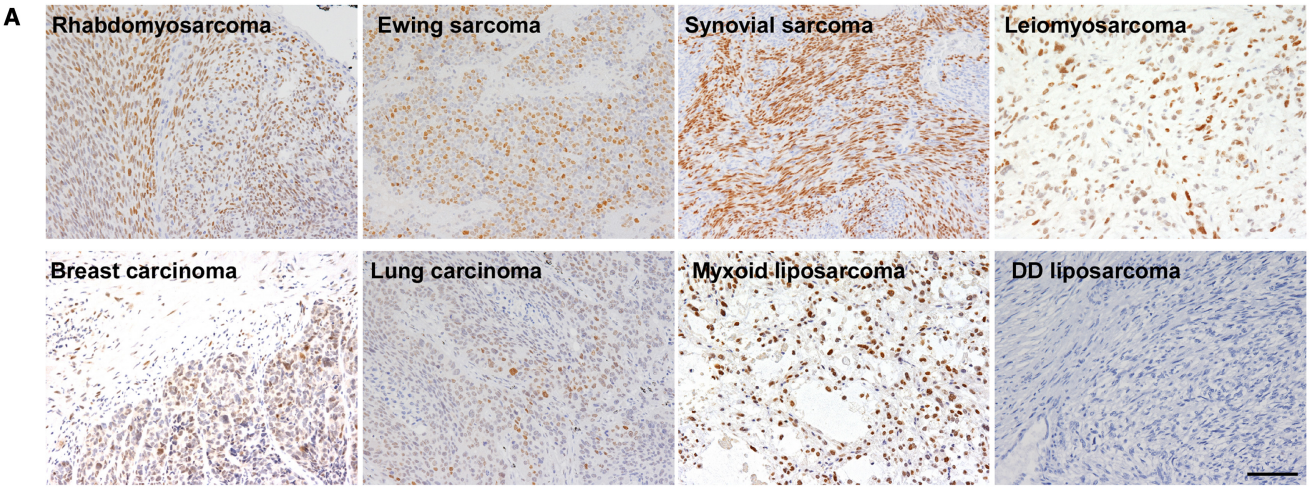

B

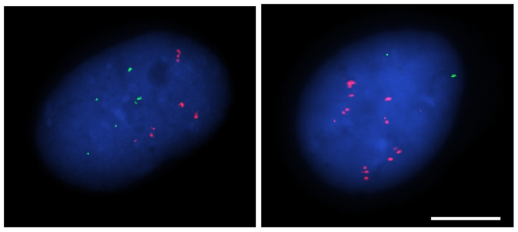

C

		Twist1$^+$	Twist1$^-$	Total	p
LMS	p53 mutated	1	7	8	
	p53 wild-type	14	13	27	
	Total	15	20	35	0.10090
LS	MDM2$^+$ (WD, DD LS)	2	8	10	
	MDM2$^-$ (Myxoid LS)	13	1	14	
	Total	15	9	24	0.00049

D

BJ cells	Oncogene combination	Nr tumors/ Nr injections
RE-vector	Ras + E1A + vector	0/10
RE-MDM2	Ras + E1A + MDM2	9/10
RE-shp53	Ras + E1A + shp53	3/4
RE-dnp53	Ras + E1A + dnp53	7/8
RE-Twist1	Ras + E1A + Twist1	5/8
RE-Twist2	Ras + E1A + Twist2	6/8

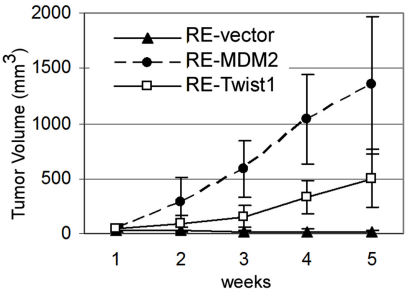

Figure 1. Twist1 Is Overexpressed in Human Sarcomas and Supports the Oncogenic Transformation of Primary Mesenchymal Cells

(A) Immunostaining for Twist1 in sarcomas and in carcinomas. Scale bar: 100 μm.

(B) FISH analysis of *TWIST1* in sarcomas overexpressing Twist1. *TWIST1* probe (RP11-960P19) is in red; chromosome 7 centromeric probe (Alpha-Satellite 7) in green. An example of copy-number gain involving the whole chromosome 7 (left panel) and of selective amplification of the *TWIST1* locus (right panel) are shown. Scale bar: 10 μm.

(C) Expression of Twist1 in LMS according to *TP53* mutation status (upper) and in LS according to MDM2 expression (lower). The p value was calculated according to the Fisher's exact test.

(D) Twist1 and Twist2 induce tumorigenic conversion of RE-BJ cells. The table indicates the number of tumors generated by each oncogenic combination in a set of injections. MDM2, a dominant-negative *TP53* allele (dnp53, R175H), and a shRNA targeting p53 (shp53) were used as positive controls. Representative images of RE-vector and RE-Twist1 xenografts are shown in the middle panel. Tumor size was measured weekly. The right panel shows the kinetics (average volume of tumors, ± SD) of representative tumors.

See also Figure S1 and Tables S1, S2, S3, and S4.

To functionally validate the role of Twist1 as an antagonist of p53 during sarcomagenesis, we then probed its ability to complement the transformation of human primary fibroblasts. We showed previously that BJ human fibroblasts upon expression of HRasV12 and E1A (RE-BJ) gain a transformed phenotype in culture but display negligible tumorigenic activity in xenograft assays. RE-BJ cells become tumorigenic following inactivation of the p53 pathway (Di Micco et al., 2006; Seger et al., 2002). We found that Twist-transduced RE-BJ also generated tumors when injected into immunocompromised mice, supporting that Twist proteins may actually sustain oncogene-induced transformation of cells of mesenchymal origin at least in part by antagonizing p53 (Figures 1D, S1C, and S1D).

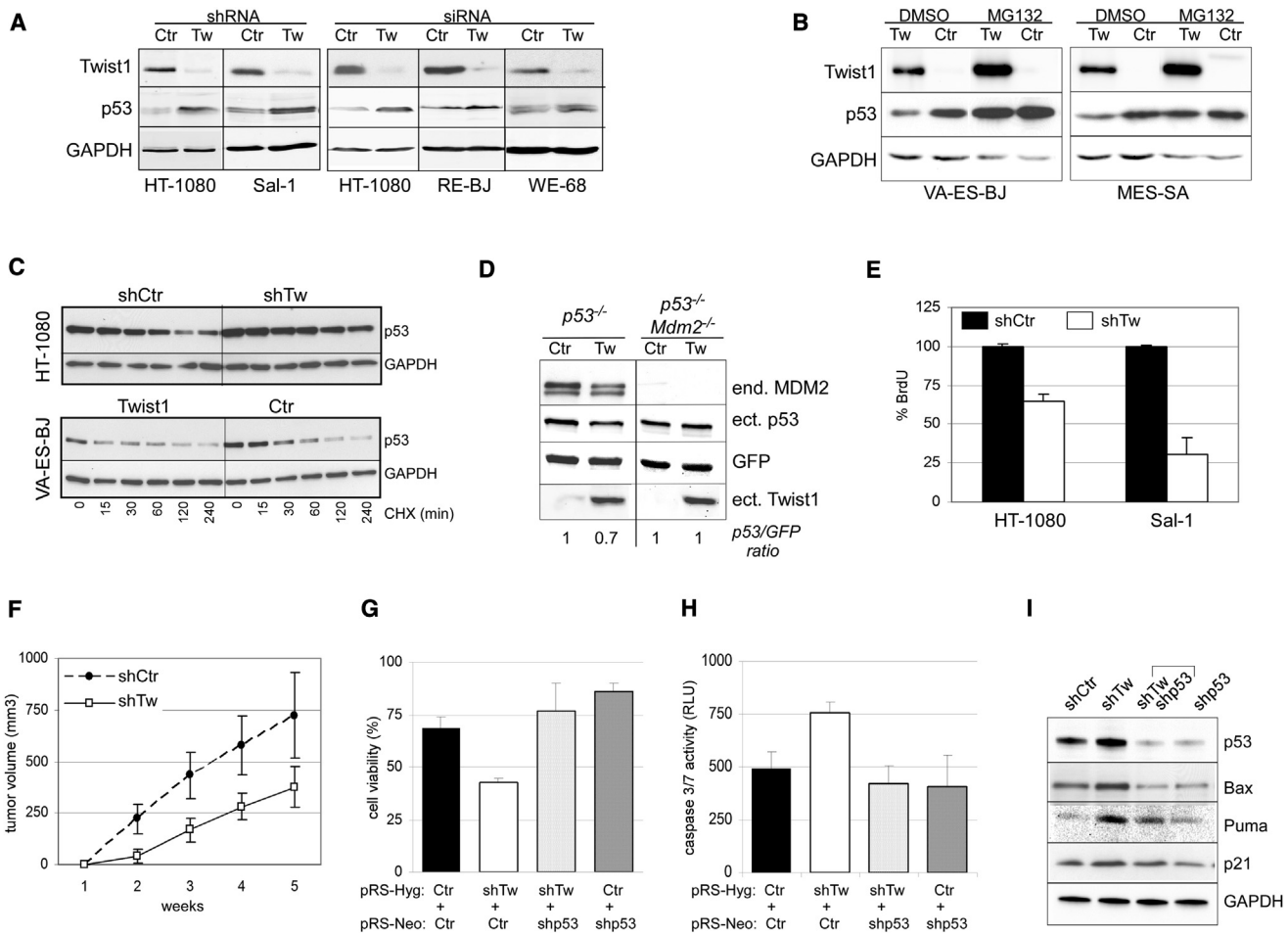

Figure 2. Modulation of Twist1 Expression Affects p53 Response and Tumorigenicity in Sarcoma Cells

(A) Immunoblot of cells silenced for endogenous Twist1 expression by either shRNA (left) or siRNA (right). As a control (Ctr), shLuc and nontargeting siRNA pool were used, respectively. Protein levels were normalized to GAPDH.

(B) Immunoblot of cells ectopically expressing either Twist1 (Tw) or GFP, as a control (Ctr). Cells were exposed to MG132 (10 μM) or vehicle (DMSO) for 4 hr, then harvested.

(C) Cycloheximide-chase assays (CHX, 100 μg/ml) in Twist1-silenced HT-1080 and in VA-ES-BJ engineered to express ectopic Twist1. shGFP (shCtr) and GFP (Ctr) were used as controls, respectively.

(D) Immunoblot of $p53^{-/-}$ and $p53^{-/-}$;$Mdm2^{-/-}$ MEF cotransfected with ectopic p53 (5 μg) and either myc-Twist1 (Tw) or empty control vector (Ctr) (15 μg). GFP (1 μg) was used as a control of transfection. p53 expression levels (ect. p53) were corrected for transfection efficiency (p53/GFP ratio). This result was confirmed on three independent experiments.

(E) BrdU incorporation assay in Twist1-silenced HT-1080 and Sal-1 cells. Histograms represent the mean plus SD.

(F) Xenograft growth of Twist1-silenced HT-1080 cells. Curves represent the average tumor volumes ± SD.

(G and H) HT-1080 cells were engineered to express combination of two shRNAs in pRS-Hyg and -Neo, as indicated. Controls (Ctr) were shGFP and shLuc. Cells were seeded overnight and then were shifted to serum-free medium. Cell viability (G) and caspase 3/7 activation (H) were assessed 48 hr after starvation. Histograms represent mean values plus SD.

(I) HT-1080 cells engineered and serum starved as in (G) and (H) were immunoblotted for the indicated proteins.

See also Figure S2.

Twist1 Enhances MDM2-Mediated Degradation of p53

We then assessed the effect of modulation of Twist expression in a series of human sarcoma cell lines expressing wild-type p53 (Figures S1A and S1B). Downregulation of the endogenous Twist1 by either stable expression of Twist1-specific shRNAs (Ansieau et al., 2008; Yang et al., 2004) or transient transfection of siRNAs stabilized p53 (Figure 2A). Conversely, ectopic Twist1 expression in $Twist1^{-}$ sarcoma cells reduced the p53 protein level, without affecting p53 transcription (data not shown). This downregulation was reversed by proteasome inhibition, suggesting that Twist1 promotes p53 proteasomal degradation (Figure 2B). Accordingly, cycloheximide (CHX)-chase assays indicated that the p53 half-life was increased from ~1 hr to ~3 hr in Twist1-silenced HT-1080 cells, whereas it was reduced from ~45 min to ~20 min in VA-ES-BJ expressing ectopic Twist1 (Figure 2C). Moreover, cotransfection of Twist1 together with p53 resulted in a slight but consistent reduction in p53 levels (~30%) in MDM2-proficient ($p53^{-/-}$) but not in MDM2-deficient

(*p53*$^{-/-}$; *Mdm2*$^{-/-}$) mouse embryo fibroblasts (MEF) null for endogenous p53 (Figure 2D), supporting a role for MDM2 in Twist1-induced downregulation of p53.

Silencing of Twist1 Activates a p53 Response in Sarcoma Cells

Under standard culture conditions, Twist1-depleted cells exhibited impaired cell growth compared to control cells, as revealed by longer doubling time (~1.3 and 1.9 times longer for HT-1080 and Sal-1, respectively; data not shown), decreased BrdU incorporation (Figure 2E), and reduced S-phase fraction (Figure S2A). Moreover, Twist1 knockdown was associated with induction of acidic β-galactosidase activity (SA-β-gal) (Figures S2B and S2C), suggesting spontaneous premature senescence, and with reduced tumorigenicity in xenograft models (Figures 2F and S2D). Twist1 depletion correlated also with enhanced sensitivity to serum starvation and UV radiation (Figures 2G, 2H, and S2C). This was paralleled by induction of p53 target genes (Figure 2I) and was rescued by silencing of p53 (Figures 2G–2I and S2E). No relevant perturbation in cell growth was observed following Twist1 silencing in sarcoma cells that were either homozygously deleted (SAOS-2) or mutated (SK-UT-1) for *TP53* or that overexpressed MDM2 (SJSA) (Figure S2A).

Twist1 antagonizes oncogene-induced apoptosis at least in part by interfering with the ARF/p53 pathway. However, a significant fraction of sarcomas and sarcoma-derived cell lines (including HT-1080, Sal-1, MES-SA, VA-ES-BJ, and WE68) are deficient for INK4a/ARF, and Twist1 can attenuate Myc-induced apoptosis in p53 wild-type/ARF null U2-OS cells (Figure S2F). This suggests that Twist1 impinges on p53 also independently of ARF.

Twist1-Mediated Antagonism of p53 Activity Does Not Require an Intact Basic Domain or Binding to p300/CBP

To shed light on the mechanisms of Twist-induced destabilization of p53, we characterized Twist1 domains required to antagonize the p53 response. Twist1 is known to regulate the transcription of several genes by binding their promoters through its basic DNA binding domain (Cakouros et al., 2010; Yang et al., 2010). We therefore investigated whether Twist1 modulated p53 response through a direct transcriptional mechanism. To this end, a series of Twist1 mutants defective for DNA binding (Spicer et al., 1996) (Figure 3A) were assayed for inhibition of p53-mediated transcription and apoptosis in E1A/Ras MEF (ER-MEF), which represent a well-defined setting of oncogene-induced/p53-dependent apoptosis (Lowe et al., 1993). In these cells, ectopic Twist expression attenuates p53-induced apoptosis (Maestro et al., 1999), whereas silencing of endogenous Twist1 results in enhanced stress sensitivity (Figures S3A–S3E). Despite loss of DNA binding activity, Twist1 basic domain mutants retained ability to protect ER-MEF from p53-mediated apoptosis (Figures 3B and S3F) and to repress a p53-responsive promoter (Figure S3G). More importantly, similar to full-length Twist1, the mutant carrying a deletion of the whole basic domain (Δb) was capable of converting nontumorigenic RE-BJ into tumorigenic cells (Figures 3C and S3H). Taken together, these data indicated that Twist1 could antagonize p53 and contribute to cancer development through an E-box-independent mechanism.

Twist1 has been hypothesized to interfere with p300/CBP-mediated activation of p53 (Ansieau et al., 2008; Hamamori et al., 1999; Shiota et al., 2008). To test this hypothesis, we generated a Twist1 mutant devoid of the major p300/CBP binding region (Δ30-60) (Figure 3A). The p300/CBP binding region overlaps Twist1 nuclear localization signal (NLS), and, therefore, the Δ30-60 mutant lost nuclear localization (Figure 3D). To circumvent this problem, an ectopic NLS (KRKK) was inserted at the N terminus (Δ30-60NLS). Despite impaired p300 binding, Twist1 Δ30-60NLS retained the power of repressing p53-mediated transcription (Figures S3G–S3I) and promoting cell survival (Figure 3D). This result demonstrates that the binding to p300/CBP is dispensable for Twist1-mediated inhibition of p53. Moreover, the fact that only the mutant expressed in the nucleus was capable of preventing p53-dependent apoptosis indicates that Twist1 requires nuclear localization to antagonize p53.

Twist and p53 Establish Tail-Tail Interaction that Involves the *Twist box* and p53 C-Terminal Regulatory Domain

It has been recently proposed that p53 may interact with the N terminus of Twist1 (Shiota et al., 2008). We then hypothesized that Twist1 could inhibit p53 response in sarcomas by directly targeting p53. Immunoprecipitation of endogenous Twist1 resulted in coprecipitation of endogenous p53 (Figure 4A), indicating that Twist1 does interact with p53 in sarcoma cells. The interaction is direct, as demonstrated by GST pull-down and coprecipitation assays using GST-Twist1 and His-p53 recombinant proteins (Figure 4B).

GST pull-down experiments confirmed the suggested weak interaction between p53 and the very N terminus of Twist1 (Figure S4A). However, we have shown that the deletion of this region does not affect the ability of Twist1 to antagonize p53-dependent transcription and apoptosis (Δ30-60NSL) (Figures 3D and S3G), ruling out a major biological relevance for this particular interaction. Instead, we found that p53 binds robustly to the C terminus of Twist1. In fact, both in vitro and in vivo (Figures S4A and S4B) coprecipitation experiments indicated that Twist1 engages a 20-aa stretch, corresponding to the highly conserved C-terminal region named *Twist box* (Bialek et al., 2004), to interact with p53 (Figure 4C).

The specificity of the binding was confirmed by GST pull-down using a *Twist box* peptide displayed from the active site loop of thioredoxin (T175-199), implying that this minimal region is both required and sufficient for p53 interaction. More importantly, *Twist box*-defective mutants were impaired in their ability to antagonize p53-depedent apoptosis (Figure 4D) and transcription (Figure S3G). This corroborates the relevance of the *Twist box* in the inhibition of p53. Intriguingly, this domain is conserved also in Twist2 and, in fact, Twist2 protected ER-MEF and bound p53 as efficiently as Twist1 (Figure 4D; Figure S4C).

Reciprocal mapping experiments revealed that p53 interacts with Twist through its C-terminal regulatory domain (aa 354–393) (p53CTD) (Figures 4E and S4D). These results were also corroborated by in silico prediction of protein:protein interaction. Docking simulation of human Twist1 and p53 models provided the best docking score for p53CTD and Twist1 *Twist box*, with

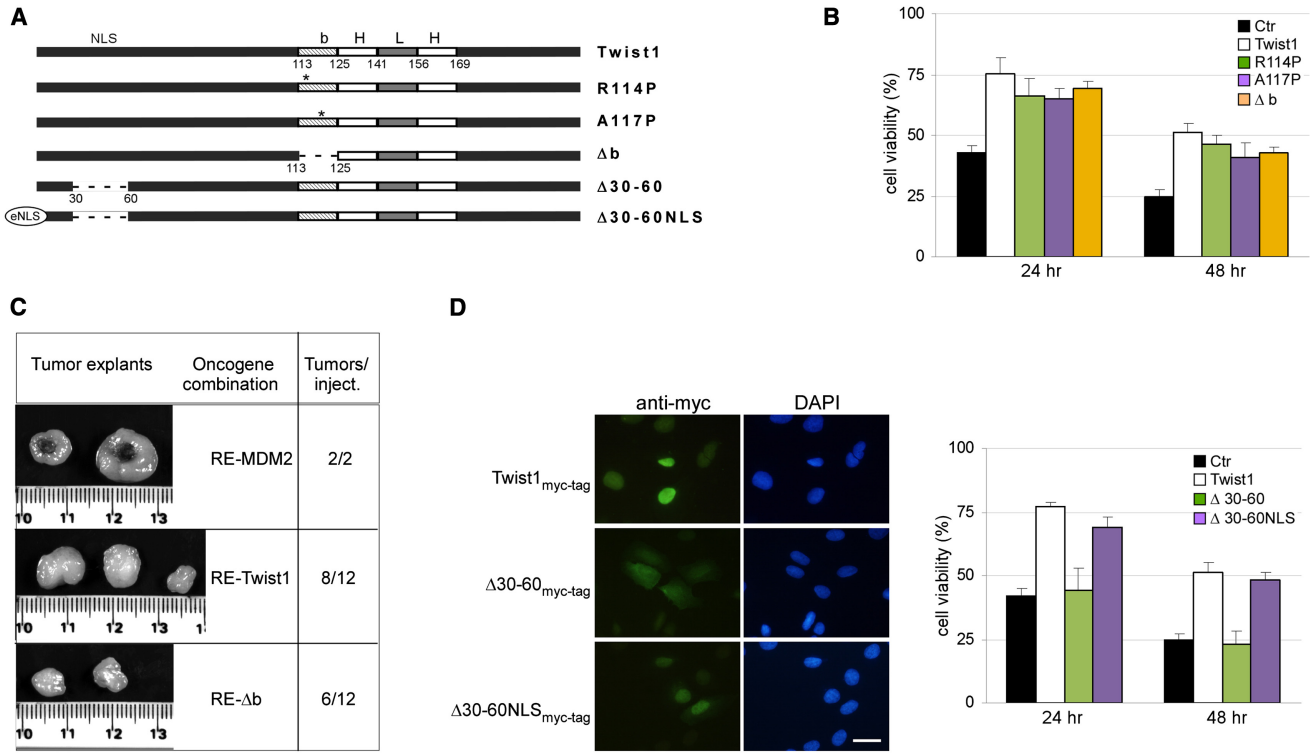

Figure 3. Twist1 Inhibits p53 also Independently of E-Box and p300/CBP Binding

(A) A schematic representation of the mouse Twist1 and various mutants. A114P and A117P carry a destabilizing proline into the basic domain (b); Δb is a whole basic-domain deletion mutant; NLS indicates Twist1 nuclear localization signal, bHLH the basic Helix-Loop-Helix domain; and eNLS denotes the ectopic nuclear localization signal.

(B) Cell viability of ER-MEF engineered as indicated after oncogene-mediated/p53-dependent apoptosis (0.1 μg/ml doxorubicin, 24 and 48 hr). Histograms indicate the mean percentage of treated/untreated cells, plus SD. Ctrl are control vector-infected cells.

(C) Representative tumor explants from RE-BJ cells engineered to express MDM2, Twist1, or Δb Twist1 (left). The number of tumors generated in a representative set of injections is reported on the right. Pictures were taken at week 5.

(D) Left: Immunofluorescence of ER-MEF engineered to express the indicated Twist1 myc-tag constructs. Nuclei are stained with DAPI. Scale bar: 50 μm. Right: Cell viability of ER-MEF engineered as indicated after apoptotic challenge (0.1 μg/ml doxorubicin, 24 and 48 hr). Histograms indicate the mean percentage of treated/untreated cells, plus SD.

See also Figure S3.

a predicted interface of the complex of 980 Å^2 and a highly significant lowest energy cluster population (187/500 individuals) (Figures 5A and 5B). In agreement with GST pull-down data, docking simulations ruled out a major role for other regions of p53 in the interaction with Twist1, including the p53 "core domain" (Cho et al., 1994) (lowest energy cluster: 55/500 individuals). The relevance of *Twist box* in Twist:p53 interaction was corroborated by the finding that single amino acid substitutions in the *Twist box* affected the binding in vitro to p53 (Figure 5C).

Twist1 Hinders p53 Phosphorylation at Ser392

Posttranslational modifications of C-terminal residues are involved in the regulation of p53 activity and stability (Xu, 2003). Intriguingly, in silico docking experiments indicated that one of the p53 residues involved in the interaction with Twist1 is the highly conserved Ser392 (Ser389 in mouse). In fact, in the Twist1:p53 complex, Ser392 is directly engaged in hydrogen bonds with Arg191 and Ala200 of Twist1 and is shielded by the Twist1 C terminus (Val189-His202) (Figures 5B and 5D).

Phosphorylation of Ser392 has been implicated in the regulation of p53 stability and activity (Cox and Meek, 2010; Hupp et al., 1992; Kapoor et al., 2000; Sakaguchi et al., 1997; Yap et al., 2004). Moreover, mice expressing a p53 mutant that cannot be phosphorylated at Ser389 (S389A) show impaired p53 response, with increased sensitivity to chemical and UV-induced carcinogenesis (Bruins et al., 2004; Hoogervorst et al., 2005).

We then hypothesized that Twist1 may affect p53 by directly inhibiting Ser392 phosphorylation. Indeed, we found that silencing of Twist1 was associated with a significant increase in the fraction of p53 phosphorylated at Ser392 (PSer392). Conversely, PSer392 was diminished in the cells engineered to express Twist1 or p53 binding-proficient Twist1 mutants but was unaffected in the cells expressing *Twist box*-deleted mutants (Figures 6A and S5A). Moreover, transient cotransfection experiments indicated that, under conditions where ectopic Twist1 efficiently promoted degradation and repressed transcriptional activity of wild-type p53, Twist1-mediated inhibition was impaired toward Ser392 mutants of p53 (Figures 6B

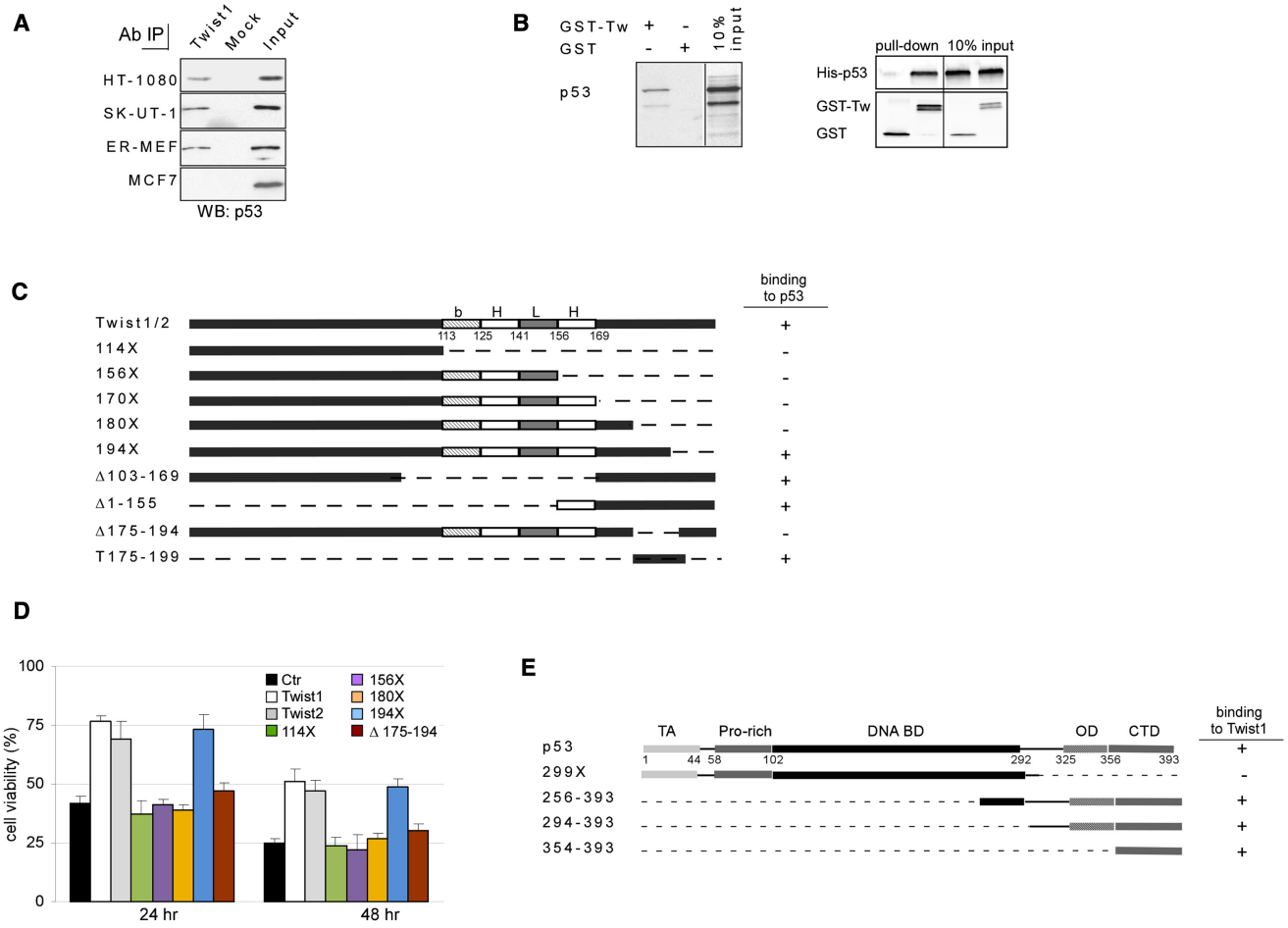

Figure 4. Twist1 and p53 Bind Directly through the C Termini

(A) Cells lysates from HT-1080, SK-UT-1, and ER-MEF were incubated with either Twist1 monoclonal antibody (Twist1) or nonimmune IgG (Mock), immunoprecipitated, and then blotted for coprecipitated p53 using anti-p53 antibodies. Twist1-negative MCF7 cells were used as a negative control. Input represents 10% of the whole cell lysate prior immunoprecipitation.

(B) Left panel: ^{35}S-labeled in vitro translated p53 (IVT-p53) was incubated with equivalent amounts of GST-Twist1 or GST, used as a negative control. Complexes were visualized by autoradiography. Right panel: recombinant His-p53 was incubated with equal amounts of glutathione agarose-bound GST or GST-Twist1. After SDS-PAGE, complexes were detected with anti-GST and anti-His antibodies.

(C) A schematic representation of the mouse Twist and various Twist1 mutants (left) and summary of their ability to interact with p53 based on GST pull-down experiments (right).

(D) Cell viability of ER-MEF engineered as indicated after apoptotic challenge (0.1 μg/ml doxorubicin, 24 hr and 48 hr). Histograms indicate the mean percentage viability plus SD.

(E) A schematic representation of human p53 and derivative mutants (left) and summary of their ability to interact with Twist1 based on GST pull-down experiments (right).

See also Figure S4.

and S5B). Finally, although it is still unclear what kinase phosphorylates Ser392 in vivo, casein kinase 2 (CK2) has been shown to target Ser392 in vitro (Cox and Meek, 2010), and we found that in vitro CK2-mediated phosphorylation at Ser392 was attenuated in the presence of recombinant Twist1 (Figure S5C).

Twist1 failed to significantly affect the acetylation of Lys373 and Lys382 of p53, two residues involved in p53 stabilization and included in the region of p53 engaged in the interaction with Twist1 (Figures S5D–S5F). Although we cannot rule out that Twist1 may alter other posttranscriptional modifications relevant for p53 activity and stability, our data indicate that Twist1 attenuates the p53 response at least in part by impinging on Ser392 phosphorylation. Intriguingly, different from Lys373 and Lys382 acetylation, Ser392 phosphorylation is triggered in response to oncogene activation, both in human (Figures S5D–S5F) and mouse fibroblasts (Figure S5G), and this correlates with p53 induction. In the same cells, oncogene-induced transformation was associated also with increased Twist1 levels (Figures S5G and S5H). This suggests that the activation of Twist1 may represent a mechanism elicited by oncogene-challenged cells to quench p53 response during transformation.

A

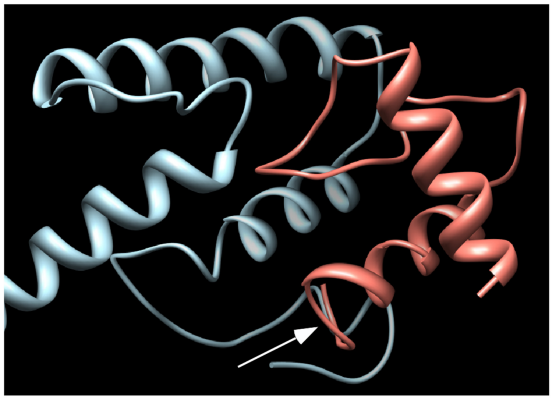

B

Human Twist1 residue and atom	Human p53 residue and atom	Distance (Å)
Ile134 O	Gly360 O	2.9
Tyr155 OH	Glu358 N	3.2
	Glu358 O	2.7
	Gly356 O	3.0
His180 NE2	Gly361 N	3.2
Arg182 NH1	Asp391 OD1	2.7
	Glu388 OE1	2.8
Arg182 NH2	Asp393 OD2	2.8
Arg191 NH1	Ser392 OG	2.8
	Asp391 OD1	2.8
	Ser392 N	3.1
Ala200 O	Ser392 N	2.9
His202 N	Asp391 OD2	3.2

C

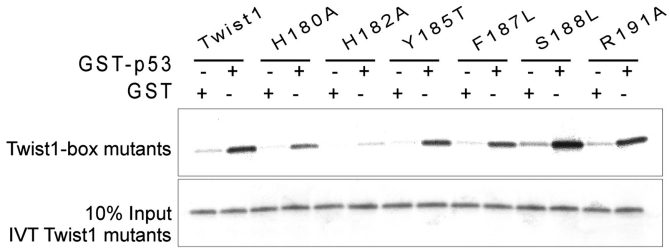

D

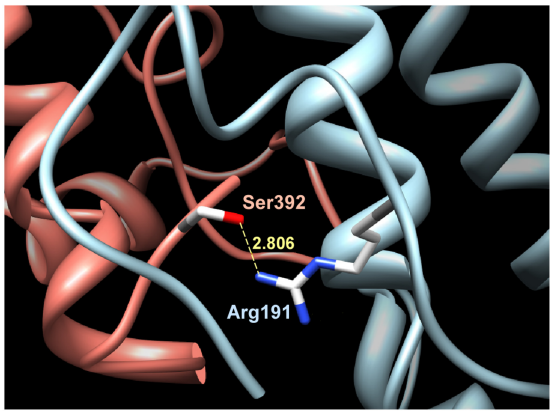

Figure 5. The *Twist box* Is Necessary for the Interaction with p53

(A) Ribbon representation of the interaction between p53 (red) and Twist1 (blue). The arrow indicates the *Twist box*:p53 interface.

(B) A summary of the residues of human Twist1 and human p53 involved in their binding, the functional groups of these residues involved in the interaction, and the distance (in Å) between the corresponding interacting functional groups as assessed by docking simulation. In mouse Twist1, the region involved in the binding spans Ile138-His206.

(C) GST or GST-p53 pull-downs of IVT-*Twist box* or IVT-*Twist box* carrying the indicated amino acid substitutions.

(D) Magnification of the ribbon representation of *Twist box* (blue):p53 CTD (red) interaction. The hydrogen bond formed between p53 Ser392 and Twist1 Arg191 and the distance between these two residues in Å are indicated in yellow.

Twist1 Facilitates p53 Degradation by Increasing the Affinity of p53 for MDM2

Modifications of p53CTD are known to modulate its susceptibility to MDM2-mediated degradation. We therefore sought to investigate the role of Ser392 in p53 degradation. CHX-chase experiments in SAOS-2 and *p53*$^{-/-}$ HCT116 cells engineered to stably express p53 mutants at codon 392 indicated that p53-S392E, a mutant mimicking constitutive phosphorylation at Ser392, displayed a longer half-life than did the p53-S392A phosphorylation-deficient mutant (Figure 6C). On a side note, we noticed that both Ser392 mutants were more tolerated compared to p53 WT, suggesting that Ser392 status affects both p53 turnover and tumor-suppressive activity. Moreover, the differential stability of Ser392 mutants was easier to appreciate if the constructs were expressed following stable retroviral infection instead of acute transfection, likely because of transfection-induced stress response.

Intriguingly, the amount of MDM2 coimmunoprecipitated with p53-S392E was significantly reduced (~50%) compared to the amount bound to the wild-type p53 and p53-S392A (Figure 6D). This suggests that phosphorylation of Ser392 makes p53 less prone to binding to MDM2, and hence to MDM2-driven degradation. In this scenario, by preventing Ser392 phosphorylation, Twist1 might affect p53:MDM2 association. In agreement with this hypothesis, we found that the increase in the overall levels of p53 detected in HT-1080 cells following Twist1 knockdown correlated with a slight but consistent decrease (~30%) in the amount of p53 complexed to MDM2 (Figures 6E and S5I).

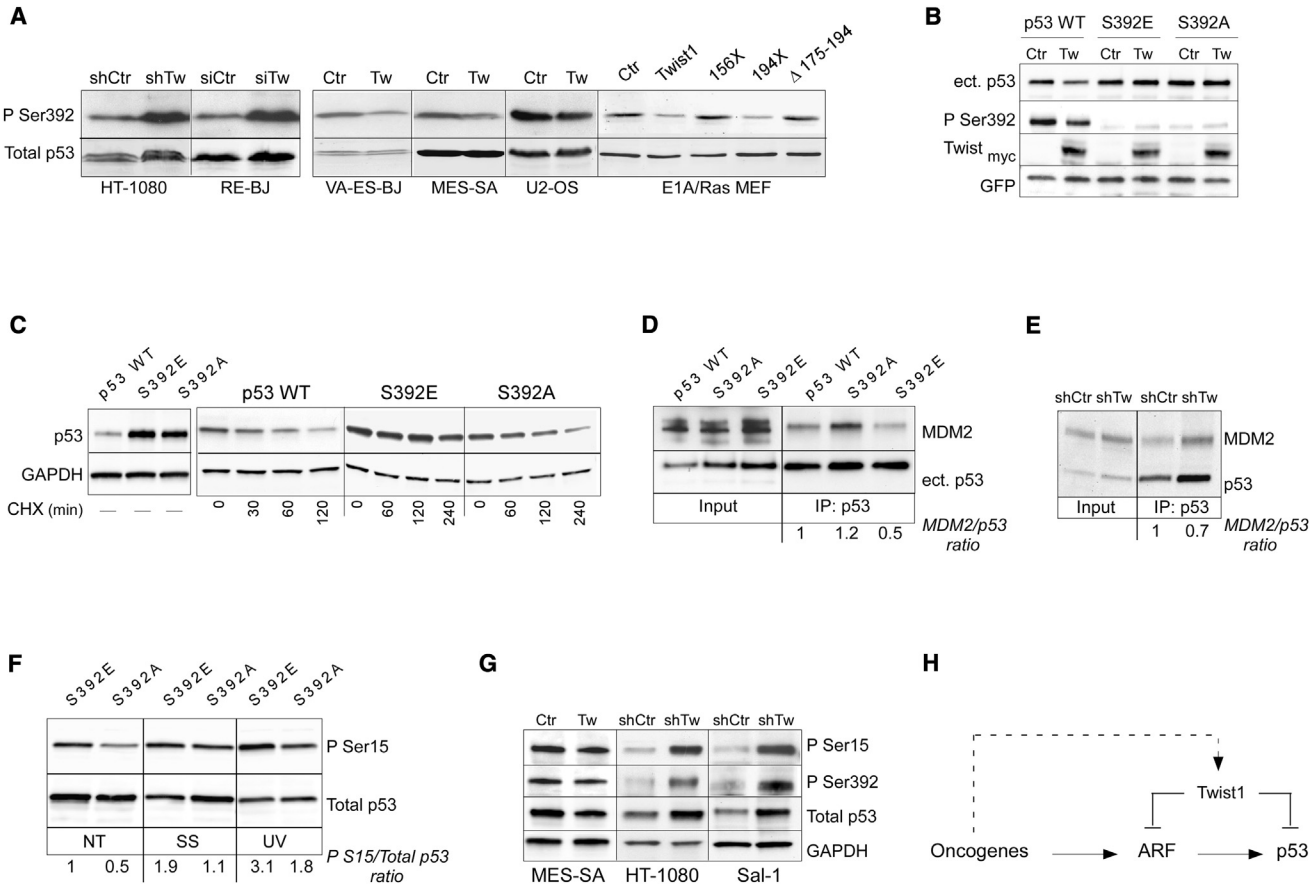

Figure 6. Twist1 Hinders Phosphorylation of p53 at Ser392 and Affects p53:MDM2 Interaction

(A) Immunoblot for p53 phosphorylated at Ser392 (P Ser392) of sarcoma cells silenced for Twist1 expression (left) or engineered to express ectopic Twist1 or Twist1 mutants (right). Because modulation of Twist1 expression affects p53 expression levels, to better appreciate the effect of Twist1 on Ser392 phosphorylation, samples were unevenly loaded to tentatively equalize the signals for total p53.

(B) Immunoblot of Twist1-negative *p53*$^{-/-}$ HCT116 transfected with wild-type p53 or p53 mutants (4 μg) as indicated together with either myc-Twist1 (Tw) or empty control vector (Ctr) (20 μg). GFP (1 μg) was included for normalization of transfection efficiency. This result was confirmed on three independent experiments.

(C) Cycloheximide-chase assays (CHX, 250 μg/ml) in SAOS-2 cells infected with retroviral vectors encoding p53 WT, p53 S392E (phospho-mimic), or p53 S392A (phospho-impaired).

(D) SAOS-2 engineered to express p53 WT, S392A, or S392E p53 were treated with MG132 (10 μM, 8 hr), then were immunoprecipitated for p53. Immunoblots were probed with anti-MDM2 and -p53 antibodies, and the amount of MDM2 coprecipitated was calculated as MDM2/p53 ratio. This result was confirmed in two independent experiments.

(E) Twist1-silenced (shTw) and control (shCtr) HT-1080 were treated with MG132 (10 μM, 8 hr), immunoprecipitated for endogenous p53, and then probed for MDM2 and p53. The amount of MDM2 bound to p53 was calculated as MDM2/p53 ratio. This experiment was done three times with two different p53 antibodies (DO-1 and CM5).

(F) Immunoblot of *p53*$^{-/-}$ HCT116 engineered to express either S392A or S392E p53, under standard conditions (NT), UV radiation (20 J/m^2) or serum starvation (30 hr).

(G) Immunoblots for p53 phosphorylation at Ser15 and Ser392 in sarcoma cells after modulation of Twist1 expression. GAPDH was used for normalization.

(H) Schematic representation of the proposed mechanisms of Twist1 contribution to oncogene-induced transformation and attenuation of p53 response.

See also Figure S5.

Thus, Twist1 seems to promote p53 degradation by maintaining p53 in an MDM2-accessible state.

It has been recently shown that, besides the canonical N-terminal region (Kussie et al., 1996; Lin et al., 1994), p53 binds MDM2 also with the CTD, and this interaction is hampered by p53CTD modifications (Poyurovsky et al., 2010). Thus, Twist1 could interfere with this alternative mechanism of MDM2-mediated degradation of p53. However, an interplay between Ser392 and Ser15 of p53 has been proposed (Kapoor et al., 2000), and phosphorylation at Ser15 is well known to inhibit MDM2 from binding N terminus p53 (Shieh et al., 1997). Therefore, we investigated a possible cross-talk between these two serines. We found that p53-S392E displayed a greater extent of phosphorylation at Ser15 than did p53-S392A (Figure 6F). Instead, constitutive phosphorylation at Ser15 (S15E) failed to affect the extent of phosphorylation at Ser392 (Figure S5J). This suggests a directional control of Ser15 phosphorylation by Ser392 status. Moreover, modulation of Twist1 expression in

sarcoma cells correlated with concordant variations in Ser392 and Ser15 phosphorylation (Figure 6G). Thus, besides interfering with the p53CTD:MDM2 interaction, Twist1 might indirectly affect also the canonical route of MDM2-mediated p53 degradation, suggesting the existence of multiple levels of controls of Twist1 over p53 (Figure 6H).

DISCUSSION

By investigating the role of Twist1 in the context of sarcomas, this study highlights an alternative mechanism of p53 inactivation and provides evidence that Twist1 promotes MDM2-mediated degradation of p53 by directly interacting with its C-terminal regulatory domain and by interfering with key phosphorylations.

We found that although Twist1 expression pattern in carcinomas is compatible with its proposed role in malignant progression, the diffuse and strong Twist1 accumulation observed in sarcomas suggests that Twist1 activation is an intrinsic component of the transformed phenotype of tumor cells of mesenchymal origin. This hypothesis is supported by the finding that, in these tumors, Twist1 accumulation often associates with *TWIST1* copy-number gain, a result that is in line with recent evidence that one of the most frequent copy-number variations in sarcomas involves the *TWIST1* locus (Menghi-Sartorio et al., 2001; Taylor et al., 2008).

In addition, we found that, in LS, Twist1 overexpression is mutually exclusive with MDM2 positivity. In LMS, Twist1 accumulation clustered among p53 wild-type tumors, although the correlation was not statistically significant. This may be in part due to the small sample size of these clinically rare tumors. On the other hand, although early studies suggested that *TP53* mutation and MDM2 overexpression were mutually exclusive, subsequent studies have demonstrated that this is not a general rule. Indeed, overexpression/amplification of MDM2 and *TP53* mutation can coexist in the same tumor, likely because both p53 and MDM2 are provided with functions independent of each other (Cordon-Cardo et al., 1994; Ito et al., 2011; Manfredi, 2010). Similarly, Twist1 is also provided with p53-independent functions that may play a role in sarcomagenesis (e.g., inhibition of differentiation) and might account for Twist1 and MDM2 coexpression observed in six LMS retaining wild-type *TP53.*

Most evidence linking Twist1 to cancer refers to the ability of Twist proteins to modulate the expression of target genes, including ARF, thus affecting p53. This study provides evidence that Twist1 affects p53 also through an E-box-independent mechanism. In fact, we found that Twist1 mutants defective for DNA binding retain the ability to interfere with the p53 response. This indicates that Twist1 may participate to tumorigenesis and promote the bypass of p53 failsafe programs apparently through molecular mechanisms different from those that facilitate EMT in carcinomas.

Intriguingly, we found that Twist1 establishes a direct interaction with p53 through the *Twist box* and that this interaction is critical for Twist1 inhibition of p53. The *Twist box* corresponds to a highly conserved 20-aa stretch at the C terminus of the protein. Through the *Twist box,* Twist binds to and inhibits RunX2 (Bialek et al., 2004), MEF2 (Spicer et al., 1996), ATF4 (Danciu et al., 2012), and RelA (Šošić et al., 2003). This suggests that the binding via *Twist box* is a leitmotif in the inhibition exerted by Twist on other transcription factors. Here, we demonstrate that Twist employs the *Twist box* to interact with the CTD regulatory domain of p53. By binding p53CTD, Twist1 hinders Ser392 phosphorylation, and this correlates with increased p53 sensitivity to degradation. Although Twist1 failed to significantly affect Lys373 and Lys382 acetylation, we cannot exclude that, by interacting with p53CTD, Twist1 may influence other modifications that affect p53 functions. Nevertheless, the fact that Ser392 is phosphorylated in response to oncogene activation and modulates p53 activity and stability corroborates the concept that Twist1 participates to sarcomagenesis at least in part by interfering with Ser392-mediated p53 activation.

How may *Twist box*:p53CTD interaction affect p53 response? Recently, Prives's group has demonstrated that, besides the canonical N terminus, p53 engages also the CTD region to bind MDM2, and this interaction is hampered by p53CTD posttranslational modifications (Poyurovsky et al., 2010). Although the authors addressed the effect of acetylation on p53CTD:MDM2 complex formation, they argued that other p53CTD modifications are likely to impinge on this interaction. By using Ser392 mutants, we collected data suggesting that Ser392 phosphorylation reduces p53 affinity to MDM2. Thus, by hindering Ser392 phosphorylation, Twist1 might favor p53CTD:MDM2 complex formation and hence p53 degradation. Yet we found that Ser392 status influences also the extent of phosphorylation at Ser15 that inhibits the interaction between N terminus p53 and MDM2. Then, by acting on Ser392, Twist1 might in turn impinge on Ser15, thus facilitating also the canonical route of MDM2-mediated degradation of p53.

Finally, in agreement with recent observations (Kogan-Sakin et al., 2011; Lee and Bar-Sagi, 2010), we found that oncogene-challenged human and mouse fibroblasts display increased levels of Twist1. This suggests a scenario where oncogenic transformation results in the induction of Twist1. In turn, Twist1 promotes the bypass of oncogene-induced p53 safeguard responses by both inhibiting the ARF/p53 signaling and by directly interacting with p53 and facilitating its degradation (Figure 6H).

In conclusion, this study sheds light on the mechanisms of Twist1-mediated inactivation of p53 and adds another important piece of information on the role of p53CTD in the regulation of p53 tumor-suppressive activity. Although focused on sarcomas, our study proposes a model that might also apply to other tumor histotypes and provides the proof of principle that targeting Twist1:p53 interaction may offer additional avenues for the treatment of tumors.

EXPERIMENTAL PROCEDURES

Immunohistochemistry and FISH

Primary sarcoma samples and corresponding normal tissues were retrieved from the Treviso General Hospital and the San Raffaele Institute tissue banks, where they were analyzed with patients' consent. Specimens were deidentified before analysis, and the study was approved by the IRB of CRO, Treviso General Hospital, and San Raffaele Institute. No patient had received radio- or chemotherapy prior to surgery. Immunohistochemistry was performed on 5-μm sections with the following antibodies: Twist1 (Twist2C1a, Santa Cruz), Twist 2 (ab6603, Abcam), p53 (DO-7, Labvision), and MDM2 (1F2, Oncogene Science). FISH was performed following standard protocols on 19 cases for which frozen material was available.

TP53 Mutation Analysis

Mutation analysis of *TP53* was performed by PCR direct-sequencing on genomic DNA extracted from paraffin-embedded tissue sections, as previously described (Dei Tos et al., 1997).

Cells, Constructs, and Protein Expression Analyses

Transfections, retroviral infections, and reporter assays were performed as previously described (Demontis et al., 2006). Acute silencing of Twist1 was achieved with ON-TARGETplus SMART pool siRNAs (Dharmacon), according to the manufacturer's instructions. Stable silencing of Twist1 was achieved by retroviral infection of previously published Twist1-specific shRNAs (Ansieau et al., 2008; Yang et al., 2004). shGFP and shLuciferase (shLuc) were used as negative controls. Protein lysates were separated by SDS-PAGE and were transferred onto nitrocellulose membrane (Protran, Whatman). Expression analyses were performed with Odyssey Infrared (Li-Cor Biosciences) and Chemidoc (BioRad) Imaging systems, using the antibodies indicated in Supplemental Experimental Procedures. Immunofluorescence and SA-β-gal staining were performed as previously described (Di Micco et al., 2006; Seger et al., 2002). GST pull-downs and in vitro CK2 assay were performed as described in Supplemental Experimental Procedures.

Apoptosis, BrdU Incorporation, and FACS Analyses

Cell viability was assessed by Trypan blue and Viacount assay (Guava PCA) and was calculated as mean percentage of cells that survived the apoptotic stress (100× viable treated cells/untreated cells). Experiments were done in triplicate on at least two different retroviral infections. Caspase 3/7 activation and BrdU incorporation were determined with the Apo-ONE Caspase-3/7 and the BrdU Kits (Promega). FACS analyses were done with the Cytomics FC 500 (Beckman Coulter).

In Vivo Tumorigenicity Assay

Experiments on animals were performed in accordance with national regulations and approved by the CRO animal ethics committee. RE-BJ cells (5×10^6) stably expressing MDM2, dnp53, shp53, or Twist were subcutaneously injected into each flank of six-week-old athymic nude mice (Hsd:Athymic nude-nu, Harlan) as previously described (Di Micco et al., 2006; Seger et al., 2002) For pRetroSuper-shLuc and pRetroSuper-shTwist HT-1080, 1×10^6 cells were used. Tumor size was monitored weekly. Mice were sacrificed at week 5. Tumor volume was calculated as $2r^3$.

Protein Modeling and Docking Simulations

Three-dimensional structure models of Twist1 and p53 were built using the web server SAM-T08 (Karplus, 2009) and further minimized by simulated annealing using the program CNS (Brünger et al., 1998). Docking calculations were carried out by the web server ClusPro 2.0 (Comeau et al., 2007).

Statistical Analysis

Data shown are means ± SD of at least three independent experiments. Comparisons of proportions were performed using two-tailed Fisher's exact test.

SUPPLEMENTAL INFORMATION

Supplemental Information includes five figures, four tables, and Supplemental Experimental Procedures and can be found with this article online at http://dx.doi.org/10.1016/j.ccr.2012.08.003.

ACKNOWLEDGMENTS

This work was supported by CRO, the Italian Association for Cancer Research (AIRC) (RM PI grant and MCO10016), the Italian Ministry of Health, and Regione Friuli Venezia-Giulia. We are grateful to M. Eilers, G. Hamilton, F. Van Valen, B. Vogelstein, D. Turner, A. Puisieux, A. Lassar, S. Lowe, G. Lozano, F. Perrin-Schmitt, and G. Del Sal for kindly providing reagents and A. Puisieux, G. Hannon, G. Del Sal, S. Romeo, S. Giordano, C. Brancolini, S. Soddu, J. Taylor, and OS1 personnel for support and suggestions. In particular, we thank V. Candotti and F. Sirocco for precious help in hectic moments.

Received: October 6, 2011
Revised: April 25, 2012
Accepted: August 4, 2012
Published: September 10, 2012

REFERENCES

Ansieau, S., Bastid, J., Doreau, A., Morel, A.P., Bouchet, B.P., Thomas, C., Fauvet, F., Puisieux, I., Doglioni, C., Piccinin, S., et al. (2008). Induction of EMT by twist proteins as a collateral effect of tumor-promoting inactivation of premature senescence. Cancer Cell *14*, 79–89.

Barnes, R.M., and Firulli, A.B. (2009). A twist of insight—the role of Twist-family bHLH factors in development. Int. J. Dev. Biol. *53*, 909–924.

Bialek, P., Kern, B., Yang, X., Schrock, M., Sosic, D., Hong, N., Wu, H., Yu, K., Ornitz, D.M., Olson, E.N., et al. (2004). A twist code determines the onset of osteoblast differentiation. Dev. Cell *6*, 423–435.

Borden, E.C., Baker, L.H., Bell, R.S., Bramwell, V., Demetri, G.D., Eisenberg, B.L., Fletcher, C.D., Fletcher, J.A., Ladanyi, M., Meltzer, P., et al. (2003). Soft tissue sarcomas of adults: state of the translational science. Clin. Cancer Res. *9*, 1941–1956.

Bruins, W., Zwart, E., Attardi, L.D., Iwakuma, T., Hoogervorst, E.M., Beems, R.B., Miranda, B., van Oostrom, C.T., van den Berg, J., van den Aardweg, G.J., et al. (2004). Increased sensitivity to UV radiation in mice with a p53 point mutation at Ser389. Mol. Cell. Biol. *24*, 8884–8894.

Brünger, A.T., Adams, P.D., Clore, G.M., DeLano, W.L., Gros, P., Grosse-Kunstleve, R.W., Jiang, J.S., Kuszewski, J., Nilges, M., Pannu, N.S., et al. (1998). Crystallography & NMR system: a new software suite for macromolecular structure determination. Acta Crystallogr. D Biol. Crystallogr. *54*, 905–921.

Cakouros, D., Raices, R.M., Gronthos, S., and Glackin, C.A. (2010). Twist-ing cell fate: mechanistic insights into the role of twist in lineage specification/differentiation and tumorigenesis. J. Cell. Biochem. *110*, 1288–1298.

Castanon, I., and Baylies, M.K. (2002). A Twist in fate: evolutionary comparison of Twist structure and function. Gene *287*, 11–22.

Cho, Y., Gorina, S., Jeffrey, P.D., and Pavletich, N.P. (1994). Crystal structure of a p53 tumor suppressor-DNA complex: understanding tumorigenic mutations. Science *265*, 346–355.

Coindre, J.M., Pédeutour, F., and Aurias, A. (2010). Well-differentiated and dedifferentiated liposarcomas. Virchows Arch. *456*, 167–179.

Comeau, S.R., Kozakov, D., Brenke, R., Shen, Y., Beglov, D., and Vajda, S. (2007). ClusPro: performance in CAPRI rounds 6-11 and the new server. Proteins *69*, 781–785.

Cordon-Cardo, C., Latres, E., Drobnjak, M., Oliva, M.R., Pollack, D., Woodruff, J.M., Marechal, V., Chen, J., Brennan, M.F., and Levine, A.J. (1994). Molecular abnormalities of mdm2 and p53 genes in adult soft tissue sarcomas. Cancer Res. *54*, 794–799.

Cox, M.L., and Meek, D.W. (2010). Phosphorylation of serine 392 in p53 is a common and integral event during p53 induction by diverse stimuli. Cell. Signal. *22*, 564–571.

Danciu, T.E., Li, Y., Koh, A., Xiao, G., McCauley, L.K., and Franceschi, R.T. (2012). The basic helix loop helix transcription factor Twist1 is a novel regulator of ATF4 in osteoblasts. J. Cell. Biochem. *113*, 70–79.

Dei Tos, A.P., Maestro, R., Doglioni, C., Piccinin, S., Libera, D.D., Boiocchi, M., and Fletcher, C.D. (1996). Tumor suppressor genes and related molecules in leiomyosarcoma. Am. J. Pathol. *148*, 1037–1045.

Dei Tos, A.P., Doglioni, C., Piccinin, S., Maestro, R., Mentzel, T., Barbareschi, M., Boiocchi, M., and Fletcher, C.D. (1997). Molecular abnormalities of the p53 pathway in dedifferentiated liposarcoma. J. Pathol. *181*, 8–13.

Demontis, S., Rigo, C., Piccinin, S., Mizzau, M., Sonego, M., Fabris, M., Brancolini, C., and Maestro, R. (2006). Twist is substrate for caspase cleavage and proteasome-mediated degradation. Cell Death Differ. *13*, 335–345.

Di Micco, R., Fumagalli, M., Cicalese, A., Piccinin, S., Gasparini, P., Luise, C., Schurra, C., Garre', M., Nuciforo, P.G., Bensimon, A., et al. (2006). Oncogene-induced senescence is a DNA damage response triggered by DNA hyper-replication. Nature *444*, 638–642.

Feng, M.Y., Wang, K., Song, H.T., Yu, H.W., Qin, Y., Shi, Q.T., and Geng, J.S. (2009). Metastasis-induction and apoptosis-protection by TWIST in gastric cancer cells. Clin. Exp. Metastasis *26*, 1013–1023.

Fletcher, C.D.M., Unni, K.K., and Mertens, F., eds. (2002). World Health Organization Classification of Tumors: Pathology and Genetics of Tumors of Soft Tissue and Bone (Lyon, France: IARC Press).

Hall, K.L., Teneriello, M.G., Taylor, R.R., Lemon, S., Ebina, M., Linnoila, R.I., Norris, J.H., Park, R.C., and Birrer, M.J. (1997). Analysis of Ki-ras, p53, and MDM2 genes in uterine leiomyomas and leiomyosarcomas. Gynecol. Oncol. *65*, 330–335.

Hamamori, Y., Sartorelli, V., Ogryzko, V., Puri, P.L., Wu, H.Y., Wang, J.Y., Nakatani, Y., and Kedes, L. (1999). Regulation of histone acetyltransferases p300 and PCAF by the bHLH protein twist and adenoviral oncoprotein E1A. Cell *96*, 405–413.

Helman, L.J., and Meltzer, P. (2003). Mechanisms of sarcoma development. Nat. Rev. Cancer *3*, 685–694.

Hoogervorst, E.M., Bruins, W., Zwart, E., van Oostrom, C.T., van den Aardweg, G.J., Beems, R.B., van den Berg, J., Jacks, T., van Steeg, H., and de Vries, A. (2005). Lack of p53 Ser389 phosphorylation predisposes mice to develop 2-acetylaminofluorene-induced bladder tumors but not ionizing radiation-induced lymphomas. Cancer Res. *65*, 3610–3616.

Hupp, T.R., Meek, D.W., Midgley, C.A., and Lane, D.P. (1992). Regulation of the specific DNA binding function of p53. Cell *71*, 875–886.

Isenmann, S., Arthur, A., Zannettino, A.C., Turner, J.L., Shi, S., Glackin, C.A., and Gronthos, S. (2009). TWIST family of basic helix-loop-helix transcription factors mediate human mesenchymal stem cell growth and commitment. Stem Cells *27*, 2457–2468.

Ito, M., Barys, L., O'Reilly, T., Young, S., Gorbatcheva, B., Monahan, J., Zumstein-Mecker, S., Choong, P.F., Dickinson, I., Crowe, P., et al. (2011). Comprehensive mapping of p53 pathway alterations reveals an apparent role for both SNP309 and MDM2 amplification in sarcomagenesis. Clin. Cancer Res. *17*, 416–426.

Kapoor, M., Hamm, R., Yan, W., Taya, Y., and Lozano, G. (2000). Cooperative phosphorylation at multiple sites is required to activate p53 in response to UV radiation. Oncogene *19*, 358–364.

Karplus, K. (2009). SAM-T08, HMM-based protein structure prediction. Nucleic Acids Res. *37* (Web Server issue), W492–W97.

Karreth, F., and Tuveson, D.A. (2004). Twist induces an epithelial-mesenchymal transition to facilitate tumor metastasis. Cancer Biol. Ther. *3*, 1058–1059.

Kogan-Sakin, I., Tabach, Y., Buganim, Y., Molchadsky, A., Solomon, H., Madar, S., Kamer, I., Stambolsky, P., Shelly, A., Goldfinger, N., et al. (2011). Mutant p53(R175H) upregulates Twist1 expression and promotes epithelial-mesenchymal transition in immortalized prostate cells. Cell Death Differ. *18*, 271–281.

Kussie, P.H., Gorina, S., Marechal, V., Elenbaas, B., Moreau, J., Levine, A.J., and Pavletich, N.P. (1996). Structure of the MDM2 oncoprotein bound to the p53 tumor suppressor transactivation domain. Science *274*, 948–953.

Kwok, W.K., Ling, M.T., Yuen, H.F., Wong, Y.C., and Wang, X. (2007). Role of p14ARF in TWIST-mediated senescence in prostate epithelial cells. Carcinogenesis *28*, 2467–2475.

Lee, K.E., and Bar-Sagi, D. (2010). Oncogenic KRas suppresses inflammation-associated senescence of pancreatic ductal cells. Cancer Cell *18*, 448–458.

Li, Q.Q., Xu, J.D., Wang, W.J., Cao, X.X., Chen, Q., Tang, F., Chen, Z.Q., Liu, X.P., and Xu, Z.D. (2009). Twist1-mediated adriamycin-induced epithelial-mesenchymal transition relates to multidrug resistance and invasive potential in breast cancer cells. Clin. Cancer Res. *15*, 2657–2665.

Lin, J., Chen, J., Elenbaas, B., and Levine, A.J. (1994). Several hydrophobic amino acids in the p53 amino-terminal domain are required for transcriptional activation, binding to mdm-2 and the adenovirus 5 E1B 55-kD protein. Genes Dev. *8*, 1235–1246.

Lowe, S.W., Ruley, H.E., Jacks, T., and Housman, D.E. (1993). p53-dependent apoptosis modulates the cytotoxicity of anticancer agents. Cell *74*, 957–967.

Maestro, R., Dei Tos, A.P., Hamamori, Y., Krasnokutsky, S., Sartorelli, V., Kedes, L., Doglioni, C., Beach, D.H., and Hannon, G.J. (1999). Twist is a potential oncogene that inhibits apoptosis. Genes Dev. *13*, 2207–2217.

Manfredi, J.J. (2010). The Mdm2-p53 relationship evolves: Mdm2 swings both ways as an oncogene and a tumor suppressor. Genes Dev. *24*, 1580–1589.

Menghi-Sartorio, S., Mandahl, N., Mertens, F., Picci, P., and Knuutila, S. (2001). DNA copy number amplifications in sarcomas with homogeneously staining regions and double minutes. Cytometry *46*, 79–84.

Mentzel, T., and Fletcher, C.D. (1995). Lipomatous tumours of soft tissues: an update. Virchows Arch. *427*, 353–363.

Poyurovsky, M.V., Katz, C., Laptenko, O., Beckerman, R., Lokshin, M., Ahn, J., Byeon, I.J., Gabizon, R., Mattia, M., Zupnick, A., et al. (2010). The C terminus of p53 binds the N-terminal domain of MDM2. Nat. Struct. Mol. Biol. *17*, 982–989.

Qin, Q., Xu, Y., He, T., Qin, C., and Xu, J. (2012). Normal and disease-related biological functions of Twist1 and underlying molecular mechanisms. Cell Res. *22*, 90–106.

Sakaguchi, K., Sakamoto, H., Lewis, M.S., Anderson, C.W., Erickson, J.W., Appella, E., and Xie, D. (1997). Phosphorylation of serine 392 stabilizes the tetramer formation of tumor suppressor protein p53. Biochemistry *36*, 10117–10124.

Seger, Y.R., García-Cao, M., Piccinin, S., Cunsolo, C.L., Doglioni, C., Blasco, M.A., Hannon, G.J., and Maestro, R. (2002). Transformation of normal human cells in the absence of telomerase activation. Cancer Cell *2*, 401–413.

Shieh, S.Y., Ikeda, M., Taya, Y., and Prives, C. (1997). DNA damage-induced phosphorylation of p53 alleviates inhibition by MDM2. Cell *91*, 325–334.

Shiota, M., Izumi, H., Onitsuka, T., Miyamoto, N., Kashiwagi, E., Kidani, A., Hirano, G., Takahashi, M., Naito, S., and Kohno, K. (2008). Twist and p53 reciprocally regulate target genes via direct interaction. Oncogene *27*, 5543–5553.

Šošić, D., Richardson, J.A., Yu, K., Ornitz, D.M., and Olson, E.N. (2003). Twist regulates cytokine gene expression through a negative feedback loop that represses NF-kappaB activity. Cell *112*, 169–180.

Spicer, D.B., Rhee, J., Cheung, W.L., and Lassar, A.B. (1996). Inhibition of myogenic bHLH and MEF2 transcription factors by the bHLH protein Twist. Science *272*, 1476–1480.

Stasinopoulos, I.A., Mironchik, Y., Raman, A., Wildes, F., Winnard, P., Jr., and Raman, V. (2005). HOXA5-twist interaction alters p53 homeostasis in breast cancer cells. J. Biol. Chem. *280*, 2294–2299.

Taylor, B.S., Barretina, J., Socci, N.D., Decarolis, P., Ladanyi, M., Meyerson, M., Singer, S., and Sander, C. (2008). Functional copy-number alterations in cancer. PLoS ONE *3*, e3179.

Tukel, T., Šošić, D., Al-Gazali, L.I., Erazo, M., Casasnovas, J., Franco, H.L., Richardson, J.A., Olson, E.N., Cadilla, C.L., and Desnick, R.J. (2010). Homozygous nonsense mutations in TWIST2 cause Setleis syndrome. Am. J. Hum. Genet. *87*, 289–296.

Valsesia-Wittmann, S., Magdeleine, M., Dupasquier, S., Garin, E., Jallas, A.C., Combaret, V., Krause, A., Leissner, P., and Puisieux, A. (2004). Oncogenic cooperation between H-Twist and N-Myc overrides failsafe programs in cancer cells. Cancer Cell *6*, 625–630.

Vesuna, F., Lisok, A., Kimble, B., and Raman, V. (2009). Twist modulates breast cancer stem cells by transcriptional regulation of CD24 expression. Neoplasia *11*, 1318–1328.

Vichalkovski, A., Gresko, E., Hess, D., Restuccia, D.F., and Hemmings, B.A. (2010). PKB/AKT phosphorylation of the transcription factor Twist-1 at Ser42 inhibits p53 activity in response to DNA damage. Oncogene *29*, 3554–3565.

Xu, Y. (2003). Regulation of p53 responses by post-translational modifications. Cell Death Differ. *10*, 400–403.

Yang, J., Mani, S.A., Donaher, J.L., Ramaswamy, S., Itzykson, R.A., Come, C., Savagner, P., Gitelman, I., Richardson, A., and Weinberg, R.A. (2004). Twist, a master regulator of morphogenesis, plays an essential role in tumor metastasis. Cell *117*, 927–939.

Yang, M.H., Hsu, D.S., Wang, H.W., Wang, H.J., Lan, H.Y., Yang, W.H., Huang, C.H., Kao, S.Y., Tzeng, C.H., Tai, S.K., et al. (2010). Bmi1 is essential in Twist1-induced epithelial-mesenchymal transition. Nat. Cell Biol. *12*, 982–992.

Yap, D.B., Hsieh, J.K., Zhong, S., Heath, V., Gusterson, B., Crook, T., and Lu, X. (2004). Ser392 phosphorylation regulates the oncogenic function of mutant p53. Cancer Res. *64*, 4749–4754.

Cancer Cell
Article

Tumor Type-Dependent Function of the Par3 Polarity Protein in Skin Tumorigenesis

Sandra Iden,[1,3,5,*] Wilhelmina E. van Riel,[1] Ronny Schäfer,[1] Ji-Ying Song,[2] Tomonori Hirose,[4] Shigeo Ohno,[4] and John G. Collard[1,*]
[1]Division of Cell Biology I
[2]Division of Experimental Animal Pathology
The Netherlands Cancer Institute, 1066 CX Amsterdam, The Netherlands
[3]Cologne Cluster of Excellence in Cellular Stress Responses in Aging-Associated Diseases (CECAD), University of Cologne, 50931 Cologne, Germany
[4]Department of Molecular Biology, Yokohama City University Graduate School of Medical Science, Yokohama 236-0004, Japan
[5]Present address: Cologne Cluster of Excellence in Cellular Stress Responses in Aging-associated Diseases (CECAD), University Hospital of Cologne, Robert-Koch-Str. 21, 50931 Cologne, Germany
*Correspondence: sandra.iden@uk-koeln.de (S.I.), j.collard@nki.nl (J.G.C.)
http://dx.doi.org/10.1016/j.ccr.2012.08.004

SUMMARY

Cell polarization is crucial during development and tissue homeostasis and is regulated by conserved proteins of the Scribble, Crumbs, and Par complexes. In mouse skin tumorigenesis, Par3 deficiency results in reduced papilloma formation and growth. Par3 mediates its tumor-promoting activity through regulation of growth and survival, since *Par3* deletion increases apoptosis and reduces growth in vivo and in vitro. In contrast, Par3-deficient mice are predisposed to formation of keratoacanthomas, cutaneous tumors thought to originate from different cellular origin and frequently observed in humans. Par3 expression is reduced in both mouse and human keratoacanthomas, indicating tumor-suppressive properties of Par3. Our results identify a dual function of Par3 in skin cancer, with both pro-oncogenic and tumor-suppressive activity depending on the tumor type.

INTRODUCTION

Cell polarity is regulated by sets of polarity proteins including the Scribble, Par3, and Crumbs polarity complexes, which have been identified in invertebrates and show conserved functions in mammals (Assémat et al., 2008). The Par3 complex, consisting of partitioning-defective (Par)3, the Ser/Thr kinase atypical PKC (aPKC), and Par6, has the most ubiquitous function, being involved, for example, in apico-basal polarity, asymmetric cell division, and polarization of neuronal and T cells (Macara, 2004). Par3, aPKC, and Par6 can form a ternary complex, but in certain processes Par3 is excluded from the aPKC-Par6 domain through aPKC-mediated phosphorylation (Morais-de-Sá et al., 2010; Horikoshi et al., 2009). Par3 binds multiple proteins including the Rac-GEF Tiam1, thereby coupling Rac activation to Par polarity signaling. Cross-talk between polarity complexes and Rho GTPases is necessary to accomplish the cytoskeletal changes required for cell polarization (Iden and Collard, 2008).

Loss of polarity is considered a prerequisite for tumor formation and progression. In *D. melanogaster*, mutations in genes of the Scribble complex (*Scribble*, *Dlg*, and *Lgl*) cause loss of apico-basal polarity and neoplastic outgrowth when mutated or combined with *Ras* mutations (Bilder, 2004). In human tumors,

Significance

Although loss of cell polarity is considered a prerequisite for tumor formation and progression, in vivo evidence demonstrating polarity protein function in mammalian tumorigenicity is limited. We show functional consequences of loss of the Par3 polarity protein in cancer. In skin, Par3 acts both as tumor promoter and tumor suppressor, depending on the tumor type involved. Par3 localizes aPKC and Ras signaling components to cell-cell contacts. Importantly, epidermal *Par3* deletion results in increased formation of Ras-induced keratoacanthoma. This tumor occurs frequently in humans, spontaneously or as an adverse effect of anticancer drugs. Chemical carcinogenesis in Par3-deficient mice provides a useful model for keratoacanthoma development relevant for human disease. Our data unravel a highly context-dependent contribution of Par3 to oncogenic processes.

the expression of polarity proteins is frequently altered though this seems to be highly context-dependent. Scribble complex proteins, similar to their tumor-suppressive function in invertebrates, show mainly reduced protein levels. In contrast, Par complex proteins are often upregulated in carcinoma (Nolan et al., 2008; Huang and Muthuswamy, 2010). Pro-oncogenic functions have been suggested particularly for aPKCι, because it seems required for transformation and tumorigenesis of pancreatic and lung cancer cells (Murray et al., 2011). In mice, Par3 deficiency is embryonically lethal (Hirose et al., 2006), and the function of Par3 during later development and in pathological situations is unknown.

Oncogenic factors such as UV radiation, chemicals, and pathogens as well as hereditary causes induce a variety of skin tumors including melanoma, basal cell carcinoma (BCC), squamous cell carcinoma (SCC), and keratoacanthoma (KA). To elucidate a potential function of the Par complex in oncogenic processes, we investigated the consequence of epidermal loss of Par3 on 7,12-dimethylbenz(a)anthracene (DMBA)-initiated and 12-O-tetradecanoylphorbol-13-acetate (TPA)-promoted skin tumorigenesis and identified tumor-promoting and -suppressing activities of Par3 in cutaneous tumors of clinical relevance.

RESULTS

Par3 Deficiency Inhibits Ras-Induced Tumorigenesis

To address a function of Par3 in the skin, we generated mice with conditional deletion of *Par3* in the epidermis and hair follicle (*K14-Cre*$^{+}$*;Par3*$^{flox/flox}$; hereafter *Par3* KO). These mice are viable and reached adulthood comparable to wild-type (WT) littermates. In control skin (*K14-Cre*$^{+}$*;Par3*$^{wt/wt}$, hereafter WT), Par3 is expressed throughout the interfollicular epidermis and the hair follicle and at much lower levels in the dermis. *Par3* KO tissue lacked epithelial Par3 immunoreactivity, and loss of Par3 was further confirmed in epidermal lysates of newborn and adult *Par3* KO mice (Figure 1A).

To examine if Par3 has a potential function in tumorigenesis, we applied a two-stage chemical skin carcinogenesis protocol. Topical treatment with the carcinogen DMBA induced oncogenic Ras mutations, and subsequent repeated treatments with the phorbol ester TPA promoted outgrowth of initiated cells resulting in benign papillomas in WT mice about 7 weeks after initiation. Interestingly, papilloma formation was delayed by about 3 weeks in *Par3* KO mice (Figure 1B), and tumor multiplicity was strongly reduced (Figures 1C and 1E; Table S1 available online). Moreover, tumors that did form grew slower in the absence of Par3 (Figure 1D), indicating that Par3 promotes Ras-induced tumor formation and growth. Typical papillomas in WT mice showed exophytic growth of squamous cells (Figure 1F). To prepare tissue lysates, we dissected from same mice both normal skin and tumors and repeated this for multiple WT and *Par3* KO littermates. The analysis of Par3 and aPKC expression in nontumor and tumor tissue lysates revealed robust levels of Par3 and aPKC in WT tumors, whereas Par3 protein was undetectable in *Par3* KO skin and tumors (Figure 1G). Together, these functional and biochemical data suggest a tumor-promoting function of Par3 in Ras-induced papillomas.

To address the mechanism of reduced tumor formation and growth in *Par3* KO mice, we tested the involvement of Par3 in epidermal proliferation and apoptosis in response to DMBA/TPA treatment of the skin. After single DMBA and subsequent dual TPA treatment, as measured by BrdU incorporation, proliferation was significantly reduced in *Par3* KO compared to WT epidermis (Figure 2A). Furthermore, Par3-deficient epidermis showed a significant increase in cells positive for cleaved caspase-3, which identifies apoptosis (Figure 2A), normally a rare event in skin. We isolated skin keratinocytes from mice with loxP-flanked Exon3 of *Par3* (Hirose et al., 2006) to further address a function of Par3 in cell survival and proliferation. In keratinocytes, the 180 kDa splice variant of Par3 shows highest expression, and self-excising Cre recombinase efficiently deleted *Par3* (Figure 2B). We expressed oncogenic Ras (RasV12) in cells (Figure 2C) and studied the role of Par3 in Ras-induced resistance to contact-mediated growth inhibition. Upon calcium switch (elevation from 20 μM Ca^{2+}, termed low calcium [LC], to 2 mM Ca^{2+}, termed normal calcium [NC]), which induces cadherin-mediated intercellular adhesion, RasV12 enabled keratinocytes continue to grow despite prolonged incubation at NC. In contrast, Par3-deficient cells showed attenuated growth (Figures 2D and 2E), suggesting that Par3 is required for Ras signaling to overcome differentiation-induced cell cycle arrest. This was not due to differential expression of major adherens junction (AJ) components because loss of Par3 did not affect the moderate Ras-mediated downregulation of E-cadherin and other AJ-associated proteins tested (Figure S2H). In addition, Par3-deficiency reduced the ability of RasV12 cells to form colonies in matrigel (Figure 2E) or soft-agar (data not shown), further supporting a growth-promoting function of Par3.

We further investigated whether Par3 is involved in activation of the phosphatidylinositol-3 kinase (PI3K)/Akt and MEK/ERK pathways, main modules mediating cell survival, proliferation, and apoptotic resistance in Ras-mediated skin tumorigenesis (Kern et al., 2011). Par3-deficient keratinocytes indeed exhibit consistently reduced ERK activation upon Ras expression and/or TPA treatment (Figures 2F and 2G) and reduced Akt activation upon Ras expression compared to WT cells (Figure S2B). Moreover, as in carcinogen-exposed skin, apoptosis was increased in starved, EGF-, or TPA-treated *Par3* KO keratinocytes as evidenced by caspase-3 and Parp1-cleavage (Figure 2H). Other stimuli such as heat shock and growth factor deprivation similarly induced a stronger apoptotic response in *Par3* KO than in WT cells (Figure S2D; data not shown). Increased Bax conformational change and caspase-9 processing in *Par3* KO cells indicated activation of the intrinsic, mitochondria-dependent apoptotic pathway in the observed apoptotic phenotype (Figures 2I, S2E, and S2F). Finally, cyclin D1 levels in *Par3* KO cells were lower than in WT cells (Figure S2C). This difference was further increased upon expression of oncogenic Ras, known to induce cyclin D1 expression (Filmus et al., 1994). Together, these results indicate that Par3 is required for Ras-induced tumor growth and promotes ERK- and Akt-mediated growth and survival signals that counterbalance apoptotic signaling.

Par3 Interacts with and Localizes aPKC in Cultured Keratinocytes

Because Par3 has been shown to act together with aPKC in several cellular systems, we analyzed the subcellular localization of Par3 and aPKC in keratinocytes. At NC, Par3 was

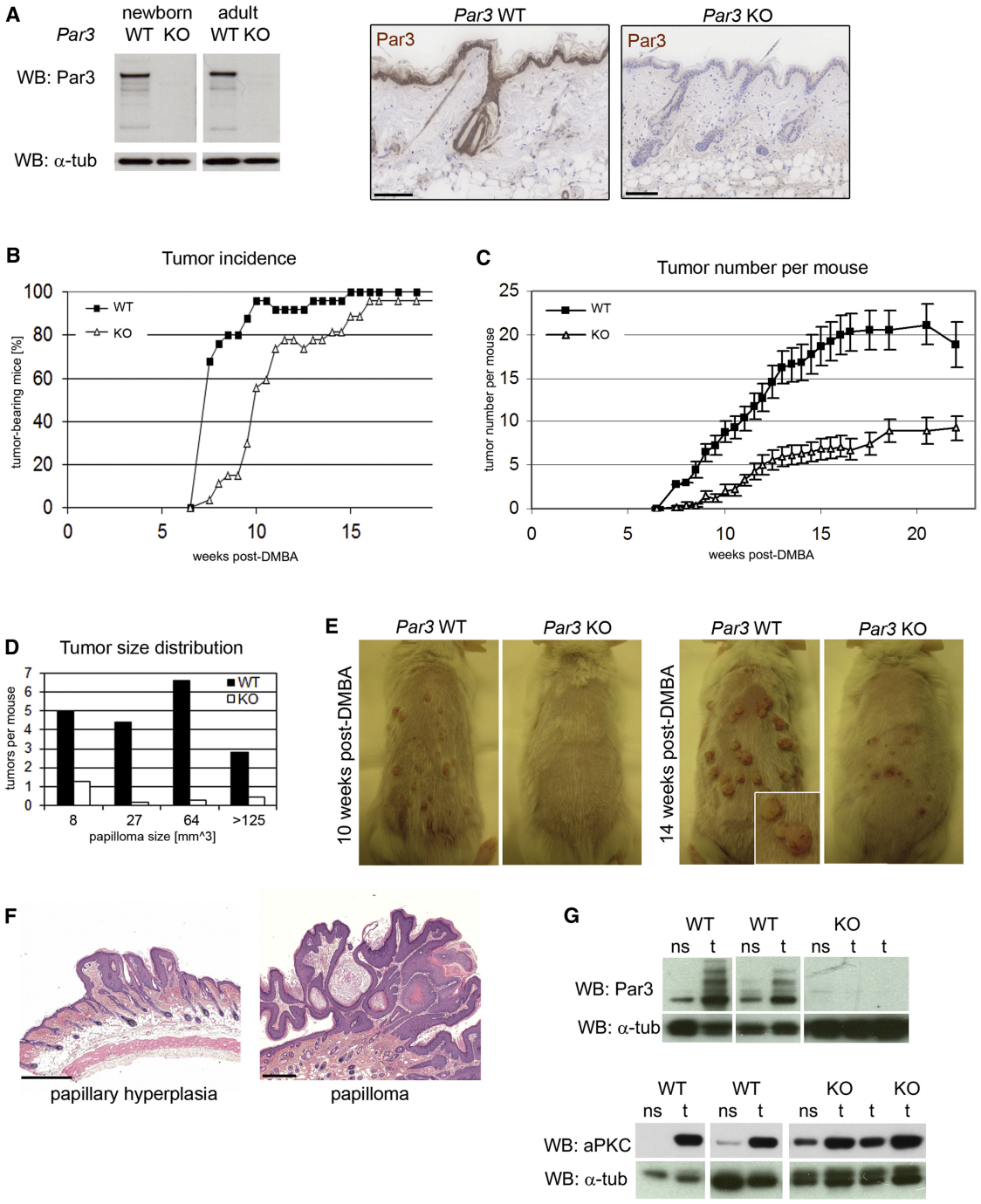

Figure 1. Mice with Epidermal *Par3* Deletion Show Reduced Ras-Mediated Tumorigenesis

(A) Western blot against Par3 and α-tubulin from epidermal lysates (left: epidermis from newborns; right: epidermis from 8 weeks old mice) and immunohistochemical Par3 staining of adult *K14-Cre*$^{+}$;*Par3*$^{wt/wt}$ (WT) or *K14-Cre*$^{+}$;*Par3*$^{flox/flox}$ (*Par3* KO) mice (right). Scale bars, 100 μm.

(B) Tumor incidence, indicated by percentage of tumor-bearing mice, in WT and epidermal *Par3* KO mice. n(WT) = 25, n(KO) = 27.

(C) Average number of tumors per mouse in WT and epidermal *Par3* KO mice (mean ± SEM).

(D) Tumor volume (length × width × height) in WT mice and epidermal *Par3* KO mice. Representative data are shown for 14.5 weeks post-DMBA.

(E) Representative photographs of TPA-treated WT and epidermal *Par3* KO mice 10 and 14 weeks after tumor initiation.

(F) Histologic sections of papillary hyperplasia and papilloma in WT mice, H&E. Scale bars, 500 μm.

(G) Western blot analysis of Par3 and aPKC expression in lysates of WT and *Par3* KO skin and tumors. Vertical white lines indicate that lanes were removed between the samples shown. ns, normal skin; t, tumor tissue; α-tub, α-tubulin.

See also Figure S1.

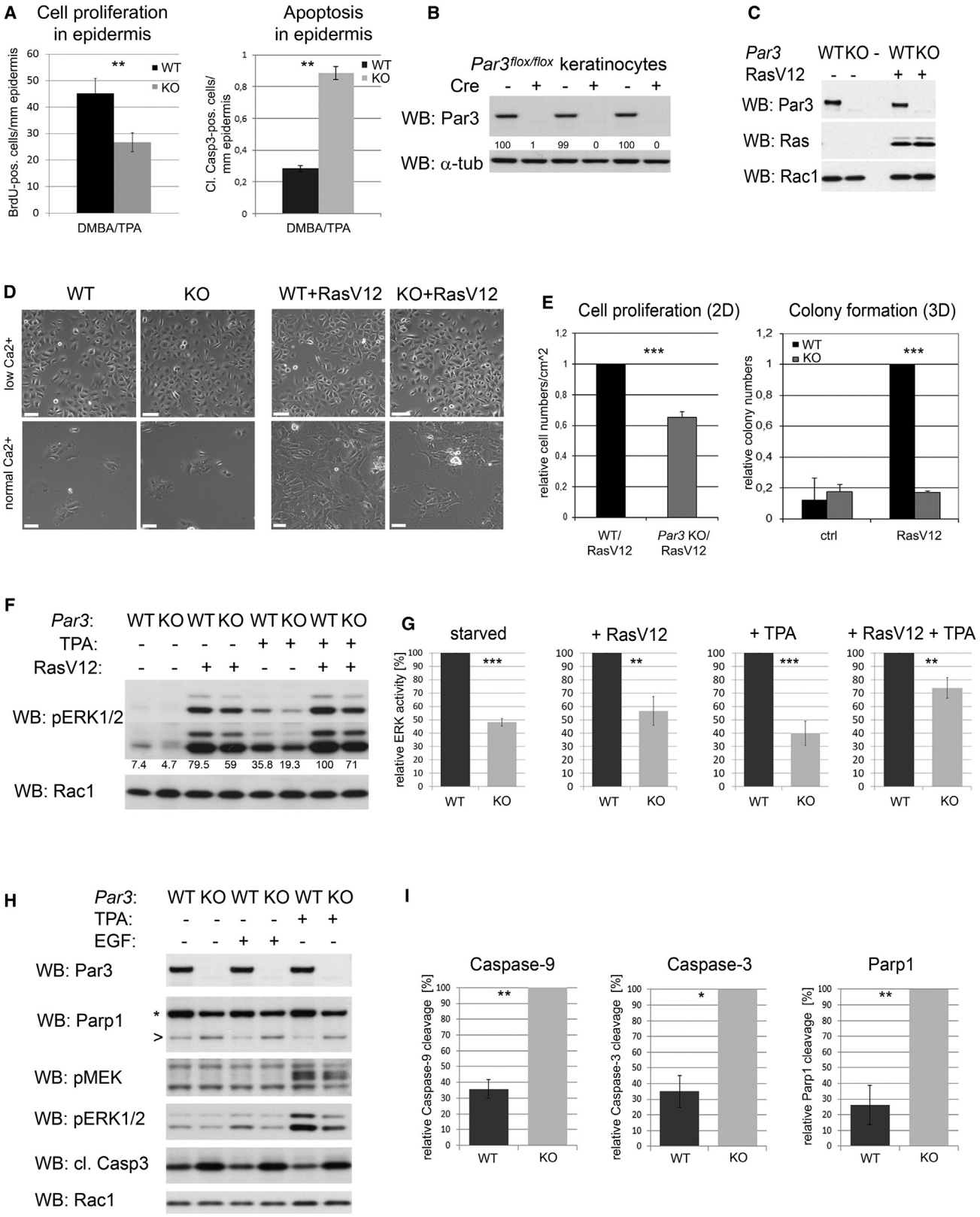

Figure 2. Reduced Proliferation and Cell Survival and Increased Apoptosis upon Epidermal *Par3* Deletion

(A) Back-skin of mice was treated once with DMBA and twice with TPA with a 3 day interval. Proliferation and apoptosis 24 hr after last treatment was quantified based on immunohistochemical analyses (mean ± SEM) (see Experimental Procedures for details).

predominantly found at ZO-1-positive cell-cell contacts of WT cells, whereas in *Par3* KO cells it was not (Figure 3A). The ZO-1 pattern was discontinuous in *Par3* KO cells in early phases of junction formation indicating impaired tight junction maturation upon loss of Par3 (6 hr NC; Figure 3A), which could be restored by myc-PAR3 expression (Figure S2A). In contrast, 48 hr after calcium switch ZO-1 distribution was comparable to WT cells (data not shown), indicating a temporary requirement of Par3 in initial steps of tight junction (TJ) formation as described for other epithelial cell types (Chen and Macara, 2005). Immunostaining revealed colocalization of Par3 and aPKC at keratinocyte TJs (Figure 3B), and co-immunoprecipitation revealed binding of both endogenous proteins in WT keratinocytes (Figure 3C), indicating the presence of a functional Par3-aPKC complex. In WT cells, we found aPKC localization at newly formed cell-cell contacts (30 min and 2 hr at NC) and at established intercellular junction of multilayered keratinocytes (3 days at NC on permeable supports) (Figure 3D). In *Par3* KO cells however, aPKC showed a diffuse cytoplasmic distribution and was absent at cell-cell contact sites, both shortly after calcium switch and in multilayers with established TJs (Figure 3D). As total aPKC levels are unaffected by *Par3* deletion (Figure 3C), our data suggest that Par3 is required for proper aPKC localization to intercellular contacts in cultured keratinocytes. Interestingly, similar to myc-PAR3, expression of membrane-targeted aPKC (aPKC-CAAX) could restore active ERK levels in *Par3* KO keratinocytes after starvation or when expressing RasV12 combined with TPA stimulation (Figures 3E and 3F). Furthermore, similar to *Par3* deletion, siRNA-mediated depletion of aPKC impaired TPA-induced ERK activation (Figure S3A) and resulted in increased apoptosis (Figure S3B), indicating that aPKC likely contributes to Par3-dependent ERK stimulation and survival.

Altered Localization of Ras-MAPK Pathway Components upon Loss of Par3

To assess how Par3 dysfunction impacts survival and growth signaling, we analyzed the subcellular localization of crucial components of the Ras signaling pathway in control and Par3-deficient epidermis, papillomas, and keratinocytes. Interestingly, endogenous Ras and its GEF Sos2 localized to cell-cell contacts of control epidermis and papilloma tissue in a pattern similar to that of Par3 (Figure 4A, top). This specific localization, however, was strongly diminished in *Par3* KO tissue (Figure 4A, bottom), suggesting that Par3 mediates the localization of Ras pathway components to intercellular adhesions. In primary keratinocytes, endogenous Ras and Par3 indeed colocalized at cell-cell contacts (Figure 4B) and both exogenous oncogenic RasV12 and endogenous Sos2 colocalized with ZO-1 (Figures 4B and 4C), indicating that they associate with TJs. RasV12 further codistributed with Par3 at cell-cell contacts in WT keratinocytes (Figure 5A, top), whereas this localization was diminished in *Par3* KO keratinocytes (Figure 5A, middle). Importantly, RasV12 localization to intercellular contacts could be restored by expression of exogenous human myc-PAR3 in *Par3* KO cells (Figure 5A, bottom), suggesting that Par3 mediates localization of active Ras to these sites. In line with the in vivo data (Figure 4A) also Sos2 displayed Par3-dependent cell-cell contact localization as evident by loss of Sos2 from these sites in *Par3* KO keratinocytes cultured at NC (Figure 5B). Finally, next to cytoplasmic and nuclear pools we observed the active form of the downstream effector ERK1/2 (pERK1/2) at cell-cell contacts in WT cells (Figure 5C), colocalizing with aPKC (Figure 5D). Similar to Ras and Sos2, pERK1/2 was not found at intercellular contacts of *Par3* KO cells (Figures 5C and 5D, right). Ras, Sos2, MEK, and ERK protein levels were unaffected by loss of Par3 in keratinocytes (Figure 5E), excluding that Par3 regulates the expression of these proteins. Together, the above data suggest that junctional Par3 mediates localization of Ras pathway components and thereby helps to assemble a functional, signaling-competent platform at intercellular contacts that efficiently stimulates growth and survival signaling in papillomagenesis.

Increased Formation of Keratoacanthoma in Par3-Deficient Mice

To examine if Par3 is important for the progression of papillomas to SCCs, mice were inspected thoroughly during the experiment. While papillomas, the predominant tumors of WT mice, showed clear exophytic growth with a narrow stem connecting tumor mass and skin (Figures 1F and S1A), *Par3* KO mice often developed tumors with initially glossy surface that rapidly grew inward (Figures 6A and 6B). This caused experiment termination 22 weeks postinitiation as tumor sizes reached >1 cm. At dissection we noticed deep protrusion of tumors into the dermis and presence of strong vascularization at the base. These tumors were histologically identified as keratoacanthoma (KA), a tumor rarely observed in mice but common in human, with typical crater-like morphology, broad tumor base and a keratin-filled center (Figures 6B, S1D, S1H, and S1I). Histopathological

(B) Western blot of cultured keratinocytes upon Cre-mediated *Par3* deletion. The 180kDa band shown reflects the dominantly expressed splice variant in keratinocytes (WT: $Par3^{fl/fl}$, KO: $Par3^{fl/fl}$ + self-excising Cre). Numbers indicate the relative Par3 expression after normalization to loading control α-tubulin.
(C) Western blot of transduced oncogenic Ras (RasV12) in WT and *Par3* KO keratinocytes. Rac served as loading control.
(D) Phase-contrast micrographs of WT and *Par3* KO keratinocytes either untreated (left) or upon expression of RasV12 (right) at growth (low Ca^{2+}, top) and differentiating (normal Ca^{2+}, bottom) conditions. Scale bars, 20 μm.
(E) Proliferation and colony formation induced by oncogenic Ras. Cell proliferation on culture plates (left) and colony formation in 3D upon seeding single cell suspensions of RasV12-infected WT and *Par3* KO keratinocytes into matrigel and incubation for 10 days at NC (right) was assessed (mean ± SD).
(F) Western blot analysis of total cell lysates to detect ERK activation in WT and *Par3* KO cells (bottom: longer exposure of top pERK blot). Serum-starved keratinocytes were infected with oncogenic Ras and/or treated with 0.68 μM TPA for indicated time points.
(G) Quantification of F, ERK activation upon loss of Par3 in starved, Ras-expressing and TPA-treated cells ($n \geq 4$) (mean ± SEM).
(H) WT and *Par3* KO cells were cultured at NC for 36 hr, serum-starved and treated with TPA or EGF. Apoptosis was indicated by caspase-3 and Parp1 cleavage, ERK pathway activity by pMEK and pERK levels. Asterisk: full-length Parp1; arrow: cleaved Parp1 fragment.
(I) Quantification of apoptosis markers upon starvation ($n \geq 3$) (mean ± SEM). Representative western blots for caspase-9 are provided in Figure S2E. *$p < 0.05$; **$p < 0.01$.
See also Figure S2.

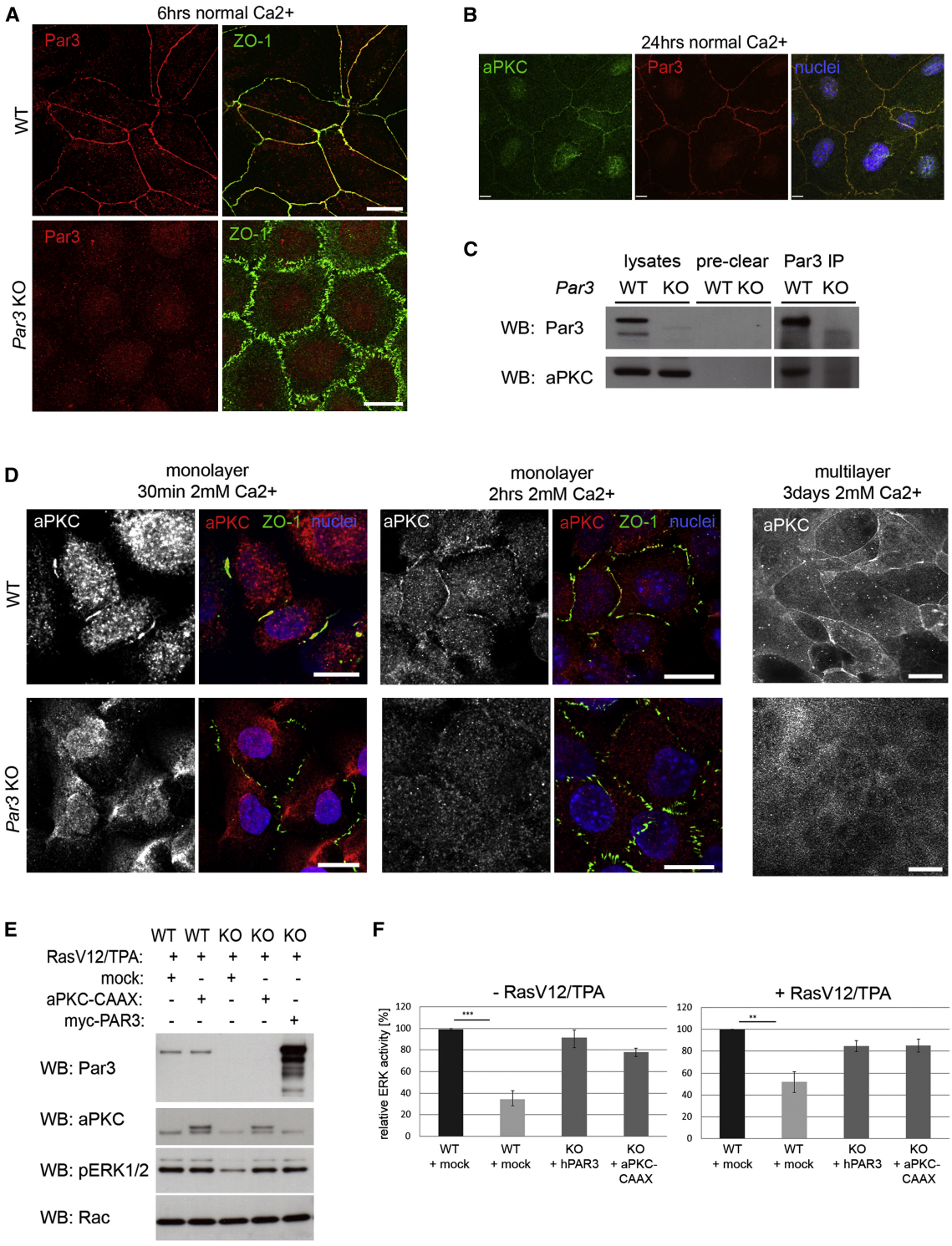

Figure 3. Par3 Interacts with aPKC and Mediates Cell-Cell Contact Localization of aPKC in Keratinocytes

(A) Endogenous Par3 and ZO-1 immunostaining 6 hr after calcium switch to NC. Continuous, thin lines of ZO-1 immunoreactivity indicate matured tight junctions. Scale bar, 10 μm.

(B) Co-immunostaining of aPKC and Par3 in WT keratinocytes cultured for 24 hr at NC. Scale bar, 10 μm.

(C) Co-immunoprecipitation of endogenous Par3 and aPKC in WT keratinocytes 6 hr after Ca^{2+} switch (see Supplemental Experimental Procedures for details). Vertical white lines indicate that lanes were removed between the samples shown.

(D) Immunostaining against aPKC and ZO-1 in WT and *Par3* KO keratinocytes. Various time points after calcium switch were analyzed as indicated on top. Scale bars, 10 μm.

analyses confirmed that at termination *Par3* KO mice had formed 6.63 KAs per mouse (91% of mice KA-positive; Table S1), whereas in WT mice only 0.53 KAs per mouse were detected (27% of WT mice KA-positive; Table S1), which were too small to be macroscopically classified as such. Formation of SCCs was in total rare at week 22 but *Par3* KO mice appeared not to be prone to SCC formation. WT mice had slightly increased SCC formation (0.4 SCCs per mouse, 20% of WT mice SCC-positive; Table S1) compared to *Par3* KO mice (0.18 SCCs per mouse, 18% of KO mice SCC-positive; Table S1). Of note, all tumors tested were positive for *Ras* codon 61 mutations (Figure S4A) described to be induced by DMBA (Finch et al., 1996), indicating that KAs were also induced by oncogenic Ras signaling. Lack of Par3 expression was confirmed in all tested *Par3* KO-derived tumors (data not shown), excluding the possibility that KAs developed from rare cells that had escaped Cre-mediated *Par3* deletion. The remarkably increased incidence and accelerated appearance of KAs in *Par3* KO mice (Figures 6C and 6D; Table S1) contrasted the reduced papilloma formation in these mice (Figures 1B, 1C, and 6D; Table S1), indicating a dual function of Par3 in development of skin tumors dependent on the tumor type.

To address further the molecular functions of Par3 in the skin and the different skin tumors, we explored the subcellular localization of Par3 and aPKC in skin tissue. Par3 was robustly expressed in epidermis and papilloma tissue, where it localized to sites of cell-cell contacts (Figure 6E, top), but was lost in the few KAs of WT mice (Figure 6E, top). Similar to cultured keratinocytes (Figure 3D), we found a requirement of Par3 for junctional localization of aPKC in vivo, as aPKC was strikingly mislocalized to the cytoplasm in Par3-deficient epidermis and tumors as well as in the rare WT KAs that displayed reduced Par3 levels (Figure 6E, middle and bottom). Instead, ZO-1 showed normal TJ distribution in WT and *Par3* KO epidermis and appeared cortically distributed but scattered both in WT papilloma and *Par3* KO KAs (Figure S4D), suggesting Par3-independent ZO-1 localization in this context. Since KAs also develop in humans, we further investigated possible similarities between Ras-induced mouse tumors and patient-derived KAs. Quantitative analyses of sections of non-diseased human skin and 10 KA tumors revealed that PAR3 was clearly detectable in basal and suprabasal layers of healthy epidermis and in epidermis adjacent to tumors, partially colocalizing with E-CADHERIN, ZO-1 and aPKC (Figure S4C). However, its expression was significantly reduced in the tumor epithelium of KAs (Figures 6G, 6H, and S4B), similarly as found in murine WT KAs. In contrast, analysis of human SCCs did not reveal significantly reduced PAR3 expression (Figure 6H, bottom panel; Figure S4B, right panel), in line with the lack of significant alterations of SCC incidence in *Par3* KO mice (Table S1). From these data we conclude that Par3 expression and localization differs in papillomas and KAs, consistent with the differential tumor outcome in mice with *Par3* deletion (Figures 1 and 6; Table S1). Analysis of keratinocytes cultured at LC versus NC indicated that depending on the cellular context and presence of cell-cell contacts Par3 is differentially required for MAPK signaling (Figure S3D). We therefore assessed if a differential activity of crucial MAPK components could be confirmed in tumor tissues. Interestingly, we observed abnormally high levels of phosphorylated active CRaf in a distinct vesicular pattern in basal layers of *Par3* KO epidermis as well as Par3-deficient KAs (Figure 7A, bottom). In contrast, in WT epidermis this active CRaf was moderately detected at cell-cell contacts of the suprabasal layers, in few vesicular structures in the basal layer and was only very weakly present in WT papilloma tissue (Figure 7A, top). These data implicate Par3 in CRaf activation and/or localization in the context of KA formation. The abundance of active CRaf in intracellular vesicles has been reported previously (Rizzo et al., 2001) and could be recapitulated in vitro in *Par3* KO but not WT keratinocytes cultured at LC (Figure 7B), suggesting that in the absence of profound intercellular adhesions cytoplasmic Par3 serves to restrict CRAF activity.

Together, the above data indicate that the tumor-suppressive function of Par3 in KA formation involves regulation of CRaf and illustrate that polarity proteins contribute to clinically relevant pathologies.

DISCUSSION

Our functional tumorigenicity studies reveal a hitherto unknown role of the Par3 polarity protein in mammalian cancer, i.e., a tumor-promoting function in papilloma formation and tumor-suppressive activity in KA formation. Previously, polarity proteins of the Scribble complex have been implicated in tumor suppression in D.*melanogaster,* in D.*rerio* and recently in mice (Bilder, 2004; Reischauer et al., 2009; Zhan et al., 2008; Pearson et al., 2011). Similarly, Par4/LKB1 shows tumor-suppressive activity (Vaahtomeri and Mäkelä, 2011), and loss of Par4/LKB1 associated with impaired epithelial integrity synergizes with oncogenic c-*myc* induced mammary tumorigenesis (Partanen et al., 2012). In the DMBA/TPA tumor model involving Ras mutations, we found that Par3 can serve either as a tumor promoter in papilloma formation or a tumor suppressor in KA formation. Par3-deficient mice did not develop spontaneous skin tumors, indicating that Par3 dysfunction in mice alone is not sufficient to drive tumorigenesis. Malignant transformation of papillomas by local invasion into the stroma was observed in 45% of the relatively small tumors found in *Par3* KO mice and in 33% of the abundant larger tumors of WT mice (Table S1), suggesting that loss of Par3 promotes Ras-mediated metastasis of tumor cells as found in *Drosophila* (Pagliarini and Xu, 2003). Similarly, local invasion by KAs was exclusively observed in *Par3* KO mice (36%; Table S1) although we cannot exclude that this is the result of the earlier onset of KAs in these mice.

Isolated epidermal keratinocytes appear to recapitulate well what is occurring during papillomagenesis. In the absence of Par3, both carcinogen-exposed epidermis and cultured

(E) Expression of myc-hPAR3 and of membrane-targeted aPKC (aPKC-CAAX) in *Par3* KO keratinocytes to restore ERK activity. RasV12-expressing cells were cultured at NC and treated with TPA.
(F) Quantification of ERK activity in WT and KO *Par3* KO keratinocytes transfected with control plasmid, myc-hPAR3 or aPKC-CAAX, either untreated (left) or upon expression of RasV12 and subsequent TPA treatment (right) (n = 3). Mean ± SEM; $^{**}p < 0.01$; $^{***}p < 0.001$.
See also Figure S3.

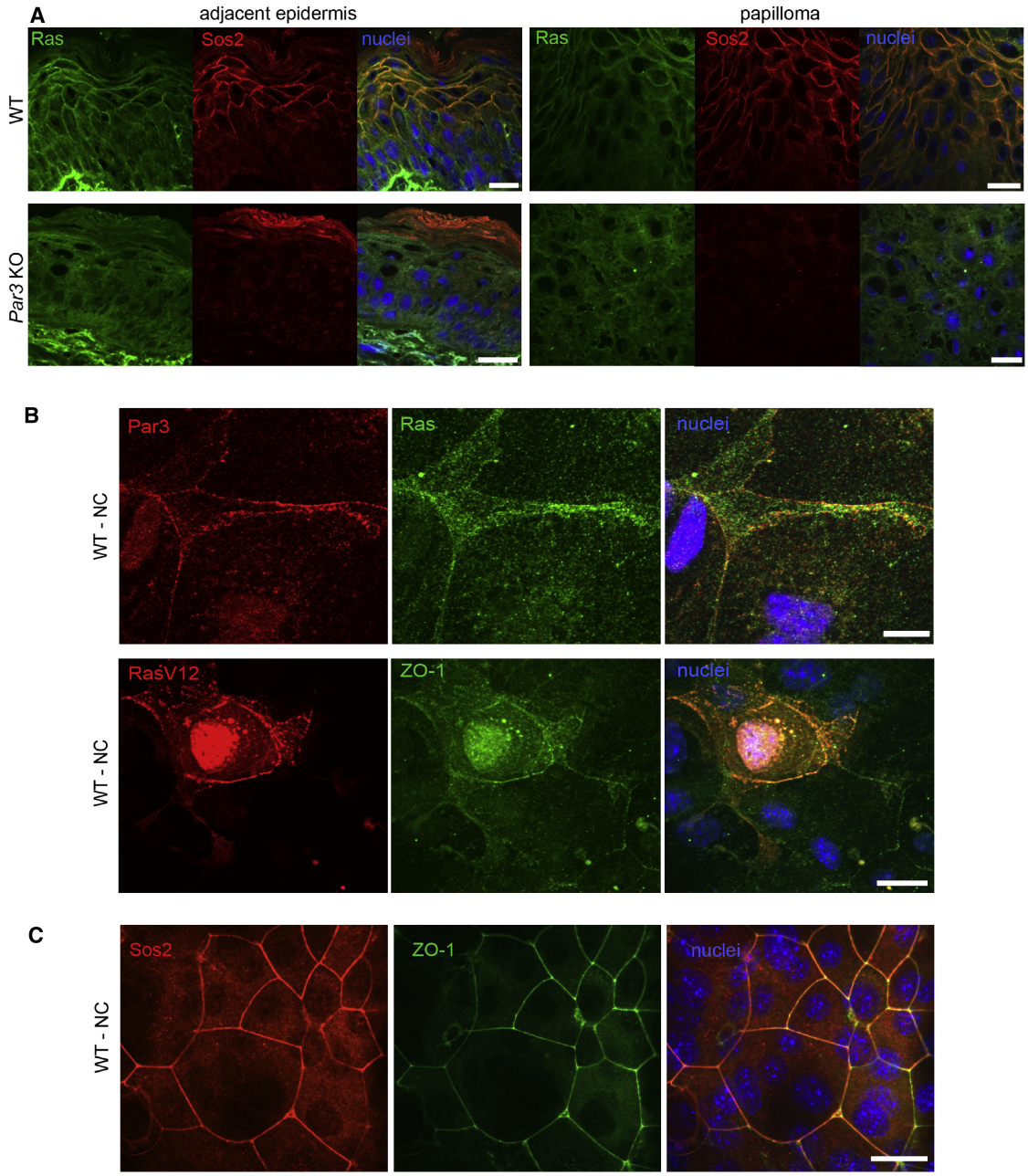

Figure 4. The Localization of Ras and the RasGEF Sos2 to Cell-Cell Contacts Is Par3-Dependent

(A) Immunostaining of Ras and the Ras-GEF Sos2 in murine epidermis adjacent (left) to papillomas (right) in WT (top) and *Par3* KO (bottom) tissues. Scale bars, 20 μm.

(B) Co-immunostaining of endogenous Par3 and Ras, and of oncogenic Ras (HA-RasV12, stained with HA-tag antibodies) with the endogenous, TJ-associated protein ZO-1 in WT keratinocytes. Scale bars, 20 μm.

(C) Co-immunostaining of the endogenous Ras-GEF Sos2 with ZO-1 in WT keratinocytes 48 hr after switch to NC. Scale bars, 20 μm.

keratinocytes show reduced proliferative responses and higher apoptotic sensitivity (Figure 2). Par3 likely promotes Ras-induced ERK- and Akt-mediated cell growth and apoptotic resistance giving rise to papillomas. To date, no direct molecular link between Par3 and Ras signaling has been reported. Recently, direct binding of Par3 to PI3K, PTEN and phosphoinositides and a positive feedback of the Par3 complex to PI3K has been postulated in the context of axon formation and establishment of plasma membrane polarity (Itoh et al., 2010; Yoshimura et al., 2006; Cain and Ridley, 2009). Our findings of reduced Akt activity upon loss of Par3 in keratinocytes suggest that such interactions also sustain survival signals in skin tumorigenesis. We further provide evidence that loss of Par3, concomitant with reduced survival signaling, results in activation of the

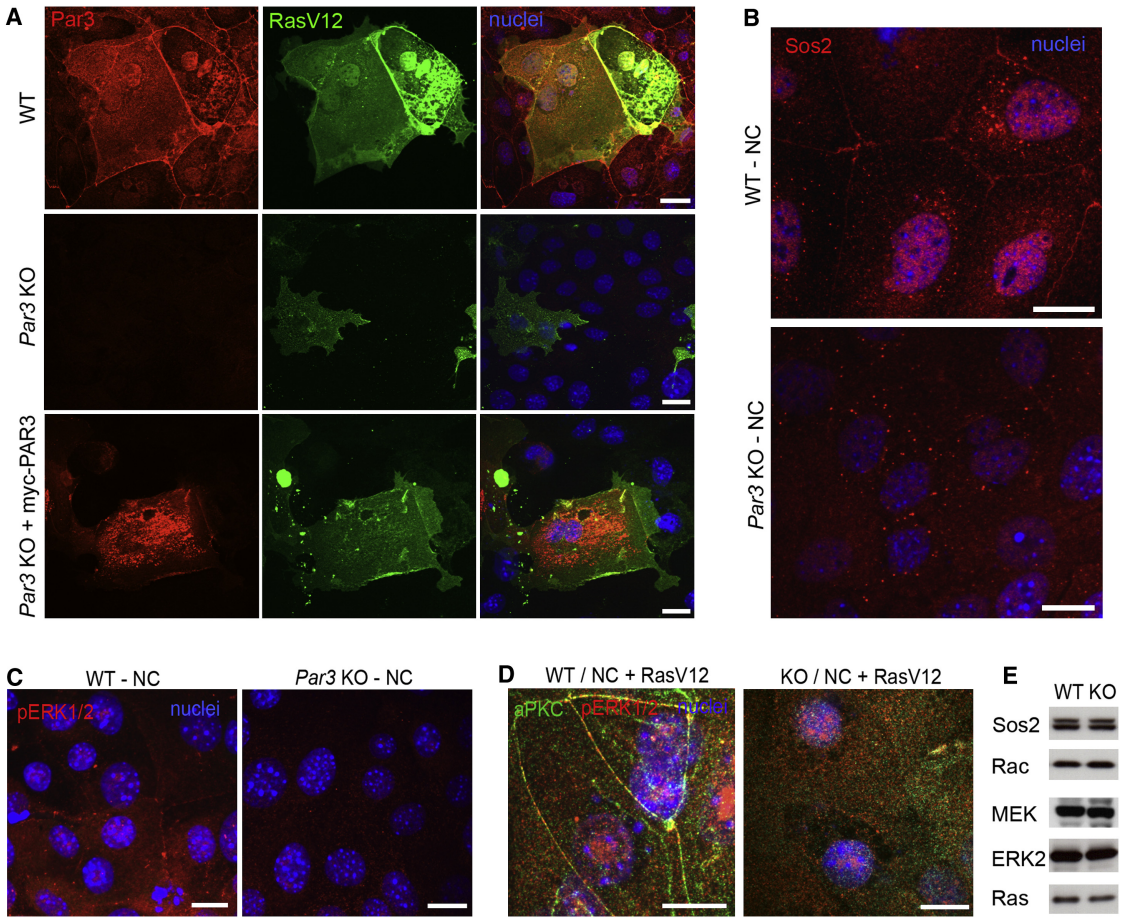

Figure 5. Mislocalization of Ras Pathway Components upon Loss of Par3 in Epidermis, Skin Tumors, and Keratinocytes

(A) Immunofluorescent co-staining of RasV12, stained with HA-tag antibodies, and Par3 in WT keratinocytes (top), in *Par3* KO cells (middle), and in *Par3* KO keratinocytes expressing myc-PAR3 (bottom). All cells were cultured at NC. Scale bars, 20 μm.

(B) Immunofluorescent staining of Sos2 to depict its localization in WT and *Par3* KO keratinocytes. Scale bars, 20 μm.

(C) Immunofluorescent staining of phosphorylated ERK1/2 in WT (left) and *Par3* KO (right) keratinocytes to detect sites of high ERK activity. Scale bars, 20 μm.

(D) Immunofluorescent staining of aPKC and active ERK (pERK1/2) to depict colocalization in WT and *Par3* KO keratinocytes expressing RasV12 and cultured at NC. Scale bars, 20 μm.

(E) Western blot analysis of Sos2, MEK, ERK2, and Ras and Rac protein levels in WT and *Par3* KO keratinocytes.

intrinsic mitochondria-dependent apoptotic pathway (Figures 2I, S2E, and S2F), which has earlier been implicated in balancing skin tumor growth in the DMBA/TPA tumor model (Cho et al., 2001) and mediating UV-induced cell death in human keratinocytes (Van Laethem et al., 2004).

We and others have shown that Par3 can cross-talk to Rho GTPase signaling through interaction with the Rac-GEF Tiam1. Tiam1 and Rac collaborate with the Par3-aPKC complex to regulate TJ biogenesis and persistent migration of keratinocytes (Iden and Collard, 2008). Similar to Tiam1-depleted cells, *Par3* KO keratinocytes are impaired in scratch-induced wound closure (Figure S2G). Interestingly, deletion of Tiam1 or Rac1 also suppresses Ras-induced papilloma formation (Malliri et al., 2002; Wang et al., 2010), suggesting that Par3 and Tiam1/Rac1 function is coupled not only during cell polarization but also in tumorigenic events downstream of Ras. Considering the striking resemblance between papilloma phenotypes upon deletion of Tiam1, Rac1 or Par3, and our previous findings that Tiam1/Rac regulates the Par3 complex in polarizing keratinocytes (Pegtel et al., 2007) we speculate that Par3 acts at the level of Tiam1/Rac in papillomagenesis. Of note, the increased KA incidence in *Par3* KO mice has not been observed in Tiam1- and Rac1-deficient mice, indicating that the tumor-suppressive effect of Par3 on KA formation is not coupled to Tiam1/Rac signaling. Moreover, in contrast to increased SCC formation in Tiam1-KO mice (Malliri et al., 2002), we could not detect a significant contribution of Par3 expression on SCC formation (Table S1). A recent report implicates the RAS/RAF/MAPK axis in formation of human SCC (Reuter et al., 2009). Due to the rapidly growing KAs, which appear much earlier than SCCs, animals needed to be sacrificed before profound SCC onset, preventing a statistically validated conclusion on the function of Par3 in SCC formation. Hence, considering the different kinetics of SCC and KA formation, we cannot exclude that SCC initiation is altered upon loss of Par3. However, we did not detect significant differences in the expression of PAR3 in

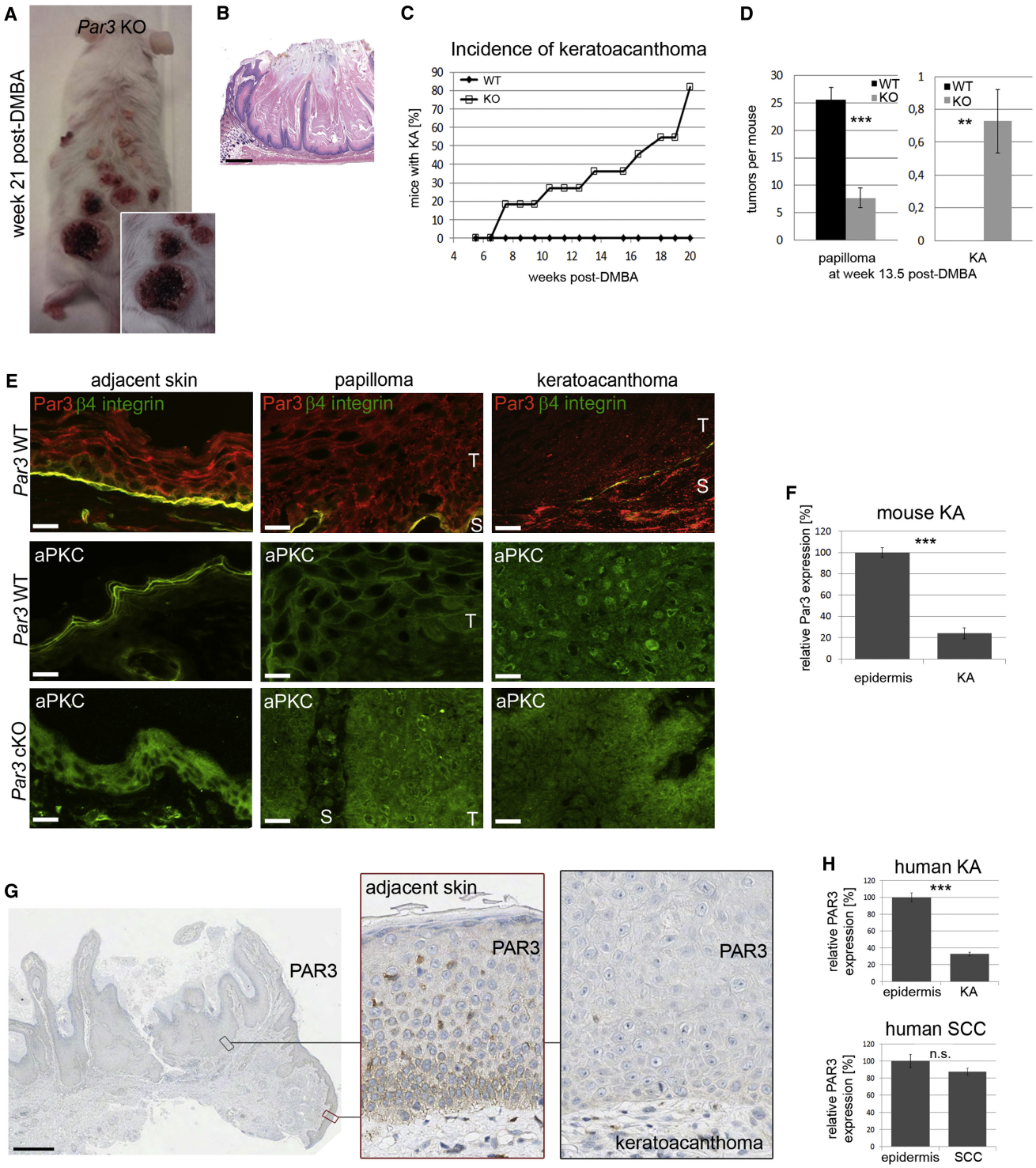

Figure 6. *Par3* cKO Mice Develop Keratoacanthomas

(A) Representative photograph of keratoacanthomas in *Par3* KO mice 21 weeks post-DMBA.

(B) Representative H&E staining of KA cross-section. Scale bar, 1 mm.

(C) KA incidence based on macroscopic analysis of WT and *Par3* KO mice. For histologic analyses, see Table S1.

(D) Number of papillomas versus KAs per mouse based on macroscopic analysis at week 13.5 post-DMBA. For histologic analyses, see Table S1.

(E) Par3 and aPKC immunostaining in cryosections of mouse epidermis, papilloma and KA. β4 integrin signal reflects the epidermal-dermal border. Scale bars, 20 μm. T, tumor; S, stroma.

(F) Quantification of Par3 protein expression in KAs of WT mice and epidermis adjacent to the tumors.

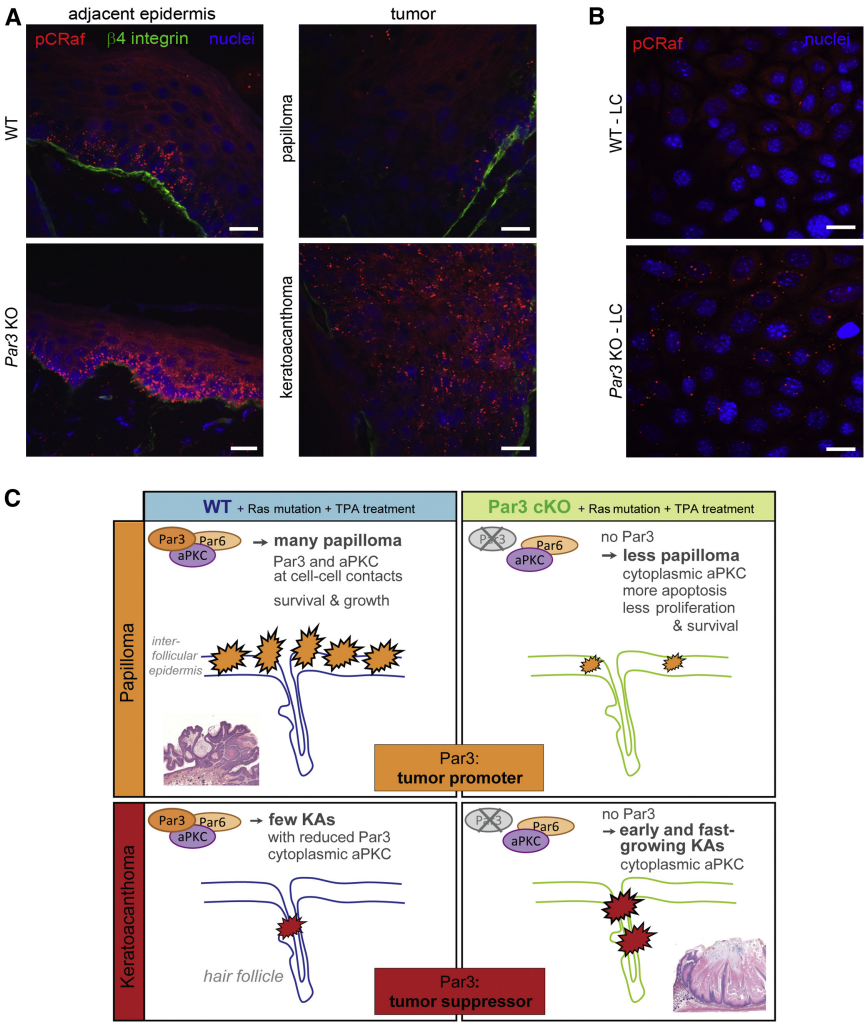

Figure 7. Altered Localization and Activity of CRaf in Par3-Deficient Epidermis and Skin Tumors

(A) Immunofluorescent staining of phosphorylated CRaf, reflecting the active form of CRaf in WT and *Par3* KO epidermis and tumor tissues. Scale bars, 20 μm.

(B) Immunofluorescent staining of phosphorylated CRaf in WT and *Par3* KO keratinocytes cultured at LC conditions. Scale bars, 20 μm.

(C) Model representing experimental skin tumorigenesis in WT and *Par3* KO mice. While papillomas likely arise mostly from suprabasal layers of the interfollicular epidermis, KAs are considered to originate from the hair follicle (Perez-Losada and Balmain, 2003). In WT epidermis and papillomas, Par3 and aPKC localize to intercellular adhesions. In the absence of Par3, papilloma formation and growth is reduced, which correlates with mislocalization of aPKC and components of the Ras pathway, impaired proliferation and survival signaling, and increased apoptosis, indicating tumor-promoting functions of Par3. In contrast, *Par3* KO mice develop significantly more KAs, suggesting a tumor-suppressive function of Par3 in hair follicular cells giving rise to KAs. This highlights opposing functions of Par3 in tumorigenesis depending on the tumor origin.

established human SCCs, in contrast to KAs (Figures 6G, 6H, and S4E), suggesting that the impact of Par3 expression on SCC formation is different as compared to KA formation. This leaves the possibility that Par3 function can be replaced by as yet unknown proteins in SCC but not KA formation.

The origin and development of KAs are not well understood. Proliferating cells of the basal and suprabasal layers of the interfollicular epidermis and the subsets of cells in the hair follicle each face a different microenvironment, which may eventually define the tumor outcome in pathologic conditions. Predominant expression of oncogenic Ras in differentiated interfollicular keratinocytes and subsequent tumor promotion induces papillomas (Bailleul et al., 1990; Greenhalgh et al., 1993; Owens and Watt, 2003). In contrast, expression of Ras in basal cells of the hair follicle results in the formation of KAs and SCCs that are independent of exogenous tumor promotion (Brown et al., 1998), indicating that the cell of KA origin resides in the hair follicle and shows little differentiation (Perez-Losada and Balmain, 2003). Par3 is expressed throughout the interfollicular epidermis and hair follicle but may act at different intracellular sites in cells giving rise to papillomas and KAs, respectively. Such cell type specific functions could explain the opposing tumor outcome observed in *Par3* KO mice (Figure 6D). While the formation of papillomas correlates with robust Par3 expression and localization to cell-cell contacts (Figures 1G and 6E), Par3 is strongly reduced in KAs and is rarely found at intercellular contact sites (Figure 6E). The differential outcome of Par3 deficiency on papilloma versus KA formation in vivo intriguingly parallels our observation that Par3 promotes growth and survival signaling in vitro only when cell-cell contacts are established. At LC conditions when Par3 is not enriched at cellular junctions it does not stimulate ERK, as *Par3* KO cells at these conditions show ERK activity equal to WT cells (Figure S3A). This suggests that junctional, but not cytoplasmic Par3, promotes cell survival and growth signaling, possibly by recruiting other proteins to intercellular adhesions. Indeed, we found that several components of the Ras-MAPK signaling pathway, including Ras, its GEF Sos2, and its effector pERK, localize to cell-cell contacts

(G) PAR3 expression in human epidermis and KA (paraffin sections). Colored boxes in overview indicate insets of KA (black) and epidermal (red) tissue. Scale bar, 100 μm.

(H) Quantification of PAR3 expression in human KAs and SCCs compared to adjacent epidermis (cryo sections). Related examples of micrographs see Figure S4B. Mean ± SEM; $^{**}p < 0.02$; $^{***}p < 0.001$.

See also Figure S4 and Table S1.

in a Par3-dependent manner, and loss of Par3 results in reduced ERK activation in cells with established cell-cell contacts. Interestingly, in human intestinal epithelial cells cortical active ERK1/2 has been recently associated with a stronger EGF-induced ERK activation as compared to cytoplasmic ERK in under-differentiated cells (Basuroy et al., 2006; Aggarwal et al., 2011). Moreover, we found that Par3 associates with aPKC in keratinocytes and observed Par3-dependent localization of aPKC to intercellular contacts both in vitro and in vivo. Importantly, in *Drosophila*, cortical aPKC induces neuroblast overgrowth, whereas cytoplasmic aPKCι is associated with poor prognosis in human ovarian and breast cancer (Grifoni et al., 2007; Kojima et al., 2008). aPKCι also mediates tumor cell growth, transformation and invasion in vitro and in experimental Ras-induced lung tumorigenesis likely by stimulating ERK signaling (Regala et al., 2009). Interestingly, ERK activity in *Par3* KO keratinocytes can be efficiently blocked by aurothiomalate (ATM) (Figure S3C), a small molecule inhibitor of the aPKC/Par6 interaction previously demonstrated to block oncogenic functions of aPKC in lung cancer (Erdogan et al., 2006; Stallings-Mann et al., 2006), indicating that in the absence of Par3 cytoplasmic aPKC can mediate ERK activity via interaction with Par6. Together, these data suggest that junctional aPKC contributes to Par3- and Ras-mediated growth and survival during papilloma formation, whereas increased KA formation as a result of loss of Par3 may involve oncogenic activities of cytoplasmic aPKC, likely in complex with Par6.

The Ras-based skin tumor model combined with loss of Par3 presented in this study provides a robust tool to study keratoacanthoma formation. Preclinical and clinical studies testing inhibitors of mutant BRaf to restrict metastatic growth of solid tumors recently provided evidence that human KAs also result from deregulated Ras signaling: 15%–31% of patients treated with the BRaf inhibitor vemurafenib (PLX4032, Roche, and Plexxikon) develop KAs or SCCs as adverse effect (Flaherty et al., 2010; Chapman et al., 2011). The *HRas* codon 61 mutation has recently, among other *Ras* mutations, been confirmed in those drug-promoted KAs harboring WT *BRaf* alleles (Oberholzer et al., 2012; Su et al., 2012). Moreover, in the DMBA/TPA mouse tumor model, which similarly induces *HRas* codon 61 mutations, vemurafenib treatment accelerated the growth of Ras-containing lesions accompanied by increased MAPK activity (Su et al., 2012), confirming that verumafenib indeed activates growth signaling in *Ras* mutant cells in vivo. BRaf inhibitors likely induce the formation of Raf dimers that leads to paradoxic CRaf activation and consequently MAPK pathway hyperactivation (Poulikakos et al., 2010; Hatzivassiliou et al., 2010; Heidorn et al., 2010). The observation of reduced Par3 expression in both mouse and human KAs (Figures 6E, 6F, 6H, and S4B) and of CRaf hyperactivation in Par3-deficient KAs (Figure 7A) therefore suggests a common mechanism of KA formation in human and mice involving *Ras* mutation and Par3 dysfunction.

In conclusion, we identified a tumor type-dependent function of Par3 in Ras-mediated skin cancer, with (pro)oncogenic and tumor-suppressive activity during papilloma and KA formation, respectively (Figure 7C). Our data underscore an important context-dependent role of polarity proteins in mammalian tumorigenesis and underlying signaling pathways. Our data further suggest that polarity protein dysfunction may differentially affect the tumor outcome in other tissues depending on the cellular context. In addition, we present a mouse tumor model of KA formation that recapitulates a human skin cancer of increasing clinical relevance.

EXPERIMENTAL PROCEDURES

Epidermal Par3 Deletion

To delete *Par3* specifically in the epidermis and hair follicle, mice with a conditional *Par3* allele (Hirose et al., 2006) were crossed with *K14-Cre(neo)* (Huelsken et al., 2001) mice. For further details see Supplemental Information. All experiments involving animals in this study were reviewed and approved by the Animal Experiments and Ethics Committee (DEC) of the Netherlands Cancer Institute and conformed the regulatory standards of the Dutch Act on Use of Laboratory animals.

Skin Tumorigenesis Experiments

Two independent DMBA/TPA-mediated two-stage chemical skin carcinogenesis experiments were performed as previously described (Malliri et al., 2002). 25 WT (*K14-Cre*$^{+}$;*Par3*$^{wt/wt}$) and 27 *Par3* cKO (*K14-Cre*$^{+}$;*Par3*$^{flox/flox}$) mice of mixed genetic background have been used initially, and a repeat experiment comprised 17 WT and 11 *Par3* cKO mice of FVB background (F8). Results were essentially the same, and representative data are shown. Mice were examined twice a week, and tumor numbers and sizes were measured. At termination, normal skin, tumor tissue, and other organs were snap-frozen or fixed for further analyses.

Tissue Processing, Histology, and Immunohistochemistry

Hematoxylin and eosin (H&E) staining and immunohistochemistry of normal skin and skin tumors were performed on formalin- or EAF-fixed 4 μm paraffin sections or 8 μm cryosections. For biochemical analysis, normal skin and tumor tissue was minced, collected in a tube and supplemented with radioimmunoprecipitation assay buffer containing protease inhibitor cocktail (SIGMA) and phosphatase inhibitors (Roche). The tissue was dissociated using a tissue homogenizator, incubated for 10 min on ice and then cleared by centrifugation. Alternatively, proteins were isolated in parallel to DNA and RNA using TRIzol Reagent according to the manufacturer's protocol (Invitrogen). Epidermal lysates were prepared from newborn and adult epidermis. Newborn epidermis was separated from the dermis after floating back-skin on ice-cold 0.5 M ammonium thiocyanate/PBS for 20 min, and adult epidermis was mechanically scraped-off the dermis. The epidermis was subsequently minced and proteins were isolated using TRIzol Reagent.

The use of human specimen involved in this study was approved by the institutional review board at the Medical Faculty of the University of Cologne. Written informed consent was obtained from patients in accordance with institutional review board policies and procedures for research dealing with tumor specimen.

Apoptosis in Mouse Epidermis

DMBA (25 ug) or TPA (10^{-4}M) or both were applied to the backs of six mice of each genotype, and mice were killed 24 hr later. Apoptotic cells in skin biopsy specimen were detected by immunohistochemistry against cleaved caspase-3. The number of positively stained cells within the epidermis was evaluated per millimeter of basement membrane using phase-contrast microscopy of at least 60 nonserial tissue sections and subsequent image analysis (Aperio, Slidepath).

Cell Proliferation in Mouse Epidermis

Control and *Par3* cKO littermates (n = 6 each) were treated with TPA alone (10^{-4} M), DMBA alone (25 μg) for 24 hr, or were treated with DMBA and subsequently treated with two doses of TPA over 7 days. At the end of the experiment, mice were injected intraperitoneally with BrdU (Sigma) at 50 mg/kg, and killed 3 hr later. Using an anti-BrdU antibody (DAKO), the number of BrdU-stained cells within the epidermis was evaluated per millimeter of basement membrane using phase-contrast microscopy of at least 30 nonserial tissue sections and subsequent image analysis (Aperio and Slidepath).

Similarly, the thickness of the interfollicular epidermis was measured as readout for net proliferation.

Antibodies

The following antibodies were used in this study: rabbit polyclonal antibodies directed against Par3 aa712-936 (Iden et al., 2006) and commercial sources (Millipore/Upstate, no. 07-330, and SIGMA-Aldrich HPA030443), aPKCzeta (C-20, Santa Cruz), PARP (no. 9542), phospho-p42/44 (Cell Signaling, no. 4370), pAkt Ser473 (Cell Signaling, no. 4060), ZO-1 (no. 61-7300, Invitrogen), cleaved caspase-3 (Cell Signaling, no. 9661), mouse-specific caspase 9 (Cell Signaling no. 9504), cyclin D1 (Upstate no. 05-815), Tiam1 (C-16, Santa Cruz), Keratin-1 (Covance, PRB149P), Tom20 (Santa Cruz, no. sc-11415), murine Bax (BD PharMingen, no. 554106), HA-tag (Y-11, Santa Cruz, no. sc-805), pcRAF Ser338 (Cell Signaling, no. 9427), Sos2 (Santa Cruz, no. sc-258), mouse monoclonal antibodies against ZO-1 (Invitrogen, no. 33-9100), Ras (BD Transduction, no. R02120), Ras (Ab-3, Millipore, no. OP-40), Rac1 (Upstate, clone 23A8, no. 05-389), ERK2 (BD Transduction, no. 610103), α-tubulin (SIGMA-Aldrich, no. T-5168, clone B-5-1-2), BrdU (DakoCytomation, no. MO744), E-cadherin (no. 610181, BD Transduction), β-catenin (BD Transduction, no. 610154), active Bax (clone 6A7, BD Pharmingen no. 556467), aPKCzeta (H-1, Santa Cruz, no. sc-17781), aPKCl/i (BD Transduction Labs, no. P20520, clone 23), HA-tag (12CA5, own hybridoma), HA-probe (F-7, Santa Cruz, no. sc-7392). For secondary detection, species-directed antibodies conjugated with AlexaFluor fluorophors (Molecular Probes) or horse radish peroxidase (GE Healthcare) were used for immunofluorescence or western blot studies, respectively.

Isolation of Primary Mouse Keratinocytes

Primary murine keratinocytes were isolated from newborn *Par3*$^{flox/flox}$ mice and cultured as previously described (Mertens et al., 2005), whereby epidermal and dermal fractions were kept separate. Primary and SV40-immortalized epidermal and dermal cells expressing typical keratinocyte marker proteins have been used in this study. Cells were plated on Collagen I-coated dishes and used up to passage 20. *Par3* was deleted by retroviral infection with self-excising Cre recombinase (Silver and Livingston, 2001). Corresponding parental cell isolations of identical passage served as control.

Tumor Promoter Treatments In Vitro

Keratinocytes were growth factor-starved for 2 hr, and then treated with either 40 ng/ml murine epidermal growth factor (BD Biosciences) or 0.68 μM TPA (SIGMA-Aldrich) for indicated time points. Lysates of adherent and floating cells were combined for subsequent biochemical analysis.

Colony Formation Assays

Cold growth factor-reduced matrigel (BD Biosciences) was diluted 1:1 in keratinocyte culture medium and 30 μl were pipetted into a chilled 96 well plate. Subconfluent keratinocytes were harvested by trypsinization, counted and seeded into a matrigel matrix to yield a final concentration of 5×10^3 cells/ml. The matrigel:cell mix was incubated at 37°C for 45 min to solidify the matrigel. Afterward, culture medium was added to the top and replaced every second day. Colony formation was followed over a period of up to 3 weeks.

Immunofluorescence Analysis: Mono- and Multilayer Tissue

For monolayer cultures, keratinocytes were seeded on Collagen I-coated 8 well or 16 well LabTek Chamber Slides (Nunc), grown until confluency and then switched to NC levels (2mM). For analysis of multilayer cultures, keratinocytes were seeded on Collagen I-coated TransWell Filters (TransWell Clear, 0.4 μm pore size, 6.5 mm diameter, Nunc), grown to confluency and then incubated at NC levels for several days. For immunofluorescence staining, monolayer and multilayer cultures were washed twice with PBS and fixed with either PFA (4% PFA in PBS 10 min at room temperature, followed by 15 min 0.5% Triton X-100 in PBS for permeabilization) or ethanol/acetone (30 min 96% ethanol on ice, followed by 3 min incubation of ice-cold acetone at RT). Cells were blocked with 5% BSA for 1 hr at RT, and subsequently incubated with primary antibodies diluted in AB buffer (10 mM Tris-HCl, 150 mM NaCl, and 0.1% BSA) in a humidified chamber overnight at 4°C. Incubation with AlexaFluor 488- and 568-conjugated secondary antibodies (Invitrogen) and TOPRO as nuclei stain (Invitrogen) was carried out for 1 hr at room temperature in AB buffer. Immunostained cells on chamber slides were mounted in Mowiol; filters with multilayer cultures were first excised and then mounted to a glass slide.

Additional experimental procedures can be found in Supplemental Experimental Procedures.

SUPPLEMENTAL INFORMATION

Supplemental Information includes four figures, one table, and Supplemental Experimental Procedures and can be found with this article online at http://dx.doi.org/10.1016/j.ccr.2012.08.004.

ACKNOWLEDGMENTS

We thank Carien Niessen and Klaus Ebnet for critically reading the manuscript. We are grateful to the NKI facilities for experimental animals, animal pathology, and digital microscopy and to the CECAD Imaging Facility in Cologne for professional support. We acknowledge Jelle Wesseling and Mark Opdam (NKI), Cornelia Mauch and Paola Zigrino (Z2 project SFB829) for providing human skin tumor samples, and Klaus Ebnet, Carien Niessen, Susanne Vorhagen, Ian Macara, David M. Livingston, and Hamid Kashkar for constructs and reagents. Furthermore, we thank members of the Division of Cell Biology I for helpful discussions and Rehan Villani for linguistic advice. This work was supported by the European Commission (TuMIC), the Dutch Cancer Society (KWF), the excellence initiative by the German federal and state governments (CECAD Cologne), and the German Research Foundation (CRC829 and CRC832).

Received: September 26, 2011
Revised: January 31, 2012
Accepted: August 6, 2012
Published: September 10, 2012

REFERENCES

Aggarwal, S., Suzuki, T., Taylor, W.L., Bhargava, A., and Rao, R.K. (2011). Contrasting effects of ERK on tight junction integrity in differentiated and under-differentiated Caco-2 cell monolayers. Biochem. J. *433*, 51–63.

Assémat, E., Bazellières, E., Pallesi-Pocachard, E., Le Bivic, A., and Massey-Harroche, D. (2008). Polarity complex proteins. Biochim. Biophys. Acta *1778*, 614–630.

Bailleul, B., Surani, M.A., White, S., Barton, S.C., Brown, K., Blessing, M., Jorcano, J., and Balmain, A. (1990). Skin hyperkeratosis and papilloma formation in transgenic mice expressing a ras oncogene from a suprabasal keratin promoter. Cell *62*, 697–708.

Basuroy, S., Seth, A., Elias, B., Naren, A.P., and Rao, R. (2006). MAPK interacts with occludin and mediates EGF-induced prevention of tight junction disruption by hydrogen peroxide. Biochem. J. *393*, 69–77.

Bilder, D. (2004). Epithelial polarity and proliferation control: links from the Drosophila neoplastic tumor suppressors. Genes Dev. *18*, 1909–1925.

Brown, K., Strathdee, D., Bryson, S., Lambie, W., and Balmain, A. (1998). The malignant capacity of skin tumours induced by expression of a mutant H-ras transgene depends on the cell type targeted. Curr. Biol. *8*, 516–524.

Cain, R.J., and Ridley, A.J. (2009). Phosphoinositide 3-kinases in cell migration. Biol Cell. *1*, 13–29.

Chapman, P.B., Hauschild, A., Robert, C., Haanen, J.B., Ascierto, P., Larkin, J., Dummer, R., Garbe, C., Testori, A., Maio, M., et al; BRIM-3 Study Group. (2011). Improved survival with vemurafenib in melanoma with BRAF V600E mutation. N. Engl. J. Med. *364*, 2507–2516.

Chen, X., and Macara, I.G. (2005). Par-3 controls tight junction assembly through the Rac exchange factor Tiam1. Nat. Cell Biol. *7*, 262–269.

Cho, S.H., Delehedde, M., Rodriguez-Villanueva, J., Brisbay, S., and McDonnell, T.J. (2001). Bax gene disruption alters the epidermal response to ultraviolet irradiation and in vivo induced skin carcinogenesis. Int. J. Mol. Med. *7*, 235–241.

Erdogan, E., Lamark, T., Stallings-Mann, M., Jamieson, L., Pellecchia, M., Thompson, E.A., Johansen, T., and Fields, A.P. (2006). Aurothiomalate inhibits

transformed growth by targeting the PB1 domain of protein kinase Ciota. J. Biol. Chem. *281*, 38450–9.

Filmus, J., Robles, A.I., Shi, W., Wong, M.J., Colombo, L.L., and Conti, C.J. (1994). Induction of cyclin D1 overexpression by activated ras. Oncogene *9*, 3627–3633.

Finch, J.S., Albino, H.E., and Bowden, G.T. (1996). Quantitation of early clonal expansion of two mutant 61st codon c-Ha-ras alleles in DMBA/TPA treated mouse skin by nested PCR/RFLP. Carcinogenesis *17*, 2551–2557.

Flaherty, K.T., Puzanov, I., Kim, K.B., Ribas, A., McArthur, G.A., Sosman, J.A., O'Dwyer, P.J., Lee, R.J., Grippo, J.F., Nolop, K., and Chapman, P.B. (2010). Inhibition of mutated, activated BRAF in metastatic melanoma. N. Engl. J. Med. *363*, 809–819.

Greenhalgh, D.A., Rothnagel, J.A., Quintanilla, M.I., Orengo, C.C., Gagne, T.A., Bundman, D.S., Longley, M.A., and Roop, D.R. (1993). Induction of epidermal hyperplasia, hyperkeratosis, and papillomas in transgenic mice by a targeted v-Ha-ras oncogene. Mol. Carcinog. *7*, 99–110.

Grifoni, D., Garoia, F., Bellosta, P., Parisi, F., De Biase, D., Collina, G., Strand, D., Cavicchi, S., and Pession, A. (2007). aPKCzeta cortical loading is associated with Lgl cytoplasmic release and tumor growth in Drosophila and human epithelia. Oncogene *26*, 5960–5965.

Hatzivassiliou, G., Song, K., Yen, I., Brandhuber, B.J., Anderson, D.J., Alvarado, R., Ludlam, M.J., Stokoe, D., Gloor, S.L., Vigers, G., et al. (2010). RAF inhibitors prime wild-type RAF to activate the MAPK pathway and enhance growth. Nature *464*, 431–435.

Heidorn, S.J., Milagre, C., Whittaker, S., Nourry, A., Niculescu-Duvas, I., Dhomen, N., Hussain, J., Reis-Filho, J.S., Springer, C.J., Pritchard, C., and Marais, R. (2010). Kinase-dead BRAF and oncogenic RAS cooperate to drive tumor progression through CRAF. Cell *140*, 209–221.

Hirose, T., Karasawa, M., Sugitani, Y., Fujisawa, M., Akimoto, K., Ohno, S., and Noda, T. (2006). PAR3 is essential for cyst-mediated epicardial development by establishing apical cortical domains. Development *133*, 1389–1398.

Horikoshi, Y., Suzuki, A., Yamanaka, T., Sasaki, K., Mizuno, K., Sawada, H., Yonemura, S., and Ohno, S. (2009). Interaction between PAR-3 and the aPKC-PAR-6 complex is indispensable for apical domain development of epithelial cells. J. Cell Sci. *122*, 1595–1606.

Huang, L., and Muthuswamy, S.K. (2010). Polarity protein alterations in carcinoma: a focus on emerging roles for polarity regulators. Curr. Opin. Genet. Dev. *20*, 41–50.

Huelsken, J., Vogel, R., Erdmann, B., Cotsarelis, G., and Birchmeier, W. (2001). beta-Catenin controls hair follicle morphogenesis and stem cell differentiation in the skin. Cell *105*, 533–545.

Iden, S., and Collard, J.G. (2008). Crosstalk between small GTPases and polarity proteins in cell polarization. Nat. Rev. Mol. Cell Biol. *9*, 846–859.

Iden, S., Rehder, D., August, B., Suzuki, A., Noda, K., Nagafuchi, A., Wolburg-Buchholz, K., Wolburg, H., Ohno, S., et al. (2006). A distinct PAR polarity protein complex physically associated with VE-cadherin in vertebrate endothelial cells. EMBO Rep. *7*, 1239–1246.

Itoh, N., Nakayama, M., Nishimura, T., Fujisue, S., Nishioka, T., Watanabe, T., and Kaibuchi, K. (2010). Identification of focal adhesion kinase (FAK) and phosphatidylinositol 3-kinase (PI3-kinase) as Par3 partners by proteomic analysis. Cytoskeleton (Hoboken). *5*, 297–308.

Kern, F., Niault, T., and Baccarini, M. (2011). Ras and Raf pathways in epidermis development and carcinogenesis. Br. J. Cancer *104*, 229–234.

Kojima, Y., Akimoto, K., Nagashima, Y., Ishiguro, H., Shirai, S., Chishima, T., Ichikawa, Y., Ishikawa, T., Sasaki, T., Kubota, Y., et al. (2008). The overexpression and altered localization of the atypical protein kinase C lambda/iota in breast cancer correlates with the pathologic type of these tumors. Hum. Pathol. *39*, 824–831.

Macara, I.G. (2004). Par proteins: partners in polarization. Curr. Biol. *14*, R160–R162.

Malliri, A., van der Kammen, R.A., Clark, K., van der Valk, M., Michiels, F., and Collard, J.G. (2002). Mice deficient in the Rac activator Tiam1 are resistant to Ras-induced skin tumours. Nature *417*, 867–871.

Mertens, A.E., Rygiel, T.P., Olivo, C., van der Kammen, R., and Collard, J.G. (2005). The Rac activator Tiam1 controls tight junction biogenesis in keratinocytes through binding to and activation of the Par polarity complex. J. Cell Biol. *170*, 1029–1037.

Morais-de-Sá, E., Mirouse, V., and St Johnston, D. (2010). aPKC phosphorylation of Bazooka defines the apical/lateral border in Drosophila epithelial cells. Cell *141*, 509–523.

Murray, N.R., Kalari, K.R., and Fields, A.P. (2011). Protein kinase Cι expression and oncogenic signaling mechanisms in cancer. J. Cell. Physiol. *226*, 879–887.

Nolan, M.E., Aranda, V., Lee, S., Lakshmi, B., Basu, S., Allred, D.C., and Muthuswamy, S.K. (2008). The polarity protein Par6 induces cell proliferation and is overexpressed in breast cancer. Cancer Res. *68*, 8201–8209.

Oberholzer, P.A., Kee, D., Dziunycz, P., Sucker, A., Kamsukom, N., Jones, R., Roden, C., Chalk, C.J., Ardlie, K., Palescandolo, E., et al. (2012). RAS mutations are associated with the development of cutaneous squamous cell tumors in patients treated with RAF inhibitors. J. Clin. Oncol. *30*, 316–321.

Owens, D.M., and Watt, F.M. (2003). Contribution of stem cells and differentiated cells to epidermal tumours. Nat. Rev. Cancer *3*, 444–451.

Pagliarini, R.A., and Xu, T. (2003). A genetic screen in Drosophila for metastatic behavior. Science *302*, 1227–1231.

Partanen, J.I., Tervonen, T.A., Myllynen, M., Lind, E., Imai, M., Katajisto, P., Dijkgraaf, G.J., Kovanen, P.E., Mäkelä, T.P., Werb, Z., and Klefström, J. (2012). Tumor suppressor function of Liver kinase B1 (Lkb1) is linked to regulation of epithelial integrity. Proc. Natl. Acad. Sci. USA *109*, E388–E397.

Pearson, H.B., Perez-Mancera, P.A., Dow, L.E., Ryan, A., Tennstedt, P., Bogani, D., Elsum, I., Greenfield, A., Tuveson, D.A., Simon, R., and Humbert, P.O. (2011). SCRIB expression is deregulated in human prostate cancer, and its deficiency in mice promotes prostate neoplasia. J. Clin. Invest. *121*, 4257–4267.

Pegtel, D.M., Ellenbroek, S.I., Mertens, A.E., van der Kammen, R.A., de Rooij, J., and Collard, J.G. (2007). The Par-Tiam1 complex controls persistent migration by stabilizing microtubule-dependent front-rear polarity. Curr. Biol. *17*, 1623–1634.

Perez-Losada, J., and Balmain, A. (2003). Stem-cell hierarchy in skin cancer. Nat. Rev. Cancer *3*, 434–443.

Poulikakos, P.I., Zhang, C., Bollag, G., Shokat, K.M., and Rosen, N. (2010). RAF inhibitors transactivate RAF dimers and ERK signalling in cells with wild-type BRAF. Nature *464*, 427–430.

Regala, R.P., Davis, R.K., Kunz, A., Khoor, A., Leitges, M., and Fields, A.P. (2009). Atypical protein kinase Ciota is required for bronchioalveolar stem cell expansion and lung tumorigenesis. Cancer Res. *69*, 7603–7611.

Reischauer, S., Levesque, M.P., Nüsslein-Volhard, C., and Sonawane, M. (2009). Lgl2 executes its function as a tumor suppressor by regulating ErbB signaling in the zebrafish epidermis. PLoS Genet. *5*, e1000720.

Reuter, J.A., Ortiz-Urda, S., Kretz, M., Garcia, J., Scholl, F.A., Pasmooij, A.M., Cassarino, D., Chang, H.Y., and Khavari, P.A. (2009). Modeling inducible human tissue neoplasia identifies an extracellular matrix interaction network involved in cancer progression. Cancer Cell *15*, 477–488.

Rizzo, M.A., Kraft, C.A., Watkins, S.C., Levitan, E.S., and Romero, G. (2001). Agonist-dependent traffic of raft-associated Ras and Raf-1 is required for activation of the mitogen-activated protein kinase cascade. J. Biol. Chem. *276*, 34928–34933.

Silver, D.P., and Livingston, D.M. (2001). Self-excising retroviral vectors encoding the Cre recombinase overcome Cre-mediated cellular toxicity. Mol. Cell *8*, 233–243.

Stallings-Mann, M., Jamieson, L., Regala, R.P., Weems, C., Murray, N.R., and Fields, A.P. (2006). A novel small-molecule inhibitor of protein kinase Ciota blocks transformed growth of non-small-cell lung cancer cells. Cancer Res. *66*, 1767–1774.

Su, F., Viros, A., Milagre, C., Trunzer, K., Bollag, G., Spleiss, O., Reis-Filho, J.S., Kong, X., Koya, R.C., Flaherty, K.T., et al. (2012). RAS mutations in cutaneous squamous-cell carcinomas in patients treated with BRAF inhibitors. N. Engl. J. Med. *366*, 207–215.

Vaahtomeri, K., and Mäkelä, T.P. (2011). Molecular mechanisms of tumor suppression by LKB1. FEBS Lett. *585*, 944–951.

Van Laethem, A., Van Kelst, S., Lippens, S., Declercq, W., Vandenabeele, P., Janssens, S., Vandenheede, J.R., Garmyn, M., and Agostinis, P. (2004). Activation of p38 MAPK is required for Bax translocation to mitochondria, cytochrome c release and apoptosis induced by UVB irradiation in human keratinocytes. FASEB J. *18*, 1946–1948.

Wang, Z., Pedersen, E., Basse, A., Lefever, T., Peyrollier, K., Kapoor, S., Mei, Q., Karlsson, R., Chrostek-Grashoff, A., and Brakebusch, C. (2010). Rac1 is crucial for Ras-dependent skin tumor formation by controlling Pak1-Mek-Erk hyperactivation and hyperproliferation in vivo. Oncogene *29*, 3362–3373.

Yoshimura, T., Arimura, N., and Kaibuchi, K. (2006). Signaling networks in neuronal polarization. J. Neurosci. *26*, 10626–10630.

Zhan, L., Rosenberg, A., Bergami, K.C., Yu, M., Xuan, Z., Jaffe, A.B., Allred, C., and Muthuswamy, S.K. (2008). Deregulation of scribble promotes mammary tumorigenesis and reveals a role for cell polarity in carcinoma. Cell *135*, 865–878.

Cancer Cell
Article

A Small Molecule Inhibitor of Ubiquitin-Specific Protease-7 Induces Apoptosis in Multiple Myeloma Cells and Overcomes Bortezomib Resistance

Dharminder Chauhan,[1,9,*] Ze Tian,[1,9] Benjamin Nicholson,[2] K.G. Suresh Kumar,[2] Bin Zhou,[3] Ruben Carrasco,[1] Jeffrey L. McDermott,[2] Craig A. Leach,[2] Mariaterresa Fulcinniti,[1] Matthew P. Kodrasov,[2] Joseph Weinstock,[2] William D. Kingsbury,[2] Teru Hideshima,[1] Parantu K. Shah,[1] Stephane Minvielle,[4] Mikael Altun,[5] Benedikt M. Kessler,[6] Robert Orlowski,[7] Paul Richardson,[1] Nikhil Munshi,[1,8] and Kenneth C. Anderson[1,*]

[1]Department of Medical Oncology, The LeBow Institute for Myeloma Therapeutics and Jerome Lipper Myeloma Center, Dana Farber Cancer Institute, Harvard Medical School, Boston, MA 02215, USA
[2]Progenra, Inc., Malvern, PA 19355, USA
[3]Institute for Nutritional Sciences, Shanghai Institute for Biological Sciences, Chinese Academy of Sciences, Shanghai, China 200031
[4]Inserm U892, Universite de Nantes, 44200 Nantes, France
[5]Department of Medical Biochemistry and Biophysics, Karolinska Institute, 171 77 Stockholm, Sweden
[6]Nuffield Department of Medicine, University of Oxford, Roosevelt Drive, Oxford OX3 7BN, UK
[7]Department of Lymphoma and Myeloma, The University of Texas M.D. Anderson Cancer Center, Houston, TX 77030, USA
[8]Veterans Administration Boston Healthcare System, Boston, MA 02115, USA
[9]These authors contributed equally to this work
*Correspondence: dharminder_chauhan@dfci.harvard.edu (D.C.), kenneth_anderson@dfci.harvard.edu (K.C.A.)
http://dx.doi.org/10.1016/j.ccr.2012.08.007

SUMMARY

Bortezomib therapy has proven successful for the treatment of relapsed/refractory, relapsed, and newly diagnosed multiple myeloma (MM); however, dose-limiting toxicities and the development of resistance limit its long-term utility. Here, we show that P5091 is an inhibitor of deubiquitylating enzyme USP7, which induces apoptosis in MM cells resistant to conventional and bortezomib therapies. Biochemical and genetic studies show that blockade of HDM2 and p21 abrogates P5091-induced cytotoxicity. In animal tumor model studies, P5091 is well tolerated, inhibits tumor growth, and prolongs survival. Combining P5091 with lenalidomide, HDAC inhibitor SAHA, or dexamethasone triggers synergistic anti-MM activity. Our preclinical study therefore supports clinical evaluation of USP7 inhibitor, alone or in combination, as a potential MM therapy.

INTRODUCTION

Normal cellular homeostasis is maintained by a balanced regulation of protein synthesis and degradation. The ubiquitin proteasome system (UPS) is a nonlysosomal intracellular protein degradation pathway mediated via proteasome holoenzyme, ubiquitin ligases, and deubiquitylating (DUB) enzymes (Hershko, 2005). Specifically, the covalent attachment of ubiquitin to target substrates leads to protein degradation via the multicatalytic 26S proteasome complex (Adams, 2004; Ciechanover, 2005); conversely, the ubiquitylation process can be reversed by DUBs, which specifically cleave the isopeptide bond at the C terminus of Ub (Nicholson et al., 2008). Deregulation of the UPS pathway is linked to the pathogenesis of various human diseases (Adams, 2004; Hoeller et al., 2006); therefore, inhibitors of the UPS pathways, either at the level of proteasome, ubiquitylating, or DUB enzymes offers great promise as a novel therapeutic strategy.

Indeed, preclinical and clinical studies provided the basis for FDA approval of the first-in-class proteasome inhibitor bortezomib for treatment of multiple myeloma (MM) (Richardson et al., 2003). Even though bortezomib therapy is a major advance, it

Significance

Deregulation of the ubiquitin-proteasome system (UPS) is linked to pathogenesis of various human diseases, including cancer. Targeting the proteasome has proven to be a successful therapy in multiple myeloma (MM) patients. Recent research efforts led to the discovery of newer agents that target enzymes modulating protein ubiquitin-conjugation/deconjugation rather than the proteasome itself, with the goal of generating more specific and less toxic antitumor agents. Here, we utilized both in vitro and in vivo MM xenograft models to show antitumor efficacy of a small molecule inhibitor of ubiquitin-specific protease-7 (USP7) P5091. Our preclinical data showing efficacy of P5091 in MM disease models provides the framework for clinical evaluation of USP7 inhibitors to improve patient outcome in MM.

has been associated with possible off-target toxicities and the development of drug-resistance (Lonial et al., 2005). More recent efforts have focused on the discovery and development of small molecule inhibitors of other major components of UPS, including inhibitors of DUBs, E1-conjugating enzyme, or E3 ubiquitin ligase. Among these, DUBs have emerged as a potential therapeutic target, given their role in several human diseases (Nicholson et al., 2007).

USP7 regulates key biological signaling pathways in tumorigenesis (Everett et al., 1997; Hu et al., 2002; Li et al., 2002; Nicholson et al., 2007), and its overexpression in prostate cancer correlates with tumor aggressiveness (Song et al., 2008). *MDM2*, a murine double minute oncogene (human ortholog *HDM2*), is a primary substrate of USP7 and negatively regulates the tumor suppressor protein p53 (Cummins et al., 2004; Li et al., 2004). MDM2 ubiquitylates p53 and targets it for proteasome-mediated degradation. Under normal conditions USP7 stabilizes MDM2 levels, which consequently drives p53 ubiquitylation and subsequent degradation. Although MDM2 has autoubiquitylase activity (Fang et al., 2000; Stommel and Wahl, 2004) and a short half-life, which can be abrogated by USP7, a more recent in vivo knockin model of inactive *MDM2* showed that it is still efficiently ubiquitylated through self-ubiquitylation-independent mechanisms (Itahana et al., 2007). Genetic ablation of *USP7* using siRNA or somatic knockout (KO) prevents USP7 from deubiquitylating MDM2, resulting in stabilization of p53 (Cummins et al., 2004; Kon et al., 2010; Li et al., 2004; Meulmeester et al., 2005). Furthermore, p53 protein levels were elevated in $USP7^{-/-}$embryos, and the embryonic lethality of $USP7^{-/-}$ mice was delayed in a $p53^{-/-}$ background (Kon et al., 2010). The functional consequences of inhibiting USP7 therefore include decreased HDM2 levels with accumulation of p53, induction of growth arrest via p21, and cell death. Mutations or deletions of p53 are late events in MM, and activation of p53 may offer a novel therapeutic strategy (Anderson, 2007). USP7 also deubiquitylates other cancer targets (PTEN, FOXO4, or claspin) and plays a role in DNA replication, apoptosis, and endosomal organization (Nicholson et al., 2007). Therapeutic strategies using USP7 inhibitors allow for specific targeting of the UPS and are therefore less likely to trigger off-target activities and associated toxicities.

Here, we demonstrate the efficacy of a small molecule inhibitor of USP7 P5091 in MM using both in vitro and in vivo models. These findings provide the proof-of-concept for evaluation of USP7 inhibitors as anti-MM agents.

RESULTS AND DISCUSSION

P5091 Is a Selective Inhibitor of USP7

P5091 is a trisubstituted thiophene with dichlorophenylthio, nitro, and acetyl substituents mediating anti-USP7 activity (Figure 1A). P5091 was discovered using a ubiquitin-phospholipase A_2 enzyme (Ub-PLA_2) reporter assay (Figure 1B) in a high-throughput screening for inhibitors of USP7 from a diversity-based library of small molecules. The structure-activity relationship (SAR) data for selected analogs of P5091 is shown in Figure 1C. Comparison of the halogen substituents of the 5-arylsulfanyl moiety of the 2-acetyl-4-nitro-5-arylsulfanylthiophenes demonstrated that the unsubstituted phenyl analog 1 was not active as a USP7 antagonist, whereas all of the 5- mono and dihalo phenylsulfanylthiophenes, including P5091 (5), exhibited USP7 inhibitory activity. In addition, the dichloro analogs (5–7) and difluoro analog were more potent than the monochloro analogs (2–4). Initial exploration of the R2 position (9–12) did not result in enhanced potency. Importantly, P5091 (Compound 5; Figure 1C) exhibited potent, specific, and selective deubiquitylating activity against USP7 (EC_{50} = 4.2 ± 0.9 μM). In contrast, P5091 did not inhibit other DUBs or other families of cysteine proteases tested (EC_{50} > 100 μM) (Figure 1D). P22074, an inactive analog of P5091, served as a negative control (Figure 1D).

To determine the USP7 inhibitory activity of P5091 in living cells, we performed competition assays between P5091 and the ubiquitin (Ub) active site probe Ub-vinyl methyl ester (HA-UbVME) (Borodovsky et al., 2002). P5091 inhibited the labeling of USP7 with HA-UbVME in a concentration-dependent manner (Figure 1E). Untreated cell lysates incubated with Ub-probes exhibited Ub-USP7 conjugate formation, as reflected by the increase in mass of USP7 of ~10 kDa. In contrast, Ub-USP7 conjugate formation was inhibited in cell lysates from P5091-treated cells at concentrations as low as 5–10 μM P5091, with a concomitant increase in the unlabeled free form of USP7. No gross difference in the labeling of other DUBs with Ub-VME was observed, even at 40 μM. The residual active USP7 may relate to the irreversibility-related potency of HA-Ub probe versus P5091 and/or kinetics of labeling of HA-Ub probe against USP7. P5091 treatment did not inhibit other DUBs, such as USP5, UCHL1, or UCHL3 (Figure S1A available online). These data demonstrate the P5091 activity against USP7 in the cellular environment.

Isopeptidase activity analyses shows that USP7 efficiently cleaves high molecular weight polyubiquitin chains (Ub7- and K48-linked ubiquitin chains), and USP7-mediated cleavage of these chains is inhibited in a dose-dependent manner by P5091 (Figure 1F). Moreover, P5091 inhibits USP7- but not USP2- or USP8-mediated cleavage of poly K48-linked ubiquitin chains (visualized by the presence or absence of monoubiquitin) (Figure S1B).

USP7 Knockout Renders Cells Resistant to P5091

To further determine whether the inhibitory effect of P5091 is mediated via USP7, we utilized human cells (HCT116 $USP7^{-/-}$) in which the *USP7* is disrupted by targeted homologous recombination (Cummins et al., 2004). P5091 decreased the viability of HCT116 (WT) cells in a time- and concentration-dependent manner; conversely, a marked reduction in P5091 cytotoxic activity was observed against HCT116 $USP7^{-/-}$ cells (Figure 1G). HCT116 $USP7^{-/-}$ cells are slow proliferating cells compared to HCT116 (WT). To exclude the possibility that the differences observed during P5091 treatment is not due to growth rate, cells were serum starved and examined for P5091 effects. In agreement with our results in Figure 1G, P5091 decreased the viability of HCT116 (WT) cells, whereas cytotoxic activity of P5091 was significantly blocked in $USP7^{-/-}$ cells (Figure S1C). $USP7^{-/-}$ mice die during early embryonic development (Kon et al., 2010). The KO selection process in HCT116 $USP7^{-/-}$ cells can contribute to the development of a compensatory mechanism for the loss of USP7 for survival. Nonetheless, our data using HCT116 $USP7^{-/-}$ cells suggests that P5091 targets USP7.

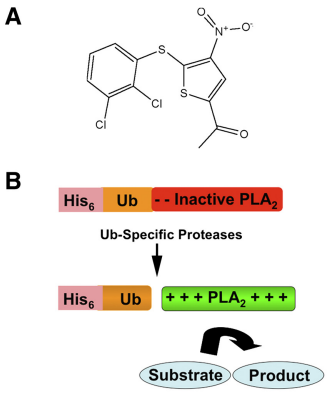

C

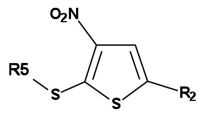

Compound #	R2	R5	USP7 inhibition EC_{50} (μM)
1	Acetyl	phenyl	>50
2	Acetyl	2-chlorophenyl	12.9 ± 4.3
3	Acetyl	3-chlorophenyl	7.0 ± 2.1
4	Acetyl	4-chlorophenyl	11.8 ± 3.0
5	Acetyl	2,3-dichlorophenyl	4.2 ± 0.9
6	Acetyl	3,5-dichlorophenyl	6.4 ± 1.4
7	Acetyl	2,4-dichlorophenyl	6.5 ± 2.6
8	Acetyl	2,4-difluorophenyl	8.0 ± 2.8
9	1-hydroxyethyl	2,4-dichlorophenyl	20.1 ± 4.3
10	Ethyl	2,3-dichlorophenyl	>50
11	n-butyl	2,4-dichlorophenyl	13.9 ± 4.2

D

Enzyme	EC_{50} (μM)	
	P5091	P22074
USP2c	>100	>100
USP5	>100	>100
USP7	4.2±0.9	>100
USP8c	>100	>100
USP15	>100	>100
USP20	>100	>100
USP21	>100	>100
USP28	>100	>100
UCH-L1	>100	>100
Caspase 3	>100	>100
Cathepsin K	>100	>100
Calpain 1	>100	>100
MMP13	>100	>100
Cathepsin D	>100	>100
EK_L	>100	>100
PLA_2	>100	>100

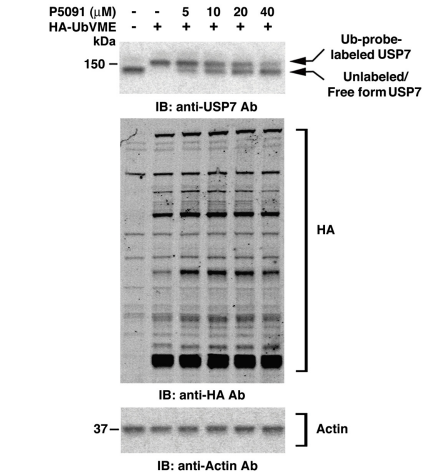

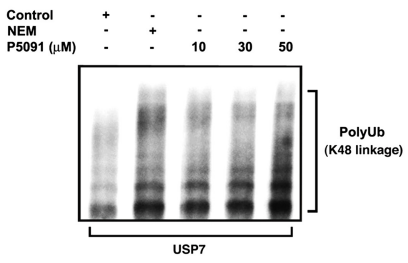

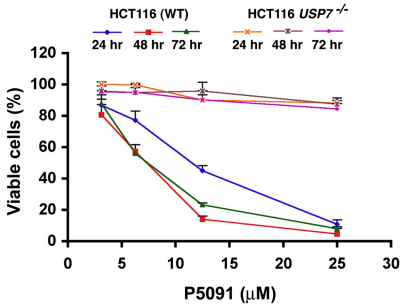

Figure 1. P5091 Is a Selective Inhibitor of USP7 Activity

(A) Chemical structure of P5091.

(B) Schematic representation of Ub-PLA_2 isopeptidase reporter assay: cleavage by the isopeptidase at the carboxy-terminal glycine of the Ub releases catalytically active PLA_2, which liberate a quantifiable fluorescent product in the presence of its substrate.

(C) Structure-activity relationship data for selected analogs of P5091 (compound 1 = P22074 and compound 5 = P5091).

(D) P5091 demonstrates potent and specific inhibition of USP7 in vitro versus other DUBs and proteases.

(E) HEK293T cells were treated with DMSO or P5091; crude cell extracts were labeled with indicated UbVME probe, followed by immunoblotting (IB) with indicated antibodies.

(F) P5091 inhibits higher molecular weight polyubiquitin chain cleavage in a dose-dependent manner. NEM (N-ethyl maleimide) is a nonspecific inhibitor of USP7 and served as control.

(G) HCT116 (WT) and HCT116 *USP7*$^{-/-}$ cells were treated with vehicle or indicated concentrations of P5091 for 24, 48, and 72 hr and then analyzed for viability using MTT assay (mean ± SD; n = 3). Error bars indicate SD.

See also Figure S1.

P5091 Targets USP7 Substrate HDM2

Genetic ablation of USP7 destabilizes its substrate, HDM2 (Cummins et al., 2004; Li et al., 2004). U20S cells were transiently transfected with HA-Ub constructs, and endogenous HDM2 ubiquitylation was analyzed by pulling down ubiquitylated proteins using Tandem Ubiquitin Binding Entities (TUBEs) (Hjerpe et al., 2009). Empty-vector/vehicle served as a control to determine the effects of HA-Ub alone on HDM2 ubiquitination (Figure 2A, lane 2, empty vector versus lane 3, HA-Ub). HA-Ub transfection alone slightly increases HDM2-ubiquitination versus empty-vector. Importantly, addition of P5091 markedly increases HDM2 ubiquitination, in particular, the band between 130–170 (lane 3 versus lane 4). The band between 130–170 kDa likely represents a predominantly multiubiquitylated form of HDM2; a similar banding pattern has been recently reported (Zhao et al., 2011). The mock pulldown (lane 1) is negative control for TUBE1 using unconjugated Agarose. Alternatively, we asked whether HDM2 stabilization is affected in the presence of P5091. P5091 accelerates the degradation of HDM2 versus control cycloheximide (CHX) alone-treated U20S cells (Figure 2B). Likewise, P5091 enhanced the degradation of HDM2 in prostate cancer cell lines (Figure S2). Together, our data suggest that USP7 inhibition by P5091 induces HDM2 polyubiquitylation and accelerates degradation of HDM2.

Prognostic relevance of USP7 in multiple myeloma proteasome inhibition has proven to be a successful treatment strategy for MM patients (Richardson et al., 2003). Because USP7 is also a component of UPS, we examined the effects of USP7 inhibition with P5091 in MM cells. Immunohistochemistry (IHC) studies using bone marrow (BM) biopsies from MM patients and normal healthy donors showed a significantly higher *USP7* expression in MM cells than in normal cells (Figure 3A). Normal plasma cells lack detectable *USP7* expression. Similar results were observed using protein extracts from MM patient tumor cells versus normal cells, and MM cell lines (Figure 3B).

We retrospectively analyzed the prognostic significance of baseline USP7 expression from BM biopsy samples on the

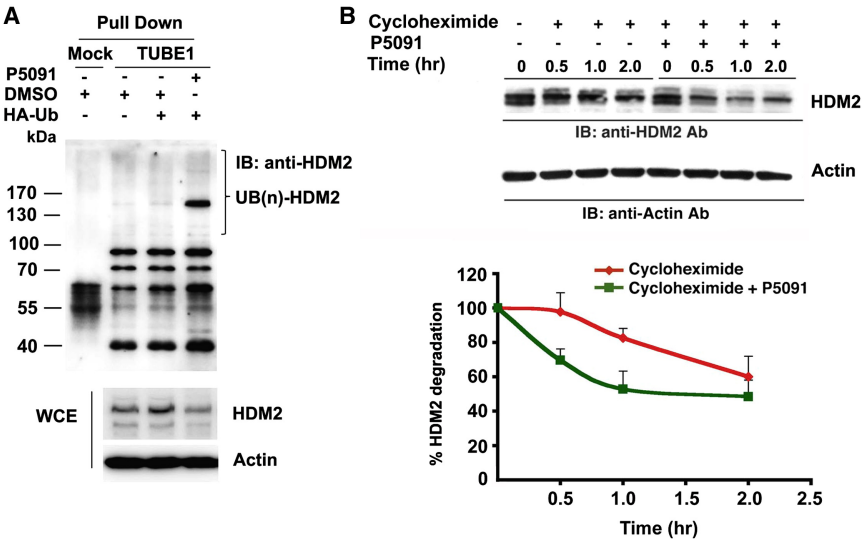

Figure 2. Effect of P5091 on USP7 Substrate HDM2

(A) U2OS cells were transfected with HA-Ub (WT), and 48 hr posttransfection, cells were treated with DMSO or P5091 (30 μM) for 4 hr. Endogenous HDM2 ubiquitylation was analyzed by pulling down ubiquitylated proteins using TUBEs (Supplemental Experimental Procedures). Cell lysates were normalized for HDM2 protein and incubated with uncojugated Agarose or TUBE1 conjugated Agarose; samples were separated by SDS-PAGE, and HDM2 ubiquitylation was detected using anti-HDM2 antibody. Whole-cell extracts (WCE) were subjected to IB using anti-HDM2 and anti-actin antibodies.

(B) U2OS cells were pretreated with either vehicle or P5091 (15 μM, IC_{50}) for 2.0–3.5 hr, followed by addition of CHX (40 μg/ml) for the indicated times. Total proteins lysates were subjected to immunoblotting with anti-HDM2 or anti-actin antibodies. Densitometry was utilized to quantify HDM2 protein levels after normalization with actin control to obtain percent HDM2 degradation (mean ± SD; n = 3).

Error bars indicate SD. See also Figure S2.

overall survival and event-free survival of 170 MM patients enrolled in a clinical trial. Results show a statistically significant inverse correlation between USP7 levels and overall survival (Figure 3C). Additionally, MM patients with lower USP7 levels survived for longer timespan with no recurrence of the disease following therapy (Figure 3D). Together, these data suggest a role of USP7 in the pathogenesis of MM and provide a rationale for targeting USP7 in MM.

P5091 Inhibits USP7 Deubiquitylating Activity, without Blocking Proteasome Activity, in MM Cells

P5091 causes significant inhibition (>50%) of USP7 activity in a concentration-dependent manner (Figure 4A). Although bortezomib blocks chymotrypsin-like (CT-L) proteasome activity, no significant inhibition of CT-L activity was observed in P5091-treated MM cells (Figure 4B). P5091 (25–50 μM) had no effect on trypsin-like (T-L)- or caspase-like (C-L) proteasome activities (Figure S3A). A comparative analysis shows that bortezomib induced a marked increase in ubiquitylated proteins (Figure 4B), whereas a modest increase in polyubiquitylation was observed in P5091-treated cells. This is likely due to the narrow USP7 substrate activity compared to bortezomib, which has a broader substrate spectrum. These data suggest that P5091 blocks USP7 activity without altering proteasome function.

P5091 Inhibits Growth in MM Cells and Overcomes Bortezomib-Resistance

P5091 induces a dose-dependent decrease in viability of various MM cell lines, including those that are resistant to conventional therapies dexamethasone (Dex) (MM.1R), doxorubicin (Dox-40), or melphalan (LR5) (IC_{50} range 6–14 μM) (Figure 4C). P5091 blocks the USP7 activity in MM at the IC_{50} of P5091 for these cells (Figure 4A and data not shown). In contrast, P22074 had no significant effect on the viability. The variable IC_{50} of P5091 against MM cell lines may be due to their distinct genetic background and/or drug-resistance characteristics (Anderson, 2007). USP7-siRNA inhibited cell proliferation; conversely, transfection of USP7 (WT) rescued cells from the growth-inhibitory effects of USP7-siRNA (Figure 4D). Immunoblot analysis shows a significant knockdown of USP7 by USP7-siRNA versus scrambled (scr)-siRNA, and restoration of USP7 levels in cells transfected with USP7 (WT) versus USP7-siRNA (Figure 4D, inset).

To determine whether P5091 similarly affects purified patient MM cells, tumor cells from eight MM patients, including those relapsing after multiple prior therapies, such as bortezomib, lenalidomide, and Dex, were treated with P5091. Patient MM was deemed to be refractory to bortezomib therapy when progressive disease occurred in spite of bortezomib treatment; in addition, most bortezomib-resistant MM was refractory to lenalidomide and Dex therapies as well. A dose-dependent decrease in the viability of all patient MM cells was noted after P5091 treatment (Figure 4E). We next examined whether tumor cells from bortezomib-resistant MM patients are affected by bortezomib treatment in vitro and whether P5091 exerts a cytotoxic effect in these cells (Figure 4F). Results demonstrate a varying sensitivity to bortezomib in vitro (10%–50% decrease in viability), albeit at much higher concentrations (12.5 nM) than normally observed IC_{50} for MM cells (3–5 nM) in three of six samples; however, all patient cells were significantly more sensitive to P5091 ($IC_{50} \leq 3$ μM). These findings show the ability of P5091 to trigger cytotoxicity, even in patient tumor cells resistant to bortezomib, Dex, or lenalidomide therapies.

To further address this issue, we utilized bortezomib-sensitive (ANBL-6.WT) and bortezomib-resistant (ANBL-6.BR) isogenic MM cell lines. Cell viability analysis showed that the IC_{50} of drugs for ANBL-6.WT or ANBL-6.BR were 2.32 nM and 12.05 nM for bortezomib and 6.83 μM and 9.85 μM for P5091. As seen in Figure 4G, the IC_{50} ratio (ANBL-6.BR/ANBL-6.WT) of P5091 is significantly less than bortezomib ($p < 0.001$), demonstrating the ability of P5091 to overcome bortezomib resistance. Finally, P5091 at the IC_{50} for MM cells does not significantly affect the

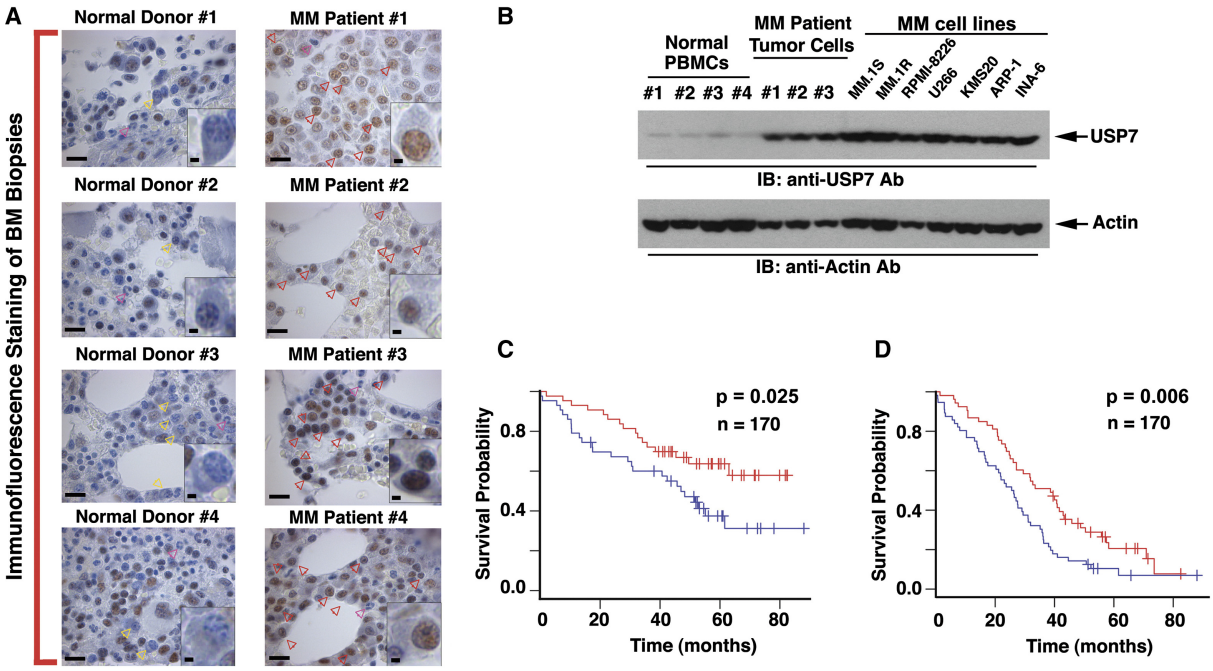

Figure 3. USP7 Expression and Prognostic Relevance in MM Cells

(A) IHC analysis of BM biopsies from normal donors and MM patients to show USP7 expression. Red arrowheads indicate USP7-positive cells (brown color). Yellow arrowheads represent normal plasma cells; magenta arrowheads are neutrophils. Scale bars, 50 μm (10 μm in insets).

(B) Purified tumor cells from MM patients, normal peripheral blood mononuclear cells (PBMCs), and MM cell lines were analyzed for USP7 expression level by IB with anti-USP7 and anti-actin antibodies.

(C and D) Kaplan-Meier plots on prognostic relevance of *USP7* expression on the overall and event-free survival for MM patients. The blue line indicates a patient group with higher *USP7* expression and shorter survival, whereas the red line represents a group of patients with lower *USP7* expression and longer survival. See Web site (http://www.ncbi.nlm.nih.gov/geo/) for gene expression data under accession number GSE39754.

viability of normal PBMCs (Figure 4H). Higher concentrations of P5091 (25 μM) decrease the viability of PBMCs by 20%–25%, suggesting that normal cells are not completely refractory to P5091. These data show a favorable therapeutic index for P5091 in MM.

P5091 Overcomes Bone Marrow Stromal Cell-Induced Growth of MM Cells

Interaction of MM cells with BMSCs triggers cytokine secretion, which mediates paracrine growth of MM cells and protects against drug-induced apoptosis (Chauhan et al., 2005b). To determine whether P5091 affects BMSCs-triggered MM cell growth, MM.1S cells were cultured with or without BMSCs in the presence or absence of various concentrations of P5091. P5091 treatment inhibited BMSCs-induced proliferation of MM.1S (Figure 4I). P5091 treatment does not affect the viability, morphology, or function of BMSCs (Figures S3B–S3D). These data suggest that P5091 not only directly targets MM cells but also overcomes the cytoprotective effects of the MM-host BM microenvironment.

We next examined whether anti-MM activity of P5091 is due to apoptosis. P5091 treatment shows accumulation of cells in early- (Ann V^+/PI^-) and late-stage (Ann V^+/PI^+) apoptosis (Figure S3E), associated with proteolytic cleavage of poly (ADP) ribose polymerase (PARP) (Figure S3F). Treatment of MM.1S and RPMI-8226 cells with P5091 induces caspase-3 cleavage and activates caspase-9 and casapse-8 apoptotic pathways (Figure S3F). Biochemical inhibition of either caspase-8 (IETD-FMK) or pan-caspase inhibitor (Z-VAD-FMK) markedly abrogates P5091-triggered cytotoxicity (Figure 4J). These findings suggest that (1) P5091 triggers both mitochondria-dependent and mitochondria-independent signaling pathways and (2) P5091-induced apoptosis is mediated, at least in part, via caspases.

Effect of P5091 on HDM2/p53/p21 Pathway in MM Cells

In agreement with our results using U20S cells (Figure 2A), P5091 increases ubiquitination of endogenous HDM2 in MM.1S cells (Figure S4A). In contrast to U20S cells, higher levels of endogenous poly-Ub HDM2 were observed in MM.1S cells in the absence of exogenous Ub transfection. Importantly, a significant increase in HDM2 ubiquitination was noted in P5091-treated cells compared to untreated cells. Even though similar bands are observed in DMSO-treated U2OS cells (Figure 2A, lanes 2 and 3) as well as in MM.1S cells (Figure S4A), P5091 treatment resulted in accumulation of band between 130–170 kDa only in U2OS cells (Figure 2A, lane 3), suggesting cell-type-specific differences in HDM2 ubiquitination that is sensitive to P5091 treatment.

USP7 regulates HDM2, HDMX, and p53 pathways (Cummins et al., 2004; Li et al., 2004). P5091 decreased HDM2 and HDMX, as well as upregulated p53 and p21 levels (Figure 5A). Pretreatment of MM.1S cells with P5091, followed by CHX

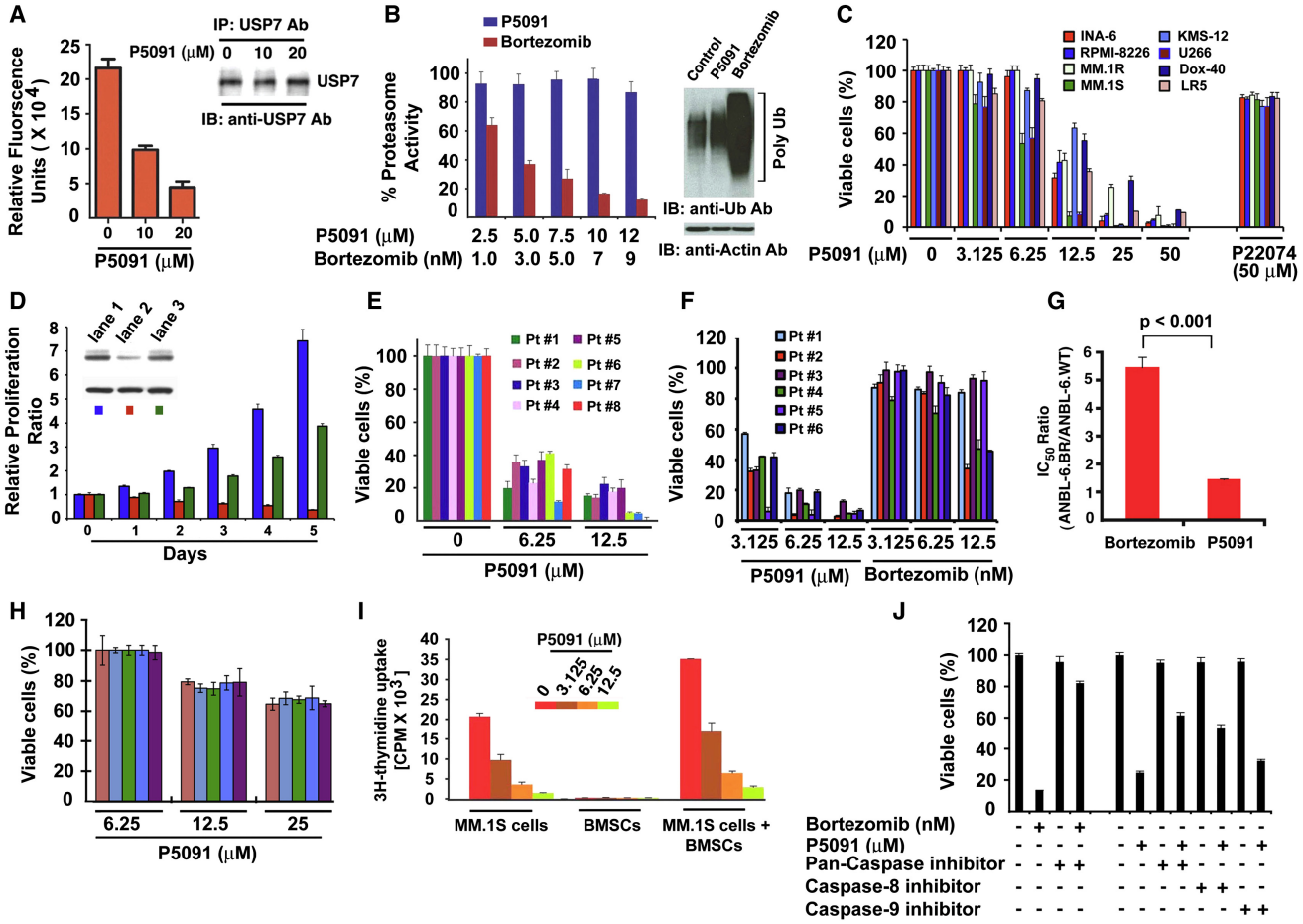

Figure 4. P5091 Inhibits USP7 Activity, Induces MM Cell Death, and Overcomes Bortezomib-Resistance

(A) MM.1S cells were treated with DMSO or with P5091 for 3 hr; cellular USP7 was immunoprecipitated under native conditions and analyzed for USP7 activity using the Ub-EK$_L$ assay ($p < 0.05$; n = 2).

(B) MM.1S cells were treated with DMSO or with P5091 or bortezomib for 3 hr; protein lysates were analyzed for proteasome activity. Raw data were normalized to percent proteasome activity in control (as 100%) versus drug-treated cells (mean ± SD; n = 3). Protein lysates from control, P5091-, or bortezomib-treated MM.1S cells were subjected to IB with anti-Ub antibody.

(C) MM cell lines were treated with DMSO or with P5091 for 48 hr, followed by assessment for cell viability (mean ± SD; $p < 0.001$ for all cell lines; n = 3).

(D) MM.1S cells were cotransfected with scr-siRNA plus empty-vector, USP7-siRNA plus empty-vector, or USP7-siRNA plus active USP7 (WT) and subjected to growth analysis using CellTiter-Glo assay (mean ± SD; n = 3). Immunoblot shows USP7 expression in cells transfected with scr-siRNA plus empty-vector (lane 1), USP7-siRNA plus empty-vector (lane 2), or USP7-siRNA plus active USP7 (WT) (lane 3) (Inset).

(E) Purified patient MM cells were treated with P5091 for 48 hr and analyzed for viability (mean ± SD of triplicate cultures; $p < 0.001$ for all patient samples).

(F) MM cells from six bortezomib-resistant patients (Pt. #1–#6) were treated in a side-by-side manner with either bortezomib or P5091 for 48 hr and analyzed for viability (mean ± SD of triplicate cultures; $p < 0.001$ for all patient samples).

(G) Bortezomib-sensitive (ANBL-6.WT) and Bortezomib-resistant (ANBL-6.BR) cells were treated with either bortezomib or P5091 for 48 hr, followed by assessment for cell viability. The bar graph shows the IC$_{50}$ ratio (ANBL-6.BR/ANBL-6.WT) of P5091 and bortezomib (mean ± SD; n = 2).

(H) Normal PBMCs were treated with P5091 for 48 hr and analyzed for viability (mean ± SD of quadruplicate cultures).

(I) MM.1S cells were cultured with or without BMSCs for 72 hr, and DNA synthesis was measured by ^{3}H-TdR uptake (mean ± SD of triplicate cultures; $p < 0.001$ for all samples).

(J) MM.1S cells were pretreated with inhibitors of caspase-8, caspase-9, or pan-caspase for 1 hr, and then P5091 (12.5 μM) or bortezomib (10 nM) was added for another 24 hr, followed by analysis of viability.

Error bars (A–J) indicate SD. See also Figure S3.

addition resulted in the rapid degradation of HDM2 and increased steady-state protein levels of p53 and p21 (Figure 5B). This increase in p53 and p21 was not due to enhanced transcription at the tested time point (Figure S4B). HDMX stability was only slightly decreased in both control and P5091-treated cells, likely because of its long half-life in human cancer cells (Li and Gu, 2011). The P5091-induced HDM2 degradation was blocked in the presence of proteasome inhibitor MG132 (Figure S4C), suggesting that HDM2 degradation is proteasome dependent.

We next examined the role of HDM2, p53, and p21 during P5091-induced cytotoxicity using loss-of-function studies and a KO cell system. HDM2-siRNA reduced HDM2 levels compared

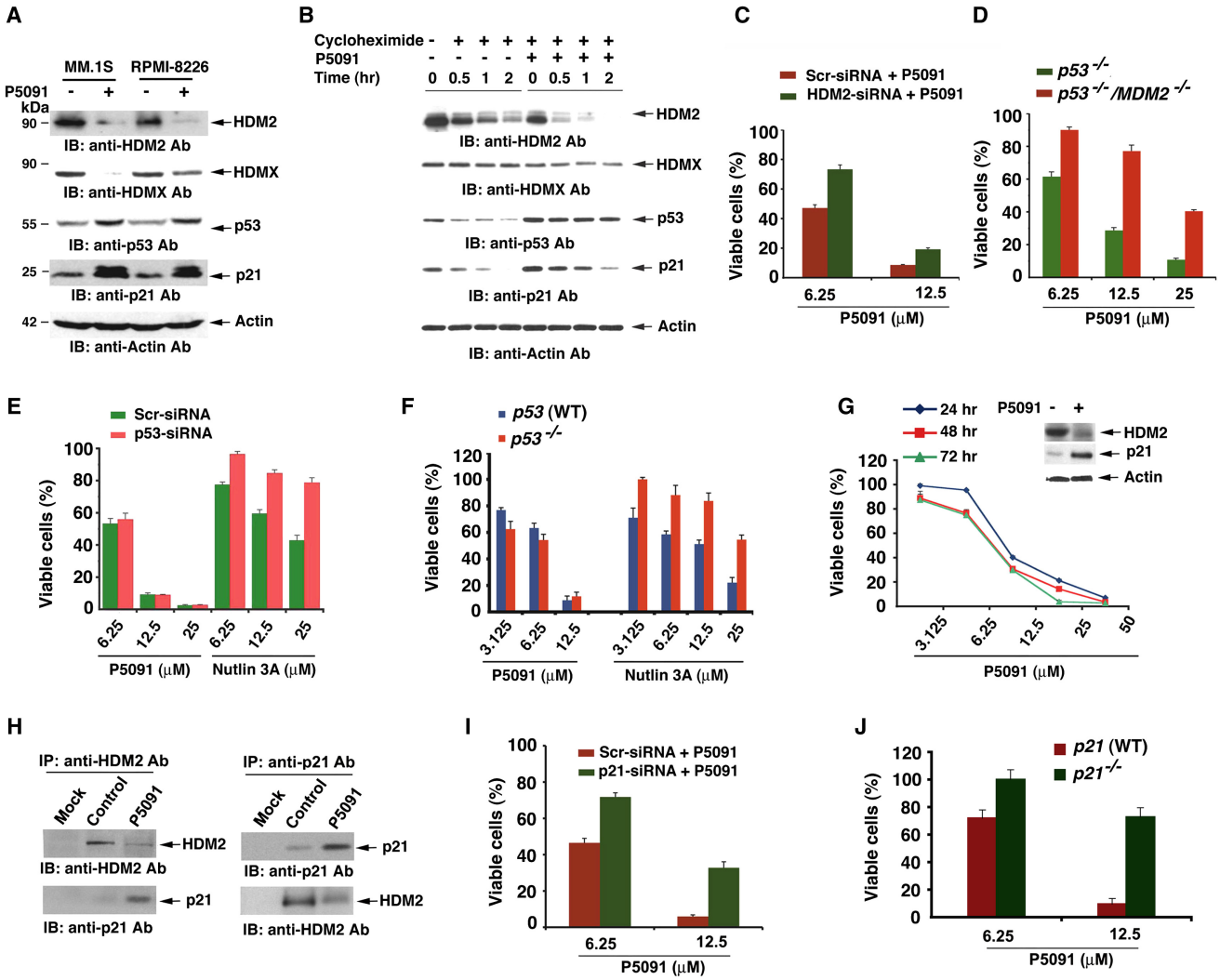

Figure 5. Mechanisms Mediating Anti-MM Activity of P5091

(A) MM.1S and RPMI-8226 cells were treated with P5091 (6.25 and 12.5 μM) for 24 hr; protein lysates were subjected to IB with anti-HDM2, anti-HDMX, anti-p53, anti-p21, or anti-actin antibodies.

(B) MM.1S cells were pretreated with P5091 (6.25 μM) for 4 hr, followed by addition of CHX (50 μg) for the final 0–120 min of the experiment. Protein lysates were subjected to IB using indicated antibodies.

(C) MM.1S cells were transfected with either scr- or HDM2-siRNA. After 24 hr of transfection, cells were treated with vehicle or indicated concentrations of P5091 for an additional 24 hr, followed by analysis of cell viability (mean ± SD; n = 3).

(D) $p53^{-/-}$ and $p53^{-/-}/MDM2^{-/-}$ MEFs were treated with P5091 for 48 hr, followed by analysis of cell viability (mean ± SD; n = 3).

(E) MM.1S cells were transfected with scr- or p53-siRNA, followed by treatment with P5091 or Nutlin-3A for 48 hr, and then analyzed for viability (mean ± SD; n = 3).

(F) HCT116 *p53* (WT) and HCT116 $p53^{-/-}$ cells were treated with DMSO, P5091, or Nutlin-3A for 72 hr, followed by assessment for cell viability (mean ± SD; n = 3).

(G) ARP-1 MM cells were treated with DMSO or P5091 for 48 hr and analyzed for cell viability (mean ± SD; n = 3). Inset: Lysates from control and P5091-treated ARP-1 cells were analyzed for HDM2 and p21 levels using IB.

(H) MM.1S cells were treated with DMSO or P5091 (6.25 μM) for 12 hr; cell lysates were immunoprecipitated with anti-p21, anti-HDM2, or corresponding isotype control (mock) antibodies, and the immune complexes were then subjected to IB with anti-HDM2 and anti-p21 antibodies.

(I) MM.1S cells were transfected with scr- or p21-siRNA, followed by treatment with P5091 for 48 hr, and then analyzed for viability (mean ± SD; n = 3). Percent cell viability was normalized (as 100%) for scr- or p21-siRNA controls, respectively.

(J) HCT116 (WT) and HCT116 $p21^{-/-}$ cells were treated with DMSO or with P5091 for 48 hr, followed by assessment for cell viability (mean ± SD; $p < 0.001$; n = 3).

Error bars in (C–G), (I), and (J) indicate SD. See also Figure S4.

to untreated scr-siRNA, and treatment of HDM2-siRNA transfected cells with P5091 further modestly decreased HDM2 levels (Figure S4D). It is likely that knocking down HDM2 alone negatively impacts the HDM2/HDMX heterocomplex, as well as overall HDM2 E3 ligase activity and polyubiquitylation status of HDM2, thereby resulting in the remaining HDM2 (in HDM2-siRNA cells) being comparatively less sensitive to the effects of P5091. As seen in Figure S4E, which shows absolute levels of viable

cells, the percentage of cell viability in HDM2 knockdown cell is 63.66% (0.322/0.506 × 100%) normalized to scr-siRNA control. Further derivation from absolute values (Figure S4E) show that the percentage of viable cells in scr- and HDM2-siRNA-transfected cells upon treatment with P5091 (6.25 and 12.5 μM) was 47.2%, 8.6%, and 73.3% and 19.2%, respectively (Figure 5C). In concert with these data, P5091 downregulated HDM2 and HDMX, as well as upregulating p53 and p21 levels, in scr-siRNA-transfected cells (Figure S4D). p53 levels were slightly increased by HDM2-siRNA knockdown and further upregulated by P5091 treatment. HDM2-siRNA, like P5091 alone, upregulated p21 levels, which remained unaffected by the combination of HDM2-siRNA and P5091. The role of HDM2 during P5091-induced cell death was further examined using $p53^{-/-}$ and $p53^{-/-}/MDM2^{-/-}$ (double KO) mouse embryonic fibroblasts (MEFs). Results demonstrate significantly reduced cytotoxicity of P5091 in $p53^{-/-}/MDM2^{-/-}$ cells versus $p53^{-/-}$ MEFs (IC_{50} of P5091 for $p53^{-/-}$: 7.72 μM and for $p53^{-/-}/MDM2^{-/-}$: 20.88 μM) (Figure 5D). Together, these data suggest that (1) the effects of HDM2-siRNA alone may not absolutely mimic the responses triggered by P5091 and (2) P5091-induced cytotoxicity is mediated in part via HDM2.

Interestingly, *p53* depletion by siRNA does not affect the P5091-induced decrease in MM.1S cell viability (Figure 5E). In contrast, p53 depletion inhibited cytotoxic effects of Nutlin-3A (Figure 5F), an MDM2-p53 interaction antagonist, suggesting its dependence of p53. We further utilized two different strategies to further address this issue: first, we used HCT116 *p53* (WT) and HCT116 $p53^{-/-}$ cells to show that P5091, but not Nutlin-3A, exerts equipotent cytotoxicity in both cell types (Figure 5F). Second, P5091 treatment decreases the viability of *p53* null ARP-1 MM cells (Figure 5G), associated with decreased HDM2 levels and increased p21 expression (Figure 5G, inset). Together, these data suggest that although P5091 increase p53 levels (Figure 5A), its cytotoxic activity is not dependent on p53. A recent report also highlighted a p53-dependent and p53-independent function of USP7 (Kon et al., 2011). Our findings have important clinical implications because 10%–15% of MM patients have p53 mutations/deletions, which confer drug resistance; a therapeutic approach using USP7 inhibition would allow for potent anti-MM activity, even in this patient population.

Our data show that besides p53, P5091 treatment also upregulates p21, a known downstream target of HDM2-p53 axis (Enge et al., 2009; Vogelstein et al., 2000; Xu et al., 2010). MDM2 inhibition is associated with induction of p21 in human cancer cells regardless of p53 status, suggesting a role of MDM2 in p21 regulation as well as p21 function in mediating p53-independent apoptosis (Wang et al., 2001, 2002; Wu et al., 2002; Zhang et al., 2003, 2004). We examined the effect of P5091 on HDM2-p21 signaling axis. Coimmunoprecipitation assays show that HDM2 is associated with p21 in MM cells and that P5091 downregualates HDM2 and upregualtes p21 (Figure 5H). Silencing of *p21* with siRNA attenuates P5091-induced cytotoxicity (Figure 5I). Similarly, treatment of HCT116 $p21^{-/-}$ cells significantly blocked P5091-triggered cytotoxicity, associated with late-stage apoptosis (Figures 5J and S4F). The P5091-induced increase in p21 protein is in concert with an earlier study showing that MDM2 negatively regulates p21 protein by directly binding to it and facilitating its proteasomal degradation (Zhang et al., 2004). Although P5091 upregulates and stabilizes p21 in MM cells, it triggers a modest accumulation of endogenous ubiquitylated p21 (Figure S4G). The mechanism(s) underlying the USP7-inhibition-mediated p21 ubiquitylation and stabilization in MM cells remains to be defined. Nonetheless, previous reports showed that p21 ubiquitylation is not a prerequisite for proteasomal degradation and that the p21 ubiquitylation may serve some function other than proteasome degradation via conformation changes (Sheaff et al., 2000; Zhang et al., 2004; Xu et al., 2010).

Overall, our mechanistic studies show that (1) P5091-induced cytotoxicity is mediated in part via HDM2-p21 signaling axis and (2) although p53 is upregulated in response to P5091 treatment, the cytotoxic activity of P5091 is not dependent on p53. It is possible that other signaling molecules besides HDM2 or p21 contribute to the overall response to P5091 because HDMX is also the downstream target of USP7 and recent studies showed interaction of USP7 with Claspin, PTEN, or FOXO4.

P5091 Inhibits Human MM Cell Growth In Vivo and Prolongs Survival in the MM.1S MM Xenograft Mouse Model

We next examined the in vivo efficacy of P5091 using human plasmacytoma xenograft and SCID-hu mouse models (Chauhan et al., 2005a). These two distinct models have been immensely useful in extensively validating novel anti-MM therapies bortezomib and lenalidomide, leading to their translation to clinical trials and FDA approval for the treatment of MM. Treatment of MM.1S tumor-bearing mice with intravenous (IV) injection of P5091 inhibits MM tumor growth and prolongs survival of these mice (Figures 6A and 6B). Examination of harvested tumors showed that P5091 inhibited USP7 activity, decreased HDM2, and increased p21 levels relative to tumors from control mice (Figure 6C). P5091 decreases proliferation in harvested tumors, as assessed by BrdU and Ki67 staining (Figures 6D and S5A). P5091 increases the number of cleaved-caspase-3- and TUNEL-positive apoptotic tumor cells versus vehicle treatment (Figures 6E and S5B). P5091 was well tolerated, since no significant weight loss in mice was observed (Figure S5C). These data show potent in vivo apoptotic activity of P5091 against MM cells.

P5091 Triggers Antiangiogenic Activity In Vivo

MM cell growth is associated with angiogenesis, and vascular endothelial growth factor (VEGF) plays a role in this process (Anderson, 2007). To determine whether P5091 triggers antiangiogenic activity, we evaluated tumors harvested from mice by immunostaining using distinct markers of angiogenesis, VEGFR2, and platelet endothelial cell adhesion molecule (PECAM1). P5091 decreases the number of VEGFR2- and PECAM1-positive cells (Figures 6Fa and 6Fb). Tumor sections were also analyzed for expression of LYVE1 (lymphatic vessel marker), ENG (endoglin/CD105), and ACTA2/α-SMA (smooth muscle cell marker). A marked decrease in the number of LYVE1- and ENG-positive cells is observed in tumors from P5091-treated mice versus control mice (Figures 6Fc and 6Fd), suggesting that P5091 exposure results in reduction of tumor vasculature. Dual immunostaining of harvested tumors with PECAM1 and ACTA2 confirms the disappearance of intact larger vessels in P5091-treated

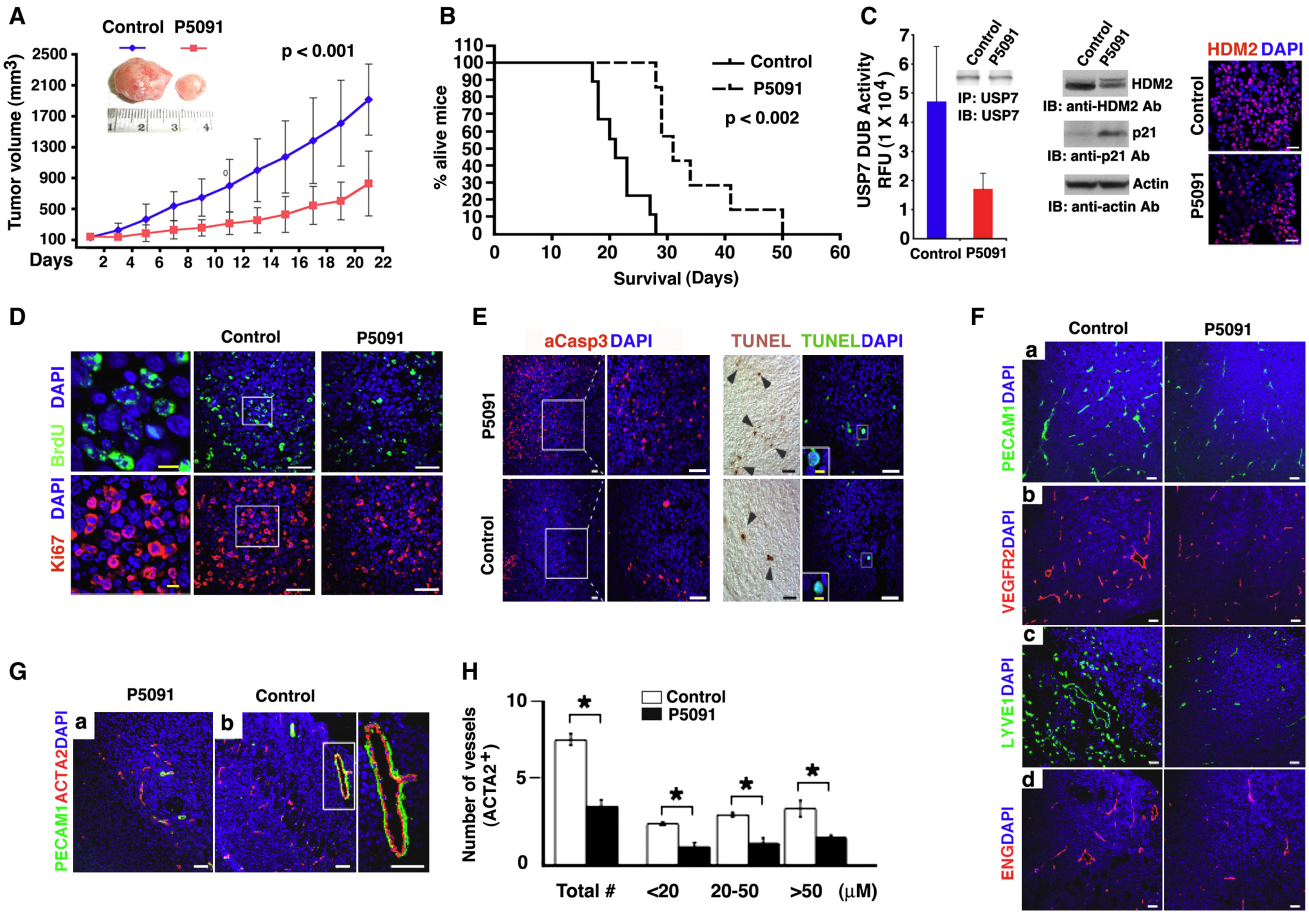

Figure 6. P5091 Inhibits Xenografted Human MM Cell Growth, Prolongs Survival, and Blocks Angiogenesis in CB-17 Mice

(A) Mice bearing human MM.1S MM tumors were treated with vehicle or P5091 (10 mg/kg; IV) twice weekly for 3 consecutive weeks. Data are presented as mean tumor volume ± SD (ten mice/group).

(B) Kaplan-Meier survival plot shows survival of mice.

(C) Tumors from vehicle or P5091-treated mice were analyzed for USP7 activity. Inset: Immunoblot shows equal USP7 protein input. HDM2 and p21 levels in mice tumors were analyzed by IB. Tumor sections from control and P5091-treated mice were immunostained with anti-HDM2 antibody and DAPI. Scale bars, 50 μm.

(D) Tumor sections from control and P5091-treated mice were immunostained with BrdU and Ki67 antibodies. Nuclear staining was performed with DAPI. White rectangle in the middle control panel represents the 5× enlarged area. White scale bars, 50 μm. Yellow scale bars, 10 μm.

(E) Apoptotic cells in tumors sectioned from control or P5091-treated mice were identified by immunostaining for activated caspase-3 (red cells), TUNEL (green cells), and DAPI (blue). White rectangle represents 5× enlarged area. Black arrowheads point at apoptotic cells. Scale bars, 50 μm (10 μm in the inset).

(F) Tumor sections from control and P5091-treated mice were subjected to immunostaining with anti-PECAM1, anti-VEGFR2, anti-LYVE1, or anti-ENG antibodies. Nuclear staining was performed with DAPI. Scale bars, 50 μm.

(G) Tumor sections from control and P5091-treated mice were subjected to dual immunostaining with PECAM1 and ACTA2. White rectangle represents 5× enlarged area. Scale bars, 50 μm.

(H) Quantification of ACTA2-positive cells shown in (G). *p < 0.05.

Error bars represent SD. See also Figure S5.

tumors (Figures 6G and 6H). These data suggest that P5091 inhibits tumor-associated angiogenic activity.

Characterization of P5091 Efficacy in Distinct Animal Models

Because our in vitro data showed that P5091 triggers apoptosis in *p53* null ARP-1 MM cells, we evaluated whether P5091 similarly affects the growth of ARP-1 cells in vivo. Treatment of ARP-1 tumor-bearing mice with P5091 inhibits MM tumor growth and prolongs survival of these mice (Figures 7A and 7B). Importantly, a marked inhibition of USP7 activity was noted in tumors from P5091-treated mice compared with tumors from control mice (Figure 7C). Although P5091 targets USP7, as tested using a panel of DUBs, we cannot rule out the possibility of involvement of yet unknown DUB, other molecules of similar homology, or other USP7 substrates in mediating biological responses. Nonetheless, our data show an early inhibition (at 3 hr) of USP7 activity in vivo in response to P5091 treatment. Blood chemistry profile of P5091-treated mice showed normal levels of bilirubin, hemoglobin, and creatinine (Figure S6A), suggesting that P5091 treatment was well tolerated.

We next compared the in vivo efficacy of P5091 with bortezomib. A head-to-head analysis of P5091 versus bortezomib at their MTD doses showed a similar tumor growth inhibition

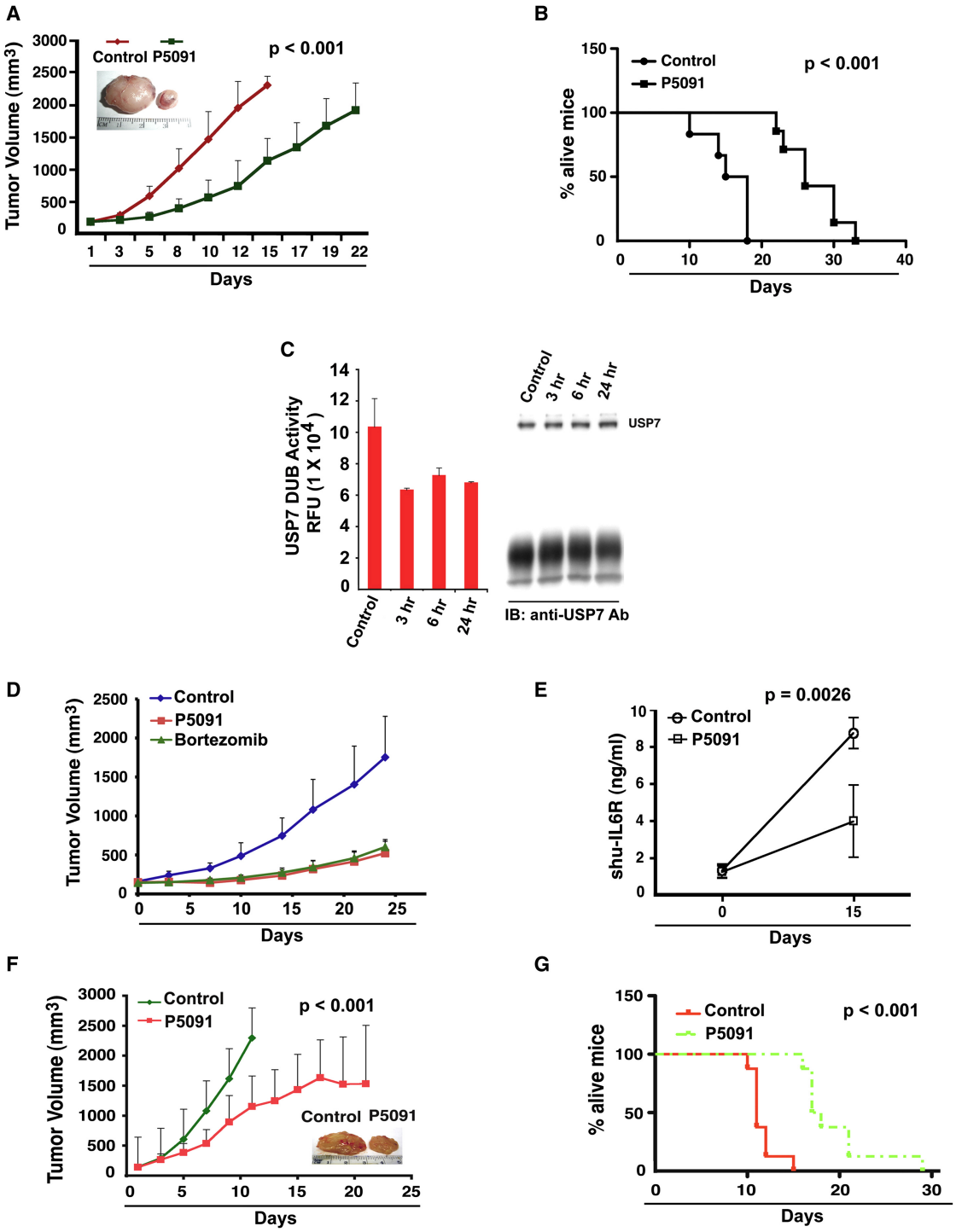

Figure 7. P5091 Targets USP7 In Vivo and Exhibits Antitumor Activity in Distinct Animal Models

(A) Mice bearing human *p53* null ARP-1 MM tumors were treated with either P5091 (10 mg/kg; IV) or vehicle control twice weekly for 3 consecutive weeks. Average and standard deviation of tumor volume (mm^3) is shown from mice versus time when tumor was measured (mean tumor volume ± SD, six mice/group).

(B) Kaplan-Meier plot shows survival in mice.

(C) Tumors from vehicle or P5091-treated mice were analyzed for USP7 activity. Immunoblot shows that equal USP7 protein input.

(D) Average and standard deviation of tumor volume (mm^3) is shown from mice (n = 5/group) versus time when tumor was measured. RPMI-8226 cells (5×10^6 cells/mouse) were implanted in the rear flank of female mice. On day 28–30, mice were randomized to treatment with vehicle, MTD doses of P5091 (20 mg/kg), or with bortezomib (1 mg/kg) on a twice-weekly schedule for 3 weeks.

(E) SCID-hu mice bearing INA-6 MM tumors (five mice/group) were treated with either vehicle alone or P5091 (10 mg/kg), and mouse serum samples were analyzed for shIL-6R.

in RPMI-8266 and MM.1S tumor-bearing mice (Figures 7D and S6B).

Because MM-host BM microenvironment confers growth, survival, and drug resistance in MM cells (Anderson, 2007), we examined whether the anti-MM activity of P5091 is retained in the presence of human BM microenvironment. For these studies, we utilized the SCID-hu model (Anderson, 2007), which recapitulates the human BM milieu in vivo. In this model, INA-6 MM cells are injected directly into human bone chips implanted subcutaneously in SCID mice, and MM cell growth is assessed by serial measurements of circulating levels of soluble human interleukin 6-receptor (shIL-6R) in mouse serum. P5091 treatment inhibited tumor growth in these mice (Figure 7E), suggesting that P5091 can trigger anti-MM activity, even in the presence of the human BM milieu. Finally, in order to determine whether P5091 induces antitumor activity in other cancer cell types, we utilized a human leukemic lymphoblast (CCRF-CEM) xenograft model. Treatment of tumor-bearing mice with P5091 inhibits leukemic tumor growth and prolongs survival of these mice (Figures 7F and 7G), supporting a broad range of antitumor activity of P5091 in cancer types. Together, our data demonstrate that P5091 reduces tumor growth, prolongs survival, and is well tolerated in vivo.

Combined Treatment with P5091 and Lenalidomide, Dex, or the HDAC Inhibitor Induces Synergistic Anti-MM Activity

Our prior preclinical studies (Anderson, 2007) have provided the basis for clinical trials of bortezomib in combination with lenalidomide, Dex, and HDAC inhibitors. Given that P5091, like bortezomib, targets the UPS, we examined whether P5091 similarly enhances the anti-MM activity of other agents. Isobogram analysis (Chou and Talalay, 1984) of synergistic anti-MM activity demonstrated that the combination of low concentrations of P5091 and lenalidomide triggers synergistic anti-MM activity (Figure 8A).

Besides proteasomal degradation, intracellular protein catabolism also occurs via an HDAC-dependent aggressome-autophagic cell death-signaling pathway. Recent clinical trials combining bortezomib and HDAC inhibitor vorinostat (SAHA) show promising outcome in MM. Combination of P5091 and SAHA triggers synergistic anti-MM activity (Figure 8B). These data confirm the potential for clinical trials combining USP7 and HDAC inhibitors. As with lenalidomide and SAHA, the combination of P5091 with conventional anti-MM agent Dex induces synergistic anti-MM activity (Figure 8C). Although definitive evidence of decreased toxicity of combination therapy awaits results of clinical trials, the synergy observed in vitro may allow for use of lower doses and decreased toxicity.

Collectively, our studies utilize MM cell lines, patient tumor cells, and MM xenograft models, as well as biochemical and genetic models, to show the antitumor activity of a USP7 deubiquitylating enzyme inhibitor P5091. The functional specificity of P5091 is confirmed using different strategies: first, cell-free-based experiments using a reporter (Ub-PLA_2)-based assay demonstrate a potent, specific, and selective inhibition of USP7 activity by P5091; second, P5091 enhances degradation of its primary substrate HDM2; third, *USP7* KO in HCT-116 cells confers resistance to P5091; and fourth, P5091 blocks USP7 DUB activity without altering proteasome activity. Treatment of MM cell lines and primary patient MM cells with P5091 inhibits growth and induces apoptosis in tumor cells, including those resistant to conventional and bortezomib therapies, without affecting the viability of normal PBMCs. P5091 triggers apoptosis in MM cells, even in the presence of the MM-host BM microenvironment. Mechanistic studies further show that P5091-triggered apoptosis in MM cells is associated with (1) activation of caspase-8, caspase-9, caspase-3, and PARP and (2) downregulation of USP7 substrate HDM2, as well as increased expression of p53 and p21. Genetic studies using siRNA and KO models show that P5091-induced cytotoxicity is, in part, mediated via HDM2-p21 and occurs independent of p53. In animal tumor model studies, P5091 is well tolerated, inhibits tumor growth, and prolongs survival. Importantly, P5091 inhibits USP7 activity in vivo and induces apoptosis in MM xenografted tumors. Immunostaining of tumor sections shows that antiangiogenic activity contributes to the overall antitumor activity of P5091. A side-by-side efficacy analysis shows a similar antitumor activity of P5091 and bortezomib at their MTD doses. Finally, combining P5091 with lenalidomide, HDAC inhibitor, or Dex induces synergistic anti-MM activity. Our preclinical studies therefore provide the rationale for the development of next-generation UPS-based therapies and specifically demonstrate the promise of therapeutics targeting USP7 to improve patient outcome in MM.

EXPERIMENTAL PROCEDURES

Cell Lines, MM Patient Cells, and Drug Sources

All studies involving human samples were performed under Dana-Farber Cancer Institute IRB committee-approved protocols, through which informed consent was obtained and deidentified samples were utilized. Human MM cell lines MM.1S, MM.1R, RPMI-8226, U266, KMS12PE, ARP-1, INA-6, Dox-40, or LR5 were cultured in RPMI-1640 medium containing 10% fetal bovine serum (FBS) and antibiotics. CCRF-CEM leukemic cells were cultured in 10% FBS and antibiotics. Human colorectal cancer cell lines HCT116 (WT), HCT116 *USP7*$^{-/-}$, HCT116 *p53*$^{-/-}$, and HCT116 *p21*$^{-/-}$ were maintained in McCoy's 5A medium with 10% FBS. Tumor cells from MM patients were purified by $CD138^+$ selection method.

Reagents for In Vitro Enzyme Assays

Recombinant full-length USP5, USP7, and SENP2 catalytic core, as well as amino terminal-tagged hexa His Ub-PLA_2 (Ub-CHOP), Ub-EK_L (Ub-CHOP2), and SUMO3-EK_L(SUMO3-CHOP2), were generated, as previously described (Nicholson et al., 2008; Tian et al., 2011). EK_L was generated by cleaving SUMO3-EK_L with SENP2 core, and mature EK_L was purified by affinity chromatography.

Ubiquitin Protease Assays

Recombinant enzymes in 20 mM Tris-HCl (pH 8.0), 2 mM $CaCl_2$, and 2 mM β-mercaptoethanol were incubated with dose ranges of P5091 for 30 min in a 96-well plate before the addition of Ub-PLA_2 and NBD C_6-HPC (Invitrogen,

(F) Mice bearing CCRF-CEM leukemic tumors were treated with either vehicle or P5091 (10 mg/kg) twice weekly for three consecutive weeks. Data are presented as mean tumor volume ± SD (eight mice/group).
(G) Kaplan-Meier survival plot shows survival of mice.
Error bars indicate SD. See also Figure S6.

A

Combination	P5091 (μM)	P5091 (Fa)	Lenalidomide (μM)	Lenalidomide (Fa)	Fa (com)	CI
1	3	0.7188	1	0.7321	0.4483	0.358
2	3	0.7188	3	0.7166	0.3676	0.265
3	3	0.7188	5	0.5975	0.3049	0.2
4	5	0.5652	1	0.7321	0.3427	0.369
5	5	0.5652	3	0.7166	0.293	0.298
6	5	0.5652	5	0.5975	0.2275	0.212
7	7	0.5256	1	0.7321	0.2532	0.334
8	7	0.5256	3	0.7166	0.2231	0.285
9	7	0.5256	5	0.5975	0.1299	0.149

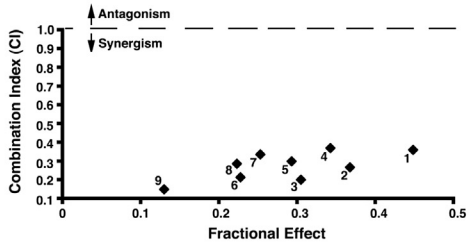

B

Combination	P5091(μM)	P5091 (Fa)	SAHA(nM)	SAHA (Fa)	Fa (com)	CI
1	3	0.7138	80	0.6612	0.4431	0.694
2	3	0.7138	120	0.6137	0.3622	0.601
3	3	0.7138	160	0.515	0.2526	0.409
4	5	0.5611	80	0.6612	0.3513	0.634
5	5	0.5611	120	0.6137	0.2644	0.486
6	5	0.5611	160	0.515	0.2289	0.453
7	7	0.5021	80	0.6612	0.2725	0.559
8	7	0.5021	120	0.6137	0.205	0.432
9	7	0.5021	160	0.515	0.1531	0.333

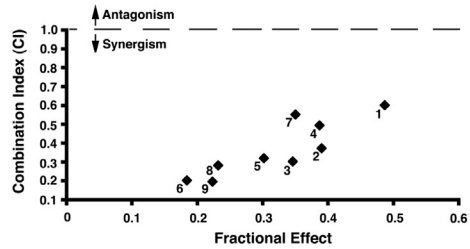

C

Combination	P5091(μM)	P5091 (Fa)	Dex(nM)	Dex (Fa)	Fa (com)	CI
1	3	0.6735	10	0.627	0.487	0.601
2	3	0.6735	20	0.5496	0.39	0.373
3	3	0.6735	30	0.5478	0.346	0.303
4	5	0.561	10	0.627	0.387	0.494
5	5	0.561	20	0.5496	0.302	0.321
6	5	0.561	30	0.5478	0.223	0.196
7	7	0.493	10	0.627	0.35	0.551
8	7	0.493	20	0.5496	0.232	0.282
9	7	0.493	30	0.5478	0.184	0.202

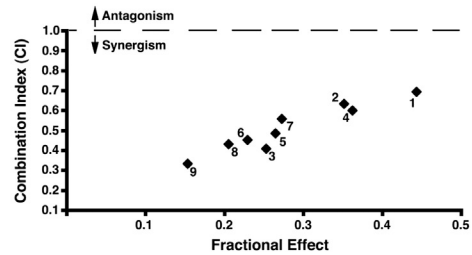

Figure 8. Combination of P5091 and Lenalidomide, SAHA, or Dex Trigger Synergistic Anti-MM Activity

(A) MM.1S cells were treated for 48 hr with P5091, lenalidomide, or P5091 plus lenalidomide and then assessed for viability using MTT assays. Isobologram analysis shows the synergistic cytotoxic effect of P5091 and lenalidomide. The graph (right) is derived from the values given in the table (left). The numbers 1–9 in graph represent combinations shown in the table. FAcom, fraction of viable cells. Combination index (CI) <1 indicates synergy.

(B) MM.1S cells were treated for 48 hr with P5091, SAHA, or P5091 plus SAHA and then assessed for viability using MTT assays. Synergistic anti-MM activity was analyzed as in (A).

(C) MM.1S cells were treated for 48 hr with P5091, Dex, or P5091 plus Dex and then assessed for viability using MTT assays. Synergistic anti-MM activity was analyzed as in (A).

Carlsbad, CA, USA) or Ub-EK_L and EK_L substrate, as previously described (Nicholson et al., 2008; Tian et al., 2011). The liberation of a fluorescent product within the linear range of the assay was monitored using a Perkin Elmer Envision fluorescence plate reader. Vehicle (2% [v/v] DMSO) and 10 mM N-ethylmaleimide (NEM) were included as controls. DUB activity and inhibition assays in living cells were performed as described (Borodovsky et al., 2002).

Ubiquitin-Linked K48 Chain Cleavage Assay

USP7 (30 nM) was preincubated with DMSO or P5091 for 30 min at room temperature (RT) before reaction with polyubiquitin chains for 20 min at 37°C. Samples were resolved by SDS-PAGE and immunoblotted with anti-Ub Ab (Sigma Chemicals, St. Louis, MO, USA).

Human Tumor Xenograft Models

All animal experiments were approved by and conformed to the relevant regulatory standards of the Institutional Animal Care and Use Committee at the Dana-Farber Cancer Institute. For the animal study, P5091 was dissolved in 4% NMP (N-methyl-2-Pyrrolidone), 4% Tween-80, and 92% Milli-Q water at a final concentration of 2 mg/ml. The human plasmacytoma xenograft model was performed as previously described (Chauhan et al., 2008). CB-17 SCID-mice (Charles River Labs, Wilmington, MA, USA) were subcutaneously inoculated with MM.1S, ARP-1, or RPMI-8226 cells in 100 μl of serum-free RPMI-1640 medium. When tumors were measurable (100–180 mm^3), mice were randomized into treatment groups. In the SCID-hu model, human fetal bone grafts were subcutaneously implanted into SCID mice. Four weeks after bone implantation, INA-6 cells were injected directly into the fetal bone implant in SCID mice; as a measure of tumor burden, mouse sera samples were analyzed for shIL-6R by ELISA (R&D Systems, Minneapolis, MN, USA). Upon detection of shIL-6R, mice were treated with vehicle or P5091, and mouse serum was analyzed for alterations in shIL-6R levels.

Statistical Analysis

Statistical significance in drug-treated versus control in vitro cultures, and in tumor xenograft models were determined by using the Student's t test. Survival of mice was measured by using the Prism GraphPad software (Systat Software, San Jose, CA, USA). Isobologram analysis (Chou and Talalay, 1984) was performed using the CalcuSyn software program (Biosoft, Ferguson, MO, USA; Cambridge, UK). A combination index (CI) less than 1.0 indicates synergistic activity.

ACCESSION NUMBERS

The raw data for expression profiling and the CEL files can be found at the Web site Gene Expression Omnibus (http://www.ncbi.nlm.nih.gov/geo/) under accession number GSE39754.

SUPPLEMENTAL INFORMATION

Supplemental Information includes six figures and Supplemental Experimental Procedures and can be found with this article online at http://dx.doi.org/10.1016/j.ccr.2012.08.007.

ACKNOWLEDGMENTS

This investigation was supported by grants from the National Institutes of Health (P50100707, PO1-CA078378, R43DK071391, and R43CA115205). M.A. is supported by VR-2011-2686. K.C.A. is an ACS Clinical Research Professor. D.C. designed research, analyzed data, and wrote the manuscript; Z.T. performed experiments and interpreted data; B.N. designed USP7 activity assay and analyzed data; B.Z. did microscopy; R.C. performed IHC; S.K., C.A.L., J.L.M., M.P.K., M.A., and B.M.K. performed DUB assays; J.W. and W.D.K. synthesized compounds; P.S., S.M., and N.M. analyzed microarray data; M.T. performed animal study; T.H. and P.R. provided clinical samples; and K.C.A. wrote the manuscript. We thank Dr. Bert Vogelstein for HCT116 USP7- and p53-KO cells. We are thankful to Dr. William G. Kaelin (DFCI, Boston, MA) for $p53^{-/-}$ cells and Dr. Guillermina Lozano (M.D. Anderson Cancer Center, Houston, TX) for $p53^{-/-}/MDM2^{-/-}$ cells. B.N., S.K., C.A.L., J.L.M., M.P.K., J.W., and W.D.K. are employees of Progenra, Inc.

Received: October 24, 2011
Revised: May 3, 2012
Accepted: August 9, 2012
Published: September 10, 2012

REFERENCES

Adams, J. (2004). The proteasome: a suitable antineoplastic target. Nat. Rev. Cancer *4*, 349–360.

Anderson, K.C. (2007). Targeted therapy of multiple myeloma based upon tumor-microenvironmental interactions. Exp. Hematol. *35* (4, Suppl 1), 155–162.

Borodovsky, A., Ovaa, H., Kolli, N., Gan-Erdene, T., Wilkinson, K.D., Ploegh, H.L., and Kessler, B.M. (2002). Chemistry-based functional proteomics reveals novel members of the deubiquitinating enzyme family. Chem. Biol. *9*, 1149–1159.

Chauhan, D., Catley, L., Li, G., Podar, K., Hideshima, T., Velankar, M., Mitsiades, C., Mitsiades, N., Yasui, H., Letai, A., et al. (2005a). A novel orally active proteasome inhibitor induces apoptosis in multiple myeloma cells with mechanisms distinct from Bortezomib. Cancer Cell *8*, 407–419.

Chauhan, D., Hideshima, T., and Anderson, K.C. (2005b). Proteasome inhibition in multiple myeloma: therapeutic implication. Annu. Rev. Pharmacol. Toxicol. *45*, 465–476.

Chauhan, D., Singh, A., Brahmandam, M., Podar, K., Hideshima, T., Richardson, P., Munshi, N., Palladino, M.A., and Anderson, K.C. (2008). Combination of proteasome inhibitors bortezomib and NPI-0052 trigger in vivo synergistic cytotoxicity in multiple myeloma. Blood *111*, 1654–1664.

Chou, T.C., and Talalay, P. (1984). Quantitative analysis of dose-effect relationships: the combined effects of multiple drugs or enzyme inhibitors. Adv. Enzyme Regul. *22*, 27–55.

Ciechanover, A. (2005). Proteolysis: from the lysosome to ubiquitin and the proteasome. Nat. Rev. Mol. Cell Biol. *6*, 79–87.

Cummins, J.M., Rago, C., Kohli, M., Kinzler, K.W., Lengauer, C., and Vogelstein, B. (2004). Tumour suppression: disruption of *HAUSP* gene stabilizes p53. Nature *428*, 1 p following 486.

Enge, M., Bao, W., Hedström, E., Jackson, S.P., Moumen, A., and Selivanova, G. (2009). MDM2-dependent downregulation of p21 and hnRNP K provides a switch between apoptosis and growth arrest induced by pharmacologically activated p53. Cancer Cell *15*, 171–183.

Everett, R.D., Meredith, M., Orr, A., Cross, A., Kathoria, M., and Parkinson, J. (1997). A novel ubiquitin-specific protease is dynamically associated with the PML nuclear domain and binds to a herpesvirus regulatory protein. EMBO J. *16*, 1519–1530.

Fang, S., Jensen, J.P., Ludwig, R.L., Vousden, K.H., and Weissman, A.M. (2000). Mdm2 is a RING finger-dependent ubiquitin protein ligase for itself and p53. J. Biol. Chem. *275*, 8945–8951.

Hjerpe, R., Aillet, F., Lopitz-Otsoa, F., Lang, V., England, P., and Rodriguez, M.S. (2009). Efficient protection and isolation of ubiquitylated proteins using tandem ubiquitin-binding entities. EMBO Rep. *10*, 1250–1258.

Hershko, A. (2005). The ubiquitin system for protein degradation and some of its roles in the control of the cell division cycle. Cell Death Differ. *12*, 1191–1197.

Hoeller, D., Hecker, C.M., and Dikic, I. (2006). Ubiquitin and ubiquitin-like proteins in cancer pathogenesis. Nat. Rev. Cancer *6*, 776–788.

Hu, M., Li, P., Li, M., Li, W., Yao, T., Wu, J.W., Gu, W., Cohen, R.E., and Shi, Y. (2002). Crystal structure of a UBP-family deubiquitinating enzyme in isolation and in complex with ubiquitin aldehyde. Cell *111*, 1041–1054.

Itahana, K., Mao, H., Jin, A., Itahana, Y., Clegg, H.V., Lindström, M.S., Bhat, K.P., Godfrey, V.L., Evan, G.I., and Zhang, Y. (2007). Targeted inactivation of Mdm2 RING finger E3 ubiquitin ligase activity in the mouse reveals mechanistic insights into p53 regulation. Cancer Cell *12*, 355–366.

Kon, N., Kobayashi, Y., Li, M., Brooks, C.L., Ludwig, T., and Gu, W. (2010). Inactivation of *HAUSP* in vivo modulates p53 function. Oncogene *29*, 1270–1279.

Kon, N., Zhong, J., Kobayashi, Y., Li, M., Szabolcs, M., Ludwig, T., Canoll, P.D., and Gu, W. (2011). Roles of HAUSP-mediated p53 regulation in central nervous system development. Cell Death Differ. *18*, 1366–1375.

Li, M., and Gu, W. (2011). A critical role for noncoding *5S* rRNA in regulating Mdmx stability. Mol. Cell *43*, 1023–1032.

Li, M., Chen, D., Shiloh, A., Luo, J., Nikolaev, A.Y., Qin, J., and Gu, W. (2002). Deubiquitination of p53 by HAUSP is an important pathway for p53 stabilization. Nature *416*, 648–653.

Li, M., Brooks, C.L., Kon, N., and Gu, W. (2004). A dynamic role of HAUSP in the p53-Mdm2 pathway. Mol. Cell *13*, 879–886.

Lonial, S., Waller, E.K., Richardson, P.G., Jagannath, S., Orlowski, R.Z., Giver, C.R., Jaye, D.L., Francis, D., Giusti, S., Torre, C., et al; SUMMIT/CREST Investigators. (2005). Risk factors and kinetics of thrombocytopenia associated with bortezomib for relapsed, refractory multiple myeloma. Blood *106*, 3777–3784.

Meulmeester, E., Maurice, M.M., Boutell, C., Teunisse, A.F., Ovaa, H., Abraham, T.E., Dirks, R.W., and Jochemsen, A.G. (2005). Loss of HAUSP-mediated deubiquitination contributes to DNA damage-induced destabilization of Hdmx and Hdm2. Mol. Cell *18*, 565–576.

Nicholson, B., Marblestone, J.G., Butt, T.R., and Mattern, M.R. (2007). Deubiquitinating enzymes as novel anticancer targets. Future Oncol. *3*, 191–199.

Nicholson, B., Leach, C.A., Goldenberg, S.J., Francis, D.M., Kodrasov, M.P., Tian, X., Shanks, J., Sterner, D.E., Bernal, A., Mattern, M.R., et al. (2008). Characterization of ubiquitin and ubiquitin-like-protein isopeptidase activities. Protein Sci. *17*, 1035–1043.

Richardson, P.G., Barlogie, B., Berenson, J., Singhal, S., Jagannath, S., Irwin, D., Rajkumar, S.V., Srkalovic, G., Alsina, M., Alexanian, R., et al. (2003). A phase 2 study of bortezomib in relapsed, refractory myeloma. N. Engl. J. Med. *348*, 2609–2617.

Sheaff, R.J., Singer, J.D., Swanger, J., Smitherman, M., Roberts, J.M., and Clurman, B.E. (2000). Proteasomal turnover of p21Cip1 does not require p21Cip1 ubiquitination. Mol. Cell *5*, 403–410.

Song, M.S., Salmena, L., Carracedo, A., Egia, A., Lo-Coco, F., Teruya-Feldstein, J., and Pandolfi, P.P. (2008). The deubiquitinylation and localization of PTEN are regulated by a HAUSP-PML network. Nature *455*, 813–817.

Stommel, J.M., and Wahl, G.M. (2004). Accelerated MDM2 auto-degradation induced by DNA-damage kinases is required for p53 activation. EMBO J. *23*, 1547–1556.

Tian, X., Isamiddinova, N.S., Peroutka, R.J., Goldenberg, S.J., Mattern, M.R., Nicholson, B., and Leach, C. (2011). Characterization of selective ubiquitin and ubiquitin-like protease inhibitors using a fluorescence-based multiplex assay format. Assay Drug Dev. Technol. *9*, 165–173.

Vogelstein, B., Lane, D., and Levine, A.J. (2000). Surfing the p53 network. Nature *408*, 307–310.

Wang, H., Nan, L., Yu, D., Agrawal, S., and Zhang, R. (2001). Antisense anti-MDM2 oligonucleotides as a novel therapeutic approach to human breast cancer: in vitro and in vivo activities and mechanisms. Clin. Cancer Res. *7*, 3613–3624.

Wang, H., Nan, L., Yu, D., Lindsey, J.R., Agrawal, S., and Zhang, R. (2002). Anti-tumor efficacy of a novel antisense anti-MDM2 mixed-backbone oligonucleotide in human colon cancer models: p53-dependent and p53-independent mechanisms. Mol. Med. *8*, 185–199.

Wu, Q., Kirschmeier, P., Hockenberry, T., Yang, T.Y., Brassard, D.L., Wang, L., McClanahan, T., Black, S., Rizzi, G., Musco, M.L., et al. (2002). Transcriptional regulation during p21WAF1/CIP1-induced apoptosis in human ovarian cancer cells. J. Biol. Chem. *277*, 36329–36337.

Xu, H., Zhang, Z., Li, M., and Zhang, R. (2010). MDM2 promotes proteasomal degradation of p21Waf1 via a conformation change. J. Biol. Chem. *285*, 18407–18414.

Zhang, Z., Li, M., Wang, H., Agrawal, S., and Zhang, R. (2003). Antisense therapy targeting MDM2 oncogene in prostate cancer: Effects on proliferation, apoptosis, multiple gene expression, and chemotherapy. Proc. Natl. Acad. Sci. USA *100*, 11636–11641.

Zhang, Z., Wang, H., Li, M., Agrawal, S., Chen, X., and Zhang, R. (2004). MDM2 is a negative regulator of p21WAF1/CIP1, independent of p53. J. Biol. Chem. *279*, 16000–16006.

Zhao, R., Yeung, S.C., Chen, J., Iwakuma, T., Su, C.H., Chen, B., Qu, C., Zhang, F., Chen, Y.T., Lin, Y.L., et al. (2011). Subunit 6 of the COP9 signalosome promotes tumorigenesis in mice through stabilization of MDM2 and is upregulated in human cancers. J. Clin. Invest. *121*, 851–865.

Transforming the Microenvironment: A Trick of the Metastatic Cancer Cell

Anuradha Budhu[1] and Xin Wei Wang[1,*]
[1]Laboratory of Human Carcinogenesis, Center for Cancer Research, National Cancer Institute, 37 Convent Drive, Bethesda, MD 20892, USA
*Correspondence: xw3u@nih.gov
http://dx.doi.org/10.1016/j.ccr.2012.08.018

Creating a permissive microenvironment is a strategy employed by tumor cells to disseminate. In this issue of *Cancer Cell*, Yang et al. identify the molecular signaling events that connect hepatitis infection with TGFβ activity and T regulatory cell recruitment to establish a favorable microenvironment for tumor metastasis.

Metastasis is a significant contributor to morbidity and mortality among cancer patients. Such patients are often considered incurable, with treatments offering either supportive care or aggressive management without curative intent. For over a century, cancer biologists have intensely explored the mechanisms underlying the emergence and spread of tumor cells (Valastyan and Weinberg, 2011). Although much progress has been made in elucidating signaling networks of metastasis, the sheer complexity of this dynamic and intricate process has thwarted our ability to define effective targets for cancer management.

An interesting form of metastases is observed in hepatocellular carcinoma (HCC) with a unique dissemination pattern within the liver, a significant proportion of which colonize inside the major branches of the portal vein, a condition called portal vein tumor thrombosis (PVTT). PVTT can lead to further liver deterioration along with ascites and esophageal bleeding, thus presenting a major treatment challenge. A few studies have explored the role of genomic alterations in PVTT and have identified critical players, such as osteopontin, in HCC metastasis (Ye et al., 2003). Profiling of the liver microenvironment of metastasis patients has shown that global shifts in inflammatory cytokines can provide a suitable niche to promote disease progression (Budhu et al., 2006). A more detailed understanding of the complex interplay of signals between tumors and the organs they invade is paramount to improving cancer patient care and in developing clinical strategies to block cancer progression.

One player at the forefront of metastasis is TGFβ. This multifunctional cytokine signals through a complex network of transduction pathways during embryonic development, cell proliferation, differentiation, angiogenesis, and wound healing. It can function as a tumor suppressor in premalignant cells by inducing apoptosis, cell cycle arrest, and immune surveillance while suppressing cytokines, chemokines, and inflammation (Ikushima and Miyazono, 2010). Its expression in many cell types allows it to orchestrate this vast set of processes. TGFβ signals through a canonical pathway via TGFβ receptors and its downstream Smad mediators to recruit a network of factors in a cell-specific and context-dependent manner to regulate target genes. The suppressive effects of TGFβ can be circumvented by malignant cells through inactivation of these components, such as mutations in TGFBR2 and SMAD4. TGFβ can also signal in a noncanonical fashion via PI3K, MAPK, and small GTP pathways. Under these circumstances, cancer cells can alter and seize TGFβ's downstream tumor suppressive signaling components to promote tumor progression. This Jekyl and Hyde nature of TGFβ can drive cancer spread via cell autonomous or nonautonomous mechanisms by impacting the host cell.

Inflammation and the tumor microenvironment play significant roles in tumor progression and are identified as hallmarks of cancer (Hanahan and Weinberg, 2011). A complex milieu of cells are at the ready in the premalignant state to fend off infection and disease, but can be usurped by tumor cells for more insidious roles such as metastatic initiation and progression. TGFβ, an immune and inflammation regulator, is frequently present in the microenvironment as a signal to prevent premalignant progression; however, malignant cells with high TGFβ may be shielded from immune surveillance, while defective TGFβ signaling can lead to chronic inflammation and the production of a pro-tumorigenic environment. Although several studies have described a dual role for TGFβ in cancer, the mechanisms underlying these roles and how they can be exploited for clinical relevance remains obscure. What causes altered TGFβ signaling in cancer? When does TGFβ act as a metastasis signal? How does TGFβ alter the tumor microenvironment? How can we use this knowledge to treat cancer?

In this issue of *Cancer Cell*, Yang et al. (2012) report that TGFβ promotes a metastasis-permissive microenviroment in the portal vein of hepatitis B virus (HBV)-positive liver cancer patients. This switch toward a progressive phenotype occurs through the recruitment of immune suppressive $CD4^+CD25^+$ T regulatory (Tregs) cells mediated by TGFβ suppression of microRNA-34a (miR-34a) and the consequent release of CCL22 activity (Figure 1). Among 288 Chinese HCC patients, Yang et al. (2012) found a strong correlation between HBV status and the presence of PVTT, concomitant with elevated TGFβ activity. In a screen of microRNAs related to metastasis, they found that reduced levels of miR-34a, a tumor suppressor previously identified in a HCC metastasis signature (Budhu et al., 2008), was associated with HBV^+ HCC and high TGFβ levels. Moreover, a quantitative assay showed that the chemokine CCL22 is a bona fide target of miR-34a. Using in vitro assays and mouse models of liver or lung metastasis, they demonstrate that TGFβ signaling, via miR-34a suppression and consequent elevation of CCL22, enhances

recruitment of Tregs to create an immune suppressive microenvironment, thereby promoting metastasis.

These results raise several interesting questions and opportunities for further exploration of TGFβ signaling and its relation to cancer and metastasis. While the patients studied by Yang et al. (2012) largely consist of HBV$^+$ patients, several other underlying etiologies play a significant role in liver cancer development. The most prominent of these are hepatitis C virus (HCV) infection, alcoholic liver disease, and obesity, all of which are major global health burdens in both developing and developed countries. In the context of viral infection, HBV and HCV promote liver cancer and progression in disparate ways. It would be of interest to determine whether TGFβ can be modulated by HCV to similarly affect miR-34a and CCL22 or different signals are activated dependent on the risk factor present for HCC.

Yang et al. (2012) have elegantly demonstrated the connection between HBV infection and the activation of Treg recruitment to promote metastasis. In future studies, it will be intriguing to decipher how HBV affects TGFβ level. Is this due to integration of the HBV-encoded HBx gene or some other mechanism? The role of TGFβ in HBV patients without PVTT will be useful in determining what drives and regulates the molecular switch to promote metastasis. It would also be of interest to determine how TGFβ suppresses miR-34a. Recent studies have shown that p53 mutation is involved in switching TGFβ from a tumor suppressor to a tumor promoter (Adorno et al., 2009) and miR-34a has been shown to be a direct target of p53 (He et al., 2007). The role of p53 in TGFβ-mediated HBV$^+$ HCC metastasis will be interesting to explore since p53 mutation occurs in certain HCC populations, while HBx can bind and inactivate p53-dependent processes.

TGFβ targeting is quite complex, and a clinically useful drug has not been successfully produced. Strategies have included reducing the ligand by siRNA, blocking ligand-receptor interactions by monoclonal antibodies, or inhibiting signaling by small molecule inhibitors (Calone and Souchelnytskyi, 2012). Yang et al.'s study has highlighted an important molecule in TGFβ-mediated metastasis, namely CCL22. This study therefore opens up an avenue to explore this secreted chemokine as a target for effective treatment of HCC metastasis. Metastasis remains the major cause of death among cancer patients. Here, Yang et al. (2012) have revealed an important signaling layer of TGFβ, which sheds light on its role in promotion of metastasis and leads to a promising therapeutic target to clinically manage aggressive cancer.

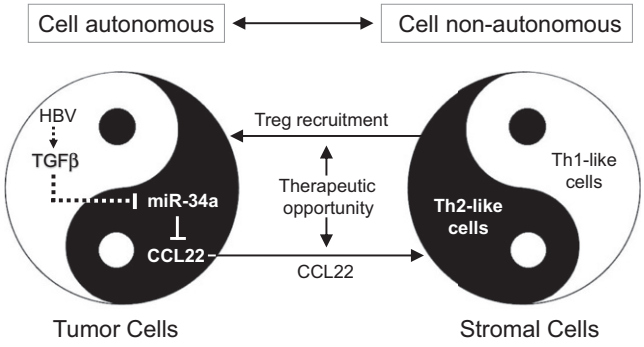

Figure 1. Cell Autonomous and Nonautonomous Activities of the TGFβ Signaling Network in Tumor and Stromal Cells

A potential therapeutic opportunity for the treatment of liver cancer metastasis is outlined. In metastatic HCC cells, TGFβ induction can be triggered by HBV infection, which then suppresses miR-34a, a suppressor of CCL22, resulting in the induction and secretion of CCL22. This chemokine, in turn, recruits Tregs to create an immune tolerant microenvironment that promotes metastatic colonization. The balancing activities of TGFβ and immune cells resemble the principle represented by the Yin-Yang symbol. Therefore, CCL22 represents a potential druggable target for metastatic HCC. The solid lines represent a direct action, and dotted lines represent a link with an unsolved mechanism.

REFERENCES

Adorno, M., Cordenonsi, M., Montagner, M., Dupont, S., Wong, C., Hann, B., Solari, A., Bobisse, S., Rondina, M.B., Guzzardo, V., et al. (2009). Cell *137*, 87–98.

Budhu, A., Forgues, M., Ye, Q.H., Jia, H.L., He, P., Zanetti, K.A., Kammula, U.S., Chen, Y., Qin, L.X., Tang, Z.Y., and Wang, X.W. (2006). Cancer Cell *10*, 99–111.

Budhu, A., Jia, H.L., Forgues, M., Liu, C.G., Goldstein, D., Lam, A., Zanetti, K.A., Ye, Q.H., Qin, L.X., Croce, C.M., et al. (2008). Hepatology *47*, 897–907.

Calone, I., and Souchelnytskyi, S. (2012). Exp. Oncol. *34*, 9–16.

Hanahan, D., and Weinberg, R.A. (2011). Cell *144*, 646–674.

He, L., He, X., Lim, L.P., de Stanchina, E., Xuan, Z., Liang, Y., Xue, W., Zender, L., Magnus, J., Ridzon, D., et al. (2007). Nature *447*, 1130–1134.

Ikushima, H., and Miyazono, K. (2010). Nat. Rev. Cancer *10*, 415–424.

Valastyan, S., and Weinberg, R.A. (2011). Cell *147*, 275–292.

Yang, P., Li, Q.-J., Feng, Y., Zhang, Y., Markowitz, G.J., Ning, S., Deng, Y., Zhao, J., Jiang, S., Yuan, Y., et al. (2012). Cancer Cell *22*, this issue, 291–303.

Ye, Q.H., Qin, L.X., Forgues, M., He, P., Kim, J.W., Peng, A.C., Simon, R., Li, Y., Robles, A.I., Chen, Y., et al. (2003). Nat. Med. *9*, 416–423.

Ready, Set, Go: The EGF Receptor at the Pancreatic Cancer Starting Line

Rushika M. Perera[1] and Nabeel Bardeesy[1,*]
[1]Massachusetts General Hospital and Harvard Medical School, Boston, MA 02114, USA
*Correspondence: bardeesy.nabeel@mgh.harvard.edu
http://dx.doi.org/10.1016/j.ccr.2012.08.019

Acinar-to-ductal metaplasia (ADM) results from pancreatic injury or KRAS activation, and is an early step in pancreatic cancer progression. In this issue of *Cancer Cell*, Ardito and colleagues and Navas and colleagues demonstrate that ADM- and KRAS-driven pancreatic cancer require EGFR signaling, revealing a mechanism for developmental reprogramming that primes tumorigenesis.

Most tissues respond to injuries such as those induced by toxins, trauma, or infections through orchestrated cellular programs that either mitigate further damage or enable regeneration. One such response is the process of metaplasia, which involves the conversion or replacement of one differentiated cell type with another in a given tissue. Metaplasia helps protect tissues as they adjust to the insult and the resulting changed environment and is usually reverted once normal conditions are reestablished. This defense mechanism comes with an unfortunate cost. It is becoming increasingly clear that sustained metaplasia can serve as an early precursor to malignant transformation in several organs, including the pancreas, stomach, and lung.

In the pancreas, acute or chronic inflammation leads to replacement of damaged acini with duct-like cells, referred to as acinar-to-ductal metaplasia (ADM) (reviewed in Reichert and Rustgi, 2011) (Figure 1). The relationship between ADM and pancreatic ductal adenocarcinoma (PDA) progression has been studied extensively in genetically engineered mouse models. In these models, oncogenic KRAS mutation—the earliest known genetic alteration in human PDA—promotes the focal development of ADM in the absence of exogenous inducers of inflammation. Rather than representing a reversible state, mutant KRAS-expressing metaplastic ducts progress into ductal precursor lesions known as pancreatic intraepithelial neoplasias (PanINs), which gradually acquire additional genetic changes including CDKN2A and/or TP53 mutation and evolve into PDA. Treatment of mice with the cholecystokinin analog cerulein, which induces pancreatic inflammation and widespread ADM, greatly accelerates PanIN formation and progression to PDA when KRAS mutations are present. Thus, it is thought that activated KRAS locks cells that have undergone ADM in the ductal state, preventing restoration of normal differentiation, and creating a reservoir of cells susceptible to additional oncogenic changes.

The first clues suggest a role for the epidermal growth factor receptor (EGFR) pathway in ADM came from transgenic mouse models in which overexpression of the EGFR ligand, TGFα, in the pancreas caused spontaneous ADM and progressive pancreatic tumorigenesis when crossed to KRAS, TP53, or CDKN2A mutant strains (Reichert and Rustgi, 2011). In vitro experiments using pancreatic explants showed that EGFR activation could act cell-autonomously in converting acinar cells into metaplastic ducts (Means et al., 2005; Miyamoto et al., 2003). The physiological relevance of this pathway has now been established in two new studies by Ardito et al. (2012) and Navas et al. (2012) in this issue of *Cancer Cell*. They employed genetic and pharmacological inactivation of EGFR in KRAS-driven mouse models to directly determine the contribution of endogenous EGFR pathway signaling to the development of ADM and PDA. Consistent with prior studies, they found that EGFR expression is upregulated in ADM and PanIN lesions in these models and in human pancreatitis specimens. Knockout of EGFR in the pancreas or treatment of mice with pharmacological EGFR inhibitors suppressed ADM provoked by activated KRAS or by cerulein. Moreover, acute EGFR inhibition resulted in apoptosis in established ADM and PanIN lesions. Importantly, Navas et al. (2012) found that EGFR knockout completely prevented PDA development in their KRAS model even in the context of deletion of CDKN2A, whereas both groups found that EGFR deletion delayed but did not eliminate PDA formation in KRAS-TP53 mutant models. Together, these results establish that EGFR is required for both the initiation and survival of ADM (and PanIN) lesions and show that its ablation restricts the development of PDA. KRAS mutations are also early initiating lesions in lung cancer and are present as later alterations in intestinal cancer. Thus, it is striking that Navas et al. (2012) found that EGFR deletion had no effect on tumorigenesis in KRAS-driven mouse models of these malignancies. Therefore, rather than playing a generic function in KRAS-mediated transformation, EGFR has specific roles in PDA initiation, acting to facilitate the developmental reprogramming of pancreatic acinar cells.

How does EGFR promote ADM? Although this remains incompletely understood, there are some intriguing leads. First, among the EGF family ligands (e.g., EGF, TGFα, and AREG), TGFα is uniquely induced during ADM both in vitro and in vivo and appears to be the main mediator of ADM. Accordingly, deletion of ADAM17, which cleaves and activates TGFα and AREG, blocks ADM to a similar extent as EGFR deletion, whereas prior studies have found that AREG fails to recapitulate the ADM phenotypes induced by TGFα (Wagner et al., 2002). TGFα is notable for its ability to cause recycling of the receptor back to the cell surface, thereby allowing for sustained moderate levels of signaling (von Zastrow

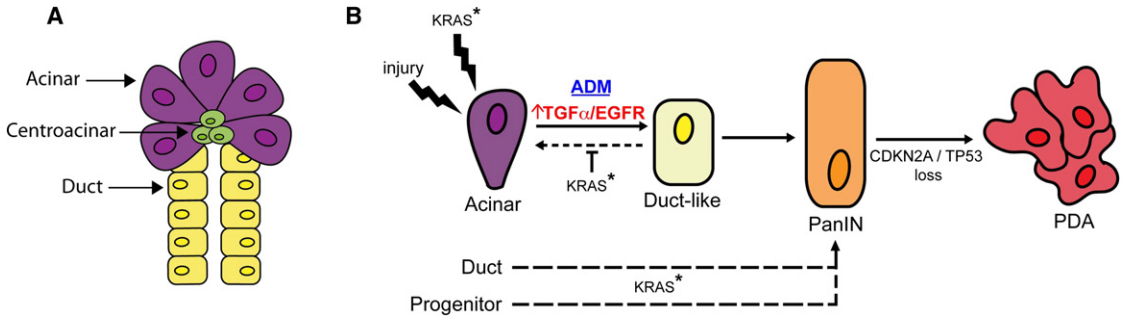

Figure 1. Role of EGFR Signaling in PDA Initiation and Progression

(A) Exocrine pancreas: acinar cells produce and secrete digestive enzymes, while ductal cells form channels that transport acinar secretions into the intestinal tract. Centroacinar cells lie at the interface between acinar and ductal cells and may have progenitor-like properties.

(B) Models of PDA progression: following injury, acinar cells undergo acinar-to-ductal metaplasia (ADM), a process that is normally reversible following resolution of the tissue damage. Activating KRAS mutation (KRAS*), the earliest oncogenic alteration in PDA pathogenesis, can also induce ADM while preventing reversion to acinar differentiation. ADM lesions can progress to pancreatic intraepithelial neoplasia (PanIN), which in turn gives rise to PDA following loss of the CDKN2A and/or TP53 tumor suppressors. EGFR signaling is required both for the initiation of ADM as well as for the survival of cells within established ADM and PanIN lesions. PDA may also originate from pancreatic duct cells and presumed pancreatic progenitors.

and Sorkin, 2007), whereas other EGFR ligands can be more potent EGFR activators but induce receptor downregulation. Hence, the selective role for ADAM17-TGFα-EGFR axis in ADM and tumor initiation suggests that a sustained threshold of EGFR activity is required for these processes. How EGFR and TGFα expression are induced in this context remains to be defined.

The signaling pathways downstream of EGFR that mediate ADM are less clear. Ardito et al. (2012) show that acute EGFR inhibition reduced levels of phospho-ERK1/2 and GTP-bound active RAS in ADM lesions in KRAS mice and acinar explants, respectively. However, Navas et al. (2012) did not observe changes in ERK1/2 activity in their model. Differences between the mouse models used in these two studies may account for some of these discrepancies. Further studies will be required to fully define the proximal effectors of EGFR signaling and associated biochemical mechanisms that facilitate ADM. In terms of more downstream pathways, prior reports have provided evidence that induction of Notch transcriptional activity contributes to ADM in vitro in response to TGFα-EGFR signaling (Miyamoto et al., 2003), and thus Notch warrants additional analysis as a potential effector of endogenous EGFR in ADM in vivo.

Does EGFR also contribute to the malignant growth of established PDA? Activated EGFR is detected in a subset of human PDAs, and EGFR inhibition shows efficacy in some patient-derived PDA xenografts and PDA cell lines (Jimeno et al., 2008). However, Erlotinib provided only limited benefit when combined with gemcitabine in a clinical trial with unselected PDA patients (Moore et al., 2007) and when administered at advanced stages in the KRAS-TP53 mouse model. This suggests that advanced PDA may have reduced dependence on EGFR signaling as compared to earlier stage lesions. Further studies will be required to ascertain how later stage cancers escape EGFR dependency and conversely to identify a molecular signature for those that remain EGFR-dependent. One such signature may involve loss of epithelial gene expression, because Ardito et al. (2012) found that EGFR expression is extinguished in poorly differentiated PDA. Moreover, published studies demonstrate that PDA cell lines showing mesenchymal features are relatively resistant to erlotinib as compared to well-differentiated PDA lines (Collisson et al., 2011).

PDA is the fourth most common cause of cancer deaths in the United States with a 5 year survival rate under 5%. Existing clinical trials with conventional and targeted therapies have only modest effects on patient outcomes, and hence new approaches to disease management are urgently needed. Since inherited predisposition to chronic pancreatitis greatly increases PDA risk and precursor lesions harboring KRAS mutations are common in otherwise normal pancreatic tissue of elderly individuals, there may be a benefit in the development of preventative strategies that eradicate ADM and PanIN lesions. The present studies support the potential of targeting TGFα-ADAM17-EGFR axis as an approach to PDA prevention.

REFERENCES

Ardito, C.M., Grüner, B.M., Takeuchi, K.K., Lubeseder-Martellato, C., Teichmann, N., Mazur, P.K., DelGiorno, K.E., Carpenter, E.S., Halbrook, C.J., Hall, J.C., et al. (2012). Cancer Cell *22*, this issue, 304–317.

Collisson, E.A., Sadanandam, A., Olson, P., Gibb, W.J., Truitt, M., Gu, S., Cooc, J., Weinkle, J., Kim, G.E., Jakkula, L., et al. (2011). Nat. Med. *17*, 500–503.

Jimeno, A., Tan, A.C., Coffa, J., Rajeshkumar, N.V., Kulesza, P., Rubio-Viqueira, B., Wheelhouse, J., Diosdado, B., Messersmith, W.A., Iacobuzio-Donahue, C., et al. (2008). Cancer Res. *68*, 2841–2849.

Means, A.L., Meszoely, I.M., Suzuki, K., Miyamoto, Y., Rustgi, A.K., Coffey, R.J., Jr., Wright, C.V., Stoffers, D.A., and Leach, S.D. (2005). Development *132*, 3767–3776.

Miyamoto, Y., Maitra, A., Ghosh, B., Zechner, U., Argani, P., Iacobuzio-Donahue, C.A., Sriuranpong, V., Iso, T., Meszoely, I.M., Wolfe, M.S., et al. (2003). Cancer Cell *3*, 565–576.

Moore, M.J., Goldstein, D., Hamm, J., Figer, A., Hecht, J.R., Gallinger, S., Au, H.J., Murawa, P., Walde, D., Wolff, R.A., et al.; National Cancer Institute of Canada Clinical Trials Group. (2007). J. Clin. Oncol. *25*, 1960–1966.

Navas, C., Hernández-Porras, I., Schumacher, A.J., Sibilia, M., Guerra, C., and Barbacid, M. (2012). Cancer Cell *22*, this issue, 318–330.

Reichert, M., and Rustgi, A.K. (2011). J. Clin. Invest. *121*, 4572–4578.

von Zastrow, M., and Sorkin, A. (2007). Curr. Opin. Cell Biol. *19*, 436–445.

Wagner, M., Weber, C.K., Bressau, F., Greten, F.R., Stagge, V., Ebert, M., Leach, S.D., Adler, G., and Schmid, R.M. (2002). Gastroenterology *122*, 1898–1912.

Strategies for p53 Reactivation in Human Sarcoma

Ted R. Hupp,[1,*] Richard L. Hayward,[2] and Borek Vojtesek[3]
[1]Institute of Genetics and Molecular Medicine
[2]Edinburgh Cancer Centre
University of Edinburgh, Edinburgh EH4 2XR, UK
[3]Regional Centre for Applied Molecular Oncology, Masaryk Memorial Cancer Institute, 656 53 Brno, Czech Republic
*Correspondence: ted.hupp@ed.ac.uk
http://dx.doi.org/10.1016/j.ccr.2012.08.020

Emerging strategies in cancer therapeutics link the genomic mutational and proteomic landscape, allowing intelligent reasoning on target selection. In this issue of *Cancer Cell*, Piccinin and colleagues use this approach to demonstrate that the mesenchymal protein Twist1 inhibits p53, providing a novel target for reactivation of p53 in human sarcoma.

One of the fundamental aims in biomedical research is the discovery of protein-protein interactions. This has led to an information explosion on biological pathway function, protein-networks, and signaling hubs. In the case of p53, this knowledge is beginning to be translated into cancer patient stratification that complements the advances already being made using gene mutation status and transcription profiling to predict therapeutic responses (Burington et al., 2011). Over 30 years of research has led to over 400 interacting proteins described for p53 that have driven exciting advances in drug development programs that target p53 inhibitors, like ubiquitin ligases (MDM2), histone de-acetylases (SIRT1 and SIRT2), and protein kinases (Aurora, CK1, and CDK; Figure 1). One of the key aims of translational biomedicine is to link this vast information on p53 interactors into clinically relevant cancer therapeutics. In this issue of *Cancer Cell*, Piccinin et al. (2012) bridge this gap and demonstrate that the mesenchymal signaling protein Twist1 forms a clinically relevant inhibitory p53 interaction in human sarcoma.

Our understanding of the genetics of human sarcoma has been facilitated by improved molecular classification using next generation sequencing technologies (Barretina et al., 2010), which has impacted clinically relevant target choice and in rational use of small molecules targeting kinases through to monoclonal antibodies targeting receptors for treating sarcoma (Figure 1). In the case of the most well studied p53 inhibitor of all, MDM2, next generation technologies have shown that *MDM2* is one of the key genes often amplified in human sarcoma (Taylor et al., 2011). Emerging translational data also demonstrate that melanomas overproducing the MDM2 homolog MDM4 form clinical settings in which to apply targeted therapeutics (Gembarska et al., 2012). In human sarcoma, the ratio of spliced MDM4 full-length and smaller isoforms better defined patients with poor survival rates than the mutation status of p53 (Lenos et al., 2012). This affirmation of MDM2 or MDM4 activation in human sarcoma provides a compelling clinical setting to investigate the potential targeting of these relatively well-characterized p53 pathway inhibitors. Current compounds targeting MDM2 protein range from lead molecules interacting with its hydrophobic peptide binding pocket (Vassilev et al., 2004) to the use of conformationally constrained peptides (e.g., stapled peptides), which offers enormous potential to develop a new generation of protein-protein interaction inhibitors to be evaluated clinically (Crunkhorn, 2011). Therefore, there is a significant potential to stratify patients in sarcoma clinical trials that might benefit from MDM2 or MDM4 targeted therapeutics.

Despite this enormous promise in targeting MDM2 to reactivate p53, human sarcomas are a very heterogeneous group of cancers arising from mesenchymal tissues within fat, muscle, peripheral nerves, fibrous tissue, or bone, and the wt-p53 alleles are not always retained. Even in sarcomas with wt-p53 alleles, MDM2 is not always the dominantly expressed p53 suppressor, and identification of such clinically relevant p53-inhibitors is a prime goal. Piccinin et al. (2012) identify such a dominant pro-oncogenic inhibitory protein interaction between Twist1 and the C terminus of p53. Targeting the Twist1-p53 complex not only provides a novel, clinically relevant approach for reactivating p53, but it also complements the existing potential to target synergistically other p53 inhibitory pathways. This knowledge will hopefully give momentum to strategically choose approaches to reactivate p53 in sarcomas by targeting these oncogenic protein-protein interaction networks (Figure 1).

Our limited knowledge of oncogenic protein-protein interactions driving sarcoma, such as Twist1-p53 or MDM2-p53, contrasts with our understanding using genomics that has divided this cancer into two types. Group I sarcomas have near-diploid karyotypes but harbor specific chromosomal translocations, most of which encode chimeric transcription fusion proteins. For example, the PAX3-FOXO1 chimera in alveolar rhabdomyosarcoma reveals how mesenchymal developmental pathways can be exploited by evolving cancers. There are over a dozen other chimeric transcription factors that reveal the genetic diversity of these sarcomas groups. Group II sarcomas are characterized by unbalanced karyotypes reflecting genome instability and mutations in p53 that result in genomic heterogeneity across tumor types. This heterogeneity is highlighted by recent whole-genome sequencing showing that some osteosarcomas and chordomas evolve through a mechanism called chromothripsis (Stephens et al., 2011), reflecting evolution from a single "catastrophic"

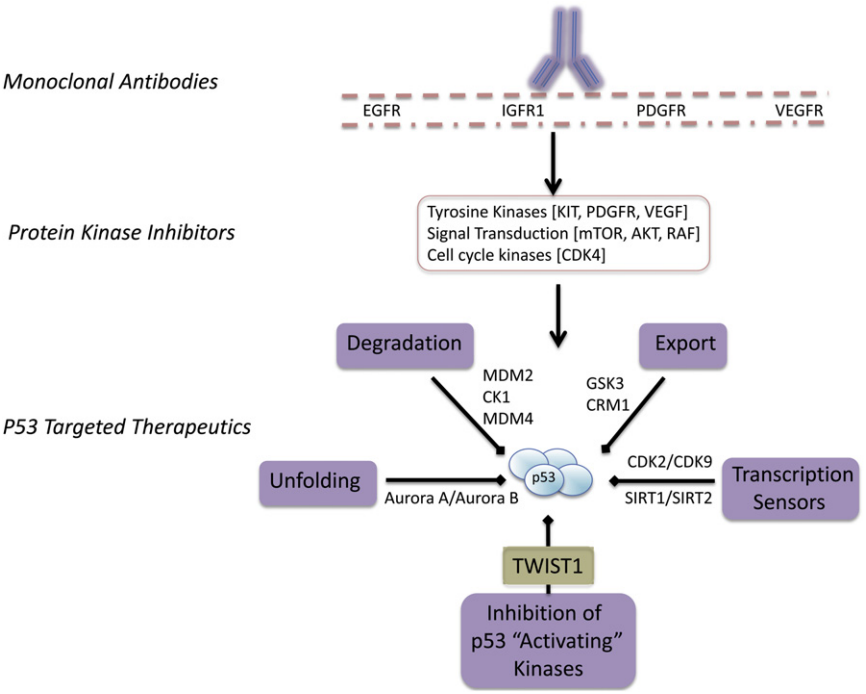

Figure 1. Therapeutic Targets in Human Sarcoma
In human sarcoma, some of the receptor-mediated regulatory pathways that have been identified as therapeutic targets include VEGFR, IGF-R1, PDGFR, and EGFR, which form the focus for monoclonal antibody-based approaches. Similarly, enzymes such as receptor tyrosine kinase growth factors or *CDK4* gene amplification highlight the potential for targeted kinase inhibitors. A subset of human sarcomas expressing wild-type p53 form clusters that might be targeted with p53-activating therapeutic molecules. The p53-inhibitory pathways whose components currently have small molecule drug leads include: (1) degradation pathways comprising MDM2, with its cofactors CK1α and MDM4; (2) unfolding and destabilization of the p53 core domain by the mitotic Aurora kinase family; (3) export pathways comprising the kinase GSK3 or the nuclear receptor CRM1; (4) transcription sensing pathways composed of kinases that regulate Pol-II transcription like CDK2/CDK9 and chromatin remodelling factors like the Sirtuins; and (5) p53 "activation" inhibitors epitomized by Twist1 that block a specific p53 activation phosphorylation. Exploiting the Twist1-p53 interface forms a novel approach for stimulating wt-p53 in certain mesenchymal cancers.

genomic instability event primarily on one chromosome.

In order to discover clinically relevant oncogenic drivers in human sarcoma, Piccinin et al. (2012) reasoned that Group I sarcomas containing the near-diploid karyotype often retain wt-p53 alleles, suggestive of oncogenic pathways that suppress p53 and bypass p53 gene mutation as a selective advantage in cancer development. In order to identify the physiological factors that might attenuate wt-p53 in sarcoma, one likely source would be developmentally programmed pathways, which are intrinsic to mesenchymal tissue, such as Twist1. The Twist1 bHLH transcription factor is involved in tissue speciation following mesoderm induction specifically during embryogenesis and plays a role in metastatic signaling through induction of EMT, and Twist1 signaling was previously implicated in silencing ARF-mediated oncogene activation of p53. The authors thus examined the mechanism whereby Twist1 might attenuate wt-p53 functions in mesenchymal-derived cancers. The authors show that Twist1 binds to the intrinsically disordered motif in the C-terminal regulatory domain of p53, a region that contains the majority of binding sites for p53-interacting proteins as well as covalent modification sites including phosphorylation, ubiquitin-like modification, and acetylation. Twist1 binding specifically attenuates an activating phosphorylation at Ser392 (CK2/FACT phosphorylation motif) implicated normally in stimulating DNA-damage activated gene expression (Bruins et al., 2008). This hypophosphorylated p53 becomes sensitized to degradation by an MDM2-dependent pathway, although the contribution of the other known p53 ubiquitin ligases, such as PirH2 or TRIM28, cannot be ruled out.

The Twist1 interaction with p53 provides another example of the now hundreds of p53 protein-protein interactions. One of the main difficulties in exploiting this vast knowledge of p53 for improving therapeutic strategies to treat cancer is that the clinical penetrance of most of these protein-protein interactions has not yet been defined. A key insight developed by Piccinin et al. (2012) at the outset was to define clinical settings where this inhibitory Twist1-p53 interaction might be clinically important to increase probability of having a future impact for patients. Over 140 human sarcomas of a large range of subtypes were screened for Twist1 expression, and over 60% exhibited strong nuclear protein expression, which in a fraction of cancers can be explained by a copy number gain. Liposarcoma and leiomyosarcoma were the types with highest percentages of Twist1 overexpression. Further, in leiomyosarcomas, there was an inverse correlation between Twist1 protein expression and p53 gene mutation. These data together suggest that there are at least two distinct pathways that drive the evolution of these sarcomas with either mutant p53 or wt-p53 and that high or low expression of Twist1 might play a role in driving these diverse evolutionary paths.

Genomics and proteomics platforms are now allowing annotation of clinically dominant pro-oncogenic driver mutations, gene expression profiling, protein-protein interactions, and potential drug targets with clinical relevance. Identifying clinical niches for such drug targets facilitates the a priori stratification of patients that might benefit from a specific therapy. However, the heterogeneity in human cancer is vast, highlighted by the diversity of sarcoma subtypes. To achieve such rational targeted therapeutics will require highly focused and integrated interdisciplinary collaborative research networks that drive patient stratification using molecular pathology, target choice, drug development, pharmaceutical engagement, and clinical trials. Some of the therapeutic possibilities in human sarcoma include using the currently available lead molecules targeting protein

kinases such as CDK4, monoclonal antibodies targeting receptors like IGF-R1 or EGFR, and peptide-mimetic MDM2 protein-interaction inhibitors that can rescue wt-p53 functions (Figure 1). We can now include the clinically relevant p53 protein interaction from Twist1 as a key target to evaluate for its therapeutic potential. There is enormous promise in drugging such protein-protein interactions, as this forms an untapped and large landscape for drug development (Crunkhorn, 2011).

REFERENCES

Barretina, J., Taylor, B.S., Banerji, S., Ramos, A.H., Lagos-Quintana, M., Decarolis, P.L., Shah, K., Socci, N.D., Weir, B.A., Ho, A., et al. (2010). Nat. Genet. *42*, 715–721.

Bruins, W., Bruning, O., Jonker, M.J., Zwart, E., van der Hoeven, T.V., Pennings, J.L., Rauwerda, H., de Vries, A., and Breit, T.M. (2008). Mol. Cell. Biol. *28*, 1974–1987.

Burington, B., Yue, P., Shi, X., Advani, R., Lau, J.T., Tan, J., Stinson, S., Stinson, J., Januario, T., de Vos, S., et al. (2011). Sci. Transl. Med. *3*, 74ra22.

Crunkhorn, S. (2011). Nat. Rev. Drug Discov. *10*, 21.

Gembarska, A., Luciani, F., Fedele, C., Russell, E.A., Dewaele, M., Villar, S., Zwolinska, A., Haupt, S., de Lange, J., Yip, D., et al. (2012). Nat. Med. Published online July 22, 2012. http://dx.doi.org/10.1038/nm.2863.

Lenos, K., Grawenda, A.M., Lodder, K., Kuijjer, M.L., Teunisse, A.F., Repapi, E., Grochola, L.F., Bartel, F., Hogendoorn, P.C., Wuerl, P., et al. (2012). Cancer Res. *72*, 4074–4084.

Piccinin, S., Tonin, E., Sessa, S., Demontis, S., Rossi, S., Pecciarini, L., Zanatta, L., Pivetta, F., Grizzo, A., Sonego, M., et al. (2012). Cancer Cell *22*, this issue, 404–415.

Stephens, P.J., Greenman, C.D., Fu, B., Yang, F., Bignell, G.R., Mudie, L.J., Pleasance, E.D., Lau, K.W., Beare, D., Stebbings, L.A., et al. (2011). Cell *144*, 27–40.

Taylor, B.S., Barretina, J., Maki, R.G., Antonescu, C.R., Singer, S., and Ladanyi, M. (2011). Nat. Rev. Cancer *11*, 541–557.

Vassilev, L.T., Vu, B.T., Graves, B., Carvajal, D., Podlaski, F., Filipovic, Z., Kong, N., Kammlott, U., Lukacs, C., Klein, C., et al. (2004). Science *303*, 844–848.

IDH1 Mutations Disrupt Blood, Brain, and Barriers

Alan H. Shih[1] and Ross L. Levine[1,*]
[1]Human Oncology and Pathogenesis Program, Leukemia Service, Department of Medicine, Memorial Sloan Kettering Cancer Center, New York, NY 10065, USA
*Correspondence: leviner@mskcc.org
http://dx.doi.org/10.1016/j.ccr.2012.08.022

The first two murine models of IDH1(R132H) mutation provide mechanistic insights into transformation. In hematopoietic cells, inhibition of TET2 and histone demethylases leads to epigenetic alterations and accumulation of hematopoietic precursors. In the central nervous system, inhibition of collagen and prolyl hydroxylases lead to altered microenvironment and defective angiogenesis.

Large-scale sequencing efforts have identified novel genes that are somatically mutated in cancer. Two of the more unexpected genes that have been implicated as recurrent mutational targets are *IDH1* and *IDH2*, which encode isocitrate dehydrogenase-1 and isocitrate dehydrogenase-2, respectively. These enzymes catalyze the conversion of isocitrate to α-ketoglutarate (αKG) in an $NADP^+$ dependent manner. Mutations in *IDH1* were first identified in colorectal cancer, and later, mutations in *IDH1*/*IDH2* were identified in brain tumors, with >70% incidence in secondary gliomas (Yan et al., 2009). Through whole-genome sequencing of a case of acute myeloid leukemia (AML), an *IDH1* mutation was identified, and *IDH1*/*IDH2* mutations were subsequently found in 12%–18% of AML cases (Mardis et al., 2009). Mutations have also been identified in thyroid cancers, chondrosarcomas, and cholangiocarcinomas.

At first it was puzzling how basic metabolic enzymes could be linked to cancer. The mutant IDH1/IDH2 enzymes have decreased enzymatic activity known at that time. However, the observations that the mutations always presented as heterozygous and at highly conserved arginine residues are more consistent with these being gain-of-function. This led to the critical finding that these mutants acquired neomorphic activity converting αKG to 2-hydroxyglutarate (2HG) (Dang et al., 2009; Ward et al., 2010). Tumor samples harboring these mutations had 2HG at levels up to ~100-fold greater than controls. Besides being an intermediate in the Krebs cycle, αKG is involved in other biochemical processes, including synthesis of glutamate, transamination of amino acids, generation of NADPH, and acting as a cofactor for dioxygenase enzymes. The structural similarity between 2HG and αKG suggested that other enzymatic processes may be competitively inhibited by elevated 2HG levels (Xu et al., 2011) (Figure 1).

Through analysis of global DNA methylation profiles in glioblastomas (GBMs), a distinct profile termed CpG island methylator phenotype with elevated genomic methylation was found to be closely associated with *IDH1* mutations (Noushmehr et al., 2010). Subsequently, it was discovered that *IDH1*/*IDH2* mutations were mutually exclusive with *TET2* mutations, a gene encoding an αKG-dependent enzyme involved in DNA demethylation, suggesting that these proteins are involved in the same pathway. Biologic significance was demonstrated through

changes in global methylation. This is reflected in the lack of changes in the differentiation pattern of CNS stem cells and failure of these mice to show evidence of glioma formation even with age.

These mouse models serve as an important step in modeling oncogenic *IDH* alleles and will undoubtedly serve as the basis for studies combining oncogenic *IDH* alleles with other mutations known to co-occur with *IDH1*/*IDH2* mutations in AML, glioma, and other malignancies. These results also raise fundamental biochemical questions as to whether specific enzymes are differentially inhibited by 2HG in a tissue-specific manner, and which of the many enzymes inhibited by 2HG are essential for transformation. In addition, further work is needed to bring greater resolution as to how epigenetic repatterning at key genes contributes to oncogenic transformation. Taken together, these studies demonstrate that *IDH1*/*IDH2* mutations will have pleiotropic effects in different contexts that contribute to transformation in different tumor types. Moreover, the development of these models provides an avenue for preclinical testing of IDH1/IDH2 inhibitors, such that we learn whether this represents a potential therapy for the subset of patients with neomorphic *IDH* disease alleles.

REFERENCES

Dang, L., White, D.W., Gross, S., Bennett, B.D., Bittinger, M.A., Driggers, E.M., Fantin, V.R., Jang, H.G., Jin, S., Keenan, M.C., et al. (2009). Nature *462*, 739–744.

Figueroa, M.E., Abdel-Wahab, O., Lu, C., Ward, P.S., Patel, J., Shih, A., Li, Y., Bhagwat, N., Vasanthakumar, A., Fernandez, H.F., et al. (2010). Cancer Cell *18*, 553–567.

Lu, C., Ward, P.S., Kapoor, G.S., Rohle, D., Turcan, S., Abdel-Wahab, O., Edwards, C.R., Khanin, R., Figueroa, M.E., Melnick, A., et al. (2012). Nature *483*, 474–478.

Mardis, E.R., Ding, L., Dooling, D.J., Larson, D.E., McLellan, M.D., Chen, K., Koboldt, D.C., Fulton, R.S., Delehaunty, K.D., McGrath, S.D., et al. (2009). N. Engl. J. Med. *361*, 1058–1066.

Noushmehr, H., Weisenberger, D.J., Diefes, K., Phillips, H.S., Pujara, K., Berman, B.P., Pan, F., Pelloski, C.E., Sulman, E.P., Bhat, K.P., et al.; Cancer Genome Atlas Research Network. (2010). Cancer Cell *17*, 510–522.

Sasaki, M., Knobbe, C.B., Itsumi, M., Elia, A.J., Harris, I.S., Chio, I.C., Cairns, R.A., McCracken, S., Wakeham, A., Haight, J., et al. (2012a). Genes Dev. Published online August 27, 2012. http://dx.doi.org/10.1101/gad.198200.112.

Sasaki, M., Knobbe, C.B., Munger, J.C., Lind, E.F., Brenner, D., Brustle, A., Harris, I.S., Holmes, R., Wakeham, A., Haight, J., et al. (2012b). Nature. Published online July 4, 2012. http://dx.doi.org/10.1038/nature11323.

Ward, P.S., Patel, J., Wise, D.R., Abdel-Wahab, O., Bennett, B.D., Coller, H.A., Cross, J.R., Fantin, V.R., Hedvat, C.V., Perl, A.E., et al. (2010). Cancer Cell *17*, 225–234.

Xu, W., Yang, H., Liu, Y., Yang, Y., Wang, P., Kim, S.H., Ito, S., Yang, C., Wang, P., Xiao, M.T., et al. (2011). Cancer Cell *19*, 17–30.

Yan, H., Parsons, D.W., Jin, G., McLendon, R., Rasheed, B.A., Yuan, W., Kos, I., Batinic-Haberle, I., Jones, S., Riggins, G.J., et al. (2009). N. Engl. J. Med. *360*, 765–773.

Tailor-Made Renal Cell Carcinoma Vaccines

Glenn Dranoff[1,2,*]
[1]Department of Medical Oncology and Cancer Vaccine Center, Dana-Farber Cancer Institute, Boston, MA 02215, USA
[2]Department of Medicine, Brigham and Women's Hospital and Harvard Medical School, Boston, MA 02215, USA
*Correspondence: glenn_dranoff@dfci.harvard.edu
http://dx.doi.org/10.1016/j.ccr.2012.08.021

Cancer vaccines are beginning to show signs of clinical activity, but major uncertainties remain regarding antigen selection, strategy for immune stimulation, patient stratification, and monitoring of elicited response. A new study of peptide vaccines in advanced renal cell carcinoma patients provides important insights into these central issues.

Recent clinical successes have validated the long-standing idea that therapeutic manipulation of endogenous immunity may achieve meaningful anti-tumor effects (Mellman et al., 2011). Perhaps the most compelling evidence marshaled to date derive from studies of blocking monoclonal antibodies against key negative immune regulatory molecules, such as cytotoxic T lymphocyte-associated antigen-4 and programmed death-1, which achieve durable tumor regressions and/or disease control in several types of malignancies. These therapeutic approaches are limited in selectivity for amplifying anti-tumor immune responses, however, and thereby sometimes provoke serious inflammatory reactions in normal tissues.

Compared to targeting immune regulatory pathways, cancer vaccines offer a stronger potential for focusing immune reactions toward tumor-specific and tumor-associated antigens, but the clinical impact of these strategies thus far has been more modest, highlighting the need for further optimization (Mellman et al., 2011). Vaccines aim to load dendritic cells (DCs), the professional antigen presenting cells of the immune system, with relevant cancer antigens and stimulate DCs to mature and migrate to regional lymph nodes, where they may efficiently prime tumor antigen-specific T and B lymphocytes. The activated T cells, particularly cytotoxic $CD8^+$ lymphocytes but also $CD4^+$ effectors, may in turn traffic systemically to metastatic deposits and thereupon effectuate tumor

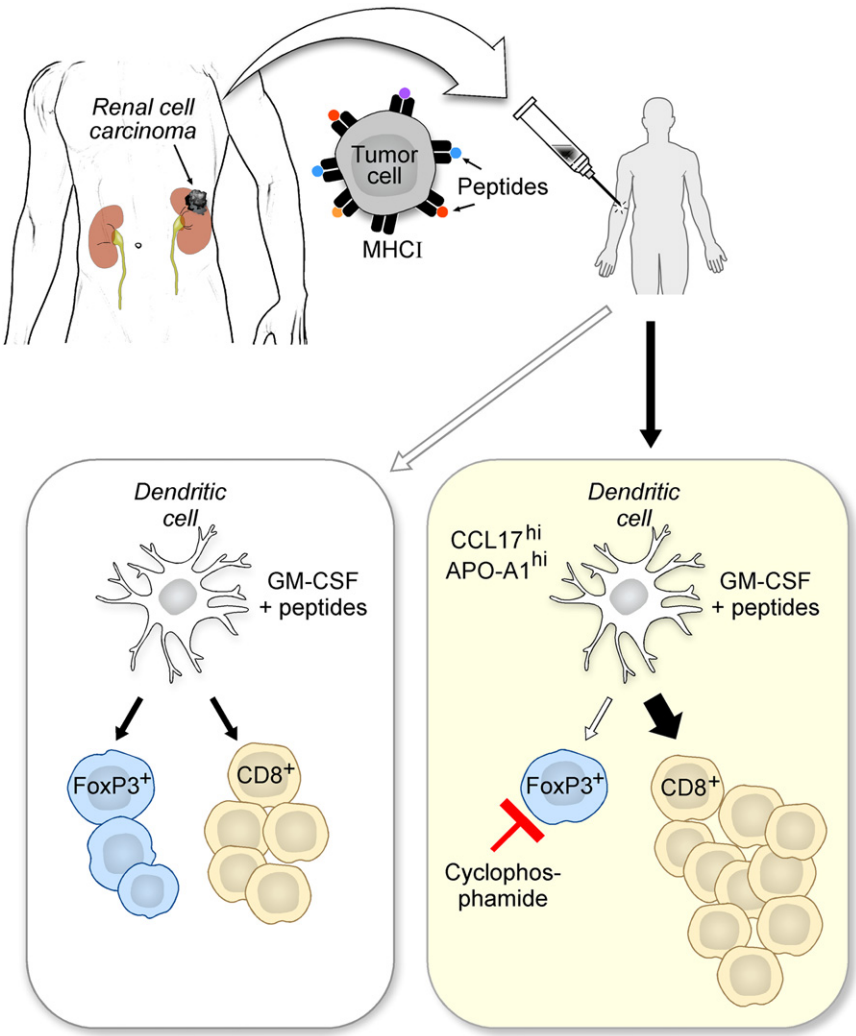

Figure 1. Schema for Developing Tailor-Made Renal Cell Carcinoma Vaccines
Naturally processed peptides derived from highly expressed oncogenic proteins are inoculated in conjunction with GM-CSF to stimulate tumor-specific $CD8^+$ cytotoxic T cells. The administration of cyclophosphamide prior to vaccination attenuates $FoxP3^+$ Tregs, resulting in more effective and durable anti-tumor immunity. High levels of apolipoprotein-A1 (APO-A1) and CCL17 are associated with superior vaccine outcome.

cell killing. Stimulated B cells may also differentiate into bone marrow-homing plasma cells that produce circulating anti-tumor antibodies.

While the general outline for a cancer vaccine may be reasonably crafted, many important details have yet to be clarified. In this context, the elegant study of renal cell carcinoma (RCC) vaccines by Walter et al. (2012) provides valuable insights into the choice of tumor antigen, method of immune priming, patient selection, and immune monitoring.

To identify relevant RCC antigens, the authors developed a multi-pronged strategy that combined biochemical, genetic, and immunologic techniques. Because the targets for $CD8^+$ cytotoxic T cells are short peptides (generated from any cellular protein) presented in the context of surface major histocompatibility complex (MHC) class I molecules, the authors purified these complexes from a large number of RCC samples and characterized the associated peptides with mass spectrometry. The expression profiles of the identified antigens were then determined, and those gene products showing the highest levels in RCC compared to normal kidney and other healthy tissues were prioritized. Lastly, the immunogenic potential of the peptides was interrogated using in vitro T cell stimulation assays with peripheral blood mononuclear cells obtained from healthy donors and RCC patients.

From this integrated analysis, the authors selected nine MHC class I peptides and one MHC class II peptide (for $CD4^+$ T cells) to serve as the antigenic components of the vaccine. The targets included sequences from the hepatocyte growth factor receptor tyrosine kinase MET, matrix metalloproteinase 7, cyclin D1, MUC-1, and two pro-angiogenic signaling molecules, all of which likely contribute to RCC progression. The choice of multiple, naturally processed peptides derived from proteins with critical oncogenic functions might reduce the emergence of antigen-loss tumor variants under immune selection.

To engender DC responses against these peptides, Walter and colleagues co-injected the cytokine granulocyte-macrophage colony stimulating factor (GM-CSF) that has been effectively employed in several earlier vaccine strategies, including Sipuleucel-T, the first FDA approved therapeutic cancer vaccine (Kantoff et al., 2010) (Figure 1). Consistent with the immunostimulatory properties of the vaccine formulation, the investigators observed that 20 of 27 evaluable patients with advanced RCC generated peptide-specific T cells in the blood that were detected with flow cytometry using MHC class I/peptide tetramers and functional assays for interferon-gamma production. Patients who mounted responses to multiple peptides showed longer survival compared to those with less intense or no responses, albeit the trial was not designed to assess clinical efficacy.

Additional immune analysis revealed that the induction of $CD8^+$ T cells to multiple peptide antigens was associated with lower numbers of FoxP3 expressing regulatory T cells (Tregs) at the time of study entry. This finding is consistent with other data indicating that Tregs negatively regulate the generation of anti-tumor cytotoxic T cells, likely reflecting their central role in maintaining immune tolerance (Josefowicz et al., 2012). Furthermore, recent work has also established the ability of GM-CSF to stimulate not only $CD8^+$ T cells, but Tregs as well, a feature that might limit vaccine potency (Jinushi et al., 2007).

Given these considerations, Walter and colleagues elected to administer a single dose of cyclophosphamide prior to the peptides/GM-CSF inoculation in an effort to attenuate Treg responses. Earlier work in murine models and small clinical trials illustrated that low doses of cyclophosphamide, which do not mediate a direct anti-tumor effect, might decrease Treg numbers (Le and Jaffee, 2012). To examine this possibility rigorously, the authors performed a Phase II trial in 68 advanced RCC patients who were randomized 1:1 to receive either the vaccine alone or a dose of cyclophosphamide prior to the first vaccine (a total of 17 vaccines were administered over several months to both groups). Indeed, cyclophosphamide reduced the numbers of circulating Tregs by approximately 20%, and this decrease was primarily in the subset of proliferating Tregs. In contrast, cyclophosphamide did not impact other lymphocyte populations analyzed, and patients who received only the vaccine did not manifest changes in Treg numbers.

Cyclophosphamide did not alter the frequency of patients who generated peptide-specific $CD8^+$ T cells, but the immune responders in this group achieved longer survival compared to immune responders who did not receive cyclophosphamide. Patients who failed to mount T cell responses displayed comparable survival regardless of cyclophosphamide treatment. Although the number of patients studied was relatively small, these results suggest that cyclophosphamide may modulate particular characteristics of vaccine responses that lead to more durable disease control. In accordance with this idea, a recent clinical trial in breast cancer that employed anti-CD25 blocking monoclonal antibodies to decrease Tregs in combination with peptide vaccines and GM-CSF similarly revealed augmented T cell responses and survival compared to earlier studies of vaccines alone (Rech et al., 2012).

To learn more about the factors that influence vaccine outcome, Walter and colleagues performed detailed immune profiling of patients prior to treatment. Among several cell types implicated in immune suppression (Gabrilovich et al., 2012), the authors found that increases in two myeloid cell populations ($CD14^+$ $HLA\text{-}DR^{-/lo}$ and $CD11b^+CD14^-CD15^+$) were associated with inferior overall survival. Moreover, among 300 soluble factors measured in the sera, high levels of apolipoprotein A1, a major constituent of high-density lipoprotein complexes, and the chemokine CCL17 were predictive for prolonged survival after vaccination. While the precise role of these proteins in immunization requires further study, one attractive possibility focuses on natural killer T (NKT) cells, a small population of lymphocytes that functions at the interface of innate and adaptive tumor immunity. NKT cells recognize lipid antigens and may activate DCs to stimulate $CD8^+$ cytotoxic T cells via a mechanism that involves CCL17 (Semmling et al., 2010).

Based on these two informative clinical trials, Walter and colleagues have launched a large Phase III trial to delineate the clinical efficacy of the peptide/GM-CSF/cyclophosphamide vaccine (IMA901) administered as a component of initial therapy for advanced RCC (http://clinicaltrials.gov number NCT01265901). Patients are randomized to sunitinib alone (the standard of care) or sunitinib plus IMA901, with overall survival as the primary endpoint. Prior work has suggested that sunitinib might be immunostimulatory, perhaps through diminishing Treg and myeloid suppressive cell numbers via inhibition of vascular endothelial growth factor receptor signaling (Gabrilovich et al., 2012). This integration of vaccines and targeted therapy represents a very promising approach to cancer treatment, and is likely to be soon followed with the addition of immunomodulatory antibodies (Vanneman and Dranoff, 2012). Overall, the careful clinical investigations of Walter and associates have helped to provide a strong framework for exploring innovative combinatorial therapies.

REFERENCES

Gabrilovich, D.I., Ostrand-Rosenberg, S., and Bronte, V. (2012). Nat. Rev. Immunol. *12*, 253–268.

Jinushi, M., Nakazaki, Y., Dougan, M., Carrasco, D.R., Mihm, M., and Dranoff, G. (2007). J. Clin. Invest. *117*, 1902–1913.

Josefowicz, S.Z., Lu, L.F., and Rudensky, A.Y. (2012). Annu. Rev. Immunol. *30*, 531–564.

Kantoff, P.W., Higano, C.S., Shore, N.D., Berger, E.R., Small, E.J., Penson, D.F., Redfern, C.H., Ferrari, A.C., Dreicer, R., Sims, R.B., et al.; IMPACT Study Investigators. (2010). N. Engl. J. Med. *363*, 411–422.

Le, D.T., and Jaffee, E.M. (2012). Cancer Res. *72*, 3439–3444.

Mellman, I., Coukos, G., and Dranoff, G. (2011). Nature *480*, 480–489.

Rech, A.J., Mick, R., Martin, S., Recio, A., Aqui, N.A., Powell, D.J., Jr., Colligon, T.A., Trosko, J.A., Leinbach, L.I., Pletcher, C.H., et al. (2012). Sci. Transl. Med. *4*, 134ra162.

Semmling, V., Lukacs-Kornek, V., Thaiss, C.A., Quast, T., Hochheiser, K., Panzer, U., Rossjohn, J., Perlmutter, P., Cao, J., Godfrey, D.I., et al. (2010). Nat. Immunol. *11*, 313–320.

Vanneman, M., and Dranoff, G. (2012). Nat. Rev. Cancer *12*, 237–251.

Walter, S., Weinschenk, T., Stenzl, A., Zdrojowy, R., Pluzanska, A., Szczylik, C., Staehler, M., Brugger, W., Dietrich, P.Y., Mendrzyk, R., et al. (2012). Nat. Med. Published online July 29, 2012. http://dx.doi.org/10.1038/nm.2883.

kinases such as CDK4, monoclonal antibodies targeting receptors like IGF-R1 or EGFR, and peptide-mimetic MDM2 protein-interaction inhibitors that can rescue wt-p53 functions (Figure 1). We can now include the clinically relevant p53 protein interaction from Twist1 as a key target to evaluate for its therapeutic potential. There is enormous promise in drugging such protein-protein interactions, as this forms an untapped and large landscape for drug development (Crunkhorn, 2011).

REFERENCES

Barretina, J., Taylor, B.S., Banerji, S., Ramos, A.H., Lagos-Quintana, M., Decarolis, P.L., Shah, K., Socci, N.D., Weir, B.A., Ho, A., et al. (2010). Nat. Genet. *42*, 715–721.

Bruins, W., Bruning, O., Jonker, M.J., Zwart, E., van der Hoeven, T.V., Pennings, J.L., Rauwerda, H., de Vries, A., and Breit, T.M. (2008). Mol. Cell. Biol. *28*, 1974–1987.

Burington, B., Yue, P., Shi, X., Advani, R., Lau, J.T., Tan, J., Stinson, S., Stinson, J., Januario, T., de Vos, S., et al. (2011). Sci. Transl. Med. *3*, 74ra22.

Crunkhorn, S. (2011). Nat. Rev. Drug Discov. *10*, 21.

Gembarska, A., Luciani, F., Fedele, C., Russell, E.A., Dewaele, M., Villar, S., Zwolinska, A., Haupt, S., de Lange, J., Yip, D., et al. (2012). Nat. Med. Published online July 22, 2012. http://dx.doi.org/10.1038/nm.2863.

Lenos, K., Grawenda, A.M., Lodder, K., Kuijjer, M.L., Teunisse, A.F., Repapi, E., Grochola, L.F., Bartel, F., Hogendoorn, P.C., Wuerl, P., et al. (2012). Cancer Res. *72*, 4074–4084.

Piccinin, S., Tonin, E., Sessa, S., Demontis, S., Rossi, S., Pecciarini, L., Zanatta, L., Pivetta, F., Grizzo, A., Sonego, M., et al. (2012). Cancer Cell *22*, this issue, 404–415.

Stephens, P.J., Greenman, C.D., Fu, B., Yang, F., Bignell, G.R., Mudie, L.J., Pleasance, E.D., Lau, K.W., Beare, D., Stebbings, L.A., et al. (2011). Cell *144*, 27–40.

Taylor, B.S., Barretina, J., Maki, R.G., Antonescu, C.R., Singer, S., and Ladanyi, M. (2011). Nat. Rev. Cancer *11*, 541–557.

Vassilev, L.T., Vu, B.T., Graves, B., Carvajal, D., Podlaski, F., Filipovic, Z., Kong, N., Kammlott, U., Lukacs, C., Klein, C., et al. (2004). Science *303*, 844–848.

IDH1 Mutations Disrupt Blood, Brain, and Barriers

Alan H. Shih[1] and Ross L. Levine[1,*]
[1]Human Oncology and Pathogenesis Program, Leukemia Service, Department of Medicine, Memorial Sloan Kettering Cancer Center, New York, NY 10065, USA
*Correspondence: leviner@mskcc.org
http://dx.doi.org/10.1016/j.ccr.2012.08.022

The first two murine models of IDH1(R132H) mutation provide mechanistic insights into transformation. In hematopoietic cells, inhibition of TET2 and histone demethylases leads to epigenetic alterations and accumulation of hematopoietic precursors. In the central nervous system, inhibition of collagen and prolyl hydroxylases lead to altered microenvironment and defective angiogenesis.

Large-scale sequencing efforts have identified novel genes that are somatically mutated in cancer. Two of the more unexpected genes that have been implicated as recurrent mutational targets are *IDH1* and *IDH2*, which encode isocitrate dehydrogenase-1 and isocitrate dehydrogenase-2, respectively. These enzymes catalyze the conversion of isocitrate to α-ketoglutarate (αKG) in an $NADP^+$ dependent manner. Mutations in *IDH1* were first identified in colorectal cancer, and later, mutations in *IDH1*/*IDH2* were identified in brain tumors, with >70% incidence in secondary gliomas (Yan et al., 2009). Through whole-genome sequencing of a case of acute myeloid leukemia (AML), an *IDH1* mutation was identified, and *IDH1*/*IDH2* mutations were subsequently found in 12%–18% of AML cases (Mardis et al., 2009). Mutations have also been identified in thyroid cancers, chondrosarcomas, and cholangiocarcinomas.

At first it was puzzling how basic metabolic enzymes could be linked to cancer. The mutant IDH1/IDH2 enzymes have decreased enzymatic activity known at that time. However, the observations that the mutations always presented as heterozygous and at highly conserved arginine residues are more consistent with these being gain-of-function. This led to the critical finding that these mutants acquired neomorphic activity converting αKG to 2-hydroxyglutarate (2HG) (Dang et al., 2009; Ward et al., 2010). Tumor samples harboring these mutations had 2HG at levels up to ~100-fold greater than controls. Besides being an intermediate in the Krebs cycle, αKG is involved in other biochemical processes, including synthesis of glutamate, transamination of amino acids, generation of NADPH, and acting as a cofactor for dioxygenase enzymes. The structural similarity between 2HG and αKG suggested that other enzymatic processes may be competitively inhibited by elevated 2HG levels (Xu et al., 2011) (Figure 1).

Through analysis of global DNA methylation profiles in glioblastomas (GBMs), a distinct profile termed CpG island methylator phenotype with elevated genomic methylation was found to be closely associated with *IDH1* mutations (Noushmehr et al., 2010). Subsequently, it was discovered that *IDH1*/*IDH2* mutations were mutually exclusive with *TET2* mutations, a gene encoding an αKG-dependent enzyme involved in DNA demethylation, suggesting that these proteins are involved in the same pathway. Biologic significance was demonstrated through

bone marrow transplant assays in which expression of IDH1/IDH2 mutant proteins or functional loss of TET2 resulted in similar changes that promote leukemogenesis (Figueroa et al., 2010). More recent work has also identified histone demethylases as potential αKG-dependent targets (Lu et al., 2012).

Two recent papers published by Sasaki et al. report the phenotype of mice expressing the IDH1(R132H) mutant from the endogenous *Idh1* locus. The first paper reports the phenotype of mice expressing IDH1(R132H) targeted to the hematopoietic system (Sasaki et al., 2012a). These mice develop hematologic abnormalities, including anemia, splenomegaly, and extramedullary hematopoiesis. These mice are characterized by hematopoietic stem/progenitor expansion, including increased numbers of LSK ($Lin^{-}Sca1^{+}cKit^{+}$) cells and lineage restricted progenitors ($CD150^{-}CD48^{+}$). Using enhanced representation bisulfite sequencing, the authors found that LSK cells from these mutant mice had significantly more methylated CpG sites compared to control LSK cells, most notably at promoter and intragenic regions. This increased global methylation is hypothesized to be secondary to inhibition of TET2. Likewise, they find increased histone methylation, particularly for H3K4me3 and H3K79me2, chromatin marks that are associated with active or poised transcription. Inhibition of Jumonji-C domain-containing histone demethylases by 2HG likely underlies this observation. These findings agree with results in *IDH1*/*IDH2* mutant AMLs that have a hypermethylation profile with a significant overlap in commonly hypermethylated genes. They also extend our mechanistic understanding of leukemogeneisis. In the subset of AMLs caused by translocations of the mixed lineage leukemia (*MLL*) gene, it is believed increased H3K79me2 activity through recruitment of DOT1L contributes to dysregulated gene expression, and it is possible that inhibition of DOT1L might reverse the phenotypic effects of mutant *IDH* alleles on hematopoietic function.

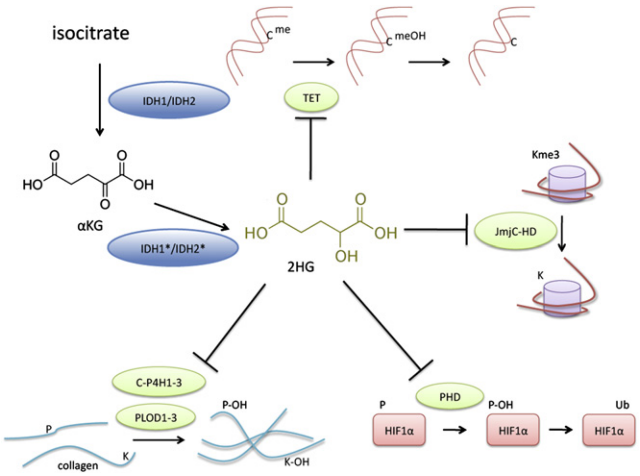

Figure 1. IDH1 Mutant Disrupts Multiple Cellular Processes
IDH1(R132H) produces 2HG, which inhibits αKG dependent dioxygenases. Inhibition of TET enzymes blocks 5-hydroxy methylcytosine modification, which leads to cytosine demethylation. Inhibition of JmjC-HDs leads to altered histone methylation on multiple histone H3 lysine residues. Inhibition of C-P4H1-3 and PLOD1-3 prevents proper prolyl and lysyl hydroxylation of collagen, which are required for their proper maturation. Inhibition of PHDs prevents HIF1α prolyl hydroxylation and subsequent ubiquitination by the von Hippel Lindau protein and degradation by the proteasome. A combination of these effects leads to epigenetic changes in the bone marrow, resulting in altered differentiation of hematopoietic progenitors and dysfunctional angiogensis in the brain, resulting in CNS hemorrhage. IDH1/IDH2 isocitrate dehydrogenase-1 and isocitrate dehydrogenase-2, IDH1*/IDH2* mutant IDH1 or IDH2; αKG, α-ketoglutarate; 2HG, 2-hydroxygluatare; TET, Tet methylcytosine dioxygenase; JmjC-HD, Jumonji-C domain-containing histone demethylases; C-P4H1-3, collagen prolyl 4-hydroxylase 1-3; PLOD1-3, procollagen-lysine, 2-oxoglutarate 5-dioxygenases 1-3; PHD, prolyl hydroxylase domain-containing proteins; HIF1α, hypoxia-inducible factor 1α; C, cytosine; P, proline; K, lysine; Ub, ubiquitin; me, methyl; OH, hydroxy.

In the second paper, Sasaki et al. (2012b) describe the phenotype of mice expressing IDH1(R132H) in the CNS using two cre strains (*Nestin* and *GFAP*). These mice develop perinatal lethality due to intracerebral hemorrhage. They noted variable penetrance in the *GFAP-cre* line; phenotypic severity correlated with levels of 2HG expression. This abnormal vascular development appears to be a consequence of 2HG-mediated inhibition of the dioxygenases that regulate collagen maturation and hypoxia-inducible transcription factors (HIF)1α and HIF2α degradation. Type IV collagen is a component of the basement membrane between astrocytes and endothelial cells. Its maturation depends on hydroxylation by procollagen-lysine, 2-oxoglutarate 5-dioxgenases 1-3 (PLOD1-3) and collagen prolyl-4-hydroxylases 1-3 (C-P4H1-3). In *Idh1* mutant mice, immature forms of collagen accumulate, and collagen fails to properly deposit along blood vessels. Accumulation of immature collagen also leads to a secondary endoplasmic reticulum (ER) stress response, which may be responsible for the increased apoptosis seen in the brain of mice expressing mutant *Idh1*. In addition, HIF1α/HIF2α are regulated by prolyl-hydroxylation, which leads to degradation by the ubiquitin-proteasome pathway through von Hippel Lindau (VHL) protein-mediated E3 ligase activity. The prolyl hydroxylase domain-containing proteins (PHDs) that regulate HIF1α/HIF2α stability belong to the dioxygenase family and are likewise another potential target of 2HG inhibition. In mutant mice, HIF1α accumulates, and the expression of HIF1α target genes, including *Vegf*, concomitantly increases. The combination of defective vessel integrity, increased ER stress, and elevated angiogenic signaling, likely leads to the intracerebral hemorrhage seen with brain-specific expression of IDH1(R132H).

Unlike the hematopoietic model, the CNS model of IDH1(R132H) expression does not suggest a putative mechanism for how glial cells expressing mutant IDH are transformed. Although abnormal angiogensis is a hallmark of GBM and brain tumor progression, *IDH1* mutations are an early event, with mutations detected more frequently in low-grade gliomas and secondary GBMs than in primary GBMs (Yan et al., 2009). Contrary to their expectation, the authors noted lower levels reactive oxygen species in mutant brain cells compared to controls. In contrast to the hematopoietic model, the authors did not note significant changes in histone methylation in the brain. Furthermore, although there was a decrease in 5-hydroxymethylcytosine (the product of TET2 enzymatic activity), the authors did not provide evidence of

changes in global methylation. This is reflected in the lack of changes in the differentiation pattern of CNS stem cells and failure of these mice to show evidence of glioma formation even with age.

These mouse models serve as an important step in modeling oncogenic *IDH* alleles and will undoubtedly serve as the basis for studies combining oncogenic *IDH* alleles with other mutations known to co-occur with *IDH1*/*IDH2* mutations in AML, glioma, and other malignancies. These results also raise fundamental biochemical questions as to whether specific enzymes are differentially inhibited by 2HG in a tissue-specific manner, and which of the many enzymes inhibited by 2HG are essential for transformation. In addition, further work is needed to bring greater resolution as to how epigenetic repatterning at key genes contributes to oncogenic transformation. Taken together, these studies demonstrate that *IDH1*/*IDH2* mutations will have pleiotropic effects in different contexts that contribute to transformation in different tumor types. Moreover, the development of these models provides an avenue for preclinical testing of IDH1/IDH2 inhibitors, such that we learn whether this represents a potential therapy for the subset of patients with neomorphic *IDH* disease alleles.

REFERENCES

Dang, L., White, D.W., Gross, S., Bennett, B.D., Bittinger, M.A., Driggers, E.M., Fantin, V.R., Jang, H.G., Jin, S., Keenan, M.C., et al. (2009). Nature *462*, 739–744.

Figueroa, M.E., Abdel-Wahab, O., Lu, C., Ward, P.S., Patel, J., Shih, A., Li, Y., Bhagwat, N., Vasanthakumar, A., Fernandez, H.F., et al. (2010). Cancer Cell *18*, 553–567.

Lu, C., Ward, P.S., Kapoor, G.S., Rohle, D., Turcan, S., Abdel-Wahab, O., Edwards, C.R., Khanin, R., Figueroa, M.E., Melnick, A., et al. (2012). Nature *483*, 474–478.

Mardis, E.R., Ding, L., Dooling, D.J., Larson, D.E., McLellan, M.D., Chen, K., Koboldt, D.C., Fulton, R.S., Delehaunty, K.D., McGrath, S.D., et al. (2009). N. Engl. J. Med. *361*, 1058–1066.

Noushmehr, H., Weisenberger, D.J., Diefes, K., Phillips, H.S., Pujara, K., Berman, B.P., Pan, F., Pelloski, C.E., Sulman, E.P., Bhat, K.P., et al.; Cancer Genome Atlas Research Network. (2010). Cancer Cell *17*, 510–522.

Sasaki, M., Knobbe, C.B., Itsumi, M., Elia, A.J., Harris, I.S., Chio, I.C., Cairns, R.A., McCracken, S., Wakeham, A., Haight, J., et al. (2012a). Genes Dev. Published online August 27, 2012. http://dx.doi.org/10.1101/gad.198200.112.

Sasaki, M., Knobbe, C.B., Munger, J.C., Lind, E.F., Brenner, D., Brustle, A., Harris, I.S., Holmes, R., Wakeham, A., Haight, J., et al. (2012b). Nature. Published online July 4, 2012. http://dx.doi.org/10.1038/nature11323.

Ward, P.S., Patel, J., Wise, D.R., Abdel-Wahab, O., Bennett, B.D., Coller, H.A., Cross, J.R., Fantin, V.R., Hedvat, C.V., Perl, A.E., et al. (2010). Cancer Cell *17*, 225–234.

Xu, W., Yang, H., Liu, Y., Yang, Y., Wang, P., Kim, S.H., Ito, S., Yang, C., Wang, P., Xiao, M.T., et al. (2011). Cancer Cell *19*, 17–30.

Yan, H., Parsons, D.W., Jin, G., McLendon, R., Rasheed, B.A., Yuan, W., Kos, I., Batinic-Haberle, I., Jones, S., Riggins, G.J., et al. (2009). N. Engl. J. Med. *360*, 765–773.

Tailor-Made Renal Cell Carcinoma Vaccines

Glenn Dranoff[1,2,*]
[1]Department of Medical Oncology and Cancer Vaccine Center, Dana-Farber Cancer Institute, Boston, MA 02215, USA
[2]Department of Medicine, Brigham and Women's Hospital and Harvard Medical School, Boston, MA 02215, USA
*Correspondence: glenn_dranoff@dfci.harvard.edu
http://dx.doi.org/10.1016/j.ccr.2012.08.021

Cancer vaccines are beginning to show signs of clinical activity, but major uncertainties remain regarding antigen selection, strategy for immune stimulation, patient stratification, and monitoring of elicited response. A new study of peptide vaccines in advanced renal cell carcinoma patients provides important insights into these central issues.

Recent clinical successes have validated the long-standing idea that therapeutic manipulation of endogenous immunity may achieve meaningful anti-tumor effects (Mellman et al., 2011). Perhaps the most compelling evidence marshaled to date derive from studies of blocking monoclonal antibodies against key negative immune regulatory molecules, such as cytotoxic T lymphocyte-associated antigen-4 and programmed death-1, which achieve durable tumor regressions and/or disease control in several types of malignancies. These therapeutic approaches are limited in selectivity for amplifying anti-tumor immune responses, however, and thereby sometimes provoke serious inflammatory reactions in normal tissues.

Compared to targeting immune regulatory pathways, cancer vaccines offer a stronger potential for focusing immune reactions toward tumor-specific and tumor-associated antigens, but the clinical impact of these strategies thus far has been more modest, highlighting the need for further optimization (Mellman et al., 2011). Vaccines aim to load dendritic cells (DCs), the professional antigen presenting cells of the immune system, with relevant cancer antigens and stimulate DCs to mature and migrate to regional lymph nodes, where they may efficiently prime tumor antigen-specific T and B lymphocytes. The activated T cells, particularly cytotoxic $CD8^+$ lymphocytes but also $CD4^+$ effectors, may in turn traffic systemically to metastatic deposits and thereupon effectuate tumor